รายงานวิจัยฉบับสมบูรณ์

(เล่มที่ 1 ของจำนวน 3 เล่ม)

โครงการ
งานวิจัยขั้นสูงทางการไหลสองสถานะและการเพิ่มความสามารถในการถ่ายเทความร้อน

โดย

ศ. ดร. สมชาย วงศ์วิเศษ

ภาควิชาวิศวกรรมเครื่องกล คณะวิศวกรรมศาสตร์

มหาวิทยาลัยเทคโนโลยีพระจอมเกล้าธนบุรี

วันที่ 31 มีนาคม 2557

สัญญาเลขที่ DPG5380003
รายงานวิจัยฉบับสมบูรณ์

โครงการ
งานวิจัยขั้นสูงทางการไหลสองสถานะและการเพิ่มความสามารถในการถ่ายเทความร้อน

โดย

ศ. ดร. สมชาย วงศ์วิเศษ
ภาควิชาวิศวกรรมเครื่องกล คณะวิศวกรรมศาสตร์
มหาวิทยาลัยเทคโนโลยีพระจอมเกล้าธนบุรี

สนับสนุนโดย

สำนักงานกองทุนสนับสนุนการวิจัย (สกว.)
สำนักงานคณะกรรมการการอุดมศึกษา (สกอ.)
มหาวิทยาลัยเทคโนโลยีพระจอมเกล้าธนบุรี

กิตติกรรมประกาศ

โครงการ “งานวิจัยขั้นสูงทางการไหลสองสถานะและการเพิ่มความสามารถในการถ่ายเทความร้อน” นี้ได้รับการสนับสนุนด้านเงินทุน จาก 3 สถาบัน ได้แก่ สำนักงานคณะกรรมการการอุดมศึกษา (สกอ.) สำนักงานกองทุนสนับสนุนการวิจัย (สกว.) และ มหาวิทยาลัยเทคโนโลยีพระจอมเกล้าธนบุรี ภายใต้ชื่อ “ทุนศาสตราจารย์วิจัยดีเด่น”

จากการได้รับทุนสนับสนุนดังกล่าวทำให้ผู้วิจัยสามารถทำงานวิจัยได้อย่างต่อเนื่องเป็นเวลา 4 ปี ผู้วิจัยพึงพอใจกับผลงานที่ได้มาเป็นอย่างมาก โดยสามารถแบ่งผลงานได้เป็น 5 ประเด็น ได้แก่

1. การสร้างองค์ความรู้ใหม่ในเรื่องของการเพิ่มประสิทธิภาพของอุปกรณ์แลกเปลี่ยนความร้อน: งานวิจัยนี้ทำให้ผู้วิจัยมีความรู้ที่ละเอียดลึกซึ้ง และสามารถมองโจทย์ที่ประชาคมวิจัยหรืออุตสาหกรรมต้องการคำตอบ ทำให้รู้ State of the art ของ งานวิจัยในสาขานี้

2. การตีพิมพ์ผลงานการค้นคิดใหม่: สามารถตีพิมพ์ ในวารสารระดับนานาชาติที่มีคุณภาพ (126 บทความ) ยื่นจด สิทธิบัตร (7 ผลงาน) และลิขสิทธิ์ (3 ผลงาน) Book chapter (3 chapters) นอกจากนั้น ผู้ทำวิจัยยังได้เขียนหนังสือ “กลศาสตร์ของไหล” หนังสือเล่มนี้สามารถใช้ประกอบการเรียนการสอนในวิชากลศาสตร์ของไหลสำหรับนิสิต นักศึกษาวิศวกรรมศาสตร์ หรือผู้ที่สนใจทั่วไป หนังสือประกอบด้วย 14 บท ผู้เขียนได้รวมผลงานที่ได้ จากงานวิจัยของตัวเองใส่เข้าไว้ในหนังสือ ซึ่งจะทำให้นักศึกษาหรือผู้อ่านได้เข้าใจเนื้อหาอย่างถ่องแท้ มีพื้นฐานที่ดีสามารถนำไปประยุกต์ใช้หรือนำความรู้ไปต่อยอดในงานวิจัยต่อไป

3. การสร้างคนที่มีความรู้ความสามารถ: จากโครงการนี้ ผู้วิจัยสามารถผลิตดุษฎีบัณฑิต ได้ 5 คน มหาบัณฑิต 9 คน และเป็นพี่เลี้ยงให้อาจารย์ทั้งในมหาวิทยาลัยของตัวเอง และมหาวิทยาลัยอื่นๆทั้งในประเทศและต่างประเทศ

4. การช่วยเหลือเชิงสาธารณะ: จากผลงานวิจัยที่ปรากฏต่อสาธารณะทำให้ผู้วิจัยได้เข้าไปมีส่วนช่วยเหลือประชาคมวิจัยต่างๆเช่นได้รับการแต่งตั้งเป็น Editor ของวารสาร Experimental Thermal and Fluid Science (Elsevier) ซึ่งเป็นวารสารระดับนานาชาติที่มีชื่อเสียง เป็นการทำชื่อเสียงให้กับประเทศชาติในอีกมิติหนึ่ง นอกจากนั้นผลงานตีพิมพ์หลายชิ้นยังได้รับการอ้างอิงจำนวนมาก (The most cited papers) จนได้รับจดหมายแสดงการให้กำลังใจจาก Thomson Reuters

5. การช่วยเหลือภาคอุตสาหกรรม: ผู้วิจัยได้ช่วยเหลือให้คำแนะนำ เพื่อเพิ่มคุณภาพของผลิตภัณฑ์ให้กับภาคอุตสาหกรรม หลายแห่ง ตัวอย่างหนึ่งได้แก่การ ช่วยเหลือบริษัท ไทย-เยอรมัน โปรดักส์ จำกัด (มหาชน) จนผลงานวิจัยมีส่วนช่วยให้ บริษัทฯ ได้รับรางวัลเกียรติยศจากรัฐสภา เมื่อวันที่ 2 ก.ย. 2556

ท้ายที่สุด ผู้เขียนขอขอบคุณ สำนักงานคณะกรรมการการอุดมศึกษา (สกอ.) สำนักงานกองทุนสนับสนุนการวิจัย (สกว.) และ มหาวิทยาลัยเทคโนโลยีพระจอมเกล้าธนบุรี ที่ให้ความช่วยเหลือเรื่องเงินทุน อธิการบดี และผู้บริหารของมหาวิทยาลัยเทคโนโลยีพระจอมเกล้าธนบุรี สมาชิกทุกคนใน FUTURE Lab เพื่อนอาจารย์ ในภาควิชาวิศวกรรมเครื่องกล คณะวิศวกรรมศาสตร์ ที่ให้ความช่วยเหลือด้วยดีอย่างไม่มีที่ติ

สมชาย วงศ์วิเศษ
ภาควิชา วิศวกรรมเครื่องกล คณะวิศวกรรมศาสตร์
มหาวิทยาลัยเทคโนโลยีพระจอมเกล้าธนบุรี

รหัสโครงการ: DPG5380003

ชื่อโครงการ: งานวิจัยขั้นสูงทางการไหลสองสถานะและการเพิ่มความสามารถในการถ่ายเทความร้อน

หัวหน้าโครงการ: ศาสตราจารย์ ดร. สมชาย วงศ์วิเศษ
ภาควิชาวิศวกรรมเครื่องกล คณะวิศวกรรมศาสตร์
มหาวิทยาลัยเทคโนโลยีพระจอมเกล้าธนบุรี

E-mail Address: somchai.won@kmutt.ac.th

ระยะเวลาโครงการ: 1 เม.ย. 2553 ถึง 31 มี.ค. 2557

1. บทคัดย่อ

กลุ่มวิจัยได้นำศาสตร์ของ การถ่ายเทความร้อนและมวล กลศาสตร์ของไหล การไหลสองเฟส และเธอร์โมไดนามิกส์ มาประยุกต์ เพื่อพัฒนาอุปกรณ์แลกเปลี่ยนความร้อนให้มีสมรรถนะสูงขึ้น ทำให้ได้ผลิตภัณฑ์ที่ประหยัดพลังงานและรักษาสิ่งแวดล้อม ความรู้ใหม่ต่างๆที่ได้จากงานวิจัยพื้นฐานเหล่านี้สามารถนำไปประยุกต์ใช้ในการออกแบบอุปกรณ์แลกเปลี่ยนความร้อนให้มีสมรรถนะสูงขึ้นได้ ซึ่งเป็นประโยชน์ต่ออุตสาหกรรมโดยตรง

โดยปกติกระบวนการแลกเปลี่ยนความร้อนระหว่างของไหลสองชนิดที่มีอุณหภูมิแตกต่างกันสามารถทำได้โดยใช้อุปกรณ์ที่เรียกว่า อุปกรณ์แลกเปลี่ยนความร้อน ถ้าอุปกรณ์แลกเปลี่ยนความร้อนถูกออกแบบมาอย่างเหมาะสม การถ่ายเทความร้อนก็จะเป็นไปอย่างมีประสิทธิภาพ การเพิ่มการถ่ายเทความร้อน ถือเป็นสิ่งหนึ่งที่จะช่วยเพิ่มสมรรถนะของอุปกรณ์แลกเปลี่ยนความร้อน ซึ่งก็เท่ากับเป็นการประหยัดพลังงานหรือเป็นการใช้พลังงานอย่างคุ้มค่า

ตัวอย่างหนึ่งของงานวิจัยคือ การเพิ่มประสิทธิภาพและลดการใช้พลังงานในระบบการทำความเย็นและการปรับอากาศ โดยทำงานวิจัยลงลึกตั้งแต่งานวิจัยพื้นฐาน เข้าสู่งานวิจัยประยุกต์ จนถึงการจดสิทธิบัตร ผลลัพธ์จากงานวิจัย อยู่ในรูปของการตีพิมพ์เผยแพร่ต่อสาธารณชนทั้งระดับชาติและระดับนานาชาติ โดยผลงานวิจัยได้ถูกนำไปอ้างอิงจำนวนมากเพื่อต่อยอดงานวิจัยหรือถูกนำไปใช้งาน ซึ่งหมายถึงเป็นการทำประโยชน์ให้สังคมโดยส่วนรวม และสร้างชื่อเสียงให้กับประเทศชาติ และเนื่องจากประเทศไทยอยู่ในเขตร้อนชื้น การทำความเย็นและการปรับอากาศถือเป็นสิ่งจำเป็นในชีวิตประจำวัน ประกอบกับประเทศไทยเป็นฐานการผลิตเครื่องปรับอากาศเพื่อการส่งออกระดับต้นๆของโลก ดังนั้นงานวิจัยและพัฒนาในเรื่องเหล่านี้จึงมีประโยชน์อย่างยิ่งต่อประเทศชาติ

2. Abstract

The research interests include two-phase flow, heat transfer enhancement and thermal system design. Generally, the process of heat exchange between two kinds of fluids of different temperatures can be accomplished with equipment called a heat exchanger. A well-designed heat

exchanger can transfer heat effectively. Heat transfer enhancement can increase the performance of a heat exchanger through the saving or cost-effective use of energy.

Since Thailand is situated in a tropical zone, air conditioners and refrigerators are considered necessary appliances in Thai daily life. Additionally, Thailand has become an important production base for air conditioner and refrigerator manufactoring, as well as a top exporter of these products to the world market. Therefore, research and development, as well as the preparation of specialists in this field is necessary.

The research team have applied the sciences of heat and mass transfer, fluid mechanics, and thermodynamics in developing higher-performance heat exchangers, the main focus being on increasing the efficiency and reducing the power consumption of air conditioners and refrigerators. The new body of knowledge gained from this basic research can be applied in designing high-performance equipment that is directly useful in the industry.

3. Executive Summary

Gas-liquid two-phase flow is one of four types of two-phase flows. It occurs commonly in both the power and the process industries and in ordinary life. Gas-liquid flows are the most complex. They combine the characteristics of the compressibility of gas and a deformable interface. Gas-liquid flow occurs in a wide variety of equipment, for example, in all condenser and evaporator of refrigeration and air conditioning system and in petroleum pipelines which carry a mixture of gas and oil. In fact, the majority of the real heat-mass transfer problems in the industries is related with changes of phase during boiling and condensation.

Boiling and condensation under the conditions of free or forced convection is an extreamly important subject that confronts engineers in the process industries. The design and analysis of refrigeration and air conditioning system, distillators, water-tube and fire-tube boiliers, process industry reboilers and condensers, surface condensers, automotive industries, pressurized water reactors in nuclear power plants, heat pumps and various kinds of heat exchanger and many other equipment in chemical and power plant are examples which are based on the knowledge of the two-phase flow and heat-mass transfer characteristics occurring during the changes of phase.

In general, the heat and mass transfer rate and the pressure drop in a considered system are the usual design parameters of interest. It is very meaningful to know the phenomena which occurs. This is because it may impose some limitation in the performance of the system, for example, a change in hydrodynamic or heat transfer characteristics. In boiling and condensation, the flow and heat transfer characteristics are very closely related and the coupling is much closer than in single-phase flows.

The exchange rates of heat, mass and momentum, pressure drop, holdup and system stability causes variations in the amount and distribution of each phase and topology of the flow. The subject of the heat transfer enhancement has been developed generally for the purpose of heat exchange applications. It is also not possible to understand the two-phase flow phenomena without a clear understanding of the flow patterns encountered.

The ability to predict the type of flow accurately is necessary before the relevant calculation techniques will be developed. The external and internal extended surfaces in forms of, for example, longitudinal or radial fins are also alternative ways to enhance the heat transfer rate between the surface and the adjacent fluid. However, while the heat transfer rate is augmented, the flow characteristic is changed and the resistance resulted from extended surface becomes higher. This is still big room to discuss and go further into detail.

The main objective of this project is to study experimentally and theoretically the two-phase gas-liquid flow characteristics and its relations with the heat-mass transfer mechanism and to enhance the heat transfer rate by considering in the view of the fluids and equipment. All these fundamental works will be concentrated on the improvement of the performance of the refrigeration and air-conditioning system.

The project is divided into various relevant related sub-projects as follows;

-Micro-Channel Heat Exchanger used for Refrigeration and Air Conditioning

-Heat and Mass Transfer Characteristics of Fin-and-Tube Evaporators used in Air conditioning system

-Saturated Pool Boiling Characteristics of New Alternative Fluorine-Based Refrigerants

-Pool Boiling Characteristics of New Alternative Refrigerants “Nano-Fluids”

-Hydrocarbon Mixtures to Replace Refrigerants used in an Automotive Air Conditioning System

-Heat Transfer, Pressure Drop and Effect of Flow Direction of Working Fluids Flowing Through a Plate Heat Exchanger Simulated as Evaporator and Condenser

-Characteristics of Refrigerant HFC-134a Flowing Through Micro-Scale Short Tube Orifices

-Vertical Upward Gas-Liquid Flow in Sinusoidal Wavy Channels

-Heat Transfer and Pressure Drop Characteristics of Refrigerant HFC-134a During Evaporation and Condensation in Annulus Coil Evaporator and Condenser

-Two-Phase Flow Patterns, Void Fraction and Pressure Drop in a Narrow Concentric Annuli

-Performance of a Vapor Compression Refrigeration Cycle Using a Two-Phase Ejector as an Expansion Device

-Experimental and Theoretical Investigations of Two-Phase Flow in Micro-Channels

-Effects of Electrohydrodynamics on the In-Tube Condensation and Boiling Heat Transfer – Enhancement of a New Alternative Refrigerant in Smooth and Micro-Fin Tubes

-Two-Phase Flow Patterns and Pressure Drop in a Small Circular Tube Vertical Bend used in Refrigeration and Air conditioning

-Forced Convective Heat Transfer Characteristic of New Alternative Refrigerants “Nano-fluid”

-Selection Charts for Fluorine-Based Capillary Tubes Used in Refrigerator and Air-Conditioner

-Effect of Geometric Parameters on the Air-Side Performance of Crimped Finned Tube Condenser used in the Air-Conditioning System

-Heat Transfer Performance of a Helically Coiled Heat Exchanger

-Performance of New Alternative Refrigerants Flowing Through Non-Adiabatic Capillary Tubes Used as An Expansion Device in Refrigeration and Air Conditioning System

-Combined Refrigeration and Solar Energy Systems

4. เนื้อหางานวิจัย

การมุ่งสู่การพัฒนาเครื่องปรับอากาศและอุปกรณ์ทำความเย็นให้มีสมรรถนะสูงขึ้น คณะวิจัย ได้ศึกษาวิธีพัฒนา คอนเดนเซอร์ และ อีวาโปเรเตอร์ ซึ่งถือเป็นอุปกรณ์แลกเปลี่ยนความร้อนที่อยู่ในวงจรการปรับอากาศและการทำความเย็น ให้สามารถแลกเปลี่ยนความร้อนระหว่าง สารทำความเย็นกับอากาศได้ดียิ่งขึ้น การศึกษาสามารถทำทั้งจากการทดลองและจากการสร้างแบบจำลองทางคณิตศาสตร์ ตัวอย่างของงานวิจัยได้แก่ การออกแบบอุปกรณ์แลกเปลี่ยนความร้อนแบบใหม่ๆซึ่งอาจเป็นแนวทางในการนำไปประยุกต์ใช้ต่อไปในอนาคต การศึกษาถึงผลของ รูปร่างของครีบที่ใช้ในการถ่ายเทความร้อน ความหนาของครีบ ระยะห่างระหว่างครีบ วัสดุที่ใช้ ลักษณะการวางท่อ ต่อสมรรถนะทางการถ่ายเทความร้อน และการลดลงของความดันของอากาศขณะไหลผ่านอุปกรณ์แลกเปลี่ยนความร้อน ทั้งที่ภาวะที่ผิวท่อด้านนอกของคอนเดนเซอร์มีสภาพแห้ง และที่ภาวะที่ผิวท่ออีวาโปเรเตอร์เปียกด้วยน้ำที่เกิดจากการควบแน่น

คณะวิจัยยังศึกษาในส่วนอุปกรณ์ระเหยซึ่งถือเป็นอุปกรณ์ที่สำคัญอีกตัวหนึ่งในวงจรการปรับอากาศและทำความเย็น ได้แก่ การนำอีเจ็กเตอร์ และ การนำท่อคาปิลลารีทั้งแบบแอเดียแบติก และ แบบนอนแอเดียแบติก มาใช้เป็นอุปกรณ์ระเหย โดยสามารถพัฒนาแบบจำลองทางคณิตศาสตร์เพื่อจำลองการไหลของสารทำความเย็นในท่อคาปิลลารี ซึ่งมีการไหลสองเฟสเป็นกลไกสำคัญ แบบจำลองดังกล่าวสามารถนำไปใช้ในการออกแบบหาขนาดท่อคาปิลลารีที่เหมาะสมที่ใช้กับสารทำความเย็นประเภทต่างๆ ที่ทำงานที่ภาวะต่างๆตามแต่กำหนด และเพื่อให้สะดวกต่อการใช้งานในภาคสนาม กลุ่มวิจัยได้พัฒนาแผนภูมิ เพื่อใช้เลือกขนาดท่อคาปิลลารี ที่เหมาะสมกับสารทำความเย็นและภาวะการใช้งานจริง

ในส่วนของสารทำงานในวงจรการปรับอากาศและการทำความเย็นซึ่งเราเรียกว่าสารทำความเย็น และคณะวิจัย ได้ศึกษาลักษณะเฉพาะในการไหลของสารทำความเย็นทางเลือกใหม่ทั้งจากการทดลองและจากการพัฒนาแบบจำลองทางคณิตศาสตร์ ทั้งในด้านการถ่ายเทความร้อนและด้านกลศาสตร์ของไหลในขณะที่สารทำความเย็นระเหย และควบแน่นภายในท่อเรียบและท่อที่ผิวภายในไม่เรียบ โดยศึกษาทั้ง

กับสารทำความเย็นบริสุทธิ์และกับสารทำความเย็นที่มีน้ำมันหล่อลื่นผสมซึ่งตรงกับสภาพการใช้งานจริง ผลลัพธ์จากการศึกษาทางด้านการถ่ายเทความร้อนจะอยู่ในรูปของสัมประสิทธิ์การถ่ายเทความร้อน สำหรับในเชิงกลศาสตร์ของไหลจะเสนอผลในรูปของ รูปแบบการไหลสองเฟสซึ่งเป็นไปได้หลากหลายรูปแบบการไหล แฟกเตอร์ความเสียดทาน และ ความดันลด สหสัมพันธ์ที่พัฒนาได้ทั้งสัมประสิทธิ์การถ่ายเทความร้อนและแฟกเตอร์ความเสียดทาน สามารถนำไปใช้ในการออกแบบอีวาโปเรเตอร์ และคอนเดนเซอร์ ได้โดยตรง นอกจากนั้นแบบจำลองทางคณิตศาสตร์ที่พัฒนาขึ้นมาสามารถนำไปเป็นแนวทางและใช้ดัดแปลงเพื่อการออกแบบอุปกรณ์แลกเปลี่ยนความร้อนที่มีลักษณะแตกต่างออกไปได้

นอกจากการศึกษาคุณสมบัติของสารทำความเย็นขณะไหลและเปลี่ยนสถานะแล้ว คณะนักวิจัยยังสามารถพัฒนาอุปกรณ์การทดลองเพื่อศึกษาการเดือดของสารทำความเย็นประเภทต่าง ๆขณะไม่มีการไหล โดยมุ่งพัฒนา เส้นโค้งการเดือด ข้อมูลดังกล่าวจะทำให้เข้าใจถึงกลไกการเดือดของสารทำความเย็นชนิดต่าง ๆ ซึ่งจะมีประโยชน์ในการออกแบบอุปกรณ์แลกเปลี่ยนความร้อนที่จะนำสารทำความเย็นนั้น ๆไปใช้ นอกจากสารทำความเย็นปกติแล้ว คณะวิจัย ได้พยายามศึกษา คุณสมบัติของสารทำความเย็นทางเลือกใหม่ที่น่าจะมีศักยภาพ อาทิ ไฮโดรคาร์บอน หรือ ของไหลนาโน ซึ่งคาดหมายว่าจะเป็นของไหลชนิดใหม่ที่มีศักยภาพในการเพิ่มการถ่ายเทความร้อนของอุปกรณ์แลกเปลี่ยนความร้อน

งานวิจัยเกือบทั้งหมดดำเนินการด้วยตัวเองภายในประเทศ ผลลัพธ์จากงานวิจัยในเรื่องที่กล่าวมาอยู่ในรูปของการตีพิมพ์เผยแพร่ต่อสาธารณะชนทั้งระดับชาติและระดับนานาชาติ โดยผลงานวิจัยได้ถูกนำไปอ้างอิงจำนวนมากเพื่อการต่อยอดงานวิจัยหรือถูกนำไปใช้งาน ซึ่งหมายถึง เป็นการทำประโยชน์ให้สังคมโดยส่วนรวม และสร้างชื่อเสียงให้กับประเทศชาติเป็นอย่างยิ่ง และเนื่องจากประเทศไทยอยู่ในเขตร้อนและชื้น การทำความเย็นและการปรับอากาศ ถือเป็นสิ่งจำเป็นในชีวิตประจำวัน ประกอบกับประเทศไทยเป็นฐานการผลิตเครื่องปรับอากาศเพื่อการส่งออกเป็นอันดับต้น ๆของโลก งานวิจัยและพัฒนา ในเรื่องเหล่านี้จะมีประโยชน์อย่างยิ่งต่อประเทศชาติ

5. Output ที่ได้จากโครงการ

5.1 ผลงานการตีพิมพ์ในวารสารระดับนานาชาติ (สามารถดู reprint ได้ในภาคผนวก ก)

1. Saisorn S, Wongwises S. (2010) The effects of channel diameter on flow pattern, void fraction and pressure drop of two-phase air-water flow in circular micro-channels *Experimental Thermal and Fluid Sciences*, 34(4) : 454-462.

2. Laohalertdecha S, Kaw-on, J., Wongwises S., (2010) The effect of the electrohydrodynamic technique on the two-phase flow pressure drop of R-134a during evaporation inside horizontal smooth and micro-fin tubes, *Heat Transfer Engineering* 31 (2): 108-118.

3. Pirompugd W, Wang CC, Wongwises S., (2010) Correlation for wet surface ratio of fin-and – tube heat exchanger, *International Journal of Heat and Mass Transfer* 53(1-3): 568-573.

4. Daungthongsuk, W., Wongwises, S., (2010) An experimental study on the heat transfer Performance and pressure drop of TiO_2-water nanofluids flowing under turbulent flow regime, *International Journal of Heat and Mass Transfer* 53(1-3): 334-344.

5. Chen, Wongwises, Yang, Wang, (2010) Two-Phase Flow Across Small Sudden Expensions and Contractions, *Heat Transfer Engineering.* 31 (4):298-309.

6. Godson Asirvatham , B.Raja, D. Mohan Lal and S. Wongwises, (2010) Enhancement of Heat Transfer using Nanofluids- An Overview, *Renewable and Sustainable Energy Reviews* 14 (2): 629-641.

7. Liu, Y.C., Wongwises, S., Wang, C.C., (2010) Air-side performance of fin and tube heat exchangers in dehumidifying conditions-Data with larger diameter, *International Journal of Heat and Mass Transfer* 53(7-8) : 1603-1608.

8. Daungthongsuk, W., Wongwises, S., (2010) Comparison of the effects of measured and computed thermophysical properties of nanofluids on heat transfer performances, *Experimental Thermal and Fluid Science* 34 (5): 616-624.

9. Laohalertdecha S, Wongwises S. (2010) The effects of corrugation pitch on the condensation heat transfer coefficient and pressure drop of R-134a inside horizontal corrugated tubes, International Journal of Heat and Mass Transfer 53(13-14): 2924-2931.

10. Dalkilic, A.S., Agra, O., Teke, I., Wongwises, S., (2010) Comparison of frictional pressure drop models during annular flow condensation of R600a in a horizontal tube at low mass flux and of R134a in a vertical tube at high mass flux, International Journal of Heat and Mass Transfer,53 (9-10): 2052-2064.

11. Nilpueng, K., Wongwises, S., (2010) Flow mechanisms of HFC-410A inside short tube orifices during flashing process, International Journal of Heat and Mass Transfer 53 (17-18) 3449-3459.

12. Saisorn, S., Kaew-on, J., Wongwises, S., (2010) Flow pattern and heat transfer characteristics of R-134a refrigerant during flow boiling in a horizontal circular mini-channel, International Journal of Heat and Mass Transfer, 53 (19-20): 4023-4038..

13. Dalkilic, A.S., Wongwises, S., (2010) An investigation of a model of the flow pattern transition mechanism in relation to the identification of annular flow of R134a in a vertical tube using various void fraction models and flow regime maps, *Experimental Thermal and Fluid Science* 34 (6): 692-705.

14. Dalkilic, A.S., Laohalertdecha, S., Wongwises, S., (2010) New experimental approach on the determination of condensation heat transfer coefficient using frictional pressure drop and void fraction models in a vertical tube,Energy Conversion and Management 51 (12): 2535-2547.

15. Dalkilic, A.S., Wongwises, S., (2010) Validation of void fraction models and correlations using a flow pattern transition mechanism model in relation to the identification of annular vertical downflow in-tube condensation of R134a, International Communications in Heat and Mass Transfer 37 (7): 827-834

16. Chingulpitak, S., Wongwises, S., (2010) Two-phase flow model of refrigerants flowing through helically coiled capillary tubes, Applied Thermal Engineering 30 (14-15) 1927-1936.

17. Suriyawong, A., Wongwises, S. (2010) Nucleate pool boiling heat transfer characteristics of TiO_2- water nanofluids at very low concentrations, Experimental Thermal and Fluid Science 34 (8) 992-999.

18. Nilpueng, K., Wongwises, S. (2010) Two-phase gas–liquid flow characteristics inside a plate heat exchanger, Experimental Thermal and Fluid Science 34: 1217-1229.

19. Godson Asirvatham, D. Mohan Lal and S. Wongwises (2010) Experimental measurement of temperature-dependent thermal conductivity and viscosity of silver-water nanofluids, Nanoscale and Microscale Thermophysical Engineering 14 (3) 152-173.

20 . Borwornsethanan, S., Wongwises, S.,(2010) Assessment of Useful Life of Lubricants Using Analytical Hierarchy Process (AHP) and Vector Projection Approach (VPA), *American Journal of Engineering and Applied Science* 32 (2) 470-475.

21. Kanokjaruvijit K, Thaworn-ngamyingsakul, C., Wongwises S. (2010) Numerical investigation of an axisymmetric laminar jet impinging on a uniform heat flux dimpled surface using finite element method, *Journal of Mechanical Science and Technology* 24 (9) 1809-1818.

22. Godson Asirvatham, L., Mohan Lal, D., Wongwises, S., (2010) Experimental Investigation on the Thermal Conductivity and Viscosity of Silver-Deionized Water Nanofluid, *Experimental Heat Transfer* 23 (4) 317-332.

23. Chingulpitak, S., Wongwises, S., (2010) Effects of Coil Diameter and Pitch on the Flow Characteristics of Alternative Refrigerants Flowing Through Adiabatic Helical Capillary Tubes, *International Communications in Heat and Mass Transfer* 37 (9): 1305-1311.

24. Naphon, P., Wongwises, S. (2010) Investigation on the jet liquid impingment heat transfer for the central processing unit of personal computers, *International Communications in Heat and Mass Transfer* 37 (7): 822-826.

25. Dalkilic, A.S., Wongwises, S. (2010) A performance comparison of vapour compression refrigeration system using various alternative refrigerants, *International Communications in Heat and Mass Transfer* 37 (9): 1340-1349.

26. Kundu, B., Mondal, P.K., Datta, S.P., Wongwises, S. (2010) Operating design conditions of a solar-powered vapor absorption cooling system with an absorber plate having different profiles: An analytical study, *International Communications in Heat and Mass Transfer* 37 (9): 1238-1245.

27. Laohalertdecha S, Wongwises S. (2011) An experimental study into the evaporation heat transfer and flow characteristics of R134a refrigerant flowing through corrugated tubes, *International Journal of Refrigeration* 34 (1):280-291.

28. Balcilar, M., Dalkilic, A.S., Wongwises, S., (2011), Artificial neural network (ANN) techniques for the determination of condensation heat transfer characteristics during downward annular flow of R134a inside a vertical smooth tube, *International Communications in Heat and Mass Transfer* 38 (1): 75-84.

29. Aroonrat K., Wongwises, S., (2011) Evaporation heat transfer and friction characteristics of R-134a flowing downward in a vertical corrugated tube, *Experimental Thermal and Fluid Science* 35 (1): 20-28.

30. Dalkilic, A.S., Wongwises, S. (2011) Experimental study on the modeling of condensation heat transfer coefficients in high mass flux region of refrigerant HFC-134a inside the vertical smooth tube in annular flow regime, *Heat Transfer Engineering* 32 (1): 33-44.
31. Dalkilic, A.S., Teke, I., Wongwises, S., (2011) Experimental Analysis for the Determination of the Convective Heat Transfer Coefficient by Measuring Pressure Drop Directly During Annular Condensation Flow of R134a in a Vertical Smooth Tube, *International Journal of Heat and Mass Transfer* 54 :1008-1014.

32. Kaew-On, J., Sakamatapan, K., Wongwises, S. (2011) Flow Boiling Heat Transfer of R-134a in a Multiport Minichannel Heat Exchangers, *Experimental Thermal and Fluid Science* 35: 364-374.

33. Nilpueng, K, Wongwises, S., (2011) Choked flow mechanism of HFC-134a flowing through ahort-tube orifices, *Experimental Thermal and Fluids Science.* 35:347-354.

34. Demir, H., Dalkilic, A.S., Kürekci, N.A., Duangthongsuk, W., Wongwises, S., (2011) Numerical investigation on the single phase forced convection heat transfer characteristics of TiO2 nanofluids in a double-tube counter flow heat exchanger *International Communications in Heat and Mass Transfer* 38:218-228.

35. Saisorn, S., Wongwises, S. (2011),Two-phase air-water flow in micro-channels: An inspection of viscosity models for pressure drop prediction, *International Communications in Heat and Mass Transfer* 38: 212-217.

36. Chingulpitak, S., Wongwises, S., (2011) A Comparison of Flow Characteristics of Refrigerants Flowing Through Adiabatic Straight and Helical Capillary Tubes, *International Communications in Heat and Mass Transfer* 38: 398-404.

37. Pongsoi, P., Pikulkajorn, S., Wang, C.C., Wongwises, S., (2011) Effect of fin pitches on the air-side performance of crimped spiral fin-and-tube heat exchangers with a multipass parallel and counter cross-flow configuration, *International Journal of Heat and Mass Transfer* 54:2234-2240.

38. Laohalertdecha S, Wongwises S. (2011) Condensation heat transfer and flow characteristics of R-134a flowing through corrugated tubes, *International Journal of Heat and Mass Transfer* 54: 2673-2682.

39. Wongwises, S., Laohalertdecha, S., Kaew-on, J., Duangthongsuk, W., Aroonrat, K., Sakamatapan, K., (2011) Evaporation heat transfer and flow characteristics of R-134a flowing through internally grooved tubes, *Heat and Mass Transfer* 47 (6): 629-640.

40. Aschariyaphotha N., Wongwises P., Humphries UW, Wongwises S., (2011) Study of storm due to Typhoon Linda 1997 in the Gulf of Thailand using a three dimensional ocean model. *Applied Mathematics and Computation* 217 (21): 8640-8654.

41. Saisorn, S., Kaew-On, J. Wongwises, S., (2011) Two-phase flow of R-134a refrigerant during flow boiling through a horizontal circular mini-channel, *Experimental Thermal and Fluid Science* 35 (2011): 887-895.

42. Ebrahimnia-Bajestan, E., Niazmand, H., Duangthongsuk, W., Renksizbulut, M., Wongwises, S., (2011) Numerical Investigation of Effective Parameters in Convective Heat Transfer of Nanofluids Flowing under a Laminar Flow Regime, *International Journal of Heat and Mass Transfer* 54 (19-20): 4376-4388.

43. Nilpueng, K., Wongwises,S. (2011) Performance characteristics of HFC-134a and HFC-410A refrigeration system using a short-tube orifice as the expansion device, *Heat and Mass Transfer* 47 (10) (2011): 1219-1227.

44. Dalkilic, A.S., Balcilar, M., Bolat, B., Wongwises, S. (2011) Investigation of empirical correlations on the determination of condensation heat transfer characteristics during downward annular flow of R134a inside a vertical smooth tube using computational numerical methods, *Journal of Mechanical Science and Technology* 25 (10): 2683-2701.

45. Godson, L., Raja.,B., D.M. Lal., Wongwises, S. (2011) Convective Heat Transfer Applications in Nanofluids and Development of Correlations, *Particuology* 9 (6): 626-631.

46. Laohalertdecha, S., Dalkilic, A.S., Wongwises, S. (2011) Correlations for evaporation heat transfer coefficient and two-phase friction factor for R-134a flowing through horizontal corrugated tubes, *International Communications in Heat and Mass Transfer*, 38 (10): 1406-1413.

47. Naphon, P., Wongwises, S. (2011) Experimental study of jet nanofluids impingement system for cooling computer processing unit, *Journal of Electronics Cooling and Thermal Control* 1: 38-44.

48. Kaewnai, S., Wongwises, S. (2011) Improvement of the Runner Design of Francis Turbine using CFD *American Journal of Engineering and Applied Science* 4(4):540-547.

49. Kaew-On, J., Sakamatapan, K., Wongwises, S. (2012) Flow boiling pressure drop of R134a in the counter flow multiport minichannel heat exchangers, *Experimental Thermal and Fluid* Science 36 (1): 107-117.

50. Nilpueng, K., Wongwises, S. (2012) Review on the Experimental Studies of Refrigerant Flow Mechanisms inside Short-Tube Orifices, *International Journal of Refrigeration* 35 (1): 27-35.

51. Dalkilic, A.S., Kürekci, N.A., Wongwises, S. (2012) Effect of void fraction and friction factor models on the prediction of pressure drop of R134a during downward condensation in a vertical tube. *Heat and Mass Transfer* 48 (1): 123-139.

52. Saha, S., Celata, G. Wongwises, S. (2012) Selected papers on advances in heat transfer, *Heat Transfer Engineering* 33 (4-5): 281-283.

53. Dalkilic, A.S., Teke, I., Wongwises, S. (2012) Heat transfer enhancement during downward laminar flow condensation of R134a in vertical smooth and micro-fin tubes, *Journal of Thermal Science and Technology* 32(1):19-31.

54. Pongsoi, P. Wongwises, S. (2012) Experimental study on the air-side performance of a multipass parallel and counter cross-flow L-footed spiral fin-and-tube heat exchanger, *Heat Transfer Engineering* 33 (15)1251-1263.

55. Pongsoi, P., Pikulkajorn, S., Wang, C.C., Wongwises, S., (2012) Effect of number of tube rows on the air-side performance of crimped spiral fin-and-tube heat exchanger with a multipass parallel and counter cross-flow configuration, *International Journal of Heat and Mass Transfer* 55 (4): 1403-1411.

56. Vahid Etminan-Farooji, Ehsan Ebrahimnia-Bajestan, Hamid Niazmand, Somchai Wongwises (2012) Unconfined laminar nanofluid flow and heat transfer around a square cylinder, *International Journal of Heat and Mass Transfer* 55 (5-6): 1475-1485.

57. Kundu, B., Wongwises, S., (2012) A decomposition analysis on convecting-radiating rectangular plate fins for variable thermal conductivity and heat transfer coefficient, *Journal of the Franklin Institute* 349 (3): 966-984.

58. Daungthongsuk, W., Wongwises, S., (2012) A dispersion model for predicting the heat transfer performance of TiO2 Water nanofluids under a laminar flow regime, *International Journal of Heat and Transfer* 55 (11-12): 3138-3146.

59. Duangthongsuk, W., Dalkilic, A.S., Wongwises, S. (2012) Convective heat transfer of Al_2O_3-water nanofluids in a microchannel heat sink, *Current Nanoscience* 8(3):317-322.

60. Nilpueng, K., Wongwises, S., (2012) A review of numerical modelling studies on short-tube orifices performance with application to air-conditioning, *International Journal of Refrigeration* 35 (4):740-749.

61. Aschariyaphotha, N., Wongwises, S. (2012) Simulations of Seasonal Current Circulations and Its Variabilities Forced by Runoff from Freshwater in the Gulf of Thailand, *The Arabian Journal for Science and Engineering* 37:1389-1404.

62. Kaewon J., Wongwises, S. (2012) New proposed two-phase multiplier and evaporation heat transfer coefficient correlations for R134a flowing at low mass flux in a multiport minichannel, *International Communications in Heat and Mass Transfer* 39 (6):853-860.

63. Balcilar, M., Dalkilic, A.S., Agra, O., Atayilmaz, S.O., Wongwises, S. (2012) A Correlation Development for predicting the Pressure Drop of various refrigerants during Condensation and Evaporation in Horizontal Smooth and Micro-fin Tubes, *International Communications in Heat and Mass Transfer* 39(7):937-944.

64. Naphon, P., Wongwises, S., Wiriyasart, S. (2012) On the thermal cooling of central processing unit of the PCs with vapor chamber *International Communications in Heat and Mass Transfer* 39 :1165-1168.

65. Yiamsawas, T., Wongwises, S. (2012) Measurement of the thermal conductivity of Titania and Alumina nanofluids, *Thermochimica Acta* 545 : 48-56.

66. Pongsoi, P., Pikulkajorn, S., Wongwises, S. (2012) Effect of fin pitches on the optimum heat transfer performance of crimped spiral fin-and-tube heat exchangers, *International Journal of Heat and Mass Transfer*, 55:6555-6566.

67. Dalkilic, A.S., Kaya, N., Tabatabei, M., Yıldız, O., Yavuz, B., Daungthongsuk, W., Wongwises, S. (2012) Forced convective heat transfer of nanofluids - A review of the recent Literature, *Current Nanoscience* 8: 949-969.

68. Yiamsawasd, T., Dalkilic, A.S., Wongwises, S. (2012) Measurement of Specific Heat of Nanofluids, *Current Nanoscience* 8: 939-944.

69. Balcilar, M., Dalkilic, A.S., Suriyawong, A., Yiamsawas, T., Wongwises, S. (2012) Investigation of pool boiling of nanofluids using artificial neural networks and correlation development techniques, *International Communications in Heat and Mass Transfer* 39 (3): 424-431.

70. Saisorn, S., Wongwises, S. (2012) A critical review of recent investigations on heat transfer in flow boiling micro-channels, *Frontier in Heat and Mass Transfer* 3-013006.

71. Saisorn, S., Wongwises, S. (2012) A critical review of recent investigations on two-phase pressure drop in flow boiling micro-channels, *Frontier in Heat and Mass Transfer* 3-013007.

72. Kaew-On, J., Chingulpitak, S., Wongwises, S. (2012) Experimental investigation of R134a flowing through adiabatic helically coiled capillary tubes, *International Journal of Air conditioning and Refrigeration* 20(1):1250001.

73. Godson, L., Raja, B., Mohan Lal, D. (2012) Wongwises, S., Convective Heat Transfer Characteristics of Silver-Water Nanofluid Under Laminar and Turbulent Flow Conditions, *The ASME Journal of Thermal Science and Engineering Applications*, Vol. 4: 031001.

74. Suriyawong, A., Dalkilic, A.S., Wongwises, S. (2012) Nucleate pool boiling heat transfer correlation for TiO_2-water nanofluids, *Journal of ASTM International* 9(5)(Paper ID JAI104409).

75. Laohalertdecha, S., Dalkilic, A.S., Wongwises, S. (2012) A Critical Review on the Heat-transfer Performance and Pressure-drop Characteristics of Various Enhanced Tubes, *International Journal of Air Conditioning and Refrigeration* 20 (4): 1230003.

76. Chingulpitak, S., Kaew-On, J., Wongwises,S. (2012) Numerical and Experimental Investigation of the Flow Characteristics of R134a Flowing Through Adiabatic Helical Capillary Tubes *International Journal of Air Conditioning and Refrigeration* 20(4): 1250019.

77. Phoolphundh, S., Hathaisamit, K., Wongwises, S. (2013) Performance of Two-stage Upflow Anaerobic Sludge Blanket (UASB) Reactor Treating Wastewater from Latex-Processing
Factory, *Journal of Environmental Engineering*. 139: 141-146.

78. Naphon, P., Wongwises, S., Wiriyasart, S. (2013) Application of two-phase vapor chamber technique for hard disk drive cooling of PCs, *International Communications in Heat and Mass Transfer* 40 : 32-35.

79. Mahian, O., Mahmud, S., Wongwises, S. (2013) Entropy Generation Between Two Rotating Cylinders in the Presence of Magnetohydrodynamic Flow using Nanofluids, *Journal of Thermophysics and Heat Transfer* 27: 161-169.

80. Aroonrat, K., Dalkilic, A.S., Wongwises, S. (2013) Experimental study on evaporative heat transfer and pressure drop of R-134a flowing downward through vertical corrugated tubes with different corrugation pitches, *Experimental Heat Transfer* 26 : 41-63.

81. Mahian, O.,Oztop, H.F., Pop, I, Mahmud, S., Wongwises, S., (2013) Design of a vertical annulus with MHD flowing using entropy generation analysis, Thermal Science 17 (4): 1013-1022.

82. Mahian, O., Oztop, H., Pop, I., Sahin, A.Z., Wongwises, S. (2013) Estimation of operational costs due to entropy generation in a vertical annulus, *International Journal of Exergy* 13(4): 472-486.

83. Wongwises, S., Ghajar, A.J., Chau, K.W., Valladares, G. O., Kundu, B., Dalkilic, A.S., Lazarus, G.A., Two-phase flow and heat transfer enhancement, *Advances in Mechanical Engineering*, 2013 Article ID 256839.

84. Mahian, O., Kianifar, A., Kalogirou, S., Pop, I., Wongwises, S. (2013) A Review of the Applications of Nanofluids in Solar Energy, *International Journal of Heat and Mass Transfer* 57: 582-594.

85. Duangthongsuk, W., Wongwises, S. (2013) An Experimental Investigation into the Heat Transfer and Pressure Drop Characteristics of a Circular Tube Fitted with Rotating Turbine-Type Swirl Generators, *Experimental Thermal and Fluid Science* 45:8-15.

86. Nilpueng, K., Wongwises, S. (2013) Numerical simulation of refrigerants flowing through short-tube orifices during flashing process, *HVAC&R* 19: 159-174.

87. Kayaci, N., Balcilar, M., Tabetebai, M., Celen, A., Yıldız, O., Dalkilic, A.S., Wongwises, S. (2013)Determination of the Single-Phase Forced Convection Heat Transfer Characteristics of TiO_2 Nanofluids Flowing in Smooth and Micro-Fin Tubes by Means of CFD and ANN Analyses *Current Nanoscience* 9: 61-80.

88. Duangthongsuk, W, Yiamsawas, T., Dalkilic, A.S.,Wongwises, S. (2013) Pool-Boiling Heat Transfer Characteristics of Al_2O_3–Water Nanofluids on a Horizontal Cylindrical Heating Surface *Current Nanoscience* 9: 56-60.

89. Aroonrat, K., Jumpholkul, C., Leelaprachakul, R., Dalkilic, A.S., Mahian, O., Wongwises, S.,Heat transfer and single-phase flow in internally grooved tubes *International Communications in Heat and Mass Transfer* 42 : 62-68.

90. Saisorn, S., Kaewon, J., Wongwises, S. (2013) An Experimental Investigation of Flow Boiling Heat Transfer of R134a in horizontal and Vertical Mini-channels, *Experimental Thermal and Fluid Science* 46:232-244.

91. Pongsoi, P., Promoppatum, P., Pikulkajorn, S., Wongwises, S. (2013) Effect of fin pitches on the Air side performance of L-footed spiral fin and tube heat exchangers, *International Journal of Heat and Mass Transfer*, 59: 75-82.

92. Asirvatham, L.G., Nimmagadda, R., Wongwises, S. (2013) Heat transfer performace of screen wick heat pipes using silver-water nonofluid, *International Journal of Heat and Mass Transfer* 60:201-209.

93. Dalkilic, A.S., Kürekci, N.A., Kincay, O., Wongwises, S. (2013) Fundamental basis and application of cold room project design: a turkish case study, *Arabian Journal for Science and Engineering* 38(5): 1115-1130.

94. Mahian, O., Oztop, H., Pop, I., Mahmud, S., Wongwises, S., (2013) Entropy generation between two vertical cylinders in the presence of MHD flow subjected to constant wall temperature, *International Communications in Heat and Mass Transfer* 44: 87-92.

95. Dalkilic, A.S., Kundu, B., Wongwises, S. (2013) An experimental investigation on the Reynolds analogy applied to annular condensation laminar flow of R134a in a vertical tube, *Arabian Journal for Science and Engineering* 38: 1493-1507.

96. Jongpradist, P., Rojbunsongsri, R., Kamnerdtong, T., Wongwises, S. (2013) Parametric study and optimization of a food can corrugation design, *Journal of Mechanical Science and Technology* 27: 2043-2052.

97. Pirompugd, W., Wongwises, S. (2013) Partially Wet Fin Efficiency for the Longitudinal Fins of Rectangular,Triangular, Concave Parabolic, and Convex Parabolic Profiles, *Journal of Franklin Institute* 350: 1424-1442.

98. Pongsoi, P., Wongwises, S. (2013) A review on nuclear power plant scenario in Thailand, *Renewable and Sustainable Energy Reviews* 24: 586-592.

99. Celen, A., Dalkilic, A.S., Wongwises, S. (2013) Experimental analysis of the single phase pressure drop characteristics of smooth and microfin tubes, *International Communications in Heat and Mass Transfer* 46: 58-66.

100. Pirompugd W, Wongwises S. (2013) Efficiencies for partially wetted spine fins: uniform cross section, conical, concave parabolic, and convex parabolic spines, *ASME Journal of Heat Transfer* 135:081903-1.

101. Sakamatapan, K., Kaewon, J.,Dalkilic, A.S., Mahian, O., Wongwises, S. (2013) Condensation heat transfer Characteristics of R-134a flowing inside the multiport minichannels, *International Journal of Heat and Mass Transfer* 64: 976-985.

102. Mahian ,O., Pop,I., Sahin,A.Z., Oztop,H., Wongwises, S. (2013) Irreversibility Analysis of a Vertical Annulus Using TiO_2/ Water Nanofluid with MHD Flow Effects, *International Journal of Heat and Mass Transfer* 64 :671-679.

103. Duangthongsuk, W., Wongwises, S.(2013) Comparison of the heat transfer performance and friction characteristics between fixed and rotating turbine-type swirl generators fitted in a small circular tube *Experimental Thermal and Fluid Science* 50:222-228.

104. Mahian, O., Kianifar A., Kleinstreuer, C., Al-Nimr, M., Pop, I., Sahin, A., Wongwises, S. (2013) A review of entropy generation in nanofluid flow, *International Journal of Heat and Mass Transfer* 65:514-532.

105. Nitiapiruk, P., Mahian, O., Dalkilic, A.S., Wongwises, S. (2013) Performance characteristics of a microchannel heat sink using TiO_2/water nanofluid and different thermophysical models, *International Communications in Heat and Mass Transfer* 47:98-104.

106. Matin, H., Mahian, O., Wongwises, S. (2013) Nanofluids flow between two rotating cylinders: Effects of thermophoresis and Brownian motion,*Journal of Thermophysics and Heat Transfer* 27(4): 748-755.

107. Asirvatham, L.G., Nimmagadda, R. (2013) Wongwises, S. Operational limitations of heat pipes with silver-water nanofluids, *ASME Journal of Heat Transfer* 135:111011-1-111011-9.

108. Yiamsawas, T., Kaewnai, S., Mahian, O., Dalkilic, A.S., Wongwises, S. (2013) Experimental studies on the viscosity of TiO_2 and Al_2O_3 nanoparticles suspended in a mixture of ethylene glycol and water for high temperature applications, *Applied Energy* 11: 40-45.

109. Balcilar, M., Aroonrat, K., Dalkilic, A.S., Wongwises, S. (2013) A numerical correlation development study for the determination of Nusselt numbers during two-phase flow of R134a inside smooth and corrugated tubes, *International Communications in Heat and Mass Transfer* 48: 141-148.

110. Mahian, O., Kianifar A., Wongwises, S. (2013) Dispersion of ZnO nanoparticles in a mixture of Ethylene Glycol-Water, Exploration of temperature-dependent density, and sensitivity analysis, *Journal of Cluster Science* 24:1103-1114.

111. Balcilar, M., Aroonrat, K., Dalkilic, A.S., Wongwises, S. (2013) A generalized numerical correlation study for the determination of pressure drop during condensation and boiling of R134a inside smooth and corrugated tubes, *International Communications in Heat and Mass Transfer* 49: 78-85.

112. Yiamsawas, T., Dalkilic, A.S., Omid, Mahian, Wongwises, S. (2013) Measurement and correlation of the viscosity of water-based Al2O3 and TiO2 nanofluids in high temperatures and comparisons with literature report, *Journal of Dispersion Science and Technology* 34: 1697-1703.

113. Kaewnai, S., Wongwises, S. (2013) Analysis of Flow through a Double-acting Impeller with a Straight Radial Blades Using CFD, *International Journal of Applied Research in mechanical Engineering* 3 (1):37-43.

114. Chingulpitak, S., Wongwises, S. (2014) Critical Review of the Current Status of Wind Energy in Thailand, *Renewable and Sustainable Energy Review* 31 : 312-318.

115. Dalkilic, A.S., Omid, M., Wongwises, S. (2014) Selection of the most suitable refrigerant for a shell and tube condenser, *Heat and Mass Transfer* 50: 183-197.

116. Balcilar, M., Dalkilic, A.S., Aroonrat, K., Wongwises, S. (2014) Neural network based analyses for the determination of evaporation heat transfer characteristics during

downward flow of R134a inside a vertical smooth and corrugated tube, *Arabian Journal for Science and Engineering*, 39: 1271-1290.

117. Laohalertdecha, S., Aroonrat, K., Dalkilic, A.S., Mahian, O., Wongwises, S. (2014) Prediction of heat transfer coefficients and friction factors for evaporation of R-134a flowing inside corrugated tubes, *Heat and Mass Transfer* 50: 469-482.

118. Esfe, M.H., Saedodin, S., Mahian, O., Wongwises, S.(2014) Heat transfer characteristics and pressure drop of COOH-functionalized DWCNTs/water nanofluid in turbulent flow at low concentrations, *International Journal of Heat and Mass Transfer* 73: 186-194.

119. Heris, S.Z., Mahian, O., Wongwises, S. (2014) A comparative experimental study on the natural convection heat transfer of the different metal oxide nanopowders suspended in turbine oil inside an inclined cavity, *International Journal of Heat and Mass Transfer* 73:231-238.

120. Celen, A., Kayaci, N., Cebi, A., Demir, H., Dalkilic, A.S., Sonmex, A.C.,Wongwises, S., (2014) Numerical investigation for the calculation of TiO2-water nanofluids pressure drop in plain and enhanced pipes, *International Communications in Heat and Mass Transfer* 53:98-108.

121. Balcilar, M., Dalkilic, A.S., Sonmex, A.C., Wongwises, S. (2014) Classification of in-tube boiling R134a data belonging to the smooth and corrugated tubes, *International Communications in Heat and Mass Transfer* 53:185-194.

122. Saisorn, S., Kuaseng, P., Wongwises, S. (2014) Heat transfer characteristics of gas-liquid flow in horizontal rectangular micro-channels, *Experimental Thermal and Fluid Science* 55: 54-61.

123. Esfe, M.H., Saedodin, S., Mahian, O., Wongwises, S., Thermal Conductivity of Al_2O_3/water nanofluids: measurement, correlation, sensitivity analysis, and comparisons with literature reports, *Journal of Thermal Analysis and Calorimetry* (in press).

124. Rashidi, I., Mahian, O., Lorenzini, G., Biserni, C., Wongwises, S., Natural Convection of Al_2O_3/water nanofluid in a square cavity: Effects of heterogeneous heating, *International Journal of Heat and Mass Transfer* (in press).

125. Sakamatapan, K., Wongwises, S., Pressure drop during condensation of R134a flowing inside a multiport minichannel, *International Journal of Heat and Mass Transfer* (in press)

126. Srisomba, R., Wongwises, S., Measurement of Void Fraction of R-134a Flowing Through Horizontal Tube, *International Communications in Heat and Mass Transfer* (accepted)

5.2 ผลงานการตีพิมพ์ในการประชุมระดับนานาชาติ

1. Dalkilic, A.S., Wongwises, S., A heat transfer model for co-current downward laminar film condensation of R134a in a vertical micro-fin tube during annular flow regime, the Eleventh UK National Heat Transfer Conference, September 6-8, Queen Mary University of London, UK.

2. Kaew-On, J., Nilpueng, K., Chingulpitak, S., Wongwises, S., An experimental study of the flow phenomena of R134a flowing through a capillary tube, FEDSM-ICNMM2010-30953: Proceedings of the 8th International Conference on Nano-channel, Micro-channel and Mini-channel, August 1-5, 2010, Montreal, Canada.

3. Saisorn, S., Kaew-On, J., Wongwises, S., Flow Boiling Heat Transfer Characteristics of R-134a in Horizontal and Vertical Mini-channels, Proceedings of the 8th International Conference on Nano-channel, Micro-channel and Mini-channel, August 1-5, 2010, Montreal, Canada.

4. Duangthongsuk, W., Wongwises, S., A Comparison on the Heat Transfer and Flow Characteristics of TiO2-Water Nanofluids Having Two Different Chemical Agents FEDSM-ICNMM2010-31020: Proceedings of the 8th International Conference on Nano-channel, Micro-channel and Mini-channel, August 1-5, 2010. Montreal, Canada.

5. Balcilar, M., Dalkilic, S.,Wongwises, S., Determination of condensation heat transfer characteristics of R134a by means of artificial intelligence method, *Proceedings of the 2010 ASME International Mechanical Engineering Congress and Exposition*, November 12-18, 2010, Vancouver, British Columbia, Canada.

6. Dalkilic, A.S., Laohalertdecha, S., Wongwises, S., Comparison of condensation frictional pressure drop models and correlations during annular flow of R134a inside a vertical tube, Thermal and Environmental Issues in Energy Systems, ASME-ATI-UTI, May 16-19, 2010, Italy.

7. Dalkilic, A.S., Wongwises, S., Experimental study on the flow regime identification in the case of co-current condensation of R134a in a vertical smooth tube, International Heat Transfer Conference, ASME, August 8-13, 2010, USA.

8. Demir, H., Dalkilic, A.S., Kurekci, N.A., Kelesoglu, B., Wongwises, S., A numerical investigation of nanofluids forced convection flow in a horizontal smooth tube, International Heat Transfer Conference, ASME, August 8-13, 2010, USA.

9. Dalkilic, A.S., Wongwises, S., Comparison of various alternative refrigerants for vapour compression refrigeration systems, accepted draft paper, ASME/JSME 8th Thermal Engineering Joint Conference, March 13-17, 2011, Honolulu, Hawaii, USA.

10. Nilpueng, K., Wongwises, S., Flashing flow mechanisms of HFC-134a and HFC-410A through short tube orifice, ASME/JSME 8th Thermal Engineering Joint Conference, March 13-17, 2011, Honolulu, Hawaii, USA.

11. Bolat, B., Balcilar, M., Dalkilic, A.S., Wongwises, S., Optimization of the relationship between the two-phase friction factor and Reynolds equivalent number model by means of genetic algorithm, ASME/JSME 8th Thermal Engineering Joint Conference, March 13-17, 2011, Honolulu, Hawaii, USA.

12.Laohalertdecha, S. Wongwises, S., Effect of pitch and depth on the condensation heat transfer of R-134a flowing through corrugated tubes, ASME/JSME 8th Thermal Engineering Joint Conference, March 13-17, 2011, Honolulu, Hawaii, USA.

13.Nilpueng, K., Wongwises, S., Two-phase flow characteristics refrigerant flowing through short-tube orifices, Proceedings of International Conference on Air-Conditioning & Refrigeration, July 6-8, 2011, Yongpyong Resort, Gangwon-Do, Korea.

5.3 การจดสิทธิบัตร (สามารถดู เอกสาร ได้ในภาคผนวก ข)

1 อุปกรณ์แลกเปลี่ยนความร้อนแบบท่อขดเป็นวง
(สิทธิบัตรเลขที่ 31282)

2 กรรมวิธีการเลือกขนาดท่อคาปิลลารีเพื่อใช้ในระบบทำความเย็นที่ใช้สารทำความเย็น R404A, R407B, R407C, R410A, R410B, R502A, R507A โดยใช้แผนภาพ
(คำขอรับสิทธิบัตรเลขที่ 0901004855)

3 วิธีการหาขนาดออริฟิซท่อสั้นที่ใช้เป็นอุปกรณ์ขยายในระบบปรับอากาศ
(คำขอรับสิทธิบัตรเลขที่ 1001001785)

4 แผนภาพสำหรับการเลือกขนาดออริฟิซท่อสั้นเพื่อใช้เป็นอุกรณ์ขยายในระบบปรับอากาศที่ใช้สารทำความเย็น R134a, R407C, R410A
(คำขอรับสิทธิบัตรเลขที่ 1001001909)

5 แผนภาพสำหรับการเลือกขนาดท่อคาปิลลารีแบบขดเพื่อใช้ในระบบทำความเย็นสำหรับสารทำความเย็น R134a, R404A.R407B, R407C, R410A
(คำขอรับสิทธิบัตรเลขที่ 11010000167)

6 อุปกรณ์เพิ่มสมรรถนะการถ่ายเทความร้อนชนิดกังหันแบบหมุนได้ภายในท่อ
(คำขอรับสิทธิบัตรเลขที่ 1101003266)

7 ท่อเพิ่มสมรรถนะการถ่ายเทความร้อนแบบร่องเกลียว
(คำขอรับสิทธิบัตรเลขที่ 1101003634)

8 อุปกรณ์เพิ่มสมรรถนะการถ่ายเทความร้อนชนิดกังหันหมุนเองได้เหนือพื้นผิวของการเดือด
(คำขอรับสิทธิบัตรเลขที่ 1201000625)

5.4 การจดลิขสิทธิ์ (สามารถดู เอกสาร ได้ในภาคผนวก ค)

1. โปรแกรมสำหรับหาขนาดท่อคาปิลลารีแบบแอไดเอบาติก
   (คำขอแจ้งข้อมูลลิขสิทธิ์เลขที่ ลข 98447 ทะเบียนข้อมูลเลขที่ ว1.1755)
2. โปรแกรมการออกแบบคอนเดนเซอร์แบบท่อติดครีบที่ระบายความร้อนด้วยอากาศ
   (คำขอแจ้งข้อมูลลิขสิทธิ์เลขที่ ลข 189622 ทะเบียนข้อมูลเลขที่ ว1.2873)
3 โปรแกรมคำนวณอัตราการไหลของสารทำความเย็นที่ไหลผ่านออริฟิซท่อสั้น
   (คำขอแจ้งข้อมูลลิขสิทธิ์เลขที่ ลข 287701 ทะเบียนข้อมูลเลขที่ ว1.4613)

5.5 <u>หนังสือ</u>(สามารถดู เอกสาร ได้ในภาคผนวก ง)

กลศาสตร์ของไหล เล่ม 1 (อยู่ในขั้นตอนการจัดพิมพ์ที่ สำนักพิมพ์แห่งจุฬาลงกรณ์มหาวิทยาลัย)

5.6 <u>Book chapters</u> (สามารถดู เอกสาร ได้ในภาคผนวก จ)

- A.S. Dalkilic, S., Wongwises, Two-Phase Heat Transfer Coefficients of R134a Condensation in vertical Downward Flow at High Mass Flux, in: A. Belmiloudi and D. Barbin (Eds.),Heat Transfer, InTech, Vienna, 2011, pp. 15-32 (ISBN 978-953-307-226-5).
- B. Kundu, S. Wongwises, Optimum Fin Profile under Dry and Wet Surface Conditions, in: A. Belmiloudi and D. Barbin (Eds.), Heat Transfer, InTech, Vienna, 2011 pp. 3-32 (ISBN 978-953-307-550-1) .
- A.S. Dalkilic, S., Wongwises, Condensation Heat Transfer in Smooth and Enhanced Geometrics: A Review of the Recent Literature, in: D. Alda and D. Ciarlo (Eds.), Refrigeration Systems, Design Technologies and Developments, Nova, New York, 2012, pp. 113-154 (ISBN 978-1-62417-229-8).

5.7 การนำผลงานไปใช้ประโยชน์

<u>เชิงวิชาการ</u>

- นักศึกษาระดับปริญญาเอกจบการศึกษา 5 คน คือ นายวีระพันธ์ ด้วงทองสุก นายศิระ สายศร นายกิตติ นิลผึ้ง นายสุริยัน เลาหเลิศเดชา และ นายจตุพร แก้วอ่อน
- นักศึกษาระดับปริญญาโทจบการศึกษา 9 คน คือ นายอดิเรก สุริยะวงศ์ นายปริญญา พงสร้อย นายคณิต อรุณรัตน์ นายศักรินทร์ ชินกุลพิทักษ์ นายทแกล้ว เยี่ยมสวัสดิ์ นายรวมศักดิ์ บุญศรี นายภูเบศร์ เที่ยงธรรม นายกิตติพงษ์ ศักดิ์อมตพันธ์ และ นางสาวปานสุนี สุวรรณกำเนิด

- เป็นพี่เลี้ยงให้นักศึกษาต่างชาติ 5 คน ได้แก่ Dr. Godson Asirvatham Lazarus Dr. Ahmet Selim Dalkilic, Dr. Balarum Kundu Mr. Omid Mahianและ Mr. Ehsan Ebrahimnia Bajestan
- เป็นพี่เลี้ยงให้อาจารย์มหาวิทยาลัยเทคโนโลยีพระจอมเกล้าธนบุรี และมหาวิทยาลัยอื่นๆ จำนวนมาก

<u>เชิงสาธารณะ</u> (สามารถดู เอกสาร ได้ในภาคผนวก ฉ)

- เป็น Reviewer พิจารณาโครงการที่เสนอขอทุนวิจัยต่างๆของ สกว.
- เป็นกรรมการบัญญัติคำศัพท์ทางวิศวกรรมเครื่องกลของราชบัณฑิตยสถาน
- เป็นกรรมการพิจารณาผลงานเพื่อเข้าสู่ตำแหน่งทางวิชาการให้มหาวิทยาลัยต่างๆ
- เป็น Reviewer พิจารณาบทความให้กับวารสารระดับชาติและระดับนานาชาติ
- เป็นวิทยากรให้องค์กร และ มหาวิทยาลัยต่างๆในเรื่องที่เกี่ยวกับงานวิจัย
- เป็น Editor ของวารสารระดับนานาชาติ Experimental Thermal and Fluid Science (Elsevier Publisher)
- เป็น Lead Guest Editor ของวารสารระดับนานาชาติ Advances in Mechanical Engineering ใน special issue เรือง “Two-Phase Flow and Heat Transfer Enhancement”.
- เป็น Guest Editor ของวารสารระดับนานาชาติ Heat Transfer Engineering (special issue)(Taylor and Francis Publisher)
- ได้รับการประกาศจาก Thomson Reuters ว่ามีบทความต่อไปนี้เป็น a highly-cited article “Trisaksri V, Wongwises S. (2009) Nucleate Pool Boiling Heat Transfer TiO_2-R141b nanofluids, *International Journal of Heat and Mass Transfer* 52 (5-6): 1582-1588.”
- ได้รับการประกาศจากวารสาร Heat and Mass Transfer ว่ามีบทความต่อไปนี้เป็น the popular paper “Srisawas, K., Wongwises S. (2009) Heat transfer characteristics of a new helically coiled crimped spiral finned tube heat exchanger, *Heat Mass Transfer* 45 (4):381-391.”
- ได้รับการประกาศจากวารสาร Experimental Thermal and Fluid Science ว่ามีบทความต่อไปนี้เป็น the most cited article “Daungthongsuk, W., Wongwises, S. (2009) Measurement of temperature-dependent thermal conductivity and viscosity of TiO_2-water nanofluids, *Experimental Thermal and Fluid Science* 33 (4): 706-714.”
(โปรดดูเอกสารในภาคผนวก ฉ)

<u>เชิงพาณิชย์</u> (สามารถดู เอกสาร ได้ในภาคผนวก ช)

ช่วยเหลือให้คำแนะนำ เพื่อเพิ่มคุณภาพของผลิตภัณฑ์ ให้กับภาคอุตสาหกรรม ได้แก่
บริษัท ไซโจเดนกิ อินเตอร์เนชันแนล จำกัด

บริษัท ซี แอร์คอน เทค จำกัด

บริษัท สมชายอินดัสตรี จำกัด

บริษัท ไทย-เยอรมัน โปรดักส์ จำกัด (มหาชน)

โดยเฉพาะอย่างยิ่งได้ให้ความช่วยเหลือบริษัท ไทย-เยอรมัน โปรดักส์ จำกัด (มหาชน) จนกระทั่งผลงานวิจัยมีส่วนช่วยให้ บริษัทฯ ได้รับรางวัลเกียรติยศจากรัฐสภา เมื่อวันที่ 2 ก.ย. 2556 (โปรดดูเอกสารในภาคผนวก ช)

(ศ. ดร. สมชาย วงศ์วิเศษ)

หัวหน้าโครงการ

ภาคผนวก ก.

ผลงานที่ตีพิมพ์ในวารสารระดับนานาชาติ

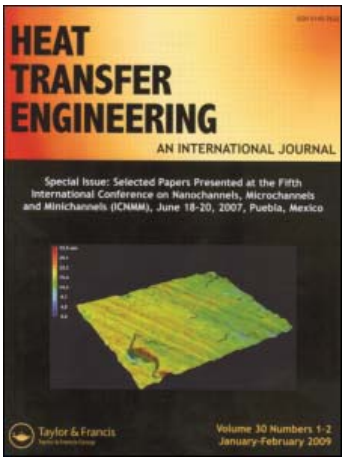

Heat Transfer Engineering
Publication details, including instructions for authors and subscription information:
http://www.informaworld.com/smpp/title~content=t713723051

The Effect of the Electrohydrodynamic on the Two-Phase Flow Pressure Drop of R-134a during Evaporation inside Horizontal Smooth and Micro-Fin Tubes

Suriyan Laohalertdecha [a]; Jatuporn Kaew-On [ab]; Somchai Wongwises [a]
[a] Fluid Mechanics, Thermal Engineering and Multiphase Flow Research Laboratory (FUTURE), Department of Mechanical Engineering, King Mongkut's University of Technology Thonburi, Bangkok, Thailand [b] Department of Physics, Faculty of Science, Thaksin University, Papayom, Phattalung, Thailand

Online Publication Date: 01 January 2010

To cite this Article Laohalertdecha, Suriyan, Kaew-On, Jatuporn and Wongwises, Somchai(2010)'The Effect of the Electrohydrodynamic on the Two-Phase Flow Pressure Drop of R-134a during Evaporation inside Horizontal Smooth and Micro-Fin Tubes',Heat Transfer Engineering,31:2,108 — 118

To link to this Article: DOI: 10.1080/01457630903285369

URL: http://dx.doi.org/10.1080/01457630903285369

Heat Transfer Engineering, 31(2):108–118, 2010

ISSN: 0145-7632 print / 1521-0537 online
DOI: 10.1080/01457630903285369

Taylor & Francis
Taylor & Francis Group

The Effect of the Electrohydrodynamic on the Two-Phase Flow Pressure Drop of R-134a during Evaporation inside Horizontal Smooth and Micro-Fin Tubes

SURIYAN LAOHALERTDECHA,[1] JATUPORN KAEW-ON,[1,2] and SOMCHAI WONGWISES[1]

[1]Fluid Mechanics, Thermal Engineering and Multiphase Flow Research Laboratory (FUTURE), Department of Mechanical Engineering, King Mongkut's University of Technology Thonburi, Bangkok, Thailand
[2]Department of Physics, Faculty of Science, Thaksin University, Papayom, Phattalung, Thailand

This article concerns the pressure drop caused by using the electrohydrodynamic (EHD) technique during evaporation of pure R-134a inside smooth and micro-fin tubes. The test section is a counter-flow concentric tube-in-tube heat exchanger where R-134a flows inside the inner tube and hot water flows in the annulus. A smooth tube and micro-fin tube having an inner diameter of 8.12 mm and 8.92 mm, respectively, are used as an inner tube. The length of the inner tube is 2.50 m. The outer tube is a smooth copper tube having an inner diameter of 21.2 mm. The electrode, which is a cylindrical stainless steel wire having diameter of 1.47 mm, is placed in the center of the inner tube. The electrical field is established by connecting a DC high voltage power supply of 2.5 kV to the electrode while the inner tube is grounded. Experiments are conducted at saturation temperatures of 10–20°C, mass fluxes of 200–600 kg/m^{2}s, and heat fluxes of 10–20 kW/m^2. The experimental results indicate that the application of EHD introduces a small pressure drop penalty. New correlations for the pressure drop are proposed for practical applications.

INTRODUCTION

Normally, heat transfer enhancement techniques can be divided into two groups: namely passive techniques and active techniques. The passive techniques require special surface geometries, such as rough surface or extended surface. The active techniques require external forces, such as fluid vibration, surface vibration, and an electrical field. An electrohydrodynamic (EHD) technique is one of the types of active techniques, which can be achieved by the interaction between the electrical field and the flow of dielectric fluid medium. This interaction creates additional fluid motion which leads to a higher heat transfer coefficient. The electrical body force density acting on the fluid element of dielectric fluid in the presence of an electrical field can be expressed as:

$$f_e = qE - \frac{1}{2}E^2\nabla\varepsilon + \frac{1}{2}\nabla\left[E^2\rho\left(\frac{\partial\varepsilon}{\partial\rho}\right)_T\right] \qquad (1)$$

The three terms on the right side of Eq. (1) represent the electrophoretic, dielectrophoretic, and electrostrictive components of the force, respectively. The first term represents the force acting on the free charges in the presence of an electrical field, called Coulomb force. The second term is a consequence of inhomogeneous or spatial change in the permittivity of the dielectric fluid due to non-uniform electrical fields, temperature

The present study was supported financially by the Joint Graduate School of Energy and Environment (JGSEE) and the Thailand Research Fund (TRF) whose guidance and assistance are gratefully acknowledged.

Address correspondence to Professor Somchai Wongwises, King Mongkut's University of Technology Thonburi, 126 Pracha-utid Road, Bangmod, Toongkru, Bangkok 10140, Thailand. E-mail: somchai.won@kmutt.ac.th

Table 1 Refrigerants, electrode and tube configurations studied by various researchers

Source	Refrigerant	Test section	Electrode geometry	Experimental condition	Supplied energy to the test section
Singh et al. [1]	R-123	Smooth stainless steel tube ID = 9.4 mm Length = 1220 mm	Cylindrical stainless steel electrode having diameter of 3 mm	T_{sat} = 27.52°C EHD = 0, 10 kV q'' = 5, 10, 20 kW/m^2 G = 50–400 kg/m^{2}s Inlet quality = 0–0.5	Hot water
Singh et al. [2]	R-134a	Smooth stainless steel tube ID = 9.4 mm Length = 1220 mm	Cylindrical stainless steel electrode having diameter of 3 mm	T_{sat} = 20.15°C EHD = 0, 10 kV q'' = 5, 10, 20 kW/m^2 G = 50–400 kg/m^{2}s Inlet quality = 0–0.5	Hot water
Salehi et al. [3]	R-404A	Micro-fin copper tube ID = 11.78 mm OD = 12.7 mm Length = 304.8 mm	Cylindrical stainless steel wire having diameter of 0.46 mm Helical electrode ID = 8.92 mm, OD = 9.84 mm	T_{sat} = 20.15°C EHD = 0–3 kV q'' = 5, 10 kW/m^2 G = 50–200 kg/m^{2}s Average quality = 0–0.8	Electric heater
Salehi et al. [4]	R-134a	1. Smooth copper tube ID = 9.5 mm OD = 11.56 mm Length = 114.3 mm 2. Corrugated copper tube with helical angle of 18 with height of ridge of 0.25 mm	Cylindrical rod	Re =500, 1000 EHD = 0–3 kV q'' = 25 kW/m^2 Inlet quality = 0–0.6	Electric heater
Bryan and Seyed-Yagoobi [5]	R-134a	Smooth copper tube ID = 14.1 mm OD = 15.9 mm Length = 100, 200, 300, 500 mm (connecting in series)	Cylindrical brass rod electrode having diameter of 1.6 mm	T_{sat} = 4.9–25.1°C EHD = 0, 5, 15 kV G = 99.9–300.7 kg/m^{2}s Inlet quality = 0–0.8	Hot water
Cotton et al. [6]	R-134a	Smooth stainless steel tube ID = 10.92 mm OD = 12.7 mm Length = 1800 mm	Cylindrical stainless steel electrode having diameter of 3.175 mm	T_{sat} = 24°C EHD = 0–8 kV q'' = 10, 20 kW/m^2 G = 100–500 kg/m^{2}s Inlet quality = 0–0.6	Hot water

gradients, and phase differences. The third term is caused by inhomogeneous electrical field strength and the variation in dielectric constant with temperature and density.

Heat transfer enhancement during evaporation using EHD has been published in the literature. Some of the works were performed by Singh et al. ([1, 2]), Salehi et al. [3, 4], Bryan and Seyed-Yagoobi [5] and Cotton et al. [6] as shown in Table 1.

It can be noted that the mass fluxes of the reported test tubes are almost all below 300 kg/s.m^2. As a consequence, the objective of this study is to study the pressure drop penalty from the use of electrohydrodynamic technique during evaporation of R-134a flowing in a horizontal smooth tube and micro-fin tube at high mass flux conditions.

EXPERIMENTAL APPARATUS

The experimental apparatus can be divided into two parts: the refrigeration test unit and the direct current (DC) high voltage power supply unit. A schematic diagram of the test apparatus is shown in Figure 1. This experimental apparatus was designed to measure the heat transfer coefficient and pressure drop of pure R-134a over the length of the test tube.

The test loop consists of a test section, refrigerant loop, heating water flow loops, sub-cooling loop, and the relevant instrumentation. For the refrigerant circulation loop, liquid refrigerant is pumped by a magnetic gear pump which is regulated by an inverter. The refrigerant flows in series through a filter/dryer, a sight glass tube, and enters the test section. The inlet quality before entering the test section is controlled by the pre-heater. The pre-heater is a spiral counter flow heat exchanger that supplies energy to control inlet quality of the refrigerant. The refrigerant leaving the test section is then condensed and sub-cooled by the chilling loop that removes heat load receiving from the pre-heater and, returns from the two-phase refrigerant to a sub-cooled state and later collects in a receiver and eventually returns to the refrigerant pump to complete the cycle.

The test section as shown in Figure 2 is a horizontal counter-flow double tube heat exchanger. The length of the heat exchanger is 2.5 m. Refrigerant temperature and the tube

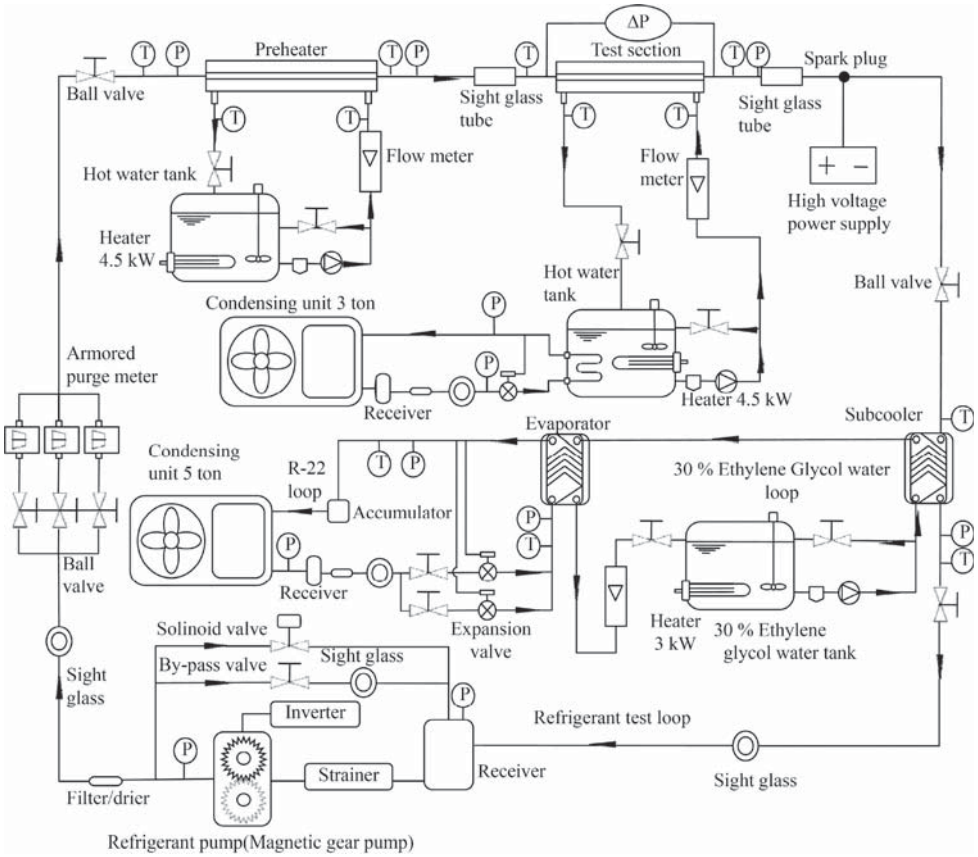

Figure 1 Schematic diagram of experimental apparatus.

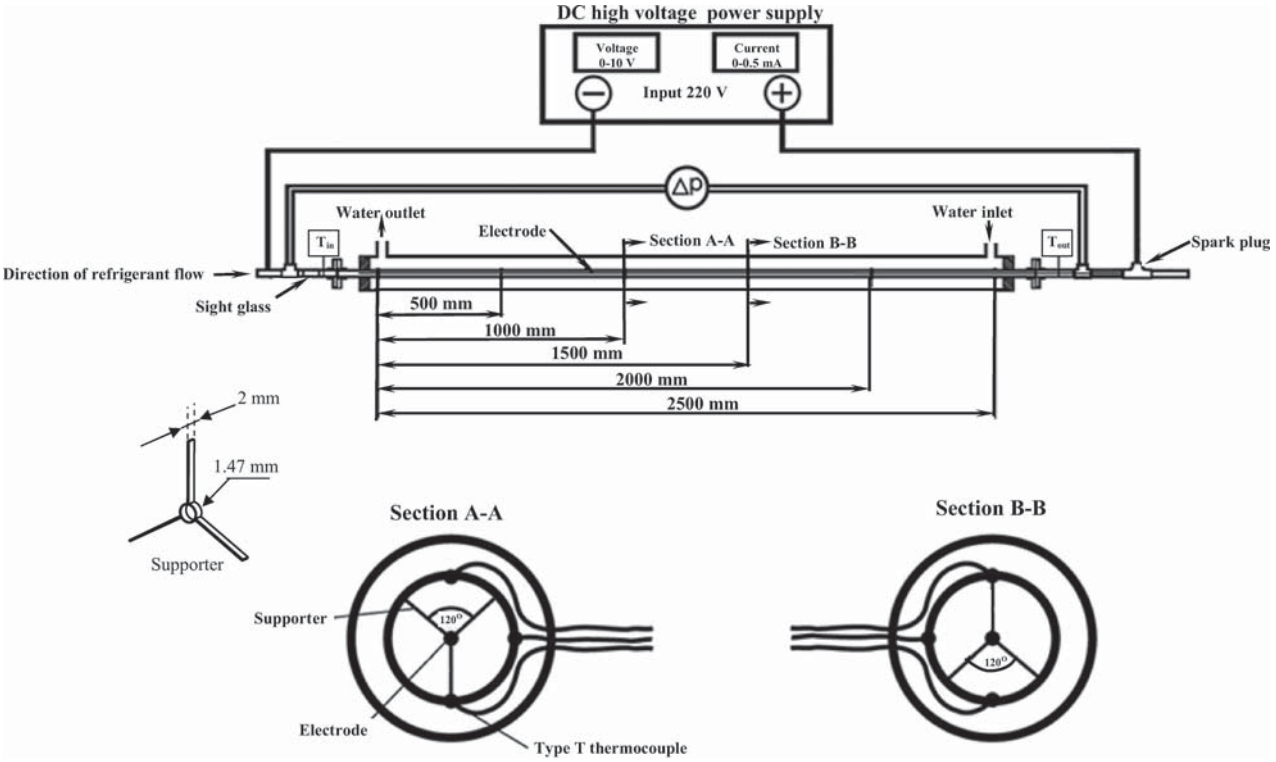

Figure 2 Schematic diagram of test section.

Table 2 Smooth tube and micro-fin tube dimensions

Parameter	Smooth tube	Micro-fin tube
Outside diameter, D_o (mm)	9.52	9.52
Bottom thickness, t (mm)	0.7	0.3
Wwetted perimeter (mm)	25.5	43.2
Maximum inner diameter, D_i (mm)	8.12	8.92
Hydraulic diameter, D_h (mm)	8.12	5.43
Cross sectional area, A_c (mm^2)	51.78	61.31
Number of fins, n	—	60
Spiral angle, β (degrees)	—	18
Fin height, e_f (mm)	—	0.2
Fin pitch, p (mm)	—	0.47
Bottom width (mm)	—	0.27
Apex angle, γ (degrees)	—	52.45
Fin tip diameter, D_t (mm)	—	8.52

wall temperatures in the test section are measured by T-type thermocouples. A total of eighteen thermocouples are soldered at the top, bottom and side at six points along the tube. All the temperature measuring devices are well calibrated in a controlled temperature bath using standard precision mercury glass thermometers. The uncertainty of the temperature measurements after considering the data acquisition system is ± 0.1°C. All static pressure taps are mounted in the tube wall. The refrigerant flow meter is a variable area type. The flow meter is specially calibrated in the range of 0–8.3 × 10^{-3} m^3/min for R-134a by the manufacturer. The differential pressure transducer and pressure gauges are calibrated against a primary standard, the dead weight tester. A stainless steel cylindrical electrode, 1.47 mm in diameter, is used in all experiments. The cylindrical electrode is supported in the center of the test section by electrically insulating spacers (Teflon type material) at intervals of 250 mm. The electrode is attached to the spacers by using a special epoxy-resin. Since the electric field is applied to the test section by a DC high voltage power supply, the electrode attached to a modified automotive spark plug serves as the charged electrode and the heat transfer surface as the receiving electrode.

The dimensions of the smooth and micro-fin tubes are shown in Table 2. The cross-section of micro-fin tube is shown in

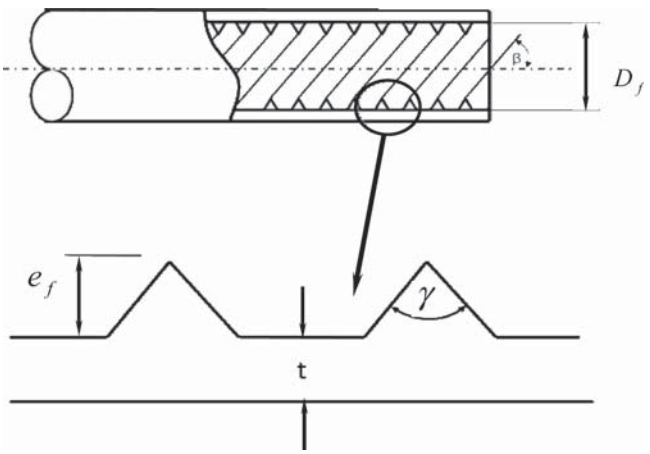

Figure 3 The cross-section of micro-fin tube.

Table 3 Experimental uncertainty

Parameter	Uncertainty
Temperature, T (°C)	±0.1°C
Pressure drop, ΔP(kPa)	±0.075 kPa
Mass flow rate of refrigerant, $\dot{m}_{ref}$	±2% Full scale
Mass flow rate of water, $\dot{m}_w$	±5% Full scale
Heat transfer rate at test section, $\dot{Q}_{TS}$	±11%
Heat transfer rate at pre-heater, $\dot{Q}_{ph}$	±8%
Heat transfer coefficient, h_{avg}	±12%
Inlet quality, x_{in}	±8%

Figure 3. The inlet water temperature is controlled by a thermostat. A differential pressure transducer and thermocouples are installed at the test section to measure the pressure drop and temperature across the test section respectively. The length between the pressure taps is 3 m.

It is necessary to realize that the maximum voltage before starting the electrical breakdown in the test section must be known and should not be exceeded during any steady-state condition. Before the two-phase experiment was performed, the heat balance between refrigerant-side and water-side of the single-phase experiment was conducted. The uncertainties of the heat balance were within 8% and 5% for the pre-heater and the test section, respectively. The uncertainties of the measured quantities and calculated parameters are shown in Table 3.

DATA REDUCTION

The data reduction of the measured results can be summarized as follows:

The inlet vapor quality of the test section ($x_{TS,in}$)

$$x_{TS,in} = \frac{i_{TS,in} - i_{f@T_{TS,in}}}{i_{fg@T_{TS,in}}} \tag{2}$$

where i_f is the enthalpy of the saturated liquid based on the temperature of the test section inlet, i_{fg} is the enthalpy of vaporization based on the temperature of the test section inlet, $i_{TS,in}$ is the refrigerant enthalpy at the test section inlet and is given by:

$$i_{TS,in} = i_{ph,in} + \frac{\dot{Q}_{ph}}{\dot{m}_{ref}} \tag{3}$$

where $i_{ph,in}$ is the inlet enthalpy of the liquid refrigerant before entering the pre-heater, $\dot{m}_{ref}$ is the mass flow rate of the refrigerant and $\dot{Q}_{ph}$ is the heat transfer rate in the pre-heater:

$$\dot{Q}_{ph} = \dot{m}_{w,ph} c_{p,w} (T_{w,in} - T_{w,out})_{ph} \tag{4}$$

where $\dot{m}_{w,ph}$ is the mass flow rate of water entering the pre-heater.

The outlet vapor quality of the test section ($x_{TS,out}$)

$$x_{TS,out} = \frac{i_{\mathrm{TS,out}} - i_{f@T_{\mathrm{TS,out}}}}{i_{fg@T_{\mathrm{TS,out}}}} \tag{5}$$

where $i_{TS,out}$ is the refrigerant enthalpy at the test section outlet, i_f is the enthalpy of the saturated liquid based on the temperature of the test section outlet, and i_{fg} is the enthalpy of vaporization. As a consequence, the outlet enthalpy of the refrigerant flow is calculated as:

$$i_{TS,out} = i_{TS,in} + \frac{\dot{Q}_{TS}}{\dot{m}_{ref}} \tag{6}$$

where the heat transfer rate in the test section is obtained from:

$$\dot{Q}_{TS} = \dot{m}_{w,TS} c_{p,w} (T_{w,in} - T_{w,out})_{TS} \tag{7}$$

where $\dot{m}_{w,TS}$ is the mass flow rate of the water entering the test section.

The average heat transfer coefficient (h_{avg})

$$h_{avg} = \frac{\dot{Q}_{TS}}{A_{inside}(T_{avg,wall} - T_{avg,sat})} \tag{8}$$

where h_{avg} is the average heat transfer coefficient, $\dot{Q}_{TS}$ is the heat transfer rate in the test section, $T_{avg,wall}$ is the average temperature of the wall, $T_{avg,sat}$ is the average temperature of the refrigerant at the test section inlet, and outlet.

$$T_{avg,sat} = \frac{T_{in,sat} + T_{out,sat}}{2} \tag{9}$$

A_{inside} is the inside surface area of the test section:

$$A_{inside} = \pi D_f L \tag{10}$$

where D_f is the inside diameter of the test tube. L is the length of the test tube. The inside diameter of the micro-fin tube is defined as the outer diameter of the micro-fin tube minus twice the minimum wall thickness.

RESULTS AND DISCUSSION

In general, the EHD technique can provide enhancement of heat transfer. However, the heat transfer enhancement should be considered together with pressure drop penalty. In the present study, the effects of electrode, supporter, mass fluxes, saturation temperatures, heat fluxes, and applied voltage of 2.5 kV on the pressure drop during evaporation of R-134a inside smooth and micro-fin tubes are experimentally investigated. The test conditions were selected to cover as much as possible of the range of inlet quality. The pressure drop is the sum of a frictional pressure drop and a momentum pressure drop. The pressure drop per unit length is obtained by dividing the measured pressure drop by the length between pressure taps. In our apparatus, the length between pressure taps is 3 m, while the length of the heat exchanger is 2.5 m.

There are two phenomena that are usually encountered inside EHD-enhanced smooth and micro-fin tubes [7]. The first is the liquid-extraction phenomenon. When a coaxial cylindrical electrode is used with a smooth tube, the highest electrical field is at the electrode surface due to its small radius of curvature

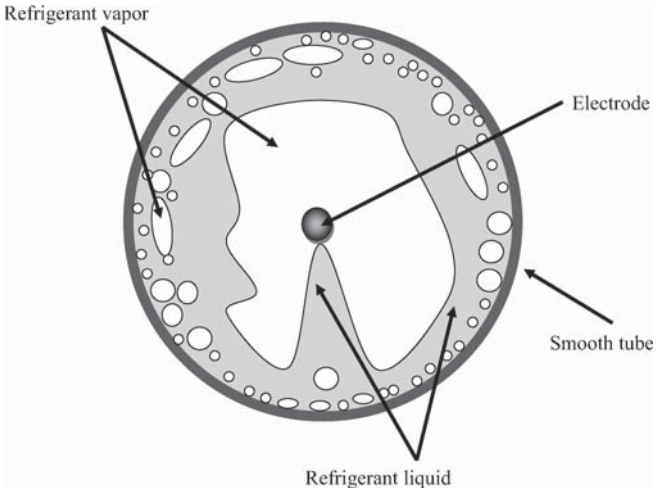

Figure 4 Liquid-extraction phenomenon [7].

since the liquid surface extends into the gas toward the electrode as shown in Figure 4. The second is the electro-convection phenomenon. When a coaxial cylindrical electrode is used with a micro-fin tube, the highest electrical field is at the tip of the fin due to its small radius of curvature (sharp) since the liquid interface is pulled toward the tip of the fin, as shown in Figure 5. Both liquid-extraction and electro-convection phenomena generate a secondary fluid motion inside the tube leading to increase in heat transfer and pressure drop.

Figures 6 and 7 show the comparisons of the measured pressure drop inside smooth and micro-fin tubes for the absence of an electrode, the presence of an uncharged electrode (0 kV), and the presence of a charged electrode (2.5 kV). The test conditions are performed at the saturation temperature (T_{sat}) of 20°C, heat flux (q") of 10 kW/m^2, and mass flux (G) of 400 kg/m^{2}s. The measured pressure drop in the absence of an electrode is obtained by Wongsa-ngam et al. [8]. These figures also show that the pressure drops obtained from both tubes increase with increasing inlet quality. At the same quality, the pressure drop obtained with the presence of an uncharged electrode (0 kV) is higher than that with the absence of an electrode up to

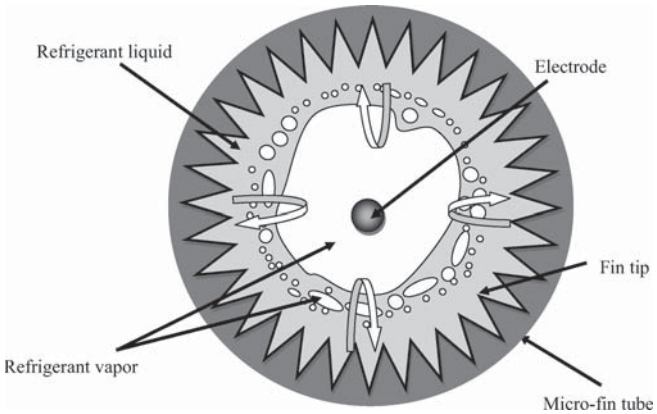

Figure 5 Electro-convection phenomenon [7].

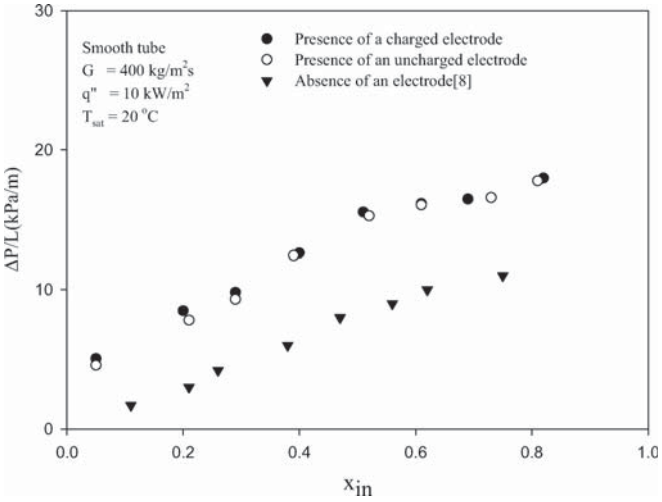

Figure 6 Pressure drop versus inlet quality for smooth tube at $T_{sat} = 20°C$, $G = 400$ kg/m^{2}s and $q'' = 10$ kW/m^2.

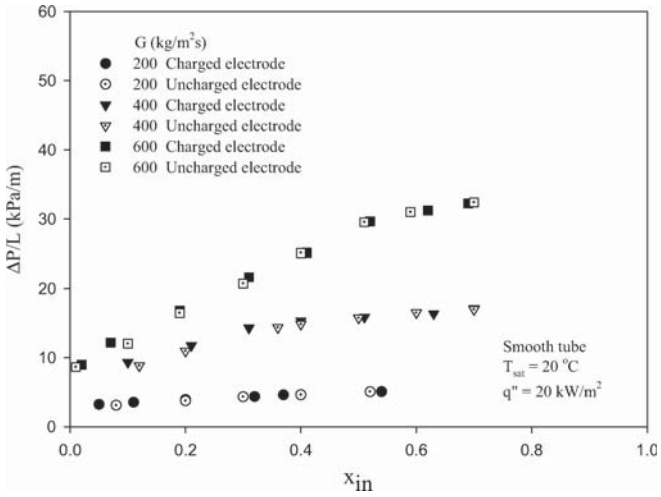

Figure 8 The effect of mass flux on the pressure drop for smooth tube at $T_{sat} = 20°C$ and $q'' = 20$ kW/m^2.

100% for smooth tube and 80% for micro-fin tube. This is because the supporter and electrode obstruct the fluid flow. The pressure drop obtained with the presence of a charged electrode is slightly higher than that with the presence of an uncharged electrode at the same inlet quality because of the instabilities at the liquid-vapor interface resulting from the molecules of refrigerant disturbed by the EHD force.

Figures 8 and 9 show the variation of the measured pressure drop with inlet quality of pure R-134a during evaporation in the smooth and micro-fin tubes for the presence of an uncharged electrode (0 kV) and for the presence of a charged electrode (2.5 kV) at a saturation temperature of 20°C and heat flux of 20 kW/m^2 for different mass fluxes of 200, 400, and 600 kg/m^2 s. These figures show that the measured pressure drops obtained from the presence of an uncharged electrode (0 kV) and the presence of a charged electrode (2.5 kV) increase with increasing inlet quality. As expected, at the same quality the pressure drops for the presence of an uncharged electrode (0 kV) and the presence of a charged electrode (2.5 kV) obtained from higher mass flux are always higher than at lower mass fluxes across the range of the inlet quality. However, the effect of the mass flux on the pressure drop can be clearly seen at higher inlet quality, i.e., the pressure drop is much higher for a higher mass flux than that for a lower mass flux. The application of EHD seems to be negligible for almost all pressure drops obtained from the broadest range of inlet quality.

Figures 10 and 11 show the variation of the measured evaporation pressure drop with inlet quality in the smooth and micro-fin tubes for the presence of an uncharged electrode (0 kV) and the presence of a charged electrode (2.5 kV) at a mass flux of 400 kg/m^2 s and saturation temperature of 20°C for different heat fluxes of 10, 15 and 20 kW/m^2. These figures also show that

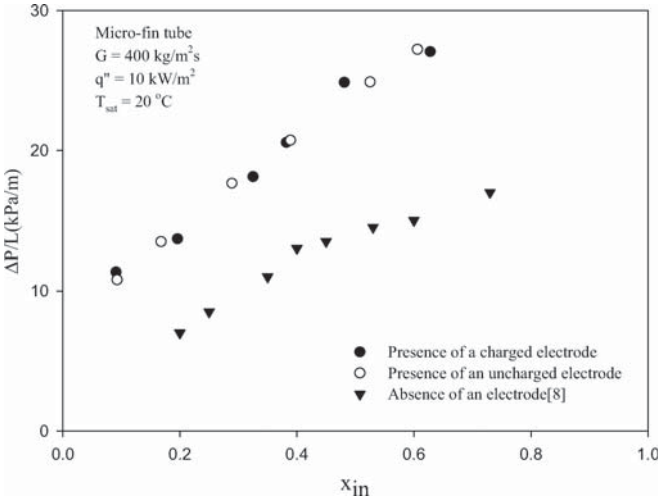

Figure 7 Pressure drop versus inlet quality for micro-fin tube at $T_{sat} = 20°C$, $G = 400$ kg/m^{2}s and $q'' = 10$ kW/m^2.

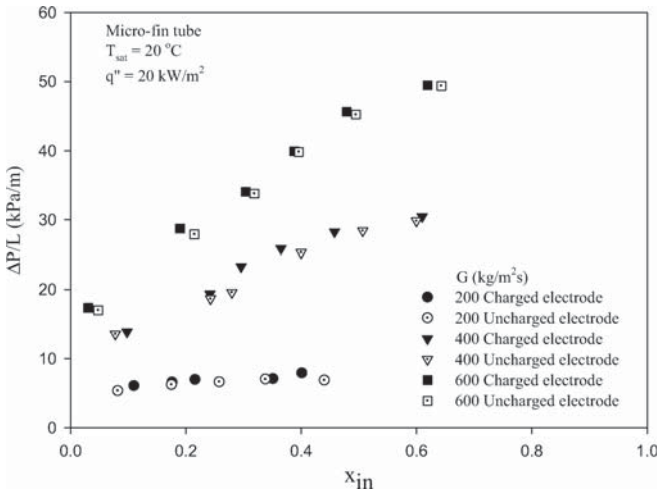

Figure 9 The effect of mass flux on the pressure drop for micro-fin tube at $T_{sat} = 20°C$ and $q'' = 20$ kW/m^2.

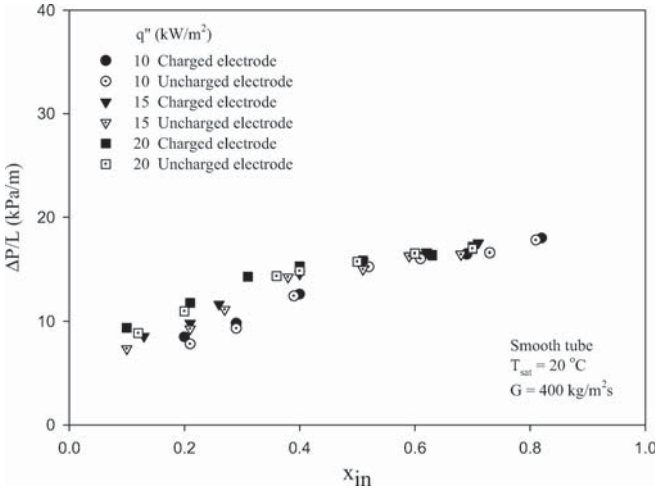

Figure 10 The effect of heat flux on the pressure drop for smoth tube at $T_{sat} = 20°C$ and $G = 400$ kg/m^{2}s.

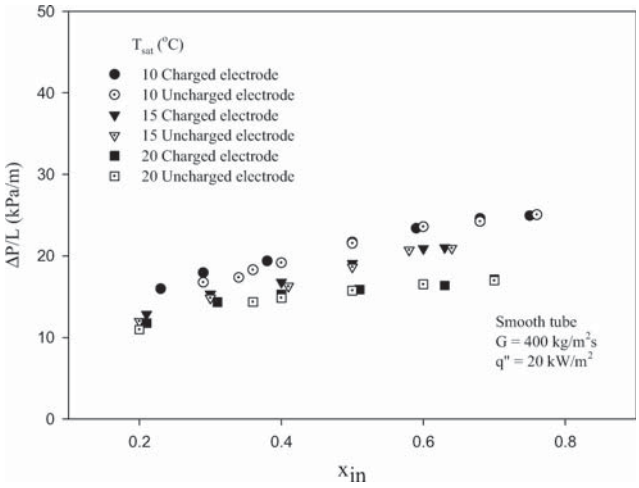

Figure 12 The effect saturation temperature on the pressure drop for smooth tube at $T_{sat} = 20°C$ and $G = 400$ kg/m^{2}s.

the pressure drops for both smooth and micro-fin tubes with the presence of an uncharged electrode (0 kV) and the presence of a charged electrode (2.5 kV) increase with increasing inlet quality. It can be seen that pressure drop increases with increasing heat flux. This is because more vapor bubbles are created at higher heat flux. This phenomenon promotes more agitation in the fluid flow, leading to the increase in pressure drop. Application of EHD voltage of 2.5 kV also has a slight effect on the pressure drop in a wide range of inlet qualities.

Figures 12 and 13 show the variation of the measured evaporation pressure drop with inlet quality in the smooth and micro-fin tubes for the presence of an uncharged electrode (0 kV) and the presence of a charged electrode (2.5 kV) at a mass flux of 400 kg/m^2 s, heat flux of 20 kW/m^2 and different saturation temperatures of 10, 15 and 20°C. These figures also show that the pressure drops increase slightly with increasing inlet quality. As expected, the pressure drop at lower saturation temperatures is higher than those at higher saturation temperatures at an equivalent inlet quality. The effect of the saturation temperature on the pressure drop is clear at higher inlet quality. The pressure drop is higher for a lower saturation temperature than that for a higher saturation temperature, and this is caused by the decrease in the mixture viscosity. The application of an EHD voltage of 2.5 kV for smooth and micro-fin tubes slightly increases the pressure drop at all saturation temperatures.

Figures 14 and 15 show the comparisons of the average measured evaporation heat transfer coefficient obtained from the smooth tube with that obtained from the micro-fin tube at a mass flux of 400 kg/m^2 s, a heat flux of 20 kW/m^2, and saturation temperatures of 20°C for the presence of an uncharged electrode and a charged electrode, respectively. It can be clearly seen that the heat transfer coefficient increases with increasing inlet quality. Both in the presence of uncharged electrode and charged electrode, the heat transfer coefficient obtained from

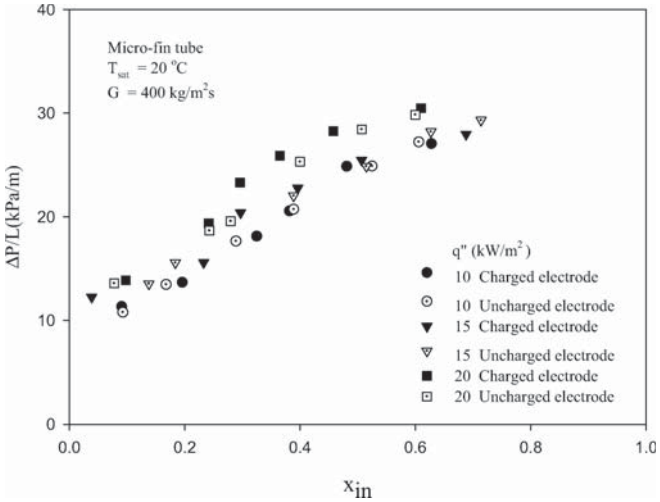

Figure 11 The effect of heat flux on the pressure drop for micro-fin tube at $T_{sat} = 20°C$ and $G = 400$ kg/m^{2}s.

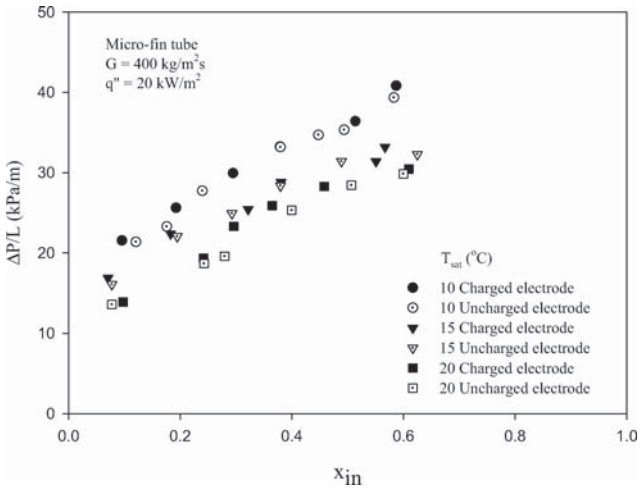

Figure 13 The effect saturation temperature on the pressure drop for micro-fin tube at $T_{sat} = 20°C$ and $G = 400$ kg/m^{2}s.

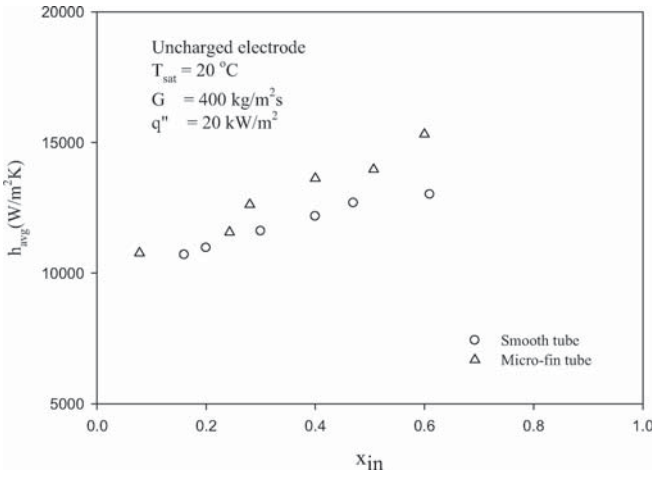

Figure 14 Heat transfer coefficient versus inlet quality for the presence of an uncharged electrode at $T_{sat} = 20°C$, $G = 400$ kg/m^{2}s, and $q'' = 20$ kW/m^2.

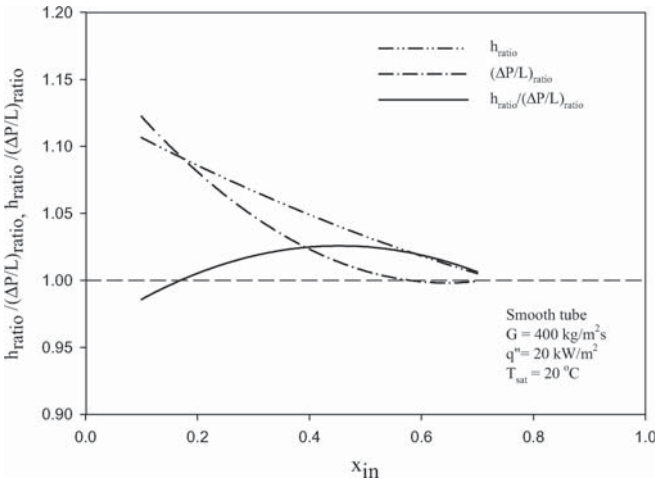

Figure 16 The heat transfer ratio and the pressure drop ratio versus inlet quality for smooth tube at $T_{sat} = 20°C$, $G = 400$ kg/m^{2}s, and $q'' = 20$ kW/m^2.

the microfin tube are higher than that obtained from the smooth tube at the same inlet quality.

In the case of a smooth tube, with the presence of charged electrode, due to liquid extraction phenomenon, the liquid-vapor interface becomes unstable. This causes the average heat transfer coefficient to be higher than in the case of uncharged electrode. In the case of micro-fin tube, due to electro-convection phenomenon, the liquid interface was pulled toward the tip of the fin causing the increase of heat transfer coefficient.

Figures 16 and 17 show the heat transfer coefficient ratio (h_{ratio}), pressure drop ratio $(\Delta P/L)_{ratio}$ and enhancement factor $((h_{ratio})/(\Delta P/L)_{ratio})$ with inlet quality at a saturation temperature of 20°C, heat flux of 20 kW/m^2 and mass flux of 400 kg/m^2 s in smooth and micro-fin tubes, respectively. The heat transfer coefficient ratio (h_{ratio}) is defined by $h_{avg,e}/h_{avg,o}$, where $h_{avg,e}$ is the heat transfer coefficient with the presence of a charged electrode (2.5 kV) and $h_{avg,o}$ is the heat transfer coefficient with the presence of an uncharged electrode (base case, 0 kV). The pressure drop ratio ($(\Delta P/L)_{ratio}$) is defined by $[(\Delta P/L)_e/(\Delta P/L)_o]$, where $(\Delta P/L)_e$ is the pressure drop with the presence of a charged electrode (2.5 kV) and $(\Delta P/L)_o$ is the pressure drop with the presence of an uncharged electrode (base case, 0 kV). From these figures it can be seen that heat transfer coefficient ratio and pressure drop ratio are decreased with an increase in inlet quality. The heat transfer coefficient ratios are all higher than the pressure drop ratio. The enhancement ratios $(h_{ratio}/(\Delta P/L)_{ratio})$ are almost always higher than 1 in the whole range of the tested inlet quality. It can be explained that the slight pressure drop penalty is compensated by the heat transfer augmentation.

Correlation for Predicting Pressure Drop

The two-phase friction pressure gradient (dp_F/dz) of smooth and micro-fin tubes may be expressed in term of two-phase

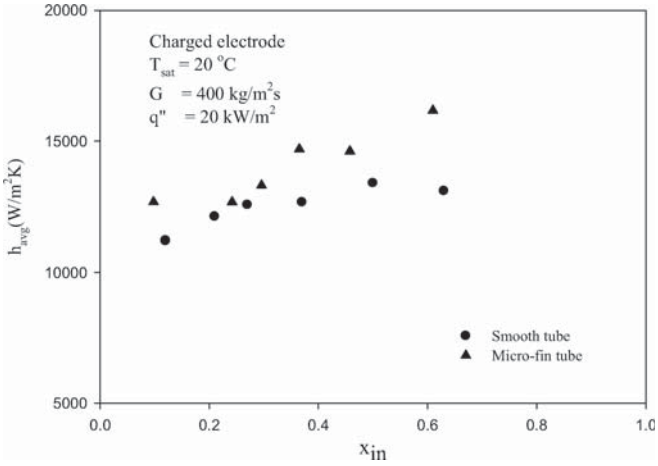

Figure 15 Heat transfer coefficient versus inlet quality for the presence of a charged electrode at $T_{sat} = 20°C$, $G = 400$ kg/m^{2}s, and $q'' = 20$ kW/m^2.

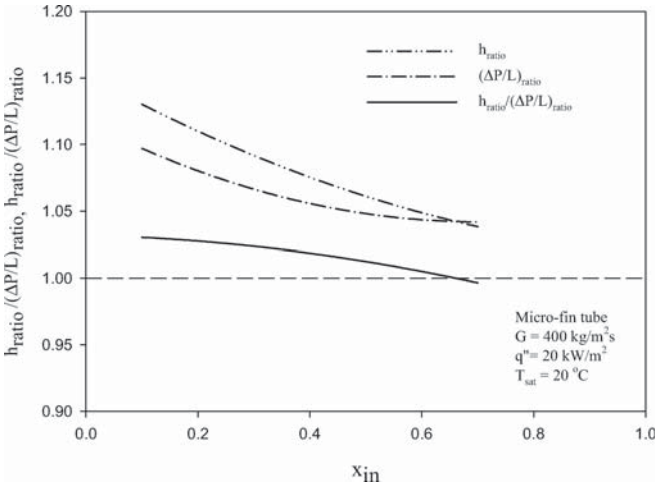

Figure 17 The heat transfer ratio and the pressure drop ratio versus inlet quality for micro-fin tube $T_{sat} = 20°C$, $G = 400$ kg/m^{2}s, and $q'' = 20$ kW/m^2.

multiplier ϕ_l^2 defined as follow:

$$\phi_l^2 = \left(\frac{dp_F}{dz}\right) / \left(\frac{dp_F}{dz}\right)_l \tag{11}$$

Martinelli parameter (X) is given by:

$$X = \sqrt{\frac{(dp_F/dz)_l}{(dp_F/dz)\,v}} \tag{12}$$

where $(dp_F/dz)_l$ and $(dp_F/dz)_v$ are the single-phase liquid and vapor pressure gradients (kPa/m) calculated by using the actual phase flow as follows:

$$(dp_F/dz)_l = \frac{2f_l G^2(1-x)^2}{D\rho_l} \tag{13}$$

and

$$(dp_F/dz)_v = \frac{2f_v G^2 x^2}{D\rho_v} \tag{14}$$

where f_l is the single phase liquid friction factor calculated from:

$$4f_l = 1.325\left[\ln\left(\frac{e/D}{3.7} + \frac{5.74}{\mathrm{Re}_l^{0.9}}\right)\right]^{-2} \tag{15}$$

And

$$\mathrm{Re}_l = \frac{GD(1-x)}{\mu_l} \tag{16}$$

where f_v is the single phase vapor friction factor calculated from:

$$4f_v = 1.325\left[\ln\left(\frac{e/D}{3.7} + \frac{5.74}{\mathrm{Re}_v^{0.9}}\right)\right]^{-2} \tag{17}$$

And

$$\mathrm{Re}_v = \frac{GDx}{\mu_v} \tag{18}$$

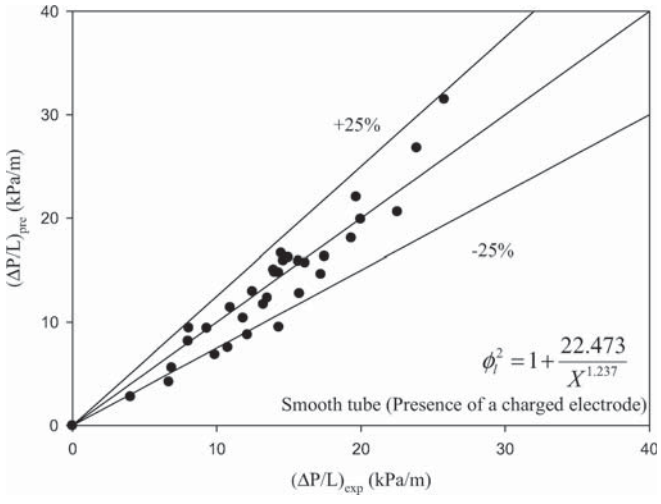

Figure 18 Predicted pressure drop versus the measured pressure drop.

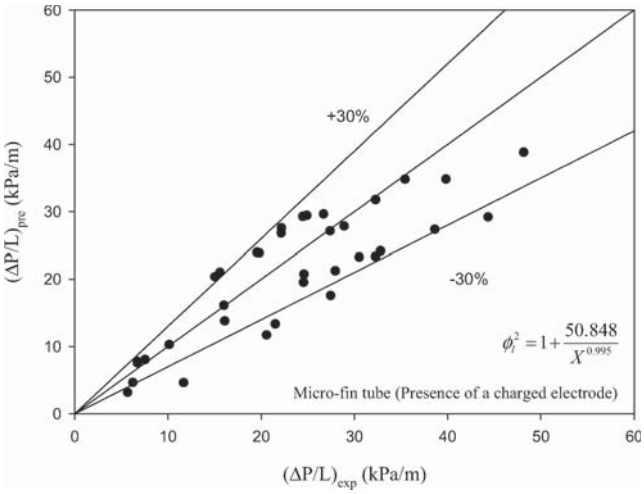

Figure 19 Predicted pressure drop versus the measured pressure drop.

For micro-fin tube the relative roughness (e/D) in Eqs. (15) and (17) are replaced by the equation: Cavalini and Zecchin [9]:

$$e/D = 0.18(e_f/D_t)/(0.1 + \cos\beta) \tag{19}$$

where e_f is the fin height. D_t is the fin tip diameter. β is the spiral angle.

For smooth tube, empirical correlation shown in Eq. (20) is developed based on the presence of a charged electrode. It is created by fitting the Martinelli parameter (X) against a two-phase multiplier.

The presence of a charged electrode the two-phase multiplier is:

$$\phi_l^2 = 1 + \frac{22.473}{X^{1.237}} \tag{20}$$

The correlation is also plotted in Figure 18. It can be explained that the present correlation can predict the pressure drop within a deviation of ±25%.

For micro-fin tube, the empirical correlation shown in Eq. (21) is developed based on the presence of a charged electrode. It is created by fitting the Martinelli parameter (X) against a two-phase multiplier.

The presence of a charged electrode the two-phase multiplier is:

$$\phi_l^2 = 1 + \frac{50.848}{X^{0.995}} \tag{21}$$

The correlation is also plotted in Figure 19. It can be explained that the present correlation can predict the pressure drop within a deviation of ±30%.

CONCLUSIONS

The present article reports the pressure drop penalty from the application of EHD force on evaporation heat transfer enhancement of R-134a in horizontal smooth and micro-fin tubes. The pressure drop obtained from the presence of an uncharged

electrode (0 kV) is higher than that from the absence of an electrode, up to 100% for smooth tube and 80% for micro-fin tube. Pressure drop results from both smooth and micro-fin tubes indicate that the application of an EHD voltage of 2.5 kV slightly increases the pressure drop across the range of tested conditions. The enhancement ratio is almost always higher than 1. The present correlation can predict the pressure drop within a deviation of ±25% for smooth tube and ±30% for micro-fin tube, respectively.

NOMENCLATURE

A_{inside}	inside surface area of test section (m^2)
A_c	cross section area (m^2)
c_p	specific heat at constant pressure (J/kg-K)
D_h	hydraulic diameter (m)
D_o	outside tube diameter (m)
D_f	inside tube diameter (m)
e_f	fin height (m)
E	electric field strength (V/m)
f_e	EHD force density (N/m^3)
G	mass flux (kg/m^2s)
h	heat transfer coefficient (W/m^2 K)
i	enthalpy (J/kg)
L	tube length (m)
$\dot{m}$	mass flow rate (kg/s)
n	number of fin
p	fin pitch (m)
P	pressure (Pa)
$\dot{Q}$	heat transfer rate (W)
q''	heat flux (W/m^2)
q	electric charge density (C/m^3)
T	temperature (°C)
u	velocity (m/s)
x	quality
X	Martinelli parameter
ϕ_l^2	two-phase multiplier

Greek Symbols

β	spiral angle (degree)
γ	apex angle (degree)
ε	electric permittivity (F/m)
ε_o	electric permittivity of free space (8.854×10^{-12}) (F/m)
ρ	density (kg/m^3)

Subscripts

avg	average
e	presence of an uncharged electrode
exp	experiment
f	saturated liquid
fg	difference in property between saturated liquid and vapor
in	inlet
l	liquid
o	presence of a charged electrode
out	outlet
ph	pre-heater
pre	prediction
ref	refrigerant
sat	saturation
TS	test section
V	vapor
w	water
wall	wall

REFERENCES

[1] Singh, A., Dessiatoun, S., Ohadi, M. M., Salehi, M., and Chu, W., In-tube Boiling Heat Transfer Enhancement of R-123 using the EHD technique. *ASHRAE Transactions: Symposia*, pp. 818–825, 1994.

[2] Singh, A., Dessiatoun, S., Ohadi, M. M., Salehi, M., and Chu W., In-tube Boiling Enhancement of R-134a Utilizing the Electric Field Effect, *ASME/JSME Thermal Engineering Conference*, vol. 2, pp. 215–223, 1995.

[3] Salehi, M., Ohadi, M. M., and Dessiatoun, S., The Applicability of the EHD Technique for Convective Boiling of Refrigerant Blends—Experiments with R-404A, *ASHRAE Transactions: Symposia,* pp. 839–844, 1996.

[4] Salehi, M., Ohadi, M. M., and Dessiatoun, S., EHD Enhanced Convective Boiling of R-134a in Grooved Channels—Application to Subcompact Heat Exchangers, *Journal of Heat Transfer*, vol. 119, pp. 805–809, 1997.

[5] Bryan, J. E., and Seyed-Yagoobi, J., Elecrohydrodynamically Enhanced Convective Boiling: Relationship between Electrohydrodynamic Pressure and Momentum Flux Rate, *Transaction of the ASME*, vol. 122, pp. 266–277, 2000.

[6] Cotton, J., Robinson, A. J., Shoukri, M., and Chang, J. S., A Two-Phase Flow Pattern Map for Annular Channels under a DC Applied Voltage and the Application to Electrohydrodynamic Convective Boiling Analysis, *International Journal of Heat and Mass Transfer*, vol. 48, pp. 5563–5579, 2005.

[7] Singh, A., Ohadi, M. M., and Dessiatoun, S., EHD Enhancement of In-tube Condensation Heat Transfer of Alternate Refrigerant R-134a in Smooth and Microfin Tubes, *ASHRAE Transactions: Symposia*, pp. 813–823, 1997.

[8] Wongsa-ngam, J., Nualboonrueng, T., and Wongwises, S., Performance of Smooth and Micro-fin Tubes in High mass Flux Region of R-134a during Evaporation, *Heat and Mass Transfer*, vol. 40, pp. 425–435, 2004.

[9] Cavallini, A., and Zecchin, R., A Dimensionless Correlation for Heat Transfer Coefficient in Forced Convection Condensation, *International Journal of Heat and Mass Transfer conference*, pp. 193–200, 1974.

Suriyan Laohalertdecha is currently a Ph.D. student at the Joint Graduate School of Energy and Environment, King Mongkut's University of Technology Thonburi, Bangmod, Thailand. He received his Master's degree in energy technology from the same department in 2005. He also received his B.Eng. degree from the Department of Mechanical Engineering at the same university in 2002. Currently, his research works concern heat transfer enhancement.

Jatuporn Kaewon is currently a Ph.D. student at the Joint Graduate School of Energy and Environment, King Mongkut's University of Technology Thonburi, Bangmod, Thailand. He received his Master's degree in energy technology from the same department in 2003. He also received his B.Eng. degree from the Department of Mechanical Engineering at the same university in 1999. He is also currently a lecturer at Thaksin University.

Somchai Wongwises is a Professor of Mechanical Engineering at King Mongkut's University of Technology Thonburi, Bangmod, Thailand. He received his Doktor-Ingenieur (Dr.-Ing.) in mechanical engineering from the University of Hannover, Germany, in 1994. His research interests include two-phase flow, heat transfer enhancement, and thermal system design. Professor Wongwises is the head of the Fluid Mechanics, Thermal Engineering and Multiphase Flow Research Lab.

International Journal of Heat and Mass Transfer 53 (2010) 568–573

Contents lists available at ScienceDirect

International Journal of Heat and Mass Transfer

journal homepage: www.elsevier.com/locate/ijhmt

Technical Note

Correlations for wet surface ratio of fin-and-tube heat exchangers

Worachest Pirompugd [a,*], Chi-Chuan Wang [b], Somchai Wongwises [c]

[a] Department of Mechanical Engineering, Faculty of Engineering, Burapha University, Saensook, Muang, Chonburi 20131, Thailand
[b] Energy and Environment Research Laboratories, Industrial Technology Research Institute, Hsinchu 310, Taiwan, ROC
[c] Fluid Mechanics, Thermal Engineering and Multiphase Flow Research Lab. (FUTURE), Department of Mechanical Engineering, King Mongkut's University of Technology Thonburi, Bangmod, Bangkok 10140, Thailand

ARTICLE INFO

Article history:
Received 10 September 2008
Received in revised form 21 August 2009
Accepted 21 August 2009
Available online 7 October 2009

Keywords:
Dehumidifying condition
Finite Circular Fin Method
Heat and mass transfer characteristics
Partially wet surface
Fin-and-tube heat exchanger

ABSTRACT

Correlations are proposed for the wet surface ratio of a fin-and-tube heat exchanger with plain and wavy fin geometry under dehumidifying conditions. The 'Finite Circular Fin Method' (FCFM) is used for data reduction. It is found that the percentage of wet surface area increases with increasing fin spacing or number of tube rows and decreasing Reynolds number. Despite the addition of tube rows or reduced fin spacing the effective surface area is increased, and its influence on a partially wet surface is apparently the opposite. This is because adding tube rows will provide a more effective temperature drop in air flow than adding fins, Moreover, the heat and mass transfer characteristics of j_h and j_m increase with an increase in the area of wet surface. Correlations for prediction of the percentage of wet surface area are proposed. These correlations can describe 83.81% of the area of wet surface to within ±10%.

1. Introduction

Fin-and-tube heat exchangers are widely-used heat transfer devices in association with applications like refrigeration and air-conditioning systems. They can be applicable to both condensers and evaporators. For a typical evaporator, the outside surface temperature of the heat exchanger is generally below the dew point temperature, and therefore condensation of water vapour takes place around the outside surfaces. As a result, simultaneous heat and mass transfer occurs and it becomes even more complicated as the condensate may interact with the air flow, yet may result in full or partial condensation along the surface. In this regard, detailed simulation of the performance of the heat exchanger is rather difficult.

The heat and mass transfer characteristics of fin-and-tube heat exchangers have been studied by many researchers (McQuiston [1,2], Beecheer and Fagan [3], Yan and Sheen [4], Mirth and Ramadhyani [5,6], Wang et al. [7–13], Pirompugd et al. [14–19]). The published data were mainly focused, however, on sensible heat transfer characteristics rather than on mass transfer characteristics. Moreover, in a typical operation some outside surface temperature is higher than the dew point temperature while the other surface is lower than the dew point temperature, indicating a partially wet surface. There were even limited studies dealing with the heat and mass transfer characteristics of fin-and-tube heat exchangers under partially wet surface conditions. Pirompugd et al. [16,17] presented the fully wet and fully dry tiny circular fin method for evaluation of heat and mass transfer characteristics under fully wet and partially wet surface conditions. Xia and Jacobi [20] formulated the logarithmic-mean temperature difference (LMTD) and logarithmic-mean enthalpy difference (LMED) methods for fully dry, fully wet, partially wet and frosted surface conditions. Pirompugd et al. [18,19] developed a new mathematical reduction method, the 'Finite Circular Fin Method (FCFM)' for fin-and-tube heat exchangers under fully dry, fully wet and partially wet surface conditions. The FCFM is capable of dividing a fin-and-tube heat exchanger into many tiny segments through which the detailed surface conditions (fully dry, fully wet, or partially wet) are taken into account. In this study, the objective is to investigate the effect of a partially wet surface on the heat and mass transfer characteristics of the plain and wavy fin-and-tube heat exchanger based on the FCFM methodology.

2. Experimentation

The experimental apparatus can be found in Pirompugd et al. [18,19]. A total of fifteen plain fin-and-tube heat exchangers and eighteen wavy fin-and-tube heat exchangers with various geometric parameters are tested in this study. The details of test samples are shown in Tables 1 and 2. The test conditions approximate those encountered with typical fan-coils and evaporators of air-conditioning applications.

* Corresponding author. Tel.: +66 818048996.
E-mail address: worapiro@yahoo.com (W. Pirompugd).

0017-9310/$ - see front matter © 2009 Elsevier Ltd. All rights reserved.
doi:10.1016/j.ijheatmasstransfer.2009.09.025

Nomenclature

A_o	total surface area, m^2	P_d	wave height, m
A_{wet}	outside surface area of wet portion, m^2	P_l	longitudinal tube pitch, m
D_c	collar diameter, m	P_t	transverse tube pitch, m
F_p	fin pitch, m	Re_{Dc}	moist air-side Reynolds number based on the collar diameter
j_h	Colburn heat transfer group or Chilton-Colburn j-factor for the heat transfer	RH_{in}	inlet relative humidity
j_m	Colburn mass transfer group or Chilton-Colburn j-factor for the mass transfer	S_p	fin spacing, m
N	number of tube row	t	fin thickness, m
		X_f	projected fin length, m

Table 1
Geometric dimensions of the sample plain fin-and-tube heat exchangers.

No.	F_p (mm)	t (mm)	D_c (mm)	P_t (mm)	P_l (mm)	N
1	1.19	0.115	8.51	25.4	19.1	1
2	1.75	0.120	10.34	25.4	22.0	1
3	1.23	0.115	8.51	25.4	19.1	2
4	1.23	0.115	7.53	21.0	12.7	2
5	1.23	0.115	10.23	25.4	19.1	2
6	1.82	0.130	10.23	25.4	22.0	2
7	1.23	0.115	10.23	25.4	19.1	4
8	1.23	0.115	7.53	21.0	12.7	4
9	1.55	0.115	10.23	25.4	19.1	4
10	1.60	0.115	8.51	25.4	19.1	4
11	2.03	0.130	10.23	25.4	22.0	4
12	2.31	0.115	10.23	25.4	19.1	4
13	1.85	0.130	10.23	25.4	22.0	6
14	2.21	0.130	10.23	25.4	22.0	6
15	3.16	0.130	10.23	25.4	22.0	6

The test conditions of the inlet-air are as follows:

Dry-bulb temperature of the air	27 ± 0.5 °C
Inlet relative humidity for the incoming air	50% and 90%
Inlet-air velocity	From 0.3 to 4.5 m/s
Inlet-water temperature	7 ± 0.5 °C
Water velocity inside the tube	1.5–1.7 m/s

3. Data reduction

In the present study, the 'Finite Circular Fin Method (FCFM)' published in our previous literature (Pirompugd et al. [18,19]) is used for calculating the heat and mass transfer characteristics of a fin-and-tube heat exchanger. The heat exchanger is divided into many tiny segments by number of tube rows, number of tube passes per row and number of fins. The surface conditions of each tiny segment can be fully wet, partially wet, or fully dry. If the surface is fully wet, the fin tip temperature is lower than the dew point temperature of moist air. Both sensible and latent heat transfers take place along this tiny segment. For the second case, where partially wet conditions prevail, in which the outside tube (including collar) temperature is lower than the dew point temperature, part of the fin temperature is higher than the dew point temperature. The last case is the fully dry condition, in which the outside tube (including collar) temperature is higher than the dew point temperature, yet only sensible heat transfer occurs on the whole area of this tiny segment. In this study, FCFM is used to explain the heat and mass transfer characteristics of fin-and-tube heat exchangers. The reduced results of the heat and mass transfer characteristics are presented in terms of dimensionless groups of j_h and j_m, respectively.

4. Results and discussion

In practice it is very interesting to examine the wet/dry surface distribution pertaining to influences such as inlet conditions and flow conditions. The partially dry condition becomes even more conspicuous when the inlet humidity is reduced. Fig. 1 shows the percentage of wet surface area for all the test samples with an inlet relative humidity of 50%. As seen from the figure, at a very low Reynolds number (<1000), the partially dry surface is hardly seen, yet

Table 2
Geometric dimensions of the sample wavy fin-and-tube heat exchangers.

No.	F_p (mm)	t (mm)	D_c (mm)	P_t (mm)	P_l (mm)	P_d (mm)	X_f (mm)	N
1	1.60	0.12	10.38	25.4	19.05	1.18	4.7625	1
2	1.64	0.12	8.62	25.4	19.05	1.58	4.7625	1
3	2.82	0.12	10.38	25.4	19.05	1.18	4.7625	1
4	2.92	0.12	8.62	25.4	19.05	1.58	4.7625	1
5	3.54	0.12	8.62	25.4	19.05	1.58	4.7625	1
6	3.63	0.12	8.62	25.4	25.40	1.68	6.3500	1
7	1.69	0.12	8.62	25.4	19.05	1.18	4.7625	2
8	1.71	0.12	8.62	25.4	19.05	1.58	4.7625	2
9	3.12	0.12	8.62	25.4	19.05	1.58	4.7625	2
10	3.17	0.12	8.62	25.4	19.05	1.18	4.7625	2
11	1.64	0.12	8.62	25.4	19.05	1.58	4.7625	4
12	1.70	0.12	8.62	25.4	19.05	1.18	4.7625	4
13	3.07	0.12	8.62	25.4	19.05	1.58	4.7625	4
14	3.14	0.12	8.62	25.4	19.05	1.18	4.7625	4
15	1.57	0.12	10.38	25.4	19.05	1.18	4.7625	6
16	1.65	0.12	8.62	25.4	19.05	1.58	4.7625	6
17	2.82	0.12	10.38	25.4	19.05	1.18	4.7625	6
18	3.06	0.12	8.62	25.4	19.05	1.58	4.7625	6

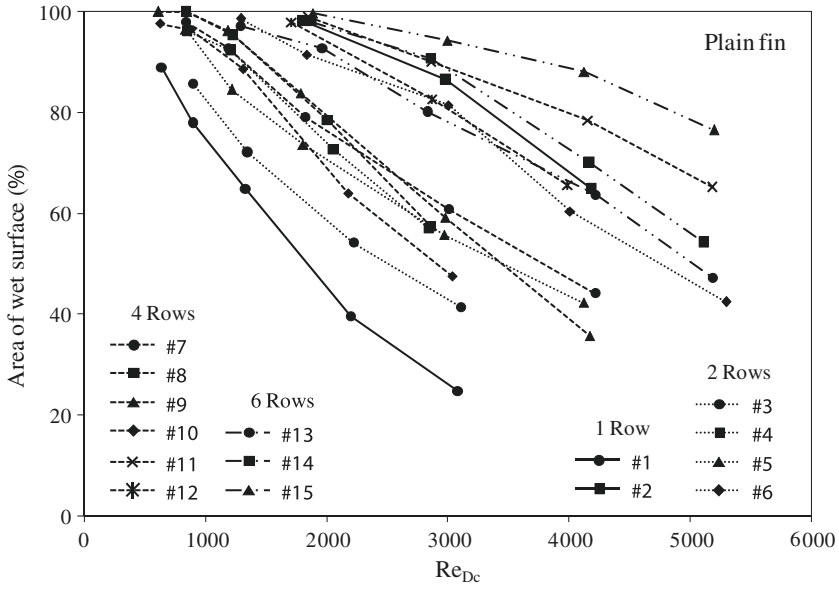

Fig. 1. Area of wet surface percentage plotted against Reynolds number.

the percentage of wet surface area drops with the rise of the Reynolds number. This is because a higher Reynolds number results in higher heat transfer coefficient, thereby leading to a smaller temperature difference and corresponding to a higher surface temperature. In this context, the temperature of part of the fin surface may exceed that of the dew point temperature and become partially dry. This phenomenon becomes more evident when the number of tube rows is reduced or when the fin spacing is reduced. Again, one of the reasons may be attributed to the heat transfer coefficient. The heat transfer coefficient usually decreases with the number of tube rows (Wang et al. [8]). This may not, however, be the main cause. As air flows into the heat exchanger under dehumidifying conditions, the temperature of the air flow decreases along the air flow direction, resulting in a rise of relative humidity as the number of tube rows rises. In essence, the surface can become wet more easily. Moreover, one can see that the percentage of the wet surface area is increased with the increase of the fin spacing. In the beginning, with more fins being added (smaller fin spacing), it is expected that the temperature of air flow will drop and should exhibit the same results as obtained when tube rows are added. The results, however, are the opposite of what we originally expected. Although extra tube rows and extra

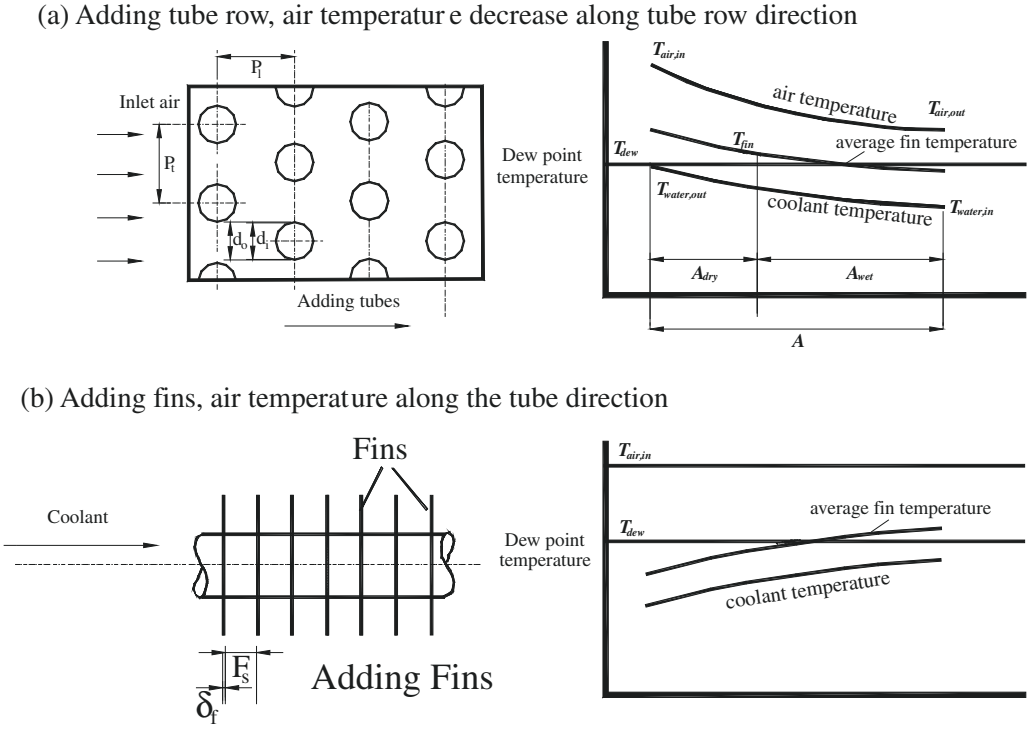

Fig. 2. A schematic showing the difference in adding surface amid adding tube rows and reducing fin spacing.

fins act similarly in increasing surface temperature, they are not the same in fact. The following schematic shows the difference between adding rows and adding fins. Note that the coolant flows into the heat exchangers parallel to each row, so adding rows may effectively reduce the air temperature along the flow direction, as seen in Fig. 2(a). In the meantime, the coolant in the tube is rising with further reduction in fin spacing (adding fins). As shown in Fig. 2(b), the inlet-air temperature remains unchanged by the addition of fins despite the average air temperature being slightly reduced. It becomes less evident for air flow temperature to fall below the dew point temperature. Accordingly, adding surface by reducing fin spacing reveals less partially wet conditions compared with adding tube rows. In fact, adding tubes is more like 'mixed flow', whereas adding fins produces a more 'unmixed' flow situation.

The heat and mass transfer characteristics are presented in the dimensionless terms of j_h and j_m, respectively. In Fig. 3a and b, the transfer characteristic of j_h and j_m increases with an increase of wet surface. In the present study, the percentage of the wet portion depends on the moist air velocity. Raising the air velocity means that the convective heat and mass transfer coefficient will be increased but the percentage of the wet portion dwindles considerably, indicating a drop in the heat and mass transfer characteristic of j_h and j_m. Moreover, it can be seen that the j_h and j_m drop with an increase of the fin spacing. This phenomenon can be described from the flow field within the fin passage. In the numerical simulation (Torikoshi et al. [21]), the entire flow region can be kept laminar and steady and the vortex forming behind the tube can be suppressed for the tight fin. The cross-stream width of the vortex region behind the tube will take place when the fin spacing increases. Then,

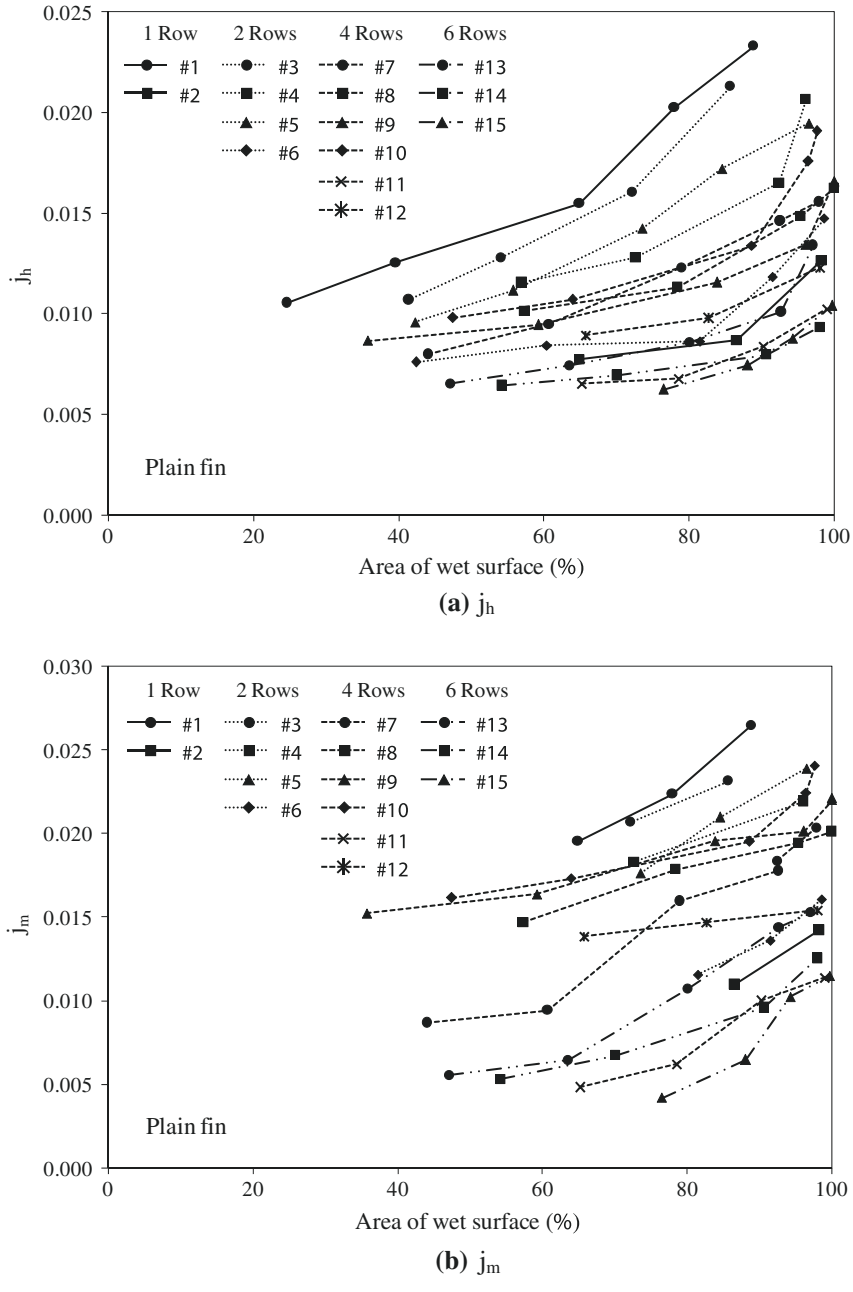

(a) j_h

(b) j_m

Fig. 3. j_h and j_m plotted against area of wet surface.

Table 3
Coefficients for the correlations.

Type	N	a_1	a_2	a_3	a_4	b_1	b_2	b_3	b_4
Plain	1	0	0	374.2	79.1	0	0	0.0115	−0.0020
	2	−391,566.8	173,756.3	−24,895.6	1272.9	−3.7345	1.6463	−0.2373	0.0109
	4	101,167.3	−49,475.7	7893.4	−281.7	−0.7475	0.3840	−0.0629	0.0030
	6	0	−5827.6	2608.3	−143.7	0	0.0084	−0.0031	0.0001
Wavy	1	0	0	−3.0062	187.3	0	0	0.0012	−0.0008
	2	0	0	−1497.3	406.8	0	0	−0.0395	0.0070
	4	0	10,363.9	−5247.6	709.7	0	−0.0786	0.0413	−0.0050
	6	−24,596.9	19,730.9	−5083.2	501.7	0.1308	−0.1024	0.0259	−0.0021

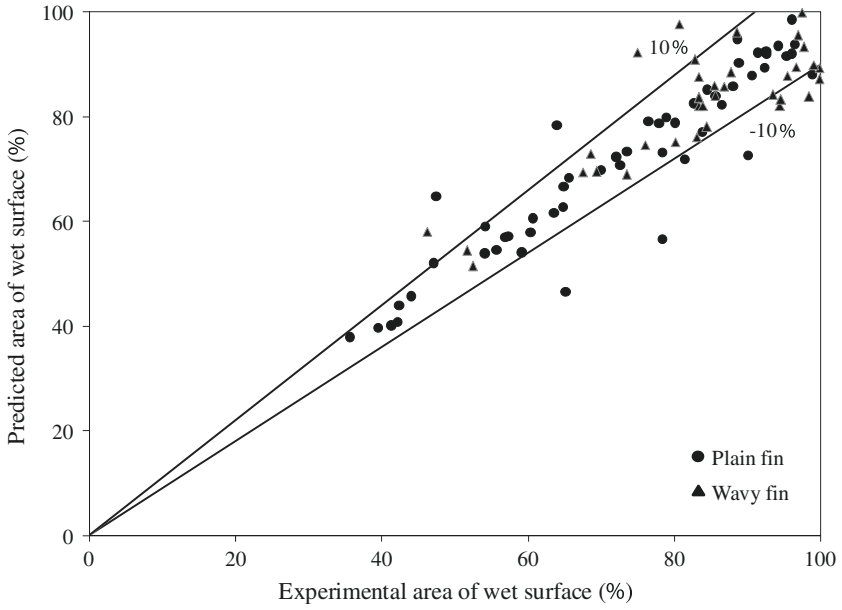

Fig. 4. Comparison of the area of wet surface between those obtained from the correlation and those obtained from experiment.

the j_h and j_m decrease with the increase in fin spacing for one-row configuration, indicating a detectable influence of fin spacing. The effect of fin spacing on j_h can be negligible when the number of tube rows is increased. This is because with the increasing number of tube rows the subsequent row can block the condensate blow-off phenomenon from the preceding row.

Using a multiple linear regression technique in a range of experimental data ($300 < Re_{Dc} < 5500$, $RH_{in} \approx 50\%$), we present the appropriate correlations of the percentage area of wet surface based on the present data as follows:

$$\frac{A_{wet}}{A_o} = \left(a_1\left(\frac{S_p}{D_c}\right)^3 + a_2\left(\frac{S_p}{D_c}\right)^2 + a_3\frac{S_p}{D_c} + a_4\right) \times e^{\left(\left(b_1\left(\frac{S_p}{D_c}\right)^3 + b_2\left(\frac{S_p}{D_c}\right)^2 + b_3\frac{S_p}{D_c} + b_4\right)Re_{D_C}\right)} \quad (1)$$

The coefficients for the equation are shown in Table 3. Detailed comparisons of the proposed correlations against the experimental data are shown in Fig. 4. It is found that the correlations can describe 83.81% of the area of the wet surface within 10%.

5. Conclusions

This study explored the partially wet characteristics of fin-and-tube heat exchangers with the help of the FCFM reduction method. A total of fifteen plain fin-and-tube heat exchangers and eighteen wavy fin-and-tube heat exchangers were tested and compared. On the basis of previous discussions, the following conclusions were drawn:

1. The percentage of wet surface area increases with the increase of the Reynolds number or fin spacing or the number of tube rows. Whether tube rows are added or fin spacing is reduced, the effective surface area is increased, and its influence on partially wet surfaces is apparently the converse. This is because adding tube rows will provide more effective temperature drop of air flow than the addition of fins.
2. The heat and mass transfer characteristic of j_h and j_m increases with an increase in the area of wet surface.
3. Correlations applicable to the present fin-and-tube heat exchangers are proposed. These correlations can describe 83.81% of the area of wet surface within ±10%.

Acknowledgments

The authors are indebted to the Thailand Research Fund (TRF), Commission on Higher Education of Thailand (CHE), Support Fund for Research and Development (No. 22/2552) from Faculty of Engineering, Burapha University, and the Energy R&D foundation funding from the Bureau of Energy of the Ministry of Economic Affairs, Taiwan, for supporting this study.

References

[1] F.C. McQuiston, Heat mass and momentum transfer data for five plate-fin tube transfer surface, ASHRAE Trans. 1 84 (1978) 266–293.
[2] F.C. McQuiston, Correlation of heat, mass and momentum transport coefficients for plate-fin-tube heat transfer surfaces with staggered tubes, ASHRAE Trans. 1 84 (1978) 294–309.
[3] D.T. Beecher, T.J. Fagan, Effects of fin pattern on the air-side heat transfer coefficient in plate finned-tube heat exchanger, ASHRAE Trans. 93 (2) (1987) 1961–1984.
[4] W.M. Yan, P.J. Sheen, Heat transfer and friction characteristics of fin-and-tube heat exchangers, Int. J. Heat Mass Transfer 43 (2000) 1651–1659.
[5] D.R. Mirth, S. Ramadhyani, Prediction of cooling-coils performance under condensing conditions, Int. J. Heat Fluid Flow 14 (4) (1993) 391–400.
[6] D.R. Mirth, S. Ramadhyani, Correlations for predicting the air-side Nusselt numbers and friction factors in chilled-water cooling coils, Exp. Heat Transfer 7 (1994) 143–162.
[7] C.C. Wang, W.L. Fu, C.T. Chang, Heat transfer and friction characteristics of typical wavy fin-and-tube heat exchangers, Exp. Therm. Fluid Sci. 14 (2) (1997) 174–186.
[8] C.C. Wang, Y.C. Hsieh, Y.T. Lin, Performance of plate finned tube heat exchangers under dehumidifying conditions, J. Heat Transfer 119 (1997) 109–117.
[9] C.C. Wang, Y.M. Tsi, D.C. Lu, Comprehensive study of convex-louver and wavy fin-and-tube heat exchangers, AIAA J. Thermophys. 12 (3) (1998) 423–430.
[10] C.C. Wang, Y.T. Lin, C.J. Lee, Investigation of wavy fin-and-tube heat exchangers: a contribution to data bank, Exp. Heat transfer 12 (1999) 73–89.
[11] C.C. Wang, K.U. Chi, Heat transfer and friction characteristics of plain fin-and-tube heat exchangers: part I: new experimental data, Int. J. Heat Mass Transfer 43 (2000) 2681–2691.
[12] C.C. Wang, Y.M. Hwang, Y.T. Lin, Empirical correlations for heat transfer and flow friction characteristics of herringbone wavy fin-and-tube heat exchangers, Int. J. Refrig. 25 (2002) 673–680.
[13] C.C. Wang, J. Lo, Y.T. Lin, C.S. Wei, Flow visualization of annular and delta winglet vortex generators in fin-and-tube heat exchanger application, Int. J. Heat Mass Transfer 45 (2002) 3803–3815.
[14] W. Pirompugd, S. Wongwises, C.C. Wang, A tube-by-tube reduction method for simultaneous heat and mass transfer characteristics for plain fin-and-tube heat exchangers in dehumidifying conditions, Heat Mass Transfer 41 (8) (2005) 756–765.
[15] W. Pirompugd, S. Wongwises, C.C. Wang, Simultaneous heat and mass transfer characteristics for wavy fin-and-tube heat exchangers under dehumidifying conditions, Int. J. Heat Mass Transfer 49 (3–4) (2006) 132–143.
[16] W. Pirompugd, C.C. Wang, S. Wongwises, A fully wet and fully dry tiny circular fin method for heat and mass transfer characteristics for plain fin-and-tube heat exchangers under dehumidifying conditions, J. Heat Transfer 129 (9) (2007) 1256–1267.
[17] W. Pirompugd, C.C. Wang, S. Wongwises, Heat and mass transfer characteristics for finned tube heat exchangers with humidification, J. Thermophys. Heat Transfer 21 (2) (2007) 361–371.
[18] W. Pirompugd, C.C. Wang, S. Wongwises, Finite circular fin method for heat and mass transfer characteristics for plain fin-and-tube heat exchangers under fully and partially wet surface conditions, Int. J. Heat Mass Transfer 50 (3–4) (2007) 552–565.
[19] W. Pirompugd, C.C. Wang, S. Wongwises, Finite circular fin method for wavy fin-and-tube heat exchangers under fully and partially wet surface conditions, Int. J. Heat Mass Transfer 51 (15–16) (2008) 4002–4017.
[20] Y. Xia, A.M. Jacobi, Air-side data interpretation and performance analysis for heat exchangers with simultaneous heat and mass transfer: Wet and frosted surfaces, Int. J. Heat and Mass Transfer 48 (2005) 5089–5102.
[21] K. Torikoshi, G. Xi, Y. Nakazawa, H. Asano, Flow and heat transfer performance of a plate-fin and tube heat Exchanger (1st report: effect of fin pitch), Tenth International Heat Transfer Conference, 1994, paper 9-HE-16, 1994, pp. 411–416.

International Journal of Heat and Mass Transfer 53 (2010) 334–344

Contents lists available at ScienceDirect

International Journal of Heat and Mass Transfer

journal homepage: www.elsevier.com/locate/ijhmt

An experimental study on the heat transfer performance and pressure drop of TiO_2-water nanofluids flowing under a turbulent flow regime

Weerapun Duangthongsuk, Somchai Wongwises *

Fluid Mechanics, Thermal Engineering and Multiphase Flow Research Laboratory (FUTURE), Department of Mechanical Engineering, King Mongkut's University of Technology Thonburi, Bangmod, Bangkok 10140, Thailand

ARTICLE INFO

Article history:
Received 9 February 2009
Received in revised form 21 August 2009
Accepted 21 August 2009
Available online 6 October 2009

Keywords:
Nanofluid
Heat transfer coefficient
Friction factor
Particle concentration

ABSTRACT

Nanofluid is a new class of heat transfer fluids engineered by dispersing metallic or non-metallic nanoparticles with a typical size of less than 100 nm in the conventional heat transfer fluids. Their use remarkably augments the heat transfer potential of the base liquids. This article presents the heat transfer coefficient and friction factor of the TiO_2-water nanofluids flowing in a horizontal double tube counter-flow heat exchanger under turbulent flow conditions, experimentally. TiO_2 nanoparticles with diameters of 21 nm dispersed in water with volume concentrations of 0.2–2 vol.% are used as the test fluid. The results show that the heat transfer coefficient of nanofluid is higher than that of the base liquid and increased with increasing the Reynolds number and particle concentrations. The heat transfer coefficient of nanofluids was approximately 26% greater than that of pure vol.%, and the results also show that the heat transfer coefficient of the nanofluids at a volume concentration of 2.0 vol.% was approximately 14% lower than that of base fluids for given conditions. For the pressure drop, the results show that the pressure drop of nanofluids was slightly higher than the base fluid and increases with increasing the volume concentrations. Finally, the new correlations were proposed for predicting the Nusselt number and friction factor of the nanofluids, especially.

1. Introduction

Conventional heat transfer fluids such as oil, water and ethylene glycol are widely used in many industries, including power generation, chemical processes, heating and cooling processes, transportation, microelectronics and other micro-sized applications. In general, the heat transfer performance of these fluids is restricted by their poor thermal properties compared to those of most solids. This is the important reason why the development of heat transfer devices is retarded. Based on industrial needs, the enhancement techniques meet an astronomical increase in heat flux and high degree of compactness of the heat transfer equipment. So, a search for high efficiency heat transfer fluid is a challenging task for today. In recent years, many researchers have attempted to develop special classes of heat transfer fluids for augmentation of their heat transfer properties. An innovative method is to suspend small solid particles in the common fluid to form fluid slurries. Different types of solid particles, such as metallic, non-metallic and polymeric can be added into fluids. In the early studies, however, use of suspended particles of millimetre or even micrometre-size demonstrated unusually high thermal enhancement, but some extreme problems are also experienced, such as poor stability of the suspension, clogging of flow channels, eroding of pipelines and increase in pressure drop in practical applications. Although the solutions show better thermal performance compared to common heat transfer fluids, they are still not suitable for use as heat transfer fluids in practical applications, especially for the mini and/or micro-channel or even electronic cooling equipment.

A decade ago, with the rapid development of modern nanotechnology, particles of nanometre-size (normally less than 100 nm) are used instead of micrometre-size for dispersing in base liquids, and they are called nanofluids. This term was first suggested by Choi [1] in 1995, and it has since gained in popularity. Compared with millimetre or micrometre sized particle suspensions, a number of researchers have reported that nanofluids have shown a number of potential advantages, such as better long-term stability, little penalty in pressure drop, and can have significantly greater thermal conductivity. As a result, many researchers have investigated the heat transfer performance and flow characteristics of various nanofluids with different nanoparticles and base fluid materials. Several following existing published articles which associate with the use of nanofluids are described in the following sections.

Pak and Cho [2] investigated experimentally the heat transfer performance of γ-Al_2O_3 and TiO_2 nanoparticles dispersed in water flowing in a horizontal circular tube with a constant heat flux

* Corresponding author. Tel.: +662 470 9115; fax: +662 470 9111.
E-mail address: somchai.won@kmutt.ac.th (S. Wongwises).

0017-9310/$ - see front matter © 2009 Elsevier Ltd. All rights reserved.
doi:10.1016/j.ijheatmasstransfer.2009.09.024

Nomenclature

C_p	specific heat, J/kg K
d	nanoparticle diameter, m
D	tube diameter, m
f	friction factor
h	heat transfer coefficient, W/m^2 K
k	thermal conductivity, W/m K
L	length of the test tube, m
$\dot{m}$	mass flow rate, kg/s
Nu	Nusselt number
ΔP	Pressure drop, Pa
Pe	Peclet number
Pr	Prandtl number
q	heat flux, W/m^2
Q	heat transfer rate, W
Re	Reynolds number
T	temperature, °C
u	mean velocity, m/s
$\dot{V}$	volume flow rate, m^3/s

Greek symbols

ϕ	volume fraction
ε	tube roughness
ρ	density, kg/m^3
α	thermal diffusivity
μ	viscosity, kg/ms

Subscripts

ave	average
f	fluid
h	heating fluid
in	inlet
m	mean
out	outlet
p	particles
nf	nanofluid
w	water
wall	tube wall

under turbulent flow conditions. The results showed that the Nusselt number of nanofluids increased with increasing Reynolds number and the volume concentration. However, they still found that the convective heat transfer coefficient of the nanofluids with 3 vol.% nanoparticles was 12% lower than that of pure water at a given condition. Finally, a new heat transfer correlation for predicting the convective heat transfer coefficient of nanofluids in a turbulent flow regime was proposed.

Li and Xuan [3] and Xuan and Li [4] studied experimentally the convective heat transfer and flow features for Cu-water nanofluids flowing through a straight tube under laminar and turbulent flow regimes with a constant heat flux. The experimental results showed that addition of nanoparticles into the base liquid remarkably enhanced the heat transfer performance of the base liquid. Moreover, the friction factor of nanofluids coincided well with that of the water. They also proposed new convective heat transfer correlations for calculating the heat transfer coefficients of the nanofluid for both laminar and turbulent flow conditions.

Tsai et al. [5] studied experimentally gold-DI water nanofluids flowing in a conventional heat pipe. The experimental results illustrated that use of the nanofluids led to a significant reduction in the thermal resistance of the heat pipe when compared with DI water at given concentrations.

Wen and Ding [6] investigated the convective heat transfer coefficient of Al_2O_3-DI water flowing through a copper tube under a constant heat flux for a laminar flow regime and placed emphasis on the entrance region in particular. Their results showed that the local heat transfer coefficient increased with increasing the Reynolds number as well as the volume concentration of nanofluids.

Yang et al. [7] investigated the convective heat transfer coefficient of graphite nanoparticles dispersed in two liquids flowing in a horizontal tube heat exchanger under laminar flow conditions. Their results showed that the heat transfer coefficient increased with the Reynolds number and the particle volume concentration. Furthermore, two graphite nanoparticle sources at the same particle loading gave different values of heat transfer coefficient. Finally, they proposed a new heat transfer correlation to predict the heat transfer coefficient of nanofluids under laminar flow conditions.

Ding et al. [8] reported on an experiment in which the local heat transfer coefficient of CNT-distilled water nanofluids flowing through a tube under a laminar flow regime. They found that the local heat transfer coefficient of CNT nanofluids is much greater than that of pure water, and the enhancement depends on the flow conditions, CNT concentration and the PH value. However, they reported that the effect of pH value is smallest compared with other parameters. They also suggest that the aspect ratio should be associated with the high enhancement of heat transfer performance of CNTs based nanofluids [9].

Heris et al. [10,11] studied experimentally the heat transfer performance of Al_2O_3-water and CuO-water nanofluids flowing in an annular concentric tube under constant wall temperature boundary condition for a laminar flow regime. The results indicated that the heat transfer coefficient increased with an increasing Peclet number as well as particle volume concentration, and CuO-water nanofluids showed smaller heat transfer enhancement than Al_2O_3-water nanofluid.

He et al. [12] investigated the heat transfer performance and flow characteristic of TiO_2-distilled water nanofluids flowing through a vertical pipe in an upward direction under a constant heat flux in both a laminar and a turbulent flow regime. Their results indicated that the local heat transfer coefficient increased with increasing nanoparticle concentration in both laminar and turbulent flow regimes at a given Reynolds number and particle size. Moreover, the results showed that the pressure drop of the nanofluids was very close to that of the base fluid.

Nguyen et al. [13] reported on an experiment in which the heat transfer coefficient of Al_2O_3 nanoparticles was dispersed in water flowing through a liquid cooling system of microprocessors under turbulent flow condition. They found that the nanofluid gave a higher heat transfer coefficient than the base liquid. Moreover, the results also showed that the nanofluid with a 36 nm particle diameter gave higher heat transfer coefficient than the nanofluid with a 47 nm particle diameter.

Ko et al. [14] investigated the pressure drop and viscosity of carbon nanotubes dispersed in distilled water flowing through a horizontal tube and also reported the effect of the CNT concentrations and preparation methods on the viscosity of nanofluids. Their results showed that the nanofluids prepared by acid treatment (TCNT) have much smaller viscosity than the ones made with surfactant (PCNT). Under laminar flow conditions, the friction factor of the PCNT nanofluids is much higher than that of the TCNT nanofluids. Moreover, both nanofluids show larger friction factors than the base fluid. In contrast, under turbulent flow conditions, the friction factor of both nanofluids becomes similar to that of the base fluids as the flow rate increases.

Chein and Chuang [15] reported experimentally on microchannel heat sink (MCHS) performance using CuO-water nanofluids as coolants.

The thermal and physical properties of nanofluids were calculated using the following equations: the Brinkman equation [16] for viscosity, the Xuan and Roetzel equation [17] for specific heat, and the Hamilton and Crosser model [18] for thermal conductivity. The results showed that the presence of nanoparticles creates greater energy absorption than pure water at a low flow rate and that there is no contribution from heat absorption when the flow rate is high.

Duangthongsuk and Wongwises [19,20] investigated the effect of thermophysical properties models on prediction of the heat transfer coefficient and also reported the heat transfer performance and friction characteristics of nanofluid, respectively. The 0.2 vol.% TiO_2 naoparticles are used to disperse in the water. The results showed that the various thermophysical models have no significant effect on the predicted values of Nusselt number of the nanofluid. The results also indicated that the heat transfer coefficient of nanofluid is slightly greater than that of water by approximately 6–11% and use of nanofluid has little penalty in pressure drop.

However, the previous work of the authors did not examine the effect of the particle concentrations on heat transfer and pressure drop of nanofluids. The authors used the existing thermophysical property model to calculate the thermal conductivity and viscosity of nanofluids, which may have caused a small error in the results. In vies of that consequence, this article is aimed at reporting the effect of particle concentration on the heat transfer performance and pressure drop of nanofluids experimentally. Moreover, the thermal conductivity and viscosity of nanofluids are measured. Finally, new heat transfer and friction factor correlations of nanofluids are proposed.

2. Sample preparation

The term 'nanofluid', meaning a two-phase mixture usually consists of nanoparticles dispersed in common liquids. In order to prepare the nanofluids by dispersing the nanoparticles in a base fluid, proper mixing, and stabilisation of the particles is required. There are three effective methods used to attain stability of suspension against sedimentation of nanoparticles, and these are summarised as follows: (1) control of ph value of the suspensions, (2) addition of surface activators or surfactants, (3) use of ultrasonic vibration. All of these techniques aim at changing the surface properties of suspended nanoparticles and suppressing formation of the cluster of particles, in order to obtain stable suspensions. In the present study, nanofluids provided by a commercial source (DEGUSSA, VP Disp. W740×) are used. This mixture is composed of TiO_2 nanoparticles with average diameter of 21 nm, dispersed in water. The original particle concentration was 40 wt%. In order to produce other required particle volume fractions, dilution with water followed by a stirring action was effected. Moreover, an ultrasonic vibrator was used to sonicate the solution continuously for approximately 2 h in order to break down agglomeration of the nanoparticles. The desired volume concentrations used in this study are 0.2%, 0.6%, 1.0%, 1.5% and 2.0%, with pH values of 7.5, 7.1, 7.0, 6.8 and 6.5, respectively. From the pH values, it can be seen that the solution chemistry of nanofluids is nearly neutral in nature. A transmission electron microscope (TEM) was used to approximate the size of the primary nanoparticles. As shown in Fig. 1, it is clear that the primary shape of nanoparticles is approximately spherical, with an average diameter of approximately 21 nm.

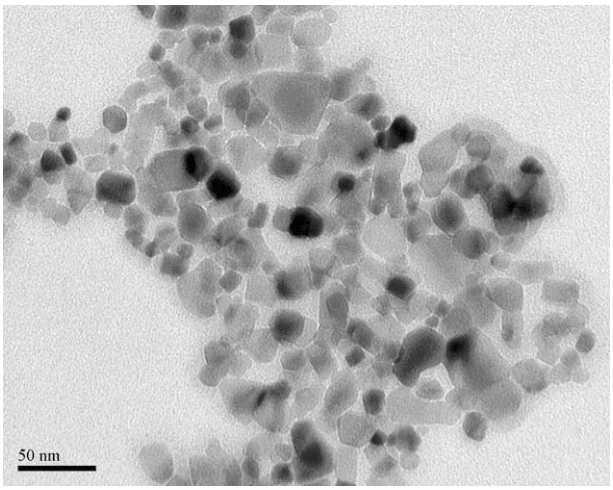

Fig. 1. TEM image of dispersed TiO_2 nanoparticles in water.

3. Experimental apparatus

3.1. Convective heat transfer coefficient and pressure drop of nanofluids

The experimental apparatus used in this study is shown schematically in Fig. 2a. It mainly consists of a test section, two receiver tanks, a magnetic gear pump, a hot water pump, a cooler tank, a hot water tank and a collection tank. The test section is a 1.5 m long counter-flow horizontal double tube heat exchanger with nanofluid flowing inside the tube while hot water flows in the annular. The inner tube is made from smooth copper tubing with a 9.53 mm outer diameter and an 8.13 mm inner diameter, while the outer tube is made from PVC tubing and has a 33.9 mm outer diameter and 27.8 mm inner diameter. The test section is thermally isolated from its upstream and downstream sections by plastic tubes in order to reduce heat loss along the axial direction. The differential pressure transmitter and T-type thermocouple are mounted at both ends of the test section to measure pressure drop and the bulk temperature of the nanofluid, respectively. Thermocouples are mounted at different longitudinal positions on the inner tube surface of the wall, each with three thermocouples equally space around the tube circumference. The inlet and exit temperatures of hot water are measured using T-type thermocouples which are inserted directly into the flow. The receiver tanks of 60 L capacity are made from stainless steel to store the nanofluid and hot water leaving from the test section. The cooler tank with a 4.2 kW cooling capacity and a thermostat is used to keep the nanofluid temperature constant. Similar to the cooler tank, a 3 kW electric heater with a thermostat was installed to keep the temperature of the hot water constant. The nanofluid flow rate is controlled by adjusting the rotation speed of the magnetic gear pump. The hot water flow rate is measured by a rotameter whereas the nanofluids flow rate is evaluated by the time taken for a given volume of nanofluid to be discharged.

In the present study, the differential pressure transmitter was calibrated using an air operated dead weight tester. The uncertainty of the pressure measurement is ±0.030 kPa. Then, a portable programmable calibrator having a maximum precision of 0.1 °C was used to calibrate all of the T-type thermocouples. Furthermore, the nanofluid flow rates were determined by electronic balance. The uncertainty of the electronic balance is ±0.0006 kg. Therefore, the uncertainty of the measured heat transfer coefficient is approximately 5%.

During the test run, wall temperatures of the test section, mass flow rates of the hot water and nanofluids, the pressure difference in the nanofluid, the inlet and exit temperatures of the hot water and nanofluids were recorded.

3.2. Measurement of the thermal conductivity and viscosity of nanofluid

The thermal conductivity and viscosity of the nanofluids are important thermophysical properties. In order to apply the nanofluids

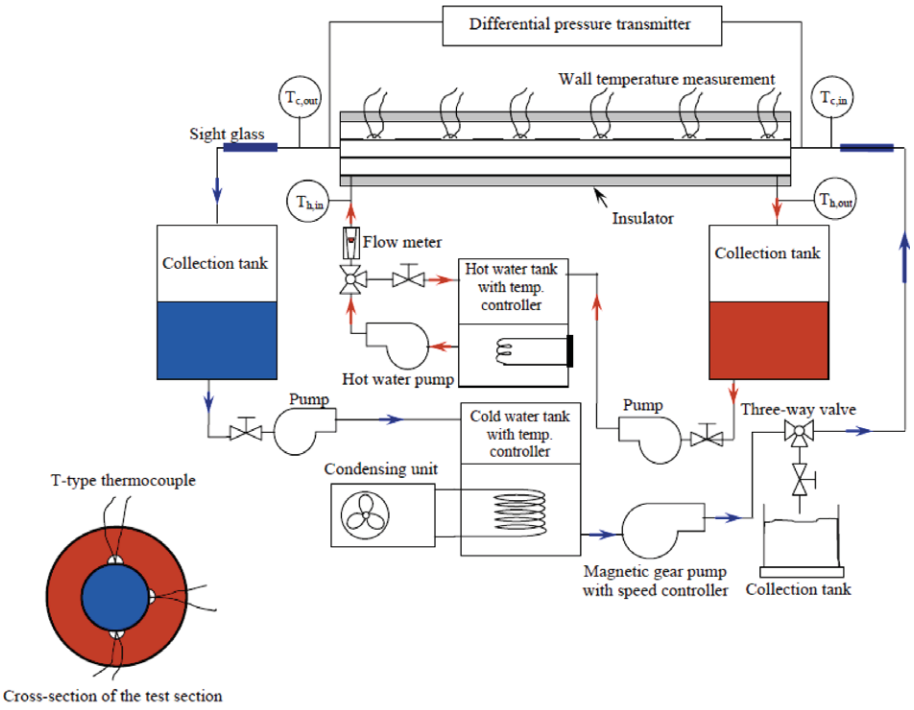

(a) Convective heat transfer coefficient and pressure drop

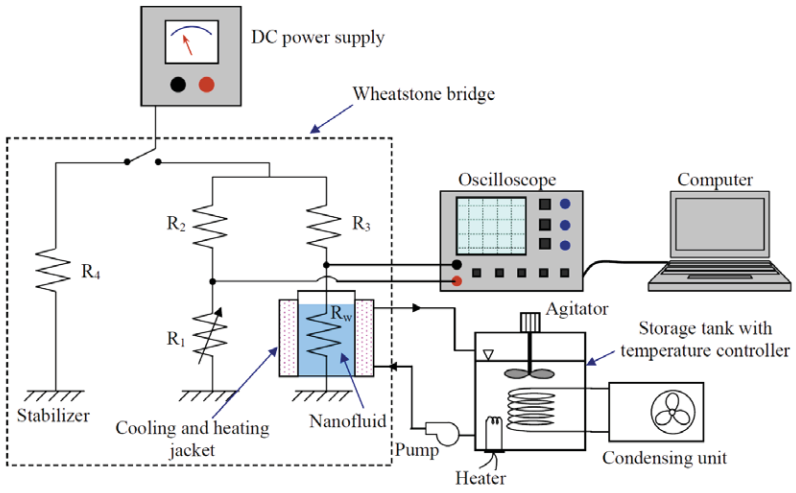

(b) Transient hot-wire apparatus

Fig. 2. Schematic diagram of the experimental apparatus.

for the practical application, the exact value of thermal conductivity and viscosity of nanofluids are needed. In the case of thermal conductivity, the transient hot-wire technique is used to measure the thermal conductivity of nanofluids. The experimental system of the transient hot-wire method is shown schematically in Fig. 2b. The main parts consist of the Wheatstone bridge, and cooling and heating jacket. In the Wheatstone bridge circuit, R_w is the resistance of the platinum wire (named hot-wire), R_1 is a potentiometer, and R_2 and R_3 are resistors. The main reasons for choosing the platinum wire as a hot-wire cell is due to its well-known relationship between temperature and resistance through a wide temperature range. The resistance–temperature coefficient of the platinum wire is 0.0039092/°C [21]. The platinum wire of 76.2 μm and length of 200 mm coated with teflon produced by OMEGA was used as a hot-wire cell. The wire length to diameter ratio of the wire is approximately 2625 for minimisation of loss due to heat conduction at both ends of the wire. A nanofluid polypropylene container of 700 mL volume, 50 mm inner diameter and 350 mm length was used as the container which is sufficiently large to be considered infinite compared with the diameter of the wire. The storage tank with temperature controller was used to keep the temperature of water constant and circulate to the cooling and heating jacket by a pump in order to keep the nanofluid temperature at the desired value. The thermal conductivity of nanofluids with various volume fractions (0.2%. 0.6%, 1.0%, 1.5% and 2.0%,) were measured at temperatures of 15 °C, 25 °C and 35 °C, respectively. Finally, the thermal conductivity of the nanofluids is calculated from:

$$k = \frac{q}{4\pi(T_2 - T_1)} \ln\left(\frac{t_2}{t_1}\right) \quad (1)$$

where k is the thermal conductivity, q is the applied electric power per unit length of the wire, and $T_2 - T_1$ is the temperature rise of the

wire between time t_1 and t_2. Then, the measured thermal conductivity of nanofluids is compared with those obtained from the well-known correlations, which are defined as follows:

One well-known formula for computing the thermal conductivity of nanofluid is the Hamilton and Crosser [18] model (H–C model), which is expressed in the following form:

$$k_{nf} = \left[\frac{k_p + (n-1)k_w - (n-1)\phi(k_w - k_p)}{k_p + (n-1)k_w + \phi(k_w - k_p)}\right]k_w \quad (2)$$

$$n = 3/\psi \quad (3)$$

In which, n is the empirical shape factor and Ψ is the sphericity, defined as the ratio of the surface area of a sphere (of the same volume as the given particle) to the surface area of the particle. The sphericity is 1 and 0.5 for the spherical and cylindrical shapes, respectively. Moreover, k_{nf} is the thermal conductivity of the nanofluid, k_p is the thermal conductivity of the nanoparticles, and k_w is the thermal conductivity of the base fluid.

The thermal conductivity of the nanofluids is calculated from the Wasp [22] model, which is defined as follows:

$$k_{nf} = \left[\frac{k_p + 2k_m - 2\phi(k_w - k_p)}{k_p + 2k_w + \phi(k_w - k_p)}\right]k_w \quad (4)$$

For spherical particles, the results given by the Wasp model coincide with those of the Hamilton and Crosser model.

An alternative formula for calculating the thermal conductivity was introduced by Yu and Choi [23], which is expressed in the following form:

$$k_{nf} = \left[\frac{k_p + 2k_w + 2(k_p - k_w)(1+\beta)^3\phi}{k_p + 2k_w - (k_p - k_w)(1+\beta)^3\phi}\right]k_w \quad (5)$$

where β is the ratio of the nanolayer thickness to the original particle radius. Normally $\beta = 0.1$ is used to calculate the thermal conductivity of the nanofluid.

Murshed et al. [24] introduced the Bruggeman model [25] for calculating the thermal conductivity of nanofluids, which is expressed as follows:

$$k_{nf} = \frac{1}{4}[(3\phi - 1)k_p + (2 - 3\phi)k_w] + \frac{k_w}{4}\sqrt{\Delta} \quad (6)$$

$$\Delta = \left[(3\phi-1)^2(k_p/k_w)^2 + (2-3\phi)^2 + 2(2 + 9\phi - 9\phi^2)(k_p/k_w)\right] \quad (7)$$

Finally, Timofeeva et al. [26] introduced the effective medium theory for computing thermal conductivity of nanofluids, which is defined as follows:

$$k_{nf} = [1 + 3\phi]k_w \quad (8)$$

In the case of viscosity measurement, the viscosity of nanofluids was measured by using the rotational rheometer (Gemini 200HR Nano, Ultra low viscosity) manufactured by Malvern-Bohlin Instruments. The measurement conditions are the same as those of the thermal conductivity measurement. Moreover, the measured data are compared with those obtained from the well-known correlations, which are summarised as follows:

Brinkman [16] suggested the equation for calculating the viscosity of the suspension, which is defined as follows:

$$\mu_{nf} = \frac{1}{(1-\phi)^{2.5}}\mu_w \quad (9)$$

Drew and Passman [27] suggested the well-known Einstein's equation for calculating viscosity, which is applicable to spherical particles in volume fractions less than 5.0 vol.%, and is defined as follows:

$$\mu_{nf} = (1 + 2.5\phi)\mu_w \quad (10)$$

Batchelor [28] introduced a correlation for calculating the viscosity of nanofluids with spherical shape nanoparticles, which is defined as:

$$\mu_{nf} = (1 + 2.5\phi + 6.2\phi^2)\mu_w \quad (11)$$

Furthermore, Wang et al. [29] proposed a model to predict the viscosity of nanofluids which is expressed as:

$$\mu_{nf} = (1 + 7.3\phi + 123\phi^2)\mu_w \quad (12)$$

where φ is the volume concentration, μ_{nf} is the viscosity of the nanofluid and μ_w is the viscosity of the base fluid.

4. Data reduction

In the present study, the TiO_2 nanoparticles dispersed in water with volume concentrations of 0.2%, 0.6%, 1.0%, 1.5% and 2.0% were used to investigate the convective heat transfer coefficient and pressure drop of the nanofluids. Thus, the heat transfer coefficient and pressure drop of nanofluids can be calculated from the following equations.

The heat transfer rate from the heating fluid is calculated from:

$$Q_w = \dot{m}_w Cp_w (T_{in} - T_{out})_w \quad (13)$$

where Q_w is the heat transfer rate of the hot water and $\dot{m}_w$ is the mass flow rate of the hot water.

The heat transfer rate into the nanofluid is defined as:

$$Q_{nf} = \dot{m}_{nf} Cp_{nf} (T_{out} - T_{in})_{nf} \quad (14)$$

where Q_{nf} is the heat transfer rate of the nanofluid and $\dot{m}_{nf}$ is the mass flow rate of the nanofluid.

The average heat transfer rate is defined as follows:

$$Q_{ave} = \frac{Q_w + Q_{nf}}{2} \quad (15)$$

where Q_{ave} is the average heat transfer rate between the hot water and the nanofluid.

In this study, the energy differences between nanofluid and heating fluid are approximately 3%.

The experimental heat transfer coefficient and Nusselt number of the nanofluid are computed from the following equation:

$$h_{nf} = \frac{q_{ave}}{T_{wall} - T_{nf}} \quad (16)$$

$$Nu_{nf} = \frac{h_{nf} D}{k_{nf}} \quad (17)$$

where h_{nf} is the heat transfer coefficient of the nanofluid, q_{ave} is the average heat flux between the hot water and the nanofluid, T_{wall} is the average temperature of the wall, T_{nf} is the bulk temperature of the nanofluid, Nu_{nf} is the Nusselt number of the nanofluid, D is the inner diameter of the test tube, and k_{nf} is the thermal conductivity of the nanofluid.

Similarly to the heat transfer coefficient, the friction factor of the nanofluid is calculated from:

$$f_{nf} = \frac{2D\Delta P_{nf} L}{u_m^2 L \rho_{nf}} \quad (18)$$

where f_{nf} is the friction factor of the nanofluid, ΔP_{nf} is the measured pressure drop of the nanofluid, L is the length of the tube, D is the diameter of the tube, ρ_{nf} is the density of the nanofluid, and u_m is the mean velocity of the nanofluid.

The density and specific heat of the nanofluids presented in the above equation are calculated by use of the Pak and Cho [2] correlations, which are defined as follows:

$$\rho_{nf} = \phi\rho_p + (1 - \phi)\rho_w \quad (19)$$

and

$$Cp_{nf} = \phi Cp_p + (1-\phi)Cp_w \quad (20)$$

where Cp_{nf} is the specific heat of the nanofluid, Cp_p is the specific heat of the nanoparticles and Cp_w is the specific heat of the base fluid.

The properties of the nanofluid shown in the above equations are evaluated from water and nanoparticles at average bulk temperature.

5. Results and discussion

5.1. The thermal conductivity of nanofluids

In order to validate the transient hot-wire system, the thermal conductivity of water was measured at temperatures of 15 °C, 25 °C and 35 °C. Then, the measured data of water were compared with the reference data presented in the standard textbook [30]. As shown in Fig. 3, the results show that the measured data gave reasonable agreement with the reference data. Furthermore, the results also show that the uncertainty of the thermal conductivity measurement is approximately 2.5%. Fig. 4 shows the thermal conductivity of TiO_2-water nanofluids as a function of temperature and particle volume concentration. The results indicated that the thermal conductivity of nanofluids substantially increases with increasing particle volume concentration as well as nanofluid temperature. Fig. 5 shows a comparison of measured values of thermal conductivity of nanofluids with the calculated values from well-known correlations. The results show that the measured thermal conductivity of the nanofluids is significantly greater than the computed value of the H–C model, Wasp model, Bruggeman model, and the effective medium theory. However, the results showed that the measured values are closer to the calculated values of the Yu and Choi equation than of the other equations.

5.2. The viscosity of nanofluids

In compliance with the thermal conductivity measurement, the viscosity of pure water was first measured for validating the experimental apparatus. The measurement conditions are the same as those of the thermal conductivity measurement. Then, the reference data presented in the standard textbook [31] were used to compare with the measured data. Fig. 6 shows the comparison of viscosity between the measured data and the reference data for water. The results show a good correspondence between the measured data and the reference data, and the uncertainty of the viscosities measurement is approximately 3.5%. As shown in Fig. 7, the results show that the viscosity of nanofluids increases with increasing particle volume concentration and also increases with decreasing nanofluid temperature. Fig. 8 shows a comparison of measured values with the predicted values from well-known correlations. The results show that the measured data of nanofluids are much larger than those of predicted values by use of the Einstein equation, Brinkman equation and Batchelor equation. However, the results also show that the measured values are rather consistent with the calculated values by using the Wang et al. equation.

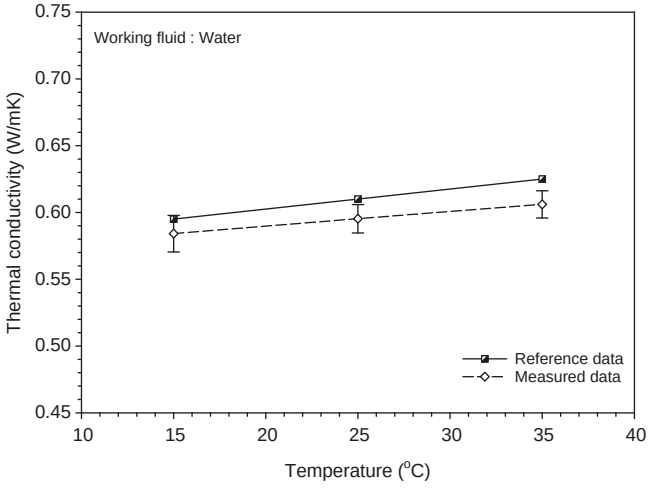

Fig. 3. Comparison of the thermal conductivity between measured data and standard data.

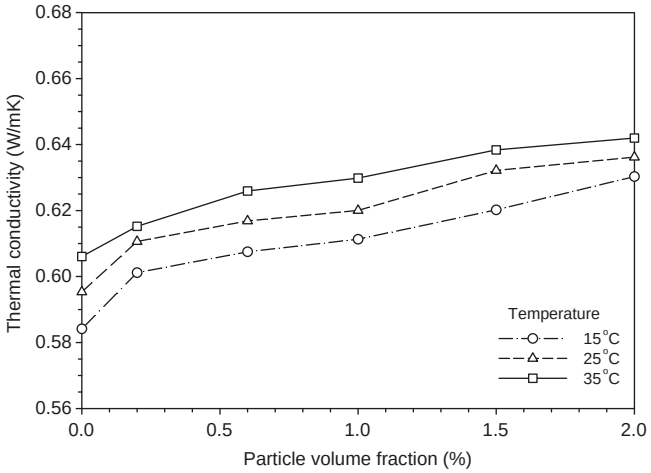

Fig. 4. Thermal conductivity of TiO_2-water nanofluids as function of temperature and volume fraction.

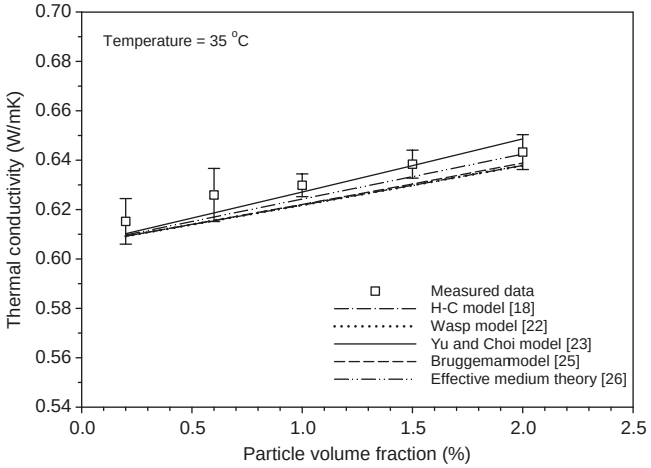

Fig. 5. Comparison of the thermal conductivity between measured data and calculated value from the other correlations.

5.3. Convective heat transfer of nanofluid

In the present study, TiO_2 nanoparticles dispersed in water for 0.2%, 0.6%, 1.0%, 1.5% and 2.0% by volume are used to investigate the heat transfer performance and the pressure drop characteristics of the nanofluid. The test conditions used in this study are summarised as follows: (1) the Reynolds number of the nanofluid varies in the approximate range of 3000–18,000, (2) the temperature of the nanofluid is 15 °C, 20 °C and 25 °C, (3) the mass flow

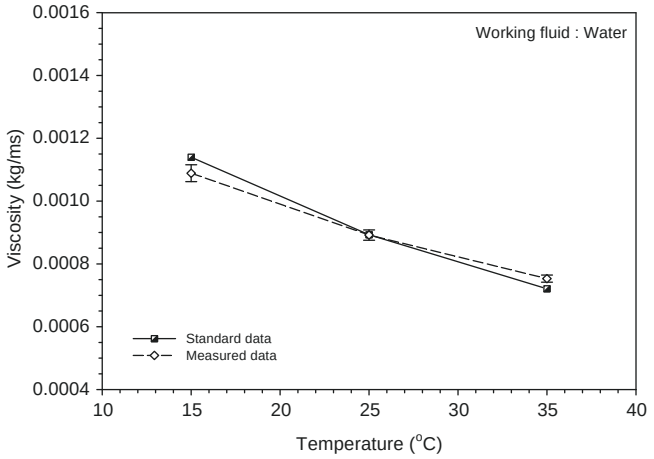

Fig. 6. Comparison of the viscosity between measured data and reference data.

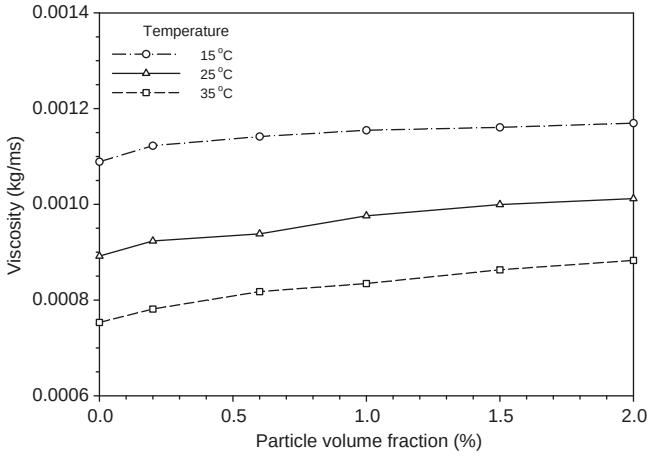

Fig. 7. Viscosity of TiO_2-water nanofluids as a function of temperature and volume fraction.

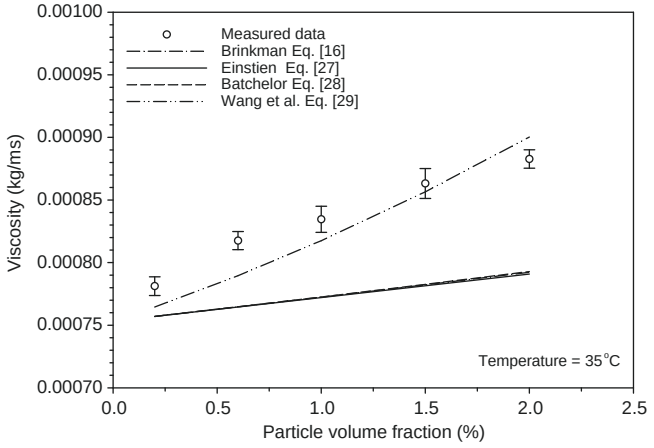

Fig. 8. Comparison of the viscosity between measured data and calculated value from the other correlations.

rates of hot water is 3 LPM and 4.5 LPM, and (4) the temperature of the hot water is 35 °C and 45 °C.

Before evaluating the heat transfer performance of the nanofluids, the pure water is used as the working fluid for estimating the reliability and accuracy of the experimental system. The results of the experimental Nusselt number are compared with those obtained from the Gnielinski equation [32], which is defined as follows:

$$Nu = \frac{(f/8)(Re - 1000)Pr}{1 + 12.7(f/8)^{0.5}(Pr^{2/3} - 1)} \tag{21}$$

where Nu is the Nusselt number, Re is the Reynolds number, Pr is the Prandtl number and f is the friction factor.

The friction factor can be calculated from the Colebrook equation [33] as follows:

$$\frac{1}{\sqrt{f}} = -2.0\log\left(\frac{\varepsilon/D}{3.7} + \frac{2.51}{Re\sqrt{f}}\right) \tag{22}$$

where ε is the roughness of the test tube.

Moreover, the existing correlations for calculating the Nusselt number for nanofluids were used for comparison with the experimental results. Up to now, there are only two correlations for predicting the heat transfer performance of nanofluids flowing in the turbulent flow regime, namely the Pak and Cho [2] and Xuan and Li [4] correlations, which are defined as follows:

The Pak and Cho correlation is defined as:

$$Nu_{nf} = 0.021 Re_{nf}^{0.8} Pr_{nf}^{0.5} \tag{23}$$

The Xuan and Li correlation is defined as:

$$Nu_{nf} = 0.0059\left(1.0 + 7.6286\phi^{0.6886} Pe_d^{0.001}\right) Re_{nf}^{0.9238} Pr_{nf}^{0.4} \tag{24}$$

The Reynolds number of the nanofluid is expressed as:

$$Re_{nf} = \frac{\rho_{nf} u_m D}{\mu_{nf}} \tag{25}$$

The Prandtl number and Peclet number of the nanofluid can be calculated from the following equation:

$$Pr_{nf} = \frac{\mu_{nf} Cp_{nf}}{k_{nf}} \tag{26}$$

$$Pe_{nf} = \frac{u_m d_p}{\alpha_{nf}} \tag{27}$$

where d_p is the diameter of the nanoparticles.

In order to calculate the Peclet number, the thermal diffusivity of the nanofluid (α_{nf}) is defined as:

$$\alpha_{nf} = \frac{k_{nf}}{\rho_{nf} Cp_{nf}} \tag{28}$$

As shown in Fig. 9, the measured Nusselt number coincided well with the calculated values for pure water.

As shown in Fig. 10, the heat transfer coefficient and the Nusselt number of the nanofluids are higher than those of the base liquid, and they increase with increasing the Reynolds number as well as the particle volume concentration for the volume concentration $\leqslant$1.0 vol.%. At 1.0 vol.%, the enhancement range between 20% and 32% is observed. However, the heat transfer coefficient for particle concentration of 1.5 vol.% is smaller than that for the volume concentration of 1.0 vol.%, but still larger than for the base liquid. It was also found that the heat transfer coefficient of nanofluid at volume fraction of 2.0 vol.% was approximately 14% **s**maller than that of pure water when compared under the same conditions. This behaviour may be due to the fact that the nanoparticles presented in the base liquid increase the thermal conductivity and the viscosity of the base liquid at the same time, and increase with increasing the particle concentrations. The increasing of the thermal conductivity leads to an increase in the heat transfer performance, whereas the increasing of the viscosity of the fluid leads to an increase in the boundary layer thickness, which results in a decrease in the heat transfer performance. As a result, for the volume

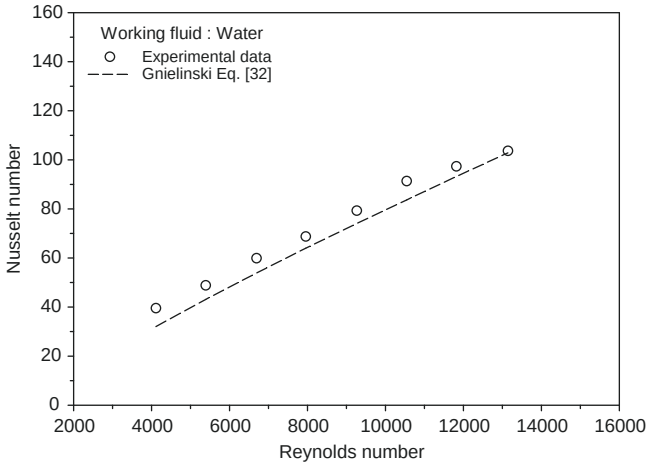

Fig. 9. Comparison between measured heat transfer coefficient and that calculated from Gnielinski equation [32].

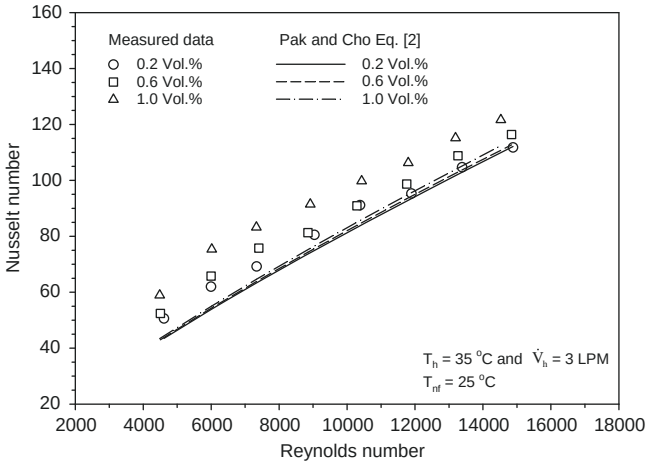

Fig. 11. Comparison of Nusselt number between the measured data and calculated values from nanofluid correlations.

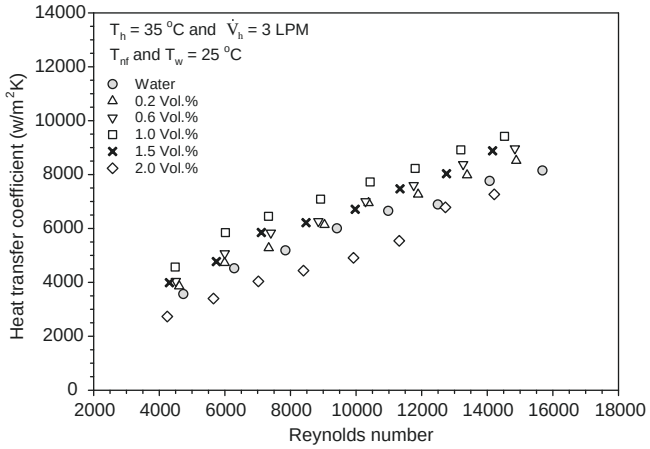

(a) Heat transfer coefficient

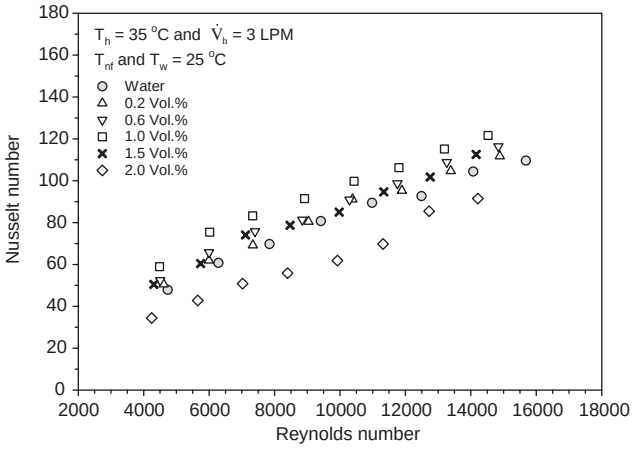

(b) Nusselt number

Fig. 10. Experimental heat transfer coefficient and Nusselt number for water and TiO_2-water nanofluids versus Reynolds number at various volume concentration.

concentration $\leqslant$1.0 vol.%, the effect of thermal enhancement may overcome the effect of the increasing of the viscosity. On the other hand, for the volume concentration of more than 1.0 vol.%, the effect of the viscosity increase may overcome the effect of thermal conductivity enhancement, which leads to a decrease in the heat transfer performance of the nanofluids. Moreover, in our opinion, the nanoparticles at higher volume concentration may become combined together, which caused the size became bigger and leads to a decrease in the heat transfer performance. According to this study, the present results are found to be different from those obtained from other researchers. For example, Xuan and Li [4] investigated experimentally the convective heat transfer and flow characteristics for Cu-water nanofluids. They found that the Nusselt number of the nanofluid is increased more than 39% for the particle volume fraction of 2.0 vol.%. He et al. [12] determined experimentally the heat transfer and flow behaviour of TiO_2-distilled water nanofluids in both laminar and turbulent flow condition. The results showed that the convective heat transfer coefficient increased more than 40% for a volume fraction of 1.1 vol.%. Nguyen et al. [13] experimentally investigated the heat transfer behaviour of Al_2O_3-water nanofluid flowing under a turbulent flow regime inside an electronic cooling system. They found that the heat transfer coefficient of nanofluids for particle volume concentration of 6.8 vol.% is greater than the base fluid by approximately 40%. However, Pak and Cho [2] experimentally studied heat transfer performance of γ-Al_2O_3 and TiO_2 nanoparticle dispersed in water flowing in a horizontal circular tube. Their results showed that the Nusselt number of nanofluids increased with an increase in the Reynolds number as well as the volume fraction. Moreover, their results still showed that the heat transfer coefficient of the nanofluids for a volume concentration of 3 vol.% was 12% lower than that of pure water under the same conditions. As mentioned above, it is difficult to explain this difference in behaviour. It may be caused by several factors, such as particle source, particle size, particle shape, particle preparation, and even solution chemistry (e.g. pH value). Therefore, more experimental works are needed in order to address the exact heat transfer behaviour of nanofluids for applying them in practical applications.

From the previous work of the authors [20], the results indicated that the Pak and Cho [2] equation can be used to predict the heat transfer performance of TiO_2-water nanofluid with a volume concentration of 0.2% and give an agreement that compares with the experimental results. At the same time, the Xuan and Li [4] correlation gives a significantly lower heat transfer coefficient compared with the measured data and the Pak and Cho correlation. However, in this study, Fig. 11 shows that Pak and Cho [2] correlation fails to predict the Nusselt number of nanofluids for volume concentrations of 0.6% and 1.0%. This may be caused by the effect of the particle concentrations, which was not considered in their correlation, and by different configuration of the test section. Thus,

a new heat transfer correlation which gives better accuracy for predicting the heat transfer performance of the nanofluids may still be required. This is an important subject for the present study.

In general, Nusselt numbers of nanofluids may be related with the parameters as follows:

$$Nu_{nf} = f(Re_{nf}, Pr_{nf}, \phi) \tag{29}$$

Considering the above mentioned, the equation for predicting the heat transfer performance of nanofluid was formed and is proposed in the following form:

$$Nu_{nf} = 0.074 Re_{nf}^{0.707} Pr_{nf}^{0.385} \phi^{0.074} \tag{30}$$

The above equation is obtained by curve fitting all the experimental data for the nanofluids. Comparisons of the experimental Nusselt number with those calculated by the proposed correlation are shown in Fig. 12. The results show good correspondence between the experimental values and the calculated values by the above equation. It is clearly seen that the majority of the data falls within ±10% of the proposed equation. The authors would like to introduce that this equation can be used for predicting the heat transfer coefficient of nanofluids with a volume concentration of $\leqslant$1.0% and a Reynolds number range between 3000 and 18,000. Moreover, it is very important to note that this equation is only established with respect to the data for TiO_2-water nanofluids.

5.4. Pressure drop of nanofluid

In order to apply the nanofluids for practical application, in addition to the heat transfer performance of the nanofluids it is necessary to study their flow features. In this study, nanofluid with 0.2, 0.6, 1.0, 1.5 and 2.0 vol.% suspended nanoparticles are used in the pressure drop test under the turbulent flow condition. Similar to the convective heat transfer coefficient of nanofluids, pure water is used as the working fluid in order to estimate the reliability and accuracy of the measured pressure.

As shown in Fig. 13, the measured friction factor agrees well with those of calculated values for pure water.

As shown in Fig. 14, the results show that the pressure drop and friction factor of the nanofluids increase with increasing Reynolds number and that there is a small increase with increasing particle concentrations. This means that using the nanofluids at higher particle volume fraction may create a small penalty in pressure drop. Moreover, although the Colebrook equation can fairly predict the pressure drop of nanofluids as shown in Fig. 14a, a new correlation

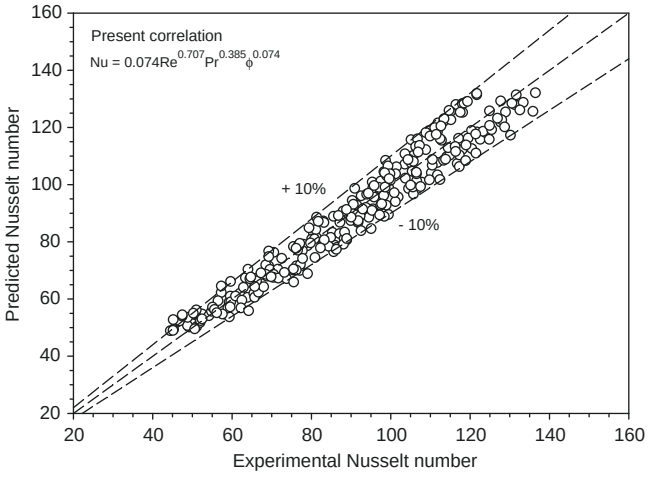

Fig. 12. Comparison of the Nusselt number of nanofluids between predicted values by presented correlation and experimental data.

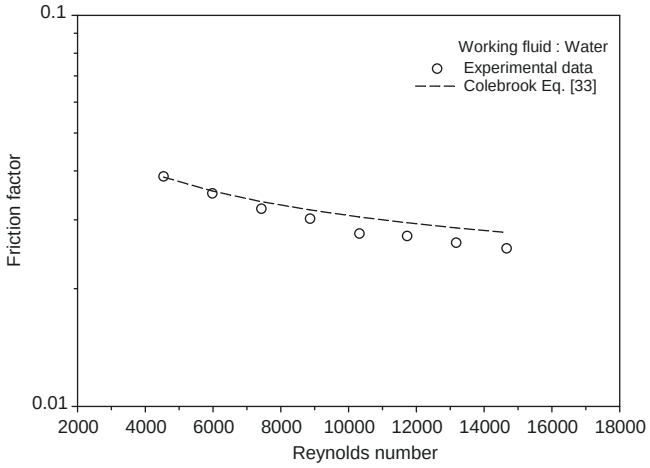

Fig. 13. Comparison between measured friction factor and that calculated from Colebrook equation [33].

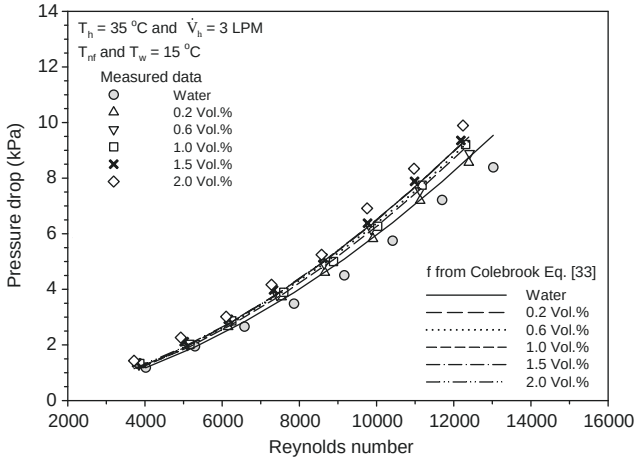

Fig. 14. Comparison of pressure drop and friction factor obtained from water and that from the TiO_2-water nanofluids at different volume fraction.

which gives better accuracy and that is easy to use for calculating the friction factor of nanofluids is still needed. Similar to the heat transfer correlation, a new equation for predicting the friction factor of nanofluids is proposed in the following form:

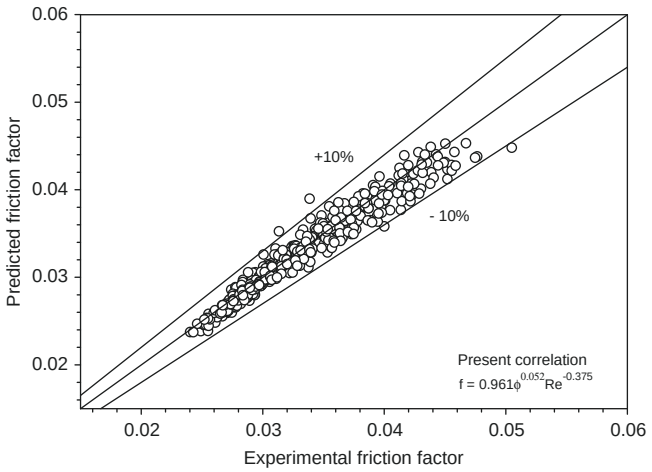

Fig. 15. Proposed pressure drop versus experimental pressure drop.

$$f_{nf} = 0.961\phi^{0.052}Re^{-0.375} \quad (31)$$

As shown in Fig. 15, the results show that the present correlation gave reasonably good agreement with the experimental data. This equation can be used to compute the friction factor of nanofluids with particle volume concentrations range between 0% and 2.0%.

6. Conclusions

The convective heat transfer performance and flow characteristic of TiO_2-water nanofluid flowing in a horizontal double tube counter-flow heat exchanger was experimentally investigated. Experiments were carried out under turbulent flow conditions. The effect of particle concentrations and the Reynolds number on the heat transfer performance and flow behaviour of nanofluids are determined. Important conclusions have been obtained and are summarised as follows:

- Dispersion of the nanoparticles into the base liquid increases the thermal conductivity and viscosity of the nanofluids, and this augmentation increases with increasing particle concentrations.
- At a particle volume concentration of $\leqslant$1.0 vol.%, the use of TiO_2-water nanofluid gives significantly higher heat transfer coefficients than those of the base fluid. For example, at the 1.0 vol.%, the heat transfer coefficient of nanofluids was approximately 26% greater than that of pure water. However, at the particle concentration of 2.0 vol.%, it was found that the heat transfer coefficient of nanofluids was roughly 14% smaller than that of pure water for the given conditions.
- The pressure drop of nanofluids increases with increasing Reynolds number and there is a small increase with increasing particle volume concentrations. This is caused by increase in the viscosity of nanofluids, and it means that nanofluids incur little penalty in pressure drop.
- The results showed that the Pak and Cho [2] correlation can predict the heat transfer coefficient of nanofluids and gives results that corresponded well only with the experimental results for the volume concentration of 0.2%. However, for the volume concentrations of 0.6% and 1.0%, the Pak and Cho equation fails to predict the heat transfer performance of the nanofluids.
- New heat transfer and friction factor correlations for predicting the Nusselt number and friction factor of TiO_2-water nanofluids are proposed in the form of $Nu = 0.074Re^{0.707}Pr^{0.385}\phi^{0.074}$, and $f = 0.961\phi^{0.052}Re^{-0.375}$, respectively. The majority of the data falls within ±10% of the proposed equation. These equations are valid in the range of Reynolds number between 3000 and 18,000 and particle volume concentrations in the range of 0 and 1.0 vol.% for Nusselt number and 0 and 2.0 vol.% for friction factor.

Acknowledgments

The authors would like to express their appreciation to the Thailand Research Fund (TRF) for providing financial support for this study. The authors also wish to thank DEGUSSA AG, Germany for the valuable donation of the nanoparticles used in the present study.

References

[1] S.U.S. Choi, Enhancing thermal conductivity of fluids with nanoparticle, ASME FED 231 (1995) 99.
[2] B.C. Pak, Y. I Cho, Hydrodynamic and heat transfer study of dispersed fluids with submicron metallic oxide particles, Exp. Heat Transfer 11 (1998) 151.
[3] Q. Li, Y. Xuan, Convective heat transfer and Flow characteristics of Cu-water nanofluid, Sci. China E 45 (2002) 408.
[4] Y. Xuan, Q. Li, Investigation on convective heat transfer and flow features of nanofluids, ASME J. Heat Transfer 125 (2003) 151.
[5] C.Y. Tsai, H.T. Chien, P.P. Ding, B. Chan, T.Y. Luh, P.H. Chen, Effect of structural character of gold nanoparticles in nanofluid on heat pipe thermal performance, Mater. Lett. 58 (2004) 1461.
[6] D. Wen, Y. Ding, Experimental investigation into convective heat transfer of nanofluids at the entrance region under laminar flow conditions, Int. J. Heat Mass Transfer 47 (2004) 5181.
[7] Y. Yang, Z.G. Zhang, E.A. Grulke, W.B. Anderson, G. Wu, Heat transfer properties of nanoparticle-in-fluid dispersions (nanofluids) in laminar flow, Int. J. Heat Mass Transfer 48 (6) (2005).
[8] Y. Ding, H. Alias, D. Wen, R.A. Williams, Heat transfer of aqueous suspensions of carbon nanotubes (CNT nanofluids), Int. J. Heat Mass Transfer 49 (1–2) (2005) 240.
[9] X.Q. Wang, A.S. Mujumdar, Heat transfer characteristics of nanofluids: a review, Int. J. Therm. Sci. 46 (2007) 1.
[10] S.Z. Heris, S.G. Etemad, M.N. Esfahany, Experimental investigation of oxide nanofluids laminar flow convective heat transfer, Int. Commun. Heat Mass Transfer 33 (2006) 529.
[11] S.Z. Heris, M.N. Esfahany, S.G. Etemad, Experimental investigation of convective heat transfer of Al2O3/water nanofluid in circular tube, Int. J. Heat Fluids Flow 28 (2) (2007) 203.
[12] Y. He, Y. Jin, H. Chen, Y. Ding, D. Cang, H. Lu, Heat transfer and flow behavior of aqueous suspensions of TiO_2 nanoparticles (nanofluids) flowing upward through a vertical pipe, Int. J. Heat Mass Transfer 50 (2007) 2272.
[13] C.T. Nguyen, G. Roy, C. Gauthier, N. Galanis, Heat transfer enhancement using Al_2O_3-water nanofluid for electronic liquid cooling system, Appl. Therm. Eng. 28 (2007) 1501.
[14] G.H. Ko, K. Ho, K. Lee, D.S. Kim, C. Kim, Y. Sohn, M. Choi, An experimental study on the pressure drop of nanofluids containing carbon nanotubes in the horizontal tube, Int. J. Heat Mass Transfer 50 (2007) 4749.
[15] R. Chein, J. Chuang, Experimental microchannel heat sink performance studies using nanofluids, Int. J. Therm. Sci. 46 (1) (2007) 57.
[16] H.C. Brinkman, The viscosity of concentrated suspensions and solution, J. Chem. Phys. 20 (1952) 571.
[17] Y. Xuan, W. Roetzel, Conceptions for heat transfer correlation of nanofluids, Int. J. Heat Mass Transfer 43 (2000) 3701.
[18] R.L. Hamilton, O.K. Crosser, Thermal conductivity of heterogeneous two-component systems, I&EC Fund. 1 (3) (1962) 187.
[19] W. Duangthongsuk, S. Wongwises, Effect of thermophysical properties models on the prediction of the convective heat transfer coefficient for low concentration nanofluid, Int. Comm. Heat Mass Transfer 35 (2008) 1320.
[20] W. Duangthongsuk, S. Wongwises, Heat transfer enhancement and pressure drop characteristics of TiO_2-water nanofluid in a double-tube counter flow heat exchanger, Int. J. Heat Mass Transfer 52 (2009) 2059.
[21] J.P. Bentley, Temperature sensor characteristics and measurement system design, J. Phy. E: Sci. Instrum. 17 (1984) 430.
[22] F.J. Wasp, Solid–liquid slurry pipeline transportation, Trans. Tech, Berlin, 1977.
[23] W. Yu, S.U.S. Choi, The role of interfacial layers in the enhanced thermal conductivity of nanofluids: a renovated Maxwell model, J. Nanoparticle Res. 5 (2003) 167.
[24] S.M.S. Murshed, K.C. Leong, C. Yang, Enhanced thermal conductivity of TiO_2-water based nanofluids, Int. J. Therm. Sci. 44 (2005) 367.
[25] D.A.G. Bruggeman, Berechnung verschiedener physikalischer konstanten von heterogenen substanzen, I. Dielektrizitatskonstanten und Leitfahigkeiten der Mischkorper aus Isotropen Substanzen, Annalen der Physik 14 (1935) 636.
[26] E.V. Timofeeva, A.N. Gavrilov, J.M. McCloskey, Y.V. Tolmachev, Thermal conductivity and particle agglomeration in alumina nanofluids: experiment and theory, Phy. Rev. 76 (2007) 061203.

[27] D.A. Drew, S.L. Passman, Theory of Multi-Component Fluids, Springer, Berlin, 1999.
[28] G.K. Batchelor, The effect of Brownian motion on the bulk stress in a suspension of spherical particles, J. Fluid Mech. 83 (1) (1977) 97.
[29] X. Wang, X. Xu, S.U.S. Choi, Thermal conductivity of nanoparticles-fluid mixture, J. Thermophys. Heat Transfer 13 (4) (1999) 474.
[30] F.P. Incropera, D.P. DeWitt, Fundamentals of Heat and Mass Transfer, Springer, 1996.
[31] R.W. Fox, A.T. McDonald, P.J. Pritchard, Introduction to Fluid Mechanics, John Wiley & Sons, 2004.
[32] V. Gnielinski, New equations for heat and mass transfer in turbulent pipe and channel flow, Int. Chem. Eng. 16 (1976) 359.
[33] C.F. Colebrook, Turbulent flow in pipes, with particular reference to the transition between the smooth and rough pipe laws, J. Inst. Civ. Eng. Lond. 11 (1939) 133.

Renewable and Sustainable Energy Reviews 14 (2010) 629–641

Contents lists available at ScienceDirect

Renewable and Sustainable Energy Reviews

journal homepage: www.elsevier.com/locate/rser

Enhancement of heat transfer using nanofluids—An overview

Lazarus Godson [a,*], B. Raja [b,1], D. Mohan Lal [a], S. Wongwises [c]

[a] Refrigeration & Air-Conditioning Division, Department of Mechanical Engineering., College of Engineering, Anna University, Chennai 600 025, Tamil Nadu, India
[b] Indian Institute of Information Technology, Design & Manufacturing-Kancheepuram Indian Institute of Technology-Madras, Chennai 600 036, Tamil Nadu, India
[c] Fluid Mechanics, Thermal Engineering and Multiphase Flow (FUTURE), Dept. of Mechanical Engineering, King Mongkut's University of Technology Thonburi, Bangmod, Bangkok 10140, Thailand

ARTICLE INFO

Article history:
Received 26 June 2009
Accepted 6 September 2009

Keywords:
Nanofluid
Convective heat transfer
Laminar flow
Turbulent flow
Nanoparticles
Dispersion
Thermal conductivity

ABSTRACT

A colloidal mixture of nano-sized particles in a base fluid, called nanofluids, tremendously enhances the heat transfer characteristics of the original fluid, and is ideally suited for practical applications due to its marvelous characteristics. This article addresses the unique features of nanofluids, such as enhancement of heat transfer, improvement in thermal conductivity, increase in surface volume ratio, Brownian motion, thermophoresis, etc. In addition, the article summarizes the recent research in experimental and theoretical studies on forced and free convective heat transfer in nanofluids, their thermo-physical properties and their applications, and identifies the challenges and opportunities for future research.

Contents

* Corresponding author. Tel.: +91 99944 55741; fax: +91 44 22203261.
E-mail addresses: godasir@yahoo.co.in (L. Godson), rajab@iiitdm.ac.in (B. Raja), mohanlal@annauniv.edu (D. Mohan Lal), somchai.won@kmutt.ac.th (S. Wongwises).
[1] Tel.: +91 44 22578556; fax: +91 44 22574691.

1364-0321/$ – see front matter © 2009 Elsevier Ltd. All rights reserved.
doi:10.1016/j.rser.2009.10.004

Nomenclature

A	cross-sectional area (m^2)
C_p	specific heat (J/kg K)
D	tube diameter (m)
h	heat transfer coefficient (W/m^2 K)
k	thermal conductivity (W/m K)
m	mass flow rate (kg/s)
Nu	Nusselt number
Pr	Prandtl number
q''	heat flux (W/m^2)
Re	Reynolds number
T	temperature (°C)

Greek symbols

β	thermal dispersion coefficient (N/m^2 K)
φ	volume fraction
ρ	density (kg/m^3)
μ	dynamic viscosity (kg/m s)
γ	particle size (nm)

Subscript

f	bulk fluid
nf	nanofluid
w	tube wall
x	axial distance
bf	base fluid
i	inner wall
o	outer wall

Abbreviation

CHF	critical heat flux
CNT	carbon nano tube
HTC	heat transfer coefficient

1. Introduction

Ever since the adverse effect of green house gases was discovered, leading to the Kyoto Protocol [1], the search for methods and technological advancement to mitigate the impact of global warming on Planet Earth became a pressing need for the research and industrial communities. The Protocol had exhorted both the developed and developing countries to show intense curiosity with a sense of participation, to find definitive ways to tackle the issue. Subsequent meetings which were held in many countries had called for a gentle decline in the production of green house gases. Even as scientists subscribed to a number of methods to tackle the carbon footprints, the global energy need and inefficient thermal-fluid systems always increased the green house gases.

A reduction in energy consumption is possible by enhancing the performance of heat exchange systems. Heat transfer is one of the most important processes in industrial and consumer products and it is worth addressing its influence over carbon footprints. For instance, the present telecommunication demand for enhanced functionality in circuit boards, results in high process density circuit boards. In such cases, the company spends more than 50% of the total electricity on the thermal management of electronic cooling systems [2]. Further, one of the most influential regulations is the 65 Dba noise limit in a central office environment compared to the 85 Dba in data centers and thus, typical air-cooling methods are unsuitable for these conditions [3]. The dozens of methods such as Fin-Foam Heat Sink, Minichannels, Microchannels, Novel interface materials, Dielectric mist cooling, Forced convective boiling, etc. and their combinations are limited to heat removal of up to 1000 W/cm^2. Some of the electronic systems like ultra-high heat flux optical devices, high-powered X-rays and lasers demand as high as 2000 W/cm^2 of heat removal [4]. Similarly, the growth of Heating Ventilation and Air-Conditioning (HVAC) and chemical processing equipment had adversely increased the carbon footprints. The paradigm shift in their design with respect to heat transfer will both simultaneously reduce the size of the heat exchangers and the energy consumption. In many industrial applications, the conventional heat transfer fluids are refrigerants, water, engine oil, ethylene glycol, etc. Even though an improvement in energy efficiency is possible from the topological and configuration points of view, much more is needed from the perspective of the heat transfer fluid. Further, enhancement in heat transfer is always in demand, as the operational speed of these devices depends on the cooling rate. New technology and advanced fluids with greater potential to improve the flow and thermal characteristics are two options to enhance the heat transfer rate and the present article deals with the latter option. One such latest advancement in heat transfer fluids, is an engineered colloidal mixture of the base fluids and nano-sized metallic particles (1–100 nm). The earlier versions of colloidal fluids such as micro-fluid substances tend to sediment and cause erosion in the moving component. However, nanofluids are claimed to be a non-agglomerated mono-dispersed particles in the base fluids, which proved to be enhancing the heat transfer more than 50% in real-time applications even when the volume ratio of the nanoparticle to base fluid is less than 0.3% [5]. As the need for more efficient heat transfer systems increases, researchers have introduced various heat transfer enhancement techniques since the middle of the 1950s. The exponential increase in the number of research articles dedicated to this subject thus far shows a noticeable growth and the importance of heat transfer enhancement technology. Some recent review articles [6–10] have covered a variety of methods for the enhancement of heat transfer. Investigation in convective heat transfer characteristics has been carried out in recent times. In this paper, the various articles related to the mechanism of nanofluid heat transfer, thermo-physical properties and pioneering experiments related to convective and boiling heat transfer of nanofluids are discussed. This article presents the recent research in natural, forced and two-phase convective heat transfer in nanofluids and its applications, and identifies the challenges and opportunities for future research.

2. Nanofluids

Enhancement of convective heat transfer and thermal conductivity of liquids was earlier made possible by mixing micron-sized particles with a base fluid (Maxwell paper) [11]. However, rapid sedimentation, erosion, clogging and high-pressure drop caused by these particles has kept the technology far from practical

use. A very small amount of nanoparticles, when dispersed uniformly and suspended stably in base fluids, can provide impressive improvements in the thermal properties of base fluids. Nanofluids, which are a colloidal mixture of nanoparticles (1–100 nm) and a base liquid (nanoparticle fluid suspensions) is the term first coined by Choi in the year 1995 [12] at the Argonne National Laboratory to describe the new class of nanotechnology based heat transfer fluids that exhibit thermal properties superior to those of their base fluids or conventional particle fluid suspensions.

The phases in the colloid are distinguishable and interact through weak surface molecular forces, preferably without any chemical reaction. Compared to micron-sized particles, nanoparticles are engineered to have larger relative surface areas, less particle momentum, high mobility, better suspension stability than micron-sized particles and importantly increase the thermal conductivity of the mixture. This makes the nanofluids a promising working medium as coolants, lubricants, hydraulic fluids and metal cutting fluids. Further, a negligible pressure drop and mechanical abrasion makes researchers subscribe to nanofluids for the development of the next generation miniaturized heat exchangers.

Based on their application, nanoparticles have been made of various materials [13–27] such as oxide ceramics, nitride ceramics, carbide ceramics, metals, semiconductors, carbon nanotubes and composite materials such as alloyed nanoparticles Al70Cu30 or nanoparticle core–polymer shell composites. In addition to nonmetallic, metallic, and other materials for nanoparticles, completely new materials and structures have been used, such as materials "doped" with molecules in their solid–liquid. The goal of nanofluids is to achieve the best possible thermal properties at the least possible volume fraction ($\varphi < 1\%$) in the base fluids. Thus, the suspension of nearly non-agglomerated or mono-dispersed nanoparticles in liquids is the key to significant enhancement in the heat transfer. In addition, Xuan and Li [28] suggested ultrasonic vibration of nanofluids and addition of surfactants to enhance the suspension.

3. Enhancement of thermal conductivity

A substantial increase in liquid thermal conductivity, liquid viscosity, and heat transfer coefficient, are the unique features of nanofluids. It is well known that at room temperature, metals in solid phase have higher thermal conductivities than those of fluids [29]. For example, the thermal conductivity of copper at room temperature is about 700 times greater than that of water and about 3000 times greater than that of engine oil. The thermal conductivity of metallic liquids is much greater than that of nonmetallic liquids. Thus, fluids containing suspended metal particles are expected to manifest enhanced thermal conductivities relative to pure fluids [30]. Masuda et al. [31] dispersed oxide nanoparticles (γ-Al_2O_3 and TiO_2 with $\varphi = 4.3\%$) particles in liquid and showed the increase in the thermal conductivity to be 32 and 11%, respectively. Grimm [32] dispersed aluminum particles ($\gamma = 80$–$1\ \mu m$) into a fluid and claimed a 100% increase in the thermal conductivity of the fluid for $\varphi = 0.5$–10%. Choi and Eastman [33] showed that the thermal conductivity of Cu–water and CNT–water nanofluids was higher compared to that of their base liquids. Eastmann et al. [34] showed that Cu–ethylene glycol (nanoparticles coated with thioglycolic acid) with $\varphi = 0.3\%$ gave a 40% increase in thermal conductivity. Recently, an attempt at the Indira Gandhi Centre for Atomic Research (IGCAR) was made, to align magnetic nanoparticles (Fe_3O_4 coated with Oelic acid) in a base fluid (hexadecane) in a linear chain using a magnetic field, which was applied to increase the thermal conductivity by 300% [35]. Further, it was proved that the thermal properties are tunable for magnetically polarizable nanofluids that consist of a colloidal suspension of magnetite nanoparticles. Moreover, the effective thermal conductivity depends also on other mechanisms of particle motion; the commonly explained physics are as follows.

3.1. Dispersion of the suspended particles

Dispersion is a system in which particles are dispersed in a continuous phase of a different composition. Surface-active substances (surfactants) can increase the kinetic stability of emulsions greatly so that, once formed, the emulsion does not change significantly over years of storage. Some of the surfactants are thiols [36], oleic acid [37,38], laurate salts, etc. Pak and Cho [39], Xuan and Li [28] and others claimed that the abnormal increase in thermal conductivity is due to uniform dispersion of the nanoparticles.

3.2. Intensification of turbulence

Even though thermal conductivity (k_{th}) is a function of primary variables such as thermodynamic pressure and temperature, in a turbulent flow the effective thermal conductivity ($k_{th} + k_{turb}$) due to the effects of turbulent eddies is many times higher than the actual value of k_{th}. Similarly in nanofluids, such intensification is believed to be possible due to the addition of nanoparticles. Xuan and Li [28]. However, Buongiorno [40] has claimed that due to the particle size, the effects of both dispersion and turbulence are negligible and not sufficient to explain the enhancement of thermal conductivity in nanofluids.

3.3. Brownian motion

It is a seemingly random movement of particles suspended in a liquid or gas and the motion is due to collisions with base fluid molecules, which makes the particles undergo random-walk motion. Thus, the Brownian motion intensifies with an increase in temperature as per the kinetic theory of particles. Keblinski et al. [41] and Koo and Kleinstreuer [42] have suggested that the potential mechanism for enhancement of thermal conductivity is the transfer of energy due to the collision of higher temperature particles with lower ones. The effectiveness of the Brownian motion decreases with an increase in the bulk viscosity.

3.4. Thermophoresis

Thermophoresis or the Sorét effect is a phenomenon observed when a mixture of two or more types of motile particles (particles able to move) is subjected to the force of a temperature gradient. The phenomenon is most significant in a natural convection process, where the flow is driven by buoyancy and temperature. The particles travel in the direction of decreasing temperature and the process of heat transfer increases with a decrease in the bulk density.

3.5. Diffusiophoresis

Diffusiophoresis (also called as Osmo-phoresis) occurs when there is a migration of particles from a lower concentration zone to a higher concentration one. However, this is not a favorable condition since the nanofluids may lose their non-agglomeration characteristics. Thus, the resulting fluid will result in a discrete spread in the particle density. Buongiorno [40] has stressed that the Brownian motion, thermophoresis and diffusiophoresis are significant in the absence of turbulent eddies.

The thermal conductivity enhancement ratio is defined as the ratio of the thermal conductivity of the nanofluid to that of the base fluid and this ratio depends on the material, size and shape of the

particle, volume concentration and the operating temperature itself. The influence of type of material on thermal conductivity enhancement has no effect for relatively low thermal conductivity particles and positive enhancement with higher thermal conductivity particles. For instance, the enhancement of thermal conductivity using metal particles is higher that the metal oxide particles. However, it is difficult to create metal particle nanofluids without particles oxidizing during the production process. A major obstacle for metal-particle nanofluids is eliminating the oxidation process during production and later during usage. Particle coating is one technique that has received some attention to solve this problem.

The smaller in particle size higher will be the enhancement. Since the surface to volume ratio will be higher for small diameter particles which results in uniform distribution of particles gives and the best enhancement. The most commonly used geometric shape of the particles is spherical and cylindrical. The cylindrical particles show an increase in thermal conductivity enhancement due to a mesh formed by the elongated particles that conducts heat through the fluid. This indicates the elongated particles are superior to spherical for thermal conductivity. The thermal conductivity enhancement increases with increased particle volume concentration. Metal oxide particle volume concentrations below φ = 4–5% produces an enhancement level up to about 30% is typical and metal particles with less than $\varphi < 1.5\%$ gives an enhancement up to 40%. The thermal conductivity of nanoparticles is more temperature sensitive than that of the base fluid. Consequently, the thermal conductivity enhancement of nanofluids is also rather temperature sensitive and a strong dependence of nanofluid thermal conductivity is due to the random motion of nanoparticles.

The physics of the above explained mechanisms is important and to be considered while studying the enhancement of thermal conductivity and the convective heat transfer of nano-sized colloidal mixture; the mechanisms are studied experimentally and theoretically by researchers and the summary of these investigations, findings and suggestions are presented in the following sections.

4. Experimental investigation

Enhancement in heat transfer was tried earlier also, with the help of suspended micro-particles. Ahuja [43,44] conducted experiments on the enhancement of heat transport in the laminar flow of water with micro-sized polystyrene suspension. The results showed a significant enhancement in the Nusselt number and heat exchanger effectiveness compared to that of a single phase liquid. Hetsroni and Rozenblit [45] investigated the thermal interaction between liquid and solid mixtures consisting of water and polystyrene particles in a turbulent flow. Interestingly, polystyrene has very low thermal conductivity close to only 0.08 W/m K. Still, the turbulence intensification and particle rotation effect are to be reasoned for an enhancement of heat transfer. The penalty in pumping power, clogging, agglomeration, sedimentation and erosion are some of the adverse effects of micro-particles. However, this issue has been eliminated with the use of stable nano-sized particulate colloids, and this has paved the way for researchers to further investigate the enhancement of convective heat transfer.

4.1. Forced convection heat transfer experiments with nanofluids

4.1.1. Experiments with metal oxide nanoparticles

Nanoparticles made from metal oxides, metals, nanotubes and graphite are widely investigated in base fluids such as water, ethylene glycol, acetone, etc. Some of the important experiments in macro, mini channels, heat pipes, etc. commonly used in many industrial heat transfer applications are discussed in the following sections.

Lee and Choi [46] used a nanofluid as a coolant in a microchannel heat exchanger and compared the enhanced cooling rates with those of conventional water-cooled and liquid-nitrogen cooled micro-channel. The intensification of turbulence or eddy, suppression of the boundary layer, dispersion of the suspended particles, besides the augmentation of thermal conductivity and the heat capacity of the fluid were suggested to be the possible reasons for heat transfer enhancement. Eastman et al. [47] conducted tests to assess the thermal performance of CuO–water with φ = 0.9% under turbulent flow conditions and the heat transfer coefficient was higher by 15% than that of pure water. Pak and Cho [39] presented an experimental investigation of the convective turbulent heat transfer characteristics of nanofluids (γAl_2O_3–water and TiO_2–water) with φ = 1–3%. The Nusselt number for the nanofluids increased with an increasing volume concentration and Reynolds number. Wen and Ding [48] assessed the convective heat transfer of nanofluids in the entrance region under laminar flow conditions. Aqueous based nanofluids containing γ-Al_2O_3 nanoparticles (γ = 27–56 nm; φ = 0.6–1.6%) with sodium dodecyl benzene sulfonate (SDBS) as the dispersant, were tested under a constant heat flux boundary condition. For nanofluids containing φ = 1.6%, the local heat transfer coefficient in the entrance region was found to be 41% higher than that of the base fluid at the same flow rate. It was observed that the enhancement is particularly significant in the entrance region, and decreases with axial distance. Particle migration was reasoned for the enhancement. Heris et al. [49] examined and proved the enhancement of in-tube laminar flow heat transfer of nanofluids (water–CuO and water–Al_2O_3) in a constant wall temperature boundary condition. Similarly, Esfahany et al. [50] presented an investigation of the laminar flow convective heat transfer of Al_2O_3–water under constant wall temperature with φ = 0.2–2.5% for Reynolds number varying between 700 and 2050. The Nusselt number for the nanofluid was found to be greater than that of the base fluid; and the heat transfer coefficient increased with an increase in particle concentration. The ratio of the measured heat transfer coefficients increases with the Peclet number as well as nanoparticle concentrations. Lai et al. [51] studied the flow behavior of nanofluids (Al_2O_3–DI water; γ = 20 nm) in a millimeter-sized stainless steel test tube, subjected to constant wall heat flux and a low Reynolds number (Re < 270). The maximum Nusselt number enhancement of the nanofluid of 8% at φ = 1% was recorded. Jung et al. [52] conducted convective heat transfer experiments for a nanofluid (Al_2O_3–water) in a rectangular micro-channel (50 μm × 50 μm) under laminar flow conditions. The convective heat transfer coefficient increased by more than 32% for φ = 1.8% in base fluids. The Nusselt number increased with an increasing Reynolds number in the laminar flow regime (5 < Re < 300) and a new convective heat transfer correlation for nanofluids in Microchannels was also proposed. Williams et al. [53] investigated the turbulent convective heat transfer behavior of alumina (Al_2O_3–water and ZrO_2–water). The convective heat transfer and pressure loss behavior of nanofluids under a fully developed turbulent flow, matched the correlations of a single-phase flow. Duangthongsuk and Wongwises [54] showed an enhancement of heat transfer at a lower concentration of TiO_2–water (φ = 0.2%) and claimed that the convective heat transfer coefficient also depends on the experimental measurement system and calibration. Jang and Choi [55] showed an enhancement of the convective heat transfer coefficient of nanofluids (Al_2O_3–water with φ = 0.3%) up to 8%. Duangthongsuk and Wongwises [56] reported an experimental study on the forced convective heat transfer under varied heat flux boundary conditions and pressure drop characteristics of a

nanofluid consisting of water and 0.2 vol.% TiO_2 nanoparticles of 21 nm diameter flowing in a horizontal double-tube counter flow heat exchanger under turbulent flow conditions. The results showed that the convective heat transfer coefficient of nanofluid is slightly higher than that of the base liquid by about 6–11%. The heat transfer coefficient of the nanofluid increases with an increase in the mass flow rate of the hot water and nanofluid. It was seen that the Gnielinski equation failed to predict the heat transfer coefficient of the nanofluid. Finally, it was also observed that the use of the oxide nanofluid has a little penalty in pressure drop.

4.1.2. Experiments with pure metal nanoparticles

Xuan and Li [57] experimentally studied the single phase heat transfer of the Cu–water nanofluid in tubes in the turbulent flow regime (Reynolds number between 10,000 and 25,000) with $\varphi = 0.3$–2.0% and proposed a heat transfer correlation. The convective heat transfer coefficient increased remarkably with the volume-fraction and with the flow velocity, with a negligible penalty in pumping power. Xuan and Li [58] measured the convective heat transfer of the Cu–water nanofluid in a small-hydraulic-diameter flat tube under laminar flow conditions. The Nusselt number of the nanofluid with $\varphi = 2\%$ increased by more than 39% compared with that of pure water. Zhou [59] investigated the enhancement of the single phase heat transfer of Cu–acetone particles with average particle sizes in the $\gamma = 80$–100 nm range and concentrations ranging from 0.0 to 4.0 g/l. Xuan et al. [60] investigated Cu–water (deionised) with $\gamma = 26$ nm and $\varphi = 0.5$–2%. The Nusselt number increased proportionately with the Reynolds number, and for the same Reynolds number the ratio of Nusselt number of Cu–water to water varied from 1.06 to 1.39 when the volume fraction of copper nanoparticles increased from 0.5 to 2.0%.

Faulkner et al. [61] investigated the convective heat transfer of a CNT–water nanofluid in a micro-channel, with a hydraulic diameter of 355 μm, a Reynolds number between 2 and 17 and $\varphi = 1.1$, 2.2 and 4.4%. The results showed an enhanced heat transfer coefficient of CNT–water at highest concentration. Yang et al. [62] investigated the convective heat transfer of graphite nanoparticles dispersed in liquid in laminar flow in a horizontal tube heat exchanger, and reported that at 2 wt% the heat transfer coefficient of the nanofluids increased, compared with that of the base fluid; at 2.5 wt% the heat transfer coefficient 22 and 15% was higher than that of pure fluid at 50 and 70 °C respectively. Ding et al. [63] tested multi-walled carbon nanotubes (MCNT with $\varphi = 0.1$–1.0% with 0.5 wt% in aqueous solution) in a horizontal tube, and obtained a maximum enhancement of heat transfer (350%) at a Reynolds number of 800. Particle re-arrangement, shear induced thermal conduction, reduction of thermal boundary layer due to the presence of nanoparticles and high aspect ratio of CNTs were reasoned for the enhancement. Yulong et al. [64] experimentally analyzed forced convective heat transfer using aqueous and ethylene glycol-based spherical titania, and aqueous-based titanate nanotubes, carbon nanotubes and nano-diamond nanofluids. For aqueous-based titania, carbon and titanate nanotube nanofluids, the convective heat transfer coefficient enhancement exceeded, by a large margin. The competing effects of particle migration on the thermal boundary layer thickness and the effective thermal conductivity were suggested to be responsible for the heat transfer enhancement.

4.1.3. Inferences from forced convection heat transfer experimental studies

The observed results from the prior work done on the convective heat transfer performance of nanofluids clearly shows, that the suspended particles outstandingly increase the heat transfer performance of the base-fluid; and the nanofluids have higher heat transfer coefficients than those of the base-fluids at the same Reynolds number. High aspect ratio nanoparticles such as carbon nanotubes resulted in greater enhancement in thermal conductivity and the heat transfer coefficient, compared to spherical and low aspect ratio nanoparticles. It has been shown in many references that the heat transfer behavior of nanofluids and the application of nanofluids for heat transfer enhancement, are influenced by the effective thermo-physical properties of nanofluids and many other factors such as particle size, shape and distribution; Brownian motion, particle–fluid interaction and particle migration also have an important influence on the heat transfer performance of nanofluids. However, because of the lack of agreement between the experimental results reported by various groups, most of the studies lack physical explanation for their observed results. All the convective studies have been performed with oxide particles, Future convective studies must be performed with metallic nanoparticles with different geometries and concentrations to consider heat transfer enhancement in laminar, transition and turbulence regions. Besides, the experimental data available for convective heat transfer are limited and insufficient to exactly predict the trend for heat transfer enhancement. Maiga et al. [65] reported that, with regard to the nanofluid thermal properties, the actual amount of experimental data available in the literature remains surprisingly small, and it is obvious that more works in this area will be published in the near future. Therefore, further research on the convective heat transfer of nanofluids is needed. Table 1 shows the summary of published experimental investigations of the convective heat transfer performance of various nanofluids.

4.2. Natural convection heat transfer experiments with nanofluids

Putra et al. [66] presented a study of the natural convection of nanofluids (Al_2O_3–water, CuO–water with $\varphi = 1$–4%) using a horizontal cylinder test section with one end heated and the other cooled. The time to reach the steady state was much lesser even at relatively high particle concentrations, due to the non-agglomerative and mono-dispersive nature of the nanofluids. The heat transfer coefficient was found to be higher at the hot wall than at the cold wall. The natural convective heat transfer is higher for the CuO–water than the Al_2O_3–water nanofluid. Wen and Ding [67] conducted experiments on nanofluids (TiO_2–water with $\varphi = 0$–1%) using two horizontally positioned aluminum discs separated by a 10 mm gap filled with nanofluid. The lower disc was heated at the bottom surface and the upper surface was open to the atmosphere. The temperature rose smoothly without any initial temperature oscillations as compared to micro-sized particles. The time to reach the steady state was also shorter and the heating surface temperature was found to increase with nanoparticle concentrations. The temperature difference between the walls increased with the volume fraction and reached 2.3 K for a $\varphi = 0.57\%$ compared to 1.5 K for pure liquid. Hwang et al. [68] theoretically presented the effects of the volume fraction, the size of nanofluids (Al_2O_3–water), and the average temperature of nanofluids on natural convective heat transfer characteristics in a rectangular cavity heated from the bottom. The results were validated with Touloukian et al. [69]. The results showed that as the volume fraction the of nanoparticles increased, the size of the nanoparticles decreased, the average temperature of nanofluids increased and the ratio of the heat transfer coefficient of nanofluids to that of base fluid decreased. Polidori et al. [70] investigated the natural convection heat transfer of Newtonian nanofluids in a laminar flow region with γ-Al_2O_3–water nanofluids whose Newtonian behavior was experimentally confirmed for $\varphi < 4\%$. The experimental investigations showed that the addition of nanoparticles deteriorated the heat transfer characteristics in the natural convective heat transfer region, whereas, the theoretical models predicted otherwise.

Table 1
Summary of experimental investigations in convective heat transfer of nanofluids.

Author	Base fluid	Particle material	Particle size	Volume fraction (vol.%)	Dimension	Flow regime, Re	Results and remarks
Pak and Cho. [39]	Water	$\gamma A1_2O_3$ TiO_2	13 nm 27 nm	1–3 1–3	ID: 1.066 cm Length: 480 cm S.S. tube	$Re = 10^4$–10^5 (turbulent flow)	Nu increased with increase in φ and Re
Eastman et al. [47]	Water	CuO	<100 nm	0.9	–	(Turbulent flow conditions)	HTC increased by >15% compared with pure water.
Wen and Ding [48]	Water	$\gamma A1_2O_3$	26–56 nm	0.6, 1, 1.6	ID: 4.5 mm Length: 970 mm Copper tube	Re = 500–2100 (laminar flow)	For φ = 1.6%, the HTC is 41% higher than the base fluid
Heris et al. [49]	Water	$A1_2O_3$ CuO	20 nm 50–60 nm	0.2–3.0 0.2–3.0	ID: 6 mm Copper tube	Re = 650–2050 (laminar flow)	HTC was high when φ increases for $A1_2O_3$, Nu is high
Esfahany etal. [50]	Water	γAl_2O_3	20 nm	0.2, 0.5, 1, 1.5, 2, 2.5	ID: 6 mm Length: 1 m Copper tube	Re = 700–2050 (laminar flow)	HTC ratio increases with φ and 22% increase with Pe
Lai et al. [51]	Water	$A1_2O_3$	20 nm	0–1%	ID: 1 mm S.S. tube	Re < 270	Nu enhancement of 8% for φ = 1%. $A1_2O_3$ nanofluid at Re = 270
Jung et al. [52]	Water	$A1_2O_3$	l0 nm	0.5–1.8%	Rectangular microchannel (50 μm × 50 μm)	5 < Re < 300	Conv. HTC increased by 32% for φ = 1.8%. Nu increases with Re
Williams et al. [53]	Water	ZrO_2	46 nm 60 nm	0.9–3.6 0.2–0.9	OD: 1.27 cm Thick. = 1.65 mm S.S. tube	9000 < Re < 63,000 (turbulent flow)	Considerable heat transfer enhancement is observed
Xuan and Li [57]	Water	Cu	<100 nm	0.3, 0.5, 0.8, 1, 1.2, 1.5, 2	ID: 10 mm Length: 800 mm Brass tube	Re = 10,000–25,000 (turbulent flow)	Conv. HTC increases with increase in φ and flow velocity
Xuan and Li [58]	Water	Cu	26 nm	0.5, 1, 1.5, 2	Hydraulic diameter = 1.29 mm	Re = 200–2000 (Laminar flow)	Nu of nanofluid with φ = 2% is 39% more than pure water
Zhou [59]	Acetone	Cu	80–100 nm	0.0–4.0 g/1	ID: 16 mm Length: 200 mm Copper tube	–	Conv. HTC increases with addition of Cu nanoparticles
Xuan and Li [60]	Water	Cu	26 nm	0.5, 1, 1.5, 2	ID: 10 mm Length: 800 mm Brass tube	Re = 1000–4000 (laminar and turbulent flow)	Nu ratio varied from 1.06 to 1.39 when φ increases from 0.5 to 2%
Faulkner et al. [61]	Water	CNT	<100 nm	1.1, 2.2, 4.4	Hydraulic diameter = 355 μm	Re = 2–17 (laminar flow)	HTC was found to be high at higher concentrations
Yang et al. [62]	Oil	Graphite	20–40 nm	0.7–1.0	ID: 4.57 mm Smooth tube	Re = 5 < 110 (laminar flow)	HTC was 22% higher at 50 °C and 15% higher at 70 °C for 2.5 wt%.
Ding et al. [63]	Water	MWCNT	100 nm	0.1–1.0 wt%	ID: 4.5 mm Length: 970 mm Copper tube	Re = 800–1200 (laminar flow)	350% enhancement was found for 0.5 wt% at Re = 800
Yulong et al. [64]	Ethylene glycol	TiO_2 CNT	–	–	–	–	Conv. HTC increases with φ and Re

4.2.1. Inferences from natural convection heat transfer experimental studies

Based on the limited experimental studies and contradictory results found in natural convective heat transfer of nanofluids, a firm conclusion cannot be drawn. However, the heat transfer enhancement of nanofluids in natural convective conditions needs further experimental and theoretical investigations, to exactly predict the behavior of nanofluids. Many factors such as particle size, shape and distribution, and the particle–fluid interactions should also be considered as significant parameters in the heat transfer performance of nanofluids in natural convective heat transfer.

4.3. Boiling heat transfer experiments with nanofluids

Boiling is an effective method of heat removal used in a variety of phase change heat exchanger like boilers, evaporators, etc. When the boiling occurs under a quiescent fluid condition, it is referred to as nucleate boiling and under a forced-flow condition; it is referred as forced convective boiling or convective vaporization. The former depends of the microstructure and the active nucleation cites (pits and crevices, Collier and Thome, [71] of the heat surface and heat flux. Whereas, the latter depend on tube dimension and mass flow rate. The nucleate boiling and its onset depends wall superheat, surface characteristics, presence of dissolved gas, the number of nucleation sites and frequency, and the bubble growth rates. Critical heat flux in pool boiling is peak heat flux under which a boiling surface can sustain nucleate boiling. Reaching the CHF causes a transition from nucleate boiling regime to film boiling regime, which undesirable and causes temperature of the heated surface to reach the melting point. Therefore, an enhanced CHF provides increase in the safety margin of the thermal system and to design compact and efficient cooling systems for electronic devices, nuclear and chemical reactors, air conditioning, etc. Further, the invention of nanofluid has paved way for investigation on improvising the heat transfer in a phase change process. The boiling heat transfer characteristics are broadly investigated with respect to enhancement, critical heat flux and hysteresis. For instance, Chang and You [72] applied micro-porous coat to increase the number of active sites and enhanced the nucleate boiling heat transfer in a plain copper/FC-72 tube by 330% and increased CHF by 100%.

Pool boiling heat transfer using nanofluids has been a subject of many investigations and incoherent results have been reported in literature regarding the same. In the past, experiments were conducted in nucleate pool boiling with varying parameters such as particle size, concentration, surface roughness, etc. and the results showing heat transfer enhancement, deterioration and negligible effect were reported [73,74]. It has been found that deterioration in heat transfer coefficient is mainly observed at higher particle concentrations (4–16% by weight) and enhance-

ments mainly at lower particle concentrations (0.32–1.25% by weight). Moreover, the relative size of the particle with respect to the surface roughness of the heating surface seems to play an important role in understanding the boiling behavior.

Yang and Maa [75] performed pool boiling experiments with Al_2O_3–water (γ = 50, 300 nm, 1 μm) and found that pool boiling performance is greatly improved for φ = 0.1–0.5% in nucleate pool boiling regime. However, micron sized particle suspensions are known to cause problems of erosion and clogging. Das et al. [76] who investigated nucleate pool boiling characteristics of Al_2O_3–water (γ = 20–50 nm; φ = 4–16%) using cartridge heater and found that the nanoparticles sediment on the heater at higher concentration, and deteriorating the boiling performance.

Das et al. [77] showed that pool boiling of nanofluids on narrow horizontal tubes (4 and 6.5 mm diameter. It was found that at this range of narrow tubes the deterioration rate boiling performance with nanofluids is less compared to large industrial tubes, which make it less inclined to local overheating in convective applications because of the relatively small size of the tube.

Bang and Chang [78,79] studied pool-boiling characteristics of Al_2O_3–water nanofluids with (φ = 4–16%) concentration at high heat flux condition. It was observed that the boiling characteristics of nanofluids deteriorated with high concentration similar to Das et al. [76] but the rate of heat transfer was different due to the difference in geometrical features of the heaters in the two studies.

Wen and Ding [80] studied pool boiling heat transfer using spherical Al_2O_3–water (γ = 10–50 nm). The results were quite different from the earlier studies. It was observed that the pure water results matched with the Rohsenow correlation and the heat transfer with nanofluids showed an enhancement in heat flux at the same wall super heat and this enhancement increased with particle volume fraction. It was also observed 40% increase in heat transfer coefficient between nanofluids and pure water. Also, the enhancement was with just 1.25 wt% of particles, which is about 0.3% by volume. Hence, the study concluded saying that this increase is much more than the measured value of thermal conductivity enhancement and hence the boiling enhancement cannot be explained by conductivity enhancement alone.

You et al. [81] performed experiments with alumina-water nanofluids of very small solid particle concentrations (0.0001–0.005% by weight) on a 10 mm square heater in sub-atmospheric conditions and found no significant change in nucleate pool boiling. Vasallo et al. [82] conducted experiments with SiO_2–water nanofluids (γ = 15–50 nm; φ = 2%) on a NiCr wire heater and found no significant change in the boiling performance at low and medium heat fluxes. But at heat fluxes near to CHF of water, it was observed that there is boiling deterioration for the 50 nm nanofluid. Similar increase in CHF is observed in many references (You et al. [81]; Bang and Chang [78,79]; Kim et al. [83,84]; Milanova et al. [85] Jackson et al. [86]).

Witharana [87] carried out experiments using Au–water nanofluids of very low solid particle concentrations (0.001% by weight) on plate heater. An enhancement of 11–21% in heat transfer coefficient was found. With increasing particle concentration the percentage enhancement in heat transfer coefficient also increased.

Nguyen et al. [88] showed enhancement of boiling heat transfer using Al_2O_3–nanofluids (γ = 47 nm) under atmospheric pressure, at various particle concentrations. The critical heat flux had considerably decreased with the augmentation of particle concentrations. For distilled water, the value of CHF was 1192 kW/m^2 which was quite close to that predicted by using the modified Zuber formula. The corresponding values for nanofluids of 0.5, 1 and 2% concentration were 744, 690, and 422 kW/m^2. Thus, the decrease of maximum heat flux was nearly 65% for 2% nanofluid as compared to distilled water.

Jung et al. [89] measured nucleate boiling heat transfer data of eight halocarbon refrigerants and made a specific correlation for halocarbon refrigerants based on the observed data. Test results showed that nucleate boiling HTCs of these halocarbon refrigerants were increased with the addition of CNTs. Especially, heat transfer was enhanced up to 36.6% at low heat flux. As the heat flux increased, the heat transfer enhancement with CNTs decreased. The developed correlation agreed best with these halocarbon refrigerants.

Tu et al. [90] carried out pool boiling experiments using Al_2O_3–water nanofluids on a 26 mm × 40 mm rectangular surface at the atmospheric pressure and an enhancement of heat transfer of 64% was recorded. Zhou [91] investigated experimentally the heat transfer characteristics of Cu–acetone based nanofluids with and without acoustic cavitation and showed that the copper nanoparticles and acoustic cavitation had significant influence on heat transfer in the fluid. The addition of nanoparticles did not affect the dependence of the heat transfer on acoustic cavitation and fluid sub-cooling. In an acoustic field, the boiling heat transfer of nanofluids was enhanced and the boiling hysteresis disappeared.

Park and Jung [92] conducted a study on nucleate boiling heat transfer coefficients of R123 and R134a, on a 152.0 mm long horizontal plain tube of 19.0 mm outside diameter with and without 1.0 vol.% of carbon nanotubes. The addition of CNTs resulted in heat transfer enhancement at low heat flux was up to 36.6%. Further, unlike conventional nanoparticles, no fouling was observed on the surface with CNTs.

Park and Jung [93] investigated pool boiling of CNT-R22 and CNT–water (φ = 1.0%) of CNTs and showed that CNTs increase boiling heat transfer coefficients of these fluids up to 28.7%. With increasing heat flux, however, the enhancement was suppressed due to vigorous bubble generation. Penetration into the thermal boundary layer by CNTs to generate more bubbles at the surface seemed to be the key element in the improvement of nucleate boiling heat transfer associated with the use of CNTs.

4.3.1. *Inferences from boiling heat transfer experimental studies*

The observations based on the studies of boiling heat transfer of nanofluids shows that the boiling performance is inversely proportional to nanoparticle concentration. However, Wen and Ding [80] have reported a trend contradictory to this. As far as the effect of nanoparticles on the boiling heat transfer performance is concerned, conflicting results were observed from these limited data. The inconsistencies indicate that the understanding of the thermal behavior of nanofluids related to the boiling heat transfer is still poor. The pool boiling is affected by the surface properties such as surface roughness, surface wettability, and surface contamination. In the reviewed studies, only the surface roughness is the most often considered parameter. Also no study on boiling of metallic nanofluids or flow boiling of nanofluids is available. Further, detailed investigations are necessary to understand the phenomena of boiling of nanofluids and the influence on the above factors.

5. Mathematical modeling

5.1. *Theoretical investigations for convective heat transfer of nanofluids*

The mixture of nanoparticles and base fluid is a multiphase problem and thus, could be approximated as either a homogeneous fluid or heterogeneous mixture. In the case of a homogeneous approach, because of the size of the nanoparticles, it has been suggested that these particles may easily be fluidized and consequently, can be considered to behave more like a single phase fluid. Further, by assuming a negligible motion slip between

the particles and the thermal equilibrium conditions, the nanofluid could be considered as a conventional single-phase fluid with averaged physical properties of individual phases [39,94]. However, because the effective properties of the nanofluids are not known precisely, the numerical predictions of this approach are not in good agreement with the experimental results. Choi et al. [95] first adopted a homogeneous model and used the conventional heat transport equations for pure fluids, such as the Dittus–Boelter correlation, to the nanofluids. In the case of a heterogeneous approach (two-phase), factors such as gravity, friction between the phases, Brownian diffusion, sedimentation, and dispersion are included in the flow model. The two-phase approach provides the possibility of understanding the functions of both the fluid phase and the solid particles in the heat transfer process, and provides a field description of both the phases.

Xuan and Roetzel [96] proposed a two-phase thermal dispersion model and assumed that the convective heat transfer enhancement in nanofluids comes from two factors, (i) higher thermal conductivity, and (ii) the thermal dispersion of the nanoparticles. In this approach, the effect of the nanoparticle/base fluid relative velocity and temperature are treated as a perturbation of the energy equation. The thermal dispersion coefficient was introduced to describe the heat transfer enhancement. Khanafer et al. [97] investigated the heat transfer enhancement in a two-dimensional enclosure utilizing the nanofluid. The effective thermal conductivity was taken as the sum of the mixture thermal conductivity evaluated from the conventional theory and a dispersion thermal conductivity. It was observed that in any of the numerical studies in convection, the effect of temperature on thermal conductivity was not considered. However, the effect of temperature on the thermal conductivity of nanofluids was proved significant from studies made by Das et al. [98].

Buongiorno [99] developed an alternative model that eliminates the shortcomings of the homogeneous and dispersion models. The homogeneous flow models are in conflict with the experimental observation and the pure-fluid correlations underpredict the heat transfer coefficient. In this model, a detailed analysis of convective transport with seven slip conditions between particles and fluid were considered, for explaining the enhancement of heat transfer with nanofluids. In these mechanisms the Brownian diffusion and thermophoresis were the two most important nanoparticles/base fluid slip mechanisms. Convective heat transfer enhancement was obtained with a decrease in viscosity and consequent thinning of the laminar sub-layer. It was observed that the radial distribution of the particle concentration (more concentration at the core than the walls) brought about by thermophoresis make the temperature profile flatten, thus giving a higher heat transfer coefficient and finally, a new correlation was developed to predict the enhanced heat transfer coefficient of nanofluids.

Behzadmehr et al. [100] applied a two-phase mixture model to study the heat transfer of nanofluids (Cu–water; $\varphi = 1\%$) for forced turbulent convection in a uniformly heated tube. The Nusselt number increased by more than 15%, was proportional to the Reynolds number and resulted in a more uniform velocity profile. The frictional coefficient decreased as the Reynolds number increased when compared with that of pure fluid. Finally, increasing particle concentration caused the Nusselt number to increase and thus, the convective heat transfer coefficient.

Maïga et al. [101] modeled the forced convection flow of a nanofluid (γAl_2O_3 with water and ethylene glycol) in a straight tube of circular cross-section. A single-phase flow was assumed to derive the governing equations to calculate the heat transfer enhancement by the nanofluids in the laminar flow as well as the turbulent flow regime, with nanofluid concentrations ranging from 0 to 10%. For laminar flow, the results indicated an increase in the heat transfer rate, particularly at the walls, with the augmentation of φ (for $\varphi = 10\%$, the product ρc_p and thermal conductivity, k increased by $\sim$18 and $\sim$33%, respectively). The heat transfer coefficient ratio h_r also increases with particle loading and particularly at the tube end (by nearly 60%). Further, averaged heat transfer enhancement was clearly more pronounced for the γAl_2O_3–ethylene glycol than for the γAl_2O_3–water nanofluid for $\varphi > 3\%$ (identical otherwise). The wall shear stress was found to increase considerably with the particle volume fraction and along the tube length. For the turbulent flow regime, the heat transfer coefficient increased steeply for a very short distance from the inlet section. The properties h_r and τ_r varied in a similar manner as in the previous case.

Roy et al. [102] modeled the hydrodynamic and thermal fields of a γAl_2O_3–water nanofluid ($\varphi = 1$–10%) in a radial laminar flow cooling system. Considerable increases in the wall shear stress were predicted on account of the increase in the fluid viscosity (a maximum of 2.5-fold increase for $\varphi = 5\%$). Overall, the study indicated that considerable heat transfer enhancement was possible and a maximum increase of twice the value of the base fluid in the case of $\varphi = 10\%$. Ding and Wen [103] modeled the effects of particle migration in pressure driven laminar flows of nanofluids and predicted the particle concentration and velocity field of nanofluids; in the transverse plane of the pipe by taking into account the effects of the shear induced and viscosity gradient induced particle vibrations as well as self-diffusion due to the Brownian motion. Two approaches were used, one was based on mass conservation law for the dispersed phase and the other on the momentum balance of the particle phase. The results indicate that the Peclet number increased rapidly with increasing particle size and Reynolds number. The Brownian motion had a significant effect on the particle migration of nanofluids and became important at Peclet numbers less than 10. At the limit of zero Peclet number, the particle concentration is uniform. Further, the smaller the particle size, the more uniform the distribution of particles in the transverse plane. The existence of an optimal particle size at which the thermal conductivity was enhanced with little penalty due to pressure drop is suggested.

Palm et al. [104] numerically investigated the enhanced heat transfer capabilities of Al_2O_3–water ($\gamma = 38$ nm; $\varphi = 1$–4%) in a radial laminar flow cooling system and used temperature-dependant nanofluid properties. The experimental results obtained using the single-phase approach indicated that property fluctuations are noticed near the injection inlet. Lower viscosities at higher temperature, decrease in wall shear stress for increase in wall heat flux and greater wall heat transfer rates were shown when compared to predictions using constant properties.

Kim et al. [105] theoretically investigated the Thermo-diffusion (Soret effect) and diffusion thermo (Dufour effect) effects on convective instabilities in binary nanofluids (the base-fluid is a binary mixture). Data from silver and copper nanofluids studies were used in this investigation, which showed that the particles caused a unique convective motion in binary nanofluids. The heat transfer enhancement by the Soret effect in binary nanofluids is more significant than that in mono-nanofluids. Further, the heat transfer coefficient of silver nanofluids was higher than that of copper, owing to the higher thermal conductivity of silver. Studies predicted that the Soret and Dufour diffusions make the nanofluids unstable and this was more profound for denser nanofluids. Further, the convective motion in nanofluids sets easily in both the effects as the concentration increased.

Mansour et al. [106] investigated the effect of the Hamilton–Crosser model and the Modified Maxwell model, to predict nanofluid (γAl_2O_3–water; $\varphi = 1$–10%) physical properties, on their thermal and hydrodynamic performance for both fully developed laminar and turbulent forced convection in a tube with uniform

Table 2
Existing convective heat transfer correlations for nanofluids.

Reference	Correlation
Pak and Cho [39]	$Nu = 0.021\,Re^{0.8}Pr^{0.5}$
Xuan and Li [57]	$Nu = 0.4328(1.0 + 11.285\varphi^{0.754}Pe_p^{0.218})Re_{nf}^{0.333}Pr_{nf}^{0.4}$ for laminar flow $Nu = 0.0059(1.0 + 7.6286\varphi^{0.6886}Pe_p^{0.001})Re_{nf}^{0.9238}$ for turbulent flow
Maiga et al. [65]	$Nu = 0.86\,Re^{0.55}Pr^{0.5}$ for constant wall heat flux $Nu = 0.86\,Re^{0.35}Pr^{0.36}$ for constant temperature
Buongiorno [40,99]	$Nu_b = \frac{(f/8)(Re-1000)Pr}{1+\delta_\nu^+\sqrt{(f/8)(Pr_\nu^{2/3}-1)}}$
Maïga et al. [118]	$Nu = 0.085\,Re^{0.71}Pr^{0.35}$ for fully developed (fd) turbulent flow

heat flux at the wall. Two models gave substantially different results for thermal conductivity, specific heat and viscosity, and the differences were more profound for higher particle loading. The expressions failed to account for the size disparity between the nanoparticles. The two models revealed in very different predictions and it was not possible to ascertain which was accurate. The study illustrated that the operational conditions or the design parameters varied significantly with the thermo-physical properties of the nanofluid.

Prakash and Giannelis [107] calculated the thermal conductivity of nanofluids (Al_2O_3–water and ethylene glycol) using temperature and concentration dependent viscosity relations. The temperature profile was obtained using the Gaussian fit to the available experimental data. The micro-convection of the alumina nanoparticle ($\gamma < 100$ nm) was included through the Reynolds and Prandtl numbers. The model was further improved by explicitly incorporating the thermal conductivity of the nano-layer surrounding the nanoparticles. The results indicated that the thermal conductivity ratio depends on both the temperature variation in viscosity and the Brownian motion. However, the thermal conductivity was more sensitive to the Reynolds number than to the Prandtl number. As a result, there is net enhancement in thermal conductivity as the temperature was increased. Studies showed that a cylindrical-shaped particle leads to much higher thermal transport than a spherical-shaped particle.

Li and Peterson [108] simulated the mixing effect of the base fluid with nanoparticles caused by the Brownian motion; they modeled and compared it with the existing experimental data available in the literature. The mixing effect predicted a significant influence on the effective thermal conductivity of nanofluids.

5.2. Inferences from theoretical studies with nanofluids

The observations based on the reviewed literature for theoretical studies in the convective heat transfer of nanofluids clearly shows, that the models developed by the various researchers have been satisfactory only under very stringent conditions. However, a generalized theoretical model should be developed by considering all the factors such as inertia, thermophoresis, Brownion motion, and gravity which influences the heat transfer characteristics and the behavior of nanofluids under convective heat transfer conditions. The correlations based on the experimental data for finding the Nusselt number of nanofluids

Table 3
Summary of theoretical investigations in convective heat transfer of nanofluids.

Author	Theoretical investigations	Approach	Results and remarks
Xuan and Li [28]	Theoretical heat transfer characteristics of transformer oil–Cu and water–Cu nanofluids	Single phase fluid approach	The heat transfer coefficient improved dramatically with decrease in particle size and not only due to thermal conductivity increase
Xuan and Roetzel [96]	Heat transfer of nanofluids	1. Single phase fluid approach 2. Dispersion model approach	Suspended particles increase the thermal conductivity. Chaotic movement of ultrafine particles and the thermal dispersion accelerates the energy exchange process
Buongiorno [40,99]	Convective transport in nanofluids	Two-component non-homogeneous equilibrium model	Brownian diffusion and thermophoresis are the two most important nanoparticles/basefluid slip mechanisms
Behzadmehr et al. [100]	Turbulent forced convection flow in a uniformly heated tube	Two phase mixture model	HTC increases with φ and Re. Higher Re resulted more uniform velocity profile
Maiga et al. [101]	Forced convection flow of nanofluid (water/Al_2O_3 and ethylene glycol/Al_2O_3) in a circular tube	Single phase fluid approach	60% enhancement in HTC was found and turbulent flow enhancement increases with Re
Roy et al. [102]	Hydrodynamic and thermal flow fields of water/Al_2O_3 nanofluid in a radial laminar flow cooling system		Two fold increase in heat transfer coefficient was observed along with wall shear stress and particle concentration
Ding and Wen [103]	Effects of particle migration in laminar flows of nanofluids	Mass conservation laws and momentum balance	Shear induced migration, viscosity gradient migration and self-diffusion. Highly non-uniform thermal conductivity profile obtained
Palm et al. [104]	Heat transfer capabilities and temperature-dependant properties of nanofluids in radial flow cooling systems	Single phase fluid approach	Temperature dependent properties lead to greater heat transfer performance with the decrease in wall shear stresses
Kim et al. [105]	Thermo diffusion (Soret effect), diffusion thermo (Dufour effect) effects in binary nanofluids	One fluid model	As the Soret and Dufour effects and φ increases the convective motion sets in easily
Mansour et al. [106]	Thermal and hydrodynamic performance for both laminar and turbulent forced convection in a tube with uniform heat flux at the wall	Single phase fluid approach	Both the models predicted increased HTC with particle concentration
Prakash and Giannelis [107]	Thermal conductivity of Al_2O_3 nanofluids using temperature and concentration dependent viscosity		Dependence of the thermal conductivity on the size of the nanoparticle, temperature viscosity and particle concentration
Maïga et al. [118]	Forced convection flow of nanofluid (water/Al_2O_3 and ethylene glycol/Al_2O_3) in a circular tube and radial channel between a pair of parallel coaxial discs	Single phase fluid approach	HTC increased by 63 and 45%. Increased heat transfer and dynamic viscosity resulted in increased wall shear stress with partial loading

from laminar to turbulent regions reported in the published literature are presented in Tables 2 and 3 gives a summary of the various theoretical investigations in the convective heat transfer of nanofluids.

6. Applications

6.1. Micro-channels

The micro-channel heat sink (MCHS) has the capability to dissipate large amounts of heat from a small area with a very high heat transfer coefficient and less fluid inventory. Using nanofluids as a coolant in the MCHS could further improve its performance. Chein and Huang [109] analyzed the performance of the MCHS (silicon channel of 100 μm × 300 μm dimension) using a Cu–water nanofluid with φ = 0.3–2%. The Nusselt number increased significantly with an increase in Re and φ. The maximum reduction in thermal resistance as compared to pure water was found to be 15% at φ = 2% and power = 3 W. The additional reduction in R_{th} is clearly due to thermal dispersion. With regard to pressure drop, no significant differences existed between the nanofluid and water flows.

Jang and Choi [110] numerically investigated the cooling performance of a silicon micro-channel heat sink under forced convective flow with nanofluid (Cu–water; γ = 6 nm and diamond–water; γ = 2 nm particle size) for φ = 1%. The nanofluids reduced the thermal resistance of the heat sink and enhanced the cooling performance by 10 and 4%, respectively. Further, the potential of employing a micro-channel heat sink with nanofluid to remove ultra high heat flux as much as 1350 W/cm^2 when the difference between the junction temperature and inlet coolant temperature is 80°C, was demonstrated.

Chein and Chuang [111] used a nanofluid (CuO–water, φ = 0.204, 0.256, 0.294 and 0.4%) with 80 nm long and 20 nm wide particles. The energy absorbed by the nanofluid was greater than that absorbed by water and was found to increase with the increase in particle volume fraction. A large temperature difference between the MCHS inlet and outlet was obtained at a low flow rate. Thermal resistance was found to reduce with an increase in the flow rate. Although the nanofluids had higher viscosity, only a marginal increase (around 5%) in the pressure drop across the MCHS was reported.

Koo and Kleinstreuer [112] simulated and analyzed the conduction-convection heat transfer of nanofluid (CuO–water and ethylene glycol, γ = 20 nm) in a micro-channel (300 μm × 50 μm). The new model incorporated static and Brownian heat transfer, and hence the thermal conductivity and dynamic viscosity were suggested to be $k_{eff} = k_{static} + k_{Brownian}$ and $\mu_{eff} = \mu_{static} + \mu_{Brownian}$. The Nusselt number for ethylene glycol based nanofluids was always higher than for water based ones, due to stronger thermal flow development effects. Moreover, the viscous dissipation effect was found to affect only ethylene glycol based nanofluids and was more important for flows through very narrow channels.

Nguyen et al. [113] investigated the heat transfer enhancement of Al_2O_3–water (γ = 36 and 47 nm) in the cooling systems of microprocessors and electronic components. The inclusion of nanoparticles in distilled water produced a considerable enhancement convective heat transfer coefficient (around 40% for φ = 6.8%) and a clear decrease of the heated component temperature was recorded. In addition, smaller nanoparticles were found to produce greater enhancement in the heat transfer coefficient.

6.2. Heat pipes

Chien et al. [114] studied heat transfer in a disk-shaped miniature heat pipe (DMHP) using nanofluid (Au–DI water; φ = 18, 37 and 55%; γ = 17 nm). The average decrease of 40% in thermal resistance was achieved as compared to that of pure DI water. Tsai et al. [115] studied a heat pipe using the Au–DI water nanofluid (γ = 8–43.7 nm) and a 37% lower thermal resistance was achieved (at γ = 21.3 nm) when compared to that of DI–water. Smaller nanoparticles have greater reduction in thermal resistance in conditions of equal aggregation. A major reduction in thermal resistance is from the evaporator section to the adiabatic section (a maximum of 56% reduction), which is attributed to the bombardment of vapor bubbles by the nanoparticles.

Kang et al. [116] investigated heat transfer in a grooved heat pipe using Ag–water and Ag–DI water (γ = 10–35 nm) with particle concentrations ranging from 1 to 100 mg/l. The results indicated that after adding a small amount of silver nanoparticles in pure water, the heat pipe wall temperature became lower than that of pipes filled only with pure water. As more nanoparticles became dispersed in the working fluid, the heat pipe wall temperature increase became smaller. The maximum reduction in thermal resistance of a heat pipe containing γ = 10 nm was 52% lower, while that containing γ = 35 nm was 81% lower than that of DI–water. The enhancement of heat pipe performance was attributed to the increase in effective liquid conductance that flattens the temperature of the fluid.

Ma et al. [117] studied the nanofluid (diamond–water; φ = 1%) behavior in an oscillating heat pipe (OHP) and thus developed an ultrahigh performance cooling device, called the nanofluid oscillating heat pipe in which when the input power was increased to the highest value, the temperature difference between the evaporator and the condenser for the nanofluid OHP was less than that for the OHP with only pure water.

7. Outlook and future challenges

Many interesting properties of nanofluids have been reported in the review. In the previous studies, thermal conductivity has received the maximum attention, but many researchers have recently initiated studies on other heat transfer properties. The use of nanofluids in a wide variety of applications appears promising. But the development of the field is hindered by (i) lack of agreement of results obtained by different researchers; (ii) poor characterization of suspensions; (iii) lack of theoretical understanding of the mechanisms responsible for changes in properties. Therefore, this article concludes by outlining several important issues that should receive greater attention in the near future. Experimental studies in the convective heat transfer of nanofluids are needed. Many issues, such as thermal conductivity, the Brownian motion of particles, particle migration, and thermophysical property change with temperature, must be carefully considered with convective heat transfer in nanofluids. Though, all the convective studies have been performed with oxide particles in high concentrations, (for example Pak and Cho [39] used 10 vol.% of Al2O3 which increased the viscosity and pumping power of the fluid), it is interesting to know the energy transport in low-concentration (<1 vol.%) nanofluids with metallic particles, since the thermal conductivity of pure metallic nanoparticles is more than 100 times higher than that of the oxide nanoparticles. Future convective studies must be performed with metallic nanoparticles with different geometries and concentrations to consider heat transfer enhancement in laminar, transition and turbulence regions. The use of nanofluids in heat pipes has shown enhancement in performance and considerable reduction in thermal resistance. However, recent studies indicate particle aggregation and deposition in micro-channel heat sinks. Further study is required in these areas to identify the reasons for and the effects of particle deposition. Finally, there appears to be hardly any research in the use of nanofluids as refrigerants. Nanoparticle-refrigerant dispersions in two-phase heat transfer applications can be studied

to explore the possibility of improving the heat transfer characteristics of evaporators and condensers used in refrigeration and air-conditioning appliances. Applied research in nanofluids which will define their future in the field of heat transfer is expected to grow at a faster pace in the near future.

8. Conclusion

The present review is a comprehensive outlook on the research progress made in the convective heat transfer characteristics of nanofluids. The salient feature that can be drawn from the reviewed literature is that nanofluids are a new class of heat transfer fluids and show greater promise for use in cooling and related technologies. From the observed results it is clearly seen, that nanofluids have greater potential for heat transfer enhancement and are highly suited to application in practical heat transfer processes. This offers an opportunity for engineers to develop highly compact and effective heat transfer equipment. Several published articles show that the heat transfer coefficient of nanofluids is much higher than that of the common-base fluid and gives little or no penalty in pressure drop. The main reason for the heat transfer enhancement of nanofluids is that the suspended nanoparticles increase the thermal conductivity of the fluids, and the chaotic movement of ultrafine particles increases fluctuation and turbulence of the fluids, which accelerates the energy exchange process. Convective heat transfer is enhanced by increasing the particle concentration and the Reynolds number. Besides, the experimental data available for convective heat transfer in laminar, transition and turbulence regions are limited and insufficient to exactly predict the trend for heat transfer enhancement. Furthermore, only very few correlations are available to exactly predict the heat transfer performance of nanofluids, and correlations which include the effect of volume fraction, particle shape and particle size are nil to-date. Therefore, further research on convective heat transfer of nanofluids, and more theoretical and experimental research works are needed in order to clearly understand and accurately predict their hydrodynamic and thermal characteristics. The trends reported in literature on nucleate boiling of nanofluids are conflicting and the results are contradicting. The authors have tried to arrive at a common reasoning for the seemingly conflicting results. Also no study on boiling of metallic nanofluids or flow boiling of nanofluids is available. Further work is required to determine the effect of surface wettability on pool boiling of nanofluids in the nucleate boiling regime especially for the low concentration metallic nanoparticles.

Generally, many researchers indicated that nanofluids behave like pure fluids because the suspended particles are ultrafine. However, at present, no formulated advanced theory exists to explain the behavior of nanofluids by considering them as multi-component materials. Greater enhancement was observed when nanofluids were used in heat pipes and in micro-channel heat sinks, as well as other applications. Further, theoretical and experimental research investigations are needed to comprehensively understand the heat transfer mechanism in nanofluids for evolving new energy efficient heat transfer fluids specific to applications.

Acknowledgements

The authors would like to thank Prof. Jacopo Buongiorno, Ph.D., Massachusetts Institute of Technology, Cambridge, MA, for rendering a helpful review and constructive suggestions during the preparation of the above research article.

References

[1] Kyoto Protocol to the United Nations framework convention on climate change; 1992.
[2] Yang J, Chan K-t, Wu X, Energy savings with energy-efficient HVAC systems in commercial buildings of Hong Kong, ICEBO2006, Shenzhen, China, (7):5–2.
[3] Thermal Management, Technical report, Alcatel-Lucent Technologies, Ireland.
[4] Das SK, Choi SUS, Yu W, Pradeep T. Nanofluids—science and technology. Wiley-Interscience; 2008.
[5] Hwang YJ, Ahn YC, Shin HS, Lee CG, Kim GT, Park HS, Lee JK. Investigation on characteristics of thermal conductivity enhancement of nanofluids. Current Applied Physics 2006;6:1068–71.
[6] Eastman JA, Phillpot SR, Choi SUS, Keblinski P. Thermal transport in nanofluids. AR Reviews. In Advance. Annual Review of Materials Research 2004;34:219–46.
[7] Keblinski P, Eastman JA, Cahill DG. Nanofluids for thermal transport. Review Feature Materials Today June, 2005.
[8] Daungthongsuk W, Wongwises S. A critical review of convective heat transfer of nanofluids. Renewable Sustainable Energy Reviews 2007;11(5):797–817.
[9] Wang XQ, Mujumdar AS. Heat transfer characteristics of nanofluids: a review. International Journal of Thermal Science 2007;46(1):1–19.
[10] Yu W, France DM, Choi SUS, Routbort JL. Review and assessment of nanofluid technology for transportation and other applications. Argonne National Laboratory; 2007. p. 1–78.
[11] Maxwell JC. Treatise on electricity and magnetism. Oxford: Clarendon Press; 1873.
[12] Choi SUS. Enhancing thermal conductivity of fluids with nanoparticles, in Developments and Applications of Non-Newtonian Flows. ASME FED 231/MD 1995;66:99–103.
[13] Dreizin EL. Metal-based reactive nanomaterials. Progress in Energy and Combustion Science 2009;35(2):141–67.
[14] Joseph Lik Hang Chau, Chih Chun Kao. Microwave plasma synthesis of TiN and ZrN nanopowders. Materials Letters 2007;61(7):1583–7.
[15] Hayashi C, Oda M. Research and applications of nano-particles in Japan. Journal of Aero solid Science 1998;29:757–60.
[16] Granqvist CG, Buhrman RA. Ultrafine metal particles. Journal of Applied Physics 1976;47:2200.
[17] Gleiter H. Nanocrystalline materials, Program. Material Science 1989;33:223–315.
[18] Neikov OD. Nanopowders, handbook of non-ferrous metal powders; 2009. p. 80–101.
[19] Fissan HJ, Schoonman J. Vapor-phase synthesis and processing of nanoparticle materials (nano): a European Science Foundation (ESF) program. Journal of Aero solid Science 1998;29:755–7.
[20] Akoh H, Tsukasaki Y, Yatsuya S, Tasaki A. Magnetic properties of ferromagnetic ultrafine particles prepared by a vacuum evaporation on running oil substrate. Journal of Crystal Growth 1978;4:495–500.
[21] Biercuk BJ, Llaguno MC, Radosavljevic M, Hyun JK, Johnson AT. Carbon nanotube composites for thermal management. Applied Physics Letters 2002;80:2767–72.
[22] Ju S, Li ZY. Theory of thermal conductance in carbon nanotube composites. Applied Physics Letters 2006;353:194–7.
[23] Yao N, Wang ZL, editors. Handbook of microscopy for nanotechnology. Boston: Kluwer Academic Publishers; 2005.
[24] Daniel MC, Astruc D. Gold nanoparticles: assembly, supramolecular chemistry, quantum-size-related properties, and applications toward biology, catalysis, and nanotechnology. Chemical Reviews 2004;104:293–346.
[25] Trindade T, O'Brien P, Pickett NL. Nanocrystalline semiconductors: synthesis, properties, and perspectives. Chemical Materials 2001;13:3843–58.
[26] Rajamathi M, Seshadri R. Oxide and chalcogenide nanoparticles from hydrothermal/solvothermal reactions. Current Opinion Solid State Material Science 2002;6:337–45.
[27] Hulteen JC, Martin CR. In: Fendler JH, editor. Nanoparticles and nanostructured films: preparation, characterization and applications. New York: Wiley; 1998.
[28] Xuan Y, Li Q. Heat transfer enhancement of nanofluids. International Journal of Heat and Fluid Flow 2000;21:58–64.
[29] Bejan A, Kraus AD. Heat transfer handbook. John Wiley and Sons Inc.; 2003.
[30] Choi SUS. Nanofluid technology: current status and future research, Korea-U.S. Technical Conference on Strategic Technologies, Vienna, VA, US; 1998.
[31] Masuda H, Ebata A, Teramae K, Hishinuma N. Alteration of thermal conductivity and viscosity of liquid by dispersing ultra-fine particles (dispersion of γ-Al_2O_3, SiO_2 and TiO_2 ultra-fine particles). Netsu Bussei (Japan) 1993;4(4):227–33.
[32] Grimm A. Powdered aluminum-containing heat transfer fluids. German Patent DE 4131516 A1 (1993).
[33] Choi SUS, Eastman JA, U.S. Patent 6,221,275 (April 2001).
[34] Eastman JA, Choi SUS, Li S, Yu W, Thomson LJ. Anomalously increased effective thermal conductivities of ethylene glycol based nanofluids containing copper nanoparticles. Applied Physics Letters 2001;78:718–20.
[35] Philip J, Laskar JM, Raj B. Magnetic field induced extinction of light in a suspension of Fe_3O_4 nanoparticles. Applied Physics Letters 2008;92.
[36] Bhat S, Maitra U. Facially amphiphilic thiol capped gold and silver nanoparticles. Journal of Chemical Sciences 2008;120(6):507–13.
[37] Frimpong RA, Hilt JZ. Poly (n-isopropylacrylamide)-based hydrogel coatings on magnetite nanoparticles via atom transfer radical polymerization. Nanotechnology 2008;(17), doi:10.1088/0957-4484/19/17/175101.
[38] Jean NC, Tan CP, Yaakob CMB, Misni M. α-Tocopherol nanodispersions: preparation, characterization and stability evaluation. Journal of Food Engineering 2008;89:204–9.

[39] Pak BC, Cho IY. Hydrodynamic and heat transfer study of dispersed fluids with sub-micron metallic oxide particles. Experimental Heat Transfer 1998;11: 151–70.
[40] Buongiorno J. Convective transport in nanofluids. Journal of Heat Transfer ASME 2006.
[41] Keblinski P, Phillpot SR, Choi SUS, Eastman JA. Mechanisms of heat flow in suspensions of nano-sized particles (nanofluids). International Journal of Heat and Mass Transfer 2002;45:855–63.
[42] Koo J, Kleinstreuer C. Impact analysis of nanoparticle motion mechanisms on the thermal conductivity of nanofluids. International Communication on Heat and Mass Transfer 2005;32(9):1111–8.
[43] Ahuja AS. Augmentation of heat transport in Laminar flow of polystyrene suspensions. I. Experiments and results. Journal of Applied Physics 1975;46 (83):408–3416.
[44] Ahuja AS. Thermal design of heat exchanger employing Laminar flow of particle suspensions. International Journal of Heat and Mass Transfer 1982;25(5):725–8.
[45] Hetsroni G, Rozenblit R. Heat transfer to a liquid–solid mixture in a flume. International Journal of Multiphase flow 2005;20(4):671–89.
[46] Lee S, Choi SUS. Application of metallic nanoparticle suspensions in advanced cooling systems. Recent advances in solid/structures and applications of metallic materials, PVP vol. 342/MD-vol 72. New York: ASME; 1996. p. 227–234.
[47] Eastman JA, Choi SUS, Li S, Soyez G, Thompson LJ, DiMelfi RJ. Novel thermal properties of nanostructure materials. Material Science Forum 1999;312:629–34.
[48] Wen D, Ding Y. Experimental investigation into convective heat transfer of nanofluids at the entrance region under laminar flow conditions. International Journal of Heat and Mass Transfer 2004;47:5181–8.
[49] Heris SZ, Etemad SGh, Nasr Esfahany M. Experimental investigation of oxide nanofluids laminar flow convective heat transfer. International Communications in Heat and Mass Transfer 2006;33(4):529–35.
[50] Heris Z, Esfahany MN, Etemad SGh. Experimental investigation of convective heat transfer of Al_2O_3/water nanofluid in circular tube. International Journal of Heat and Fluid Flow 2007;28(2):203–10.
[51] Lai WY, Duculescu B, Phelan PE, Prasher RS. Convective heat transfer with nanofluids in a single 1.02-mm tube. In: Proceedings of ASME International Mechanical Engineering Congress and Exposition (IMECE 2006); 2006.
[52] Jung J-Y, Oh HS, Kwak HY. Forced convective heat transfer of nanofluids in microchannels. In: Proceeding of ASME International Mechanical Engineering Congress and Exposition (IMECE 2006); 2006.
[53] Williams W, Buongiorno J, Hu L-W. Experimental investigation of turbulent convective heat transfer and pressure loss of alumina/water and zirconia/water nanoparticle colloids (nanofluids) in horizontal tubes. ASME Journal of Heat Transfer 2008;130:1–6.
[54] Duangthongsuk W, Wongwises S. Effect of thermo-physical properties models on the prediction of the convective heat transfer coefficient for low concentration nanofluid. International Communications in Heat and Mass Transfer 2008;35(10):1320–6.
[55] Jang SP, Choi SUS. Role of Brownian motion in the enhanced thermal conductivity of nanofluids. Applied Physics Letters 2004;84:4316–8.
[56] Duangthongsuk W, Wongwises S. Heat transfer enhancement and pressure drop characteristics of TiO_2–water nanofluid in a double-tube counter flow heat exchanger. International Journal of Heat and Mass Transfer 2009;52(7–8):2059–67.
[57] Xuan Y, Li Q. Investigation on convective heat transfer and flow features of nanofluids. Journal of Heat Transfer 2003;125:151–5.
[58] Xuan Y, Li Q. Flow and heat transfer performances of nanofluids inside small hydraulic diameter flat tube. Journal of Engineering Thermophysics 2004;25(2):305–7.
[59] Zhou DW. Heat transfer enhancement of copper nanofluid with acoustic cavitation. Int Journal of Heat and Mass Transfer 2004;47:3109–17.
[60] Li Q, Xuan Y, Jiang J, Xu JW. Experimental investigation on flow and convective heat transfer feature of a nanofluid for aerospace thermal management. Journal of Astronautics 2005;26:391–4.
[61] Faulkner D, Rector DR, Davison JJ, Shekarriz R. Enhanced heat transfer through the use of nanofluids in forced convection. In: Proceedings of ASME Heat Transfer Div; 2004. p. 219–24.
[62] Yang Y, Zhang ZG, Grulke EA, Anderson WB, Wu G. Heat transfer properties of nanoparticles-in-fluid dispersions (nanofluids) in laminar flow. International Journal of Heat and Mass Transfer 2005;48:1107–16.
[63] Ding Y, Alias H, Wen D, Williams RA. Heat transfer of aqueous suspensions of carbon nanotubes (CNT nanofluids). International Journal of Heat and Mass Transfer 2006;49:240–50.
[64] Ding Y, Chen H, He Y, Lapkin A, Yeganeh M, Siller L, Butenko YV. Forced convective heat transfer of nanofluids. Advanced Powder Technology 2007;18(6):813–24.
[65] Maiga SEB, Palm SJ, Nguyen CT, Roy G, Galanis N. Heat transfer enhancements by using nanofluids in forced convection flows. International Journal of Heat and Fluid Flow 2005;26:530–46.
[66] Putra N, Roetzel W, Das SK. Natural convection of nano-fluids. International Journal of Heat and Mass Transfer 2003;39:775–84.
[67] Wen D, Ding Y. Formulation of nanofluids for natural convective heat transfer applications. International Journal of Heat and Fluid Flow 2005; 26:855–64.
[68] Hwang KS, Lee J-H, Jang SP. Buoyancy-driven heat transfer of water-based Al_2O_3 nanofluids in a rectangular cavity. International Journal of Heat and Mass Transfer 2007;50(19):4003–10.
[69] Touloukian YS, Powell RW, Ho CY, Klemens PG. Thermo-physical properties of materials, vol. 2. New York: Plenum Press; 1970.
[70] Polidori G, Fohanno S, Nguyen CT. A note on heat transfer modeling of Newtonian nanofluids in laminar free convection. International Journal of Thermal Science 2007;46(8):739–44.
[71] Collier J, Thome JR. Boiling and condensation. Oxford University press; 1994.
[72] Chang JY, You SM. Enhanced boiling heat transfer from microporous surfaces: effects of a coating composition and method. International Journal of Heat and Mass Transfer 1997;40:4449–60.
[73] Trisaksri V, Wongwises S. Critical review of heat transfer characteristics of nanofluids. Renewable and Sustainable Energy Reviews 2007;11(3):512–23.
[74] Trisaksri V, Wongwises S. Nucleate pool boiling heat transfer of an alternative refrigerant with nanoparticle suspension. International Journal of Heat and Mass Transfer 2009;52(5–6):1582–8.
[75] Yang YM, Maa JR. Boiling of suspension of solid particles in water. International Journal of Heat and Mass Transfer 1984;27:145–7.
[76] Das SK, Putra N, Roetzel W. Pool boiling characterization of nano-fluids. International Journal of Heat and Mass Transfer 2003;46:851–62.
[77] Das SK, Putra N, Roetzel W. Pool boiling nano-fluids on horizontal narrow tubes. International Journal of Multiphase Flow 2003;29:1237–47.
[78] Bang IC, Chang SH. Boiling heat transfer performance and phenomena of Al_2O_3–water nano-fluids from a plain surface in a pool. International Journal of Heat and Mass Transfer 2005;48:2407–19.
[79] Bang IC, Chang SH. Direct observation of a liquid film under a vapor environment in a pool boiling using a nanofluid. Applied Physics Letters 2005;86(13): 134107-1–7.
[80] Wen D, Ding Y. Experimental investigation into the pool boiling heat transfer of aqueous based alumina nanofluids. Journal of Nanoparticle Research 2005;7:265–74.
[81] You SM, Kim JH, Kim KM. Effect of nanoparticles on critical heat flux of water in pool boiling of heat transfer. Applied Physics Letters 2003;83(16):3374–6.
[82] Vassallo P, Kumar R, D'Amico S. Pool boiling heat transfer experiments in silica-water nano-fluids. International Journal of Heat and Mass Transfer 2004;47(2):407–11.
[83] Kim H, Kim J, Kim M. Experimental study on CHF characteristics of water–TiO_2 nano-fluids. Nuclear Engineering and Technology 2006;38(1).
[84] Kim SJ, Bang IC, Buongiorno J, Hu LW. Surface wettability change during pool boiling of nanofluids and its effect on critical heat flux. International Journal of Heat and Mass Transfer 2007;50:4105–16.
[85] Milanova D, Kumar R, Kuchibhatla S, Seal S. Heat transfer behavior of oxide nanoparticles in pool boiling experiment. In: Proceedings of 4th International Conference on Nanochannels, Microchannels and Minichannels; 2006.
[86] Jackson JE, Borgmeyer BV, Wilson CA, Cheng P, Bryan JE. Characteristics of nucleate boiling with gold nanoparticles in water. In: Proceedings of IMECE 2006; 2006.
[87] Witharana S. Boiling of refrigerants on enhanced surfaces and boiling of nanofluids. Ph.D. thesis. Royal Institute of Technology, Stockholm, Sweden; 2003.
[88] Nguyen CT, Galanis N, Roy G, Divoux S, Gilbert D. Pool boiling characteristics of water-alumina nanofluids 2006, doi:10.1615/IHTC13.p8.20.
[89] Jung D, Kim Y, Ko Y, Song K. Nucleate boiling heat transfer coefficients of pure halogenated refrigerants. International Journal of Refrigeration 2003;26: 240–8.
[90] Tu JP, Dinh N, Theofanous T. An experimental study of nanofluid boiling heat transfer. In: Proceedings of 6th International Symposium on Heat Transfer; 2004.
[91] Zhou DW. Heat transfer enhancement of copper nanofluid with acoustic cavitation. International Journal of Heat and Mass Transfer 2004;47:3109–17.
[92] Park K-J, Jung D. Boiling heat transfer enhancement with carbon nanotubes for refrigerants used in building air-conditioning. Energy and Buildings 2007;39(9):1061–4.
[93] Park K-J, Jung D. Enhancement of nucleate boiling heat transfer using carbon nanotubes. International Journal of Heat and Mass Transfer 2007;50(21): 4499–502.
[94] Landau LD, Lifshitz EM. Electrodynamics of continuous media, translated by Sykes JB, Bell JS, Oxford: Pergamon Press; 1960.
[95] Choi S, Zhang Z, Yu W, Lockwood F, Grulke E. Anomalously thermal conductivity enhancement of in nanotube suspensions. Applied Physics Letters 2001;79(14):2252–4.
[96] Xuan Y, Roetzel W. Conceptions for heat transfer correlation of nanofluids. International Journal of Heat and Mass Transfer 2000;43:3701–7.
[97] Khanafer K, Vafai K, Lightstone M. Buoyancy-driven heat transfer enhancement in a two-dimensional enclosure utilizing nanofluids. International Journal of Heat and Mass Transfer 2003;46:3639–53.
[98] Das SK, Choi SUS, Patel HE. Heat transfer in nanofluids—a review. Heat Transfer Engineering 2006;27(10):3–19.
[99] Buongiorno J. Convective heat transfer enhancement in nanofluids. Heat and Mass Transfer Conference, January, 2006, HMT-2006-C335.
[100] Behzadmehr A, Saffar-Avval M, Galanis N. Prediction of turbulent forced convection of a nanofluid in a tube with uniform heat flux using two phase approach. International Journal of Heat and Fluid Flow 2007;28(2): 211–9.

[101] Maiga SEB, Nguyen CT, Galanis N, Roy G. Heat transfer behaviors of nanofluids in a uniformly heated tube. Superlattices and Microstructures 2003.
[102] Roy G, Nguyen CT, Lajoie PR. Numerical investigation of laminar flow and heat transfer in a radial flow cooling system with the use of nanofluids. Superlattices and Microstructures 2003.
[103] Ding Y, Wen D. Particle migration in a flow of nanoparticles suspensions. Powder Technology 2005;149:84–92.
[104] Palm SJ, Roy G, Nguyen CT. Heat transfer enhancement with the use of nanofluids in radial flow cooling systems considering temperature-dependent properties. Applied Thermal Engineering 2006;26(17–18):2209–18.
[105] Kim J, Kang YT, Choi CK. Soret and Dufour effects on convective instabilities in binary nanofluids for absorption application. International Journal of Refrigeration 2007;30(2):323–8.
[106] Mansour RB, Galanis N, Nguyen CT. Effect of uncertainties in physical properties on forced convection heat transfer with nanofluids. Applied Thermal Engineering 2007;27(1):240–9.
[107] Prakash M, Giannelis EP. Mechanism of heat transfer in nanofluids. Journal of Computer-Aided Materials Design. doi:10.1007/s10820-006-9025-x.
[108] Li CH, Peterson GP. Mixing effect on the enhancement of the effective thermal conductivity of nanoparticle suspensions (nanofluids). International Journal of Heat and Mass Transfer 2007;23(May). doi: 10.1016/j.ijheatmasstransfer.2007.03.015.
[109] Chein R, Huang G. Analysis of microchannel heat sink performance using nanofluids. Applied Thermal Engineering 2005;25:3104–14.
[110] Jang SP, Choi SUS. Cooling performance of a microchannel heat sink with nanofluids. Applied Thermal Engineering 2005;26:2457–63.
[111] Chein R, Chuang J. Experimental microchannel heat sink performance studies using nanofluids. International Journal of Thermal Science 2006.
[112] Koo J, Kleinstreuer C. Laminar nanofluid flow in micro heat-sinks. International Journal of Heat and Mass Transfer 2005;48:2652–61.
[113] Nguyen CT, Roy G, Gauthier C, Galanis N. Heat transfer enhancement using Al_2O_3–water nanofluid for an electronic liquid cooling system. Applied Thermal Engineering 2007;27(8):1501–6.
[114] Chien H-T, Tsai C-I, Chen P-H, Chen P-Y. Improvement on thermal performance of a disk shaped miniature heat pipe with nanofluid. IEEE ICEPTD; 2003. p. 381–391.
[115] Tsai CY, Chien HT, Ding PP, Chan B, Luh TY, Chen PH. Effect of structural character of gold nanoparticles in nanofluid on heat pipe thermal performance. Materials Letters 2004;58:1461–5.
[116] Kang SW, Wei WC, Tsai SH, Yang SY. Experimental investigation of silver nano-fluid on heat pipe thermal performance. Applied Thermal Engineering 2006;26:2377–82.
[117] Ma HB, Choi SUS, Tirumala M. Effect of nanofluid on the heat transport capability in an oscillating heat pipe. Applied Physics Letters 2006;88:116–43.
[118] Sidi el Bécaye Maïga, Nguyen CT, Galanis N, Roy G, Maré T, Coqueux M. Heat transfer enhancement in turbulent tube flow using Al_2O_3 nanoparticle suspension. International Journal of numerical methods for heat and fluid flow 2006;16(3):275–92.

International Journal of Heat and Mass Transfer 53 (2010) 1603–1608

Contents lists available at ScienceDirect

International Journal of Heat and Mass Transfer

journal homepage: www.elsevier.com/locate/ijhmt

Technical Note

Airside performance of fin-and-tube heat exchangers in dehumidifying conditions – Data with larger diameter

Young-Chang Liu [a], Somchai Wongwises [b], Wen-Jeng Chang [c], Chi-Chuan Wang [a,d,*]

[a] Energy and Environment Research Laboratories, Industrial Technology Research Institute, Hsinchu 310, Taiwan
[b] Fluid Mechanics, Thermal Engineering and Multiphase Flow Research Lab. (FUTURE), Department of Mechanical Engineering, King Mongkut's University of Technology Thonburi, Bangmod, Bangkok 10140, Thailand
[c] Department of Mechanical and Computer Aided Engineering Feng Chia University, Taichung, Taiwan
[d] Department of Mechanical Engineering, National Chiao Tung University, Hsinchu 300, Taiwan

ARTICLE INFO

Article history:
Received 22 September 2009
Received in revised form 15 November 2009
Accepted 15 November 2009
Available online 13 January 2010

Keywords:
Fin-and-tube heat exchanger
Plain fin
Dehumidification

ABSTRACT

This study presents the airside performance of the fin-and-tube heat exchangers having plain fin geometry with a larger diameter tube (D_c = 15.88 mm) under dehumidifying condition. A total of nine samples of heat exchangers subject to change of the number of tube row and fin pitch are made and tested. It is found that the effect of fin pitch on the sensible j factor is, in general, diminished with the rise of tube row. However, there is a unique characteristic of fin pitch at a shallow tube row, the heat transfer performance is first increased at a wider pitch but a further increase of fin pitch lead to a falloff of heat transfer performance due to interactions amid flow development and bypass flow. The influence of tube row on the airside performance is rather small for both heat transfer and frictional characteristics at a fin pitch of 2.1 mm and when the Reynolds number is less than 4000. A slight deviation of this effect is encountered when fin pitch is increased to 2.54 mm or 3.1 mm due to condensate adhered phenomena.

1. Introduction

Fin-and-tube heat exchangers are widely-used heat transfer devices in applications like refrigeration and air conditioning systems. Its easier manufacturing, simpler construction, lower cost, and relatively easy in maintenance makes it one of the most commonly used heat exchangers. They can be applicable to both heating and cooling. Once the cooling process takes place below dew point temperature, condensate forms on the surface and result in a complex heat and mass transfer interactions. The heat transfer characteristics of fin-and-tube heat exchangers under this dehumidifying conditions had been studied by many researchers (e.g. McQuiston [1,2], Beecheer and Fagan [3], Yan and Sheen [4], Mirth and Ramadhyani [5,6], Wang et al. [7], Pirompugd et al. [8,9]). The published literatures offer considerable test results of plain fin data in wet condition.

However, the foregoing tests were conducted for typical heat exchangers of small air-conditioners where nominal tube diameters of 9.52, 7.94 or 7 mm were generally employed. In typical applications like fan-coil or ventilator, exploitation of larger diameter like 15.88 mm is also very common. Unfortunately, there is very limited performance data of the fin-and-tube heat exchanger with larger diameter tube in the open literature and is virtually no data available in dehumidifying conditions. Hence, the objective of the present study is to provide relevant performance data to the database.

2. Experimental setup

The schematic diagram of the experimental air circuit assembly is shown in Fig. 1. It consists of a closed-loop wind tunnel in which air is circulated by a variable speed centrifugal fan (7.46 kW, 10 HP). The air duct is made of galvanized sheet steel and has an 850 mm × 550 mm cross-section. The dry-bulb and wet-bulb temperatures of the inlet-air are controlled by an air-ventilator that can provide a cooling capacity of up to 21.12 kW (6RT). The air flow-rate measurement station is an outlet chamber set up with multiple nozzles. This setup is based on the ASHRAE 41.2 standard [10]. A differential pressure transducer is used to measure the pressure difference across the nozzles. The air temperatures at the inlet and exit zones across the sample heat exchangers are measured by two psychrometric boxes based on the ASHRAE 41.1 standard [11].

The working medium for the tube side is cold water. A thermostatically controlled reservoir provides cold water at selected temperatures. The temperature differences on the water side are measured by two pre-calibrated RTDs. The water volumetric flow

* Corresponding author. Address: Energy and Environment Research Laboratories, Industrial Technology Research Institute, Hsinchu 310, Taiwan. Tel.: +886 3 5916294; fax: +886 3 5820250.
E-mail address: ccwang@itri.org.tw (C.-C. Wang).

0017-9310/$ - see front matter © 2009 Elsevier Ltd. All rights reserved.
doi:10.1016/j.ijheatmasstransfer.2009.12.015

Nomenclature

A_c	minimum flow area, m^2
A_f	fin surface area, m^2
$A_{p,i}$	inside surface area of tubes, m^2
A_o	total surface area, m^2
b'_p	slope of the air saturation curved between the outside and inside tube wall temperature, J kg^{-1} K^{-1}
b'_r	slope of the air saturation curved between the mean water temperature and the inside wall temperature, J kg^{-1} K^{-1}
$b'_{w,f}$	slope of the air saturation curved at the mean water film temperature of fin surface, J kg^{-1} K^{-1}
$b'_{w,p}$	slope of the air saturation curved at the mean water film temperature of tube surface, J kg^{-1} K^{-1}
$C_{p,a}$	moist air specific heat at constant pressure, J kg^{-1} K^{-1}
D_c	collar diameter, m
D_h	hydraulic diameter, m
f	Fanning friction factor
F_p	fin pitch, m
G_c	maximum mass flux at minimum flow area, kg m^{-2} s^{-1}
$h_{c,o}$	sensible heat transfer coefficient, W m^{-2} K^{-1}
h_i	inside heat transfer coefficient, W m^{-2} K^{-1}
j	Colburn j factor
k_p	thermal conductivity of tube, W m^{-1} K^{-1}
L	streamwise duct length, m
N	number of tube row
P_l	longitudinal tube pitch, m
P_t	transverse tube pitch, m
Pr	Prandtl number of air
ΔP	pressure drop, Pa
$\dot{Q}_a$	air side heat transfer rate, W
$\dot{Q}_{avg}$	average heat transfer rate, W
$\dot{Q}_r$	water side heat transfer rate, W
Re_{Dc}	air side Reynolds number based on the collar diameter
Re_{Dh}	Reynolds number based on hydraulic diameter
RH_{in}	inlet relative humidity
$U_{o,w}$	wet surface overall heat transfer coefficient, based on enthalpy difference, kg m^{-2} s^{-1}
x_p	wall thickness, m
x^+	inverse Graetz number
σ	contraction ratio
$\eta_{f,wet}$	fully wet fin efficiency
ρ	air density, kg m^{-3}
δ_f	fin thickness, m

rate is measured by a magnetic flow meter with a ±0.001 L/s precision. All the temperature measuring probes are resistance temperature devices (Pt100), with a calibrated accuracy of 0.05 °C. In the experiments, only the data that satisfy the ASHRAE 33-78 [12] requirements (namely, the energy balance condition, $|\dot{Q}_r - \dot{Q}_a|/\dot{Q}_{avg}$, is less than 0.05, where $\dot{Q}_r$ is the water-side heat transfer rate for and $\dot{Q}_a$ air-side heat transfer rate) are considered in the final analysis. Detailed geometry used for the present plain fin-and-tube heat exchangers is tabulated in Table 1. The test fin-and-tube heat exchangers are tension wrapped having a "L" type fin collar. The test conditions of the inlet-air are as follow:

Dry-bulb temperature of the air	27 ± 0.5 °C
Inlet relative humidity for the incoming air	50% and 80%
Inlet-air velocity	From 1 to 4 m/s
Inlet-water temperature	7 ± 0.5 °C
Water velocity inside the tube	1.5–1.7 m/s

The test conditions approximate those encountered with typical fan-coils and evaporators of air-conditioning applications. Uncertainties reported in the present investigation, following the single-sample analysis proposed by Moffat [13]. The maximum uncertainty occurred at the smallest frontal velocity and is less than ±4.7% for reduction of the sensible heat transfer coefficient whereas it is within ±6% for the frictional reduction.

3. Data reduction

Basically, the present reduction method is analogous to Threlkeld's approach [14]. Details of the reduction process can be found from the previous studies by Wang et al. [7]. Notice that the Threlkeld method is an enthalpy-based reduction method. A brief description of the reduction of heat and mass transfer is given as follows:

The overall heat transfer coefficient is related to the individual heat transfer resistance (Myers, [15]) as follows;

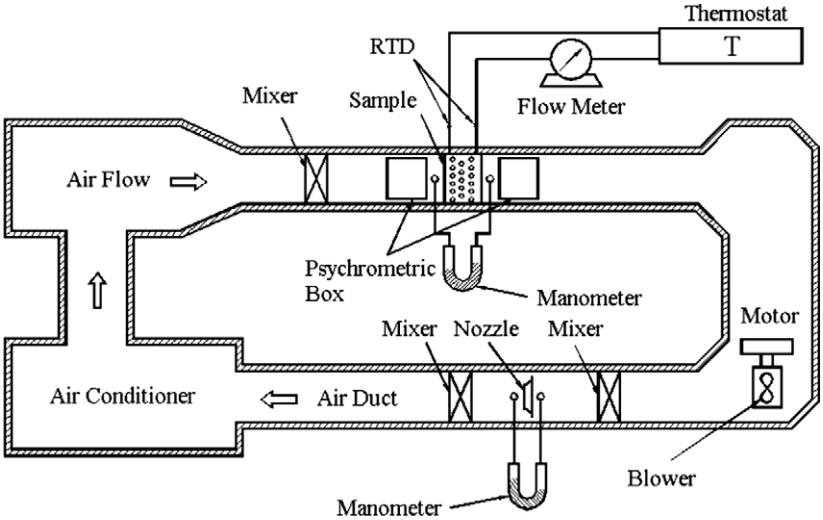

Fig. 1. Schematic of the test apparatus.

Table 1
Detailed geometric parameters of the test samples.

No.	Fin type	F_p (mm)	δ_f (mm)	D_c (mm)	P_t (mm)	P_l (mm)	N, row
1	Plain	2.12	0.12	16.68	38.1	33	2
2	Plain	2.54	0.12	16.68	38.1	33	2
3	Plain	3.17	0.12	16.68	38.1	33	2
4	Plain	2.06	0.12	16.68	38.1	33	4
5	Plain	2.54	0.12	16.68	38.1	33	4
6	Plain	3.13	0.12	16.68	38.1	33	4
7	Plain	2.12	0.12	16.68	38.1	33	8
8	Plain	2.54	0.12	16.68	38.1	33	8
9	Plain	3.17	0.12	16.68	38.1	33	8

$$\frac{1}{U_{o,w}} = \frac{b'_r A_o}{h_i A_{p,i}} + \frac{b'_p x_p A_o}{k_p A_{p,m}} + \frac{1}{h_{o,w}\left(\frac{A_{p,o}}{b'_{w,p} A_o} + \frac{A_f \eta_{f,wet}}{b'_{w,m} A_o}\right)} \tag{1}$$

where

$$h_{o,w} = \frac{1}{\frac{C_{p,a}}{b'_{w,m} h_{c,o}}} \tag{2}$$

The tube-side heat transfer coefficient, h_i, is evaluated from the Gnielinski correlation. The four quantities ($b'_{w,m}$, $b'_{w,p}$, b'_p, and b'_r) in Eq. (1) involving enthalpy–temperature ratios must be evaluated in

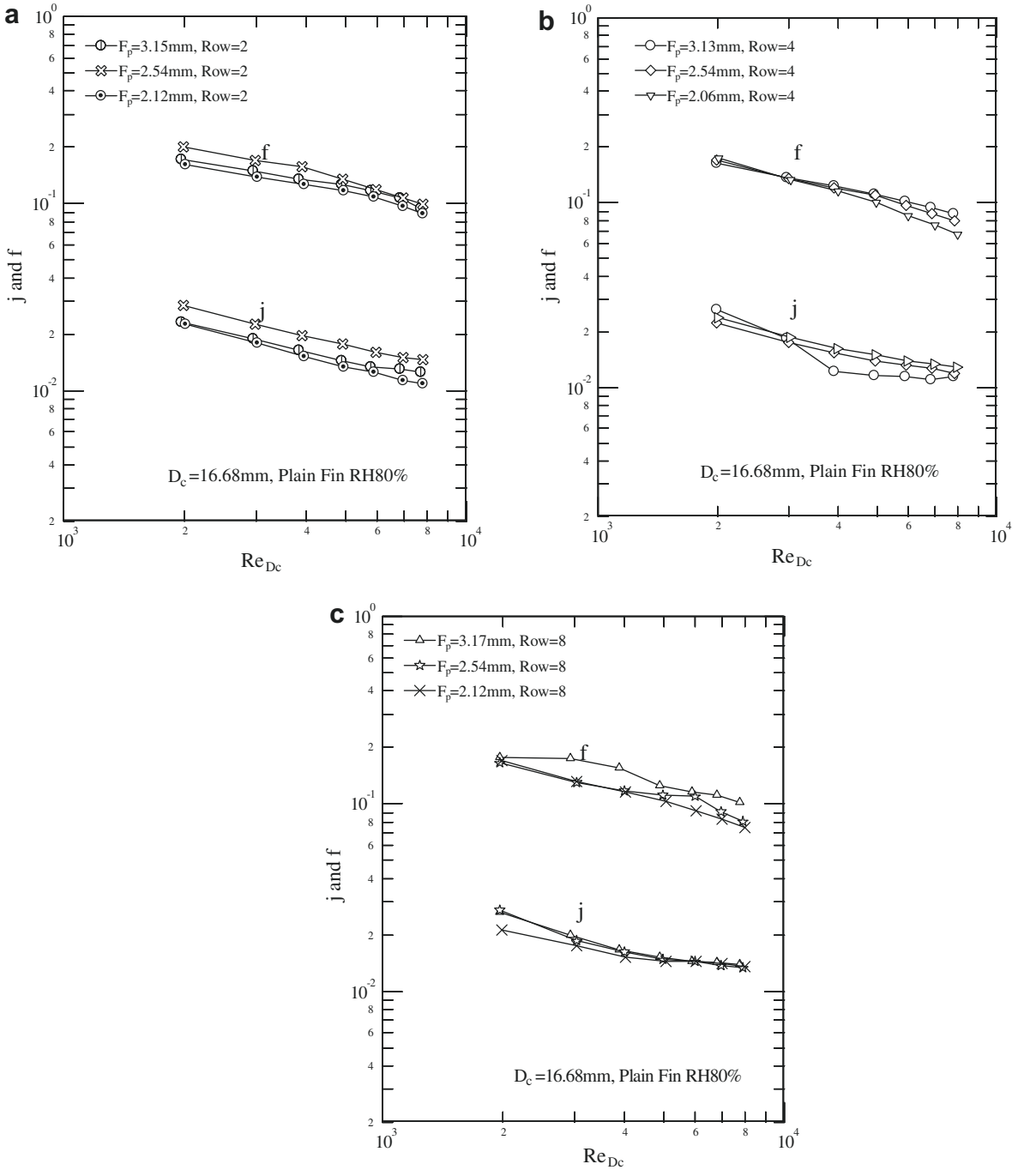

Fig. 2. Effect of fin pitch on heat transfer and friction characteristics (a) $N = 2$; (b) $N = 4$ and (c) $N = 8$ (RH = 80%).

advance. A detailed evaluation of these four terms can be found from Wang et al. [7]. The heat transfer performance is in terms of the Colburn j factor, i.e,

$$j = \frac{h_{c,o}}{G_c C_{p,a}} \mathrm{Pr}^{2/3} \tag{3}$$

The reduction of the friction factor of the heat exchanger is evaluated from the pressure drop equation proposed by Kays and London [16] as

$$f = \frac{A_c}{A_o}\frac{\rho_i}{\rho_m}\left[\frac{2\rho_i \Delta P}{G_c^2} - (1+\sigma^2)\left(\frac{\rho_i}{\rho_o} - 1\right)\right] \tag{4}$$

Related explanation and calculation of the terminology can be seen from Wang et al. [7].

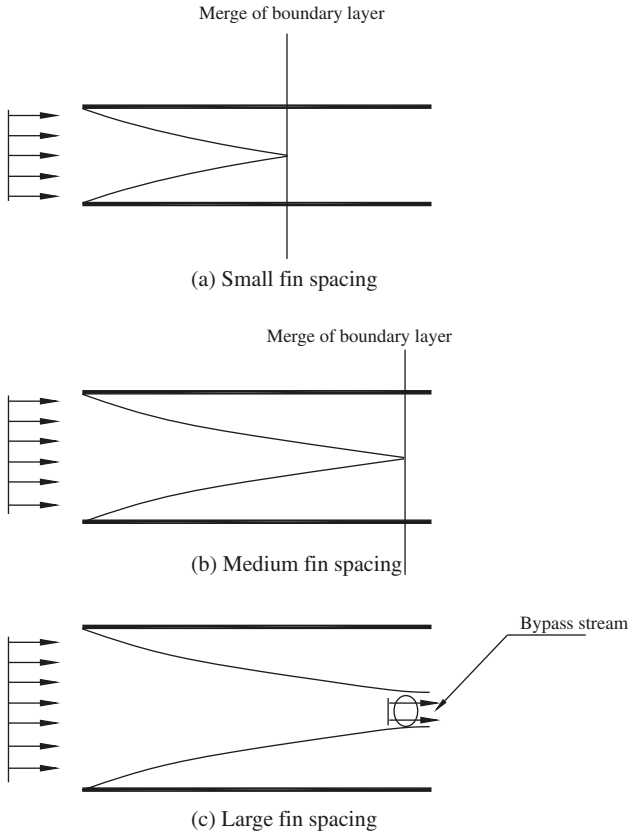

Fig. 3. Schematic of flow development alongside the fin channel: (a) small fin spacing, (b) medium fin spacing and (c) large fin spacing.

4. Results and discussion

A typical result concerning the effect of fin pitch on the airside performance for RH = 80% is schematically shown in Fig. 2. The corresponding tube rows are 2, 4, and 8, respectively. As expected, the friction factors and the sensible j factors decrease with increase of the Reynolds number. The effect of fin pitch on the sensible j factor is, in general, diminished with the rise of tube row. This is because more tube rows provide significantly mixing, thereby leading to a hardly detectable difference of j factor as the row number is increased to 8. However, there is a unique feature of the j factor for $N = 2$. The j factor shows appreciable increase when the fin pitch is increased from 2.12 mm to 2.54 mm, and a further rise to $F_p = 3.15$ mm yields a detectable drop of heat transfer performance. In fact it falls back to that of $F_p = 2.12$ mm. The special phenomenon is actually related to the developing characteristics of thermal and flow field. For further illustration of this phenomenon, one can examine the corresponding reciprocal of the inverse Graetz number x^+, which is defined as

$$x^+ = \frac{L/D_h}{\mathrm{Re}_{D_h}\mathrm{Pr}} \tag{5}$$

where L is the streamwise duct length and Pr is the Prandtl number. The flow may be considered to be fully developed when $x^+ > 0.1$ [17]. In general, the heat transfer performance within the heat exchanger is quite complex for it related to the interactions amid tubes and fins. For a shallow row number like $N = 2$, the effect of tube row is comparatively small, hence one can check the associated influence of development of flow field within channels. A close examination of the present test samples of $N = 2$ using Eq. (5) indicates that the contribution of development and fully developed region are quite corresponding. In this regard, one can realize the whole picture about the heat transfer performance subject to change of fin spacing as schematically shown in Fig. 3. For a smaller fin pitch as shown in Fig. 3(a), the flow develops along the

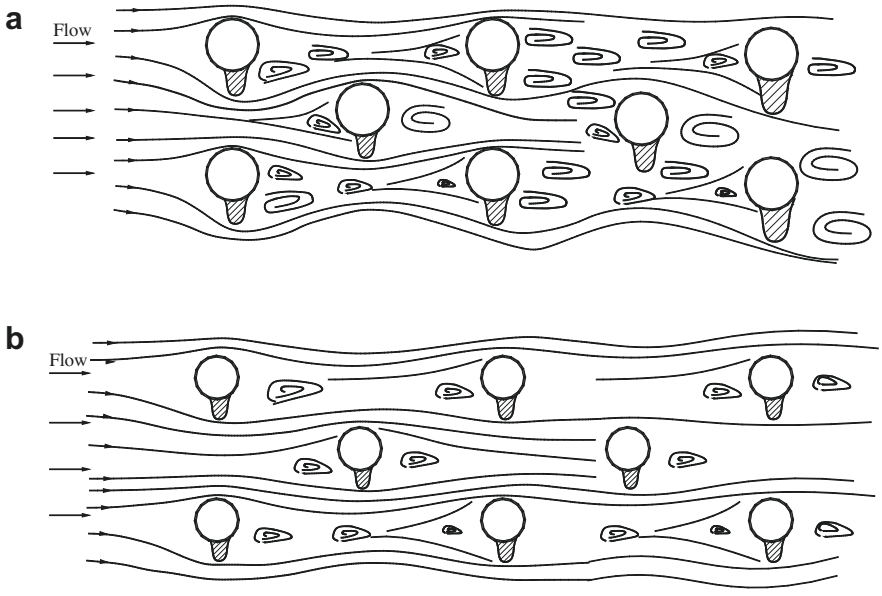

Fig. 4. Schematic of secondary flow subject to vapor shear (a) large fin spacing and (b) small fin spacing.

channel and merge accordingly somewhere alongside the channel, resulting in a comparatively low heat transfer performance. A further increase of fin spacing as seen in Fig. 3(b) will delay the conglomeration of boundary layer and increase the development length which gives rise to an increase of heat transfer performance. In the meantime, there will be no merge of boundary layer with a further increase of fin spacing as seen in Fig. 3(c). The nascent sign would suggest that the heat transfer performance will continue to rise since there is no boundary layer conglomeration. However, as clearly seen in Fig. 3(c), a bypass flow stream at the center region will offset the heat transfer gain from the development. In this sense, the heat transfer performance reveals a fallback when the fin spacing is sufficient large. However, it must be emphasized that this is applicable for shallow tube row where mixing caused by tubes is not so intensive.

In the meantime, the corresponding influence of fin pitch on the friction factor shows a slight scattering despite the variation is not so prominent. However, one can still see a marginal increase of friction factor for $N = 8$. The results are not in line with those in dry condition. For heat exchangers under completely dry operation, Rich [18] concluded that the friction factors were essentially independent of the number of tube row. The recent experimental data having larger diameter tube by Liu et al. [19] also support this finding. It is likely that the slight rise of friction factor with the fin pitch is associated with the condensate drainage. For a better understanding about the influence of condensate, Fig. 4(a) presents a cartoon to demonstrate how the friction factor may be slightly increased at a larger row number and a wider fin pitch. With a larger fin pitch, the effective vapor shear inside the fin spacing is comparatively small, the condensate is therefore easier to accumulate and

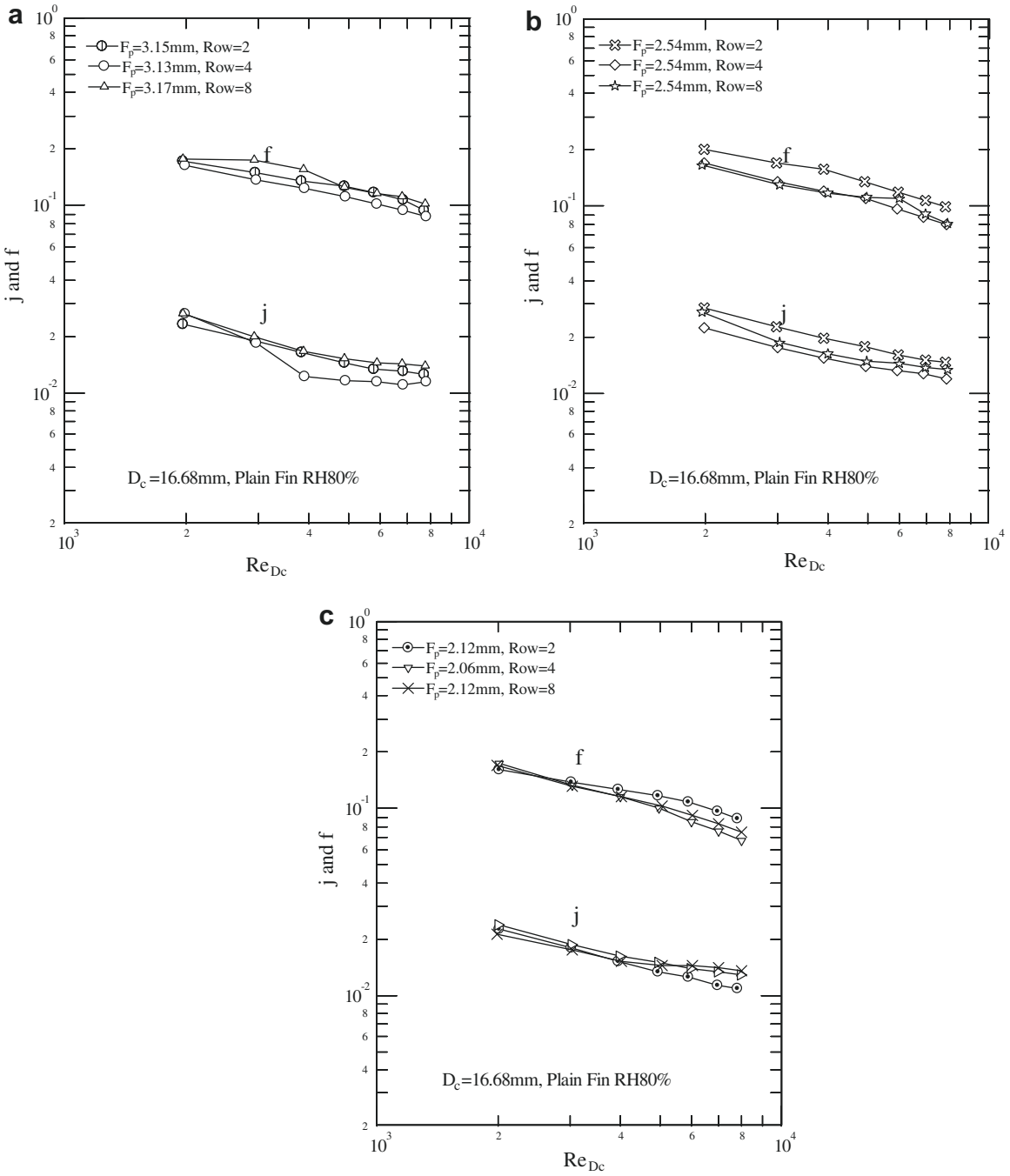

Fig. 5. Effect of the number of tube row on the heat transfer and friction characteristics: (a) $F_p = 2.1$ mm, (b) $F_p = 2.54$ mm and (c) $F_p = 3.15$ mm.

hang upon the surface. As a result, it is prone to having a higher frictional characteristic, yet the phenomenon may become more pronounced as the number of tube row is increased. On the other hand, the effect of vapor shear is reinforced at a smaller fin pitch and the condensate is easier to be removed from the surface. As a consequence, lower frictional performance is shown in Fig. 4(b) as the effect of secondary flow is reduced. Notice that condensate drainage within fin-and-tube heat exchanger is a very complex phenomenon for it interacts with both fin and tube surfaces.

Results regarding to the influence of the number of tube row on the airside performance are shown in Fig. 5. In general, the influence of tube row becomes less conceived when the fin pitch is reduced to 2.1 mm. As can be seen from Fig. 5(a), for a Reynolds number less than 4000, there is hardly any effect of the number of tube row on both heat transfer and frictional performance. By contrast, the sensible heat transfer j factors decrease with the rise of tube row when the Reynolds number is increased further. This is associated with the condensate blow off. The condensate is easier to adhere to the fin surface when the Reynolds number is low, resulting in a less influence of tube row. In the meantime, the adhered condensate may be blown off the fin surfaces when vapor shear is increased. Conversely, this phenomenon is not so significantly seen when the fin spacing is increased. This is because large condensate is prone to suspending between fins whereas smaller condensate just rolls alongside the fin, leading to this inconsistency.

5. Conclusion

This study presents the airside performance of the fin-and-tube heat exchangers having plain fin geometry with a larger diameter tube (D_c = 15.88 mm) under dehumidifying conditions. A total of nine samples of heat exchangers subject to change of the number of tube row and fin pitch are made and tested. Tests are conducted in a wind tunnel at controlled environment. Major conclusions of this study are summarized as follows:

(1) The effect of fin pitch on the sensible j factor is, in general, diminished with the rise of tube row. However, there is a distinct feature of the heat transfer performance occurring at a shallow row number (N = 2). The heat transfer performance is first increased when the fin pitch is increased from 2.12 mm to 2.54 mm, followed by a conceivable falloff if the fin pitch is increased to 3.15 mm. This unique characteristic is associated with the interaction between flow field development and bypass flow.
(2) The effect of fin pitch on the friction factor is somehow slightly scattering. There is a slight increase in friction factor for a tube row of eight. This is especially observable when the fin pitch is large. It is found that this phenomenon is related to condensate retention.
(3) The influence of tube row on the airside performance is rather small for both heat transfer and frictional characteristics. However, there is a slight deviation of this effect when fin pitch is increased to 2.54 mm or 3.1 mm. This is due to the condensate blown off phenomenon.

Acknowledgments

The authors would like to express gratitude for the Energy R&D foundation funding from the Bureau of Energy of the Ministry of Economic, Taiwan, Thailand Research Fund (TRF) and King Mongkut's University of Technology Thonburi for supporting the research.

References

[1] F.C. McQuiston, Heat mass and momentum transfer data for five plate-fin tube transfer surface, ASHRAE Trans. Part 1 84 (1978) 266–293.
[2] F.C. McQuiston, Correlation of heat, mass and momentum transport coefficients for plate-fin-tube heat transfer surfaces with staggered tubes, ASHRAE Trans. Part 1 84 (1978) 294–309.
[3] D.T. Beecher, T.J. Fagan, Effects of fin pattern on the air-side heat transfer coefficient in plate finned-tube heat exchanger, ASHRAE Trans. 93 (2) (1987) 1961–1984.
[4] W.M. Yan, P.J. Sheen, Heat transfer and friction characteristics of fin-and-tube heat exchangers, Int. J. Heat Mass Transfer 43 (2000) 1651–1659.
[5] D.R. Mirth, S. Ramadhyani, Prediction of cooling-coils performance under condensing conditions, Int. J. Heat Fluid Flow 14 (4) (1993) 391–400.
[6] D.R. Mirth, S. Ramadhyani, Correlations for predicting the air-side Nusselt numbers and friction factors in chilled-water cooling coils, Exp. Heat Transfer 7 (1994) 143–162.
[7] C.C. Wang, Y.C. Hsieh, Y.T. Lin, Performance of plate finned tube heat exchangers under dehumidifying conditions, J. Heat Transfer 119 (1997) 109–117.
[8] W. Pirompugd, S. Wongwises, C.C. Wang, A tube-by-tube reduction method for simultaneous heat and mass transfer characteristics for plain fin-and-tube heat exchangers in dehumidifying conditions, Heat Mass Transfer 41 (8) (2005) 756–765.
[9] W. Pirompugd, C.C. Wang, S. Wongwises, A fully wet and fully dry tiny circular fin method for heat and mass transfer characteristics for plain fin-and-tube heat exchangers under dehumidifying conditions, J. Heat Transfer 129 (9) (2007) 1256–1267.
[10] ASHRAE Standard 41.2-1987, Standard methods for laboratory air-flow measurement, American Society of Heating, Refrigerating and Air-Conditioning Engineers, Inc., Atlanta GA, 1987.
[11] ASHRAE Standard 41.1-1986, Standard method for temperature measurement, American Society of Heating, Refrigerating and Air-Conditioning Engineers, Inc., Atlanta, GA, 1986.
[12] ASHRAE Standard 33-78, Method of testing forced circulation air cooling and air heating coils, American Society of Heating, Refrigerating and Air-Conditioning Engineers, Inc., Atlanta, GA, 1978.
[13] R.J. Moffat, Describing the uncertainties in experimental results, Exp. Thermal Fluid Sci. 1 (1987) 3–17.
[14] J.L. Threlkeld, Thermal Environmental Engineering, Prentice-Hall, Inc., New-York, 1970.
[15] R.J. Myers, The Effect of Dehumidification on the Air-Side Heat Transfer Coefficient for a Finned-Tube Coil, M.S. Thesis, University of Minnesota, Minneapolis, 1967.
[16] W.M. Kays, A.L. London, Compact Heat Exchanger, third ed., McGraw-Hill, New York, 1984. A.L.
[17] J.E. Sergent, A. Krum, Thermal Management Handbook for Electronic Assemblies, McGraw-Hill, New York, 1998.
[18] D.G. Rich, The effect of the number of tube rows on heat transfer performance of smooth plate fin-and-tube heat exchanger, ASHRAE Trans. 81 (1) (1975) 307–317.
[19] Y.C. Liu, R. Hu, R.B.C. Yang, I.Y. Chen, I.Y.C.C. Wang, Sensible airside performance of fin-and-tube heat exchangers – data with larger diameter tube, ASHRAE Trans. 114 (1) (2008) 379–386.

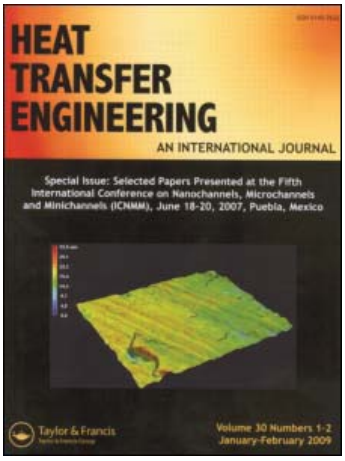

Heat Transfer Engineering

Publication details, including instructions for authors and subscription information:
http://www.informaworld.com/smpp/title~content=t713723051

Two-Phase Flow Across Small Sudden Expansions and Contractions

Ing Young Chen [a]; Somchai Wongwises [b]; Bing-Chwen Yang [c]; Chi-Chuan Wang [cd]
[a] Mechanical Engineering Department, National Yunlin University of Science and Technology, Yunlin, Taiwan [b] Department of Mechanical Engineering, King Mongkut's University of Technology Thonburi, Bangmod, Thailand [c] Energy & Environment Research Laboratories, Industrial Technology Research Institute, Hsinchu, Taiwan [d] Department of Mechanical Engineering, National Chiao Tung University, Hsinchu, Taiwan

Online publication date: 13 November 2009

To cite this Article Chen, Ing Young, Wongwises, Somchai, Yang, Bing-Chwen and Wang, Chi-Chuan(2010) 'Two-Phase Flow Across Small Sudden Expansions and Contractions', Heat Transfer Engineering, 31: 4, 298 — 309
To link to this Article: DOI: 10.1080/01457630903312056
URL: http://dx.doi.org/10.1080/01457630903312056

Heat Transfer Engineering, 31(4):298–309, 2010

ISSN: 0145-7632 print / 1521-0537 online
DOI: 10.1080/01457630903312056

Taylor & Francis
Taylor & Francis Group

Two-Phase Flow Across Small Sudden Expansions and Contractions

ING YOUNG CHEN,[1] SOMCHAI WONGWISES,[2] BING-CHWEN YANG,[3] and CHI-CHUAN WANG[3,4]

[1]Mechanical Engineering Department, National Yunlin University of Science and Technology, Yunlin, Taiwan
[2]Department of Mechanical Engineering, King Mongkut's University of Technology Thonburi, Bangmod, Thailand
[3]Energy & Environment Research Laboratories, Industrial Technology Research Institute, Hsinchu, Taiwan
[4]Department of Mechanical Engineering, National Chiao Tung University, Hsinchu, Taiwan

Two-phase flow approaching singularities such as abrupt expansions and sudden contractions is widely encountered in typical industrial and heat exchanging devices. There have been some studies concerning this subject but they mostly are applicable for larger channels. In this study, the first attempt is made to review the existing efforts concerning two-phase flow across sudden expansions/contractions and to examine the applicability of the existing correlations with respect to the recent data in small channels. The second part of this study presents some newly measured pressure drops and observed flow patterns pertaining to some special flow phenomena by expansion/contraction. For an abrupt expansion, it is found that the existing correlations all fail to provide a reasonably predictive capability against the newly collected data. Furthermore, a unique flow pattern called "liquid jet-like flow pattern" occurs at a very low quality region of total mass flux of 100 $kg{\cdot}m^{-2}{\cdot}s^{-1}$, and it raises a setback phenomenon of pressure drop. By contrast, an appreciable increase of pressure difference is seen when the liquid jet-like flow pattern is completely gone. A similar conclusion is drawn for the data of contractions. For the correlations/predictive models, the homogeneous model gives satisfactory prediction for conventional macro-channels but fails to do so when the channels become smaller. This is especially pronounced for a small-diameter tube with a Bond number being less than 1, in which the effect of surface tension dominates.

INTRODUCTION

In recent years, utilization of mini- and micro-channels has become quite attractive in heat exchanging devices. However, the length of the mini-/micro-channel is normally shorter than that in a macro-channel to eliminate the accompanied high pressure loss. This eventually leads to another problem of accurate estimation of the total pressure drop in the mini/micro system. Flow of two-phase mixtures across sudden expansions and contractions is relevant in many applications, including heat-exchanging equipment and connection pipelines. As the two-phase mixture flows through the sudden area changes, the flow might form a separation region at a sharp corner and cause an irreversible pressure loss. For the macro system, this loss is usually regarded as a minor loss, but its role becomes more and more crucial as the channel size gets smaller and shorter. Accurate methods for predicting the pressure drop in such systems are therefore important. This is particularly true for modern cooling systems where numerous channels or micro-channels are exploited to distribute the working fluid. There have been some developed correlations applicable to the pressure loss for the conventional tubes; however, very few investigations have been reported for this abrupt pressure change with respect to mini-channels (Abdelall et al. [1], Chen et al. [2, 3]). Applicability of the existing correlations/models to this area is quite ambiguous. It is therefore essential to examine the corresponding applicability.

The authors acknowledge the financial support provided by the Energy Bureau and Department of Industrial Technology both from the Ministry of Economic Affairs. The last author acknowledges a visiting professorship for his short stay in King Mongkut's University of Technology Thonburi, during the period of writing this article in Thailand.

Address correspondence to Dr. Chi-Chuan Wang, Senior Lead Researcher, D100 EEL/ITRI, Bldg. 64, 195-6, Sec. 4, Chung Hsing Rd., Chutung, Hsinchu, Taiwan, 310. E-mail: ccwang@itri.org.tw

LITERATURE REVIEW

For single-phase flow, by combining with the pressure balance equation, the static pressure difference subject to the

sudden expansion is related to the kinetic energy of the flow:

$$\frac{\Delta P_e}{\frac{G^2}{2\rho}} = -2\sigma_A(1-\sigma_A) \tag{1}$$

where the mass flux density (G) and velocity (u) are calculated based on the smaller cross-sectional area of the inlet tube. The negative sign indicates a pressure recovery whose value varies from zero to a maximum of 0.5 at $\sigma_A = 0.5$. Analogously, the pressure loss subject to sudden contraction is normally in terms of the contraction loss coefficient (K) and multiplication of kinetic energy of the flow:

$$\frac{\Delta P_c}{\frac{G^2}{2\rho}} = K \tag{2}$$

where σ_A is the passage cross-sectional area ratio and $0 < \sigma_A < 1$, and total mass flux (G) and velocity (u) are calculated based on the smaller cross-sectional area of the outlet tube. The value of K is related to the Reynolds number and contraction ratio, and it is close to 0.5 and 1.0 with a very small cross-sectional area ratio ($\sigma_A < 0.05$) (Kays and London [4]).

For single-phase flow through the contraction, Chisholm [5] combined the static pressure drop to the vena contracta (ΔP_{iv}) and the pressure recovery downstream of the vena contracta (ΔP_{vc}) to give the total static pressure drop at the contraction (ΔP_c):

$$\Delta P_{iv} = \left(\frac{G^2}{2\rho_L}\right)\left[(\sigma_A C_C)^{-2} - 1\right] \tag{3}$$

$$\Delta P_{VC} = \frac{\left(\frac{G}{\sigma_A}\right)^2}{\rho_L}\left[C_c^{-1} - 1\right] \tag{4}$$

$$\Delta P_C = \Delta P_{iv} - \Delta P_{vc} = \left(\frac{G^2}{2\rho_L}\right)\left[\frac{1}{(\sigma_A C_C)^2} - 1 - \frac{2\left(C_C^{-1}-1\right)}{\sigma_A^2}\right] \tag{5}$$

By comparing Eq. (2) with Eq. (5), the contraction loss coefficient can be found as:

$$K = \frac{1}{(\sigma_A C_C)^2} - 1 - \frac{2\left(C_C^{-1}-1\right)}{\sigma_A^2} \tag{6}$$

The contraction coefficient C_C correlated by Chisholm [5] is given as follows:

$$C_C = \frac{1}{[0.639(1-\sigma_A)^{0.5}+1]} \tag{7}$$

Another contraction coefficient C_C proposed by Geiger [6] is:

$$C_C = 1 - \frac{(1-\sigma_A)}{[2.08(1-\sigma_A)+0.5371]} \tag{8}$$

Two-Phase Pressure Change Across Sudden Expansion

For the two-phase pressure change across sudden expansion, Romie [7] derived the following expression for sudden enlargement:

$$\Delta P_e = \frac{-G^2\sigma_A(1-\sigma_A)}{\rho_L}\left[\begin{array}{l}\left(\frac{(1-x)^2}{(1-\alpha_{in})} + \frac{(\rho_L/\rho_G)x^2}{\alpha_{in}}\right) - \\ \sigma_A\left(\frac{(1-x)^2}{(1-\alpha_{\exp})} + \frac{(\rho_L/\rho_G)x^2}{\alpha_{\exp}}\right)\end{array}\right] \tag{9}$$

where the subscript "in" denotes upstream of expansion whereas "exp" represents downstream of expansion. If the void fraction remains unchanged, Eq. (9) becomes

$$\Delta P_e = \frac{-G^2\sigma_A(1-\sigma_A)}{\rho_L}\left[\frac{(1-x)^2}{(1-\alpha)} + \frac{(\rho_L/\rho_G)x^2}{\alpha}\right] \tag{10}$$

Richardson [8] simplified the energy balance model and assumed that the pressure recovery is proportional to the kinetic energies of the phases, yielding:

$$\Delta P_e = -0.5G^2\left(1-\sigma_A^2\right)\left[\frac{\sigma_A\left(1-x^2\right)}{\rho_L(1-\alpha)}\right] \tag{11}$$

Assuming that a heterogeneous flow and a loss of dynamic pressure head takes place in the liquid phase, Lottes [9] derived:

$$\Delta P_e = \frac{-G^2\sigma_A(1-\sigma_A)}{\rho_L(1-\alpha)^2} \tag{12}$$

By considering the pressure rise in a sudden expansion with irreversible flow induced in a rough tube, Chisholm and Sutherland [10] also developed a heterogeneous model based on the momentum balance:

$$\Delta P_e = -G^2\sigma_A(1-\sigma_A)(1-x)^2 \times \left[\frac{\left(1+C_h/X_{CH}+1/X_{CH}^2\right)}{\rho_L}\right] \tag{13}$$

where

$$X_{CH} = \left(\frac{\rho_G}{\rho_L}\right)^{0.5}\frac{(1-x)}{x} \tag{14}$$

$$C_h = \left\{1 + 0.5\left[1-\left(\frac{\rho_G}{\rho_L}\right)\right]^{0.5}\right\}\left\{\left(\frac{\rho_L}{\rho_G}\right)^{0.5} + \left(\frac{\rho_G}{\rho_L}\right)^{0.5}\right\} \tag{15}$$

The model of Chisholm and Sutherland [10] was compared with the bubbly flow data ($\alpha < 0.35$) for an air–water mixture. Although their predictions remain reasonably good, their model slightly underestimated the data (Attou et al. [11]).

Based on some test data, Wadle [12] proposed a formula to describe the pressure recovery in an abrupt diffuser. The model includes an artificial constant K in connection with different working fluids ($K = 0.667$ for steam-water, $K = 0.83$ for air–water):

$$\Delta P_e = -\left(1-\sigma_A^2\right)\frac{1}{2}G^2K\left[\frac{(1-x)^2}{\rho_L}+\frac{x^2}{\rho_G}\right] \tag{16}$$

From the mechanical energy equation without friction dissipation, Collier and Thome [13] derived the following expression:

$$\Delta P_e = \frac{-G^2\left(1-\sigma_A^2\right)}{2\left(\frac{x}{\rho_G}+\frac{1-x}{\rho_L}\right)}\left[\frac{(1-x)^3}{(1-\alpha)^2\rho_L^2}+\frac{x^3}{\alpha^2\rho_G^2}\right] \tag{17}$$

For estimation of the void fraction α, a very simple correlation was recently proposed by Kawahara et al. [14] as

$$\alpha = \frac{0.03\beta^{0.5}}{\left(1-0.97\beta^{0.5}\right)} \tag{18}$$

where β is the gas volumetric flow ratio, given as $\beta = j_G/(j_G + j_L)$, j_L is the superficial liquid velocity, and j_G is the superficial gas velocity. For homogeneous flow, Eq. (10) becomes:

$$\Delta P_e = -G^2\sigma_A(1-\sigma_A)\left[\frac{(1-x)}{\rho_L}+\frac{x}{\rho_G}\right] \tag{19}$$

Since the gas phase and liquid phase have different velocities, particularly for a large density difference between the gas and liquid phases, more realistic models and additional parameters are needed for the pressure recovery calculation.

Based on an annular-mist flow model accompanied with mass and momentum balance, Schmidt and Friedel [15] proposed a rather complex formula:

$$\Delta P_e = \frac{G^2\left[\frac{\sigma_A}{\rho_{eff}}-\frac{\sigma_A^2}{\rho_{eff}}-f_e\rho_{eff}\left(\frac{x}{\rho_G\alpha}-\frac{(1-x)}{\rho_L(1-\alpha)}\right)\left(1-\sqrt{\sigma_A}\right)^2\right]}{1-\Gamma_e(1-\sigma_A)} \tag{20}$$

where

$$\frac{1}{\rho_{eff}} = \frac{x^2}{\rho_G\alpha}+\frac{(1-x)^2}{\rho_L(1-\alpha)}+\frac{\alpha_E\rho_L(1-\alpha)}{1-\alpha_E} \times\left[\frac{x}{\rho_G\alpha}-\frac{1-x}{\rho_L(1-\alpha)}\right]^2 \tag{21}$$

$$\alpha = 1-\frac{2(1-x)^2}{1-2x+\sqrt{1+4x(1-x)\left(\frac{\rho_L}{\rho_G}-1\right)}} \tag{22}$$

$$\alpha_E = \frac{1}{S}\left[1-\frac{1-x}{1-x(1-0.05We^{0.27}\mathrm{Re}^{0.05})}\right] \tag{23}$$

$$S = \frac{x}{1-x}\frac{(1-\alpha)}{\alpha}\frac{\rho_L}{\rho_G} \tag{24}$$

$$We = G^2x^2\frac{d}{\rho_G\sigma}\frac{(\rho_L-\rho_G)}{\rho_G} \tag{25}$$

$$\mathrm{Re} = \frac{G(1-x)d}{\mu_L} \tag{26}$$

$$\Gamma_e = 1-\sigma_A^{0.25} \tag{27}$$

$$f_e = 4.9\times10^{-3}x^2(1-x)^2\left(\frac{\mu_L}{\mu_G}\right)^{0.7} \tag{28}$$

By applying the momentum balance within the boundary of the conical jet for an incompressible and adiabatic flow, Attou and Bolle [16] obtained a correlation for the two-phase flow pressure recovery from a sudden expansion.

$$\Delta P_e = -\sigma_A(1-\sigma_A)\theta_\sigma^r G^2\Phi + \frac{\left(1-\theta_\sigma^r\right)\sigma_A(1-\sigma_A)G^2}{\rho_L} \tag{29}$$

where $\Phi = x^2/(\alpha\rho_G) + (1-x)^2/[(1-\alpha)\rho_L]$, $\theta_\sigma = 3/[1+\sigma_A^{0.5}+\sigma_A]$, and r is a correction factor related to the physical properties of the mixture. For a gas quality $x = 0$, Eq. (29) can be reduced to $\Delta P_e = -\sigma_A(1-\sigma_A)G^2/\rho_L$. The best fitting to the correction factor is $r = 1$ for a steam–water mixture and $r = -1.4$ for an air–water mixture. The predictive ability of Eq. (29) associated with the air–water and steam–water data is around 23.4% or less (mean deviation). The correlation is particularly good for small mass velocities, but it is inapplicable to high quality flows.

More recently, Abdelall et al. [1] investigated air–water pressure drops caused by abrupt flow area expansions in two small tubes. The tube diameters were 1.6 and 0.84 mm, respectively. Their measured two-phase pressure difference indicated the occurrence of significant velocity slip. Assuming an ideal annular flow regime in accordance with minimum kinetic energy of the flowing mixture (slip ratio $S = (\rho_L/\rho_G)^{1/3}$) leads to a reasonable agreement between the data and the predictions. However, in practice the slip ratio is actually varying along the flow path. The pressure drop across the sudden expansion (ΔP_e) is the difference between the reversible pressure change (ΔP_{eR}) and the irreversible pressure changes (ΔP_{eI}), i.e., $\Delta P_e = \Delta P_{eR} - \Delta P_{eI}$. For an incompressible and adiabatic flow,

$$\Delta P_{eR} = \frac{-0.5\rho_h G^2\left(1-\sigma_A^2\right)}{\rho''^2} \tag{30}$$

$$\Delta P_{eI} = 0.5\rho_L G^2\left[\frac{2\rho_L\sigma_A(\sigma_A-1)}{\rho'}-\frac{\rho_h\rho_L(\sigma_A-1)}{\rho''^2}\right] \tag{31}$$

Where

$$\rho_h = \left[\frac{x}{\rho_G}+\frac{(1-x)}{\rho_L}\right]^{-1} \tag{32}$$

$$\rho' = \left[\frac{(1-x^2)}{\{\rho_L (1-\alpha)\}} + \frac{x^2}{(\rho_G \alpha)} \right]^{-1} \quad (33)$$

$$\rho'' = \left[\frac{(1-x)^3}{\rho_L^2 (1-\alpha)^2} + \frac{x^3}{(\rho_G^2 \alpha^2)} \right]^{-1/2} \quad (34)$$

To apply Eqs. (30) and (31), an empirical relation between α and x is needed. The predictions of the Abdelall et al. slip flow model [1] are only slightly higher than the experimental data, but the simplified momentum balance model, Eq. (8), by Collier and Thome [13] significantly overpredicts the data.

Two-Phase Pressure Change Across Sudden Contraction

Geiger [6] measured pressure drops for steam–water mixtures flowing through sudden contraction with area ratios (σ_A) of 0.398, 0.253, and 0.144. His data were compared with the homogeneous model, momentum equation, and mechanical energy equation across the contractions. The homogeneous model gave the best predictions of the data.

McGee [17] had also measured the steam–water mixtures flowing through sudden contraction using the same test rig as Geiger [6], but with different test sections and conditions (σ_A = 0.608, 0.546). The predictions by homogeneous model when compared with his test data are quite satisfactory. The predictions by the momentum and mechanical energy equations were much lower than the test data. This deviation is believed to be due to the assumption of no mechanical energy loss for the acceleration of the fluids at the downstream of the contraction.

For two-phase flow, the frictional pressure drop due to contraction can be estimated using a homogeneous flow model as recommended by Collier and Thome [13]:

$$\Delta P_c = \left(\frac{G^2}{2\rho_L} \right) \left[\left(C_C^{-1} - 1 \right)^2 + \left(1 - \sigma_A^2 \right) \right] \left[1 + x \left(\frac{\rho_L}{\rho_G} - 1 \right) \right] \quad (35)$$

The mass flux G is calculated based on the cross-sectional area of the outlet tube with smaller cross-sectional area.

Chisholm [5] also used his contraction loss coefficient K, Eq. (5), in association with the homogeneous model, i.e.,

$$\Delta P_c = \left(\frac{G^2}{2\rho_L} \right) \left[\frac{1}{(\sigma_A C_C)^2} - 1 - \frac{2\left(C_C^{-1} - 1 \right)}{\sigma_A^2} \right] \times \left[1 + x \left(\frac{\rho_L}{\rho_G} - 1 \right) \right] \quad (36)$$

Furthermore, Chisholm [5] introduced a constant B coefficient for flow through a discrete interval in evaluating the contraction loss:

$$\Delta P_c = \Delta P_{cL} \left[1 + \left(\frac{\rho_L}{\rho_G} - 1 \right) \left(Bx(1-x) + x^2 \right) \right] \quad (37)$$

$$B = \frac{\left\{ \frac{1}{K_O} \left(\frac{1}{(\sigma_A C_C)^2} - 1 \right) - \frac{2}{(K_O C_C \sigma_A^2)} + \frac{2}{(\sigma_A^2 K_O^{0.28})} \right\}}{\frac{1}{(\sigma_A C_C)^2} - 1 - \frac{2}{(C_C \sigma_A^2)} + \frac{2}{\sigma_A^2}} \quad (38)$$

where ΔP_{cL} is the contraction pressure drop for total flow assumed liquid across the same sudden contraction as shown in Eq. (5), contraction coefficient C_C is given in Eq. (7), and K_O is given as

$$K_o = \begin{cases} \left(1 + x \left(\frac{\rho_L}{\rho_G} - 1 \right) \right)^{0.5} & \text{for} \quad X > 1 \\ \left(\frac{\rho_L}{\rho_G} \right)^{0.25} & \text{for} \quad X \le 1 \end{cases} \quad (39)$$

where X is the Martinelli parameter.

Based on the momentum and mass transfer balance, Schmidt and Friedel [18]developed a new pressure drop model for sudden contraction that incorporates all of the relevant boundary conditions. In this model all the relevant physical parameters were also included in their sudden expansion paper [15]. In addition, the influence of liquid entrainment (α_E) in the gas stream is included, along with relevant parameters like area ratio (σ_A), mass flux (G), gas quality (x), mean void fraction (α), surface tension (σ), the viscosity and density of the gas and liquid phases (μ_G, μ_L, ρ_G, ρ_L), and slip ratio (S), to calculate the effective two-phase density (ρ_{eff}). Their test sections incorporated inlet tube diameters in the range of 44.2–72.2 mm and with outlet tubes in the range of 17.2–44.2 mm. The model predicts several experimental data sets with different physical properties. The comparison of the model and test results is fair, with 80% of the data sets being predicted within ±30%. For incompressible and adiabatic flow, the equation for pressure drop across a sudden contraction is given as:

$$\Delta p_c = \frac{G^2 \left[\frac{1}{\rho_{eff}} - \frac{\sigma_A}{\rho_{eff}} + f_{con} \rho_{eff} \left(\frac{x}{\rho_G \alpha} - \frac{1-x}{\rho_L (1-\alpha)} \right)^2 (1 - \sigma_A^{1/2})^2 \right]}{1 + \Gamma_{con} \left(\frac{1}{\sigma_A} - 1 \right)} \quad (40)$$

where f_{con} is the total fiction factor for the contraction, α is the void fraction, ρ_{eff} is the effective density, Γ_{con} is the base pressure coefficient for the contraction, Re is the Reynolds number, and *We* is the Weber number; ρ_{eff}, α, α_E, S, We, and Re are given in Eqs. (19)–(24) and

$$\Gamma_{con} = 0.77 \sigma_A \left(1 - \sigma_A^{0.306} \right) \quad (41)$$

$$f_{con} = 5.2 \times 10^{-3} x^{0.1} (1-x) \left(\sigma_A \frac{\mu_L}{\mu_G} \right)^{0.8} \quad (42)$$

Abdelall et al. [1] investigated air–water pressure drops caused by abrupt flow area expansion and contraction in a very small test section. The larger and small tube diameters were 1.6 and 0.84 mm, respectively. Assuming incompressible gas and liquid phases, and assuming x and α remained constant across

the sudden contraction, the pressure drop across the sudden contraction was derived as

$$\Delta P_c = G^2 \left\{ \frac{\rho_h \left(\frac{1}{C_C^2} - \sigma_A^2 \right)}{2\rho''^2} + \frac{(1 - C_C)}{\rho'} \right\} \tag{43}$$

where ρ_h, ρ' *and* ρ'' are given in Eqs. (32)–(34).

The contraction coefficient C_C, Eq. (7), given by Geiger [6], is utilized in the Abdelall et al. correlation, as in Eq. (43). The two-phase flow pressure change across the sudden contraction data was found significantly lower than the predictions of the homogeneous model. It may be attributed to the significant velocity slip at the vicinity of the flow area change. As a consequence, Abdelall et al. reappraised the suitability of homogeneous flow and concluded that the slip ratio model may be more relevant to accelerating two-phase flow (Moody [19]). Using the Zivi [20] model with the assumption of an ideal annular flow regime, the slip ratio becomes:

$$S = \frac{u_G}{u_L} = \frac{(1 - \alpha)\,\rho_L x}{[(1 - x)\rho_G \alpha]} = \left(\frac{\rho_L}{\rho_G} \right)^{\frac{1}{3}} \tag{44}$$

where u_G and u_L are the actual gas and liquid velocities of gas and liquid phases, respectively. The void fraction (α) is calculated from Eq. (44) by using gas quality and gas and liquid densities. Subsequently Eq. (43) is combined with the slip flow model to give a relatively close agreement with Abdelall et al.'s experimental data. An attempt was also made to correlate the two-phase pressure change data at the contraction point in terms of the Martinelli parameter (X), yielding

$$X = \left(\frac{u_L}{u_G} \right)^{0.1} \left(\frac{1}{x} - 1 \right)^{0.9} \left(\frac{\rho_G}{\rho_L} \right)^{0.5} \tag{45}$$

$$\frac{\Phi_{cL}}{X} = 120\,(X\mathrm{Re}_L)^{-0.7} \tag{46}$$

where $\Phi_{cL} = \Delta P_c / \Delta P_{cL}$ is the two-phase multiplier with all liquid flow through the contraction, and ΔP_{cL} is the pressure drop assuming total flow to be liquid flow. Re_L is the Reynolds number in the smaller tube (considering total flow to be liquid). Thus, the two-phase pressure change at the sudden contraction can be predicted by

$$\Delta P_c = \Delta P_{cL} X \left[120\,(X\mathrm{Re}_L)^{-0.7} \right] \tag{47}$$

From the foregoing review of the two-phase pressure change across the sudden contraction, most of the investigations are related to the abrupt area change for the upstream and downstream having round tube configuration and the tube sizes are generally above 10 mm. However, it should be mentioned that configuration variation across singularity (e.g., from rectangular to round) is very common in practice. Hence the first objective of this study is to provide new test data regarding to this influence. Further, it will be shown in subsequent comparisons that most of the proposed correlations/models are only applicable to their own database. In addition, a flow visualization experiment is also carried out to link with certain special pressure drop phenomenon.

EXPERIMENTAL SETUP

The test rig shown in Figure 1 is designed to conduct tests with air–water mixtures. Air is supplied from an air compressor and then stored in a compressed-air storage tank. Air flows through a pressure reducer and, depending on the mass flux range, is measured by three Aalborg mass flow meters for different ranges of flow rates with measurement uncertainty ranging from 0.5 to 2%. The water flow loop consists of a variable-speed gear pump that delivers water, and the water volumetric flow rate is detected by a magnetic flow meter with 0.001 L/s resolution. A self-made Y-shape mixer having a spring insert that provides good mixing amid air and water is placed ahead of the test section. An extra calming test section with a length of 300 mm after the mixer is used before the mixture goes into the test section. The gas quality is calculated from the measured air flow rate and water flow rate, namely,

$$x = \frac{\dot{m}_G}{\dot{m}_G + \dot{m}_L}$$

The total mass flux (G) of air and water flow rate evaluated at the entrance of rectangular test section range from 100 to 700 $\mathrm{kg \cdot m^{-2} \cdot s^{-1}}$ with gas quality (x) varying from 0.001 to 0.8. The corresponding uncertainties for x are within ±4.3%. The inlet temperatures of air and water are near 25°C. The pressure drops of the air–water mixtures are measured by three Yokogawa EJ110 differential pressure transducers having an adjustable span of 1300 to 13,000 Pa. Resolution of this pressure differential transducer is 0.3% of the measurements. The drilled holes of the pressure taps are perpendicular to the test sections with a diameter of 0.5 mm. Pressure measurements are made at nine locations along the inlet tube and along the rectangular channel as shown in Figure 1. For validation of the present test setup, measurements of the single-phase pressure drops for air and water alone are in terms of friction factors to compare with the friction factor equations for laminar and turbulent flows in rectangular channels. The results are in line with the known correlations having a deviation within ±5%. Leaving the test section, the air–water mixture is separated by an open water tank in which the air is vented and the water is recirculated. The air and water temperatures are measured by resistance temperature device (Pt100Ω) having a calibrated accuracy of 0.1 K (calibrated by Hewlett-Packard quartz thermometer probe with quartz thermometer, models 18111A and 2804A). Observations of flow patterns are obtained from images produced by a high-speed camera of Redlake Motionscope PCI 8000s. The maximum camera shutter speed is 1/8000 s. The high-speed camera can be placed at any position along the rectangular channels or at the side view of the abrupt change of flow area.

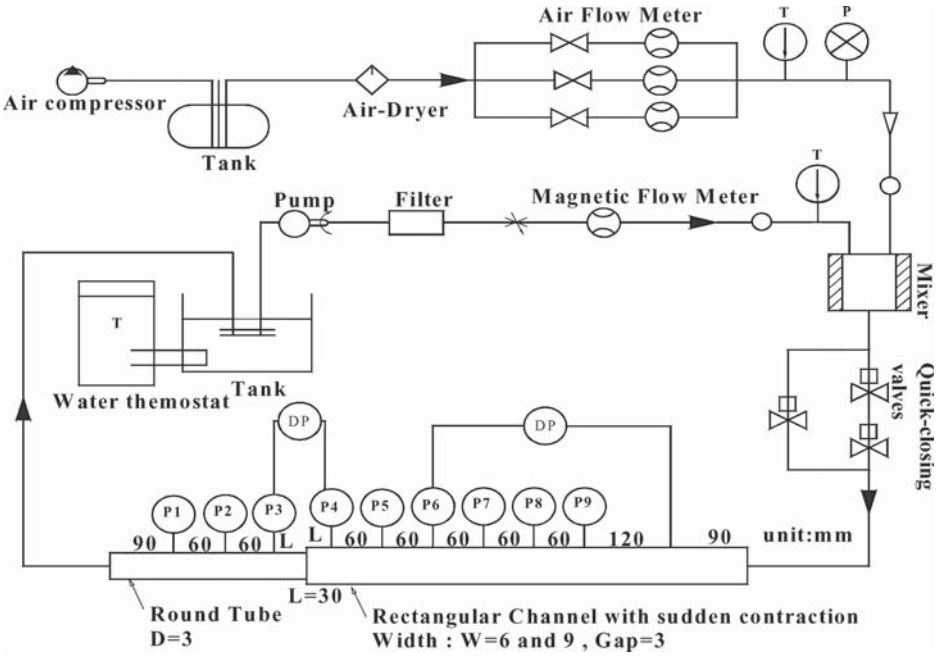

Figure 1 Schematic of test rig and test section.

The test sections are made of transparent acrylic resin, so that the flow pattern and flow structure at the vicinity of the abrupt cross-sectional area change can be visualized. For the expansion test sections, the test sections have the dimensions of gap $(G) \times$ width $(W) = 3 \times 6$ mm and 3×9 mm, and thus the corresponding aspect ratio $A = g/W = 0.333$–ß0.50. These test sections are also arranged in horizontal longitudinal (HL, the wide side is vertical) and the intersection between the rectangular and round tube is well fabricated to avoid any irregularity. The area ratio for the abrupt flow area change (σ_A) is in the range of $0.26 \sim 0.39$. The schematic and the dimensions of the test sections are also shown in Figure 1.

Figure 2a shows a typical change of static pressure along the axis for flow across the expansion. Due to the deceleration of the flow in the transitional region, the static pressure initially increases at the expansion area. After the pressure reaches the maximum, the pressure gradient merges with the downstream pressure gradient line. The pressure change at the sudden expansion is defined as the pressure difference for upstream and downstream fully developed pressure gradient lines extended to the expansion position, i.e., ΔP_{exp}, as shown in Figure 2a. Similarly, Figure 2b represents the variation of static pressure along the flow direction across singularity (for expansion and contraction). When flow approaches the contraction, due to the acceleration of the flow in the transitional region, the static pressure initially decreases to the contraction area. After the pressure reaches the minimum, the pressure increases to a downstream point and then merges with the downstream fully developed pressure gradient line. The pressure change at the sudden contraction is defined as the pressure difference at the interception of singularity evaluated using the fully developed pressure

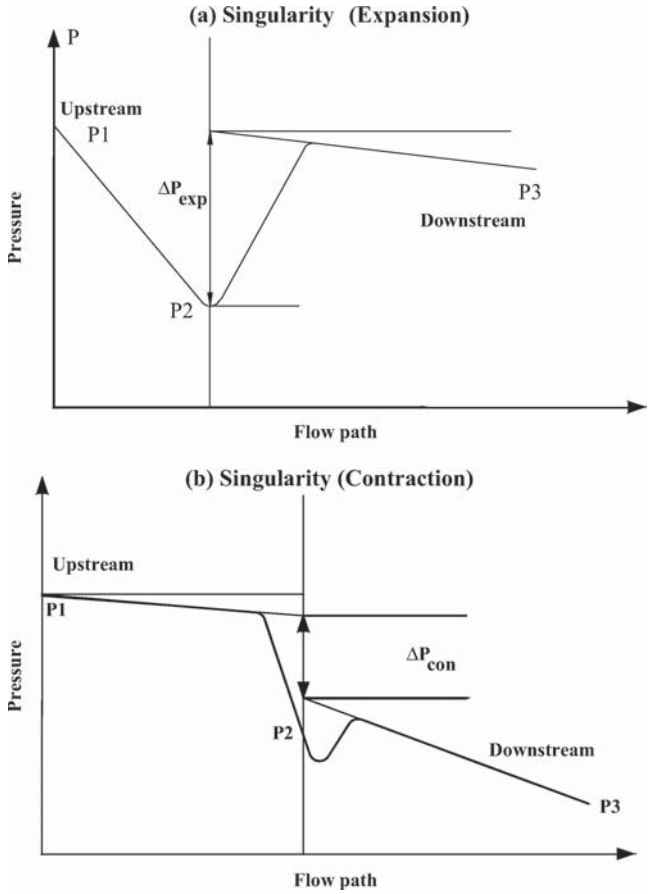

Figure 2 Definition of pressure drop subject to the influence of (a) sudden enlargement and (b) abrupt contraction.

gradients from upstream and downstream, respectively, i.e., ΔP_{con}, as shown in Figure 2b.

Some previous investigations used a single pressure differential transducer to measure the difference across the sudden contraction. This kind of measurement cannot actually reflect the pressure loss and pressure recovery across the abrupt area change. In this study, several pressure transducers are utilized for measuring the local pressures in the upstream and downstream parts of the test sections as shown in Figure 1. The measured axial pressures versus the pressure tap positions are plotted in a figure to setup the fully developed pressure gradient lines in the upstream and downstream for further obtaining the corresponding pressure change at the sudden contraction/expansion.

RESULTS AND DISCUSSION

Results for Expansion

The corresponding measured pressure drops subject to the sudden enlargement is shown in Figure 3. In general, the pressure drops increase with the rise of vapor quality. However, a notable drop of pressure difference is seen for $G = 100$ kg·m^{-2}·s^{-1} near a vapor quality of 0.01. A similar phenomenon was also reported by Schmidt and Friedel [15]. They also found that the pressure difference occurs at the very low quality region (∼0.005–0.02, depending on the mass flux) and argued that this phenomenon is not due to experimental errors but is associated with the flow pattern changes. For better understanding about this unique phenomenon, one can examine the variation of the corresponding flow pattern. Photographs that are representative of the observed flow patterns for 9 × mm and 6 × mm rectangular channels with a mass flux density of 100 kg·m^{-2}·s^{-1} and vapor qualities ranging from 0.001 to 0.5 are displayed in Figure 4 to show the flow progress in the presence of abrupt enlargement. As seen in Figure 4, for $G = 100$ kg·m^{-2}·s^{-1} at $x = 0.001$ flowing into the 9 × mm enlarged section, the original flow pattern before flowing across the sudden enlargement is elongated bubbly flow, which turns into slug flow after the abrupt area change. This is due to the considerable increase of cross-sectional area, leading to a decline of velocity and to aggregation of elongated bubble.

Note that the original liquid flow gathers at the bottom due to gravity. Hence, as the vapor quality is increased further, the entering flow contains sufficient momentum to become a jet-like (Figure 4c, $x = 0.01$) pattern. However, the liquid jet front heads towards the bottom section since its accompanied liquid momentum is unable to sustain itself against the gravity. For a further increase of vapor quality (Figure 4d, $x = 0.05$), the liquid jet spreads more evenly around the periphery pertaining to the higher momentum. The liquid jet-like flow pattern is similar to the quasi-free-jet pattern observed by Attou et al. [11]. The confined free-jet pattern appears to be conical with a small opening angle. With a further increase of vapor quality, the

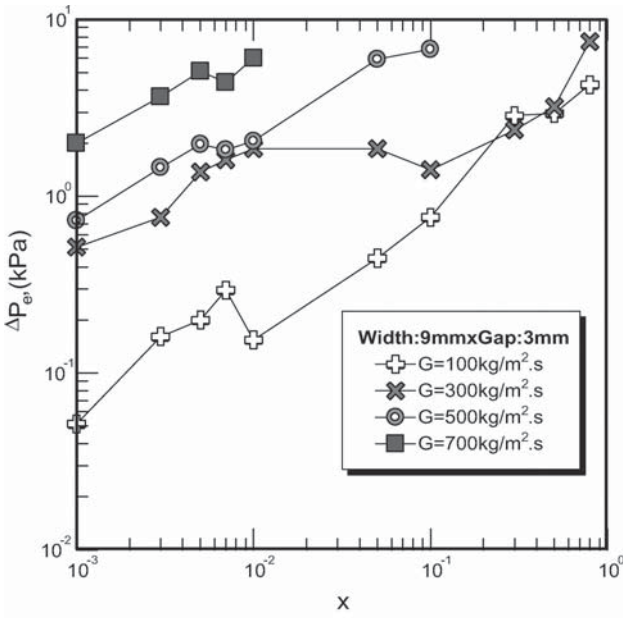

(a) Width: 9 mm x Gap: 3 mm

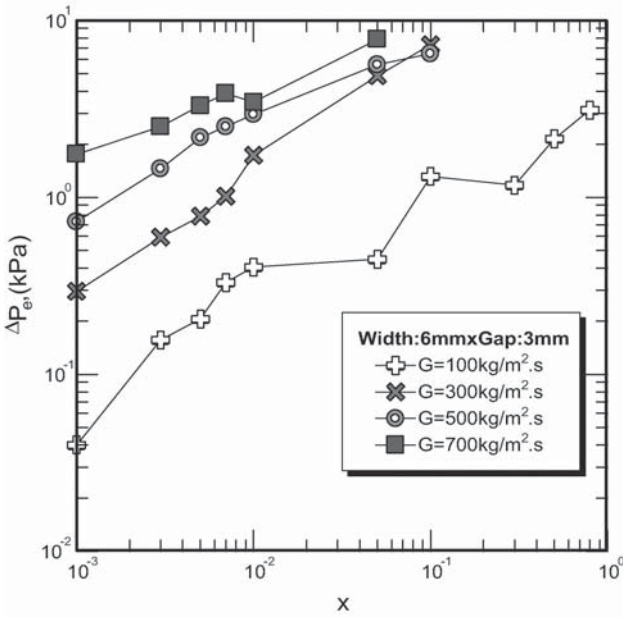

(b) Width: 6 mm x Gap: 3 mm

Figure 3 Measured pressure changes as a function of mass flux and gas quality.

inherited momentum can easily break up the liquid into droplets and a quite uniformly spread film around the whole rectangular section. The flow pattern is thus an annular flow pattern (e.g., Figure 4f, $x = 0.5$). The unique "liquid jet-like" flow pattern persists at the entrance of the 9 × mm test section. This flow pattern, however, is not seen for the 6 × mm test section as seen from Figures 4g–l. However, by comparing the foregoing observed flow patterns, one can see the unusual phenomenon

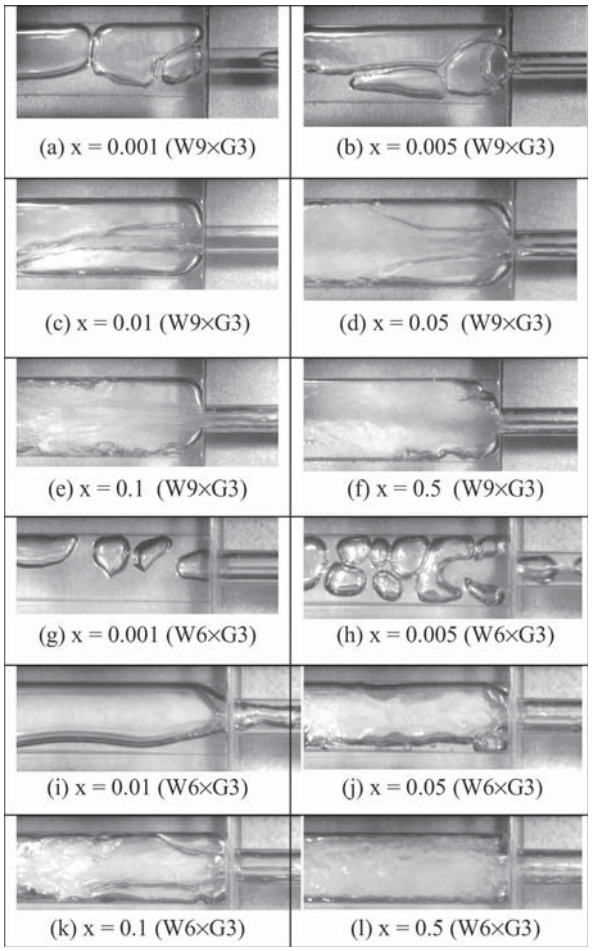

Figure 4 Progress of flow pattern for sudden enlargement vs. quality at $G = 100\ \mathrm{kg{\cdot}m^{-2}{\cdot}s^{-1}}$.

is actually related to the liquid jet-like flow pattern. When the liquid jet flows across the sudden enlargement, part of its momentum is conserved and the gas flow is alongside the liquid jet. In this regard, the corresponding expansion pressure change decreases.

In fact, some of the measured pressure difference data of this study also reveal a flat or slightly leveled-off phenomenon versus vapor quality (e.g., $G = 300\ \mathrm{kg{\cdot}m^{-2}{\cdot}s^{-1}}$). A close examination of the data suggests that this region is also related to the "liquid jet-like" flow pattern. The observations suggest that a conceivable reduction of the pressure difference is encountered when liquid jet-like flow pattern prevails, yet a flattening or leveling off of the pressure difference is seen when the liquid jet-like flow is less pronounced. By contrast, one can find an appreciable increase of pressure difference when the liquid jet-like flow pattern is completely gone. Apparently the confinement effect of this test section is the main cause for the disappearance of this flow pattern. Note that the distance from the brim of the small diameter tube at the intersection of the abrupt enlargement to the upper or lower surface of the rectangular tube for the 9 × 3 mm tube is two times larger than that of the 6 × 3 mm tube. Hence, the liquid flowing out of the smaller diameter tube touches the adjacent walls comparatively easily, thereby eliminating the "liquid jet-like" flow pattern accordingly. In addition, the size of air bubbles of the 6 × 3 mm tube (Figure 4g) is much smaller than that of the 9 × 3 mm tube at $x = 0.001$ (Figure 4a).

For a higher mass flux of 300 $\mathrm{kg{\cdot}m^{-2}{\cdot}s^{-1}}$, progress of flow pattern change is somewhat similar to that at $G = 100\ \mathrm{kg{\cdot}m^{-2}{\cdot}s^{-1}}$ except that the development of flow pattern moves toward a lower quality region. However, the liquid jet-like flow pattern is rather unclear at higher gas quality in both test sections. Therefore, the leveling-off phenomenon of the expansion pressure loss is almost unseen.

The measured pressure differences subject to abrupt enlargement are compared with the foregoing models/correlations described in the literature review. In total, nine models and correlations were used for comparison; detailed comparisons indicated that none of the models/correlations can predict the present test results with an acceptable accuracy. There are several possible causes for this significant departure. The first one is attributable to the evaluation of void fraction. Note that most of the models/correlations require information on a void fraction, except for the homogeneous model, the Chisholm and Sutherland [10] correlation, and the Wadle correlation [12]. This eventually involves suitable selection of the correlation of void fraction. In this study, the void fraction correlation being used is identical to those suggested in previous researchers. However, one still sees a tremendous digression from these comparison charts. The second cause of this deviation is related to the geometric difference. The previous geometries are mostly at a much larger scale, except those by Abdelall et al. [1]. Furthermore, previous studies are generally applicable for round/round sudden enlargement, while the present experiments are conducted for round/rectangular transformation. The best predictive abilities for the previous models are those by Wadle [12] with a mean deviation around 200%. The deviation is calculated as $\frac{1}{N}(\sum_{1}^{N}\frac{|\Delta P_{PRED}-\Delta P_{EXP}|}{\Delta P_{EXP}}) \times 100\%$, where N is the number of total data points. The results imply that further efforts should be made for seeking a better correlation.

Results for Contraction

Figure 5 shows the measured two-phase pressure drops subject to the sudden contraction for the 6 × 3 mm and 9 × 3 mm channels, respectively; each test section has 40 data points. In general, the contraction pressure drops increase with the quality and mass flux. However, a noticeable drop of the pressure loss is encountered at a low mass quality region ($x < 0.1$). This phenomenon was also observed by Schmidt and Friedel [18] for their air–water data at $G = 1000\ \mathrm{kg{\cdot}m^{-2}{\cdot}s^{-1}}$, where a local peak of pressure drop versus vapor quality is seen at a low mass flow quality. This phenomenon was characterized as a change of flow pattern in the inlet pipe or outlet pipe. In this study, a notable pressure drop is seen for $G = 100\ \mathrm{kg{\cdot}m^{-2}{\cdot}s^{-1}}$ and a gas quality

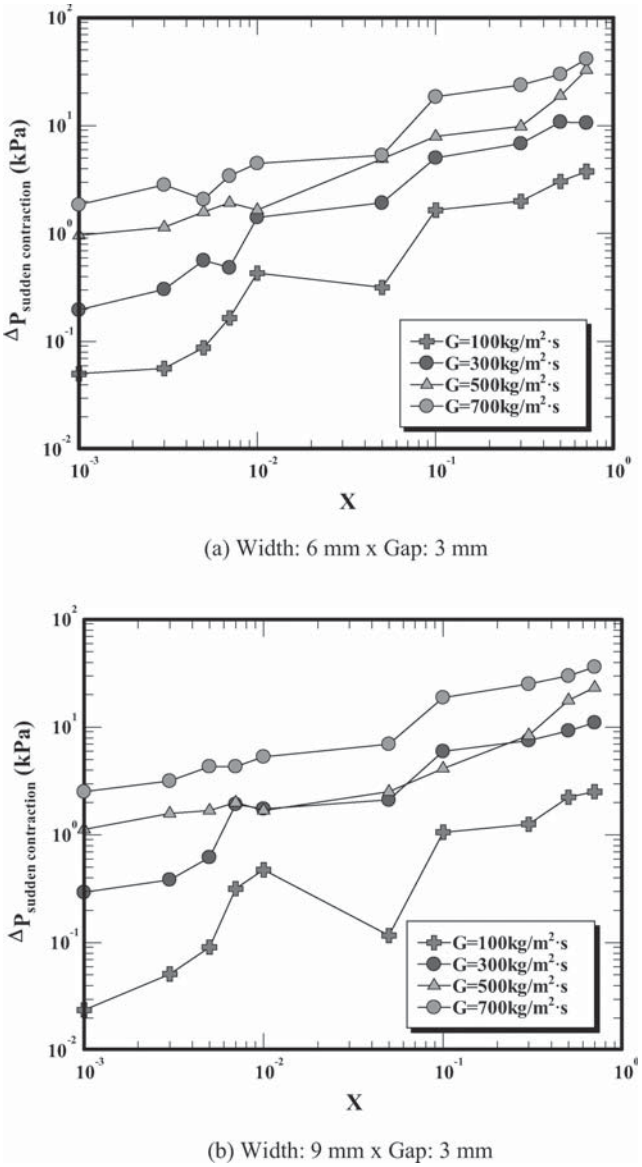

Figure 5 Measured pressure change as a function of mass flux and quality for (a) 6 mm × 3 mm and (b) 9 mm × 3 mm channel.

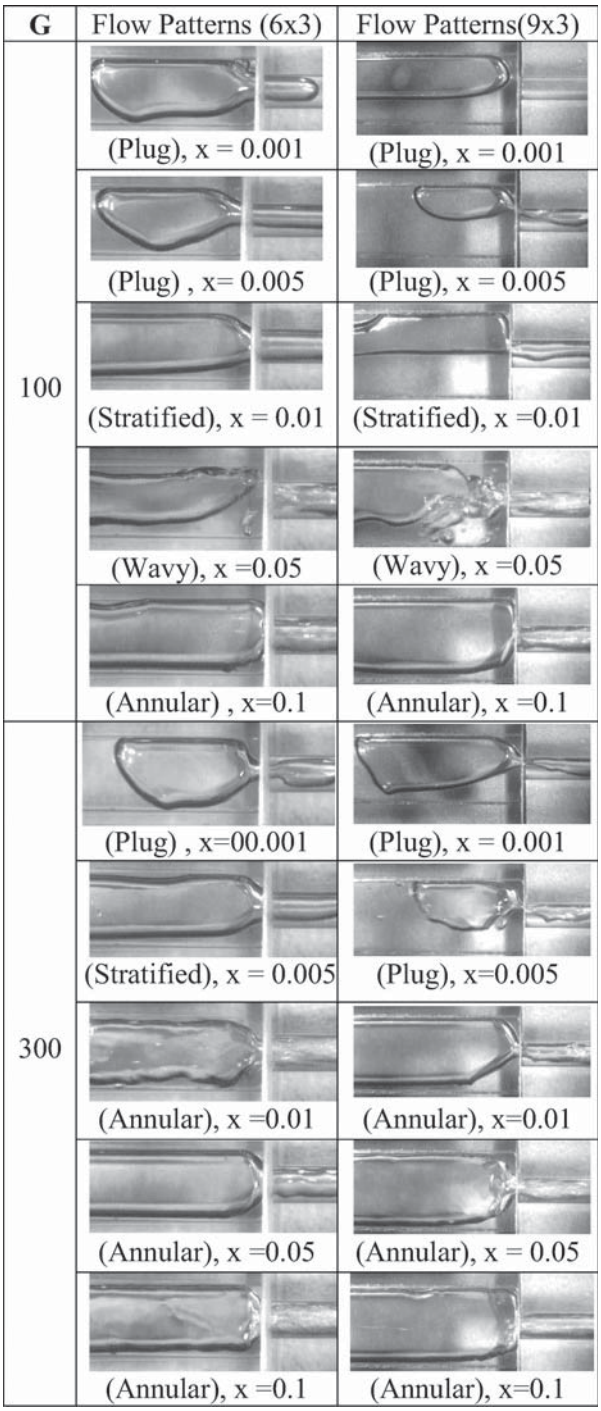

Figure 6 Progress of flow pattern vs. quality across the sudden contractions for $G = 100$ and 300 kg·m^{-2}·s^{-1}.

of 0.05 as shown in Figure 5. For further understanding about the phenomenon, one can see the progress of the flow pattern subject to the influence of contraction from Figure 6. As shown in the figure, for a mass flux of 100 kg·m^{-2}·s^{-1} at a low quality less than 0.01, one can see that the intermittent flow pattern prevails before and after the contraction. Although the stratified flow might persist after the contraction, one can see that the vena contracta is clearly absent. Note that the mentioned vena contracta is slightly different from that in single-phase flow. For single-phase flow, the vena contracta represents the point in a fluid stream where the diameter of the jet stream is the least, such as in the case of a stream issuing out of a nozzle. Here the observed vena contracta denotes the gas stream surrounded by liquid with the smallest diameter of gas core.

With the rise of vapor quality ($x = 0.01$–0.1), the vena contracta is observable for the major flow pattern after the contraction turn into an annular flow pattern. As delineated by Collier and Thome [13], the presence of the vena contracta effectively converted the accelerated and pressure energy into kinetic energy with little or no frictional dissipation from upstream. This

will certainly offset the irreversible pressure loss caused by the singularity. Beyond the vena contracta position, the conditions are similar to those of sudden enlargement through which considerable frictional dissipation occurs. In essence, the considerable deflection of the contraction pressure drop is associated with the transition of forming the vena contracta. For a larger mass flux like $G = 300\ \mathrm{kg{\cdot}m^{-2}{\cdot}s^{-1}}$, the vena contracta is still seen even at a very low quality range of 0.001–0.005. However, the rising frictional contribution with mass flux will counteract the occurrence of vena contracta, thereby leading to a comparatively small influence of vena contracta on the pressure drop. In addition, formation of vena contracta also shifts toward a smaller gas quality, giving rise to an early deflection of pressure drop at a lower gas quality. However, it should be mentioned that this phenomenon becomes less and less pronounced when the mass flux is increased. This is because the increasing frictional performance counterbalances the effect of the vena contracta.

To test the validity of the foregoing described models/correlations from the existing literatures, the measured two-phase pressure drop data subject to abrupt contraction in two test sections are compared with the previously described homogeneous model (Collier and Thome [13]), and correlations of Chisholm [5], Schmidt and Friedel [18], and Abdelall et al. [1]. The detailed comparisons and relevant mean deviations for the models/correlations give fair predictions of the present data, but none of them can accurately predict the entire database. Note that most of the existing data were conducted for the geometry from round/rectangular to round/rectangular configuration, while the present test section is from rectangular to round tube configuration. The average mean deviations of the relevant predictions are 49.15%, 54.12%, 50.8%, 64.5%, and 74.8% by the homogeneous model (Eq. 35), Chisholm homogeneous model (Eq. 36), Chisholm correlation (Eq. 37), Schmidt and Friedel correlation (Eq. 40), and Abdelall et al. correlation (Eq. 43), respectively. Also, the Abdelall et al. simplified correlation (Eq. 43) gave a mean deviation of more than 100%. The homogeneous model gives better predictive ability than the others, which had also been indicated by Geiger [6] and McGee [17]. For homogeneous predictions, the data with higher pressure drop give a good agreement with the predictions. Note that the flow patterns for these data with good predictions are actually annular flow. However, the data for all slug and stratified flows, where buoyancy force plays a significant role, are greatly over the predictions.

There are some pressure drop data for two-phase flow across sudden contractions available from the literature, as mentioned earlier. For comparison purposes, the present data and some available data along with some databases (Geiger [6]; McGee [17]; Schmidt and Friedel [18]; Abdellal et al. [1]) are compared with the relevant correlations and models. In general, the homogeneous predictions give a very good agreement with the two data sets reported by Geiger [6] and McGee [17], with corresponding mean deviations of 19.93% and 16.81%, respectively. The mean deviations for the data of Schmidt and Friedel [18] and the present data are 43.46% and 49.15%, respectively. Nevertheless, the homogeneous model significantly overpredicted the data of Abdelall et al. [1] with 468.79% mean deviation, which was also previously reported by these authors. The possible cause for this large deviation is associated with the micro-tubes (with one inner diameter of 1.60 mm and the other of 0.84 mm) being tested. For these micro-tubes, influence caused by surface tension takes control. For obtaining a better predictive ability, one should also take into account the influence of surface tension force (Tripplet et al. [21]). The balance of buoyancy and surface tension force can be represented by the Bond number (Bo) as:

$$Bo = \frac{g(\rho_L - \rho_G)(D/2)^2}{\sigma} \tag{48}$$

When the value of Bo is near or less than 1.0, the stratified flow pattern is not able to exist in most of the two-phase flow conditions. Chen et al. [2] had utilized the Bond number (Bo) to count for the force balance between buoyancy and surface tension in development of the two-phase frictional pressure drop correlation in small tubes. From the foregoing comparison, it is found that the homogeneous model gives good predictive ability but fails to predict the Abdelall et al. microchannel data. By examining the corresponding Bond number for these five databases, it is found that the departure of the predictive ability of homogeneous model is strongly related to the Bond number. In that regard, it is suggested that the influence of Bond number should be included in future development of the correlation.

CONCLUSIONS

Two-phase flow approaching singularities such as abrupt expansion and sudden contraction is widely encountered in typical industrial and heat-exchanging devices. For conventional channels where the flow path may be comparatively long, the associated pressure drops relative to the total pressure drops may be small and are often neglected. However, with smaller and smaller channels being introduced (such as mini- or microchannels) to the real world, one can no longer ignore their influence, and the need for more accurate estimation of the expansion/contraction loss becomes evident. There have been some studies concerning this subject but mostly applicable for larger channels. The major effort of this study is to review the existing efforts concerning two-phase flow across sudden expansions/contractions and to examine the applicability of the existing correlations with respect to the recent data in small channels. The second part of this study is to present some newly measured pressure drops and observed flow patterns pertaining to influence of expansion/contraction. For an abrupt expansion, it is found that the existing correlations all fail to provide a reasonably predictive capability versus the newly collected data. Furthermore, a unique flow pattern called a "liquid jet-like flow pattern" occurs at a very low quality region of $G = 100\ \mathrm{kg{\cdot}m^{-2}{\cdot}s^{-1}}$, and it raises a setback phenomenon of

pressure drop. By contrast, an appreciable increase of pressure difference is seen when the liquid jet-like flow pattern is completely gone. Similar conclusion is drawn to the data of contractions. For the correlations/predictive models, the homogeneous model gives satisfactory prediction for conventional macrochannels but fails to do so when the channels become smaller. This is especially pronounced for a small-diameter tube with a Bond number being less than 1, in which the effect of surface tension dominates. It is also found that most existing correlations can only predict their own database, and extrapolation of their correlations outside their test range is questionable. Hence, it is suggested that the Bond number should be introduced to modify the existing homogeneous model.

NOMENCLATURE

A	aspect ratio, gap/width, $0 \leq A \leq 1$
C_h	Chisholm's factor, defined in Eq. (15)
Bo	Bond number, defined in Eq. (48)
C_C	contraction coefficient
d	internal diameter of circular tube, m
D_h	hydraulic diameter, m
f	friction factor
f_{con}	total fiction factor for the contraction
g	rectangular channel gap, mm
G	total mass flux, $kg \cdot m^{-2} \cdot s^{-1}$
j_L	superficial liquid velocity, $m \cdot s^{-1}$
j_G	superficial gas velocity, $m \cdot s^{-1}$
K	loss coefficient
$\dot{m}$	mass flow rate, $kg \cdot s^{-1}$
P	pressure, Pa
ΔP_c	pressure change across the sudden contraction, Pa
ΔP_{cL}	pressure drop across the sudden contraction for total flow assumed liquid, Pa
ΔP_{iv}	static pressure drop to the vena contracta, Pa
ΔP_{vc}	pressure recovery downstream of the vena contracta, Pa
ΔP_e	pressure change across the sudden expansion, Pa
ΔP_{eI}	irreversible pressure changes across the sudden expansion, Pa
ΔP_{eR}	reversible pressure changes across the sudden expansion, Pa
dP/dz	frictional pressure gradient, $Pa \cdot m^{-1}$
Re	Reynolds number, $\rho ud/\mu$
S	slip ratio
u	mean axial velocity in the small tube, $m \cdot s^{-1}$
x	gas quality
W	rectangular channel width, mm
We	Weber number
Γ_{con}	base pressure coefficient for the contraction
X	Martinelli parameter
X_{CH}	correlation parameter for Chisholm and Sutherland [10]; see Eq. (14)

Greek Symbols

σ	surface tension, $N \cdot m^{-1}$
σ_A	flow cross-sectional area contraction ratio
α	mean void fraction
α_E	mean volumetric liquid entrained in the gas flow
μ	viscosity, $N \cdot s \cdot m^{-2}$
Φ_{cL}	two-phase multiplier with all liquid flow through the contraction
β	gas volumetric flow ratio, $=j_G/(j_G + j_L)$
ρ	density, $kg \cdot m^{-3}$
ρ'	fictitious mixture density defined in Eq. (33), $kg \cdot m^{-3}$
ρ''	fictitious mixture density defined in Eq. (34), $kg \cdot m^{-3}$
ρ_{eff}	effective density defined in Eq. (21), $kg \cdot m^{-3}$

Subscripts

con	contraction
EXP	experiments
G	gas-phase
h	homogeneous
L	liquid-phase
PRED	values for correlation or model predictions

REFERENCES

[1] Abdelall, E. F., Hahm, G., Ghiaasiaan, S. M., Abdel-Khalik, S. I., Jeter, S. S., Yoda, M., and Sadowski, D. L., Pressure Drop Caused by Abrupt Flow Area Changes in Small Channels, *Experimental Thermal & Fluid Science*, vol. 29, pp. 425–434, 2005.

[2] Chen, I. Y., Yang, K. Y., and Wang, C. C., An Empirical Correlation for Two-Phase Frictional Performance in Small Diameter Tubes, *International Journal of of Heat and Mass Transfer*, vol. 45, pp. 3667–3671, 2002.

[3] Chen, I. Y., Liu, C. C., Chien, K. H., and Wang, C. C., Two-phase Flow Characteristics Across Sudden Expansion in Small Rectangular Channel, *Experimental Thermal & Fluid Science*, vol. 32, pp. 696–706, 2007.

[4] Kays, W. M., and London, A. L., *Compact Heat Exchangers,* 3rd ed., McGraw-Hill, New York, p. 112, 1984.

[5] Chisholm, D., *Two-Phase Flow in Pipelines and Heat Exchangers,* George Godwin, London, pp. 175–192, 1983.

[6] Geiger, G. E., *Sudden Contraction Losses in Single and Two-Phase Flow*, Ph.D. Thesis, University of Pittsburgh, Pittsburgh, PA, 1964.

[7] Romie, F., Private communication to P. Lottes (see Lottes [9]).

[8] Richardson, B., *Some Problems in Horizontal Two-Phase*, *Two-Component Flow*, Report ANL-5949, 1958.

[9] Lottes, P. A., Expansion Losses in Two-Phase Flow, *Nuclear Science and Engineering*, vol. 9, pp. 26–31, 1961.

[10] Chisholm, D., and Sutherland, L. A., Prediction of Pressure Gradients in Pipeline System During Two-Phase Flow, *Proc. Institute of Mechanical Engineers*, vol. 184, pt. 3C, pp. 24–32, 1969.

[11] Attou, A., Giot, M., and Seynhaeve, M., Modeling of Steady Two-Phase Bubbly Flow Through a Sudden Enlargement, *International Journal of Heat and Mass Transfer*, vol. 40, pp. 3375–3383, 1997.
[12] Wadle, M., A New Formula for the Pressure Recovery in an Abrupt Diffuser, *International Journal of Multiphase Flow*, vol. 15, pp. 241–256, 1989.
[13] Collier, J. G., and Thome, J. R., *Convective Boiling and Condensation*, 3rd ed., Oxford, New York, pp. 109–111, 1994.
[14] Kawahara, A. A., Chung, P. M. Y., and Kawaji, M., Investigation of Two-Phase Flow Pattern, Void Fraction and Pressure Drop in a Microchannel, *International Journal of Heat and Mass Transfer*, vol. 28, pp. 1411–1435, 2002.
[15] Schmidt, J., and Friedel, L., Two-Phase Flow Pressure Change Across Sudden Expansions in Duct Areas, *Chemical Engineering Communications*, vol. 141–142, pp. 175–190, 1995.
[16] Attou, A., and Bolle, L., A New Correlation for the Two-phase Pressure Recovery Downstream From a Sudden Enlargement, *Chemical Engineering Technology*, vol. 20, pp. 419–423, 1997.
[17] McGee, J. W., *Two-Phase Flow Through Abrupt Expansions and Contractions*, Ph.D. Thesis, University of North Carolina at Raleigh, 1996.
[18] Schmidt, J., and Friedel, L., Two-Phase Flow Pressure Drop Across Sudden Contractions in Duct Areas, *International Journal of Multiphase Flow*, vol. 23, pp. 283–299, 1997.
[19] Moody, F. J., Maximum Flow Rate of a Single Component, Two-Phase Mixture, *ASME Journal of Heat Transfer*, vol. 86, pp. 134–142, 1965.
[20] Zivi, S. M., Estimation of Steady State Void Fraction by Means of Minimum Entropy Production, *Journal of Heat Transfer*, vol. 86, pp. 247–252, 1964.
[21] Tripplet, K. A., Ghiasiaan, S. M., Abdel-Khlik, S. L., LeMouel, A., and McCord, B. N., Gas–Liquid Two-Phase Flow in Microchannels, Part II: Void Fraction and Pressure Drop, *International Journal of Multiphase Flow*, vol. 25, pp. 395–410, 1999.

Ing Youn Chen is a professor at mechanical engineering of National Yunlin University of Science and Technology, Taiwan. He received his B.S. in mechanical engineering from National Taiwan University in 1971, and received his M.S. in 1979 and Ph.D. in 1984 in mechanical engineering from the University Wisconsin–Milwaukee. He joined Sundstrand and McDonell Douglas space companies from 1985 to 1989 and from 1989 to 1994, respectively. In this period, he was involved in the analysis and testing of two-phase thermal control system for the international space station. Currently, he conducts teaching and research in two-phase flow and heat transfer areas. He is also a reviewer for several international journals.

Somchai Wongwises is a professor in the Department of Mechanical Engineering at King Mongkut's University of Technology Thonburi, Bangmod, Thailand. He received his Doktor Ingenieur (Dr.-Ing.) in mechanical engineering from the University of Hannover, Hannover, Germany, in 1994. His research interests include two-phase flow, heat transfer enhancement, and thermal system design. He is the head of the Fluid Mechanics, Thermal Engineering, and Two-Phase Flow Research Laboratory.

Bing-Chwen Yang is a senior researcher in the Energy & Environment Research Laboratory, Industrial Technology Research Institute (ITRI), Hsinchu, Taiwan. He received his M.S. from the Department of Mechanical Engineering at the University of South Carolina in 1988 and his Ph.D. from the Department of Mechanical Engineering at Pennsylvania State University in 1992. He joined ITRI in 1992. His research areas include heat transfer, two-phase systems, micro cooling systems, and air-conditioning technology. He is the division head of the Residential & Commercial Energy Saving Technology Division in EEL, ITRI. He is also a committee member of ASHRAE technology committee 8.6 for cooling towers.

Chi-Chuan Wang is a senior lead researcher in the Energy & Environment Research Laboratory, Industrial Technology Research Institute (ITRI), Hsinchu, Taiwan. He received his B.S., M.S., and Ph.D. all in mechanical engineering from National Chiao-Tung University, Hsinchu, Taiwan during 1978–1989. He joined ITRI in 1989. His research areas include enhanced heat transfer, multiphase systems, micro-scale heat transfer, and heat pump technology. He is also a regional editor of the *Journal of Enhanced Heat Transfer* and an associate editor of *Heat Transfer Engineering*.

International Journal of Heat and Mass Transfer 53 (2010) 2052–2064

Contents lists available at ScienceDirect

International Journal of Heat and Mass Transfer

journal homepage: www.elsevier.com/locate/ijhmt

Comparison of frictional pressure drop models during annular flow condensation of R600a in a horizontal tube at low mass flux and of R134a in a vertical tube at high mass flux

A.S. Dalkilic [a,*], O. Agra [a], I. Teke [a], S. Wongwises [b,*]

[a] Heat and Thermodynamics Division, Department of Mechanical Engineering, Yildiz Technical University, Yildiz, Besiktas, Istanbul 34349, Turkey
[b] Fluid Mechanics, Thermal Engineering and Multiphase Flow Research Lab. (FUTURE), Department of Mechanical Engineering, King Mongkut's University of Technology Thonburi, Bangmod, Bangkok 10140, Thailand

ARTICLE INFO

Article history:
Received 28 May 2009
Received in revised form 13 December 2009
Accepted 13 December 2009
Available online 27 January 2010

Keywords:
Condensation
Pressure drop
Horizontal flow
Downward flow
R600a
R134a

ABSTRACT

This study compares well-known two-phase pressure drop models with the experimental results of a condensation pressure drop of (i) R600a in a 1 m long horizontal smooth copper tube with an inner diameter of 4 mm, outer diameter of 6 mm and (ii) R134a in a 0.5 m vertical smooth copper tube with an inner diameter of 8.1 mm and outer diameter of 9.52 mm. Different vapour qualities (0.45–0.9 for R600a and 0.7–0.95 for R134a), various mass fluxes (75–115 kg m^{-2} s^{-1} for R600a and 300–400 for R134a kg m^{-2} s^{-1}) and different condensing temperatures (30–43 °C for R600a and 40–50 °C for R134a) were tested under annular flow conditions. The quality of the refrigerant in the test section was calculated considering the temperature and pressure obtained from the experiment. The pressure drop across the test section was directly measured with a differential pressure transducer. The most agreeable correlations of various available options were then identified according to the results of analysis during annular flow regime.

1. Introduction

The two-phase flow occurs when the two phases, separated from each other by a distinct interface, flow simultaneously. Gas–liquid flows can be observed in many industrial applications such as oil–gas flow in oil pipelines, steam–water flow in nuclear reactors, steam flows in heat pipes and vapour–liquid flow of refrigerants in cooling and air-conditioning applications. This study is concerned with an annular flow regime for the liquid and vapour flow of R600a and R134a in horizontal and vertical tubes respectively.

The actual technologies of nuclear reactors, the aerospace industry, microelectronics, cooling systems, refrigeration, the automotive industry, process industry etc. are characterised by a disposition towards using packages of large power conversion or heat transfer in small volumes. There has been a recent fast development of better, more effective, heat exchangers together with a demand for more compact systems, higher energy efficiency and lower material costs. Heat exchangers are devices that are commonly used to transfer heat between two or more fluids at different temperatures. They are used in a wide variety of applications, e.g. refrigeration and air conditioning systems, power engineering and other thermal processing plants.

One of the major contributors to the depletion of the ozone layer are the hydrochlorofluorocarbon refrigerants used in the refrigeration and air conditioning industries. More compact equipment with higher system operating efficiency for air conditioning has been investigated following changes in efficiency standards. Refrigerant mixtures with enhanced surfaces have been developed as an alternative solution to replace hydrochlorofluorocarbon refrigerants. Accurate methods for the determination of the thermal and fluid-dynamic behaviour of new refrigerants need to be researched in order to improve the efficiency of heat exchangers.

The use of natural refrigerants such as hydrocarbons is one of the possible solutions to avoid the use of CFCs, HCFCs and HFCs. In spite of the prohibition due to safety concerns placed on the use of flammable hydrocarbon refrigerants a few decades ago for normal refrigeration and air conditioning applications, some of the flammable refrigerants have, nevertheless, been used in certain applications according to Kruse [1] and Jung et al. [2]. Recently, isobutene (R600a), propane (R290) and propylene (R1270) have been used for such heat transfer applications as are found in refrigerators, freezers, and heat pumps. Besides this, R429A and R432A including dim ethyl ether (DME, RE170), have been proposed as alternatives to R134a and R22. Unfortunately, some of the new

* Corresponding authors. Tel.: +90 2123832819; fax: +90 2122616659 (A.S. Dalkilic), Tel.: +66 24709115; fax: +66 24709111 (S. Wongwises).
E-mail addresses: dalkilic@yildiz.edu.tr (A.S. Dalkilic), somchai.won@kmutt.ac.th (S. Wongwises).

0017-9310/$ - see front matter © 2009 Elsevier Ltd. All rights reserved.
doi:10.1016/j.ijheatmasstransfer.2009.12.051

Nomenclature

Bo	Bond number
c_p	specific heat, J kg^{-1} K^{-1}
d	internal tube diameter, m
f	friction factor
Fr	Froude number
G	mass flux, kg m^{-2} s^{-1}
g	gravitational acceleration, m s^{-2}
i	enthalpy, J kg^{-1}
i_{fg}	latent heat of condensation, J kg^{-1}
j	superficial velocity
L	length of test tube, m
m	mass flow rate, kg s^{-1}
N_{coff}	confinement number
P	pressure, N m^{-2}
Re	Reynolds number
S	slip ratio
Q	heat transfer rate, W
We	Weber number
x	average vapor quality
X	Lockhart and Martinelli parameter
z	axial coordinate, m
ΔP	pressure drop, Pa
ΔT_{sat}	$T_{sat} - T_{wi}$, °C

Greek symbols

α	void fraction
ϕ	two-phase multiplier
ψ	surface tension parameter
ε	height of roughness
Ω	modifier to the Friedel correlation
σ	surface tension, N m^{-1}
ρ	density, kg m^{-3}
μ	dynamic viscosity, kg m^{-1} s^{-1}

Subscripts

avg	average
evap	evaporator
exp	experimental
F	frictional term
G	gravitational term
g	gas/vapor
go	gas only
i	inlet
int	interfacial
l	liquid
lo	liquid only
M	momentum term
o	outlet
ph	preheater
ref	refrigerant
sat	saturation
t	test section
TP	two-phase
TS	test section
w	water
wi	inner wall

alternative refrigerants have additional problems such as extensive heat transfer degradation during condensation due to the zeotropic characteristics of the refrigerant. For that reason, there is still room for research on alternative refrigerants such as R600a, R744 and R407C.

Annular flow conditions along the tube length include convective condensation which occurs for many applications inside tubes. Annular two-phase flow is one of the most important flow regimes, and is characterised by a phase interface separating a thin liquid film from the gas flow in the core region. Two-phase annular flow occurs widely in film heating and cooling processes, particularly in power generation, and especially in nuclear reactors. This flow regime has received the most attention, both analytically and experimentally, because of its practical importance and the relative ease with which analytic treatment may be applied. In addition to this, condensate distribution inside the tube wall is almost symmetric, and there is high velocity vapour flow in the core during annular flow.

The two-phase pressure drop is a significant design parameter in many engineering applications such as the chemical process industry, the nuclear industry, the petroleum industry, refrigeration and air conditioning applications and space applications. There have been a number of investigations into this subject in the literature due to its importance. The frictional, acceleration, and gravitational components form the two-phase total pressure drop in tubes. Determination of void fraction is necessary for computing the acceleration and gravitational components and, in a similar way, determination of whether either the two-phase friction factor or the two-phase frictional multiplier is also necessary for computing the frictional component of pressure drop.

The Lockhart and Martinelli [3], Chisholm [4] and Friedel [5,6] correlations are generally used for the determination of pressure drop in conventional channels. Some modifications to account for specific geometry or flow conditions are made in these correlations. In spite of their large deviations from the data for small channels in the condensation process, they have still been used as the basis for many recent correlations.

Condensation phenomena inside horizontal tubes represent an important issue in the chemical process and power industries. Shell side condensation is rarely preferred to tube side condensation when the coolant is air or a process gas, or when the condensing refrigerant is at high pressure, dirty or corrosive. For tube side condensers, the horizontal orientation is most commonly applied.

Lee et al. [7,8] examined the condensing heat transfer coefficients and pressure drop of hydrocarbons (R-290, R-600a, R-1270) in the evaporator and condenser, and compared them with those of R22. A tube diameter of 12.7 mm was used for this experiment. As a result of the experimental study it was determined that the condensing heat transfer coefficients and pressure drop of the hydrocarbons in both cases were higher than those of R22 under similar test conditions.

In a study performed by Wen et al. [9] the condensing heat transfer coefficients and pressure drop of the R290, R600 and R290/R600 refrigerants during their condensation inside a serpentine with a 2.46 mm diameter were examined and compared with those for the R134a refrigerant. As a result of these experiments it was determined that the condensing heat transfer coefficients of the hydrocarbons are higher than those of the R134a refrigerant under the same conditions.

Condensation inside vertical tubes usually occurs in nuclear reactors. In the design of passive containment cooling systems (PCCS), the presence of non-condensable gases inside condensed steam is an important technical problem. These kinds of condensers have vertical stainless steel tubes, almost 50 mm in diameter, immersed in a tank of water under atmospheric pressure conditions outside the containment.

Goodykoontz and Dorsch [10] investigated the local condensation heat transfer coefficients and pressure distribution of R113 for the mass fluxes of 21–455 kg m^{-2} s^{-1} in a 7.4–15.9 mm i.d. vertical tube. Kim and No [11] developed a turbulent film condensation model including pressure drop for high pressure steam in a 46 mm i.d. vertical tube. Ma et al. [12] studied the two-phase friction factors of downward flow of R113 for the mass fluxes of 400–800 kg m^{-2} s^{-1} in 20.8 mm i.d. smooth and micro-fin tubes.

To the best of the authors' knowledge, apart from the authors' previous publications [13–28], there has been insufficient work dealing with the heat transfer characteristics during downward condensation in small diameter tubes, and, moreover, no work on condensation of new generation refrigerant R600a inside horizontal tubes. Although some information is currently available on the frictional pressure drop in annular flow, room still remains for further discussion of whether it gives reliable predictions of frictional pressure drop in the high mass flux region of R134a inside vertical tubes and in the low mass flux region of the alternative, environmentally friendly refrigerant R600a inside horizontal tubes. Moreover, there are plenty of experimental and theoretical studies in the literature on the condensation of refrigerants in horizontal smooth tubes but their working fluids are mainly ozone depleting substances such as CFCs and HCFCs. It should also be noted that the reported mass fluxes, heat fluxes, condensation pressures and dimensions of the test tubes do not include studied parameters. Therefore, the main aim of this study was to extend the existing pressure drop data for R134a and R600a according to the specific experimental conditions respectively tested. The results obtained from analysis of the various experimental data at different saturation temperatures, mass fluxes and vapour qualities were used to determine the best predictive models.

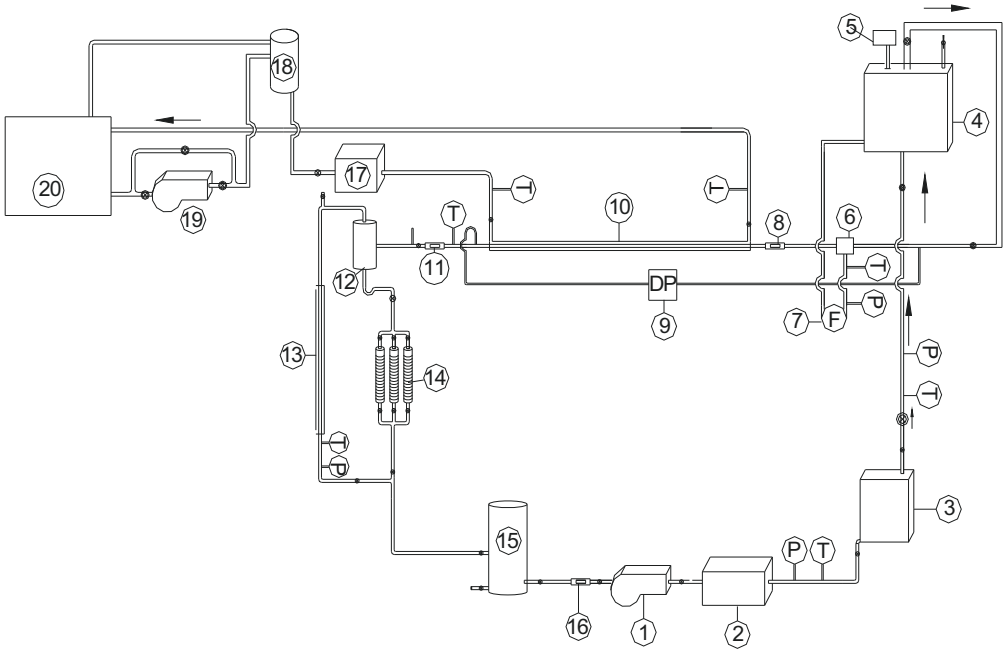

1- Refrigerant Pump 2- Filter 3- Primary heater 4- Evaporater 5- Level gauge 6- Liquid-gas mixture chamber 7- Flow meter 8- Sight glass 9- Differancial Pressure Transmitter 10- Test section 11- Sight glass 12- Liquid/Gas Seperator 13- Air-cooled condenser 14- Scaled vessels 15- R600a Reserve Tank 16- Sight glass 17- Flow meter 18- R134a reserve tank 19- Cooling water reserve tank 20- Water pump

Fig. 1. Schematic diagram of experimental apparatus for the condensation of R600a. [21].

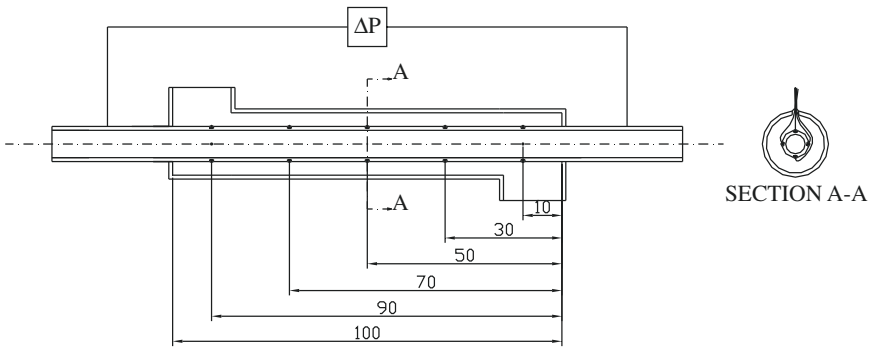

Fig. 2. Schematic diagram of test section for the condensation of R600a [22].

2. Experimental apparatus and procedure

2.1. Experimental apparatus for the condensation of R600a inside a horizontal tube

The experimental apparatus prepared for this study which is illustrated in schematic form in Fig. 1, comprised three major units, namely: the refrigerant cycle, the cooling water cycle and a data collection unit made up of 20 components. Since R600a exhibits combustible and explosive characteristics when mixed with air, special care was taken to ensure that the experiment apparatus was of ex-proof quality. The refrigerant was transferred to the test area using an ex-proof Lewa Ecodos diaphragm pump with a precisely adjustable stroke and flow rate. To identify the flow rate of the refrigerant, a coriolis-type flow meter with a measuring range of 0–250 kg h^{-1} capable of measuring with a precision of ±0.10% was employed. To ensure that the refrigerant pumped to the test tube had the desired vapour quality at the inlet of the test tube, an evaporator (4) was installed in the system. A schematic illustration of this evaporator has been given in the author's previous publications [21,22].

The lower part of the evaporator yields saturated fluid and the upper part yields saturated steam. Different vapour qualities needed to be obtained for the purposes of the experimental study and this is achieved as the steam leaving the evaporator passes through the specially designed mixing chamber (6). Here it amalgamates with the liquid surface at a determined rate to form an annular flow with no droplets. Annular flow is obtained in the mixing chamber. The liquid–steam mixture in annular form passes through a specially designed 10-cm sight glass of the same diameter as a test tube (Fig. 2). To keep the heat loss minimised in the sight glasses mounted on the inlet and outlet of the test tube (8, 11), the glasses were coated with acetate and insulated by means of the air layer between.

The test area is comprised of two concentric circular tubes. The inner one is of copper and the outer one has a Plexiglas construction. The copper tube used as the test tube (10) has an outer diameter of 6 mm and inner diameter of 4 mm, and the Plexiglas tube has an inner diameter of 16 mm. To determine the pressure drop occurring on the inlet and outlet of the test area, a differential pressure transmitter (9) calibrated at a measuring range of 0–500 mm-wg with a precision of ±0.075% was installed in the apparatus. A T-type thermocouple with a diameter of 0.3 mm was installed on the test tube to measure the surface temperature. Large, u-type grooves were slotted onto the walls of the tested copper tube, and thermocouples were mounted in horizontal form and attached to the tube to prevent wing effect. In the experimental study, the $(T_{sat} - T_{wi})$ difference was measured directly with a gauge developed on the data collection unit as illustrated in the author's previous publications [21,22]. The refrigerant leaving the test area reaches a liquid/vapour separator (12) where the liquid and vapour content of the refrigerant is separated. The refrigerant flows to the pressure-resistant graduated cups (14) to determine the quantity of the condensate. On the other hand, its vapour is driven to the air-cooled condenser (13) installed in the apparatus, condenses there and is then transferred to the receiver in liquid form. To bring the cooling water received from a container to the desired temperature, it is first heated and then accumulated in constant the water that will be transferred to the test area at constant temperature from getting impacted by vibrations due to the pump, it is accumulated in another reservoir (18) fitted close to the test area. From this reservoir, the cooling water flows to the test area under its own static pressure. After the cooling water leaves this reservoir at constant flow rate it passes through a turbine-type Honsberg flow meter with a capacity of 2–10 l h^{-1} to reach the test area. The temperature of the cooling water is measured by means of RTDs fitted on the inlet and outlet of the test area. The flow of the cooling water and the refrigerant in the test area is designed in a counter flow pattern to ensure an almost constant $(T_{sat} - T_{wi})$ temperature difference along the tube. In the cooling cycle when the refrigerant was circulating, pressures were measured by means of Bourdon Haenni-type pressure transmitters with a measuring

Table 1
Uncertainty of experimental parameters.

Condensation of R600a inside horizontal tube		Condensation of R134a inside vertical tube	
Parameters	Uncertainty	Parameters	Uncertainty
T_{sat} (°C)	0.069	T_{sat} (°C)	0.19
x_i	±1.11–2.16%	x_i	±6.96–8.24%
ΔT_{sat} (K)	±0.07	ΔT_{sat} (K)	±0.191
$(T_{w,o} - T_{w,i})_t$ (K)	±0.02	$(T_{w,o} - T_{w,i})_t$ (K)	±0.045
$(T_{w,i} - T_{w,o})_{evap}$ (K)	±0.011	$(T_{w,i} - T_{w,o})_{evap}$ (K)	±0.13
m_{ref} (g s^{-1})	±0.019	m_{ref} (g s^{-1})	±0.023
$m_{w,t}$ (g s^{-1})	±0.281	$m_{w,t}$ (g s^{-1})	±0.35
$m_{w,evap}$ (g s^{-1})	–	$m_{w,evap}$ (g s^{-1})	±0.38
q_t (kW m^{-2})	±2.1–3.3%	q_t (kW m^{-2})	±6.55-8.93%
q_{evap} (kW m^{-2})	±3.78–4.9%	q_{evap} (kW m^{-2})	±12–14.81%
ΔP_t (kPa)	±0.123	ΔP_t (kPa)	±0.13

Table 2
Operating conditions of the study.

Refrigerant	HFC-134a	HC-600a
Test tube material, inner diameter d, length L	Copper, ϕ8.1 mm, 500 mm	Copper, ϕ4 mm, 1000 mm
Range of condensing pressure, P_{sat} (bar)	10–12	4–5.73
Range of condensing temperature, T_{sat} (°C)	40–50	30–43
Range of mass flux, G (kg m^{-2} s^{-1})	300–400	75–115
Range of liquid Reynolds number, Re_l	628.74–4630.31	208.33–1571.42
Range of vapour Reynolds number, Re_g	139990–237243	21375–48875
Range of Lockhart–Martinelli number, X	0.015–0.12	0126–0.89
Range of average vapour quality, x	0.7–0.95	0.45–0.9

Table 3
Frictional pressure drop models and correlations.

Number	Frictional pressure drop model/correlation	Model/correlation
1 Experimental frictional pressure drop [15]	$(\Delta P)_G = g(\alpha\rho_g + (1-\alpha)\rho_l)L \quad \alpha = \frac{1}{1+\left(\frac{1-x}{x}\right)\left(\frac{\rho_g}{\rho_l}\right)S} \quad S = \left(1 - x + x\frac{\rho_l}{\rho_g}\right)^{1/2}$	
	$\left(\frac{dP}{dz}\right)_M = -G^2\frac{d}{dz}\left[\frac{x^2}{\rho_g\alpha} + \frac{(1-x)^2}{\rho_1(1-\alpha)}\right] \left(\frac{dP}{dz}\right)_F = \left(\frac{dP}{dz}\right)_{\text{Exp}} - \left(\frac{dP}{dz}\right)_G - \left(\frac{dP}{dz}\right)_M$	
2 Lockhart and Martinelli [3]	$X = \left[\frac{(dP/dz)_l}{(dP/dz)_g}\right]^{1/2} \quad \phi_l^2 = 1 + \frac{C}{X} + \frac{1}{X^2} \quad \left(\frac{dP}{dz}\right)_l = \frac{f_l G^2(1-x)^2}{2d\rho_l} \quad \left(\frac{dP}{dz}\right)_g = \frac{f_g G^2 x^2}{2d\rho_g}$	
	$\text{Re}_l = \frac{Gd(1-x)}{\mu_l} \quad f_l = \frac{64}{\text{Re}}\,(\text{laminar}) \quad f_l = \frac{0.316}{(\text{Re}_l^{0.25})}\,(\text{turbulent}) \quad \text{Re}_g = \frac{Gdx}{\mu_g}$	
	$f_g = \frac{0.184}{\text{Re}_g^{0.2}}\,(\text{turbulent}) \quad \left(\frac{\Delta P}{L}\right)_F = \phi_l^2\left(\frac{dP}{dz}\right)_l$	
	C: 20 / 12 / 10 / 5 — Liquid: Turbulent / Laminar / Turbulent / Laminar — Vapor: Turbulent / Turbulent / Laminar / Laminar	
3 Chisholm [4]	$Y = \sqrt{\frac{(dP/dz)_{go}}{(dP/dz)_{lo}}} \quad \left(\frac{dP}{dz}\right)_{lo} = \frac{f_{lo}G^2}{2d\rho_l} \quad \left(\frac{dP}{dz}\right)_{go} = \frac{f_{go}G^2}{2d\rho_g}$	
	$\phi_{lo}^2 = 1 + (Y^2-1)[Bx^{(2-n)/2}(1-x)^{(2-n)/2} + x^{(2-n)}] \quad n = \begin{cases} \text{Re}_{lo} \le 2100 \\ \text{Re}_{lo} > 2100 \end{cases}$	
	$f = 8\left[\left(\frac{8}{\text{Re}}\right)^{12} + \left\{\left[2.457\ln\left(\frac{1}{\left(\frac{7}{\text{Re}}\right)^{0.9} + 0.27\varepsilon/d}\right)\right]^{16} + \left(\frac{37530}{\text{Re}}\right)^{16}\right\}^{-1.5}\right]^{1/12}$	
	$B = \begin{cases} 55/\sqrt{G} \\ 520/\left(Y\sqrt{G}\right) \\ 15000/\left(Y^2\sqrt{G}\right) \end{cases} \text{ for } \begin{matrix} 0 < Y < 9.5 \\ 9.5 < Y < 28 \\ 28 < Y \end{matrix} \quad \left(\frac{\Delta P}{L}\right)_F = \phi_{lo}^2\left(\frac{dP}{dz}\right)_{lo}$	
4 Friedel et al. [5–6]	$E = (1-x)^2 + x^2\frac{\rho_l f_{go}}{\rho_g f_{lo}} \quad F = x^{0.78}(1-x)^{0.24} \quad H = \left(\frac{\rho_l}{\rho_g}\right)^{0.91}\left(\frac{\mu_g}{\mu_l}\right)^{0.19}\left(1 - \frac{\mu_g}{\mu_l}\right) \quad We = \frac{G^2 d}{\rho_{TP}\sigma}$	
	$\rho_{TP} = \left(\frac{x}{\rho_g} + \frac{1-x}{\rho_l}\right)^{-1} \quad Fr = \frac{G^2}{gd\rho_{TP}^2} \quad \phi_{lo}^2 = E + \frac{3.24FH}{Fr^{0.045}We^{0.035}} \quad \left(\frac{\Delta P}{L}\right)_F = \phi_{lo}^2\left(\frac{dP}{dz}\right)_{lo}$	
5 Chen et al. [33]	$\Omega = \begin{cases} \frac{0.0333\text{Re}_{lo}^{0.45}}{\text{Re}_g^{0.09}(1+0.4\exp(-Bo))} & Bo < 2.5 \\ \frac{We^{0.2}}{(2.5+0.06Bo)} & Bo \ge 2.5 \end{cases} \quad We = \frac{G^2 d}{\sigma\rho_{TP}} \quad Bo = g(\rho_l - \rho_g)\left(\frac{(d/2)^2}{\sigma}\right) \frac{dP}{dz} = \left(\frac{dP}{dz}\right)_{\text{Friedel}}\Omega$	
6 Cavallini et al. [34–35]	$E = (1-x)^2 + x^2\frac{\rho_l f_{go}}{\rho_g f_{lo}} \quad F = x^{0.6978} \quad H = \left(\frac{\rho_l}{\rho_g}\right)^{0.3278}\left(\frac{\mu_g}{\mu_l}\right)^{-1.181}\left(1 - \frac{\mu_g}{\mu_l}\right)^{3.477} \quad We = \frac{G^2 d}{\sigma\rho_{avg}}$	
	$\phi_{lo}^2 = E + \frac{1.262FH}{We^{0.1458}} \quad \left(\frac{\Delta P}{L}\right)_F = \phi_{lo}^2\left(\frac{dP}{dz}\right)_{lo}$	
7 Garimella et al. [36–37]	$\alpha = \left[1 + \left(\frac{1-x}{x}\right)^{0.74}\left(\frac{\rho_v}{\rho_l}\right)^{0.65}\left(\frac{\mu_l}{\mu_g}\right)^{0.13}\right]^{-1} \quad \text{Re}_l = \frac{Gd(1-x)}{\mu_l(1+\sqrt{\alpha})} \quad \text{Re}_g = \frac{Gdx}{\mu_g\sqrt{\alpha}} \quad f = \frac{64}{\text{Re}}\,(\text{laminar})$	
	$\psi = \frac{j_l\mu_l}{\sigma} \quad f = \frac{0.316}{\text{Re}^{0.25}}\,(\text{turbulent}) \left(\frac{dP}{dz}\right)_l = \frac{f_l G^2(1-x)^2}{2d\rho_l} \quad \left(\frac{dP}{dz}\right)_g = \frac{f_g G^2 x^2}{2d\rho_g}$	
	$X = \left[\frac{(dP/dz)_l}{(dP/dz)_g}\right]^{1/2} \quad j_l = \frac{G(1-x)}{\rho_l(1-\alpha)} \quad \frac{f_{\text{int}}}{f_l} = Ax^a\text{Re}_l^b\psi^c \quad \text{Re}_l < 2100\ A = 1.308\times10^{-3}$	
	$a = 0.4273\ b = 0.9295\ c = -0.1211 \quad \frac{\Delta P}{L} = \frac{1}{2}f_{\text{int}}\frac{G^2x^2}{\rho_g 2^{2.5}}\frac{1}{d}$	
8 Mishima and Hibiki [38]	$\phi_l^2 = 1 + \frac{C}{X} + \frac{1}{X^2} \quad C = 21(1 - e^{-0.319d}) \quad \left(\frac{\Delta P}{L}\right)_F = \phi_l^2\left(\frac{dP}{dz}\right)_l$	
	X should be calculated from Lockhart and Martinelli [3].	
9 Wang et al. [39]	$G > 200\ \text{kg m}^{-2}\text{s}^{-1} C = 4.56610^{-6}X^{0.128}\text{Re}_{lo}^{0.938}\left(\frac{\rho_l}{\rho_g}\right)^{-2.15}\left(\frac{\mu_l}{\mu_g}\right)^{5.1} \quad \text{Re}_{lo} = \frac{Gd}{\mu_l}\left(\frac{\Delta P}{L}\right)_F = \phi_l^2\left(\frac{dP}{dz}\right)_l$	
	$G < 200\ \text{kg m}^{-2}\text{s}^{-1}\phi_g^2 = 1 + 9.4X^{0.62} + 0.564X^{2.45} \left(\frac{\Delta P}{L}\right)_F = \phi_g^2\left(\frac{dP}{dz}\right)_g \phi_l^2 = 1 + \frac{C}{X} + \frac{1}{X^2}$	
	$(dP/dz)_l$ and $(dP/dz)_g$ should be calculated from Lockhart and Martinelli [3].	
10 Wilson et al. [40]	$\phi_{lo}^2 = 12.82Xtt^{-1.47}(1-x)^{1.8} \quad X_{tt} = \left(\frac{(1-x)}{x}\right)^{0.9}\left(\frac{\rho_g}{\rho_l}\right)^{0.5}\left(\frac{\mu_l}{\mu_g}\right)^{0.1} \quad \left(\frac{\Delta P}{L}\right)_F = \phi_{lo}^2\left(\frac{dP}{dz}\right)_{lo}$	
11 Souza et al. [41]	$\phi_l^2 = 1.376 + C_1 X_{tt}^{-C_2} \ Fr_l < 0.7 \begin{cases} C_1 = 4.172 + 5.48\ Fr_l \\ C_2 = 1.773 - 0.169Fr_l \end{cases} Fr_l \ge 0.7\ C_1 = 7.242$	
	$C_2 = 1.655\ Fr_l = \frac{G}{\rho_l\sqrt{gd}}\left(\frac{dP}{dz}\right)_l = \frac{f_l G^2(1-x)^2}{2d\rho_l}\frac{1}{\sqrt{f_l}} = -2\log\left(\frac{(\varepsilon/d)}{3.7} + \frac{2.51}{\text{Re}_l\sqrt{f_l}}\right)$	
	$\text{Re}_l = \frac{Gd(1-x)}{\mu_l}\left(\frac{\Delta P}{L}\right)_F = \phi_l^2\left(\frac{dP}{dz}\right)_l$	
12 Tran et al. [42]	$\phi_l^2 = 1 + (4.3Y^2 - 1)\ N_{conf}x^{0.875} + x^{1.75} N_{conf} = \frac{\left[\frac{\sigma}{g(\rho_l - \rho_g)}\right]^{1/2}}{d} \left(\frac{\Delta P}{L}\right)_F = \phi_{lo}^2\left(\frac{dP}{dz}\right)_{lo}$	
	$(dP/dz)_{lo}$ should be calculated from Chisholm [4].	
13 Lee and Lee [43]	$\phi_l^2 = 1 + \frac{C}{X} + \frac{1}{X^2} \ C = A\lambda^q\psi^r\text{Re}_{lo}^s \ \lambda = \frac{\mu_l^2}{\rho_l\sigma d} \ \psi = \frac{\mu_l j}{\sigma} \ \left(\frac{\Delta P}{L}\right)_F = \phi_l^2\ \left(\frac{dP}{dz}\right)_l$	

Liquid	Vapor	A	q	R	s	X Range	Re_{lo} range
Laminar	Laminar	6.833×10^{-8}	−1.317	0.719	0.557	0.776–14.176	175–1480
Laminar	Turbulent	6.185×10^{-2}	0	0	0.726	0.303–1.426	293–1506
Turbulent	Laminar	3.627	0	0	0.174	3.276–79.415	2606–17642
Turbulent	Turbulent	0.408	0	0	0.451	1.309—14.781	2675–17757

range of 0–10 bars and precision of ±0.2%. Temperatures were measured by means of RTDs.

2.2. Experimental apparatus for the condensation of R134a inside a vertical tube

Detailed descriptions of the experimental apparatus for studying condensation of R134a inside a vertical tube can be found in the authors' previous publications.

3. Data reduction

The data reduction of the measured results can be analysed as follows:

3.1. The inlet vapor quality of the test section ($x_{TS,i}$)

$$x_{TS,i} = \frac{i_{TS,i} - i_{l@T_{TS,i}}}{i_{fg@T_{TS,i}}} \quad (1)$$

Table 4
Main parameters of models and correlations.

Model number	Main parameters of equations																						
	μ_l	μ_g	ρ_l	ρ_g	ρ_{TP}	σ	x	d	G	α	S	j	ψ	f_l	f_g	f	Re	Re_l	Re_g	Re_{lo}	Re_{go}	Bo	X	We	Fr
1			x	x			x		x	x	x														
2			x	x				x	x					x	x			x	x				x		
3			x	x			x	x	x							x				x	x				
4	x	x	x	x	x	x		x																x	x
5			x	x	x	x		x	x								x					x		x	
6	x	x	x	x	x	x	x	x	x															x	
7	x	x	x	x		x	x	x	x			x				x		x	x				x		
8	x	x	x	x			x																x		
9	x	x	x	x			x		x											x			x		
10	x	x	x	x			x																x		
11	x		x				x	x	x					x				x							x
12			x	x		x	x	x								x									
13	x	x	x	x		x	x	x				x	x							x			x		

Table 5
Deviations of models according to the operating conditions during condensation tests of R134a.

R134a	Model/Correlation number and deviation (%)														
T_{sat}(°C)	P_{sat} (bar)	G (kg m^{-2} s^{-1})	x_{avg}	2	3	4	5	6	7	8	9	10	11	12	13
40	10	300	0.9	39.16	44.22	20.66	8.01	−12.59	33.41	−92.18	39.14	29.52	44.84	91.58	–
40	10	300	0.8	41.77	43.48	24.38	13.29	0.53	34.65	−64.62	40.75	9.75	−21.21	91.24	–
40	10	300	0.75	15.51	37.74	26.66	17.45	10.32	35.24	−48.64	30.40	−11.27	−48.65	90.00	–
40	10	300	0.7	3.82	33.54	26.01	17.88	12.14	34.26	−28.64	21.32	−20.31	−50.08	89.08	–
50	12	300	0.9	33.61	39.92	13.71	6.05	−12.86	25.56	−102.40	35.61	15.08	19.48	88.87	–
50	12	300	0.8	24.75	28.72	3.00	−4.64	−18.96	14.04	−107.55	26.72	−21.16	−78.16	86.88	–
50	12	300	0.75	−26.26	18.14	4.14	−0.79	−6.93	12.13	−68.99	5.31	−56.91	−97.61	84.83	–
50	12	300	0.7	−44.75	8.44	−2.79	−7.23	−12.36	−57.79	−74.63	−8.00	−75.99	−124.35	82.97	–
40	10	400	0.95	42.67	53.27	33.92	14.28	9.40	45.51	−28.29	46.42	39.99	37.71	92.91	–
40	10	400	0.9	39.16	50.06	33.05	14.09	14.77	42.91	−112.63	43.42	17.78	−47.16	92.07	–
40	10	400	0.85	25.02	46.64	32.84	14.86	18.25	41.71	−38.37	29.63	3.59	−31.55	91.20	–
40	10	400	0.8	15.81	43.36	32.58	15.58	20.48	6.11	−27.31	20.01	−6.24	−43.74	90.37	–
50	12	400	0.95	34.51	40.48	14.77	−4.49	−8.47	27.94	−105.63	32.60	15.97	−2.73	88.89	–
50	12	400	0.9	28.64	43.45	22.27	5.55	7.24	32.23	−159.57	36.79	2.19	−85.81	89.30	–
50	12	400	0.85	8.74	40.20	23.08	7.67	13.01	31.28	−51.55	20.12	−15.32	−56.16	88.50	–
50	12	400	0.8	−3.07	36.42	23.12	8.85	16.28	−29.97	−43.25	9.22	−27.70	−77.67	87.58	–

Table 6
Deviations of models according to the operating conditions during condensation tests of R600a.

R600a	Model/correlation number and deviation (%)														
T_{sat} (°C)	P_{sat} (bar)	G (kg m^{-2}s^{-1})	x_{avg}	2	3	4	5	6	7	8	9	10	11	12	13
30	4	85	0.9	−13.15	16.18	−63.44	33.68	–	−78.45	22.26	−61.24	–	–	77.73	–
30	4	85	0.8	−24.72	5.04	−75.91	28.60	–	−86.69	16.88	−71.78	–	–	73.58	–
30	4	85	0.75	−30.96	−4.61	−78.68	27.19	–	−80.64	16.34	−70.82	–	–	69.03	–
30	4	85	0.7	−39	−15.11	−84.47	23.91	–	−83.02	13.17	−75.06	–	–	64.94	–
30	4	75	0.9	−2.21	27.48	−57.20	38.78	–	30.27	29.32	−25.63	–	–	80.27	–
30	4	75	0.8	−13.10	16.45	−64.77	35.12	–	29.58	25.64	−30.63	–	–	75.71	–
30	4	75	0.75	−22.36	5.28	−71.92	31.78	–	30.01	22.70	−32.73	–	–	70.99	–
30	4	75	0.6	−27.21	−6.80	−71.65	30.70	–	36.47	23.79	−23.39	–	–	65.04	–
43	5.73	115	0.85	−32.15	1.33	−49.56	26.94	–	8.98	10.19	−59.07	–	–	73.99	–
43	5.73	115	0.7	−76.56	−44.79	−81.53	9.71	–	−5.98	−11.27	−90.22	–	–	57.77	–
43	5.73	115	0.65	−112.89	−87.01	−109.83	−5.89	–	−17.80	−29.28	−112.70	–	–	42.95	–
43	5.73	115	0.55	−147.17	−129.39	−138.16	−21.67	–	−27.32	−45.93	−129.53	–	–	27.48	–
43	5.73	95	0.85	−9.49	22.09	−34.80	39.13	–	27.19	26.80	−29.22	–	–	77.94	–
43	5.73	95	0.7	−33.86	−5.39	−49.68	31.27	–	25.55	17.96	−36.66	–	–	66.93	–
43	5.73	95	0.6	−49.13	−26.20	−60.73	24.89	–	25.51	12.26	−37.26	–	–	58.50	–
43	5.73	95	0.45	−69.40	−54.37	−80.71	13.74	–	24.80	3.72	−36.88	–	–	46.82	–

where $i_{l@T_{TS,i}}$ is the enthalpy of the saturated liquid based on the temperature of the test section inlet, $i_{fg@T_{TS,i}}$ is the enthalpy of vaporization based on the temperature of the test section inlet, and $i_{TS,i}$ is the refrigerant enthalpy at the test section inlet, given by:

$$i_{TS,i} = i_{ph,i} + \frac{Q_{ph}}{m_{ref}} \tag{2}$$

where $i_{ph,i}$ is the inlet enthalpy of the liquid refrigerant before entering the pre-heater, m_{ref} is the mass flow rate of the refrigerant, and Q_{ph} is the heat transfer rate in the pre-heater:

$$Q_{ph} = m_{w,ph} c_{p,w} (T_{w,i} - T_{w,o})_{ph} \tag{3}$$

where $m_{w,ph}$ is the mass flow rate of the water entering the preheater, $c_{p,w}$ is the specific heat of water, and $(T_{w,i} - T_{w,o})_{ph}$ is the temperature difference between inlet and outlet positions of the preheater.

3.2. The outlet vapor quality of the test section ($x_{TS,o}$)

$$x_{TS,o} = \frac{i_{TS,o} - i_{l@T_{TS,o}}}{i_{fg@T_{TS,o}}} \tag{4}$$

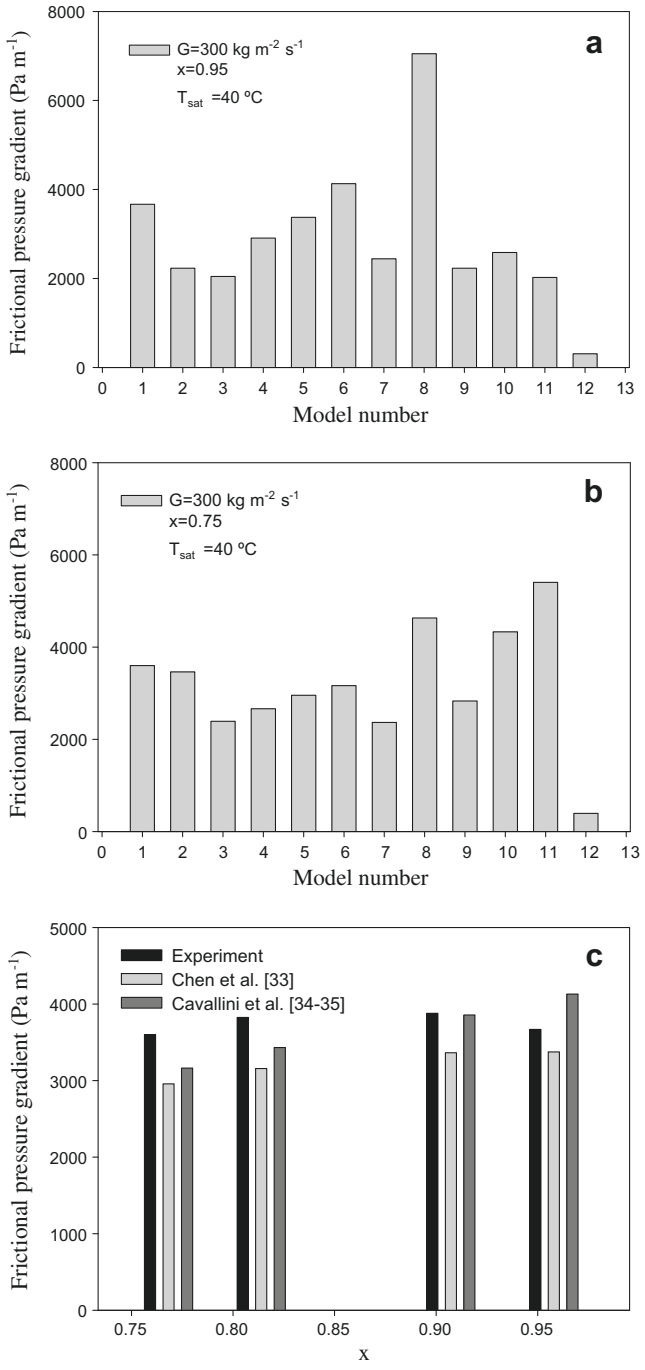

Fig. 3. Comparison of frictional pressure drop correlations at different vapour qualities of R134a for the mass flux of 300 kg m^{-2} s^{-1} and condensation temperature of 40 °C inside vertical tube.

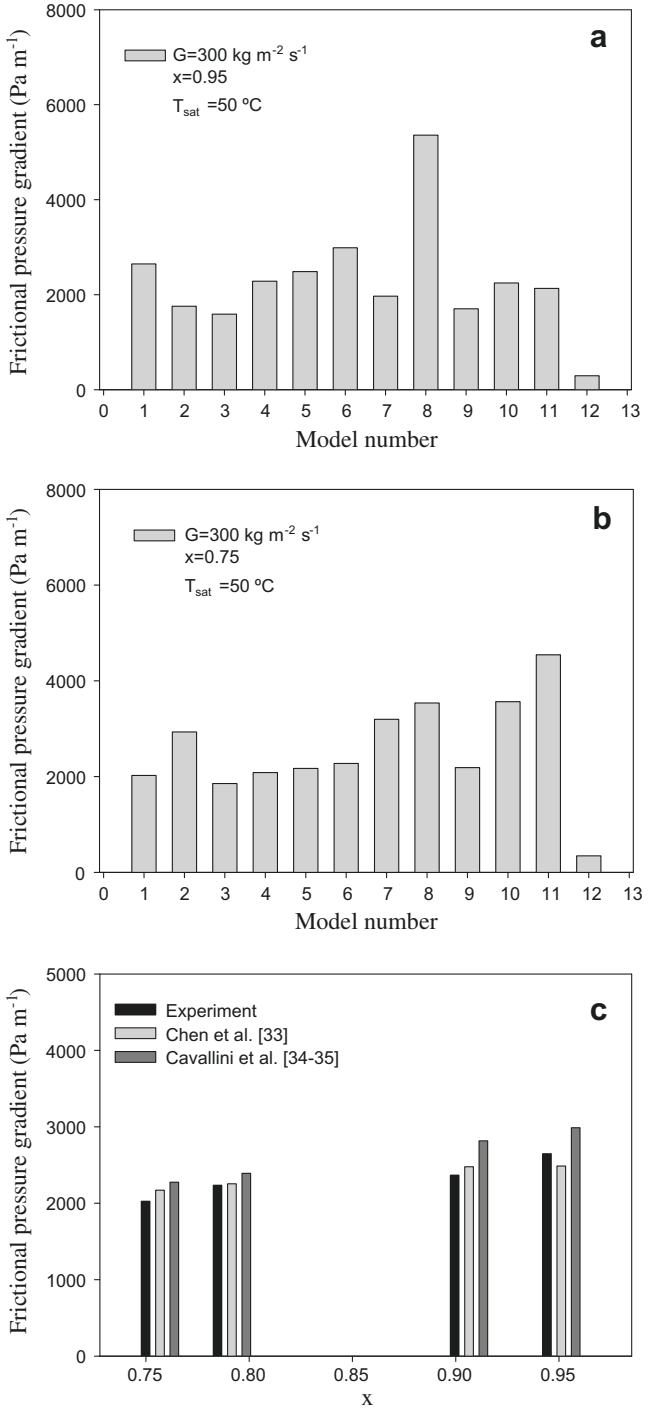

Fig. 4. Comparison of frictional pressure drop correlations at different vapour qualities of R134a for the mass flux of 300 kg m^{-2} s^{-1} and condensation temperature of 50 °C inside vertical tube.

where $i_{TS,o}$ is the refrigerant enthalpy at the test section outlet, $i_{l@T_{TS,o}}$ is the enthalpy of the saturated liquid based on the temperature of the test section outlet, and $i_{fg@T_{TS,o}}$ is the enthalpy of vaporization. The outlet enthalpy of the refrigerant flow is calculated from

$$i_{TS,o} = i_{TS,i} - \frac{Q_{TS}}{m_{ref}} \tag{5}$$

where the heat transfer rate, Q_{TS}, in the test section is obtained from:

$$Q_{TS} = m_{w,TS} c_{p,w} (T_{w,o} - T_{w,i})_{TS} \tag{6}$$

where $m_{w,TS}$ is the mass flow rate of the water entering the test section, and $(T_{w,o} - T_{w,i})_{TS}$ is the temperature difference between water at the outlet and inlet positions.

3.3. Uncertainties

The maximum uncertainties are shown in Table 1. The largest uncertainties occurred in the low mass flux region. The uncertainties of the experimental frictional pressure drop were around ±0.123 in the horizontal tube for R600a, ±0.13 in the vertical tube for R134a. The procedures of Kline & McClintock [29] were used for the calculation of all uncertainties. Operating conditions of the study are given in Table 2.

4. Results and discussion

The following paragraphs present a summary of the operating conditions of the models and correlations, and these are presented in Table 3. The main variables of them are shown in Table 4 and deviations of them according to the experimental frictional pressure drop are shown in Tables 5 and 6. A comparison of experimental frictional condensation pressure drop against predicting models using relevant annular flow of measured data during downward condensation of R134a at high mass flux in a vertical smooth tube, and condensation of R600a at low mass flux in a horizontal smooth tube over a range of experimental conditions is shown in Figs. 3–10.

Based on Hewitt and Robertson's [30] flow pattern map for the vertical tube and Tandon et al.'s [31] flow pattern map for the horizontal tube, the data shown in all figures was collected in an annular flow regime and also checked by sight glass at the inlet and outlet of the test section. In order to obtain annular flow conditions at various high and low mass fluxes, a specific vapour quality range is kept at approximately between 0.7–0.95 in the 0.5 m long test tube for R134a, and at between 0.45–0.9 in the 1 m long test tube for R600a. In the present study various pressure drop models and correlations are used to show the similarity of annular flow correlations which are independent of tube orientation (horizontal or vertical). Chen et al. [32] also mentioned this similarity in their article.

Frictional pressure drop can be determined using the Lockhart and Martinelli method [3] which expresses the division of viscous drag to vapour kinetic energy in horizontal and vertical tubes. This method was developed for adiabatic flow of air-benzene, kerosene and for water inside 1.5–26 mm tubes. Chisholm [4] developed a two-phase multiplier based on Lockhart and Martinelli parameters [3] using steam in a tube. It is used for vertical and horizontal tubes in the literature. Friedel [5,6] proposed a two-phase multiplier considering surface tension effects with 25000 data points during adiabatic flow through the vertical and horizontal channels with hydraulic diameters of more than 1 mm. Moreover, the proportion of vapour dynamic viscosity to liquid dynamic viscosity was below 1000 in his study. Chen et al. [33] accounted for the effects of surface tension and mass flux including Bond and Weber numbers in their model. They condensed R410A at 5–15 °C in several horizontal tubes ranging from 3.17 to 9 mm in diameter for the mass fluxes of 50–600 kg m^{-2} s^{-1}. They also coupled air–water at room temperature in several horizontal tubes ranging from between 1.02 and 7.02 mm in diameter for the mass fluxes of 50–3000 kg m^{-2} s^{-1}. Cavallini et al. [34,35] modified Friedel's [5,6] correlation to develop an annular flow model during the condensation of R22, R134a, R125, R32, R236ea, R407C, R410A in a 8 mm i.d. horizontal tube for the mass fluxes of 100–750 kg m^{-2} s^{-1} at saturation tempera-

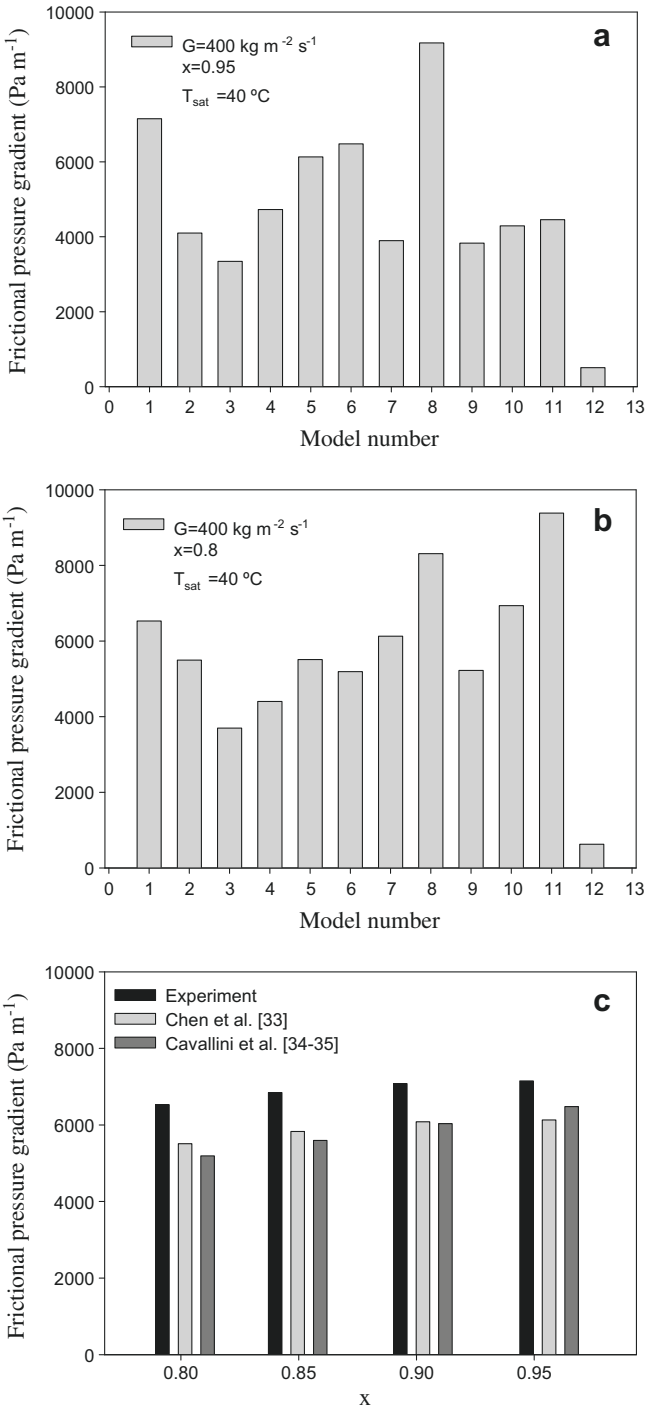

Fig. 5. Comparison of frictional pressure drop correlations at different vapour qualities of R134a for the mass flux of 400 kg m^{-2} s^{-1} and condensation temperature of 40 °C inside vertical tube.

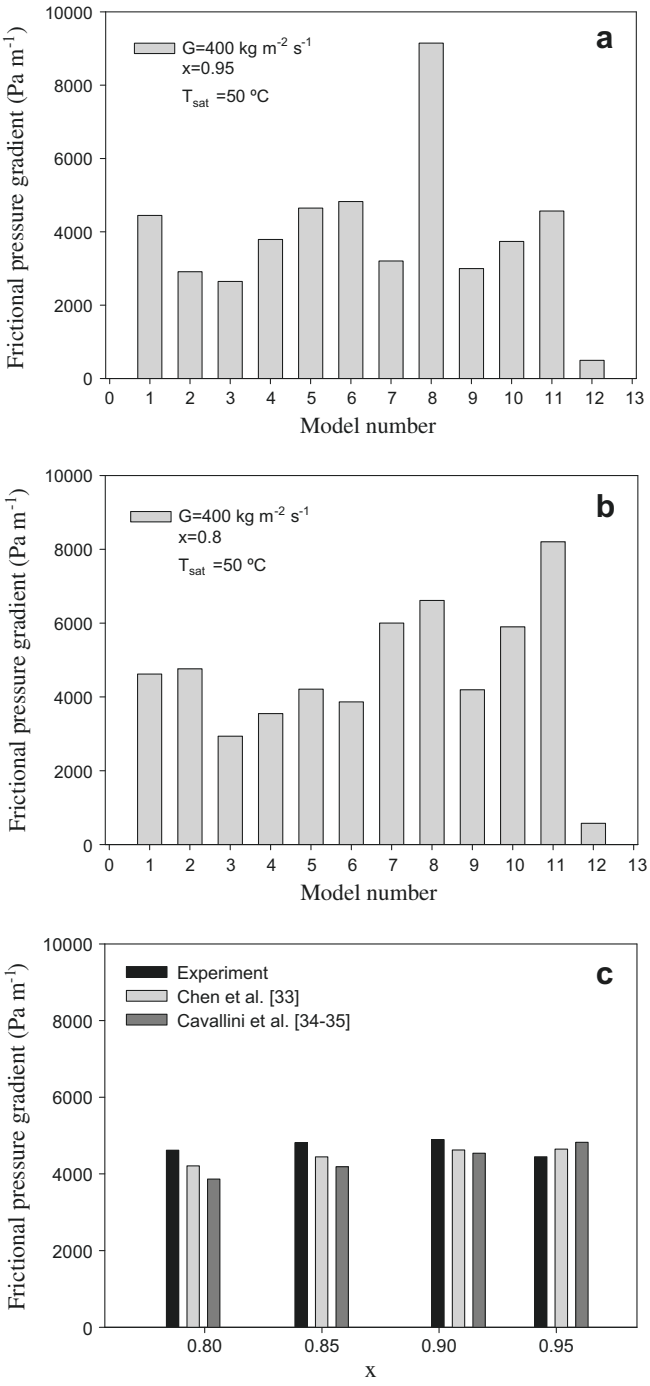

Fig. 6. Comparison of frictional pressure drop correlations at different vapour qualities of R134a for the mass flux of 400 kg m^{-2} s^{-1} and condensation temperature of 50 °C inside vertical tube.

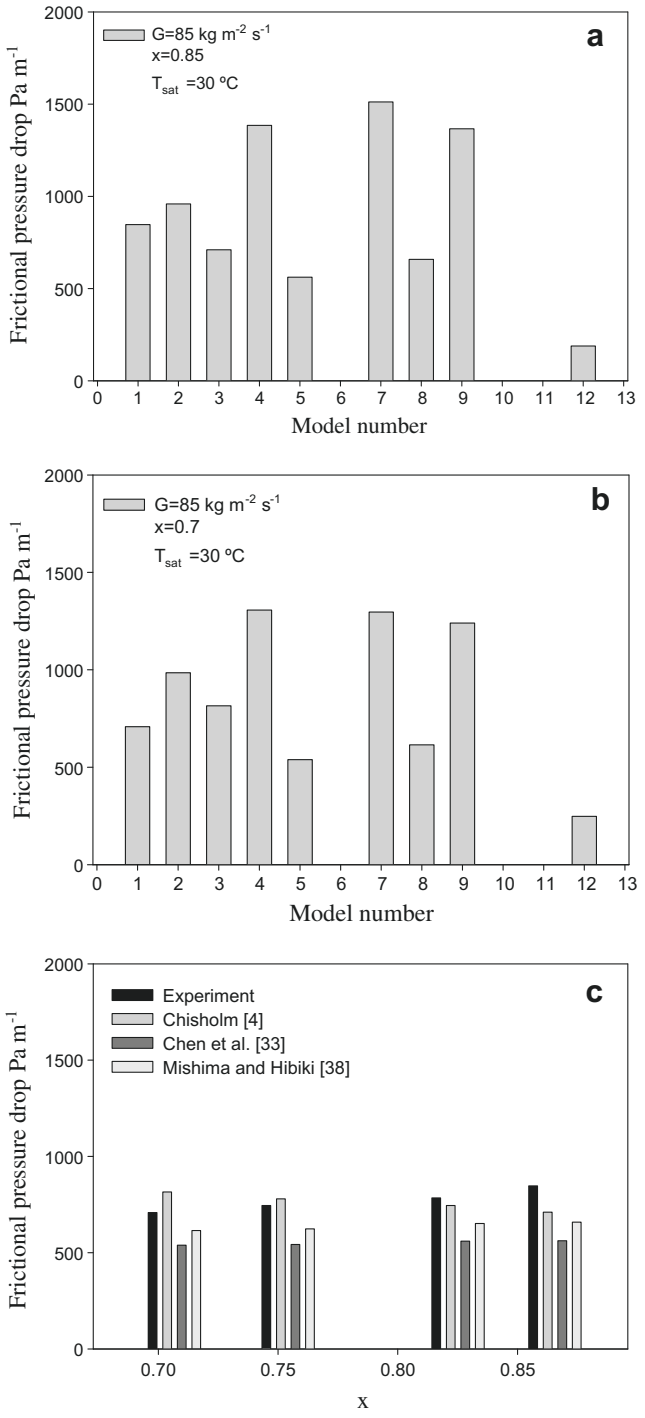

Fig. 7. Comparison of frictional pressure drop correlations at different vapour qualities of R600a for the mass flux of 85 kg m^{-2} s^{-1} and condensation temperature of 30 °C inside horizontal tube.

tures between 30–50 °C. As a result of the study, a model for predicting condensing heat transfer coefficient was developed by means of frictional pressure drop. Garimella et al. [36,37] developed a flow regime based model for intermittent and annular/mist/disperse flow regimes regarding the condensation of R134a in 0.5–4.91 mm i.d. horizontal tubes at the condensing temperature of 52 °C for mass fluxes of between 150–750 kg m^{-2} s^{-1}. Mishima et al. [38] investigated two-phase upward flow of air–water in 1–4 mm i.d. vertical tubes. Their model has limitations when it comes to accounting for the superficial velocities of vapour and liquid of phases. Wang et al. [39] studied the two-phase flow pattern of R22, R134a and R407C in a 6.5 mm i.d. horizontal tube for the mass fluxes of 50–700 kg m^{-2} s^{-1} at the condensing temperatures of 2.6–20 °C. Wilson et al. [40] condensed R134a and R410A in several 1.84–7.79 mm in diameter, horizontal, flattened, round, smooth, axial and helical micro-fin tubes for mass fluxes of between 75–400 kg m^{-2} s^{-1} at saturation temperatures of 35 °C. Souza et al. [41] showed the effect of oil in R12 and R134a on the pressure drop in a horizontal flattened tube with a hydraulic diameter of 10.9 mm for the mass fluxes of 200–600 kg m^{-2} s^{-1}. Tran et al. [42] boiled R134a, R12 and R113 in

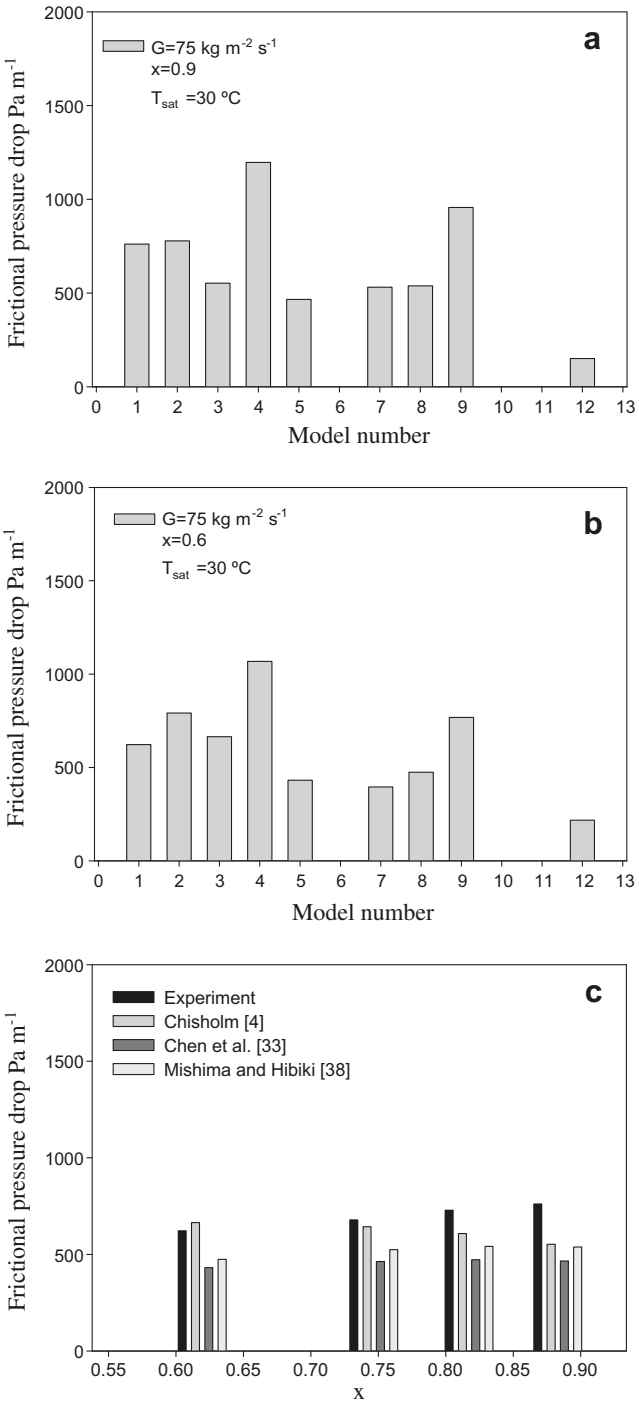

Fig. 8. Comparison of frictional pressure drop correlations at different vapour qualities of R600a for the mass flux of 75 kg m^{-2} s^{-1} and condensation temperature of 30 °C inside horizontal tube.

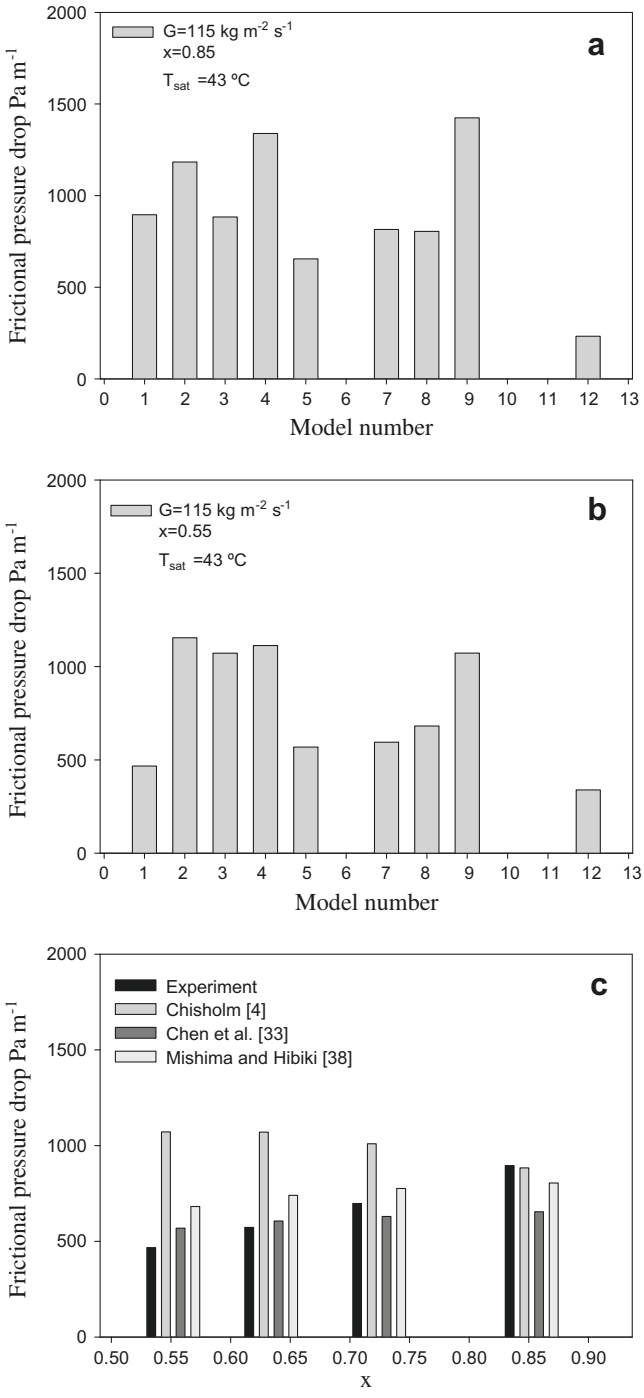

Fig. 9. Comparison of frictional pressure drop correlations at different vapour qualities of R600a for the mass flux of 115 kg m^{-2} s^{-1} and condensation temperature of 43 °C inside horizontal tube.

small diameter horizontal circular (2.4, 2.46, 2.92 mm) and rectangular tubes (4.06 × 1.7 mm) at boiling pressures between 138–836 kPa and for mass fluxes of between 33–832 kg m^{-2} s^{-1}. They proposed a pressure drop correlation modifying Chisholm [4]'s correlation to consider surface tension effects. Lee and Lee [43] studied the air–water couple to develop a two-phase multiplier for small hydraulic diameter (0.4 × 20 mm, 1.2 × 20 mm, 4 × 20 mm) rectangular horizontal channels. Their model has limitations with the Reynolds number and Lockhart and Martinelli [3] parameter.

The experimental frictional pressure drop shown in Table 3 and defined as model number 1 is calculated by means of the extraction of the gravitational component and of the component due to momentum change from the total measured pressure drop regarding condensing fluid of R134a in a vertical tube. It should be noted that the gravitational term of total measured pressure drop is neglected for the condensation of R600a in the horizontal tube. The experimental frictional pressure drop value is assumed to be the comparative value in all the figures and in Tables 5 and 6. The importance of void fraction models used for the determination of gravitational and momentum terms of pressure drop has been

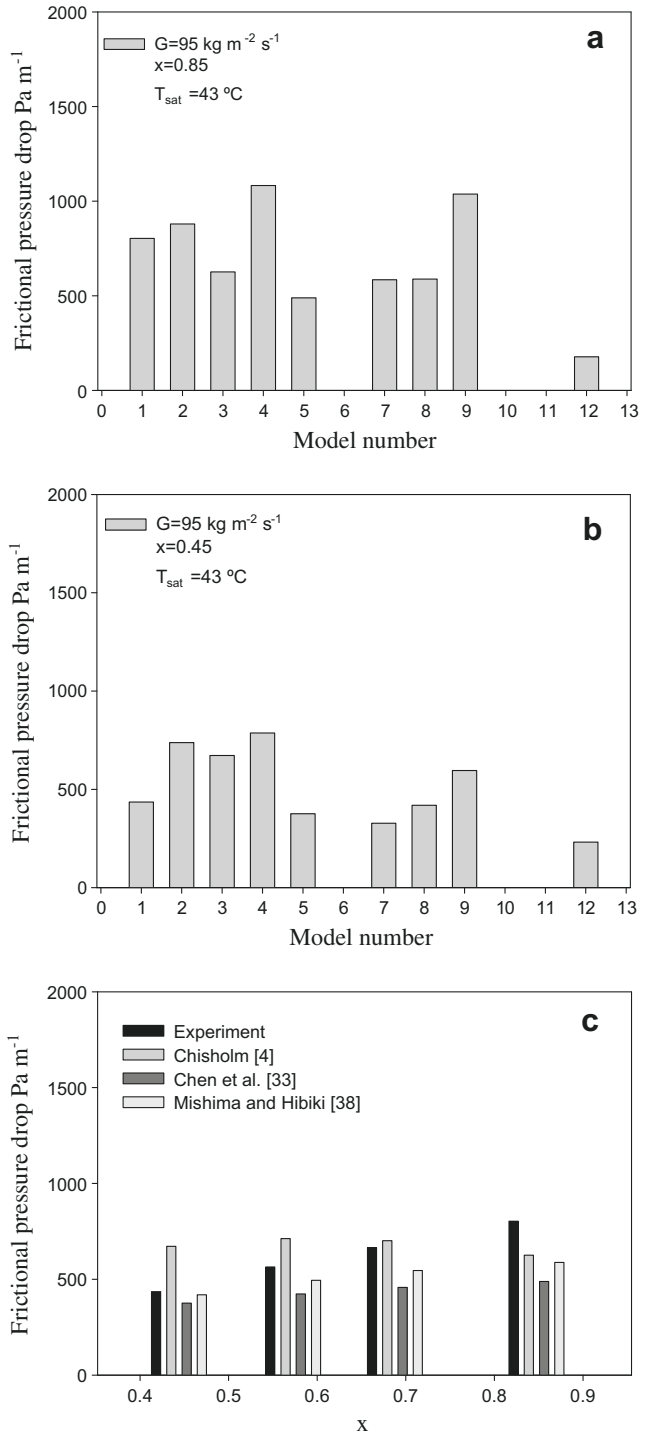

Fig. 10. Comparison of frictional pressure drop correlations at different vapour qualities of R600a for the mass flux of 95 kg m^{-2} s^{-1} and condensation temperature of 43 °C inside horizontal tube.

examined in great detail in the author's previous studies [13,16,17].

The main parameters of frictional pressure drop models and correlations mentioned in this study are shown in Table 4. They are necessary for the validation of experimental results characterising the flow and accurate predictions for untested conditions. Single phase–two phase pressure drop gradients (liquid only/vapour only), friction factors (liquid only/vapour only), Reynolds numbers, Bond numbers, Weber numbers, Froude numbers and Lockhart and Martinelli parameters were used as the main variables in the models and correlations given in Table 3. Reynolds number gives a measure of the ratio of inertial forces to viscous forces characterising different flow regimes such as laminar or turbulent flow. Bond number expresses the ratio of body forces to surface tension forces; low Bond numbers indicate surface tension domination of the system. Weber number is defined as a measure of the relative significance of the fluid's inertia compared to its surface tension. It is useful in analysing thin film flows where there is an interface between two different fluids, and the formation of droplets and bubbles. The Froude number is used to compare inertial and gravitational forces. The Lockhart and Martinelli parameter is used in internal two-phase flow calculations expressing the liquid fraction of a flowing fluid. Other important parameters belong to fluid and geometric parameters such as mass flux, vapour quality, surface tension, density, dynamic viscosity in the frictional models and correlations.

The data on the effects of heat flux, mass flux and condensation temperature on the pressure drop are discussed in the authors previous publications [13,15,18] in detail. As can be seen from the figures, pressure drop decreases with decreasing mass flux and increases with increasing vapour quality for the same condensing temperature as expected. In addition to this, calculating from the figures frictional pressure drop values at high condensing temperatures are lower than those at a low condensing temperature for the same mass flux. Therefore, the different pressure drop characteristics should be accounted for in the comparison of the heat transfer performance of fluids in spite of the same condensing temperature and mass velocity due to far different operating pressures.

In Figs. 3–6, experimental condensation frictional pressure drop data for R134a inside a vertical tube are plotted against the various models and correlations shown in Table 3 according to the condensation temperatures of 40 and 50 °C for the mass fluxes of 300 and 400 kg m^{-2} s^{-1}.

It is found that all data belong to the comparison of Cavallini et al.[34,35] and Chen et al.'s [33] correlations with the experimental frictional pressure drop fall within ±20% for all the mass fluxes and condensing temperatures of R134a. These correlations were the most predictive correlations according to the various experimental conditions in Table 5. The model of Cavallini et al. [34,35] and Chen et al.'s [33] operating conditions explained above seems similar to that of our study except for tube orientation. Moreover, Chen et al. [33] used the Bond number in their model and this is especially significant at high vapour qualities. In addition to this, the majority of the data calculated by the Lockhart and Martinelli [3], Friedel [5], Wang et al [39] and the Wilson et al. [40] correlations all fall within ±30%. On the other hand, the Lee and Lee [43] correlation is found to be incompatible with the experimental data due to the inappropriate operating conditions and lack of flow parameters in the equations. Nevertheless, the Garimella et al. [37], the Mishima et al. [38], the Souza et al. [41] and the Tran et al. [42] correlations also have poor agreement with the experimental data. Deviations of all models and correlations for the condensation of R134a inside vertical tube according to the different experimental conditions can be clearly seen in Table 5.

In Figs. 7–10 the experimental condensation frictional pressure drop data of R600a inside horizontal tube are plotted against the various models and correlations shown in Table 3 according to the condensation temperatures of 30 and 43 °C for the mass fluxes of 75, 85, 95 and 115 kg m^{-2} s^{-1}.

The majority of the data belonging to the comparison of frictional pressure drops for the Chisholm [4], Chen et al. [33] and Mishima and Hibiki [38]correlations fall within ±30% for the all mass fluxes and condensing temperatures of R600a. These correlations were the most predictive correlations according to the various experimental conditions in Table 6. Mishima and Hibiki [38]

developed Chisholm's [4] correlation for small diameter tubes and the Chen et al. [33] correlation emphasises the importance of surface tension force which should be taken into account as compared to gravitational force for two-phase flow in small diameter tubes in low mass flux regions due to low vapour shear forces. On the other hand, the Cavallini et al. [34,35], Lee and Lee [43], Wilson et al. [40] and Souza et al. [41] correlations are found to be incompatible with the experimental data due to their inappropriate operating conditions and the lack of flow parameters in the equations. Nevertheless, the Lockhart and Martinelli [3], Friedel et al. [5,6], Garimella et al. [37], Tran et al [42] and Wang et. al. [39] correlations have poor agreement with the experimental data. Deviations of all models and correlations for the condensation of R600a inside a horizontal tube according to the different experimental conditions can be clearly seen from Table 5.

In addition to these explanations, the pressure drop per length shown in Figs. 3–10 is obtained from dividing the measured pressure drop by the length between pressure taps. In our apparatus, the length between pressure taps is 0.7 m for the vertical tube, 1.5 m for the horizontal tube.

5. Conclusion

The aim of this investigation was to compare frictional pressure drop values obtained from various pressure drop models at high mass flux during downward annular flow condensation of R134a in a vertical, smooth, 8.1 mm i.d. copper tube, and at low mass flux during annular flow condensation of R600a in a horizontal, smooth, 4 mm i.d. copper tube.

In this study, accurate and repeatable condensation pressure drop data were taken and their applicability to the various pressure drop models under different operating conditions was examined. This study performed tests for the validation of models with different operating conditions. Moreover, there is little research on the parameters used in this study described in the current literature. The content of this study is expected to fill this gap in the literature.

Chisholm's void fraction correlation [4] is used to calculate the gravitational and momentum pressure drop. Frictional pressure drop is obtained from measured total pressure drop data. The model by Cavallini et al. [34,35] and Chen et al. [33] valid for the annular flow regime can determine condensation frictional pressure drop values fairly well for R134a. On the other hand, only Chen et al. [33]'s correlation from this couple can predict the data well for the new hydrocarbon R600a. It can be seen that, due to its incompatible operating conditions as explained above, Lee and Lee's model [41] disappears in Figs. 3–6 and Table 5 for the condensation of R134a inside vertical tube and Cavallini et al. [34,35], Lee and Lee [43], Wilson et al. [40] and Souza et al.'s [41] models disappear in Figs. 7–10 and Table 6 for the condensation of R600a inside a horizontal tube due to their values which are extremely higher than others.

According to the analysis in this paper, it is shown that annular flow models are independent of tube orientation provided that annular flow regime exists along the tube length and that they are capable of predicting condensation pressure drop inside the tested tubes.

Acknowledgements

The present study was financially supported by Yildiz Technical University (YTU) and King Mongkut's University of Technology Thonburi (KMUTT). The first author thank KMUTT for providing him with a Post-doctoral fellowship, while the fourth author acknowledge the financial support provided by the Thailand Research Fund.

References

[1] H. Kruse, The state of the art of the hydrocarbon technology in household refrigeration, in: Proceedings of the International Conference on Ozone Protection Technologies, Washington, DC, 1996, pp. 179–188.
[2] D. Jung, C. Kim, K. Song, B. Park, Testing of propane/isobutene mixture in domestic refrigerators, Int. J. Refrig. 23 (2000) 517–527.
[3] R.W. Lockhart, R.C. Martinelli, Proposed correlation of data for isothermal two-phase, two-component flow in pipes, Chem. Eng. Prog. 45 (1949) 39–48.
[4] D. Chisholm, Pressure gradients due to friction during the flow of evaporating two-phase mixtures in smooth tubes and channels, Int. J. Heat Mass Transfer 16 (1973) 347–358.
[5] L. Friedel, Improved friction pressure drop correlation for horizontal and vertical two-phase pipe flow, Eur. Two-phase Flow Group Meeting Pap. E2 18 (1979) 485–492.
[6] L. Friedel, Pressure drop during gas/vapor–liquid flow in pipes, Int. J. Chem. Eng. 20 (1980) 352–367.
[7] Ho-Saeng Lee, Jung-In Yoon, Jae-Dol Kim, P.K. Bansal, Condensing heat transfer and pressure drop characteristics of hydrocarbon refrigerants, Int. J. Heat Mass Transfer 46 (2006) 1922–1927.
[8] Ho-Saeng Lee, Jung-In Yoon, Jae-Dol Kim, P.K. Bansal, Characteristics of condensing and evaporating heat transfer using hydrocarbon refrigerants, Appl. Therm. Eng. 26 (2006) 1054–1062.
[9] Mao-Yu Wen, Ching-Yen Ho, Jome-Ming Hsieh, Condensation heat transfer and pressure drop characteristics of R-290 (propane), R600(butane), and a mixture of R290/R600 in the serpentine small-tube bank, Appl. Therm. Eng. 26 (2006) 2045–2053.
[10] J.H. Goodykoontz, R.G. Dorsch, Local heat transfer and pressure distributions for Freon-113 condensing in downward flow in a vertical tube, NASA TN D-3952, 1967.
[11] S.J. Kim, H.C. No, Turbulent film condensation of high pressure steam in a vertical tube, Int. J. Heat Mass Transfer 43 (2000) 4031–4042.
[12] X. Ma, A. Briggs, J.W. Rose, Heat transfer and pressure drop characteristics for condensation of R113 in a vertical micro-finned tube with wire insert, Int. Commun. Heat Mass Transfer 31 (2004) 619–627.
[13] A.S. Dalkilic, S. Laohalertdecha, S. Wongwises, Effect of void fraction models on the two-phase friction factor of R134a during condensation in vertical downward flow in a smooth tube, Int. Commun. Heat Mass Transfer 35 (2008) 921–927.
[14] A.S. Dalkilic, S. Yildiz, S. Wongwises, Experimental investigation of convective heat transfer coefficient during downward laminar flow condensation of R134a in a vertical smooth tube, Int. J. Heat Mass Transfer 52 (2009) 142–150.
[15] A.S. Dalkilic, S. Laohalertdecha, S. Wongwises, Two-phase friction factor in vertical downward flow in high mass flux region of refrigerant HFC-134a during condensation, Int. Commun. Heat Mass Transfer 35 (2008) 1147–1152.
[16] A.S. Dalkilic, S. Laohalertdecha, S. Wongwises, Effect of void fraction models on the film thickness of R134a during downward condensation in a vertical smooth tube, Int. Commun. Heat Mass Transfer 36 (2009) 172–179.
[17] A.S. Dalkilic, S. Laohalertdecha, S. Wongwises, A comparison of the void fraction correlations of R134a during condensation in vertical downward laminar flow in a smooth and microfin tube, in: Proceedings of the First International Conference on Micro/Nanoscale Heat Transfer, ASME, January 06–09, Taiwan, 2008.
[18] A.S. Dalkilic, S. Laohalertdecha, S. Wongwises, Two-phase friction factor obtained from various void fraction models of R-134a during condensation in vertical downward flow at high mass flux, in: Proceedings of the first International Conference on Heat Transfer, ASME, August 10–14, USA, 2008.
[19] A.S. Dalkilic, S. Wongwises, Intensive literature review of condensation inside smooth and enhanced tubes, Int. J. Heat Mass Transfer 52 (2009) 3409–3426.
[20] A.S. Dalkilic, Investigation of the Convective Heat Transfer Coefficient During Condensation in Vertical Tubes, Ph.D. Thesis, Yildiz Technical University, İstanbul, Turkey, 2007.
[21] O. Agra, I. Teke, Experimental investigation of condensation of hydrocarbon refrigerants (R600a) in a horizontal smooth tube, Int. Commun. Heat Mass Transfer 35 (2008) 1165–1171.
[22] O. Agra, Condensation of Refrigerants in a Horizontal Tube in Annular Flow Regime, Ph.D. Thesis, Yildiz Technical University, Istanbul, Turkey, 2007.
[23] A.S. Dalkilic, S. Laohalertdecha, S. Wongwises, Experimental investigation on heat transfer coefficient of R134a during condensation in vertical downward flow at high mass flux in a smooth tube, Int. Commun. Heat Mass Transfer 36 (2009) 1036–1043.
[24] A.S. Dalkilic, S. Laohalertdecha, S. Wongwises, Experimental investigation on the condensation heat transfer and pressure drop characteristics of R134a at high mass flux conditions during annular flow regime inside a vertical smooth tube, Summer Heat Transfer Conference, ASME, July 19–23, USA, 2009.
[25] A.S. Dalkilic, O. Agra, Experimental apparatus for the determination of condensation heat transfer coefficient for R134a and R600a flowing inside vertical and horizontal tubes, Summer Heat Transfer Conference, ASME, July 19–23, USA, 2009.
[26] A.S. Dalkilic, S. Laohalertdecha, S. Wongwises, Experimental research on the similarity of annular flow models and correlations for the condensation of R134a at high mass flux inside vertical and horizontal tubes, International

Mechanical Engineering Congress and Exposition, ASME, November 13–19, USA, 2009.
[27] A.S. Dalkilic, S. Wongwises, A heat transfer model for co-current downward laminar film condensation of R134a in a vertical micro-fin tube during annular flow regime, Eleventh UK National Heat Transfer Conference, September 6–8, Queen Mary University of London, UK, 2009.
[28] H. Demir, O. Agra, S.O. Atayilmaz, Generalized neural network model of alternative refrigerant (R600a) inside a smooth tube, Int. Commun. Heat Mass Transfer 36 (2009) 744–749.
[29] S.J. Kline, F.A. McClintock, Describing uncertainties in single sample experiments, Mech. Eng. (1953).
[30] G.F. Hewitt, D.N. Robertson, Studies of two-phase flow patterns by simultaneous x-ray and flash photography, Rept AERE-M2159, UKAEA, Harwell, 1969.
[31] T.N. Tandon, H.K. Varma, C.P. Gupta, Heat transfer during forced convection condensation inside horizontal tube, Int. J. Refrig. 18 (1995) 210–214.
[32] S.L. Chen, F.M. Gerner, C.L. Tien, General film condensation correlations, Exp. Heat Transfer 1 (1987) 93–107.
[33] I.Y. Chen, K.S. Yang, Y.J. Chang, C.C. Wang, Two-phase pressure drop of air–water and R-410a in small horizontal tubes, Int. J. Multiph. Flow 27 (2001) 1293–1299.
[34] A. Cavallini, G. Censi, D. Del Col, L. Doretti, G.A. Longo, L. Rossetto, Experimental investigation on condensation heat transfer and pressure drop of new HFC refrigerants (R134a, R125, R32, R410A, R236ea) in a horizontal smooth tube, Int. J. Refrig. 24 (2007) 73–87.
[35] A. Cavallini, G. Censi, D. Del Col, L. Doretti, G.A. Longo, L. Rossetto, Condensation of halogenated refrigerants inside smooth tubes, HVAC R. Res. 8 (2002) 429–451.
[36] S. Garimella, Condensation flow mechanisms, pressure drop and heat transfer in microchannels, in: S. Kakac, L.L. Vasiliev, Y. Bayazitoglu, Y. Yener (Eds.), Microscale Heat Transfer-Fundamental and Applications, Kluwer Academic Publishers, The Netherlands, 2005.
[37] S. Garimella, A. Agarwal, J.D. Killion, Condensation pressure drop in circular microchannels, Heat Transfer Eng. 26 (2005) 1–8.
[38] K. Mishima, T. Hibiki, Some characteristics of air–water two-phase flow in small diameter vertical tubes, Int. J. Multiph. Flow 22 (1996) 703–712.
[39] C.C. Wang, C.S. Chiang, D.C. Lu, Visual observation of two-phase flow pattern of R-22, R-134a, and R-407C in a 6.5-mm smooth tube, Exp. Ther. Fluid Sci. 15 (1997) 395–405.
[40] M.J. Wilson, T.A. Newell, J.C. Chato, C.A. Infante Ferreira, Refrigerant charge, pressure drop, and condensation heat transfer in flattened tubes, Int. J. Refrig. 26 (2003) 442–451.
[41] D.A.L. Souza, M.D.M. Pimenta, Prediction of pressure drop during horizontal two-phase flow of pure and mixed refrigerants, in: Proceedings of the 1995 ASME/JSME Fluids Engineering and Laser Anemometry Conference and Exhibition, August 13–18, Hilton Head, SC, ASME, NewYork, NY, 1995, pp. 161–171.
[42] T.N. Tran, M.C. Chyu, M.W. Wambsganss, D.M. France, Two-phase pressure drop of refrigerants during flow boiling in small channels: an experimental investigation and correlation development, Int. J. Multiph. Flow 26 (2000) 1739–1754.
[43] H.J. Lee, S.Y. Lee, Pressure drop correlations for two-phase flow within horizontal rectangular channels with small heights, Int. J. Multiph. Flow 27 (2001) 783–796.

Experimental Thermal and Fluid Science 34 (2010) 454–462

Contents lists available at ScienceDirect

Experimental Thermal and Fluid Science

journal homepage: www.elsevier.com/locate/etfs

The effects of channel diameter on flow pattern, void fraction and pressure drop of two-phase air–water flow in circular micro-channels

Sira Saisorn [a], Somchai Wongwises [b,*]

[a] Energy Division, The Joint Graduate School of Energy and Environment (JGSEE), King Mongkut's University of Technology Thonburi, Bangmod, Bangkok 10140, Thailand
[b] Fluid Mechanics, Thermal Engineering and Multiphase Flow Research Lab. (FUTURE), Department of Mechanical Engineering, King Mongkut's University of Technology Thonburi, Bangmod, Bangkok 10140, Thailand

ARTICLE INFO

Article history:
Received 17 November 2008
Received in revised form 17 February 2009
Accepted 17 February 2009

Keywords:
Two-phase flow
Micro-channel
Flow pattern
Void fraction
Pressure drop

ABSTRACT

Two-phase air–water flow characteristics are experimentally investigated in horizontal circular micro-channels. Test sections are made of fused silica. The experiments are conducted based on three different inner diameters of 0.53, 0.22 and 0.15 mm with the corresponding lengths of 320, 120 and 104 mm, respectively. The test runs are done at superficial velocities of gas and liquid ranging between 0.37–42.36 and 0.005–3.04 m/s, respectively. The flow visualisation is facilitated by systems mainly including stereozoom microscope and high-speed camera. The flow regime maps developed from the observed flow patterns are presented. The void fractions are determined based on image analysis. New correlation for two-phase frictional multiplier is also proposed for practical applications.

1. Introduction

Two-phase flow in micro-channel flow passages has been studied over the years. The clarifications of micro-scale effects on two-phase flow and heat transfer characteristics have become more necessary due to the rapid development of microstructure devices used for several engineering applications including medical devices, high heat-flux compact heat exchangers, and cooling systems of various types of equipment such as high performance micro-electronics, supercomputers, high-powered lasers.

In addition to the attractive phenomena caused by the significant role of surface effects, this emerging field enables us to develop powerful miniature devices for operation in a domain which seemed to be unfeasible in the past. However, it is obvious that a comprehensive understanding of the trends and parameters dominating flow behavior in mini- and micro-channels is still lacking. Thus, fundamental heat transfer and flow characteristics problems encountered in the development and processing of micro-electronic-mechanical-systems (MEMS) have become a significant challenge in the design and control of these micro-systems. Because of the requirement for new solutions to dissipate heat and maintain uniform temperature distributions in modern devices, a clear understanding of the major mechanisms affecting micro-scale heat transfer is essential for optimum design and process control of micro-systems.

Two-phase flow and heat transfer characteristics in small channels such as micro-channels and mini-channels are likely to be strongly dependent on surface tension effects in addition to viscosity and inertia forces, resulting in significant differences in two-phase flow phenomena between ordinarily sized channels and small channels. Several investigators have proposed criteria to address the definition of a micro-channel. The proposed channel classifications are often based on different parameters. For instance, arbitrary channel classifications based on the hydraulic diameter D_h have been proposed. Recently, Mehendale et al. [1] employed the hydraulic diameter as an important parameter for defining heat exchangers and Kandlikar [2] proposed criteria for small flow channels used in engineering applications.

In the past decade, there have been a relatively small amount of publications available for both mini-channels and micro-channels compared to those for ordinarily sized channels.

Triplett et al. [3,4] studied adiabatic two-phase air-deionized water (DI water) flow characteristics in micro-channels with hydraulic diameter ranging from 1.1 to 1.5 mm. The flow patterns observed were bubbly, slug, churn, slug–annular and annular. The measured void fraction and two-phase pressure drop in the relevant flow regimes were also investigated. The void fraction data were obtained, based on the image analysis.

Serizawa et al. [5] investigated the visualization of the two-phase flow pattern in circular micro-channels. The flowing mixture

* Corresponding author. Tel.: +66 2 470 9115; fax: +66 2 470 9111.
E-mail address: somchai.won@kmutt.ac.th (S. Wongwises).

0894-1777/$ - see front matter © 2009 Published by Elsevier Inc.
doi:10.1016/j.expthermflusci.2009.02.006

of air and water in channels of 20, 25 and 100 μm in diameter and that of steam and water in a channel of 50 μm in diameter were conducted experimentally. Two-phase flow patterns obtained from both air–water and steam-water flows were quite similar and their detailed structures were described. The study confirmed that the surface wettability had a significant effect on the two-phase flow patterns in very small channels.

Chung and Kawaji [6] performed an experiment in order to distinguish two-phase flow characteristics in micro-channels from those in mini-channels. Four different circular diameters ranging from 50 to 526 μm were employed to examine a scaling effect on nitrogen–DI water two-phase flow. The results including the flow patterns, void fraction and two-phase pressure drop were analyzed.

The applicability of several widely used viscosity models to the pressure drop prediction of air–water flow through a 0.53 mm diameter channel was examined by Saisorn and Wongwises [7]. The other relevant models for the two-phase flow pressure drop prediction in micro-channels were also examined by Kawahara et al. [8], Chung and Kawaji [6], Saisorn and Wongwises [9,10], and Triplett et al. [4].

Although some information is currently available on flow pattern, void fraction, and pressure drop in micro-channels, there still remains room for further research.

The aim of this paper is to compare the two-phase air–water flow characteristics in different size micro-channels. The results are compared based on flow pattern, void fraction and two-phase frictional pressure drop.

2. Experimental apparatus and procedure

The experiments were carried out using the apparatus along with the instruments as shown in Figs. 1 and 2. The corresponding details are described as follows. Fig. 1 illustrates a schematic diagram of the test facility. Air, nitrogen gas, water and de-ionized water are used as working fluids in the system. Instead of a conventional pump, which may contribute to pulsation and fluid contamination, either air or nitrogen gas and the liquid-filled tank are combined and operated as a pneumatic pump to supply a constant flow rate of liquid through test section. The mixing chambers as shown in Fig. 2 are designed to introduce the air–water mixture smoothly along the channel. The mixture flows freely from the channel outlet where atmospheric pressure is realized. The gas flow rates were able to be measured by four sets of rotameters within the range of 5–50 sccm, 0.05–0.5, 0.2–2.0, 1–10 SCFH, respectively. For liquid flow rate measurements, an electronic balance (320 ± 0.001 g) was used to measure the weight of the liquid flowing freely from the outlet over a time. The test sections used in this work are fused silica tubes with inner diameters of 0.53 mm (320 mm length), 0.22 mm (120 mm length) and 0.15 mm (104 mm length). The single-phase and two-phase pressure drops across the test section were determined by two pressure transduc-

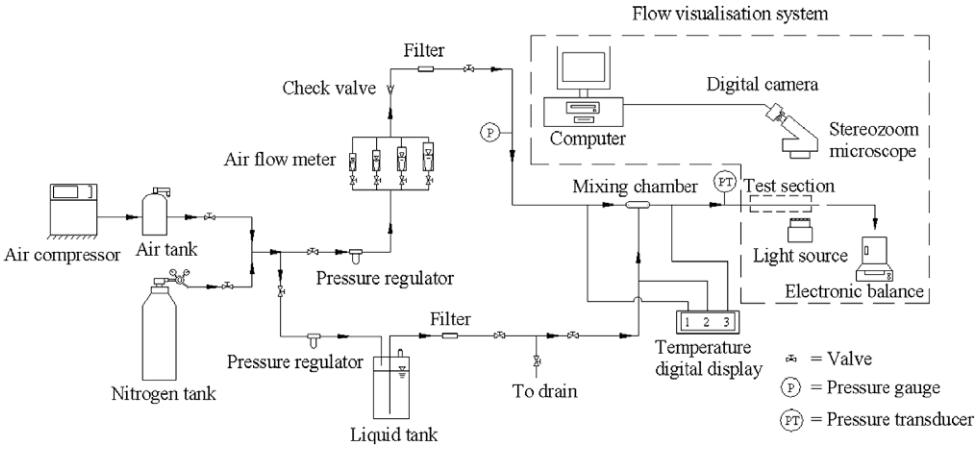

Fig. 1. Experimental apparatus.

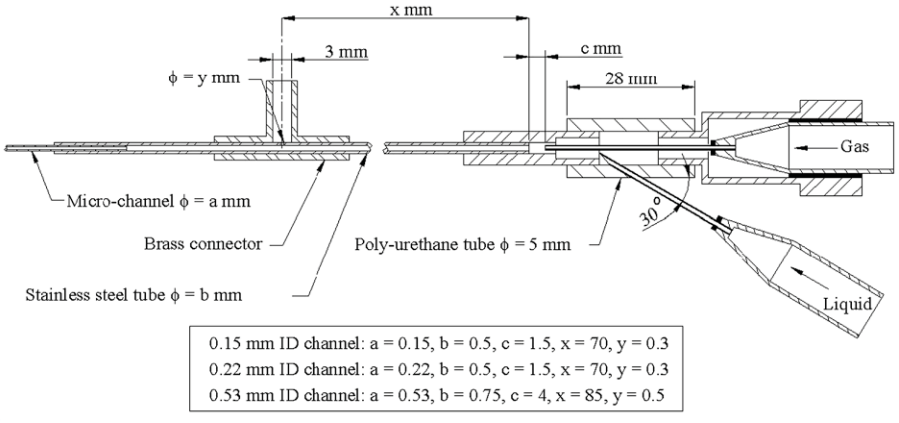

Fig. 2. Mixing chamber.

ers installed at the channel inlet. The low range pressure transducer was calibrated from 0 to 250 kPa with a ±0.5 kPa accuracy and the high range one was calibrated from 0 to 1000 kPa with a ±2 kPa accuracy. Type T thermocouples were used to measure fluid temperatures. The degree of uncertainty of the temperature measurements was ±0.1 °C.

The detailed formation of each flow pattern is registered by precise stereozoom microscope (Nikon SMZ-1) having a continuous zoom ranging between 0.7× and 3.0×, including 20× eyepieces mounted together with a camera system (Fujifilm FinePix S7000) having shutter speeds of 1/15 to 1/10,000 s and a frame rate of 30 frames per second. According to the above system, a magnified image of up to 60 times can be obtained. In this study, however, the magnification is adjusted so that the appropriate view field (L/D = 10) is obtained. The region near the channel outlet is always selected as the viewing window available for the captured image. An adjustable light source consisting of 150 watt halogen lamp and dimmer is placed under the test section to provide illumination for the flow visualization. The lighting condition can be refined by placing the frosted glass between the light source and the test section.

The single-phase flow experiments with different fluids were the first to be performed. Following this, the two-phase flow experiments were conducted at various gas and liquid flow rates. In this work, the gas flow rate was increased by small increments, while the liquid flow rate was kept constant at a pre-selected value. The system was allowed to approach steady conditions before the fluid flow rates, flow patterns and pressure drops were recorded. Visual observation shows that different flow patterns may occur with gas–liquid co-current flow in a horizontal microchannel. The main systems composing of stereozoom microscope and high-speed camera are located above the test section to facilitate the flow visualisation. The image analysis was carried out to estimate the void fraction based on the scale provided by micrometer.

3. Results and discussion

3.1. Flow pattern

A camera used in this work is Fujifilm FinePix S7000 by which the flow in the test section can be photographed with shutter speeds of 1/15–1/10,000 s. For video system, the recording speed or frame rate of the camera is 30 frames per second. In the present work, two groups of images, including a number of images extracted from the video files and a set of photographed images shot by the camera, are analysed for flow regime identification.

For a given experimental condition, the first step for the analysis is to open a video file to see the fluids flowing through the test section. With the image processing software, around 300 images are extracted from the video file to conduct the flow regime identification. The identification process for the channels with diameters of 0.53 and 0.22 mm is done based on the flow pattern which is mostly observed under a given flow condition. In the case of a 0.15 mm diameter channel, the process is done according to grouping method associated with the appearance of flow patterns.

The image analysis is used for void fraction estimation and thus, high quality of images is needed for the process. As a consequence of this requirement, the other group of the photographs (around 50–70 images for each flow condition) shot by the camera are analysed for void fraction and are selected to illustrate the flow structure as presented in Fig. 3.

Fig. 3 shows typical photographs of various flow patterns obtained from the test sections. Based on different channels, the flow patterns are observed as follows.

3.1.1. 0.53 mm diameter channel

Four different flow patterns covering slug flow, throat-annular flow, churn flow and annular–rivulet flow are observed.

Slug flow, which occurs at a relatively low air velocity, is characterized by elongated bubble flowing in the axial direction.

Throat-annular flow is considered as a unique flow pattern in micro-channels because this flow pattern has never been observed in the ordinarily sized channels under normal gravity conditions.

Churn flow is characterized by a disruption near the bubble tail of the slug flow pattern.

Annular–rivulet flow corresponds to the situation that both annular flow and rivulet flow appear interchangeably as discussed in Saisorn and Wongwises [9].

3.1.2. 0.22 mm diameter channel

Based on a 0.22 mm diameter channel, the observed flow patterns include throat-annular flow, annular flow and annular–rivulet flow. It should be noted that annular flow is characterized by the stable flowing of the water film on the tube wall and continuous air in the tube core whereas annular–rivulet flow concerns with the simultaneous appearance of both annular flow and rivulet flow. The rivulet flow is a flow pattern characterized by the flowing of a river-like water stream on the tube surface.

3.1.3. 0.15 mm diameter channel

There are four different flow patterns observed in a 0.15 mm diameter channel. These flow patterns are liquid-alone flow, throat-annular flow, serpentine-like gas core flow, which is characterized by small ripple on the gas–liquid interface, and annular flow. It is important to note that such four flow patterns tend to appear alternately with time even at a given flow condition. This unstable appearance was also reported by Serizawa et al. [5], Kawahara et al. [8] and Wu and Cheng [11]. The flow regimes for the 0.15 mm circular micro-channel can be defined according to the appearance of the flow patterns as follows.

(a) In the region of low gas flow rates, an alternating flow mode consisting of liquid-alone flow, annular flow, and either or both of throat-annular flow and serpentine-like gas core flow is observed. A new flow pattern referred to as liquid/unstable annular alternating flow (LUAAF) is represented to describe these flow characteristics.
(b) A flow mode represented by liquid/annular alternating flow (LAAF) pertains to the alternating appearance of liquid-alone flow and annular flow (AF). This flow mode occurs in the region of high liquid flow rates.
(c) In the region of high gas flow rates, the flow is quite stable and only annular flow is observed.

3.2. Flow regime map

Parameters used in the presentation of flow pattern data are the phase superficial velocities. The superficial velocities of gas (j_G) and liquid (j_L) refer to the situation where the designated phase flows alone in the channel. The present flow pattern transition maps pertaining to two-phase air–water flow in horizontal circular microchannels with diameters of 0.53, 0.22 and 0.15 mm are shown in Fig. 4. The lines along with the flow pattern names indicated on the figure refer to the transition boundaries corresponding to different channels. An interesting point, which can be seen from the comparison, is that the variation of channel diameter tends to have no significant effects on the vicinity relating to the gas core flow with deformed interface. The throat-annular flow regime based on both channels with diameters of 0.53 and 0.22 mm corresponds well with LUAAF regime obtained from a 0.15 mm diameter

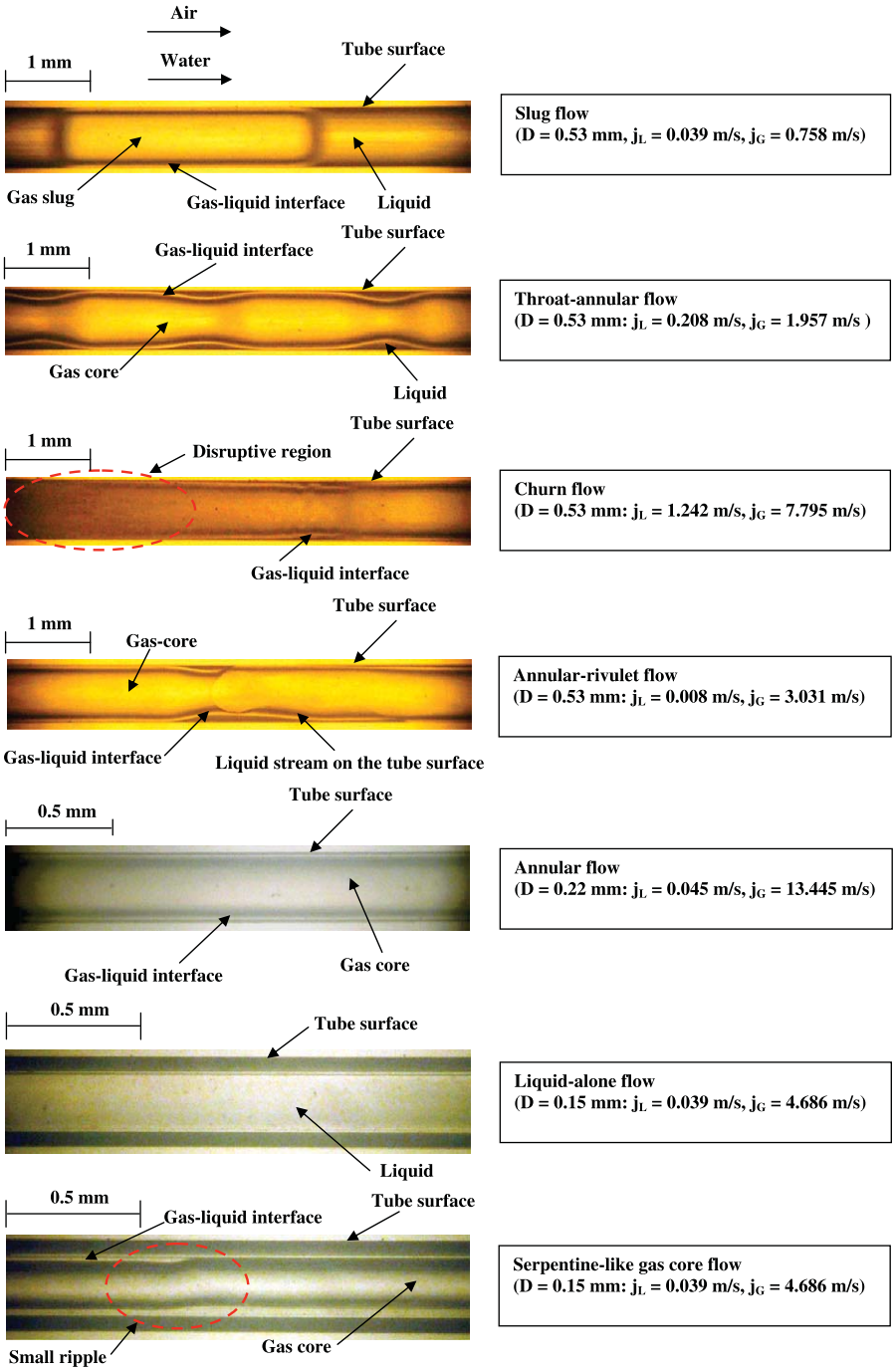

Fig. 3. Photographs of two-phase flow patterns.

channel. However, in this region, generally observed in only small channels, the interfacial waves appearing in the gas core flow patterns become thin as the channel diameter is decreased. The cause for this is due to the dominant role of surface tension on the gas–liquid interface.

The present flow pattern maps are also compared with the transition lines by Garimella et al. [12] and Revellin and Thome [13] who conducted the experiments with the phase change of refrigerant R134a in micro-channels.

The criteria for intermittent flow to wavy flow (or annular flow) transition was proposed by Garimella et al. [12] as follows:

$$x \leqslant \frac{a}{G+b} \tag{1}$$

where x denotes mass quality, G represents mass velocity and a and b are given by

$$a = 69.5673 + 22.595e^{0.2586d} \tag{2}$$

$$b = -59.9899 + 176.8137e^{0.3826d} \tag{3}$$

where d stands for tube diameter in mm. The data points which follow these criteria are considered to be located on the intermittent flow regime and the others refer to either annular regime or wavy regime. Figs. 5–7 show the comparisons of the present data with the transition criteria by Garimella et al. [12]. For a 0.53 mm diameter channel illustrated in Fig. 5, all flow pattern data, including slug flow, throat-annular flow, churn flow and annular–rivulet flow, lie

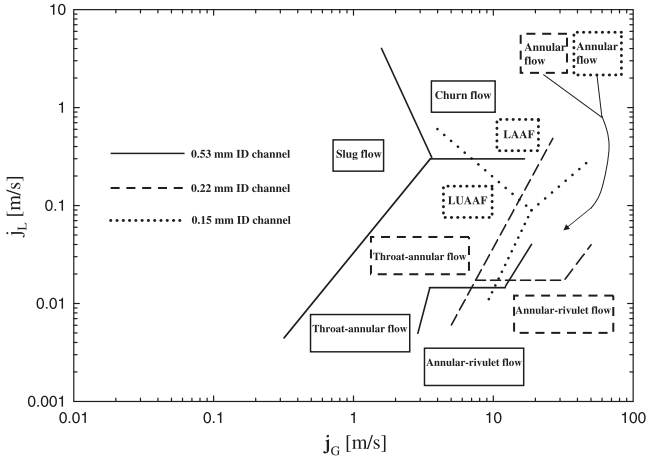

Fig. 4. Comparison of flow pattern maps.

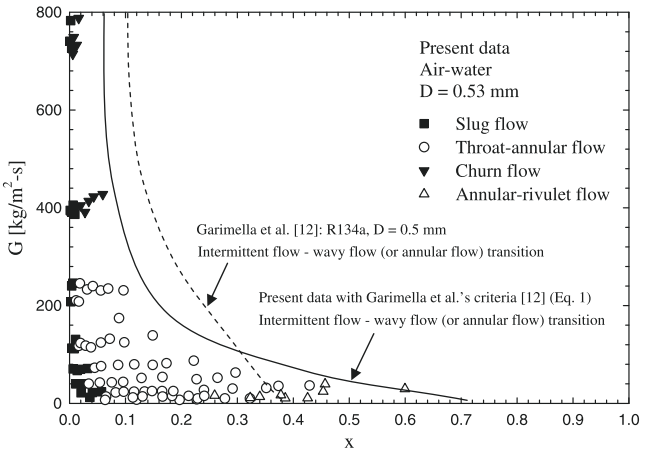

Fig. 5. Comparison of the flow patterns for a 0.53 mm diameter channel with the transition criteria by Garimella et al. [12].

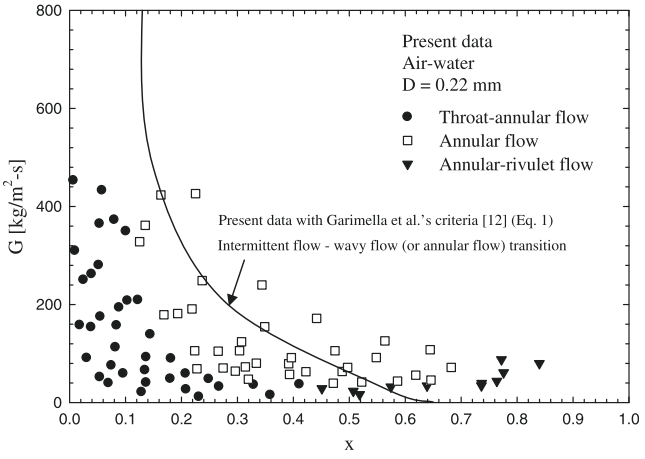

Fig. 6. Comparison of the flow patterns for a 0.22 mm diameter channel with the transition criteria by Garimella et al. [12].

in the intermittent flow regime and agree with the transition line by Garimella et al. [12]. Also, such transition criteria seem to be in fair agreement with the present data for the other two channels as shown in Figs. 6 and 7.

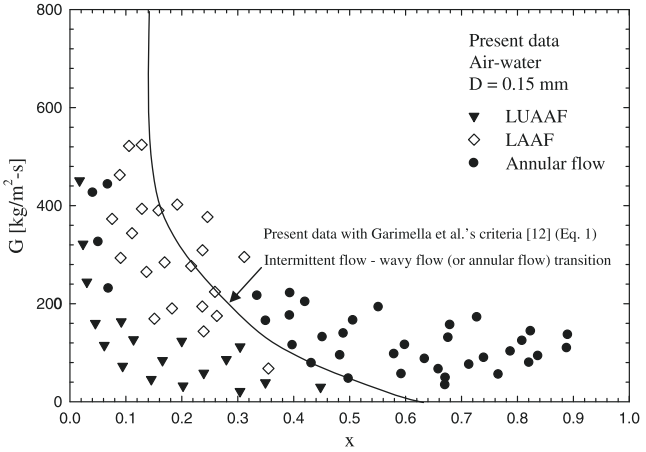

Fig. 7. Comparison of the flow patterns for a 0.15 mm diameter channel with the transition criteria by Garimella et al. [12].

The present data for the channel with the diameter of 0.53 mm is compared with the transition lines by Revellin and Thome [13] for flow boiling of R134a in a 0.51 mm diameter channel, in Fig. 8. The dash lines along with the flow pattern names indicated on the figure stand for the present transition boundaries whereas the solid lines and the names refer to the transition boundaries proposed by Revellin and Thome [13]. The comparison shows that bubbly flow, bubbly/slug flow, slug flow and slug/semi-annular flow obtained from Revellin and Thome [13] are located in the vicinity of slug flow regime of the present study. Their semi-annular flow regime, which corresponds to gas core flow with deformed interface, is found to agree well with our throat-annular flow pattern. In the region of high gas flow rates, our annular–rivulet flow is established, which is in relative agreement with their annular flow.

3.3. Void fraction

Void fraction is also one of the most important parameters used to evaluate the gravitational and accelerational terms in the total pressure drop of two-phase gas–liquid flow in various channels. Different methods available for void fraction estimation have been used by previous researchers.

Conventional methods such as a constant electric current method generally used to measure void fraction in ordinarily sized

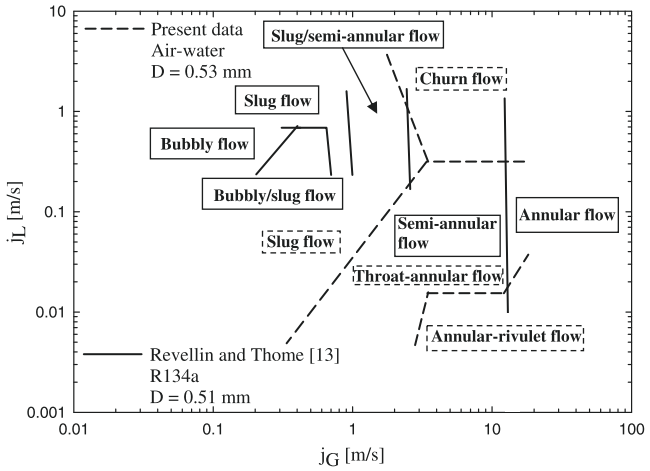

Fig. 8. Comparison of the present transition lines for a 0.53 mm diameter channel with the lines of Revellin and Thome [13].

channels were carried out by Kariyasaki et al. [14] to obtain void fractions in channels with three different diameters of 1, 2.4, and 4.9 mm. In a method based on quick-closing valves, Wongwises and Pipathattakul [15] measured void fraction in an inclined narrow annular channel with a hydraulic diameter of 4.5 mm.

For channels with hydraulic diameters of less than around 1 mm, it may be convenient to estimate volumetric void fraction by image analysis.

As previously mentioned, there are two sources of images which are obtained from flow visualisation. For a given flow condition, the first group of the images refers to approximately 300 images extracted from the video file and the other group stands for around 50–70 photographed images shot by the camera. The flow pattern identification is conducted based on both groups whereas the latter group, which corresponds to the images photographed with high shutter speed, is available for void fraction estimation.

In the present work, the void fraction is the average value estimated from about 50–70 photographed images. The image analysis is considered by assuming symmetrical volumes, covering spherical and ellipsoidal segments as well as cylinders, formed by gas–liquid interface. The volumetric void fraction was determined, based on the micrometer scale with an accuracy of ±0.05 mm and the effect of the curvature radius of the tube, which is firstly introduced by Kawahara et al. [8], is taken into account for the estimation. The uncertainty is around ±13% for the channels with diameters of 0.53 and 0.22 mm, and around ±39% for the 0.15 mm diameter channel.

The void fraction data obtained from a 0.53 mm diameter channel were found to agree well with the linear relationship of Eq. (4) which corresponds to the homogeneous flow model.

$$\alpha = \beta. \tag{4}$$

The Armand-type correlation of Eq. (5) recommended for small channel [6] was found to represent well the data for a 0.22 mm diameter channel.

$$\alpha = 0.833\beta. \tag{5}$$

For the two-phase flow in a channel having a diameter of 0.15 mm, the measured void fractions were found to be no longer linear relationship. Instead, the data were correlated well by the empirical form of Eq. (6) which is proposed by Kawahara et al. [8]. The non-linear relationship is mainly attributed to the highly frequent appearance of the gas core flow patterns which are inherent flow with large slip ratios. In addition, Kwak et al. [16] reported that void fraction data, obtained based on two-phase air–DI water flow through a fractal-like branching flow network, showed the non-linear relationship as well.

$$\alpha = \frac{C_1\beta^{0.5}}{1 - C_2\beta^{0.5}}. \tag{6}$$

In Eqs. (4)–(6), α represents volumetric void fraction, β represents volumetric quality, C_1 and C_2 are obtained based on the experimental data and are equal to 0.036 and 0.945, respectively.

According to the above discussion, Fig. 9 illustrates the measured results along with the data obtained from previous researchers.

3.4. Two-phase frictional pressure drop

Prior to obtaining data for the frictional pressure drop and two-phase multiplier, measurements of the total pressure drop are taken under various different conditions. In this work, the total pressure drop of a two-phase flow in each horizontal channel is composed of three terms: frictional pressure drop, accelerational

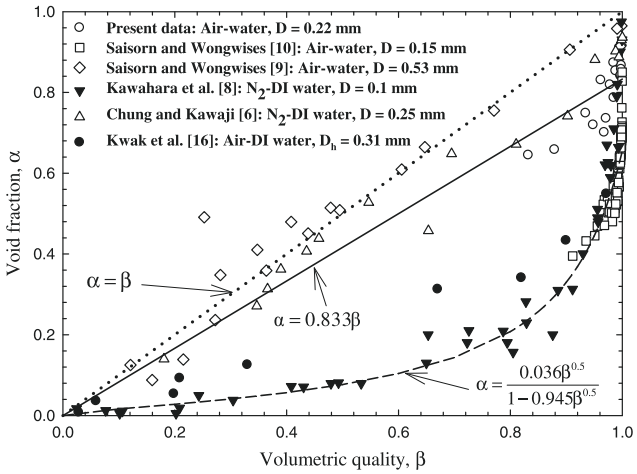

Fig. 9. Void fraction data for different channels.

pressure drop and pressure drop due to sudden contraction. According to the recent publication reported by Abdelall et al. [17], they reported that their data concerned with the air–water two-phase pressure drop in the circular micro-channel having abrupt flow area section agree very well with the slip model rather than with the homogeneous model. Therefore, it is important to note that the pressure drop due to sudden contraction should be carefully evaluated and a comprehensive review of the relevant calculations can be seen in Saisorn and Wongwises [10]. For the largest channel with a diameter of 0.53 mm, very small differences of up to 2% were indicated when the predictions obtained from the Abdelall et al.'s correlation [17] were compared with those from the homogeneous model. Nevertheless, for the other smaller channels, the sudden contraction pressure drops based on the Abdelall et al.'s correlation [17] were up to 98% lower than those calculated using the homogeneous flow model. Such considerable differences obtained from the other smaller channels are mainly due to the relatively high slip ratio as indicated in Fig. 9.

Finally, the two-phase frictional pressure drop in this study is determined by subtracting the accelerational term and sudden contraction term from the total pressure drop. For the sudden contraction term, the homogeneous flow model can be applicable in a 0.53 mm diameter channel whereas the Abdelall et al.'s correlation [17] is used for calculating in the other smaller channels. Fig. 10 shows frictional pressure drop data for different size channels. As

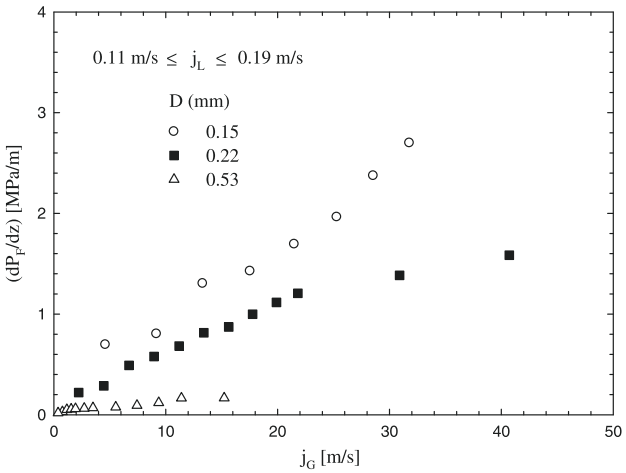

Fig. 10. Frictional pressure drop data for different channels.

expected, reducing the channel diameter increases the frictional pressure drop.

3.4.1. Two-phase frictional multiplier

The two-phase frictional multiplier for a smooth circular tube can be proposed in the form of the Lockhart–Martinelli correlation as follows:

$$\phi_L^2 = 1 + \frac{C}{\chi} + \frac{1}{\chi^2}, \tag{7}$$

where ϕ_L^2 represents two-phase frictional multiplier, χ represents Lockhart–Martinelli parameter. The constant C in the equation is the parameter which indicates the two-phase flow condition. The value of this parameter proposed by Chisholm [18] varies from 5 to 20 depending on the flow condition of the gas and liquid. For instance, the constant $C = 20$ when the gas and liquid flow is in the turbulent region and $C = 5$ if the two-phase flow is in the laminar region, which corresponds to the present study.

Mishima and Hibiki [19] proposed a correlation for the value of C as a function of the channel diameter and thus, the relationship between ϕ_L^2 and χ is given by

$$\phi_L^2 = 1 + \frac{21(1 - e^{-319D_h})}{\chi} + \frac{1}{\chi^2} \tag{8}$$

where D_h stands for hydraulic diameter.

Recently, English and Kandlikar [20] proposed a correlation which was modified, based on the Mishima and Hibiki's correlation [19] as shown in Eq. (9).

$$\phi_L^2 = 1 + \frac{C(1 - e^{-319D_h})}{\chi} + \frac{1}{\chi^2} \tag{9}$$

where the value of C depends on the flow condition and is similar to that proposed by Chisholm [18]. For the present data, the two-phase flow is in the laminar region and hence C = 5 is recommended for the calculation.

It is found from Figs. 11–13 that mass flux plays the most important role on the frictional multiplier data dealing with a 0.53 mm diameter channel but the dominating effect decreases thereafter with decreasing the channel diameter. The reason for this may be due to a level of the interaction between gas and liquid phases. According to Eq. (7), the level of the interaction corresponding to momentum coupling between the two phases can be implicitly represented by C parameter relating to the experimental data. Fig. 14 shows the data of C parameter obtained from different channels. It is found that the C parameter decreases with decreasing channel diameter. Additionally, the trend is similar way as that reported by Fujita et al. [21] and Lee and Lee [22].

In addition to mass flux, Figs. 15–17 illustrate that the orderly distribution of the data shows the dependence of flow pattern on the frictional multiplier.

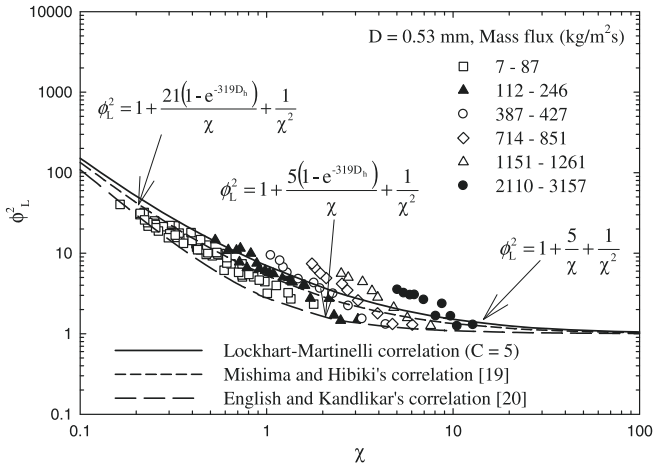

Fig. 11. Two-phase frictional multiplier data with various mass flux values for a 0.53 mm diameter channel.

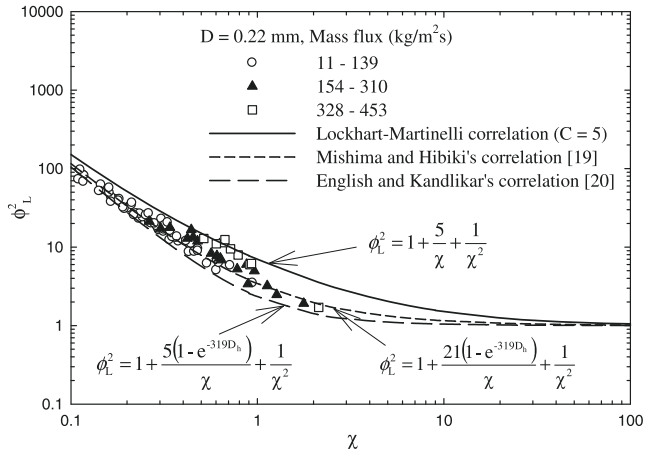

Fig. 12. Two-phase frictional multiplier data with various mass flux values for a 0.22 mm diameter channel.

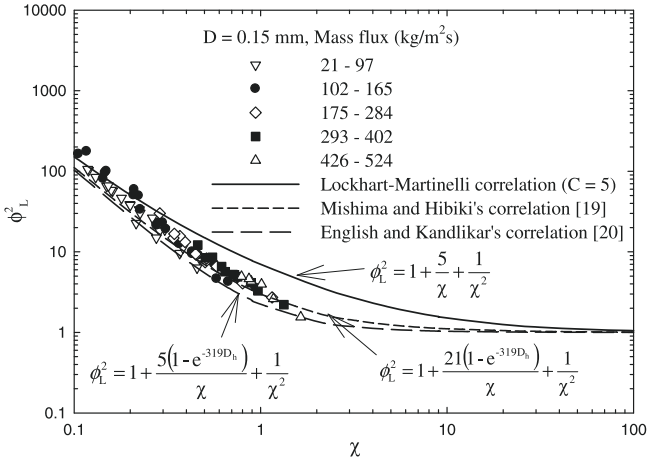

Fig. 13. Two-phase frictional multiplier data with various mass flux values for a 0.15 mm diameter channel.

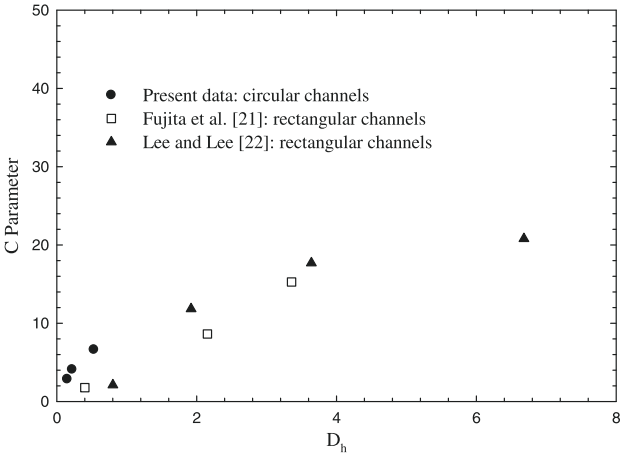

Fig. 14. C parameter versus channel diameter.

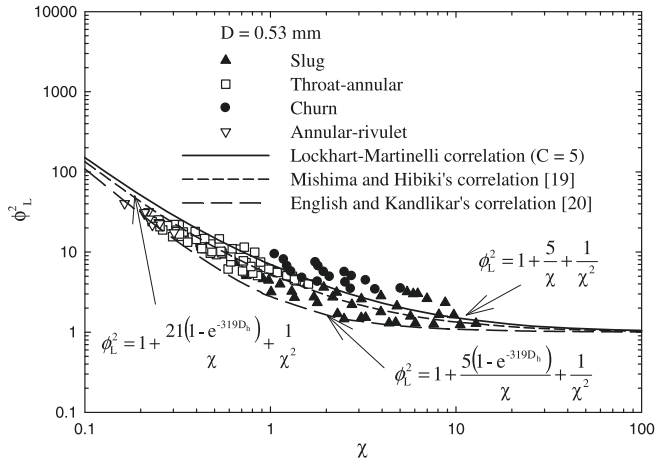

Fig. 15. Two-phase frictional multiplier data with various flow patterns for a 0.53 mm diameter channel.

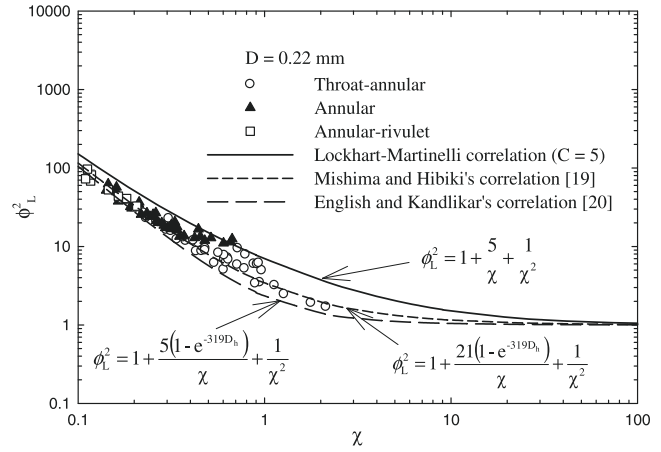

Fig. 16. Two-phase frictional multiplier data with various flow patterns for a 0.22 mm diameter channel.

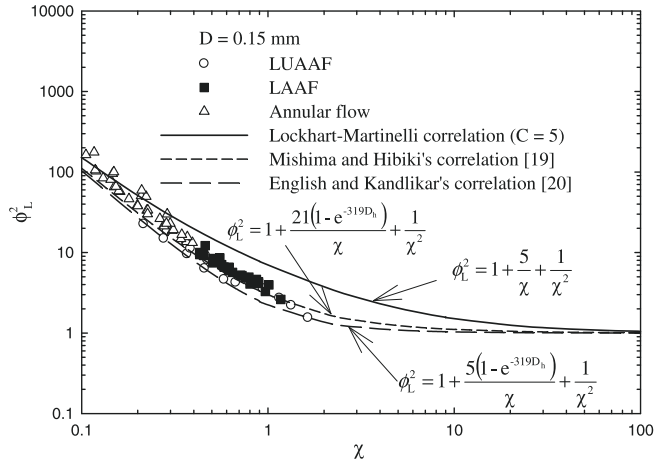

Fig. 17. Two-phase frictional multiplier data with various flow patterns for a 0.15 mm diameter channel.

Concerned with the comparisons between the pressure drop correlations and the measured data, it is found that the Lockhart–Martinelli correlation with $C = 5$ seems to be able to fairly predict the results only obtained from the largest channel whereas the Mishima and Hibiki's correlation [19] tends to be predictable for all three channels. The correlation proposed by English and Kandlikar [20] shows good agreement with the data in the range of very low mass flux values.

The pressure drop data are also compared with the correlation, working for refrigerants under certain condition, which is proposed by Muller-Steinhagen and Heck [23]. The correlation is given by the following equation:

$$\left(\frac{dP_F}{dz}\right)_{TP} = \left\{\left(\frac{dP_F}{dz}\right)_{LO} + 2x\left[\left(\frac{dP_F}{dz}\right)_{GO} - \left(\frac{dP_F}{dz}\right)_{LO}\right]\right\}(1-x)^{1/3} + \left(\frac{dP_F}{dz}\right)_{GO} x^3 \quad (10)$$

where $(dP_F/dz)_{TP}$ is two-phase frictional pressure gradient, $(dP_F/dz)_{LO}$ represents frictional pressure gradient for the total flow having liquid properties and $(dP_F/dz)_{GO}$ denotes frictional pressure gradient for the total flow having gas properties. Fig. 18 shows all present data compared with the predictions by Muller-Steinhagen and Heck [23]. The comparison shows that 60% of the present data fall within ±25% of the prediction by Muller-Steinhagen and Heck [23]. According to this comparison, the mean absolute error is around 0.13 MPa/m and the mean relative error is around 24%.

Although the pressure drop correlations presented by Mishima and Hibiki [19] and English and Kandlikar [20] were proposed at micro-scale, they do not take into account the mass velocity, viscous and surface tension effects which have significant influence on the two-phase flow in micro-channel. In this study, thus, the correlation for C parameter, proposed by Lee and Lee [22], which is developed based on two-phase air–water flow through horizontal rectangular channels with hydraulic diameter ranging from 0.78 to 6.67 mm is modified here to determine the value of C for the present test sections.

Based on all experimental data, a new correlation which takes into account the major effects dominating in the two-phase flow through micro-channel is expressed by

$$C = 7.599 \times 10^{-3} \lambda^{-0.631} \psi^{0.005} Re_{LO}^{-0.008} \quad (11)$$

where Re_{LO} represents the all-liquid Reynolds number as given below.

$$Re_{LO} = \frac{GD}{\mu_L} \quad (12)$$

where G is mass velocity and μ_L denotes liquid viscosity. λ and ψ are dimensionless parameters, introduced by Suo and Griffith [24], which are defined as

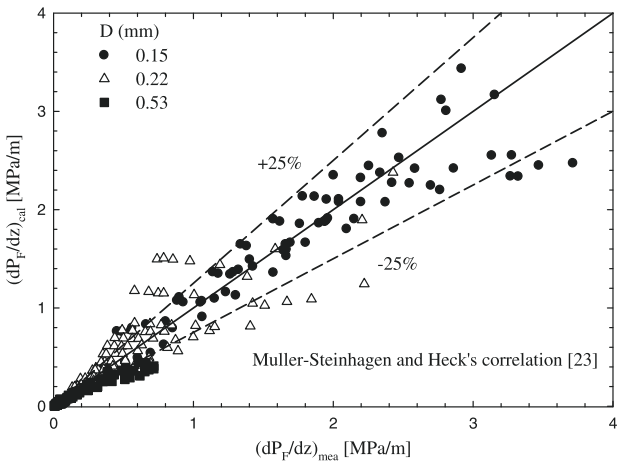

Fig. 18. Comparison of the experimental data with predictions by Muller-Steinhagen and Heck [23].

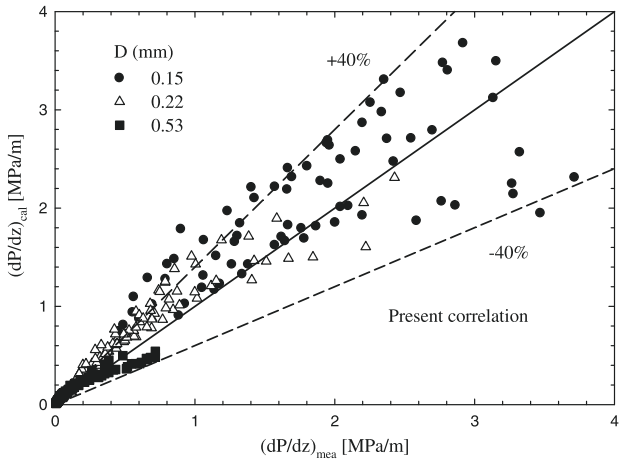

Fig. 19. Prediction of the frictional pressure drop.

$$\lambda = \frac{\mu_L^2}{\rho_L \sigma D} \tag{13}$$

$$\psi = \frac{\mu_L j}{\sigma} \tag{14}$$

where σ, ρ_L and j stand for surface tension, liquid density and total superficial velocity, respectively.

Fig. 19 shows the two-phase frictional pressure gradient obtained from measurement, $(dP/dz)_{mea}$ plotted against the two-phase frictional pressure gradient obtained from prediction, $(dP/dz)_{pre}$. Based on 285 data points, the mean absolute error is 0.2 MPa/m and the mean relative error is 47.98%, and around 52 percent of the data fall within ±40% of the proposed correlations.

The present correlation is obtained based on the channels with diameters of 0.53, 0.22 and 0.15 mm. The constant and all exponents are obtained from the data regression analysis. A notable point for the present correlation is addressed as follow. The exponent for all-liquid Reynolds number is very small, indicating that the C parameter is not strongly dependent on the mass velocity, especially in relatively small diameters. This point is also evident by Figs. 11–13.

4. Conclusion

Two-phase air–water flow is carried out in channels with diameters of 0.15, 0.22 and 0.53 mm which are made of fused silica. The gas superficial velocity and liquid superficial velocity are varied in a range of 0.37–42.36 m/s and 0.005–3.04 m/s, respectively. Seven different flow patterns including slug flow, throat-annular flow, churn flow, annular–rivulet flow, annular flow, liquid-alone flow and serpentine-like gas core flow are observed from the present test sections. The relationships dealing with void fraction are obtained, based on the measured data. The trend of the void fraction in a 0.15 mm diameter channel is no longer linear relationship. The two-phase pressure drop data indicate that mass flux and flow regime have a detectable effect on the two-phase frictional multiplier. A new correlation taking into account the major effects in two-phase flow through circular micro-channels is developed from the present data.

Acknowledgements

The authors would like to express their appreciation to the Thailand Research Fund (TRF) and the Joint Graduate School of Energy and Environment (JGSEE) for providing financial support for this study.

References

[1] S.S. Mehendale, A.M. Jacobi, R.K. Ahah, Fluid flow and heat transfer at micro- and meso-scales with application to heat exchanger design, Appl. Mech. Rev. 53 (2000) 175–193.
[2] S.G. Kandlikar, Fundamental issues related to flow boiling in mini-channels and micro-channels, Exp. Therm. Fluid Sci. 26 (2002) 389–407.
[3] K.A. Triplett, S.M. Ghiaasiaan, S.I. Abdel-Khalik, D.L. Sadowski, Gas–liquid two-phase flow in microchannels Part I: two-phase flow patterns, Int. J. Multiphase Flow 25 (1999) 377–394.
[4] K.A. Triplett, S.M. Ghiaasiaan, S.I. Abdel-Khalik, A. LeMouel, B.N. McCord, Gas–liquid two-phase flow in microchannels Part II: void fraction and pressure drop, Int. J. Multiphase Flow 25 (1999) 395–410.
[5] A. Serizawa, Z. Feng, Z. Kawara, Two-phase flow in micro-channels, Exp. Therm. Fluid Sci. 26 (2002) 703–714.
[6] P.M.-Y. Chung, M. Kawaji, The effect of channel diameter on adiabatic two-phase flow characteristics in microchannels, Int. J. Multiphase Flow 30 (2004) 735–761.
[7] S. Saisorn, S. Wongwises, An inspection of viscosity model for homogeneous two-phase flow pressure drop prediction in a horizontal circular micro-channel, Int. Commun. Heat Mass Transfer 35 (2008) 833–838.
[8] A. Kawahara, P.M.-Y. Chung, M. Kawaji, Investigation of two-phase flow pattern, void fraction and pressure drop in a microchannel, Int. J. Multiphase Flow 28 (2002) 1411–1435.
[9] S. Saisorn, S. Wongwises, Flow pattern, void fraction and pressure drop of two-phase air–water flow in a horizontal circular micro-channel, Exp. Therm. Fluid Sci. 32 (2008) 748–760.
[10] S. Saisorn, S. Wongwises, An experimental investigation of two-phase air–water flow through a horizontal circular micro-channel, Exp. Therm. Fluid Sci. 33 (2009) 306–315.
[11] H.Y. Wu, P. Cheng, Liquid/two-phase/vapor alternating flow during boiling in microchannels at high heat flux, Int. Commun. Heat Mass Transfer 30 (2003) 295–302.
[12] S. Garimella, J.D. Killion, J.W. Coleman, An experimentally validated model for two-phase pressure drop in the intermittent flow regime for circular microchannels, J. Fluid Eng. 124 (2002) 205–214.
[13] R. Revellin, J.R. Thome, A new type of diabatic flow pattern map for boiling heat transfer in microchannels, J. Micromech. Microeng. 17 (2007) 788–796.
[14] A. Kariyasaki, T. Fukano, A. Ousaka, M. Kagawa, Characteristics of time-varying void fraction in isothermal air–water co-current flow in horizontal capillary tube, Trans. JSME 57 (1991) 4036–4043.
[15] S. Wongwises, M. Pipathattakul, Flow pattern, pressure drop and void fraction of two-phase gas–liquid flow in an inclined narrow annular channel, Exp. Therm. Fluid Sci. 30 (2006) 345–354.
[16] Y. Kwak, D. Pence, J. Liburdy, V. Narayanan, Gas–liquid flows in a fractal-like branching flow network, in: Engineering Conference International Heat Transfer and Fluid Flow in Microscale III, Whistler, BC, Canada, September 21–26, 2008.
[17] F.F. Abdelall, G. Hahn, S.M. Ghiaasiaan, S.I. Abdel-Khalik, S.S. Jeter, M. Yoda, D.L. Sadowski, Pressure drop caused by abrupt flow area changes in small channels, Exp. Therm. Fluid Sci. 29 (2005) 425–434.
[18] D. Chisholm, A theoretical basis for the Lockhart–Martinelli correlation for two-phase flow, Int. J. Heat Mass Transfer 10 (1967) 1767–1778.
[19] K. Mishima, T. Hibiki, Some characteristics of air–water two-phase flow in small diameter vertical tubes, Int. J. Multiphase Flow 22 (1996) 703–712.
[20] N.J. English, S.G. Kandlikar, An experimental investigation into the effect of surfactants on air–water two-phase flow in minichannels, Heat Transfer Eng. 27 (2006) 99–109.
[21] H. Fujita, T. Ohara, M. Hirota, H. Furuta, Gas-liquid flows in flat channels with small channel clearance, in: Proceedings of the Second International Conference on Multiphase Flow'95, Kyoto, Japan, IA3-37-IA3-44, 1995.
[22] H.J. Lee, S.Y. Lee, Pressure drop correlations for two-phase flow within horizontal rectangular channels with small heights, Int. J. Multiphase Flow 27 (2001) 783–796.
[23] H. Muller-Steinhagen, K. Heck, A simple friction pressure drop correlation for two-phase flow in pipes, Chem. Eng. Process. 20 (1986) 297–308.
[24] M. Suo, P. Griffith, Two-phase flow in capillary tubes, Trans. ASME J. Heat Transfer (1964) 576–582.

Experimental Thermal and Fluid Science 34 (2010) 616–624

Contents lists available at ScienceDirect

Experimental Thermal and Fluid Science

journal homepage: www.elsevier.com/locate/etfs

Comparison of the effects of measured and computed thermophysical properties of nanofluids on heat transfer performance

Weerapun Duangthongsuk [a,b], Somchai Wongwises [b,*]

[a] Department of Mechanical Engineering, South-East Asia University, Bangkok, Thailand
[b] Fluid Mechanics, Thermal Engineering and Multiphase Flow Research Laboratory (FUTURE), Department of Mechanical Engineering, King Mongkut's University of Technology Thonburi, Bangmod, Bangkok 10140, Thailand

ARTICLE INFO

Article history:
Received 22 April 2009
Received in revised form 31 October 2009
Accepted 2 November 2009

Keywords:
Thermophysical property
Heat transfer performance
Nanofluid
Particle volume concentration

ABSTRACT

This article reports a comparison of the differences between using measured and computed thermophysical properties to describe the heat transfer performance of TiO_2–water nanofluids. In this study, TiO_2 nanoparticles with average diameters of 21 nm and a particle volume fraction of 0.2–1 vol.% are used. The thermal conductivity and viscosity of nanofluids were measured by using transient hot-wire apparatus and a Bohlin rotational rheometer, respectively. The well-known correlations for calculating the thermal conductivity and viscosity of nanofluids were used for describing the Nusselt number of nanofluids and compared with the results from the measured data. The results show that use of the models of thermophysical properties for calculating the Nusselt number of nanofluids gave similar results to use of the measured data. Where there is a lack of measured data on thermophysical properties, the most appropriate models for computing the thermal conductivity and viscosity of the nanofluids are the models of Yu and Choi and Wang et al., respectively.

1. Introduction

Nanofluids are innovative heat transfer fluids engineered by dispersing metallic or non-metallic nanoparticles with typical sizes of less than 100 nm in conventional heat transfer fluids. This term was coined by Choi [1] in 1995, and has since gained popularity. Normally, common heat transfer fluids such as oil, water, and ethylene glycol are used as the heat transfer fluid, and they are widely used in many industries in power generation, chemical processes, heating and cooling processes, transportation, microelectronics, and other micro-sized applications. However, these fluids have poor heat transfer properties compared with those of most solids, and this is the primary hindrance to the development of heat transfer equipment. The key idea is to disperse small solid particles in common base liquids in order to enhance their heat transfer properties. In recent years, with the rapid development in the field of nanotechnology, particles that are nanometer sized (normally less than 100 nm), instead of micrometer sized are dispersed in conventional base liquids in order to avoid problem of abrasion of the flow channel. Many researchers demonstrated that nanofluids have created various potential advantages, such as better long-term stability, and little penalty in term of drop in pressure, and can have drastically greater thermal conductivity compared with millimeter or even micrometer sized particle suspensions. Although nanofluids have significant potential for use in advanced thermal applications, they remain in the early stages of development. A decade ago, a number of researchers reported the heat transfer and flow characteristics of the different nanofluids. Moreover, Trisaksri and Wongwises [2], Duangthongsuk and Wongwises [3] and Wang and Mujumdar [4] reviewed the literature on the general heat transfer characteristics of nanofluids, especially. In our opinion, however, before starting to determine the heat transfer performance of nanofluids, it is first necessary to know about their thermophysical properties, especially thermal conductivity and viscosity. Many researchers have used well-known correlations for predicting the thermophysical properties of nanofluids and many researchers have measured these properties. Their works have been both theoretical and experimental. The sample investigations which have reported the heat transfer of nanofluids are summarized below.

Pak and Cho [5] evaluated the heat transfer performance of γ-Al_2O_3 and TiO_2 nanoparticles dispersed in water flowing in a horizontal circular tube under a turbulent flow regime experimentally. The experimental results of Masuda et al. [6] were used to obtain the relative thermal conductivity of nanofluids, while the viscosity of nanofluids was measured using a Brookfield viscometer. The results indicated that the Nusselt number of nanofluids increased with increases in the Reynolds number as well as the increases in the particle concentration. Moreover, their results also showed

* Corresponding author. Tel.: +662 470 9115; fax: +662 470 9111.
E-mail address: somchai.won@kmutt.ac.th (S. Wongwises).

0894-1777/$ - see front matter © 2009 Elsevier Inc. All rights reserved.
doi:10.1016/j.expthermflusci.2009.11.012

Nomenclature

Cp	specific heat, J/kg K
D	tube diameter, m
f	friction factor
h	heat transfer coefficient, W/m^2 K
k	thermal conductivity, W/m K
$\dot{m}$	mass flow rate, kg/s
Nu	Nusselt number
Pr	Prandtl number
q	heat flux, W/m^2
Q	heat transfer rate, W
Re	Reynolds number
T	temperature, °C

Greek symbols

ϕ	particle volume fraction
ε	tube roughness
ρ	density, kg/m^3
μ	viscosity, kg/m s

Subscripts

ave	average
f	fluid
h	heating fluid
in	inlet
out	outlet
p	particles
nf	nanofluid
w	water
wall	tube wall

that the heat transfer coefficient of the nanofluids with a particle volume fraction of 3% was around 12% smaller than that of pure water in the same condition. Finally, a novel heat transfer equation for computing the Nusselt number of nanofluids was proposed.

Li and Xuan [7] and Xuan and Li [8] reported experimentally the heat transfer performance and flow characteristics of Cu–DI water nanofluids flowing through a straight tube under laminar and turbulent flow conditions. The thermal conductivity and viscosity of nanofluids were measured. The results indicated that the heat transfer coefficient of nanofluids was remarkably higher than that of water and the friction factor of nanofluids coincided well with that of the water. Furthermore, new convective heat transfer correlations were proposed to calculate the heat transfer coefficients of the nanofluids for both laminar and turbulent flow conditions.

Wen and Ding [9] investigated the convective heat transfer coefficient of Al_2O_3–DI water flowing through a copper tube under a laminar flow regime experimentally. A KD2 thermal property meter was used to measure the thermal conductivity of nanofluids at 22 °C. The Einstein equation was used for calculating the viscosity of nanofluids. The experimental results indicated that the local heat transfer coefficient increased with increases in the Reynolds number as well as increases in the particle volume concentration. Moreover, the results also showed that the Shah correlation for laminar flow and the Dittus–Boelter equation for turbulent flow failed to predict the Nusselt number of nanofluids.

Ali et al. [10] studied the heat and mass transfer between air and falling film with ultrafine Cu nanoparticles in a cross flow configuration numerically. The thermophysical properties of nanofluids were calculated from the following existing formulas: the Hamilton and Crosser model (H–C model) [11] for thermal conductivity and the Brinkman equation [12] for viscosity. The results indicated that the dehumidification and cooling process increased under the following conditions: a low air Reynolds number, a high Cu particle volume fraction, increases in the height and length of the channel, and decreases in the channel width.

Roy et al. [13] investigated the heat transfer and wall shear stress of radial laminar flow in a cooling system of water–γ-Al_2O_3 nanofluids compared with water, glycol, and oil, numerically. The H–C model was used to compute the thermal conductivity and the equation of Wang et al. [14] was used to calculate the viscosity of nanofluids. Their results showed that the heat transfer rate and wall shear stress were higher with increases in the particle concentration as well as increases in the Reynolds number.

Ali and Vafai [15] reported numerical formulations to determine the effects of the inclination angle of parallel-and-counter-flow on heat and mass transfer between air and falling desiccant film, with suspended Cu nanoparticles. The H–C model was used to calculate the thermal conductivity whereas the Brinkman equation was used to compute the viscosity of nanofluids. The results indicated that the dehumidification and cooling process of air and the regeneration process of the liquid desiccant were enhanced by an increasing inclination angle for both parallel-and-counter flow channels.

Yang et al. [16] studied the heat transfer performance of graphite nanoparticles dispersed in two liquids flowing in a horizontal tube heat exchanger under laminar flow regimes. The thermal conductivity and viscosity of nanofluids were measured using a transient hot-wire apparatus and a capillary viscometer, respectively. The experimental results indicated that the heat transfer coefficient increased with increases in the Reynolds number and in the particle volume concentration. Two graphite nanoparticle sources at equal particle concentrations gave different values of the heat transfer coefficients. The results also showed that the calculated values of the Nusselt number using Li and Xuan's correlation [7] gave a higher value than the measured data did. Finally, a new heat transfer correlation for predicting the Nusselt number of nanofluids under laminar flow conditions was proposed by modifying the Seider–Tate equation (1936).

Ding et al. [17] investigated the local heat transfer coefficient of CNT-distilled water nanofluids flowing through a horizontal tube under a laminar flow regime, experimentally. A KD2 thermal property meter and a Bohlin CVO rheometer were used to measure the thermal conductivity and viscosity of nanofluids, respectively. The results showed that the local heat transfer coefficient of CNT nanofluids is much higher than that of pure water. This enhancement depends on the flow conditions, CNT concentration, and the pH value. However, they indicated that the effect of pH value is smallest compared with other parameters. Heris et al. [18,19] reported an experimental study of the heat transfer performance of Al_2O_3–water and CuO–water nanofluids flowing in an annular concentric tube under a laminar flow regime. The Einstein equation was used to calculate the viscosity of nanofluids whereas the H–C model and Yu and Choi [20] model were used to compute the thermal conductivity of nanofluids. The experimental results showed that the heat transfer coefficient increased with an increasing Peclet number and particle volume concentration. Moreover, their results also indicated that CuO–water nanofluids showed smaller heat transfer enhancement than Al_2O_3–water nanofluids.

He et al. [21] studied experimentally the heat transfer performance and pressure drop characteristic of TiO_2–distilled water nanofluids flowing through a vertical pipe in an upward direction

in both the laminar and turbulent flow regimes. A KD2 thermal property meter and a Bohlin CVO rheometer were used to measure the thermal conductivity and viscosity of nanofluids, respectively. The experimental results showed that the local heat transfer coefficient increased with an increasing concentration of nanoparticles in both the laminar and turbulent flow regimes at a given Reynolds number and particle size. The results also showed that the pressure drop of the nanofluids was very close to that of the base fluid.

Nguyen et al. [22] studied the heat transfer coefficient of Al_2O_3–water nanofluids flowing through an electronic liquid cooling system under turbulent flow conditions, experimentally. The Chon et al. equation [23] was used to calculate the thermal conductivity of nanofluids. The results showed that the Nusselt number of the nanofluids was much higher than that of the base liquid. Moreover, their results also indicated that the nanofluid with a 36 nm particle diameter gave a higher heat transfer coefficient than the nanofluid which was 47 nm in size.

Ko et al. [24] reported an experimental study of the pressure drop of carbon nanotubes dispersed in distilled water flowing through a horizontal tube. An AR2000 viscometer (TA Instruments) was used to measure the viscosity of nanofluids. The results showed that the nanofluids prepared by the acid treatment (TCNT) had much smaller viscosities than those made with surfactant (PCNT). Moreover, both nanofluids showed larger friction factors than the base fluids did.

Chein and Chuang [25] studied experimentally the heat transfer performance of a microchannel heat sink (MCHS) using CuO–water nanofluids as coolants. The thermal conductivity of nanofluids was calculated using the H–C model while the Brinkman equation was used to compute the viscosity. The results indicated that the presence of nanoparticles creates greater energy absorption than pure water at a low flow rate and there is no contribution from heat absorption when the flow rate is high.

Duangthongsuk and Wongwises [26] reported experimentally the heat transfer performance and pressure drop characteristics of TiO_2–water nanofluid flowing in a horizontal double tube counter flow heat exchanger. The Yu and Choi model was used to calculate the thermal conductivity of the nanofluids while the Einstein equation was used to compute the viscosity of the nanofluids. The results showed that the heat transfer coefficient of 0.2 vol.% nanofluid is slightly larger than that of water by about 6–11%. Moreover, the results also showed that use of nanofluid has a small penalty in terms of pressure drop.

Santra et al. [27] investigated the heat transfer behaviour of Cu–water nanofluids flowing through two isothermally heated parallel plates, numerically. The thermal conductivity and viscosity of nanofluids were calculated using the Patel et al. [28] equation and Brinkman equation, respectively. Their results showed that the local Nusselt number of nanofluids is larger than that of base fluid and increases with increases in the Reynolds number as well as with increases in the particle volume fraction.

Moreover, the other aspect of heat transfer performance of nanofluids such as pool boiling heat transfer is shown in the published article of Trisaksri and Wongwises [29].

As mentioned above, it is evident that some researchers measured the thermophysical properties of nanofluids and used them to evaluate the heat transfer performance and flow characteristics. However, some researchers used existing well-known equations to calculate the thermophysical properties of nanofluids. Many researchers (for example [5,9,14,21,30–32]) reported that the thermophysical properties model underestimated the viscosity and thermal conductivity of nanofluids. Mansour et al. [33] and Duangthongsuk and Wongwises [34] reported the effect of the thermophysical properties on the calculation of the heat transfer performance of nanofluid; however, they did not consider the discrepancy between use of the measured values and use of the calculated values of thermophysical properties to describe the Nusselt number of nanofluids. So far, this article has aimed to report the difference between the use of measured values and the use of calculated values of themophysical properties, which affects the Nusselt number of nanofluids.

2. Sample preparation

In the present study, nanofluids provided by a commercial source (DEGUSSA, VP Disp. W740×) are used as working fluid. This mixture is composed of TiO_2 nanoparticles with an average diameter of 21 nm dispersed in water. The original particle concentration was 40 wt.%. In order to produce other required particle volume fractions, dilution with water followed by a stirring action was effected. Moreover, an ultrasonic vibrator was used to sonicate the solution continuously for about 2 h in order to break down agglomeration of the nanoparticles. The desired volume concentrations used in this study were 0.2%, 0.6%, and 1.0% with pH values of 7.5, 7.1, and 7.0, respectively. From the pH values, it can be seen that the solution chemistry of nanofluids is nearly neutral in nature. A transmission electron microscope (TEM) was used to approximate the size of the primary nanoparticles. As shown in Fig. 1, it is clear that the primary size of nanoparticles is approximately spherical with an average diameter of around 21 nm.

3. Experimental apparatus

The experimental system used in the present study is shown schematically in Fig. 2. It mainly consists of a test section, two receiver tanks, a magnetic gear pump, a hot water pump, a cooler tank, a hot water tank, and a collection tank. The test section is a 1.5 m long counter-flow horizontal double tube heat exchanger with nanofluid flowing inside the tube while hot water flows in the annular. The inner tube is made from smooth copper tubing with a 9.53 mm outer diameter and a 0.7 mm thickness while the outer tube is made from PVC tubing and has a 33.9 mm outer diameter and 3 mm thickness. The test section is thermally isolated from its upstream and downstream sections by plastic tubes in order to reduce the heat loss along the axial direction. The differential pressure transmitter and T-type thermocouple are mounted at both ends of the test section to measure the pressure drop and the bulk temperature of the nanofluid, respectively. Thermocouples are mounted at different longitudinal positions on the inner

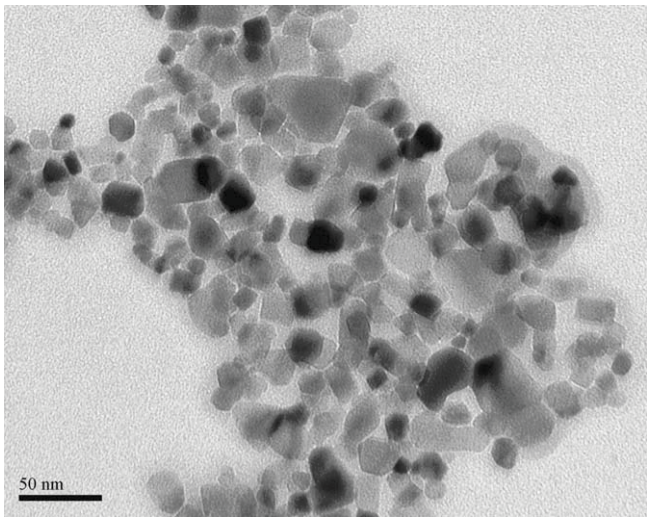

Fig. 1. TEM image of dispersed TiO_2 nanoparticles in water.

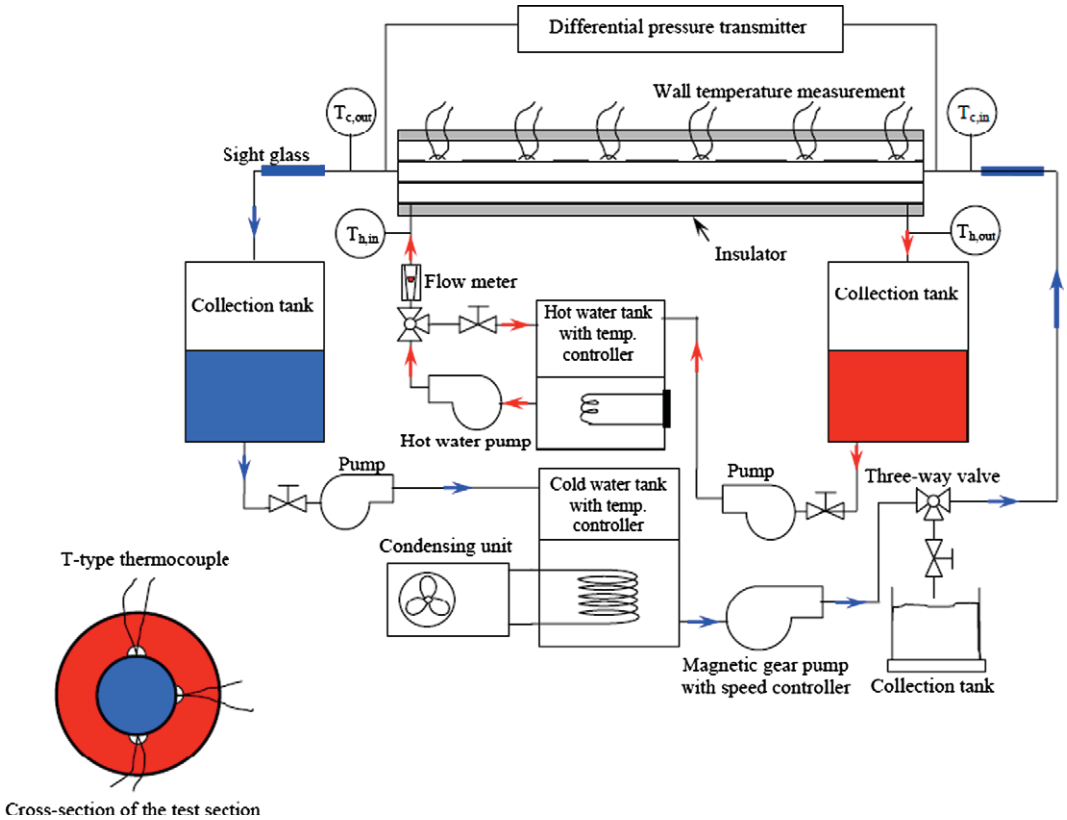

Fig. 2. Schematic diagram of the experimental apparatus.

tube surface of the wall, each with three thermocouples equally spaced around the tube circumference. The inlet and exit temperatures of hot water are measured using T-type thermocouples which are inserted into the flow directly. The receiver tanks of 60 L are made from stainless steel to store the nanofluid and hot water leaving from the test section. The cooler tank with a 4.2 kW cooling capacity and a thermostat is used to keep the nanofluid temperature constant. Similar to the cooler tank, a 3 kW electric heater with a thermostat was installed to keep the temperature of the hot water constant. The nanofluid flow rate was controlled by adjusting the rotation speed of the magnetic gear pump. The hot water flow rate was measured by a rotameter while the nanofluid flow rate was evaluated directly from the time taken for the exact mass of nanofluid to be discharged. For each speed of the pump, five measurements were done. The average of all data was used in the present study.

A portable programmable calibrator was used to calibrate all T-type thermocouples with a maximum precision of 0.1 °C. The nanofluid mass flow rates were determined by electronic balance. The uncertainty of the electronic balance was ±0.0006 kg. Maximum uncertainty of the nanofluid mass flow rate was evaluated as 2.2%. This uncertainty was taken into account to calculation of the uncertainty of the Nusselt number.

Moreover, the uncertainty of the hot water mass flow rate is ±7% (full scale). As mentioned above, it can be evidently seen that the uncertainty of the measured Nusselt number depends on the temperature measurement, and nanofluid and hot water flow rate measurement. The uncertainty of the measured Nusselt number was evaluated from the Root Mean Sum Square Method and found as 5%.

During the test run, wall temperatures of the test section, mass flow rates of the hot water and nanofluids, and the inlet and exit temperatures of the hot water and nanofluids were measured.

This study is a continuation of the authors' previous work. The details of the measurement of the thermal conductivity and viscosity of nanofluids, including the effect of temperature on these properties are presented in our previous article [35].

4. Data reduction

In this study, TiO_2–water nanofluids with particle volume concentrations of 0.2%, 0.6%, and 1.0% are used to evaluate the heat transfer performance of nanofluids. Thus, the Nusselt number of nanofluids can be computed from the following equation.

The heat transfer rate from the heating fluid is calculated from:

$$Q_w = \dot{m}_w Cp_w (T_{in} - T_{out})_w \tag{1}$$

where Q_w is the heat transfer rate of the hot water and $\dot{m}_w$ is the mass flow rate of the hot water.

The heat transfer rate into the nanofluid is computed from:

$$Q_{nf} = \dot{m}_{nf} Cp_{nf} (T_{out} - T_{in})_{nf} \tag{2}$$

where Q_{nf} is the heat transfer rate of the nanofluid and $\dot{m}_{nf}$ is the mass flow rate of the nanofluid.

The average heat transfer rate is defined as follows:

$$Q_{ave} = \frac{Q_w + Q_{nf}}{2} \tag{3}$$

where Q_{ave} is the average heat transfer rate between the hot water and the nanofluid.

In the experiments, only the data that satisfy the energy balance conditions ($|Q_w - Q_{nf}|/Q_{ave}$ are less than 3%), are considered in the analysis.

Finally, the Nusselt numbers of the nanofluid are computed from the following equations.

$$h_{nf} = \frac{q_{ave}}{T_{wall} - T_{nf}} \tag{4}$$

$$\mathrm{Nu}_{nf} = \frac{h_{nf} D}{k_{nf}} \tag{5}$$

where h_{nf} is the heat transfer coefficient of the nanofluid, q_{ave} is the average heat flux between the hot water and the nanofluid, T_{wall} is the average temperature of the wall, T_{nf} is the bulk temperature of the nanofluid, Nu_{nf} is the Nusselt number of the nanofluid, D is the inner diameter of the test tube and k_{nf} is the thermal conductivity of the nanofluid.

5. Thermophysical properties of nanofluid

The well-known correlations for calculating the thermophysical properties of the nanofluid which are often cited by a number of researchers are expressed as follows:

5.1. Thermal conductivity

One well-known equation for computing the thermal conductivity of nanofluid is the Hamilton and Crosser [11] model, which is expressed in the following form:

$$k_{nf} = \left[\frac{k_p + (n-1)k_w - (n-1)\phi(k_w - k_p)}{k_p + (n-1)k_w + \phi(k_w - k_p)}\right] k_w \tag{6}$$

$$n = 3/\psi \tag{7}$$

where n is the empirical shape factor and ψ is the sphericity, defined as the ratio of the surface area of a sphere (with the same volume as the given particle) to the surface area of the particle. The sphericity is 1 and 0.5 for the spherical and cylindrical shapes, respectively. Moreover, ϕ is the volume concentration, k_{nf} is the thermal conductivity of the nanofluid, k_p is the thermal conductivity of the nanoparticles and k_w is the thermal conductivity of the base fluid.

Moreover, the thermal conductivity of the nanofluids is calculated from Yu and Choi [20], which is expressed in the following form

$$k_{nf} = \left[\frac{k_p + 2k_w + 2(k_p - k_w)(1+\beta)^3\phi}{k_p + 2k_w - (k_p - k_w)(1+\beta)^3\phi}\right] k_w \tag{8}$$

An alternative formula for calculating the thermal conductivity was introduced by the Wasp [36] model, which is defined as follows:

$$k_{nf} = \left[\frac{k_p + 2k_w - 2\phi(k_w - k_p)}{k_p + 2k_w + \phi(k_w - k_p)}\right] k_w \tag{9}$$

where β is the ratio of the nanolayer thickness to the original particle radius. Normally $\beta = 0.1$ is used to calculate the thermal conductivity of the nanofluid. For spherical particles, the results given by the Wasp model coincide with those of the H–C model.

Murshed et al. [37] introduced the Bruggeman model [38] for calculating the thermal conductivity of nanofluids which is expressed as follows:

$$k_{nf} = \frac{1}{4}[(3\phi - 1)k_p + (2 - 3\phi)k_w] + \frac{k_w}{4}\sqrt{\Delta} \tag{10}$$

$$\Delta = \left[(3\phi - 1)^2(k_p/k_w)^2 + (2 - 3\phi)^2 + 2(2 + 9\phi - 9\phi^2)(k_p/k_w)\right] \tag{11}$$

Finally, Timofeeva et al. [39] introduced the effective medium theory for computing the thermal conductivity of nanofluids, which is defined as follows:

$$k_{nf} = [1 + 3\phi]k_w \tag{12}$$

5.2. Viscosity

Brinkman [12] suggested an equation to calculate the viscosity of the suspension, which is defined as follows:

$$\mu_{nf} = \frac{1}{(1-\phi)^{2.5}}\mu_w \tag{13}$$

In addition, Wang et al. [14] proposed a model to predict the viscosity of nanofluids which is expressed as:

$$\mu_{nf} = (1 + 7.3\phi + 123\phi^2)\mu_w \tag{14}$$

Drew and Passman [40] suggested the well-known Einstein's equation for calculating viscosity, which is applicable to spherical particles in volume fractions less than 5.0 vol.% and is defined as follows:

$$\mu_{nf} = (1 + 2.5\phi)\mu_w \tag{15}$$

Furthermore, Batchelor [41] introduced a correlation for calculating the viscosity of nanofluids with spherical shape nanoparticles which is defined as:

$$\mu_{nf} = (1 + 2.5\phi + 6.2\phi^2)\mu_w \tag{16}$$

where μ_{nf} is the viscosity of the nanofluid and μ_w is the viscosity of the base fluid.

5.3. Density and specific heat

The density and specific heat of the nanofluids are calculated by use of the Pak and Cho [5] correlations, which are defined as follows:

$$\rho_{nf} = \phi\rho_p + (1-\phi)\rho_w \tag{17}$$

and

$$Cp_{nf} = \phi Cp_p + (1-\phi)Cp_w \tag{18}$$

An alternative equation to compute the specific heat of the nanofluids was suggested by Xuan and Roetzel's equation [42], which is defined as

$$(\rho Cp)_{nf} = \phi(\rho Cp)_p + (1-\phi)(\rho Cp)_w \tag{19}$$

where Cp_{nf} is the specific heat of the nanofluid, Cp_p is the specific heat of the nanoparticles, and Cp_w is the specific heat of the base fluid.

Up to now, there are several models proposed for calculating the relevant properties. However, only a few correlations have been favorably accepted and often cited by a number of researchers.

For thermal conductivity of nanofluids, the models used in the present study are very famous. These models were developed based on theoretical investigation and always used and cited by many researchers. These models can be used to estimate the thermal conductivity of nanofluids. .

Similarly, the viscosity of nanofluids can be calculated using different existing formulas obtained for two-phase mixtures. The first well-known equation is the Einstein's equation. This relation has been found to be valid for particle concentration less than 2 vol.%. Then, this equation was extended to a more generalized form by Brinkman [12]. Moreover, one more well-known relation for calculating the viscosity of nanofluid was proposed by Bachelor [41], in 1977. The effect of Brownian motion of particles in a statistically homogeneous suspension was taken into account in this

model and this model was often cited by a number of researchers as well as Wang et al. [14] equation.

For the specific heat of the nanofluid, up to now, there are only two well-known models to calculate the specific heat of nanofluids which are Pak and Cho model [5] and Xuan and Roetzel model [42], respectively. The first model is based on the volume fraction whereas the second model is based on heat capacity concept. Both models are often cited by a number of researchers for calculating the specific heat of nanofluid.

As aforementioned, it is clearly seen that the correlations used in this study are based on the results published in open literature and often used and cited by many outstanding researchers. That is the reason for choosing these models to calculate the thermophysical properties of nanofluids for comparing with the experimental data.

The properties of the nanofluid shown in the above equations are calculated from water and nanoparticles at average bulk temperature.

6. Results and discussion

The measurement results of the thermal conductivity and viscosity of the nanofluids were expressed in a previous paper by the author [35]. In respect of the heat transfer performance, TiO_2 nanoparticles dispersed in water at 0.2%, 0.6%, and 1.0% by volume

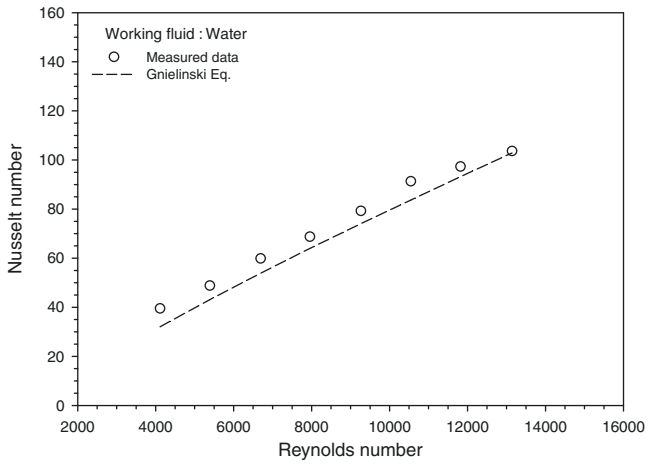

Fig. 3. Comparison between measured heat transfer coefficient and that calculated from Gnielinski equation [39].

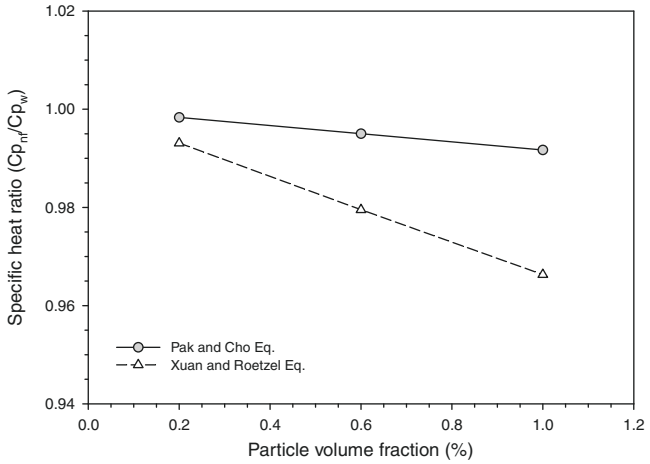

Fig. 4. Comparison of the specific heat equations of nanofluid as a function of particle volume fraction.

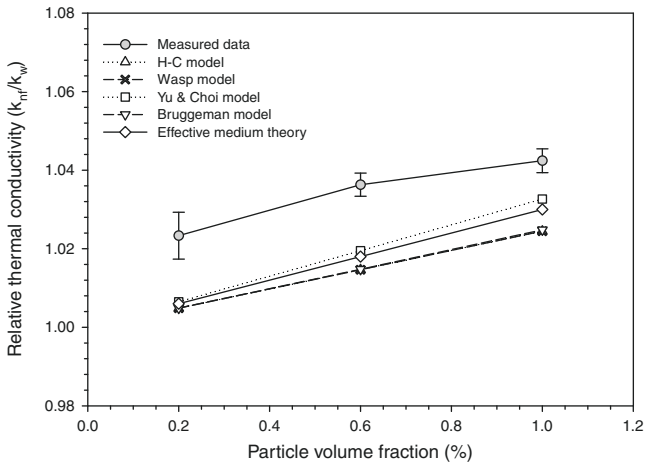

Fig. 5. Comparison of the relative thermal conductivity of nanofluids between measured data and the well-known correlations.

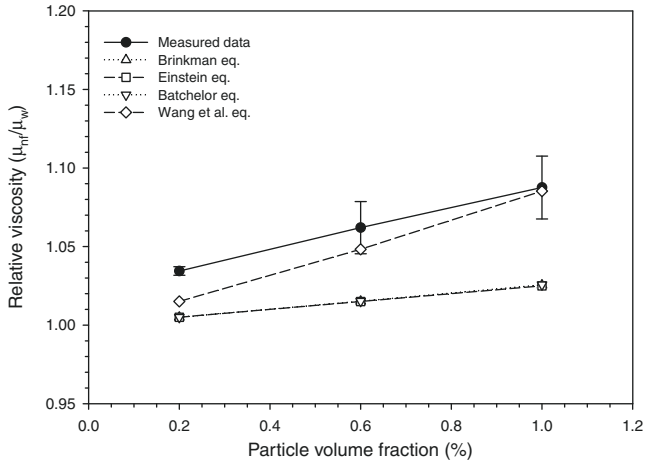

Fig. 6. Comparison of the relative viscosity of nanofluid between measured data and the well-known correlations.

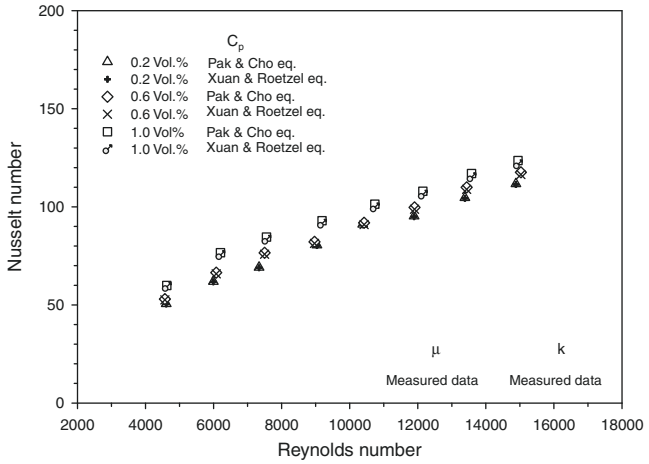

Fig. 7. Effect of the specific heat equations on the prediction of the Nusselt number of nanofluids.

are used to investigate the Nusselt number of the nanofluid. However, before measuring the Nusselt number of the nanofluids, the pure water is used as the test fluid to estimate the reliability and accuracy of the experimental system. The results of the experimental Nusselt number are compared with those obtained from the Gnielinski equation [43], which is defined as follows:

$$\mathrm{Nu} = \frac{(f/8)(\mathrm{Re} - 1000)\mathrm{Pr}}{1 + 12.7(f/8)^{0.5}(\mathrm{Pr}^{2/3} - 1)} \tag{20}$$

where Nu is the Nusselt number, Re is the Reynolds number, Pr is the Prandtl number and f is the friction factor.

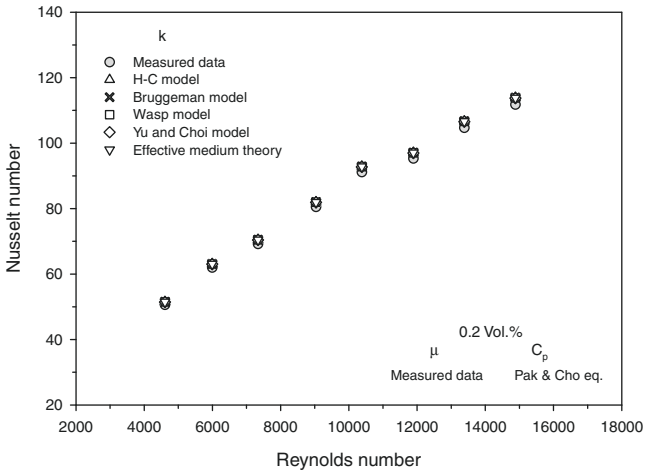

(a) at 0.2 vol.%

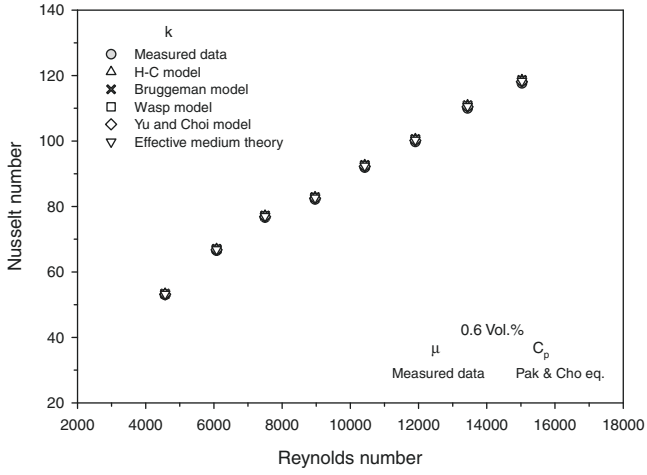

(b) at 0.6 vol.%

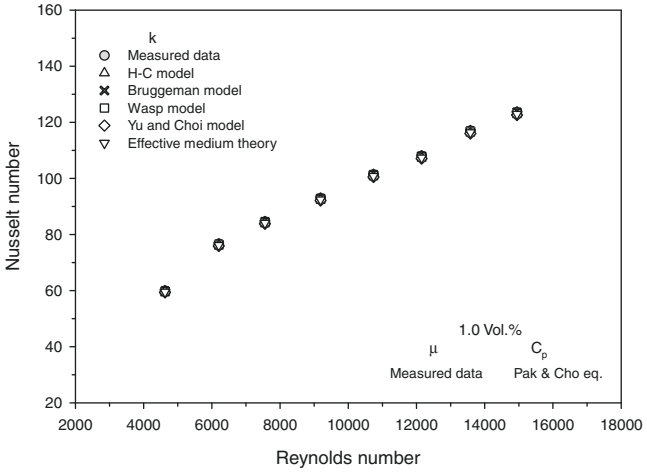

(c) at 1.0 vol.%

Fig. 8. Effect of the thermal conductivity value of nanofluid on the prediction of the Nusselt number of nanofluids.

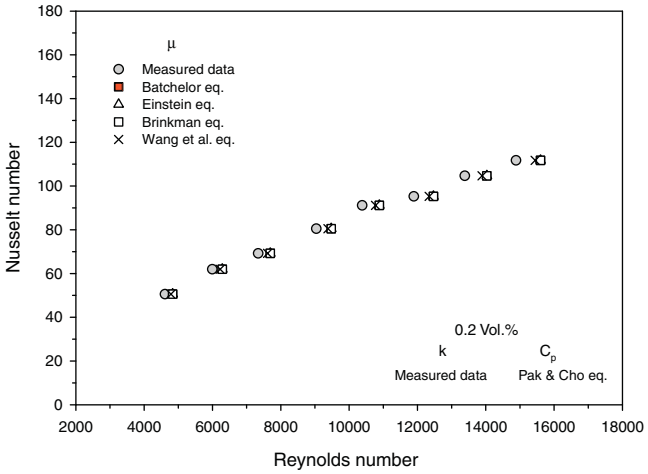

(a) at 0.2 vol.%

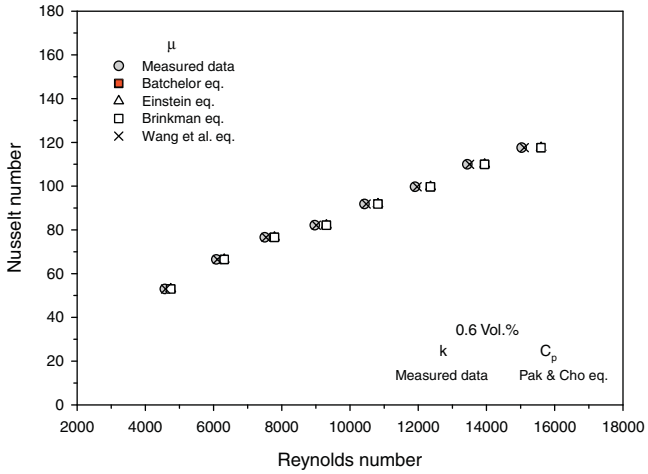

(b) at 0.6 vol.%

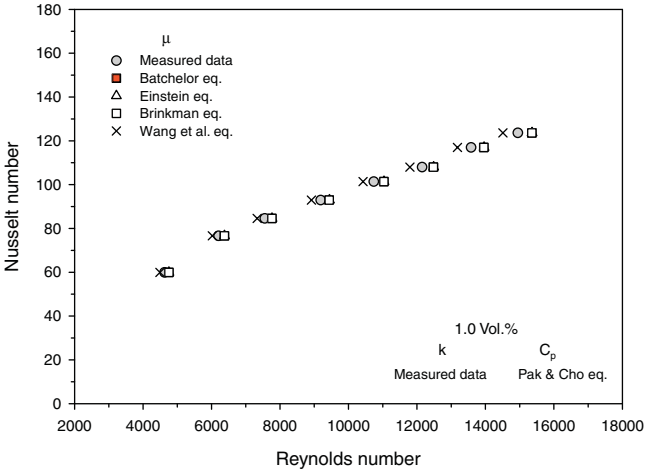

(c) at 1.0 vol.%

Fig. 9. Effect of the viscosity value of nanofluid on the describing of the Nusselt number of nanofluids.

The friction factor can be calculated from Colebrook's equation [44] as follows:

$$\frac{1}{\sqrt{f}} = -2.0\log\left(\frac{\varepsilon/D}{3.7} + \frac{2.51}{\mathrm{Re}\sqrt{f}}\right) \quad (21)$$

where ε is the roughness of the test tube.

As shown in Fig. 3, the measured Nusselt number coincided well with the calculated values for pure water.

Fig. 4 shows the specific heat ratio (Cp_{nf}/Cp_w) as a function of the particle volume concentrations. The figure shows that the two different specific heat equations give significantly different values of the specific heat ratio. Similarly, Figs. 5 and 6 show the variation between relative thermal conductivity (k_{nf}/k_w) and viscosity (μ_{nf}/μ_w) of nanofluids as a function of the particle volume concentrations, respectively. As shown in Fig. 5, it is clearly seen that all of the well-known correlations for computing the thermal conductivity of nanofluids give results that are remarkably lower than those given by the measured data. The results showed that the Yu and Choi equation gives results closest to the measured data in comparison to the H–C model, Wasp model, Bruggeman model, and even effective medium theory. Similar to the thermal conductivity, Fig. 6 shows that the Wang et al. equation for calculating the viscosity of nanofluids give results closest to the measured data in comparison to the Brinkman equation, Einstein equation, and Batchelor equation.

As mentioned above, it is evident that the various models and the measured data give difference results for evaluating the thermophysical properties of nanofluids. The following figures illustrate how big the difference is between the use of the measured data and use of the various models to describe the heat transfer performance of the nanofluids.

Fig. 7 shows that the Nusselt number increases with increases in the Reynolds number as well as in the particle volume concentrations. The results also indicated that the specific heat models have no significant effect on the prediction of the Nusselt number. Fig. 8a–c shows the effect of the thermal conductivity value on the calculation of the Nusselt number of nanofluids for particle volume concentrations of 0.2%, 0.6%, and 1.0%, respectively. The results showed that the different values of thermal conductivity give similar results for evaluating the Nusselt number of nanofluids. Similarly to the effect of the thermal conductivity, Fig. 9a–c shows the effect of the viscosity value on the description of the Nusselt number of nanofluid. The results indicated that the different values of viscosity give similar results in evaluating the Nusselt number of the nanofluids. However, the results also showed that use of the viscosity model to describe the Nusselt number of nanofluids gives different values compared with use of the measured data, by about 2–3%. In addition, the calculated values from the Wang et al. equation are closer to the results of the measured data than to the calculated values using the other correlations.

Since the models for determining various properties of nanofluids were developed from theoretical basis, it may be expected that the effect of model predictions on the results for the use of another nanofluids should give the same results.

7. Conclusions

The discrepancies between use of the measured data and use of the well-known correlations of the thermal conductivity and viscosity of nanofluid to describe the Nusselt numbers of nanofluids were investigated. TiO_2–water nanofluids with particle volume concentrations of 0.2%, 0.6%, and 1.0% flowing under turbulent flow conditions were tested. The results showed that all of the well-known correlations underestimate the thermal conductivity and viscosity of nanofluids compared with the measured data. Moreover, the different models gave different results. However, the use of the thermophysical models for calculation of the Nusselt number of nanofluids gave differences of a few percentage points when compared with the measured data. Due to lack of measured data on the thermophysical properties of the nanofluids, the use of the Yu and Choi model for thermal conductivity and the Wang et al. equation for viscosity to describe the Nusselt number of the nanofluids gave good agreement with the use of the measured data. Finally, measurement of the thermophysical properties of nanofluids is an important way to address the transport behaviour of nanofluids.

Acknowledgments

The authors would like to express their appreciation to the Thailand Research Fund (TRF) for providing financial support for this study. The authors also wish to thank DEGUSSA AG, Germany for the valuable donation of the nanoparticles used in the present study.

References

[1] S.U.S. Choi, Enhancing thermal conductivity of fluids with nanoparticle, ASME Fluids Engineering Division (FED) 231 (1995) 99-105.
[2] V. Trisaksri, S. Wongwises, Critical review of heat transfer characteristics of the nanofluids, Renewable and Sustainable Energy Reviews 11 (3) (2007) 512–523.
[3] W. Duangthongsuk, S. Wongwises, A critical review of convective heat transfer of nanofluids, Renewable and Sustainable Energy Reviews 11 (2007) 797–817.
[4] X.Q. Wang, A.S. Mujumdar, Heat transfer characteristics of nanofluids: a review, International Journal of Thermal Sciences 46 (2007) 1–19.
[5] B.C. Pak, Y.I. Cho, Hydrodynamic and heat transfer study of dispersed fluids with submicron metallic oxide particles, Experimental Heat Transfer 11 (1998) 151–170.
[6] H. Masuda, A. Ebata, K. Teramae, N. Hishinuma, Alteration of thermal conductivity and viscosity of liquid by dispersing ultra-fine particles (dispersion of Al_2O_3, SiO_2 and TiO_2 ultra-fine particles), Netsu Bussei (Japan) 7 (4) (1993) 227–233.
[7] Q. Li, Y. Xuan, Convective heat transfer and flow characteristics of Cu–water nanofluid, Science in China E 45 (2002) 408–416.
[8] Y. Xuan, Q. Li, Investigation on convective heat transfer and flow features of nanofluids, ASME Transactions, Journal of Heat Transfer 125 (2003) 151–155.
[9] D. Wen, Y. Ding, Experimental investigation into convective heat transfer of nanofluids at the entrance region under laminar flow conditions, International Journal of Heat Mass Transfer 47 (2004) 5181–5188.
[10] A. Ali, K. Vafai, A.R.A. Khaled, Analysis of heat and mass transfer between air and falling film in a cross flow configuration, International Journal of Heat Mass Transfer 47 (2004) 743–755.
[11] R.L. Hamilton, O.K. Crosser, Thermal conductivity of heterogeneous two-component systems, Industrial & Engineering Chemistry Fundamentals 1 (3) (1962) 187–191.
[12] H.C. Brinkman, The viscosity of concentrated suspensions and solution, Journal of Chemical Physics 20 (1952) 571–581.
[13] G. Roy, C.T. Nguyen, P.R. Lajoie, Numerical investigation of laminar flow and heat transfer in a radial flow cooling system with the use of nanofluids, Superlattices and Microstructures 35 (2004) 497–511.
[14] X. Wang, X. Xu, S.U.S. Choi, Thermal conductivity of nanoparticles–fluid mixture, Journal of Thermophysics Heat Transfer 13 (4) (1999) 474–480.
[15] A. Ali, K. Vafai, An Investigation of heat and mass transfer between air and desiccant film in an inclined parallel and counter flow channels, International Journal of Heat Mass Transfer 47 (2004) 1745–1760.
[16] Y. Yang, Z.G. Zhang, E.A. Grulke, W.B. Anderson, G. Wu, Heat transfer properties of nanoparticle-in-fluid dispersions (nanofluids) in laminar flow, International Journal Heat Mass Transfer 48 (6) (2005) 1107–1116.
[17] Y. Ding, H. Alias, D. Wen, R.A. Williams, Heat transfer of aqueous suspensions of carbon nanotubes (CNT nanofluids), International Journal Heat Mass Transfer 49 (1–2) (2005) 240–250.
[18] S.Z. Heris, S.G. Etemad, M.N. Esfahany, Experimental investigation of oxide nanofluids laminar flow convective heat transfer, International Communication in Heat and Mass Transfer 33 (2006) 529–535.
[19] S.Z. Heris, M.N. Esfahany, S.G. Etemad, Experimental investigation of convective heat transfer of Al_2O_3/water nanofluid in circular tube, International Journal of Heat Fluids Flow 28 (2) (2007) 203–210.
[20] W. Yu, S.U.S. Choi, The role of interfacial layers in the enhanced thermal conductivity of nanofluids: a renovated Maxwell model, Journal of Nanoparticle Research 5 (2003) 167–171.
[21] Y. He, Y. Jin, H. Chen, Y. Ding, D. Cang, H. Lu, Heat transfer and flow behavior of aqueous suspensions of TiO_2 nanoparticles (nanofluids) flowing upward through a vertical pipe, International Journal Heat Mass Transfer 50 (2007) 2272–2281.

[22] C.T. Nguyen, G. Roy, C. Gauthier, N. Galanis, Heat transfer enhancement using Al_2O_3–water nanofluid for electronic liquid cooling system, Applied Thermal Engineering 28 (2007) 1501–1506.
[23] C.H. Chon, K.D. Kihm, S.P. Lee, S.U.S. Choi, Empirical correlation finding the role of temperature and particle size for nanofluid (Al_2O_3) thermal conductivity enhancement, Applied Physics Letters 87 (15) (2005) 153107–153110.
[24] G.H. Ko, K. Ho, K. Lee, D.S. Kim, C. Kim, Y. Sohn, M. Choi, An experimental study on the pressure drop of nanofluids containing carbon nanotubes in the horizontal tube, International Journal Heat Mass Transfer 50 (2007) 4749–4753.
[25] R. Chein, J. Chuang, Experimental microchannel heat sink performance studies using nanofluids, International Journal of Thermal Sciences 46 (1) (2007) 57–66.
[26] W. Duangthongsuk, S. Wongwises, Heat transfer enhancement and pressure drop characteristics of TiO_2–water nanofluid in a double-tube counter flow heat exchanger, International Journal of Heat Mass Transfer 52 (2009) 2059–2067.
[27] A.K. Santra, S. Sen, N. Chakraborty, Study of heat transfer due to laminar flow of copper–water nanofluid through two isothermally heated parallel plates, International Journal of Thermal Sciences 48 (2009) 391–400.
[28] H.E. Patel, T. Pradeep, T. Sundararajan, A. Dasgupta, N. Dasgupta, S.K. Das, A micro-convection model for thermal conductivity of nanofluid, Pramana Journal of Physics 65 (2005) 863–869.
[29] V. Trisaksri, S. Wongwises, Nucleate pool boiling heat transfer of TiO_2-R141b nanofluids, International Journal of Heat Mass Transfer 52 (2009) 1582–1588.
[30] S. Lee, S.U.S. Choi, S. Li, J.A. Eastman, Measuring thermal conductivity of fluids containing oxide nanoparticles, Journal of Heat Transfer 121 (1999) 280–289.
[31] B.X. Wang, L.P. Zhou, X.F. Peng, A fractal model for predicting the effective thermal conductivity of liquid with suspension of nanoparticles, International Journal of Heat Mass Transfer 46 (2003) 2665–2672.
[32] J. Koo, C. Kleinstreuer, A new thermal conductivity model for nanofluids, Journal of Nanoparticle Research 6 (2004) 577–588.
[33] R.D. Mansour, N. Galanis, C.T. Nguyen, Effect of uncertainties in physical properties on forced convection heat transfer with nanofluids, Applied Thermal Engineering 27 (1) (2007) 240–249.
[34] W. Duangthongsuk, S. Wongwises, Effect of thermophysical properties models on the prediction of the convective heat transfer coefficient for low concentration nanofluid, International Communication in Heat and Mass Transfer 35 (2008) 1320–1326.
[35] W. Duangthongsuk, S. Wongwises, Measurement of temperature-dependent thermal conductivity and viscosity of TiO_2–water nanofluids, Experimental Thermal and Fluid Science 33 (2009) 706–714.
[36] F.J. Wasp, Solid–Liquid Slurry Pipeline Transportation, Trans Tech, Berlin, 1977.
[37] S.M.S. Murshed, K.C. Leong, C. Yang, Enhanced thermal conductivity of TiO_2–water based nanofluids, International Journal of Thermal Sciences 44 (2005) 367–373.
[38] D.A.G. Bruggeman, Berechnung verschiedener physikalischer konstanten von heterogenen substanzen. I. Dielektrizitatskonstanten und Leitfahigkeiten der Mischkorper aus Isotropen Substanzen, Annalen der Physik 14 (1935) 636–679.
[39] E.V. Timofeeva, A.N. Gavrilov, J.M. McCloskey, Y.V. Tolmachev, Thermal conductivity and particle agglomeration in alumina nanofluids: experiment and theory, Physical Review 76 (2007) 061203.
[40] D.A. Drew, S.L. Passman, Theory of Multi Component Fluids, Springer, Berlin, 1999.
[41] G.K. Batchelor, The effect of Brownian motion on the bulk stress in a suspension of spherical particles, Journal of Fluid Mechanics 83 (1) (1977) 97–117.
[42] Y. Xuan, W. Roetzel, Conceptions for heat transfer correlation of nanofluids, International Journal of Heat Mass Transfer 43 (2000) 3701–3707.
[43] V. Gnielinski, New equations for heat and mass transfer in turbulent pipe and channel flow, International Chemical Engineering 16 (1976) 359–368.
[44] C.F. Colebrook, Turbulent flow in pipes with particular reference to the transition between the smooth and rough pipe laws, Journal of the Institution of Civil Engineers, London 11 (1939) 133–156.

International Journal of Heat and Mass Transfer 53 (2010) 2924–2931

Contents lists available at ScienceDirect

International Journal of Heat and Mass Transfer

journal homepage: www.elsevier.com/locate/ijhmt

The effects of corrugation pitch on the condensation heat transfer coefficient and pressure drop of R-134a inside horizontal corrugated tube

Suriyan Laohalertdecha [a,b], Somchai Wongwises [b,*]

[a] The Joint Graduate School of Energy and Environment (JGSEE), King Mongkut's University of Technology Thonburi, Bangmod, Bangkok 10140, Thailand
[b] Fluid Mechanics, Thermal Engineering and Multiphase Flow Research Lab. (FUTURE), Department of Mechanical Engineering, King Mongkut's University of Technology Thonburi, Bangmod, Bangkok 10140, Thailand

ARTICLE INFO

Article history:
Received 15 April 2009
Received in revised form 10 December 2009
Accepted 10 December 2009
Available online 1 March 2010

Keywords:
Condensation
Heat transfer coefficient
Pressure drop
Smooth tube
Corrugated tube

ABSTRACT

The heat transfer coefficient and pressure drop of R-134a inside a horizontal smooth tube and corrugated tubes are experimentally investigated. The test section is a 2.0 m long counter-flow concentric double tube heat exchanger with refrigerant flowing in the inner tube and cooling water flowing in the annulus. A smooth tube and corrugated tubes having inner diameters of 8.7 mm are used as an inner tube. The corrugation pitches are 5.08, 6.35, and 8.46 mm, respectively. The corrugation depth of all corrugated tubes is fixed at 1.5 mm. The outer tube is made from smooth copper tube having an inner diameter of 21.2 mm. The test runs are performed at the saturation temperatures of 40, 45, and 50 °C, heat fluxes of 5 and 10 kW/m^2, and mass fluxes ranging from 200 to 700 kg/m^2 s. The results obtained from the corrugated tubes are compared with that of the smooth tube. It is found that the corrugation pitches have a significant effect on the heat transfer coefficient and pressure drop augmentations.

1. Introduction

Heat exchangers can be improved by using various enhancement techniques. In general, enhancement techniques can be divided into two groups: namely active and passive techniques. The active technique requires external forces such as an electric field or acoustic or surface vibration, whereas the passive technique requires special surface geometries such as a rough surface, extended surface, or fluid additives. Both active and passive techniques were used by several researchers over a century ago to increase the heat transfer rate in heat exchangers [1].

Micro-fin tubes have been successfully implemented in the air-conditioning and refrigeration industries for effectively tube-side performance. This success is because of their ability to significantly improve the heat transfer coefficient [2–5] with only a moderate increase of the friction penalty.

The corrugated tube is a kind of tube having corrugation on the surface that is expected to increase the heat transfer coefficient with a very small increase of the friction penalty, by mixing the fluid boundary layers and also by limiting the growth of fluid boundary layers close to the heat transfer surfaces. Corrugated tubes are sometimes chosen in the design of industrial shell-and-tube heat exchangers. The size of these heat exchangers can be reduced considerably by using corrugated tubes instead of smooth tubes. Heat transfer enhancement using corrugated tubes has been studied by several researchers as shown in Table 1. The heat transfer and flow characteristics of working fluid in enhanced tubes have been studied by a number of researchers, and some examples of the most productive studies are described below.

Dong et al. [6] studied the turbulent friction and heat transfer characteristics of four spirally corrugated tubes with various geometrical parameters. Their results indicated that the spirally corrugated ribs have an effect on the enhancement of heat transfer but not as large as the effect on the increases in friction.

Barba et al. [7] presented the experimental results of heat transfer and pressure drop in corrugated tube, which is used in the chemical and food industries for single-phase flow at moderate Reynolds numbers of $100 < Re < 800$. The working fluid used in their study is ethylene glycol, which is a highly viscous Newtonian fluid. The inside Nusselt number in the corrugated tube is improved very significantly in comparison to those in the smooth wall, while the friction factor increases up to a factor of 2.45–1.83. Based on the experimental data, Nusselt number and friction factor correlations are proposed for the periodically fully developed region.

Rainieri and Pagliarini [8] studied the thermal performances of corrugated tubes in order to increase convective heat transfer. Axial symmetrical and helical corrugated tubes with different pitch values were considered. The tests were conducted at Reynolds numbers ranging between 90 and 800. The results showed that the helical corrugation induces significant swirl components.

* Corresponding author. Tel.: +662 470 9115; fax: +662 470 9111.
E-mail address: somchai.won@kmutt.ac.th (S. Wongwises).

0017-9310/$ - see front matter © 2010 Published by Elsevier Ltd.
doi:10.1016/j.ijheatmasstransfer.2010.01.037

Nomenclature

A	surface area of the test section (m^2)
c_p	specific heat at constant pressure (J/kg K)
D	diameter (m)
e	corrugation depth (mm)
G	mass flux (kg/m^2 s)
h	heat transfer coefficient (W/m^2 K)
i	enthalpy (J/kg)
k	thermal conductivity (W/m K)
L	length of the test tube (m)
$LMTD$	logarithmic mean temperature difference
m	mass flow rate (kg/s)
Nu	Nusselt number
p	corrugation pitch (mm)
Pr	Prandtl number
Q	heat transfer rate (W)
Re	Reynolds number
q''	heat flux (W/m^2)
T	temperature (°C)
x	average quality
X	Martinelli parameter

Greek letters

α	void fraction
β	helix angle (deg)
ε	relative roughness (m)
ρ	density (kg/m^3)
ϕ_l^2	two-phase multiplier
μ	dynamic viscosity (Pa s)
ΔP	pressure drop (Pa/m)

Subscripts

a	acceleration
avg	average
f	friction factor
in	inlet
i	inside
l	liquid
out	outlet
o	outside
ph	pre-heater
ref	refrigerant
sat	saturation
TS	test section
v	vapor
w	water
$wall$	tube wall

Among all these previous studies, the most productive studies have continually been performed by Zimparov [9]. Extended performance evaluation criteria for enhanced heat transfer surfaces at constant wall temperature were studied. Zimparov [10] presented heat transfer and isothermal friction pressure drop results of two three-start and two single-start spirally corrugated tubes combined with five twisted tape inserts with different relative pitches. The friction factors and inside heat transfer coefficients obtained from these tubes were higher than those obtained from the smooth tube. Moreover, Zimparov [11,12] applied a simple mathematical model for predicting the friction factors and heat transfer coefficients in a spirally corrugated configuration combined with a twisted tape insert flowing in the turbulent flow regime. The calculated friction factors and heat transfer coefficients were compared with the experimental data. The results showed that the agreement between predicted and experimental data is fairly good.

Vicente et al. [13,14] experimentally studied the mixed convection heat transfer and isothermal pressure drop in corrugated tubes for laminar, transition, and turbulent flow regions. At a high Rayleigh number, the Nusselt number obtained from these tubes is 30% higher than that obtained from the smooth tube. The friction factors of the corrugated tube were between 5% and 25% higher than those of the smooth tube.

Naphon et al. [15] studied the heat transfer and pressure drop characteristics of water flowing in horizontal double pipes with helical ribs. Nine test sections with different characteristic parameters were tested, namely helical rib height to diameter h/d = 0.12, 0.15, and 0.19 and helical rib pitch to diameter p/d = 1.05, 0.78, and 0.63. It was found that the helical ribs have a significant effect on the heat transfer and pressure drop augmentations. Both the proposed correlations for the heat transfer coefficient and friction factor give good agreement with the present data to within 15%.

Targanski and Cieslinski [16] studied the evaporation for the pure R407C and R407C/oil mixtures in two smooth tubes and two enhanced tubes, experimentally. The advantages of the micro-fin tube and corrugated tube were quantified and discussed. Test runs were performed as follows: inlet and outlet vapor quality were set at 0 and 0.7, respectively, and mass flux density ranged from 250 to 500 kg/m^2 s. The experiments were conducted at an average saturation temperature of 0 °C. It was found that the corrugated tube and micro-fin tube had a significant effect on the heat transfer coefficient and pressure drop augmentations.

Bilen et al. [17] experimentally investigated the heat transfer and friction characteristics of an air flow in different grooved tubes under turbulent flow regime. Reynolds numbers ranging from 10,000 to 38,000 were tested. The circular, trapezoidal, and rectan-

Table 1
Experimental investigation on the corrugated tube with various working fluid and tube configurations.

Sources	D (mm)	e/D	p/D	β (deg)	Phase
Dong et al. [6]	16.04–22.82	0.0243–0.0398	0.438–0.623	78.8–82.1	Single phase
Barba et al. [7]	14.5	0.103	0.793	45	Single phase
Rainieri and Pagliarini [8]	14	0.107	1.143–4.571	–	Single phase
Zimparov [9]	13.68–13.73	0.0407–0.0569	4.7–15.3	67.4–68	Single phase
Zimparov [10]	13.39–13.65	0.0371–0.0441	2.4–7.7	79.3–82.2	Single phase
Zimparov [11]	12.44–13.90	0.0224–0.0569	7.45–21.17	67.4–90	Single phase
Zimparov [12]	12.44–13.90	0.0224–0.0569	7.45–21.17	67.4–90	Single phase
Vicente et al. [13]	18	0.0239–0.0572	0.608–1.229	68–80	Single phase
Vicente et al. [14]	18	0.0239–0.0572	0.608–1.229	68–80	Single phase
Naphon et al. [15]	8.1	0.12–0.19	0.63–1.05	45	Single phase
Targanski and Cieslinski [16]	8.8	0.0511	0.681	77.75	Two phase
Bilen et al. [17]	36	0.0833	0.333–0.416	90	Single phase

gular grooves were used as the test section. The tube's length-to-diameter ratio was 33. The maximum heat transfer enhancements were up to 63% for the circular groove, 58% for the trapezoidal groove, and 47% for the rectangular groove in comparison with the smooth tube at the given Reynolds number.

In the above literature review, a number of researchers mainly focused on the effects of the corrugation on the heat transfer coefficient and pressure drop of single-phase flows in corrugated tubes. Moreover, although many papers have been published on two-phase flow, only one of these papers concerned the evaporation of refrigerants inside corrugated tube; this was carried out by Targanski and Cieslinski [16]. It can also be noted that most of the works were conducted by employing tubes having inside diameters greater than 10 mm, the data obtained from tubes having inside diameters less than 10 mm are relatively small. As a consequence, the objective of this work is to study the heat transfer coefficient and pressure drop during condensation of R-134a inside horizontal corrugated tubes having inside diameters of 8.7 mm.

2. Experimental apparatus

A schematic diagram of the test apparatus is shown in Fig. 1. The experimental apparatus was designed to determine the heat transfer coefficient and pressure drop of pure R-134a over the length of the test tube. The test loop consists of a test section, refrigeration loop, cooling water flow loops, subcooling loop, and the relevant instrumentation. The objective of the water loop before the test section is to provide controlled inlet quality. The second water loop located in the test section can provide controlled heat output from the test section. The subcooling loop is used to prevent any two-phase flow condition of the refrigerant occurring before it enters the refrigerant pump.

For the refrigeration circulating loop, liquid refrigerant is discharged by a gear pump regulated by an inverter. The refrigerant passes in series through a filter/dryer, sight glass tube, flow meter, and pre-heater and enters the test section. The inlet quality before entering the test section is controlled by the pre-heater. The pre-heater is a spiral counter-flow heat exchanger that supplies energy to provide a controlled inlet quality for vaporization of the refrigerant. Leaving the test section, the refrigerant is then condensed and subcooled by the chilling loop that removes the heat input from the pre-heater and test section, returns from the two-phase refrigerant to a subcooled state, collects later in a receiver, and eventually returns to the refrigerant pump to complete the cycle.

The test section is a horizontal counter-flow double tube heat exchanger. The length of the heat exchanger is 2.0 m. The detailed dimensions of the heat exchanger and the location of the thermocouples can be seen in Fig. 2. Fig. 3 shows a drawing of a helically corrugated tube and nomenclature to describe the geometry. The dimensions of the test section are shown in Table 2.

The inlet temperature of the water is controlled by a thermostat. A differential pressure transducer and thermocouples are installed in the test section to measure the pressure drop and temperature across the test section. The length between pressure taps is 2.5 m. The system pressure of the refrigerant flow is mainly controlled by a low temperature thermostat.

Refrigerant temperature and the tube wall temperatures in the test section are measured by T type thermocouples. A total of 15 thermocouples are soldered at the top, bottom, and side at five points along the tube as shown in Fig. 2. All the temperature measuring devices are well calibrated in a controlled temperature bath using standard precision mercury glass thermometers. The uncertainty of the temperature measurements after considering the data acquisition system is ±0.1 °C. All static pressure taps are mounted

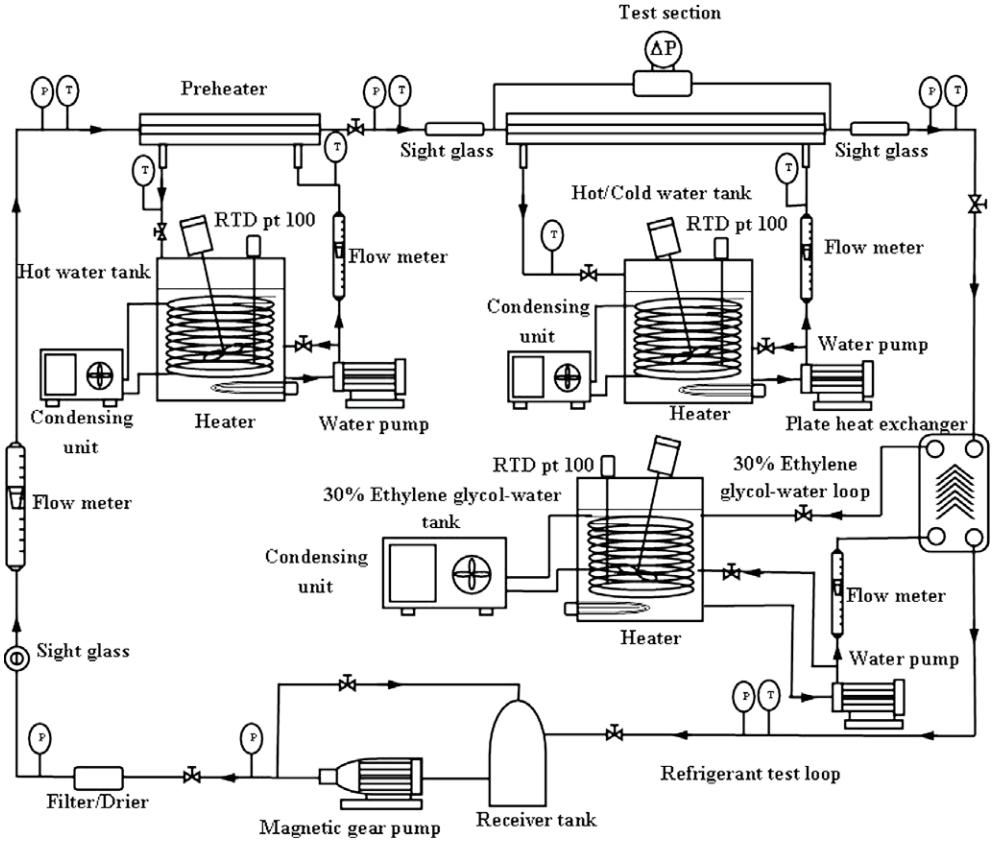

Fig. 1. Schematic diagram of experimental apparatus.

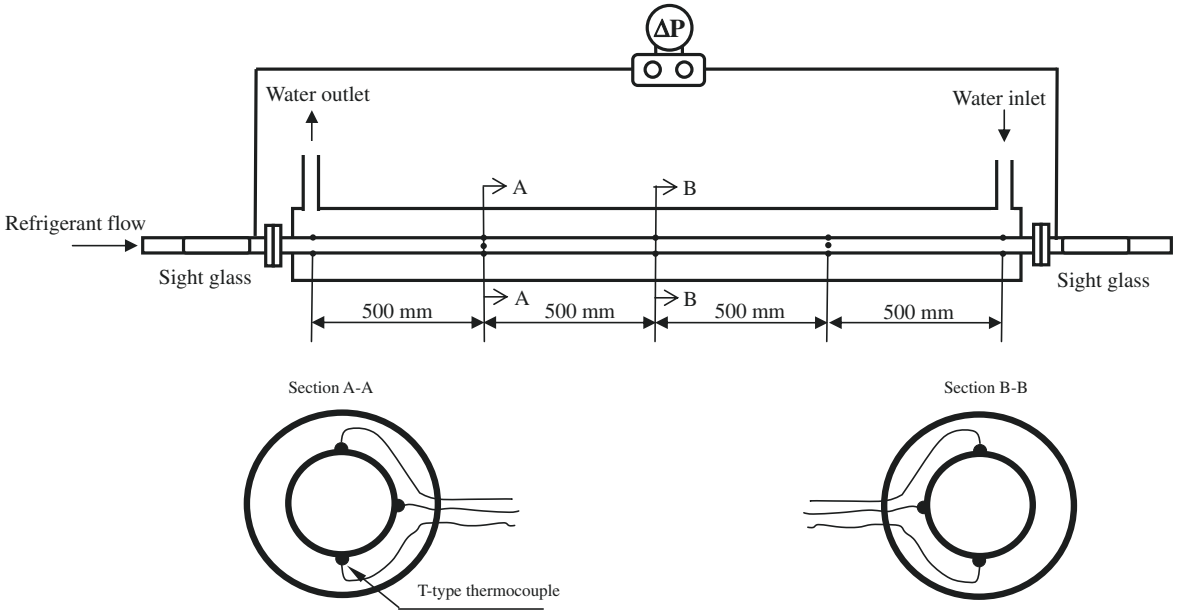

Fig. 2. Schematic diagram of the test section.

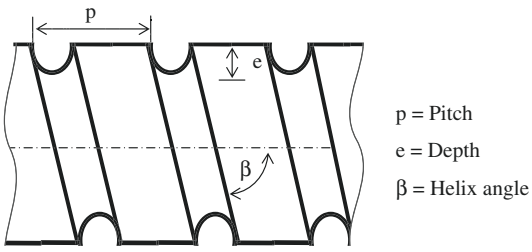

Fig. 3. Drawing of a helically corrugated tube.

in the tube wall. The refrigerant flow meter is a variable area type. The flow meter is specially calibrated in the range of 0.2–3.4 LPM for R-134a by the manufacturer. Also, the differential pressure transducer is calibrated by the manufacturer.

Experiments were conducted with various flow rates of refrigerant, vapor qualities of refrigerant entering the test section, heat fluxes, and temperatures of refrigerant condensing in the test section. In the experiments, the refrigerant flow rate in the test section was controlled by adjusting the speed of the magnetic gear pump. To vary the vapor qualities at the inlet of the test section, the heating water flow rate and the cooling water flow rate were varied by small increments while the refrigerant flow rate was kept constant. The cold water in the test section was circulated by centrifugal pump to remove heat from the refrigerant to the water. During each experiment, the heat transferred from the test section was kept at a desired value. This might be obtained by simultaneously adjusting and controlling the temperature and flow rate of the cold water entering the test section. The system was allowed to approach the steady state before any data were recorded. After stabilization, temperatures on the tube wall, refrigerant temperatures at the locations mentioned above, inlet and outlet temperatures of the heating water and cooling water, and flow rates of heating water, cooling water, and refrigerant were recorded. The pressure drop was measured by a pressure transducer installed between the inlet and outlet of the test section. It was possible to carry out the experiments by increasing the refrigerant flow rate while the saturation temperature in the test section was kept constant. The accuracies of the direct measurements and the uncertainties, which are calculated from the root mean sum square method, are shown in Table 3.

3. Data reduction

The data reduction of the measured results can be summarized as follows:

3.1. The vapor quality at the test section inlet ($x_{TS,in}$)

$$x_{TS,in} = \frac{i_{TS,in} - i_{f@T_{TS,in}}}{i_{fg@T_{TS,in}}} \quad (1)$$

where $i_{f@T_{TS,in}}$ is the enthalpy of the saturated liquid based on the temperature of the test section inlet, $i_{fg@T_{TS,in}}$ is the enthalpy of

Table 2
The dimensions of the test section.

Parameter	Smooth tube	Corrugated tube		
Depth, e (mm)	–	1.5	1.5	1.5
Pitch, p (mm)	–	5.08	6.35	8.46
Helix angle, β (deg)	–	79.47	76.56	74.20
Outside diameter, D_o (mm)	9.52	9.52	9.52	9.52
Inside diameter, D_i (mm)	8.7	8.7	8.7	8.7
Inside tube area, A_i (mm^2)	54,663	82,789	76,773	72,045
Length of the test tube, L (mm)	2000	2000	2000	2000

Table 3
Uncertainties of measured quantities and calculated parameters.

Parameter	Uncertainty
Temperature, T (°C)	±0.1
Pressure drop, ΔP (kPa)	±0.075%
Mass flow rate of refrigerant, m_{ref}	±2% full scale
Mass flow rate of water, m_w	±5% full scale
Heat transfer rate at test section, Q_{TS}	±12.9%
Heat transfer rate at pre-heater, Q_{ph}	±8.5%
Condensation heat transfer coefficient, h	±18.8%
Average quality, x	±5.2%

vaporization based on the temperature of the test section inlet, and $i_{TS,in}$ is the refrigerant enthalpy at the test section inlet given by

$$i_{TS,in} = i_{ph,in} + \frac{Q_{ph}}{m_{ref}} \tag{2}$$

where $i_{ph,in}$ is the inlet enthalpy of the liquid refrigerant before entering the pre-heater, m_{ref} is the mass flow rate of the refrigerant, and Q_{ph} is the heat transfer rate in the pre-heater:

$$Q_{ph} = m_{w,ph} c_{p,w} (T_{w,in} - T_{w,out})_{ph} \tag{3}$$

where $m_{w,ph}$ is the mass flow rate of water entering the pre-heater.

3.2. The vapor quality at the test section outlet ($x_{TS,out}$)

$$x_{TS,out} = \frac{i_{TS,out} - i_{f@T_{TS,out}}}{i_{fg@T_{TS,out}}} \tag{4}$$

where $i_{TS,out}$ is the refrigerant enthalpy at the test section outlet, $i_{f@T_{TS,out}}$ is the enthalpy of the saturated liquid based on the temperature of the test section outlet, and $i_{fg@T_{TS,out}}$ is the enthalpy of vaporization based on the temperature of the test section outlet. As a consequence, the outlet enthalpy of the refrigerant flow is calculated as

$$i_{TS,out} = i_{TS,in} - \frac{Q_{TS}}{m_{ref}} \tag{5}$$

where Q_{TS} is the heat transfer rate in the test section is obtained from

$$Q_{TS} = m_{w,TS} c_{p,w} (T_{w,out} - T_{w,in})_{TS}. \tag{6}$$

where $m_{w,TS}$ is the mass flow rate of the water entering the test section.

3.3. The heat transfer coefficient (h)

$$h = \frac{1}{\left(\frac{1}{U_i}\right) - \left(\frac{1}{2k}\right) D_i \ln\left(\frac{D_o}{D_i}\right) - \left(\frac{D_i}{D_o}\right)\left(\frac{1}{h_o}\right)} \tag{7}$$

where U_i is the overall heat transfer coefficient, k is the thermal conductivity of tube material, and h_o is the outside heat transfer coefficient.

$$U_i = \frac{Q_{TS}}{A_i (LMTD)} \tag{8}$$

where A_i is the inside tube surface and $LMTD$ is the logarithmic mean temperature difference.

$$LMTD = \frac{\Delta T_1 - \Delta T_2}{\ln\left(\frac{\Delta T_1}{\Delta T_2}\right)} \tag{9}$$

$$\Delta T_1 = T_{ref,in} - T_{w,out} \tag{10}$$

$$\Delta T_2 = T_{ref,out} - T_{w,in} \tag{11}$$

where $T_{w,in}$ and $T_{w,out}$ denote the inlet and outlet temperatures of the water on the annulus. $T_{ref,in}$ and $T_{ref,out}$ are the inlet and outlet refrigerant temperatures.

Average outside heat transfer coefficient is calculated as

$$h_o A_o = \frac{Q_{TS}}{T_{wall,avg} - T_{w,avg}} \tag{12}$$

where A_o is the outside test tube surface, $T_{wall,avg}$ is the average wall temperature, and $T_{w,avg}$ is the average cooling water temperature flowing inside annulus.

3.4. The frictional pressure drop (ΔP_f)

The total pressure drop, ΔP_{total}, is expressed as the sum of the two different components, as follows:

$$\Delta P_{\text{total}} = \Delta P_f + \Delta P_a \tag{13}$$

The two terms on the right-hand side represent the frictional pressure drop (ΔP_f) and accelerational pressure drop (ΔP_a). The accelerational pressure drop, ΔP_a, was proposed by Tran [18]:

$$\Delta P_a = G^2 \left(\left(\frac{x_{out}^2}{\rho_v \alpha_{out}} + \frac{(1-x_{out})^2}{\rho_l (1-\alpha_{out})} \right) - \left(\frac{x_{in}^2}{\rho_v \alpha_{in}} + \frac{(1-x_{in})^2}{\rho_l (1-\alpha_{in})} \right) \right) \tag{14}$$

where α is the void fraction and is presented by Zivi's correlation [19] as follows:

$$\alpha = \left(1 + \frac{(1-x)}{x} \left(\frac{\rho_v}{\rho_l} \right)^{\frac{2}{3}} \right)^{-1} \tag{15}$$

The frictional pressure drop, ΔP_f, can be obtained by subtracting the accelerational pressure drop from the total measured pressure drop.

4. Results and discussion

In the present study, the effects of corrugation pitch on the condensation heat transfer coefficient and pressure drop of R-134a inside horizontal corrugated tubes are experimentally investigated. Before measuring the two-phase heat transfer and pressure drop, a single-phase heat transfer test is first conducted to check the energy balance in the test section. The results indicate that the energy balance between the cold water and the refrigerant is within 10% for all runs. This ensures that the heat loss from the test section is rather small and the test section is appropriate for the measurement.

To check the suitability of the above experimental system for the present measurement, the single-phase liquid R-134a heat transfer data are measured first and compared with the well known correlations from the Dittus–Boelter [20] equation and the Gnielinski [21] equation, which are defined as follows.

The Dittus–Boelter equation is defined as

$$Nu = \frac{hD}{k} = 0.023 Re^{0.8} \mathrm{Pr}^{0.4} \tag{16}$$

An alternative formula for calculating the Nu was introduced by the Gnielinski equation, which is defined as

$$Nu = 0.012 (Re^{0.87} - 280) \mathrm{Pr}^{0.4} \tag{17}$$

The friction factor data were compared with the well known correlation from the Haaland equation [22] and the Blasius equation, which are defined as follows.

The Haaland equation is defined as

$$\frac{1}{\sqrt{f}} = -1.8 \log \left[\left(\frac{6.9}{Re} + \left(\frac{\frac{\varepsilon}{D}}{3.7} \right)^{1.11} \right) \right] \tag{18}$$

The Blasius equation is presented in the following form:

$$f = \frac{0.316}{Re^{\frac{1}{4}}} \tag{19}$$

As shown in Figs. 4 and 5, an agreement between the experimental results and the calculated values for single-phase liquid R-134a can be seen.

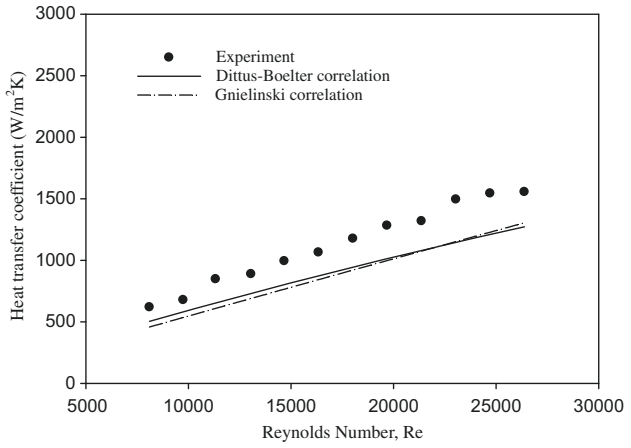

Fig. 4. Comparison of the present data for the single-phase liquid R-134a heat transfer coefficients obtained from the present study with those obtained from Dittus–Boelter and Gnielinski correlations.

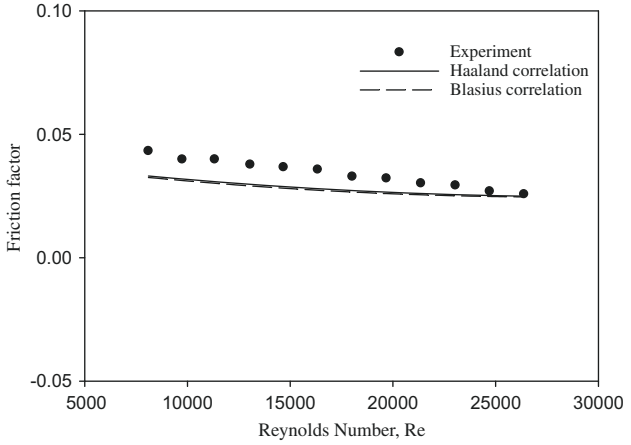

Fig. 5. Comparison of the present data for the single-phase liquid R-134a friction factor obtained from the present study with those obtained from Haaland and Blasius correlations.

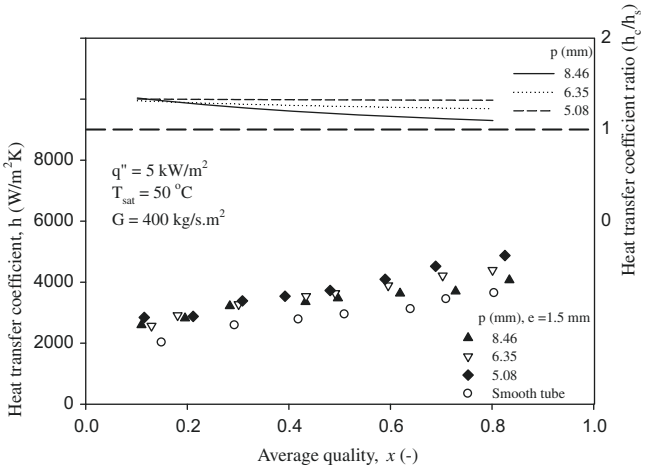

Fig. 6. Heat transfer coefficient versus average quality at T_{sat} = 50 °C, G = 400 kg/m^2 s and q'' = 5 kW/m^2.

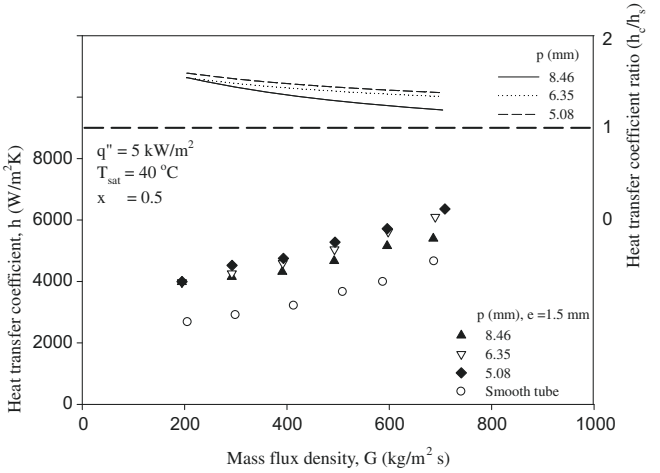

Fig. 7. Heat transfer coefficient versus mass flux at T_{sat} = 40 °C, q'' = 5 kW/m^2, and x = 0.5.

4.1. Heat transfer coefficient

Fig. 6 demonstrates the variation of the average condensation heat transfer coefficient with average quality in the smooth and corrugated tubes at a mass flux of 400 kg/m^2 s, heat flux of 5 kW/m^2, and saturation temperatures of 50 °C, respectively. During the condensation, the liquid film thickness gradually increases and the thermal resistance is therefore increased, resulting in a decrease in the heat transfer rate. A smaller liquid film thickness together with higher vapor velocity at the vapor–liquid interface results in an increase in the heat transfer coefficient when the average quality is higher. The results reveal that the average heat transfer coefficient increases with increasing average quality.

At the same average quality, the average condensation heat transfer coefficient in the smooth tube is lower than that in corrugated tubes across the range of the average quality. This is because the corrugated tube has a significant effect on mixing of the condensate film at the tube wall and increasing the turbulent flow.

The effect of the corrugation pitch on the heat transfer coefficient can be seen: the heat transfer coefficient tends to increase as the corrugation pitch decreases. This is because the lower corrugation pitch promotes turbulence of the refrigerant flow and mixing of the condensate film. These agitations are mainly due to corrugation of the surface. The ratio of the convective heat transfer coefficient of the corrugated tube to that of the smooth tube varies from 1.1 to 1.5 under the same average quality. This means that the corrugated tubes had a heat transfer coefficient approximately 10–50% higher than that of the smooth tube.

Fig. 7 displays the variation of the heat transfer coefficient with mass flux in smooth and corrugated tubes at a heat flux of 5 kW/m^2, saturation temperature of 40 °C, and average quality of 0.5. The figure shows that the average heat transfer coefficient increases with increasing mass flux. The heat transfer coefficient obtained from the smooth tube is relatively low when compared with that obtained from corrugated tubes. The reason for this is similar to the explanation concerning the corrugation pitch mentioned above. However, the maximum heat transfer coefficient ratio of the corrugated tube is up to 50% higher than that of the smooth tube. It is obtained at the lowest mass flux of 200 kg/m^2 s, saturation temperature of 40 °C, and heat flux of 5 kW/m^2.

4.2. Comparison of experimental data with existing correlations for heat transfer coefficient

Fig. 8 shows a comparison of the experimental data for smooth tube with the existing correlations proposed by Aker et al. [23], Traviss et al. [24], Cavallini and Zechin [25], Chen et al. [26], Dob-

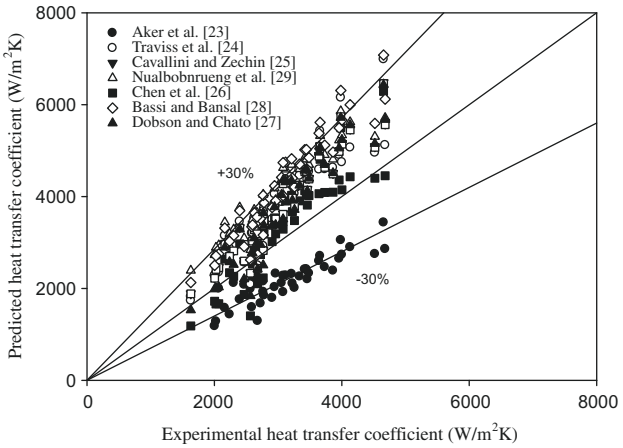

Fig. 8. Comparison of present R-134a heat transfer coefficient data with existing correlation.

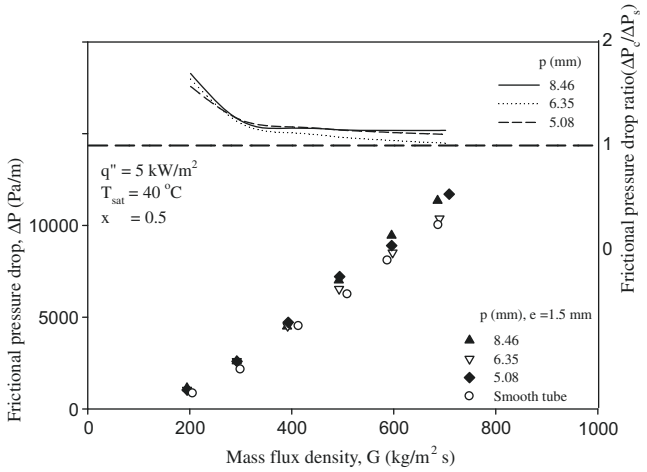

Fig. 10. Pressure drop versus mass flux at T_{sat} = 40 °C, q'' = 5 kW/m^2 and x = 0.5.

son and Chato [27], Bassi and Bansal [28], and Nualboonrueng et al. [29] for smooth tubes. Almost all the correlations give agreement with the present data to be within 30%.

4.3. Pressure drop

Fig. 9 shows the variation in the frictional pressure drop with average quality. The frictional pressure drop can be obtained by subtracting the accelerational pressure drop from the total measured pressure drop. The pressure drops are obtained by dividing the measured pressure drop by the length between pressure taps. In our apparatus, the length between pressure taps is 2.5 m while the length of the heat exchanger is 2 m. These figures show that for smooth and corrugated tubes, the frictional pressure drop increases with increasing average quality. The frictional pressure drop obtained from the corrugated tube is significantly higher than that obtained from the smooth tube. This is due to (1) drag forces exerted on the flow field by the corrugation, (2) flow blockage due to area reduction, (3) turbulence augmentation, and (4) rotational flow produced by the corrugation depth (Vicente et al., [13,14]. The ratio of the frictional pressure drop of the corrugated tube to that of the smooth tube varies from 1.0 to 1.7 under the same average quality. This means that the corrugated tubes had a frictional pressure drop approximately 0–70% higher than that of the smooth tube.

Fig. 10 displays the variation of the frictional pressure drop with mass flux in smooth and corrugated tubes at a heat flux of 5 kW/m^2, saturation temperature of 40 °C, and average quality of 0.5. The figure illustrates that the frictional pressure drop increases with increasing mass flux. Compared with the smooth tube, the frictional pressure drop obtained from the corrugated tube is relatively high. However, the maximum frictional pressure drop ratio of the corrugated tube is up to 70% higher than that of the smooth tube. It is obtained at the lowest mass flux of 200 kg/m^2 s, saturation temperature of 40 °C, and heat flux of 5 kW/m^2.

4.4. Comparison of experimental data with existing correlations for pressure drop

The two-phase frictional multiplier for the smooth tube can be calculated by using the Lockhart–Martinelli correlation as follows:

$$\phi_l^2 = 1 + \frac{C}{X} + \frac{1}{X^2} \tag{20}$$

The constant C in the above equation is the parameter which indicates the two-phase flow condition. The value of this parameter proposed by Chisholm [30] varies from 5 to 20 depending on the flow condition of the vapor and liquid. For instance, the constant

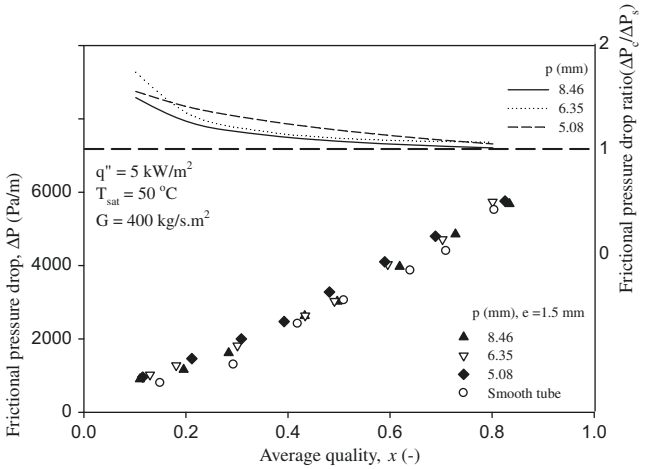

Fig. 9. Pressure drop versus average quality at T_{sat} = 50 °C, G = 400 kg/m^2 s and q'' = 5 kW/m^2.

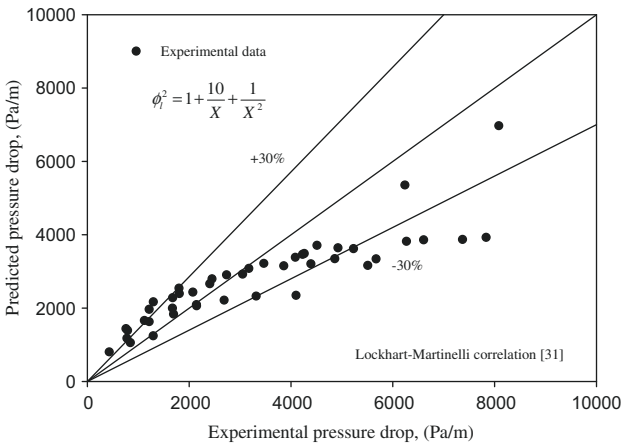

Fig. 11. Comparison of present R-134a pressure drop data for smooth tube with existing correlation.

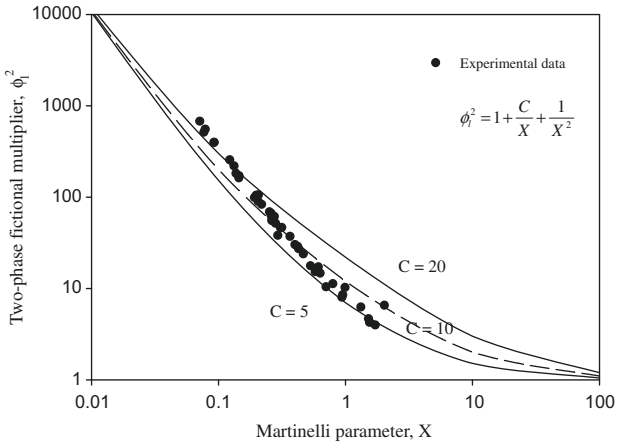

Fig. 12. The two-phase frictional multiplier versus Martinelli parameter.

$C = 20$ when the vapor and liquid flow is in the turbulent region and $C = 5$ when the two-phase flow is in the laminar region. Fig. 11 displays the frictional pressure drop for the smooth tube and shows the comparison of the experimental data with the existing correlation proposed by Lockhart and Martinelli [31] by using $C = 10$. The results showed that this correlation gives good agreement with the present data to be within 30%. The relationships of the two-phase multiplier with the Martinelli parameter are plotted in Fig. 12. As shown in this figure, almost all the measured data are in the region between $C = 5$ and $C = 20$.

5. Conclusion

The effects of corrugation pitch on the condensation heat transfer coefficient and pressure drop of R-134a inside horizontal corrugated tubes are experimentally investigated. A smooth tube and corrugated tubes having inner diameters of 8.7 mm are used as the inner tube. The corrugation pitches are 5.08, 6.35, and 8.46 mm. The corrugation depth of all corrugated tubes is fixed as 1.5 mm. The test runs are performed at saturation temperatures of 40–50 °C, heat fluxes of 5 and 10 kW/m^2, and mass fluxes ranging from 200 to 700 kg/m^2 s. The experimental results show that the average heat transfer coefficient and pressure drop increase with increasing mass flux as well as average quality. In addition, the results obtained from the corrugated tubes are compared with those obtained from the smooth tube. It is found that the corrugation pitches have a significant effect on the heat transfer coefficient and pressure drop augmentations. The maximum heat transfer coefficient ratio and frictional pressure drop ratio of the corrugated tube are up to 50% and 70% higher than those of the smooth tube, respectively.

Acknowledgments

The present study was supported by the Joint Graduate School of Energy and Environment, King Mongkut's University of Technology Thonburi, Office of the Higher Education Commission and the Thailand Research Fund, whose guidance and assistance are gratefully acknowledged.

References

[1] A. Bejan, A.D. Kraus, Heat Transfer Handbook, Wiley, New Jersey, 2003. pp. 1029–1130.
[2] L.M. Schlager, M.P. Pate, A.E. Bergles, Evaporation and condensation heat transfer and pressure drop in horizontal, 12.7-mm micro-fin tubes with refrigerant 22, J. Heat Transfer 112 (1989) 1041–1047.
[3] V. Shinohara, M. Tobe, Development of an improved thermofin tube, Hitachi Cable Rev. 4 (1985) 47–50.
[4] C.S. Kuo, C.C. Wang, In-tube evaporation of HCFC-22 in a 9.52 mm micro-fin/smooth tube, Int. J Heat Mass Transfer 39 (1996) 2559–2569.
[5] Y. Kim, K. Seo, J.T. Chung, Evaporation heat transfer characteristics of R-410A in 7 and 9.52 mm smooth/micro-fin tubes, Int. J. Refrig. 25 (2002) 716–730.
[6] Y. Dong, L. Huixiong, C. Tingkuan, Pressure drop, heat transfer and performance of single-phase turbulent flow in spirally corrugated tubes, Exp. Therm. Fluid Sci. 24 (2001) 131–138.
[7] A. Barba, S. Rainieri, M. Spiga, Heat transfer enhancement in a corrugated tube, Int. Commun. Heat Mass Transfer 29 (2002) 313–322.
[8] S. Rainieri, G. Pagliarini, Convective heat transfer to temperature dependent property fluids in the entry region of corrugated tubes, Int. J. Heat Mass Transfer 45 (2002) 4525–4536.
[9] V. Zimparov, Enhancement of heat transfer by a combination of three-start spirally corrugated tubes with a twisted tape, Int. J. Heat Mass Transfer 44 (2001) 551–574.
[10] V. Zimparov, Enhancement of heat transfer by a combination of a single-start spirally corrugated tubes with a twisted tape, Exp. Therm. Fluid Sci. 25 (2002) 535–546.
[11] V. Zimparov, Prediction of friction factors and heat transfer coefficients for turbulent flow in corrugated tubes combined with twisted tape inserts. Part 1: friction factors, Int. J. Heat Mass Transfer 47 (2004) 589–599.
[12] V. Zimparov, Prediction of friction factors and heat transfer coefficients for turbulent flow in corrugated tubes combined with twisted tape inserts. Part 2: heat transfer coefficients, Int. J. Heat Mass Transfer 47 (2004) 385–393.
[13] P.G. Vicente, A. Garcia, A. Viedma, Experimental investigation on heat transfer and friction factor characteristics of spirally corrugated tubes in turbulent flow at different Prandtl number, Int. J. Heat Mass Transfer 47 (2004) 671–681.
[14] P.G. Vicente, A. Garcia, A. Viedma, Mixed convection heat transfer and isothermal pressure drop in corrugated tubes for laminar and transition flow, Int. Commun. Heat Mass Transfer 31 (2004) 651–662.
[15] P. Naphon, M. Nuchjapo, J. Kurujareon, Tube side heat transfer coefficient and friction factor characteristics of horizontal tubes with helical rib, Energy Convers. Manag. 47 (2006) 3031–3044.
[16] T. Targanski, J.T. Cieslinski, Evaporation of R407C/oil mixtures inside corrugated and micro-fin tubes, Appl. Therm. Eng. 27 (2007) 2226–2232.
[17] K. Bilen, M. Cetin, H. Gul, T. Balta, The investigation of groove geometry effect on heat transfer for internally grooved tubes, Appl. Therm. Eng. 29 (2009) 753–761.
[18] T.N. Tran, Pressure drop and heat transfer study of two-phase flow in small channels, Ph.D. Dissertation, Texas Tech University, Texas, 1998.
[19] S.M. Zivi, Estimation of steady-state steam void-fraction by mean of the principle of minimum entropy production, Trans. ASME J. Heat Transfer 86 (1964) 247–252.
[20] F.W. Dittus, L.M.K. Boelter, Heat transfer in automobile radiators of the tubular tube, Pub. Eng. 2 (1930) 443.
[21] V. Gnielinski, New equations for heat and mass transfer in turbulent pipe and channel flow, Int. Chem. Eng. 16 (1976) 359–368.
[22] S.E. Haaland, Simple and explicit formulas for the friction factor in turbulent pipe flow, J. Fluids Eng. (1983) 89–90.
[23] W.W. Aker, H.A. Beans, O.K. Crosser, Condensation heat transfer within horizontal tubes, Chem. Eng. Prog. Symp. 55 (1959) 171–176.
[24] D.P. Traviss, W.M. Rohsenow, A.B. Baron, Forced-convection condensation inside tubes: a heat transfer equation for condenser design, ASHRAE Trans. 79 (1973) 157–165.
[25] A. Cavallini, R. Zechin, A dimensionless correlation for heat transfer coefficient in forced-convection condensation, in: Proceedings of the Fifth International Heat Transfer Conference, Japan, vol. 3, 1974, pp. 309–313.
[26] S.L. Chen, F.M. Gerner, C.L. Tien, General film condensation correlation, Exp. Heat Transfer 1 (1987) 93–107.
[27] M.K. Dobson, T.J. Chato, Condensation in smooth horizontal tubes, J. Heat Transfer 120 (1998) 193–213.
[28] R. Bassi, P.K. Bansal, In-tube condensation of mixture of R134a and ester oil: empirical correlations, Int. J. Refrig. 26 (2003) 402–409.
[29] T. Naulboonrueng, J. Kaew-on, S. Wongwises, Two-phase condensation heat transfer coefficients of HFC-134a at high mass flux in smooth and micro-fin tubes, Int. Commun. Heat Mass Transfer 30 (2003) 577–590.
[30] D. Chisholm, Pressure gradients due to friction during the flow of evaporating two-phase mixtures in smooth tubes and channels, Int. J. Heat Mass Transfer 16 (1973) 347–358.
[31] R.W. Lockhart, R.C. Martinelli, Proposed correlation of data for isothermal, two-phase two-component flow in pipes, Chem. Eng. Prog. 45 (1949) 39–48.

Experimental Thermal and Fluid Science 34 (2010) 692–705

Contents lists available at ScienceDirect

Experimental Thermal and Fluid Science

journal homepage: www.elsevier.com/locate/etfs

An investigation of a model of the flow pattern transition mechanism in relation to the identification of annular flow of R134a in a vertical tube using various void fraction models and flow regime maps

A.S. Dalkilic [a,*], S. Wongwises [b,*]

[a] Heat and Thermodynamics Division, Department of Mechanical Engineering, Yildiz Technical University, Yildiz, Besiktas, Istanbul 34349, Turkey
[b] Fluid Mechanics, Thermal Engineering and Multiphase Flow Research Lab. (FUTURE), Department of Mechanical Engineering, King Mongkut's University of Technology Thonburi, Bangmod, Bangkok 10140, Thailand

ARTICLE INFO

Article history:
Received 19 August 2009
Received in revised form 4 December 2009
Accepted 28 December 2009

Keywords:
Condensation
Flow regime map
Vertical down flow
R134a
Phase change

ABSTRACT

In the present study, new experimental data are presented for literature on the prediction of film thickness and identification of flow regime during the co-current downward condensation in a vertical smooth copper tube having an inner diameter of 8.1 mm and a length of 500 mm. R134a and water are used as working fluids in the tube side and annular side of a double tube heat exchanger, respectively. Condensation experiments are done at mass fluxes of 300 and 515 kg m^{-2} s^{-1}. The condensing temperatures are between 40 and 50 °C; heat fluxes are between 12.65 and 66.61 kW m^{-2}. The average experimental heat transfer coefficient of the refrigerant HFC-134a is calculated by applying an energy balance based on the energy transferred from the test section. A mathematical model by Barnea et al. based on the momentum balance of liquid and vapor phases is used to determine the condensation film thickness of R134a. The comparative film thickness values are determined indirectly using relevant measured data together with various void fraction models and correlations reported in the open literature. The effects of heat flux, mass flux, and condensation temperature on the film thickness and condensation heat transfer coefficient are also discussed for the laminar and turbulent flow conditions. There is a good agreement between the film thickness results obtained from the theoretical model and those obtained from six of 35 void fraction models in the high mass flux region of R134a. In spite of their different valid conditions, six well-known flow regime maps from the literature are found to be predictive for the annular flow conditions in the test tube in spite of their different operating conditions.

1. Introduction

In spite of a large number of flow pattern identification studies of horizontal and upward flow, few investigators have examined flow regime maps for downward flow.

The orientation and interaction of the liquid and vapor phases inside the tubes are among the most significant characteristics of two-phase flow. These phenomena are related to flow regime and flow pattern. A specific kind of geometric distribution of the phases is called a flow pattern or flow regime. The interfacial area of the phases is affected by geometry, and thus mass, momentum, and energy exchange between phases have come to play important roles in the design. Different flow patterns may occur depending on the tube position, the geometry of the tube, flow rates, superficial velocities, and physical properties such as density, viscosity, and surface tension of the two phases. Generally, flow patterns are observed by visual inspection and include bubble flow, slug flow, churn flow, wispy-annular flow, and annular flow for vertical flow, and bubble flow, plug flow, stratified flow, wavy flow, slug flow, and annular flow for horizontal flow. However, Hubbard and Dukler [1] classified the flow patterns as separated flow patterns (stratified flow, annular flow), intermittent flow patterns (elongated bubble flow, slug/plug flow, churn/froth flow), and dispersed flow patterns (bubble flow, dispersed bubble flow).

Two-phase annular flow occurs widely in film heating and cooling processes, particularly in power generation and especially in nuclear reactors. This flow regime has received the most attention, both analytically and experimentally, because of its practical importance and the relative ease with which analytical treatment may be applied. Annular two-phase flow is characterized by a phase interface separating a thin liquid film from the gas flow in the core region. In addition to this, condensate distribution inside the tube wall is almost symmetric and there is high velocity vapor

* Corresponding authors. Tel.: +90 212 3832819; fax: +90 212 2616659 (A.S. Dalkilic), tel.: +66 2 470 9115; fax: +66 2 470 9111 (S. Wongwises).
E-mail addresses: dalkilic@yildiz.edu.tr (A.S. Dalkilic), somchai.won@kmutt.ac.th (S. Wongwises).

0894-1777/$ - see front matter © 2010 Elsevier Inc. All rights reserved.
doi:10.1016/j.expthermflusci.2009.12.011

Nomenclature

A	inside surface area, m^{-2}
C	coefficient for the friction factor
c_p	specific heat, J kg^{-1} K^{-1}
d	internal tube diameter, m
f	friction factor
F_r	Froude rate parameter
G	mass flux, kg m^{-2} s^{-1}
g	gravitational constant, m s^{-2}
h	heat transfer coefficient, W m^{-2} K^{-1}
i	enthalpy, J kg^{-1}
i_{fg}	latent heat of condensation, J kg^{-1}
j	superficial velocity in Hewitt and Robertson's map
K	coefficient in Smith correlation
L	length of test tube, m
m	mass flow rate, kg s^{-1}
Re	Reynolds number
S	perimeter over which the stress acts, m
s	slip ratio
T	temperature, °C
Q	heat transfer rate, W
u	velocity, m s^{-1}
x	mean vapor quality
X	Lockhart–Martinelli parameter
We	Weber number
ΔT	vapor side temperature difference, $T_{sat} - T_{wi}$, °C

Greek symbols

σ	surface tension, N m^{-1}
ρ	density, kg m^{-3}
λ	property parameter of Baker flow regime map
ψ	property parameter of Baker flow regime map
μ	dynamic viscosity, kg m^{-1} s^{-1}
δ	film thickness, m
$\overline{\delta}$	dimensionless form of film thickness
α	void fraction
τ	shear stress, N m^{-2}
v	kinematic viscosity, m^2 s^{-1}

Subscripts

a	air
cond	condensate
corr	correlation
exp	measured
g	gas/vapor
H	homogen
i	inlet
int	interfacial
l	liquid
mdl	model
o	outlet
ph	preheater
ref	refrigerant
s	superficial for one phase flow alone in the pipe
sat	saturation
T	total
TS	test section
w	water
wi	inner wall

Exponentials

n	exponent in Eq. (20)
m	exponent in Eq. (21)

flow in the core during annular flow. In this flow regime, it is generally true that due to the breakup of the disturbance wave, part of the liquid phase is entrained as droplets into the gas core. It is also accepted that mass, momentum, and energy transfers are strongly affected by entrainment of the droplets to the gas core.

Two-dimensional flow pattern maps are used to determine flow patterns depicting flow regime transition boundaries. It is usually preferred that their coordinates have dimensional values such as superficial velocities and mass fluxes instead of dimensionless variables such as Weber number. Flow regime maps can be categorized into two groups: experimental flow pattern maps and mechanistic flow pattern maps. The first is obtained from a large number of experimental data and limited by its experimental parameters such as fluid properties, tube diameter, and mass flux. The second is built up from examination of various transition mechanisms using fundamental equations and its range for different experimental conditions is wider than the first one due to having incorporated system parameters. The most widely recommended flow pattern maps for vertical tubes are those of Barnea et al. [2], Fair [3], Hewitt and Robertson [4], Chen et al. [5], Zhao and Bi [6], and for horizontal tubes, those of Baker [7], Mandhane et al. [8], Thome [9], El Hajal et al. [10], Coleman and Garimella [11,12], Kattan et al. [13], Taitel and Dukler [14], Weisman et al. [15], Breber et al. [16], Soliman [17], Tandon et al. [18], and Mederic et al. [19].

Void fraction is an important parameter and is always used to determine the flow pattern transition, heat transfer coefficient, and two-phase pressure drop and is defined as the cross-sectional area occupied by the vapor in relation to the area of the flow channel. Two-phase separated flow is commonly analyzed using the slip flow model. In this model, it is assumed that the separated phases have different uniform velocities. By contrast, the homogeneous model is defined as an ideal case, as it assumes a homogeneous mixture providing uniform velocities for both phases, and for that reason it is the simplest method of determination of the void fraction.

In the technical literature, numerous studies have been carried out on the modeling of the void fraction and can be divided into several groups: general void fraction models and correlations [20–25]), K_H parameter-based void fraction models and correlations [26–28], flow regime-based void fraction models and correlations [29–31], Lockhart and Martinelli parameter-based void fraction models and correlations [32–40], and slip ratio void fraction models and correlations [10,41–52]. A brief and comprehensive overview of these works is presented in the authors' previous publications [53,56,59,60].

This paper provides a comprehensive review of the published literature on flow regime maps in relation to a flow transition model having a relationship between the film thickness and void fraction models and correlations. The experiments include a wide range of high mass fluxes with different saturation temperatures as they relate to 380 data points of R134a belonging to the condensation heat transfer database of FUTURE Lab in KMUTT. Apart from the authors' previous publications [53–65], few studies exist in the literature for the investigation of heat transfer characteristics in a small diameter vertical tube during co-current down flow condensation, and besides this, there is no study with the experimental parameters of this work and its content in the open literature. In this study, determination of the condensation film thickness is presented by means of the model of Barnea et al. [2] and verified by relating the void fraction models and correlations. In addition to this, the changes

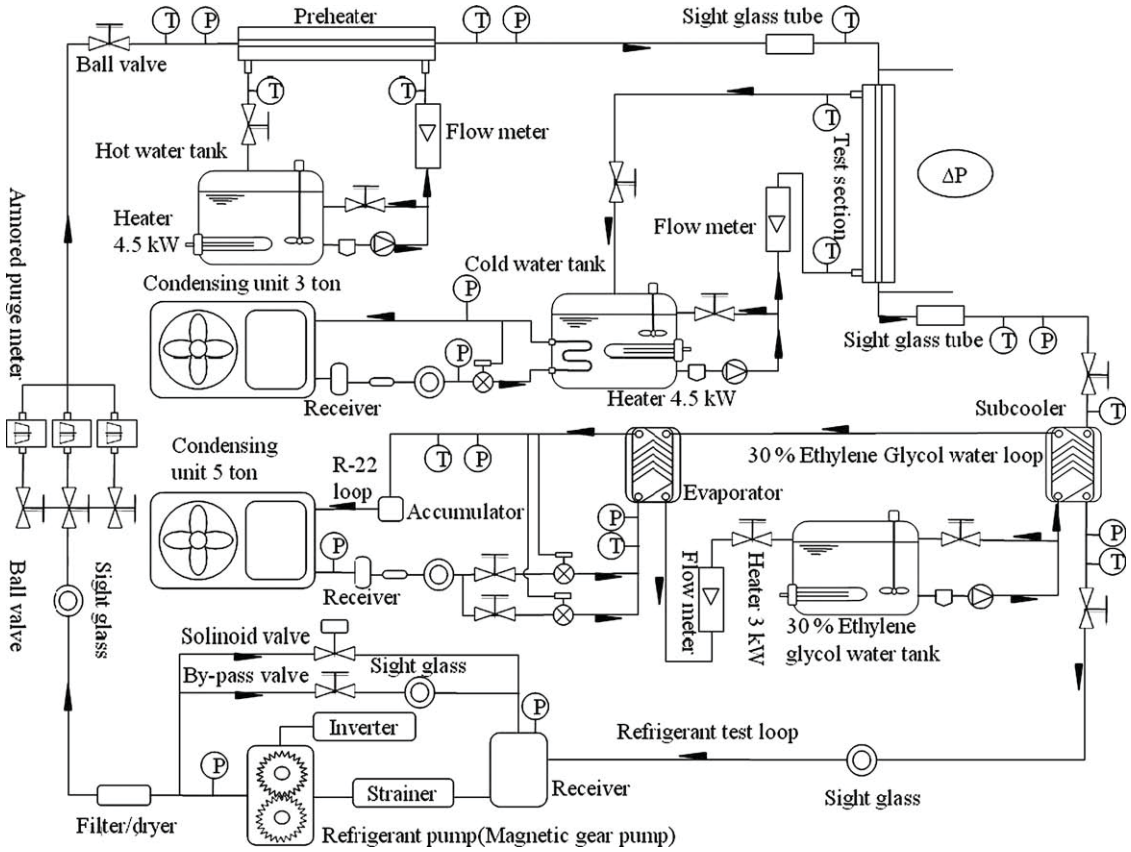

Fig. 1. Schematic diagram of experimental apparatus.

in the heat transfer coefficient, vapor quality and condensation temperature difference between the tube wall and refrigerant with film thickness and verification of the void fraction values obtained from the flow transition model are investigated. Moreover, flow regime identification is performed using various flow pattern maps valid for horizontal and vertical tubes to show the independence of the annular flow regime from tube orientation [58,66].

2. Experimental apparatus and method

A schematic diagram of the test apparatus is shown in Fig. 1. The refrigerant loop consists of a pre-heating loop, test section, cooling loop and chilling loop. The refrigerant is circulated by a gear pump controlled by an inverter. The refrigerant flows in series through a filter/dryer, a sight glass tube, a refrigerant flow meter and a preheater and enters the test section. A spiral counter-flow double tube heat exchanger is designed to supply heat to control the inlet quality of the refrigerant before entering the test section. After exiting the test section, the chilling loop condenses and subcools the refrigerant and removes the heat input from the pre-heater and test section, and ejects it into the surroundings. After leaving the chilling loop, the refrigerant changes from the two-phase refrigerant to a sub-cooled state. Eventually, the refrigerant returns to the refrigerant pump to complete the cycle.

The test section, well insulated with a proper material to minimize the heat loss, is a vertical counter-flow tube-in-tube heat exchanger with refrigerant flowing downward (co-current liquid and vapor of R134a's down flow) in the inner tube and cooling water

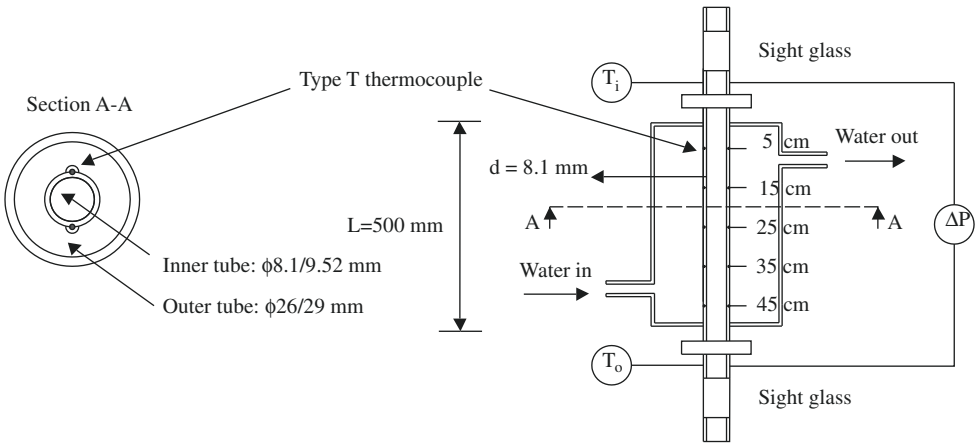

Fig. 2. Schematic diagram of test section.

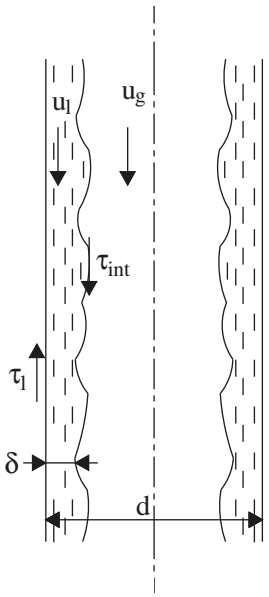

Fig. 3. System model for analysis of annular downward vertical flow.

Table 1
Coefficients of the Eqs. (20) and (21) according to flow types.

Flow types	Laminar flow	Turbulent flow
Coefficients		
n	1	0.2
m	1	0.2
C_l	16	0.046
C_g	16	0.046

flowing upward in the annulus. The inner and outer tubes are made from smooth vertical copper having inner diameters of 8.1 and 26 mm, respectively. The length of the heat exchanger is 0.5 m. Fig. 2 shows the detailed dimensions of the heat exchanger and the location of the thermocouples.

T-type thermocouples are used to measure refrigerant temperature and the tube wall temperatures in the test section. A total of ten thermocouples are located on the sidewall at five points along the test tube. A thermostat is used to control the inlet temperature of the water. All the temperature measuring devices are calibrated in a controlled temperature bath using standard precision mercury glass thermometers. The uncertainty of the temperature measurements is ±0.1 °C. All static pressure taps are mounted on the tube wall. The refrigerant flow meter is a variable area type. The flow meter was calibrated in the range of 0–2.2 gal min^{-1} for HFC-134a by the manufacturer. Pressure drop is measured by a differential pressure transducer installed between the inlet and outlet of the test section. The length between pressure taps is 0.7 m. A low temperature thermostat is used to control the system pressure of the refrigerant flow. The differential pressure transducer and pressure gauges are calibrated against a primary standard, the dead weight tester. All signals from thermocouples and pressure transducers are recorded by a data logger. Tests are performed in the steady state.

3. Data reduction and experimental uncertainty

The data reduction of the measured results can be analyzed as follows:

3.1. The inlet vapor quality of the test section ($x_{TS,i}$)

$$x_{TS,i} = \frac{i_{TS,i} - i_{l@T_{TS,i}}}{i_{fg@T_{TS,i}}} \tag{1}$$

where $i_{l@T_{TS,i}}$ is the enthalpy of the saturated liquid based on the inlet temperature of the test section, $i_{fg@T_{TS,i}}$ is the enthalpy of vapor-

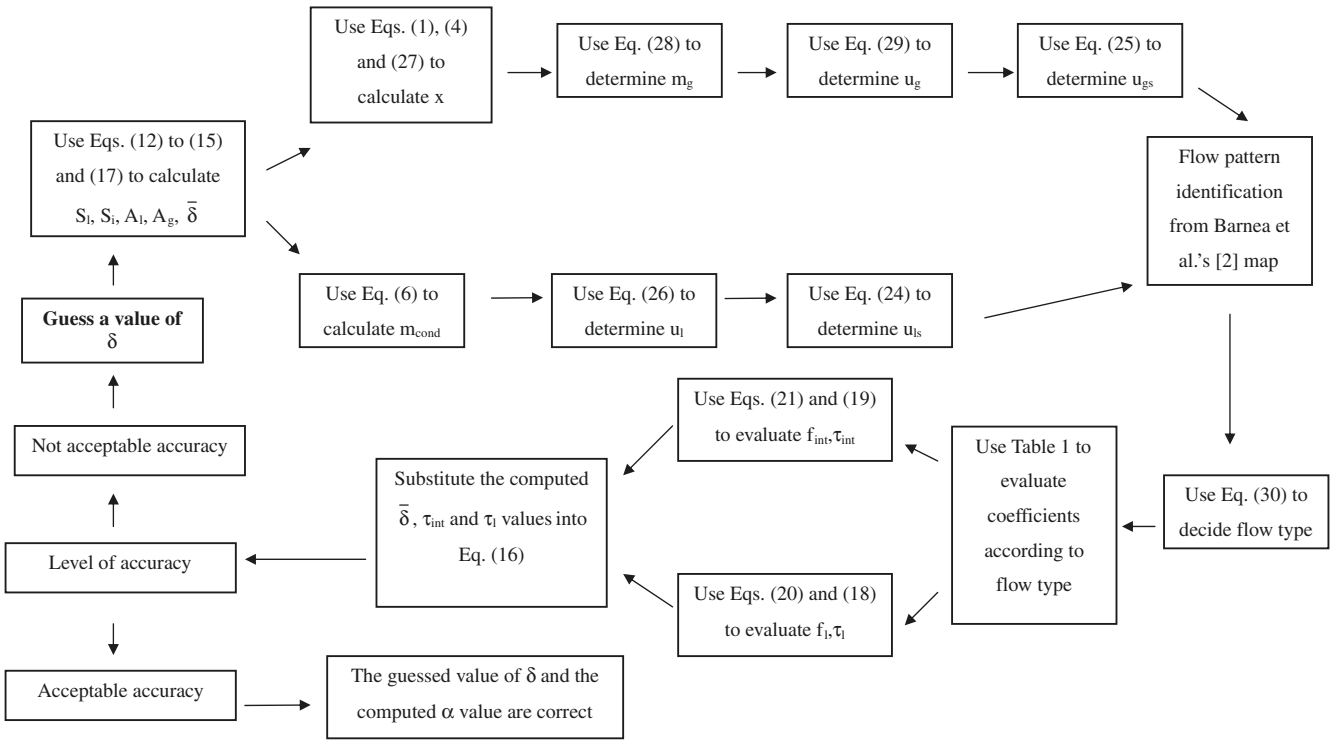

Fig. 4. Flow chart of iteration process.

ization based on the inlet temperature of the test section, $i_{TS,i}$ is the refrigerant enthalpy at the test section inlet and is given by:

$$i_{TS,i} = i_{ph,i} + \frac{Q_{ph}}{m_{ref}} \tag{2}$$

where $i_{ph,i}$ is the inlet enthalpy of the liquid refrigerant before entering the pre-heater, m_{ref} is the mass flow rate of the refrigerant, and Q_{ph} is the heat transfer rate in the pre-heater:

$$Q_{ph} = m_{w,ph} c_{p,w} (T_{w,i} - T_{w,o})_{ph} \tag{3}$$

where $m_{w,ph}$ is the mass flow rate of the water entering the pre-heater, $c_{p,w}$ is the specific heat of water, $(T_{w,i} - T_{w,o})_{ph}$ is the temperature difference between inlet and outlet positions of the preheater.

3.2. The outlet vapor quality of the test section ($x_{TS,o}$)

$$x_{TS,o} = \frac{i_{TS,o} - i_{l@T_{TS,o}}}{i_{fg@T_{TS,o}}} \tag{4}$$

where $i_{TS,o}$ is the refrigerant enthalpy at the test section outlet, $i_{l@T_{TS,o}}$ is the enthalpy of the saturated liquid based on the outlet temperature of the test section, and $i_{fg@T_{TS,o}}$ is the enthalpy of vaporization. The outlet enthalpy of the refrigerant flow is calculated as follows:

$$i_{TS,o} = i_{TS,i} - \frac{Q_{TS}}{m_{ref}} \tag{5}$$

where the heat transfer rate, Q_{TS}, in the test section is obtained from:

$$Q_{TS} = m_{w,TS} c_{p,w} (T_{w,o} - T_{w,i})_{TS} \tag{6}$$

where $m_{w,TS}$ is the mass flow rate of the water entering the test section, and $(T_{w,o} - T_{w,i})_{TS}$ is temperature difference between outlet and inlet position of the test section.

3.3. The average heat transfer coefficient

$$h_{exp} = \frac{Q_{TS}}{A_{wi}(T_{ref,sat} - T_{wi})} \tag{7}$$

where h_{exp} is the experimental average heat transfer coefficient, Q_{TS} is the heat transfer rate in the test section, T_{wi} is the average temperature of the inner wall, $T_{ref,sat}$ is the average saturation temperature of the refrigerant at the test section inlet and outlet, and A_{wi} is the inside surface area of the test section:

$$A_{wi} = \pi d L \tag{8}$$

where d is the inside diameter of the test tube. L is the length of the test tube.

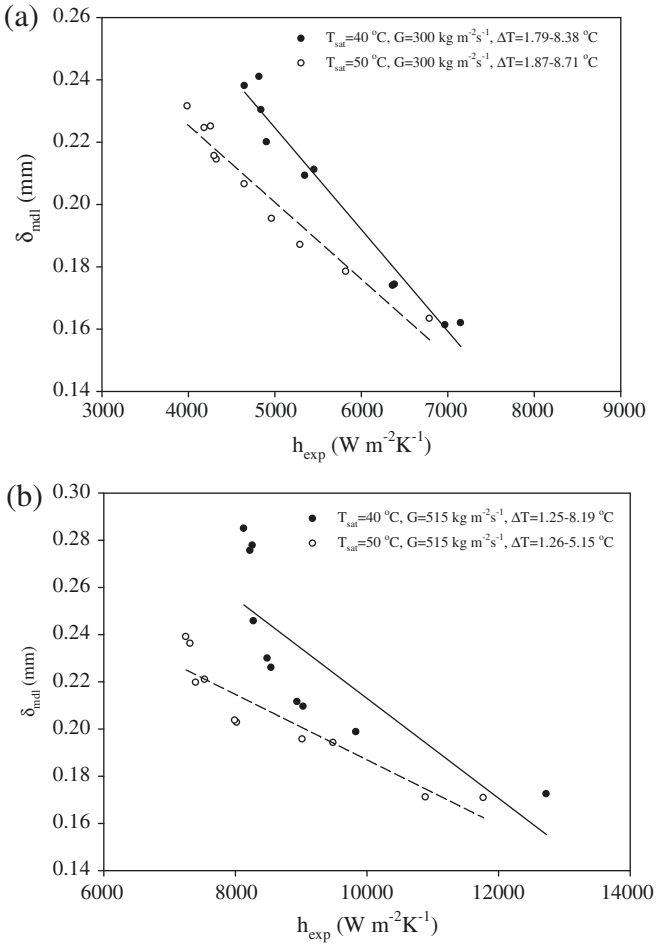

Fig. 5. Comparison of film thickness obtained from model regarding heat transfer coefficient at different condensation temperatures and ΔT_{sat} for the mass fluxes of 300 kg m^{-2} s^{-1} (a) and 515 kg m^{-2} s^{-1} (b) for the laminar flow data.

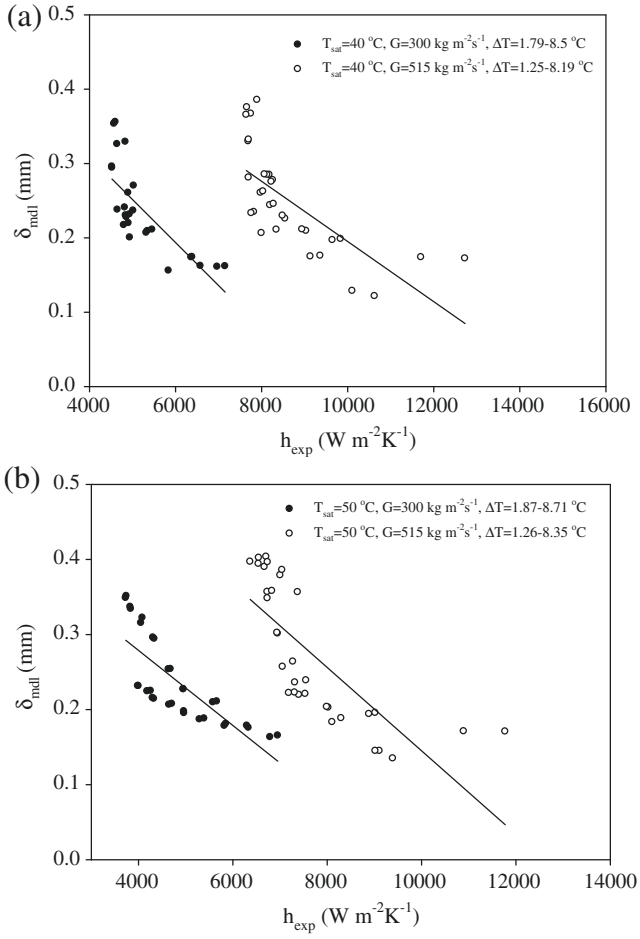

Fig. 6. Comparison of film thickness obtained from model regarding heat transfer coefficient at different condensation temperatures and ΔT_{sat} for the mass fluxes of 300 kg m^{-2} s^{-1} (a) and 515 kg m^{-2} s^{-1} (b) for the laminar flow data.

3.4. Uncertainties

The uncertainties of the Nusselt number and condensation heat transfer coefficient in the test tube varied from ±7.64% to ±10.71%. It should be noted that similar ranges of uncertainty with minimum and maximum values exist in the literature. The procedures of Kline and McClintock [67] were used for the calculation of all uncertainties. Various uncertainty values of the study can be seen from authors' previous works [54,61,63].

3.5. Calculation procedure for the annular flow model

The steady-state physical model of downward annular flow condensation of R134a in a vertical tube is shown in Fig. 3. Details of the development of the relationship among the film thickness and the flow parameters and flow pattern transition mechanisms can be seen in Barnea et al. [2].

Momentum balances of liquid and vapor phases can be defined respectively as follows:

$$-A_l\left(\frac{dP}{dx}\right)-\tau_l S_l+\tau_{int}S_i+\rho_l A_l g=0 \tag{9}$$

$$-A_g\left(\frac{dP}{dx}\right)-\tau_{int}S_i+\rho_g A_g g=0 \tag{10}$$

Eqs. (9) and (10) can be rearranged, equating pressure drop as:

$$\tau_{int}S_i\left(\frac{1}{A_l}+\frac{1}{A_g}\right)+g(\rho_l-\rho_g)-\tau_l\frac{S_l}{A_l}=0 \tag{11}$$

Flow cross-sectional areas and perimeters over which the stress acts are expressed respectively as:

$$S_l=\pi d \tag{12}$$

$$S_i=\pi(d-2\delta) \tag{13}$$

$$A_l=\pi(d\delta-\delta^2) \tag{14}$$

$$A_g=\pi\left(\frac{d}{2}-\delta\right)^2 \tag{15}$$

Eq. (16) can be obtained from the substitution of Eqs. (12)–(15) into Eq. (11)

$$\frac{\tau_{int}}{d(\overline{\delta}-\overline{\delta}^2)(1-2\overline{\delta})}+g(\rho_l-\rho_g)-\frac{\tau_l}{d(\overline{\delta}-\overline{\delta}^2)}=0 \tag{16}$$

where the dimensionless form of film thickness is determined as:

$$\overline{\delta}=\frac{\delta}{d} \tag{17}$$

Liquid shear stress and interfacial shear stress are calculated respectively as follows:

$$\tau_l=f_l\frac{\rho_l u_l^2}{2} \tag{18}$$

$$\tau_{int}=f_i\frac{\rho_g(u_g-u_l)^2}{2} \tag{19}$$

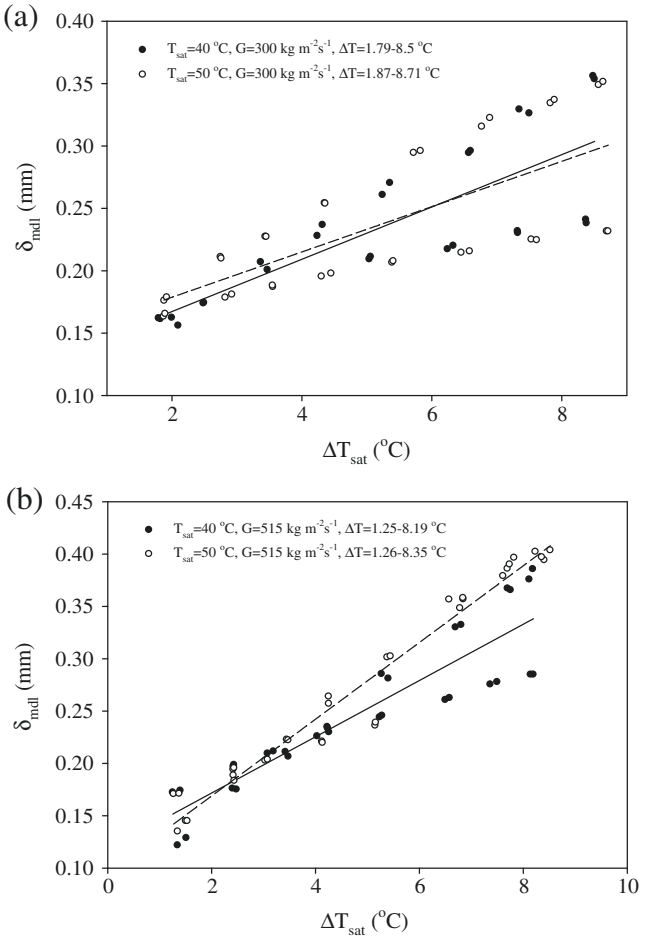

Fig. 7. Comparison of film thickness obtained from model regarding ΔT_{sat} at different condensation temperatures for the mass fluxes of 300 kg m^{-2} s^{-1} (a) and 515 kg m^{-2} s^{-1} (b) for the laminar and turbulent flow data.

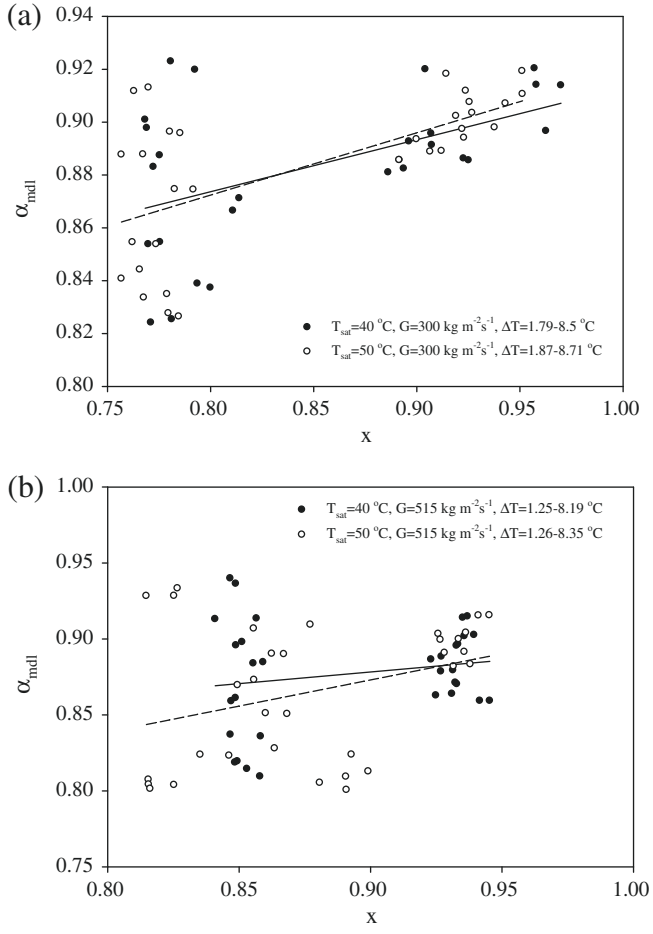

Fig. 8. Comparison of film thickness obtained from model regarding vapor quality at different condensation temperatures and ΔT_{sat} for the mass fluxes of 300 kg m^{-2} s^{-1} (a) and 515 kg m^{-2} s^{-1} (b) for the laminar and turbulent flow data.

where the liquid and interfacial friction factor are evaluated respectively as:

$$f_l = C_l\left(\frac{d_l u_l}{\nu_l}\right)^{-n} \tag{20}$$

$$f_{int} \cong f_g = C_g\left(\frac{d_g u_g}{\nu_g}\right)^{-m} \tag{21}$$

where

$$d_l = \frac{4A_l}{S_l} = 4d(\bar{\delta} - \bar{\delta}^2) \tag{22}$$

$$d_g = \frac{4A_g}{S_g} = (1 - 2\bar{\delta})d \tag{23}$$

$$u_l = \frac{u_{ls}}{4(\bar{\delta} - \bar{\delta}^2)} \tag{24}$$

$$u_g = \frac{4u_{gs}}{1 - 4\bar{\delta} + 4\bar{\delta}^2} \tag{25}$$

It should be noted that the coefficients of Eqs. (20) and (21) can be obtained from Table 1 using Eq. (30).

Condensate flow rate can be obtained from Eq. (6), and thus condensate velocity is determined from Eq. (26) as:

$$m_{cond} = \rho_l A_l u_l \tag{26}$$

Vapor flow rate is obtained from Eq. (27), and thus vapor velocity is determined as follows:

$$x = \frac{x_{TS,i} + x_{TS,o}}{2} \tag{27}$$

$$m_g = x m_T \tag{28}$$

$$m_g = \rho_g A_g u_g \tag{29}$$

Liquid Reynolds number can be determined to decide if flow is laminar or turbulent as:

$$\mathrm{Re}_l = \frac{Gd(1-x)}{\mu_l}\begin{cases} < 2300 & \text{laminar} \\ > 2300 & \text{turbulent} \end{cases} \tag{30}$$

The void fraction value from the model is estimated using an estimated film thickness value shown in Fig. 4, assuming $\delta \ll d$ as follows:

$$\alpha = \frac{A_g}{A} = \left(1 - \frac{\delta}{r}\right)^2 = 1 - \frac{4\delta}{d} \tag{31}$$

The film thickness, void fraction, and interfacial shear can be determined using an iterative technique for specified mass flux, vapor quality, condensation pressure, and thermo physical properties. After estimating a value for film thickness, Eqs. (12), (13), (14), (15), and (17) should be used to evaluate the dimensionless film thickness value, flow areas, and perimeters of phases. By means of Eqs. (1), (4), and (27), desired vapor quality can be calculated. Using Eqs. (28), (29), and (25), mass flux, velocity, and the superficial form of vapor are determined respectively and at the

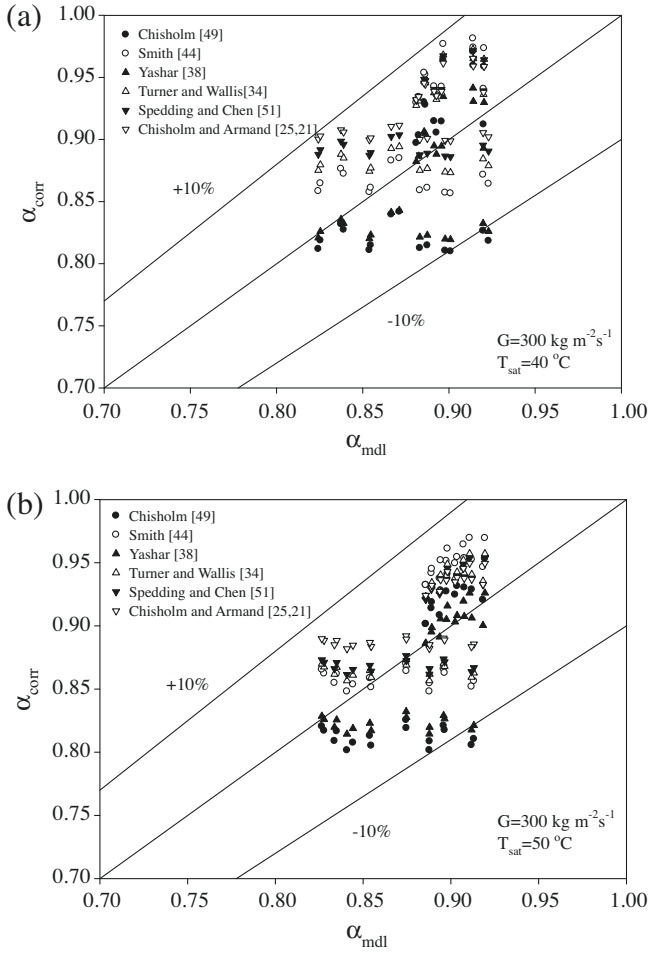

Fig. 9. Comparisons between the model and calculated void fraction values for the mass flux of 300 kg m^{-2} s^{-1} at the condensing temperatures of 40 °C (a) and 50 °C (b) using laminar and turbulent flow data.

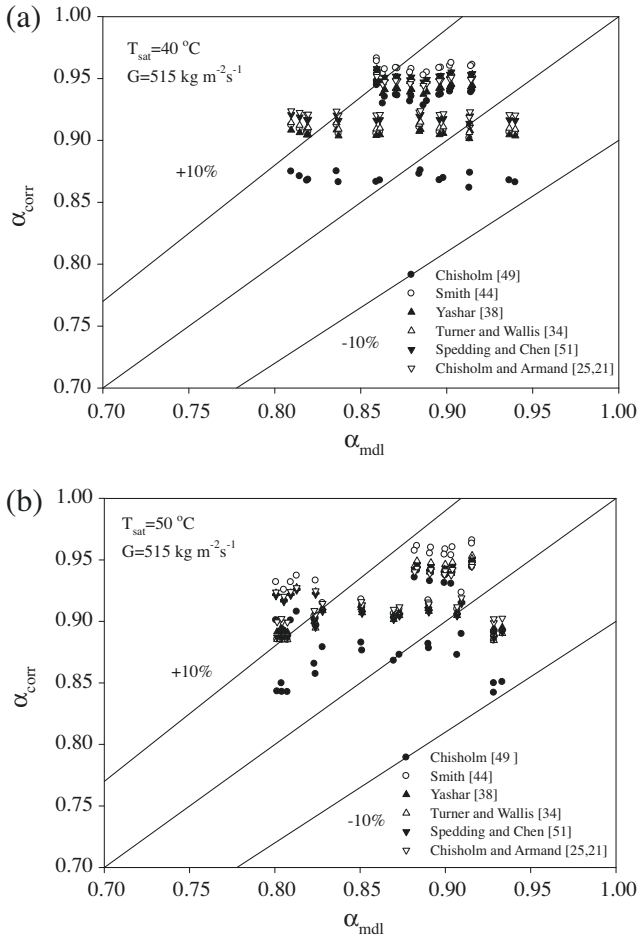

Fig. 10. Comparisons between the model and calculated void fraction values for the mass flux of 515 kg m^{-2} s^{-1} at the condensing temperatures of 40 °C (a) and 50 °C (b) using laminar and turbulent flow data.

Table 2
Agreed void fraction models and correlations.

Void fraction model/correlation	Model/correlation
Chisholm and Armand model [25,21]	$\alpha = \frac{1}{\alpha_H + (1-\alpha_H)^{0.5}}\alpha_H \quad \alpha_H = \frac{1}{1+\left(\frac{1-x}{x}\right)\left(\frac{\rho_g}{\rho_l}\right)s} \quad s = 1$
Turner and Wallis two-cylinder model [34]	$\frac{1-\alpha}{\alpha} = A\left(\frac{1-x}{x}\right)^p \left(\frac{\rho_g}{\rho_l}\right)^q \left(\frac{\mu_l}{\mu_g}\right)^r$

Correlation or model	A	p	q	r
Homogeneous	1	1	1	0
Zivi	1	1	0.67	0
Turner-Wallis	1	0.72	0.4	0.08
Lockhart-Martinelli	0.28	0.64	0.36	0.07
Thom	1	1	0.89	0.18
Baroczy	1	0.74	0.65	0.13

Yashar correlation [38]	$\alpha = (1 + F_t^{-1} + X)^{-0.321} \quad F_t = \left(\frac{x^3 G^2}{\rho_g^2 g d(1-x)}\right)^{0.5} \quad X = \left(\frac{1-x}{x}\right)^{0.9}\left(\frac{\rho_g}{\rho_l}\right)^{0.5}\left(\frac{\mu_l}{\mu_g}\right)^{0.1}$
Smith model [43]	$\alpha = \left\{1 + \left(\frac{\rho_g}{\rho_l}\right)K\left(\frac{1}{x}-1\right) + \left(\frac{\rho_g}{\rho_l}\right)(1-K)\left(\frac{1}{x}-1\right)\left[\frac{\left(\frac{\rho_l}{\rho_g}\right)+K\left(\frac{1}{x}-1\right)}{1+K\left(\frac{1}{x}-1\right)}\right]\right\}^{-1} \quad K = 0.4$
Chisholm correlation [48]	$\alpha = \frac{1}{1+\left(\frac{1-x}{x}\right)\left(\frac{\rho_g}{\rho_l}\right)s} \quad s = \left(1 - x + \frac{x\rho_l}{\rho_g}\right)^{1/2}$
Spedding and Chen correlation [51]	$\alpha = \left(1 + 2.22\left(\frac{1-x}{x}\right)^{0.65}\left(\frac{\rho_g}{\rho_l}\right)^{0.65}\right)^{-1}$

same time condensation rate, velocity, and the superficial velocity of the liquid phase are calculated using Eqs. (6), (26), and (24) respectively. It should be noted that having the superficial vapor and liquid velocities, flow identification of data can be performed from the flow pattern map of Barnea et al. [2]. After deciding the flow type using Eq. (30) and selecting coefficients from Table 1, interfacial and liquid friction factors and shear stresses can be obtained from Eqs. (21), (20), (19), and (18) respectively. The estimated dimensionless film thickness value and calculated interfacial and liquid shear values are substituted into Eq. (16). These values are updated and the film thickness value is repeatedly estimated until convergence. If the level of accuracy is acceptable, the values of estimated film thickness and void fraction value calculated by Eq. (31) are correct. This procedure can also be seen in Fig. 4.

In addition to the above explanations, the variables below are used in the calculations of flow pattern maps in the paper as follows:

Superficial momentum fluxes of the liquid and gas phases can be determined respectively for the calculations of Hewitt and Roberts' flow pattern map [4] as follows:

$$\rho_l j_l^2 = \frac{[G(1-x)]^2}{\rho_l} \tag{32}$$

$$\rho_g j_g^2 = \frac{[Gx]^2}{\rho_g} \tag{33}$$

The property parameters of Baker's flow regime map [7] and the liquid and vapor phases of mass flux are defined respectively as follows:

$$\lambda = \left[\frac{\rho_g}{\rho_a}\frac{\rho_l}{\rho_w}\right]^{1/2} \tag{34}$$

$$\psi = \left(\frac{\sigma_w}{\sigma}\right)\left[\left(\frac{\mu_l}{\mu_w}\right)\left(\frac{\rho_w}{\rho_l}\right)^2\right]^{1/2} \tag{35}$$

$$G_l = G(1-x) \tag{36}$$

$$G_g = Gx \tag{37}$$

The Weber number in the flow regime map of Chen et al. [5] can be determined as follows:

$$We = \left[\frac{\rho d u^2}{\sigma}\right] \tag{38}$$

It should be noted that u_{ls} obtained from Eq. (24) and u_{gs} obtained from Eq. (25) can used as velocity term in Eq. (38).

4. Results and discussion

The present study is performed to study the relationship between void fraction models and the annular flow model of Barnea et al. [2] and to investigate the well-known flow pattern maps to verify the annular flow conditions of experimental data for the downward two-phase flow of R134a in a vertical round tube with an inner diameter of 8.1 mm. Pure HFC-134a was used in the experiments. The effect of the temperature difference between the saturated temperature of the vapor and the inlet wall temperature of the tube (ΔT_{sat}), mass flux, vapor quality, and condensation temperature on the heat transfer coefficients and void fraction are shown in Figs. 5–8. It should be noted that R134a was entering the test section as pure saturated vapor in the figures

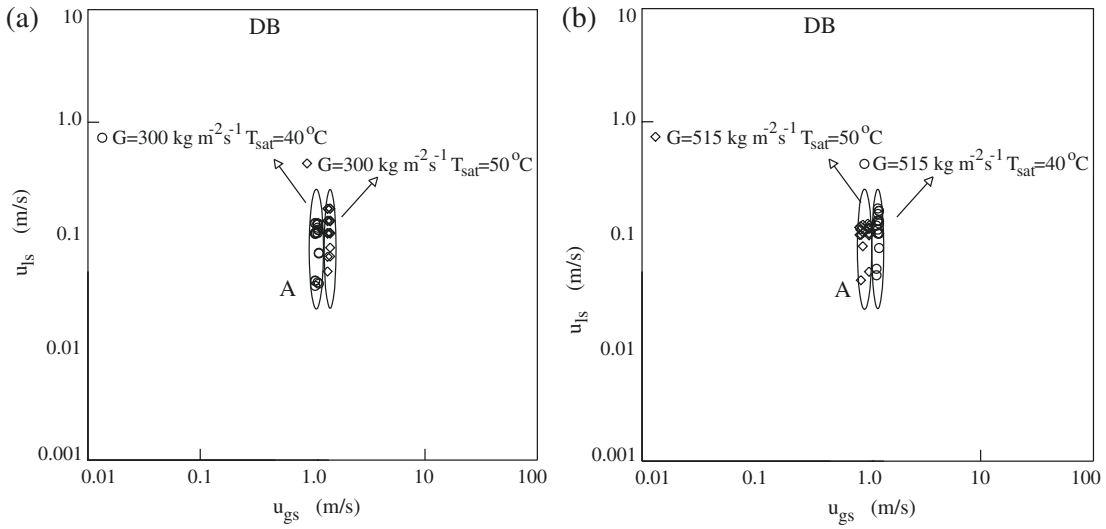

Fig. 11. Flow pattern identification of the experimental data by means of Barnea et al. [2] flow regime map for the mass fluxes of 300 kg m^{-2} s^{-1} (a) and 515 kg m^{-2} s^{-1} (b) at the condensing temperatures of 40–50 °C.

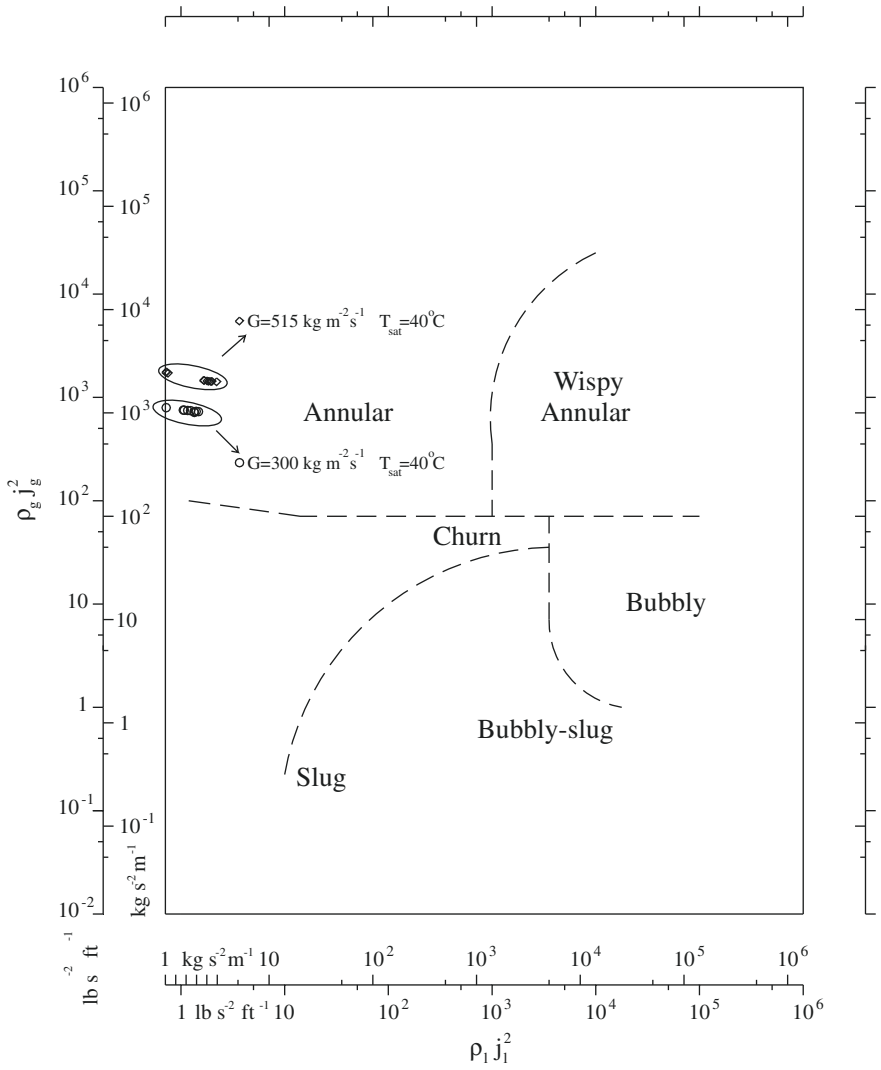

Fig. 12. Flow pattern identification of the experimental data by means of Hewitt and Robertson [4] flow regime map for the mass fluxes of 300–515 kg m^{-2} s^{-1} at the condensing temperature of 40 °C.

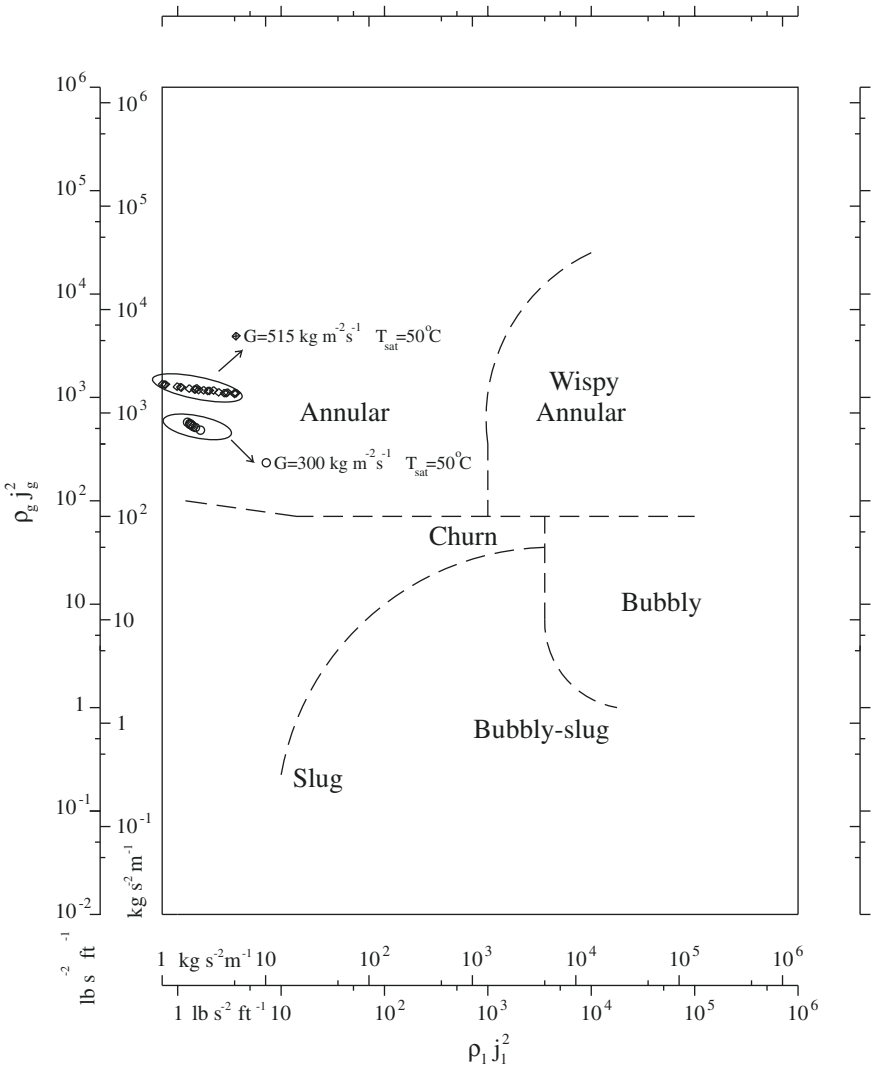

Fig. 13. Flow pattern identification of the experimental data by means of Hewitt and Robertson [4] flow regime map for the mass fluxes of 300–515 kg m^{-2} s^{-1} at the condensing temperature of 50 °C.

of laminar flow. Discussion of the results will be given in turn as follows:

Fig. 5 shows the relationship between the mean film thickness obtained from the model of Barnea et al. (Eq. (17)) and the experimental heat transfer coefficient (Eq. (7)) for the condensation temperatures of 40–50 °C at the mass fluxes of 300 kg m^2 s^{-1} (a) and 515 kg m^{-2} s^{-1} (b) for laminar flow data (Eq. (30)) in a vertical smooth tube. It can be seen that film thickness decreases with increasing heat transfer coefficient; in other words, film thickness decreases with decreases in ΔT_{sat} for similar test conditions. The increase in heat flux in relation to ΔT_{sat} in Eq. (7) increases the condensation rate. In other words, the film thickness on the tube wall increases due to the constant latent heat of condensation for a specific saturation temperature of condensation. It can also be seen that low condensation temperature conditions (40 °C) give larger condensation heat transfer coefficients than high condensation temperature conditions (50 °C) at the same condensing temperature differences for a constant film thickness value. Low condensation pressures, in other words, high temperature differences and alteration of physical properties at low pressure, cause higher local heat transfer coefficients than high condensation pressure.

Fig. 6 shows the same relationship as Fig. 5 for the mass fluxes of 300–515 kg m^{-2} s^{-1}. The effect of the mass flux on the condensation heat transfer coefficient with the condensation temperatures of 40 °C (a) and 50 °C (b) can be seen for the same mass flux in this figure. It can be clearly seen that heat transfer coefficients increase with increasing mass fluxes for a constant film thickness value. This is due to the increase in vapor velocity of R134a.

Fig. 7 shows the relationship between the mean film thickness obtained from the model of Barnea (Eq. (17)) and ΔT_{sat} in the test tube for the mass fluxes of 300 kg m^{-2} s^{-1} (a) and 515 kg m^{-2} s^{-1} (b) and condensing temperatures of 40–50 °C. Trend lines of data indicate that the average film thickness increases with increases in ΔT_{sat} for similar test conditions as explained in the above paragraphs. Verification of the reliability of the calculated film thickness from the model is checked using different condensing temperatures.

Fig. 8 shows the relationship between the void fraction obtained from the model of Barnea et al. (Eq. (31)) and vapor quality in the test tube for the mass fluxes of 300 kg m^{-2} s^{-1} (a) and 515 kg m^{-2} s^{-1} (b) and condensing temperatures of 40–50 °C. Comparison of the void fraction at higher and lower average vapor qualities and smaller liquid film thickness together with higher vapor velocity at the vapor–liquid interface shows an increase in the void fraction when the average quality is higher. Trend lines of data are in accordance with this basic knowledge of in-tube condensation.

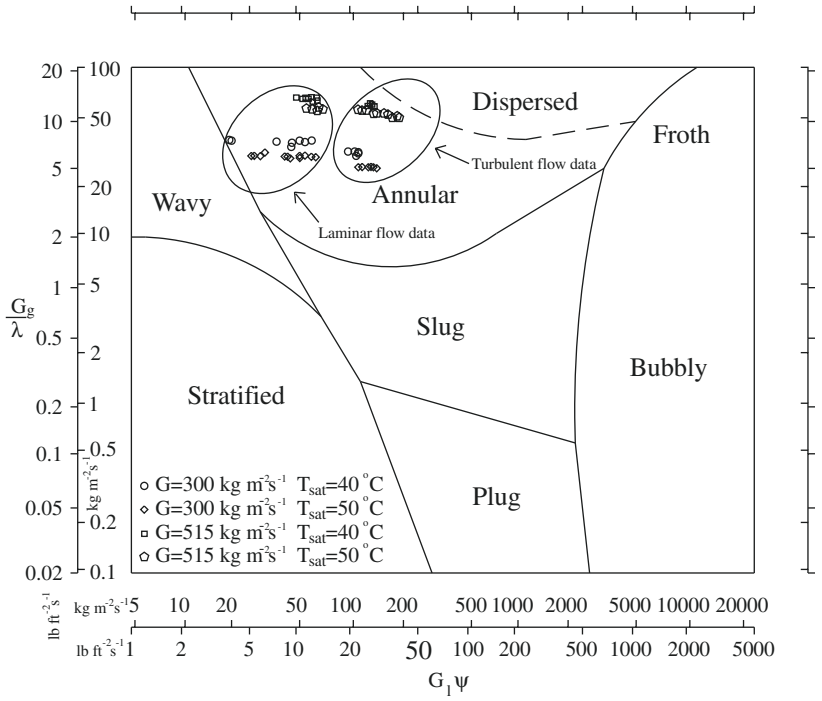

Fig. 14. Flow pattern identification of the experimental data by means of Baker [7] flow regime map for the mass fluxes of 300–515 kg m^{-2} s^{-1} at the condensing temperatures of 40–50 °C.

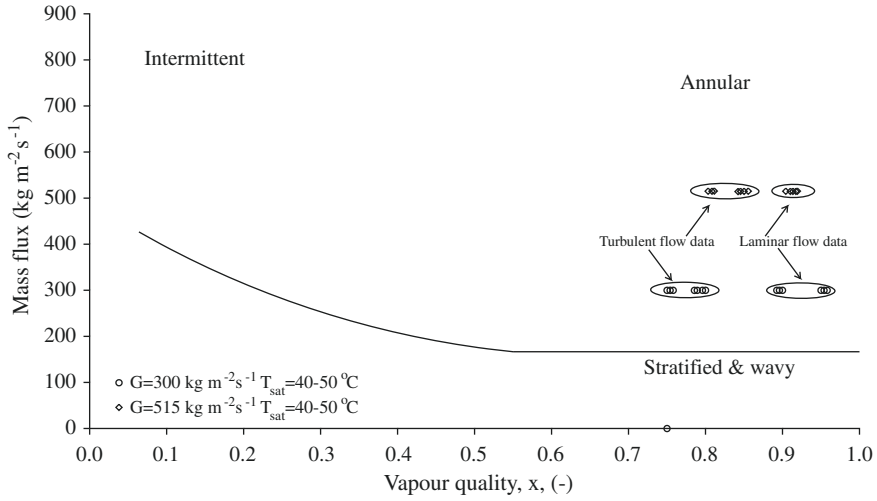

Fig. 15. Flow pattern identification of the experimental data by means of Thome [9] flow regime map for the mass fluxes of 300–515 kg m^{-2} s^{-1} at the condensing temperatures of 40–50 °C.

In Figs. 9 and 10, comparison of the void fraction obtained from the model of Barnea et al. (Eq. (31)) with the most predictive void fraction and correlations shown in Table 2 are presented with a 10% deviation line for the minimum mass flux of 300 kg m^{-2} s^{-1} (Fig. 9) and maximum mass flux of 515 kg m^{-2} s^{-1} (Fig. 10) according to the condensation temperatures of 40 °C (Figs. 9a and 10a) and 50 °C (Figs. 9b and 10b). It is clearly seen from the figures that the void fraction models and correlations of Turner and Wallis [34] and Spedding and Chen [51] have the best predictability of experimental data among 35 void fraction models and correlations given in the authors' previous publications [53,56,59,60]. In addition to this, the majority of the data calculated by the void fraction models of Chisholm and Armand [25,21], Yashar et al. [38], Smith [43], and Chisholm [48] and correlations fall within ±10% and has a good agreement with experimental data.

In Figs. 11–17, well-known flow pattern maps valid for horizontal and vertical tube orientations are presented with the plotted experimental data of the current study. These flow pattern maps are used to show the similarity of annular flow conditions which are independent of tube orientation (horizontal or vertical). Chen et al. [66] also mentioned this similarity in their article. In addition to this, the data shown in these figures were checked by sight glass at the inlet and outlet of the test section. Verification of visual control of the flow regime in the test tube is done using these flow pattern maps in the literature. The flow regime map of Barnea et al. [2] is shown in Fig. 11 for the mass fluxes of 300 kg m^{-2} s^{-1} (a) and

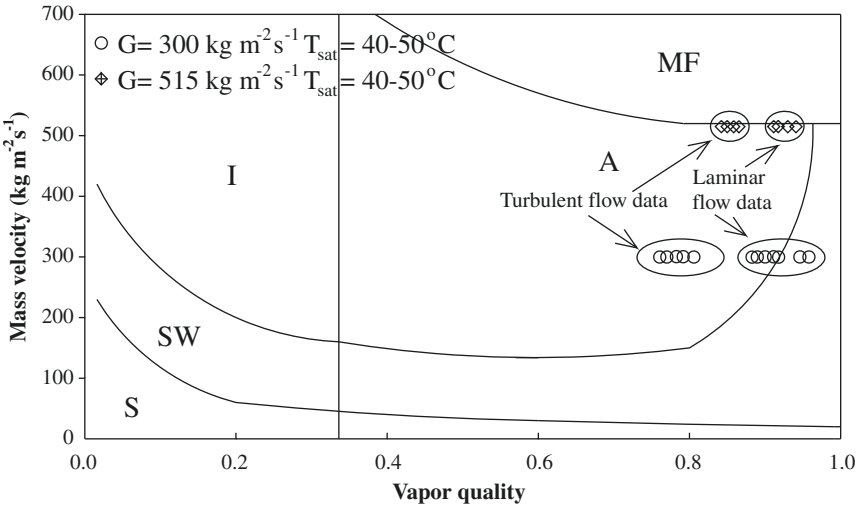

Fig. 16. Flow pattern identification of the experimental data by means of Kattan et al. [13] flow regime map for the mass fluxes of 300–515 kg m^{-2} s^{-1} at the condensing temperatures of 40–50 °C.

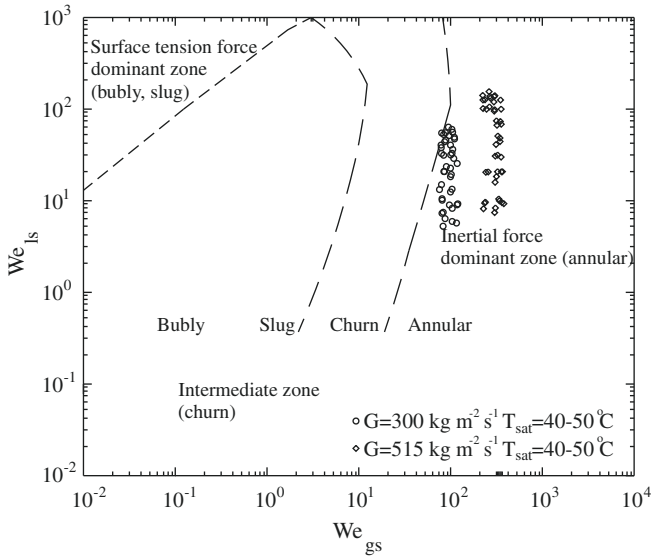

Fig. 17. Flow pattern identification of the experimental data by means of Chen et al. [5] flow regime map for the mass fluxes of 300–515 kg m^{-2} s^{-1} at the condensing temperatures of 40–50 °C.

515 kg m^{-2} s^{-1} (b) at the condensing temperatures of 40 and 50 °C respectively. It is developed for the downward condensation of air–water at the condensing pressure of 0.1 MPa inside 2.5–51 cm i.d. vertical tubes. The results from the analysis using the annular flow model of Barnea et al. [2] were plotted on their map using u_{ls} and u_{gs}, obtained from Eqs. (24) and (25) respectively, as coordinates. The plotted data are in the annular flow area on the map. It shows the accuracy of calculations and visual observation of flow regime by means of sight glasses. Hewitt and Robertson's flow regime map [4] is shown in Figs. 12 and 13 for the mass fluxes of 300–515 kg m^{-2} s^{-1} at the condensing temperatures of 40 °C (Fig. 12) and 50 °C (Fig. 13) separately. It is obtained for the downward condensation of air–water at low pressure and **water-steam at high pressure inside 1–3 cm i.d. vertical tube. Baker's flow regime map [7] is shown in Fig. 14 for the mass fluxes of 300–515 kg m^{-2} s^{-1} at the condensing temperatures of 40–50 °C. It is produced from other researchers' data including condensation of air–water and natural gas oil in horizontal tubes. Thome's flow regime map [9] is shown in Fig. 13 for the mass fluxes of 300–515 kg m^{-2} s^{-1} at the condensing temperatures of 40–50 °C. It is prepared by means of several different experimental conditions belonging to boiling and evaporation for 0.9–10 mm i.d. horizontal tubes up to 64 bars. The flow regime map of Kattan et al. [13] is shown in Fig. 16 for the mass fluxes of 300–515 kg m^{-2} s^{-1} at the condensing temperatures of 40–50 °C. It is the reference flow regime map of Thome [9] and is based on boiling experiments. The flow regime map of Chen et al. [5] is shown in Fig. 17 for the mass fluxes of 300–515 kg m^{-2} s^{-1} at the condensing temperatures of 40–50 °C; these experiments were done for the boiling of R134a at 6–14 bars during vertical upward flow in 1.1–4.26 mm i.d. tubes. It can be clearly seen from these figures that all the data were collected in the annular flow regime sections of these figures.

A large number of graphics could be generated from the output of the calculations; however, due to repetition of similar characteristics of trend lines in figures, only typical results are shown for limited data. It should also be noted that detailed information on the explanations above and some additional figures with different experimental parameters related to this study can be seen in the authors' previous publications [53–65].

5. Conclusion

Co-current downward condensation heat transfer of R134a was experimentally investigated in a 8.1 mm i.d. vertical smooth tube. Accurate and repeatable heat transfer data during annular flow are obtained. There are few researches on the parameters and content of such cases in the literature. For this reason, the results of this study are expected to fill a gap in the literature. The validation process of the investigated annular flow model and correlation development was accomplished by using a large number of data points in each case. The following results were obtained:

A study on the theoretical model of the flow regime transition mechanism of Barnea et al. [2] was performed using experimental data in an algorithm to determine accurate film thickness and void fraction values under the various test conditions. The effects of various relevant parameters such as condensing temperature, condensation temperature difference, vapor quality, and mass flux on the film thickness and void fraction are discussed and investigated in detail. In order to verify the results of calculations, the data obtained from various void fraction correlations were compared. The void fraction models and correlations of Turner and Wallis

[34], Spedding and Chen [51], Chisholm and Armand [25,21], Yashar et al. [38], Smith [43], and Chisholm [48] are found to be in good agreement with the void fraction values obtained from the model of Barnea et al. [2] in the ±10% error band.

According to the flow regime identification analysis in the paper, the flow pattern maps of Barnea et al. [2], Hewitt and Robertson [4], Baker [7], Thome [9], Kattan et al. [9], and Chen et al. [5] are capable of predicting the annular flow regime conditions checked by sight glasses in the experimental apparatus.

Acknowledgements

The authors are indebted to the Department of Mechanical Engineering, King Mongkut's University of Technology Thonburi (KMUTT) and the Thailand Research Fund for supporting this study. Especially, the first author wishes to thank KMUTT for providing him with a Post-doctoral fellowship.

References

[1] M.G. Hubbard, A.E. Dukler, The characterization of flow regimes for horizontal twophase flow, in: Proceedings of the Heat Transfer and Fluid Mechanics Institute, Stanford University Press, 1966.
[2] D. Barnea, O. Shoham, Y. Taitel, Flow pattern transition for vertical downward two phase flow, Chemical Engineering Science 37 (1982) 741–744.
[3] J.R. Fair, What you need to know to design thermosyphon reboilers, Petroleum Refiner 39 (2) (1960) 105.
[4] G.F. Hewitt, D.N. Robertson, Studies of Two-Phase Flow Patterns by Simultaneous X-ray and Flash Photography, Rept. AERE-M2159, UKAEA, Harwell, 1969.
[5] L. Chen, Y.S. Tian, T.G. Karayiannis, The effect of tube diameter on vertical two-phase flow regimes in small tubes, International Journal of Heat and Mass Transfer 49 (2006) 4220–4230.
[6] T.S. Zhao, Q.C. Bi, Co-current air–water two-phase flow patterns in vertical triangular microchannels, International Journal of Multiphase Flow 27 (2001) 765–782.
[7] O. Baker, Design of pipe lines for simultaneous flow of oil and gas, Oil and Gas Journal 26 (1954) 185–195.
[8] J.M. Mandhane, G.A. Gregory, K. Aziz, A flow pattern map for gas–liquid flow in horizontal pipes, International Journal Multiphase Flow 1 (1974) 537–553.
[9] J.R. Thome, Update on advances in flow pattern based two-phase heat transfer models, International Journal of Heat and Mass Transfer 29 (2005) 341–349.
[10] J. El Hajal, J.R. Thome, A. Cavallini, Condensation in horizontal tubes, part 1: two-phase flow pattern map, International Journal of Heat and Mass Transfer 46 (2003) 3349–3363.
[11] J.W. Coleman, S. Garimella, Characterization of two-phase flow patterns in small diameter round and rectangular tubes, International Journal of Heat and Mass Transfer 42 (1999) 2869–2881.
[12] J.W. Coleman, S. Garimella, Two-phase flow regimes in round, square and rectangular tubes during condensation of refrigerant R134a, International Journal of Heat and Mass Transfer 26 (2003) 117–128.
[13] N. Kattan, J.R. Thome, D. Favrat, Flow boiling in horizontal tubes. Part 1: development of a diabatic two-phase flow pattern map, Journal of Heat Transfer 120 (1998) 140–147.
[14] Y. Taitel, A.E. Dukler, A model for prediction flow regime transitions in horizontal and near horizontal gas–liquid flow, AIChE Journal 22 (1976) 47–55.
[15] J. Weisman, D. Duncan, J. Gibson, T. Crawford, Effects of fluid properties and pipe diameter on two-phase flow patterns in horizontal lines, International Journal Multiphase Flow 5 (1979) 437–462.
[16] G. Breber, J.W. Palen, J. Taborek, Prediction of horizontal tube-side condensation of pure components using flow regime criteria, Journal of Heat Transfer 102 (1980) 471–476.
[17] H.M. Soliman, On the annular-to-wavy flow pattern transition during condensation inside horizontal tubes, Canadian Journal of Chemical Engineering 60 (1982) 475–481.
[18] T.N. Tandon, H.K. Varma, C.P. Gupta, A new flow regime map for condensation inside horizontal tubes, Journal of Heat Transfer 104 (1982) 763–768.
[19] B. Mederic, P. Lavieille, M. Miscevic, Heat transfer analysis according to condensation flow structures in a minichannel, Experimental Thermal and Fluid Science 30 (2006) 785–793.
[20] R.H. Huq, J.L. Loth, Analytical two-phase flow void fraction prediction method, Journal of Thermo Physics 6 (1992) 139–144.
[21] A.A. Armand, The resistance during the movement of a two-phase system in horizontal pipes, Izvestiya Vsesoyuznogo Teplotekhnicheskogo Instituta 1 (1946) 16–23.
[22] D. Chisholm, A.D.K. Laird, Two phase flow in rough tubes, Transactions of ASME 80 (1958) 276–286.
[23] D. Steiner, Heat transfer to boiling saturated liquids, VDI-Warmeatlas (VDI Heat Atlas), in: Verein Deutscher Ingenieure (Ed.), VDI-Gessellschaft Verfahrenstechnik und Chemie-ingenieurwesen (GCV), Translator: J.W. Fullarton, Dusseldorf, 1993.
[24] T. Harms, D. Eckart, A. Groll, J. Braun, A void fraction model for annular flow in horizontal tubes, International Journal of Heat and Mass Transfer 46 (2003) 4051–4057.
[25] D. Chisholm, Two Phase Flow in Pipelines and Heat Exchangers, George Godwin in Association with The Institution of Chemical Engineers, London, 1983.
[26] A.A. Armand, G.G. Treschev, The resistance during the movement of a two-phase system in horizontal pipes, Izvestiya Vsesoyuznogo Teplotekhnicheskogo Instituta 1 (1946) 16–23.
[27] S.G. Bankoff, A variable density single-fluid model for two-phase flow with particular reference to steam–water flow, Transactions ASME Journal of Heat Transfer 82 (1960) 265–272.
[28] V. Czop, D. Barbier, S. Dong, Pressure drop, void fraction and shear stress measurements in adiabatic two-phase flow in coiled tube, Nuclear Engineering Design 149 (1994) 323–333.
[29] T.N. Tandon, H.K. Varma, C.P. Gupta, A void fraction model for annular two-phase flow, International Journal of Heat and Mass Transfer 28 (1985) 191–198.
[30] D. Graham, J.C. Chato, T.A. Newell, Heat transfer and pressure drop during condensation of refrigerant 134a in an axially grooved tube, International Journal of Heat and Mass Transfer 42 (1999) 1935–1944.
[31] G.A. Hughmark, Holdup in gas–liquid flow, Chemical Engineering Progress 58 (1962) 62–65.
[32] P.J. Hamersma, J. Hart, A pressure drop correlation for gas/liquid pipe flow with a small liquid holdup, Chemical Engineering Science 42 (1987) 1187–1196.
[33] R.W. Lockhart, R.C. Martinelli, Proposed correlation of data for isothermal two-phase, two-component flow in pipes, Chemical Engineering Progress 45 (1949) 39–48.
[34] J.M. Turner, G.B. Wallis, The Separate-Cylinders Model of Two-Phase Flow, Paper No. NYO-3114-6. Thayer's School Eng., Dartmouth College, Hanover, NH, USA, 1965.
[35] G.B. Wallis, One-Dimensional Two-Phase Flow, McGraw-Hill, 1965. pp. 51–54.
[36] P. Domanski, D. Didion, Computer modeling of the vapor compression cycle with constant flow area expansion device, Building Science Series, National Bureau of Standards of USA, 1983.
[37] M.J. Wilson, T.A. Newell, J.C. Chato, C.A. Infante Ferreira, Refrigerant charge, pressure drop and condensation heat transfer in flattened tubes, International Journal of Refrigeration 26 (2003) 442–451.
[38] D.A. Yashar, T.A. Newell, J.C. Chato, Experimental Investigation of Void Fraction During Horizontal Flow in Smaller Diameter Refrigeration Applications, ACRC TR-141, Air Conditioning and Refrigeration Center, University of Illinois, Urbana–Champaign, IL, 1998.
[39] A. Premoli, D. Francesco, A. Prima, An empirical correlation for evaluating two-phase mixture density under adiabatic conditions, in: European Two-Phase Flow Group Meeting, Milan, Italy, 1970.
[40] A. Kawahara, M. Kawaji, P.M.Y. Chung, M. Sadatomi, K. Okayama, Effects of channel diameter and liquid properties on void fraction in adiabatic two-phase flow through microchannels, Heat Transfer Engineering 26 (2005) 13–19.
[41] S.M. Zivi, Estimation of steady-state steam void-fraction by means of the principle of minimum entropy production, Transactions ASME Journal of Heat Transfer Series C 86 (1975) 247–252.
[42] G. Rigot, Fluid capacity of an evaporator in direct expansion, Plomberie 328 (1973) 133–144.
[43] S.L. Smith, Void fractions in two-phase flow: a correlation based upon an equal velocity head model, Proceedings of the Institution of Mechanical Engineers 36 (1969) 647–664.
[44] S. Levy, Steam slip theoretical prediction from momentum model, Transactions ASME Journal of Heat Transfer Series C 82 (1960) 113–124.
[45] H. Fauske, Critical two-phase, steam–water flows, in: Proceedings of the 1961 Heat Transfer and Fluid Mechanics Institute, Stanford University Press, Stanford, CA, pp. 79–89.
[46] J.R.S. Thom, Prediction of pressure drop during forced circulation boiling of water, International Journal of Heat and Mass Transfer 7 (1964) 709–724.
[47] C.J. Baroczy, Correlation of liquid fraction in two-phase flow with application to liquid metals, Chemical Engineering Progress Symposium Series 61 (1965) 179–191.
[48] D. Chisholm, Pressure gradients due to friction during the flow of evaporating two-phase mixtures in smooth tubes and channels, International Journal of Heat and Mass Transfer 16 (1973) 347–358.
[49] N. Madsen, A void fraction correlation for vertical and horizontal bulk-boiling of water, AIChE Journal 21 (1975) 607–608.
[50] F.W. Ahrens, Heat pump modeling, simulation and design, in: Proceedings of the NATO Advanced Study Institute on Heat Pump Fundamentals, Espinho, Spain, 1980.
[51] P.L. Spedding, J.J. Chen, Holdup in two phase flow, International Journal of Multiphase Flow 10 (1984) 307–339.
[52] J.J.J. Chen, A further examination of void-fraction in annular two-phase flow, International Journal of Heat Mass Transfer 29 (1986) 1760–1763.
[53] A.S. Dalkilic, S. Laohalertdecha, S. Wongwises, Effect of void fraction models on the two-phase friction factor of R134a during condensation in vertical downward flow in a smooth tube, International Communications in Heat and Mass Transfer 35 (2008) 921–927.
[54] A.S. Dalkilic, S. Yildiz, S. Wongwises, Experimental investigation of convective heat transfer coefficient during downward laminar flow condensation of

R134a in a vertical smooth tube, International Journal of Heat and Mass Transfer 52 (2009) 142–150.
[55] A.S. Dalkilic, S. Laohalertdecha, S. Wongwises, Two-phase friction factor in vertical downward flow in high mass flux region of refrigerant HFC-134a during condensation, International Communications in Heat and Mass Transfer 35 (2008) 1147–1152.
[56] A.S. Dalkilic, S. Laohalertdecha, S. Wongwises, Effect of void fraction models on the film thickness of R134a during downward condensation in a vertical smooth tube, International Communications in Heat and Mass Transfer 36 (2009) 172–179.
[57] A.S. Dalkilic, S. Wongwises, Intensive literature review of condensation inside smooth and enhanced tubes, International Heat and Mass Transfer 52 (2009) 3409–3426.
[58] A.S. Dalkilic, S. Laohalertdecha, S. Wongwises, Experimental investigation on heat transfer coefficient of R134a during condensation in vertical downward flow at high mass flux in a smooth tube, International Communications in Heat and Mass Transfer 36 (2009) 1036–1043.
[59] A.S. Dalkilic, S. Laohalertdecha, S. Wongwises, A comparison of the void fraction correlations of R134a during condensation in vertical downward laminar flow in a smooth and micro-fin tube, in: Proceedings of the 1st International Conference on Micro/Nanoscale Heat Transfer, January 06–09, ASME, Taiwan, 2008.
[60] A.S. Dalkilic, S. Laohalertdecha, S. Wongwises, Two-phase friction factor obtained from various void fraction models of R-134a during condensation in vertical downward flow at high mass flux, in: Proceedings of the 1st International Conference on Heat Transfer, August 10–14, ASME, USA, 2008.
[61] A.S. Dalkilic, S. Laohalertdecha, S. Wongwises, Experimental investigation on the condensation heat transfer and pressure drop characteristics of R134a at high mass flux conditions during annular flow regime inside a vertical smooth tube, in: Summer Heat Transfer Conference, July 19–23, ASME, USA, 2009.
[62] A.S. Dalkilic, O. Agra, Experimental apparatus for the determination of condensation heat transfer coefficient for R134a and R600a flowing inside vertical and horizontal tubes, in: Summer Heat Transfer Conference, July 19–23, ASME, USA, 2009.
[63] A.S. Dalkilic, S. Laohalertdecha, S. Wongwises, Experimental research on the similarity of annular flow models and correlations for the condensation of R134a at high mass flux inside vertical and horizontal tubes, in: International Mechanical Engineering Congress and Exposition, November 13–19, ASME, USA, 2009.
[64] A.S. Dalkilic, S. Wongwises, A heat transfer model for co-current downward laminar film condensation of R134a in a vertical micro-fin tube during annular flow regime, in: Eleventh UK National Heat Transfer Conference, September 6–8, Queen Mary University of London, 2009.
[65] A.S. Dalkilic, O. Agra, I. Teke, S. Wongwises, Comparison of frictional pressure drop models during annular flow condensation of R600a in a horizontal tube at low mass flux and of R134a in a vertical tube at high mass flux, International Journal of Heat and Mass Transfer, in press, doi:10.1016/j.ijheatmasstransfer.2009.12.051.
[66] S.L. Chen, F.M. Gerner, C.L. Tien, General film condensation correlations, Experimental Heat Transfer 1 (1987) 93–107.
[67] S.J. Kline, F.A. McClintock, Describing uncertainties in single sample experiments, Mechanical Engineering (1953) 3–8.

International Journal of Heat and Mass Transfer 53 (2010) 3449–3459

Contents lists available at ScienceDirect

International Journal of Heat and Mass Transfer

journal homepage: www.elsevier.com/locate/ijhmt

Flow mechanisms of HFC-410A inside short-tube orifices during flashing process

Kitti Nilpueng, Somchai Wongwises *

Fluid Mechanics, Thermal Engineering and Multiphase Flow Research Lab (FUTURE), Department of Mechanical Engineering, King Mongkut's University of Technology Thonburi, Bangmod, Bangkok 10140, Thailand

ARTICLE INFO

Article history:
Received 4 January 2010
Received in revised form 26 February 2010
Accepted 26 February 2010
Available online 3 May 2010

Keywords:
Expansion device
Short-tube orifice
Temperature distribution
Metastable flow
Choked flow

ABSTRACT

New experimental data of HFC-410A flow mechanisms, including pressure and temperature distributions, flow pattern, and mass flow rate inside a short-tube orifice are studied. Different short-tube orifice lengths of 10 mm, 15 mm, and 20 mm, with short-tube orifice diameters ranging from 0.849 to 1.096 mm were manufactured for this experiment. The test runs are done at upstream pressures ranging from 2100 to 2600 kPa, and with a degree of subcooling between 4 and 12 °C. The results show that the refrigerant flow mechanisms in the entrance region and inside a short-tube orifice agree with incompressible flow theory, but the refrigerant flow mechanisms in the exit region are similar to choked flow in a theoretical compressible flow. The temperature distribution inside a short-tube orifice is directly related to the pressure distribution. The mass flow rate is directly proportional to the upstream pressure and degree of subcooling, whereas it is strongly affected by the short-tube diameter. The downstream pressure has insignificant effects on the mass flow rate and pressure distribution inside a short-tube orifice. However, the downstream pressure has a slight effect on the temperature distribution inside a short-tube orifice.

1. Introduction

In recent years, hydrofluorocarbon (HFC) refrigerants and HFC refrigerant mixtures have been developed for use as alternatives to chlorofluorocarbon (CFC) and hydrochlorofluorocarbon (HCFC) refrigerants which are applied in refrigeration and air-conditioning systems, because the chlorine molecules from these refrigerants destroy the earth's ozone layer. Although the change of refrigerant properties will help to protect the environment, it may lead to a change in system performance. Therefore, in order to obtain the proper system performance with the new HFC refrigerants, performance data are required for each component.

An expansion device is another basic component of a refrigeration system. The main purpose of the expansion device is to reduce the pressure of the refrigerant from the condenser pressure to the evaporator pressure and to regulate the mass flow rate of refrigerant flowing from the condenser to the evaporator at a rate equal to the evaporation rate in the evaporator. During the flow of liquid refrigerant through the expansion device, the pressure decreases rapidly below the saturation pressure and the refrigerant is changed from a subcooled liquid or saturated liquid to a liquid–vapour mixture. This behaviour is defined as a flashing process. The short-tube orifice is one type of expansion device popularly used in residential and automotive air-conditioning systems. The advantages of a short-tube orifice are its simplicity, low initial cost, high reliability, and ease of maintenance. To obtain appropriate operation and performance of refrigeration systems using short-tube orifices as expansion devices, the flow of refrigerant should be choked flow. Under choked flow conditions, the flow of refrigerant through the short-tube orifice corresponds to the critical flow rate, which is the maximum flow rate that can be attained by reducing the downstream pressure under given upstream conditions. Consequently, an understanding of the flow mechanisms of the refrigerant through a short-tube orifice under choked flow conditions is very important for the proper design of the system.

During past decades, the performance characteristics of short-tube orifices have been studied by a number of researchers. Recent studies associated with flow patterns, pressure and temperature distributions and mass flow rate under choked flow conditions inside the short-tube orifice are outlined in the following paragraphs.

1.1. Flow pattern

For two-phase flow studies, it is not possible to understand flow phenomena without a clear understanding of the flow patterns, as these influence the two-phase pressure drop, holdup, system stability, and exchange rate of momentum, heat, and mass during the phase-change heat transfer process. Therefore, identification of the flow pattern inside the channel is very useful for developing suitable calculation techniques. Investigations of refrigerant flow pattern inside short-tube orifices have been published by some researchers.

* Corresponding author. Tel.: +662 470 9115; fax: +662 470 9111.
E-mail address: somchai.won@kmutt.ac.th (S. Wongwises).

0017-9310/$ - see front matter © 2010 Elsevier Ltd. All rights reserved.
doi:10.1016/j.ijheatmasstransfer.2010.04.005

Pasqua [1] studied the characteristics of subcooled and saturated liquid CFC-12 flow inside glass short tubes. For subcooled liquids entering short tubes, he found that the liquid flashed inside the short tube when the downstream pressure was near or below the saturation pressure. The fluid inside the short tube was described as a metastable inner core of liquid surrounded by a two-phase annular ring. The diameter of the metastable liquid core decreased as the fluid proceeded to the tube exit. Aaron and Domanski [2] observed the flow pattern of subcooled liquid HCFC-22 at the inlet and outlet of short tubes with $5 < L/D < 20$. They stated that the microscopic bubbles suspended in the liquid covered the short-tube outlet in a homogeneous form over several inches when the downstream pressure was close to saturation pressure. Kim [3] investigated experimentally the flow pattern of two-phase and subcooled liquid HCFC-22 and HFC-134a through short-tube orifices with a length to diameter ratio ranging between 7 and 20. The results showed that the liquid refrigerant did not flash in the inlet region although the pressure was lower than the saturation pressure. The flashing point moved to the outlet section of the short-tube when increasing the degree of subcooling. Nilpueng and Wongwises [4] investigated experimentally the two-phase flow pattern of HFC-134a through short-tube orifices. The results showed that flow patterns could be divided into two types: metastable liquid flow, and two-phase flow. In the metastable liquid flow region, the liquid refrigerant which looked like a cone shape flowed in the central core of the tube while a two-phase flow which had many tiny bubbles mixed in the liquid refrigerant surrounded the liquid refrigerant. In the two-phase flow region, there were many tiny bubbles mixed with the liquid refrigerant.

1.2. Pressure and temperature distribution

The pressure and temperature distributions of refrigerant inside a short-tube are some of the most important parameters required for the selection of the proper short-tube size for given operating conditions and capacity. However, it is found that the pressure and temperature distributions have been studied and published by only a few previous researchers.

The pressure distribution of HCFC-22 inside a short-tube orifice was measured by Aaron and Domanski [2]. In their experiment, six pressure taps which were bored to 0.08 mm were located along a short-tube orifice. The results indicated that a large variation of pressure appeared at the inlet and outlet of the short-tube orifice. The pressure tended to recover and slightly decrease inside the tube after the refrigerant flowed through the inlet section. Kim [3] studied the pressure profile of HCFC-22 and HFC-134a through a short-tube orifice. He reported that the pressure was lower than the saturation pressure when the flow of refrigerant passed through the inlet section. The pressure profile along the short-tube was increased as the degree of subcooling was increased. Liu et al. [5] investigated the pressure profile of R744 flow through short-tube orifices. They described that the rapid change of velocity and abrupt inlet loss of fluid were the cause of a large pressure drop at the inlet while the large pressure drop at the outlet was produced by the great expansion of refrigerant. The average pressure inside the short-tube increased when the upstream pressure was increased. The pressure and temperature distributions of HFC-134a inside a short-tube orifice were studied by Nilpueng and Wongwises [4] and Nilpueng and Wongwises [6]. The results indicated that the pressure greatly decreased at the inlet, then slightly increased and steadily decreased inside the tube. They concluded that the refrigerant in the short-tube orifice exists under non-equilibrium thermodynamic conditions.

1.3. Mass flow rate

In order to achieve an appropriate operation and performance of refrigeration systems, it is very important to quantify the maximum flow rate through a short-tube orifice. Consequently, the mass flow rate of refrigerant inside a short-tube orifice under choked flow conditions was investigated by several researchers.

Mei [7] investigated the flow of subcooled liquid HCFC-22 through short-tubes with $7.5 < L/D < 11.9$. He reported that first-stage choking occurred at a degree of subcooling of 22.2 °C. However, there was no indication of second-stage choking in the normal heat pump operating range. The effects of upstream subcooling, upstream pressure, downstream pressure, tube length, tube diameter, entrance chamfering, and exit chamfering on the flow rate of HCFC-22 through a short-tube were examined by Aaron and Domanski [2], Kim[3], and Kim and O'Neal [8]. Their results showed that the mass flow rate depends on upstream pressure and upstream subcooling, but that it is insensitive to downstream pressure due to approximate choking. Aaron and Domanski [2] recommended that the L/D ratio should be greater than 5 in order to achieve choked flow. The mass flow rate of HFC-134a along a short-tube was reported by Kim [3], Singh et al. [9], Tu et al. [10] and Nilpueng and Wongwises [6]. Their results showed that the short-tube orifice diameter has a significant effect on the increase in flow rate. In addition, Nilpueng and Wongwises [6] recorded that the choked flow phenomenon disappeared inside a short-tube orifice when L/D was less than 2.91. Payne and O'Neal [11] studied the flow rate of HFC-407C through short-tube orifices with diameters of 1.09–1.94 mm. They found that the addition of oil to the refrigerant increased the mass flow rate by more than 12% for two-phase flow entering the short tube; but, it had little effect on mass flow rate at a high degree of subcooling. Liu et al. [5] studied the flow of R744 through short-tube orifices. Short tubes with lengths between 8.02 and 25.42 mm and diameters between 0.83 and 1.53 mm were tested. The results showed that choked flow existed under a wide range of operating conditions. Kim et al. [12] investigated the mass flow rate of HFC-410A through short-tube orifices at upstream pressures approaching the critical point. They found that the decrease of mass flow rate with a reduction of subcooling became more significant when upstream pressure increased beyond 3.604 kPa, due to a higher density change.

As described above, it can be clearly seen that previous published papers have reported the flow mechanisms of CFC and HCFC refrigerants through short-tube orifices. But, the studies on HFC refrigerants and HFC refrigerant mixtures inside short-tube orifices have been investigated by only a few previous research works; especially, HFC-410A which is favourably used to replace HCFC-22 in domestic air conditioners and heat pumps. The main purpose of the present paper is to study the HFC-410A refrigerant flow mechanisms inside short-tube orifices, including pressure and temperature distributions, flow pattern, mass flow rate, metastable flow, and choked flow. The effects of the relevant parameters, i.e., upstream pressure, downstream pressure, degree of subcooling, short-tube diameter, and short-tube length on flow pattern, mass flow rate, and pressure distribution that have never been observed before are also investigated.

2. Experimental apparatus

The experimental apparatus described in Nilpueng and Wongwises [4] was used in the present study. A schematic diagram of the test facility is provided in Fig. 1. The system consists of three main loops: the refrigerant loop, the hot water loop and the cold water loop. The refrigerant loop consists of the main refrigeration system components: compressor, condenser, short-tube orifice (test

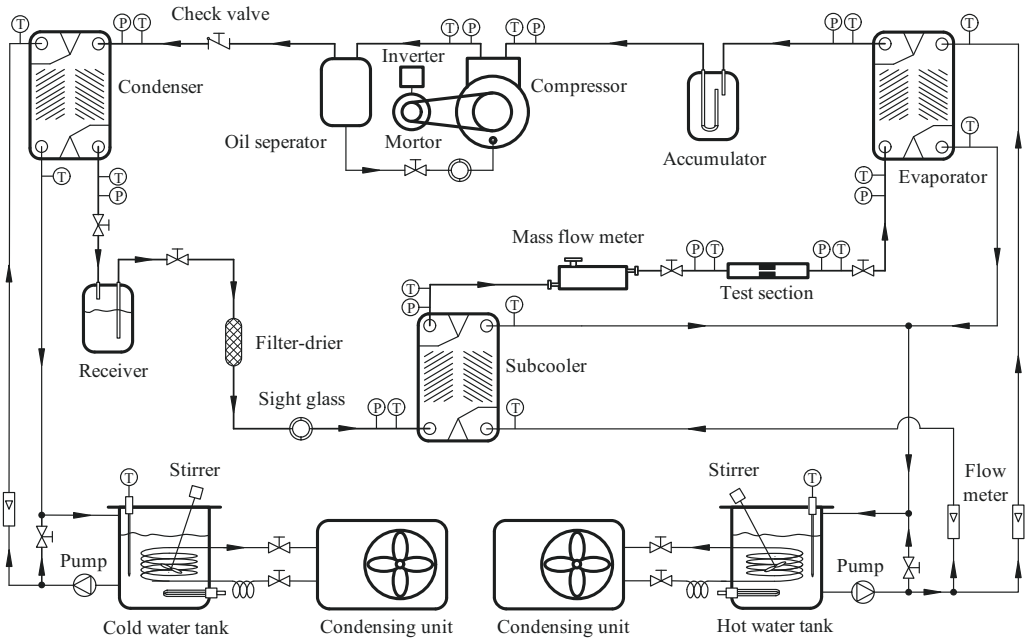

Fig. 1. Schematic diagram of experimental apparatus.

section), evaporator, and other accessory parts: oil separator, liquid receiver, filter/drier, sight glass, sub-cooler and accumulator. A commercial HFC-410A is used as the working fluid. A two-cylinder single stage reciprocating compressor, driven by an electric motor, is used to discharge the refrigerant. The speed of the motor is varied so as to provide a wide range of mass flow rates by means of an inverter. A helical oil separator is used to minimize the effect of lubricating oil on refrigerant flow through short-tube orifices. The efficiency of oil separation is approximately 99%. Compact plate heat exchangers are used as condenser, evaporator and subcooler.

In this experiment, the hot water loop and cold water loop are used for transferring heat to evaporator and from condenser, respectively. An electric heater and a separated refrigeration system are installed in the water tank so as to control the water temperature. The hot water is supplied from a hot water tank by the circulating pump and passes through the flow meter and evaporator. The downstream pressure of the test section is controlled by adjusting the temperature and the flow rate of hot water. The condenser rejects heat to the water coming from a cold water tank. The upstream pressure of the test section is regulated by adjusting the temperature of the cold water. The degree of subcooling of the refrigerant entering the test section is adjusted by varying the flow rate of water to the sub-cooler. The test runs are chosen to cover a wide range of working conditions of an air-conditioner and heat pump. The upstream pressures are set at 2100, 2250, 2400 and 2600 kPa, while downstream pressures are varied between 1000 and 1250 kPa. The degree of subcooling is varied from 4 to 12 °C.

There are two groups of short-tube orifices used in the experiment. The first group consists of the specially designed glass short-tube orifices, which permit visual observation of the flow patterns of refrigerant inside the tubes. The other group is made of brass and is used to study the temperature and pressure distributions. Table 1 lists the short-tube orifices used in this study. A specially designed short-tube orifice is used to observe the flow behaviour of refrigerant inside the tube (Fig. 2). It consists of glass short-tube orifices, a glass tube, acrylic tube, brass connector, copper tube, rubber o-ring and attachment set. Glass short-tube orifices were manufactured from glass capillary tube so as to allow

Table 1
Dimension of the short-tube orifices.

Short tube	Diameter (mm)	Length (mm)
1	0.851	10
2	0.849	15
3	0.869	20
4	0.961	10
5	0.961	15
6	0.935	20
7	1.096	10
8	1.085	15
9	1.091	20

the visualization of refrigerant flow inside short-tube orifices. The glass short-tube orifice and the glass tube are fitted into the acrylic tube. The brass connectors are used to link the copper tube with the glass tube. The rubber o-rings are inserted between the glass short-tube orifice, glass tube, and brass connector in order to prevent leakage of refrigerant. The glass short-tube orifice is supported by the attachment set to resist high pressure. The flow pattern of refrigerant inside the short-tube orifice is registered by a digital camera (Sumsung Digimax V3) with shutter speed of 1/2000 s, mounted together with a 20× magnification lens.

Fig. 3 shows a schematic diagram of the short-tube orifice for pressure and temperature distribution measurements. Six pressure and temperature taps are drilled at 0.2 mm diameter along the orifices using a wire cutting machine. Two pressure and temperature taps are drilled to 0.5 mm before and after the short-tube orifice. The thermocouples are installed into a 2 mm diameter hole without disturbance in the flow field and fixed with special glue applied to the outside of the short-tube orifice. The thermocouples are insulated with a 6.4 mm thick Aeroflex standard sheet to reduce the effect of heat transfer on measurement errors.

A microscope (Olympus BX51) is used to measure the diameter of the short-tube orifice. The length of the short-tube orifice is measured with a digital calliper. The accuracies of diameter and length measurements are ±0.001 mm and ±0.01 mm, respectively. The pressure distribution inside the short-tube orifice was detected by pressure transducers calibrated from 0 to 30 bar with

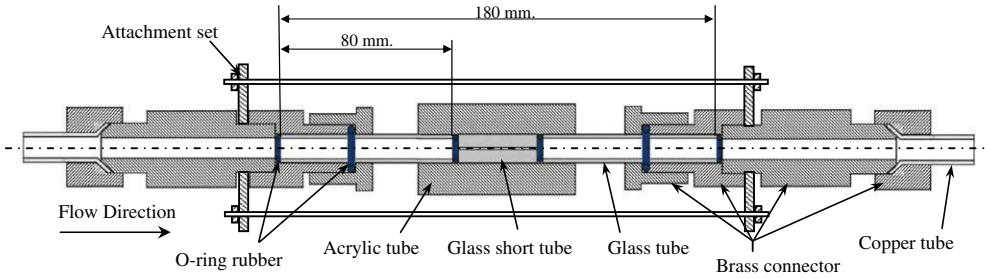

Fig. 2. Schematic diagram of test section for visual observation.

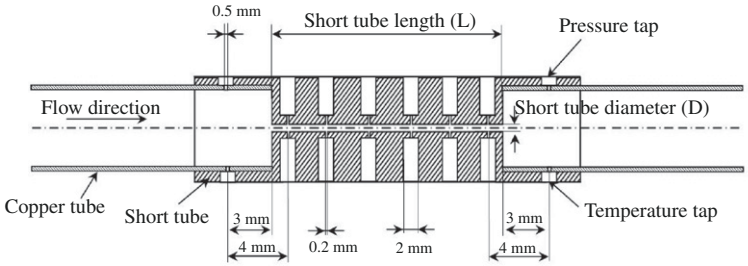

Fig. 3. Schematic diagram of test section for measuring pressure and temperature distribution.

±20 mbar accuracy. T-type thermocouples were used to measure fluid temperature. The uncertainty of the temperature measurement was ±0.1 °C. The differential transducer had an accuracy of ±0.1% of its calibrated span. The flow rate of refrigerant through the short-tube orifice was measured by a Coriolis mass flow meter (ABB FCM2000) with an accuracy of ±0.25%.

3. Results and discussion

This study presents the flow mechanisms of HFC-410A, including pressure distribution, temperature distribution, flow pattern, metastable flow, choked flow and mass flow rate, inside a short-tube orifice during a flashing process. The effects of operating conditions and short-tube orifice dimensions on the flow mechanisms are also explained.

3.1. Pressure and temperature distributions

One of the purposes of the refrigerant expansion device is to reduce the refrigerant pressure from the condenser pressure to the evaporator pressure, which also results in a temperature drop. Therefore, knowledge of the pressure and temperature distributions inside short-tube orifices is important for the proper design and selection of short-tube orifices.

The pressure and temperature distributions of HFC-410A along a short-tube orifice are shown in Fig. 4. It is found from the figure that the pressure and temperature greatly decrease in the entrance region, slightly increase over a short length and gradually decrease thereafter inside the short-tube orifice, and rapidly decrease in the exit region. In addition, it can be seen that the temperature distribution inside the short-tube orifice is directly related to the pressure distribution. This is because the refrigerant pressure is lower than the saturation pressure corresponding to upstream pressure after the flow of refrigerant passes the entrance plane. This means that the liquid refrigerant changes into a liquid–vapour mixture and the temperature varies directly with pressure.

The large pressure drop in the entrance region can occur because the refrigerant flow area is constricted into *vena contracta*. Therefore, the upstream pressure is suddenly converted into kinetic energy and becomes the minimum pressure in the *vena contracta*. Moreover, it is also found that a pressure loss is produced due to an inertial effect and wall shear stress in the entrance region. The results from this study show that the minimum pressure appears about 1 mm from the entrance plane. The cause of the pressure rise and pressure decrease inside the short-tube can be explained by the slight increase of flow area in the entrance region and shear stress between refrigerant and tube wall inside the short-tube orifice, respectively. Considering the pressure variation in the exit region, this implies that the flow behaviour of the refrigerant does not conform to incompressible fluid flow theory, but is similar to the compressible flow through a converging nozzle when the velocity in the exit plane reaches sonic speed. Under these conditions, the pressure reduces discontinuously from the exit plane to the downstream pressure value.

The effect of upstream pressure on the pressure and temperature distributions of refrigerant inside a short-tube orifice is shown in Fig. 5. It can be clearly seen from this figure that the average pressure and temperature inside the short-tube orifice increase as the upstream pressure is boosted. This is because the refrigerant velocity is increased when the pressure difference between upstream and downstream pressure is increased. Therefore, the pressure loss due to sudden contraction and wall friction is augmented. The reason for the temperature variation inside the short-tube orifice is similar to that described above. However, it is observed that the increase of upstream pressure causes a slight decrease of downstream temperature even though the downstream pressure is unchanged.

Fig. 6 shows the pressure and temperature distributions along a short-tube orifice at different degrees of subcooling. The augmentation of the degree of subcooling leads to an increase of the pressure drop in the entrance region while the average pressure and temperature inside the short-tube orifice are lowered. It is also found that the downstream temperature is slightly decreased when the degree of subcooling is increased. This is due to the fact

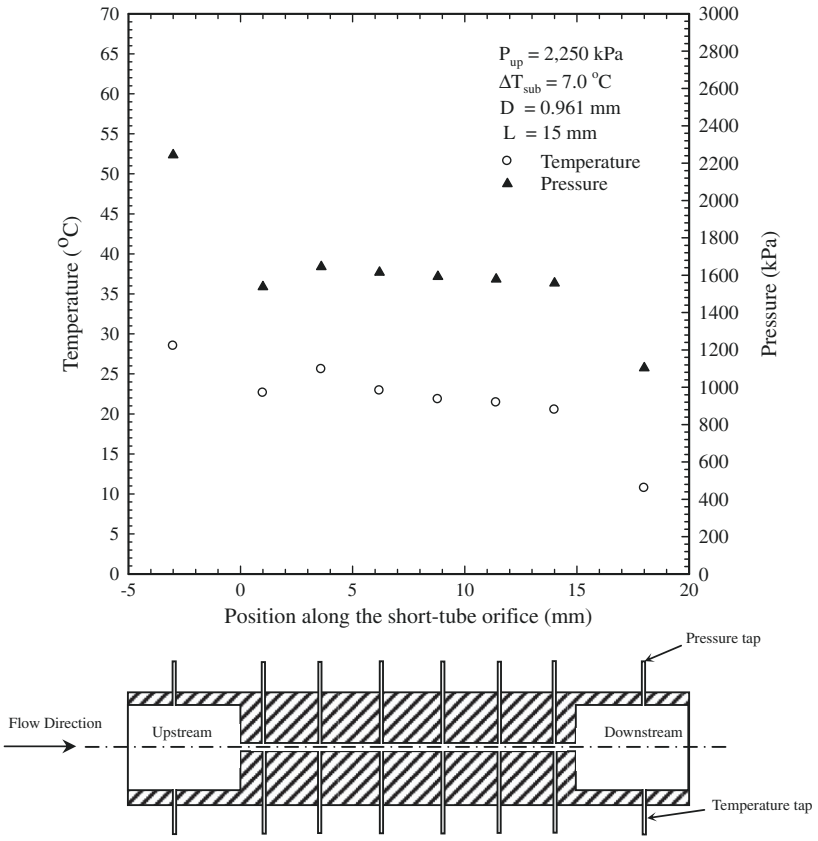

Fig. 4. Pressure and temperature distribution of HFC-410A inside a short-tube orifice.

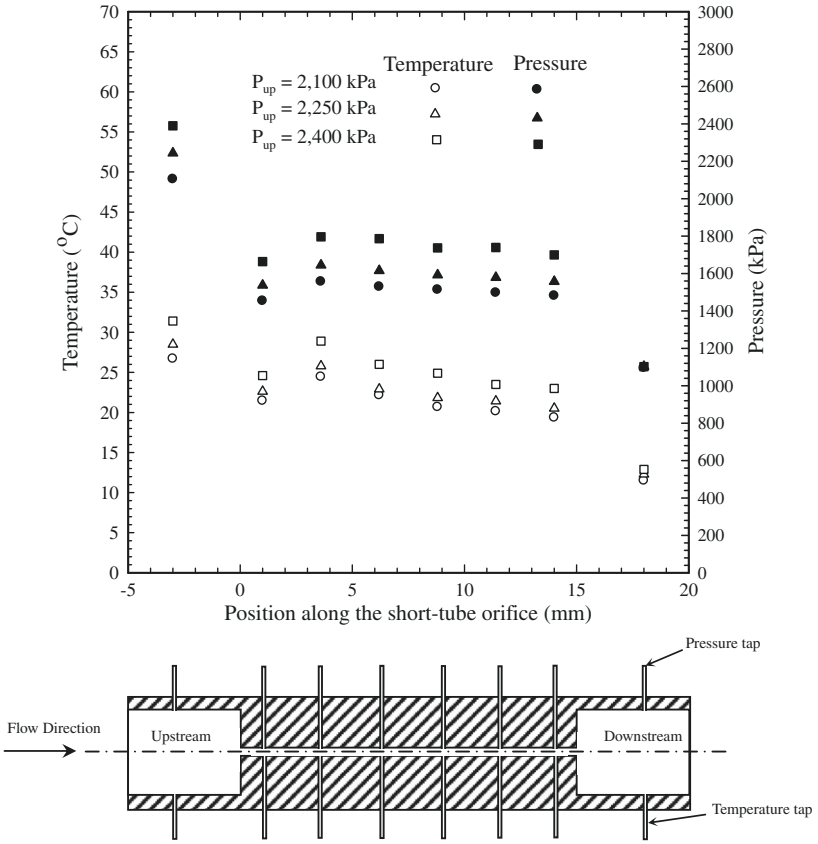

Fig. 5. Effect of upstream pressure on the pressure and temperature distribution at $D = 0.961$ mm, $L = 15$ mm, $\Delta T_{sub} = 7.8–8.5$ °C and $P_{down} = 1100$ kPa.

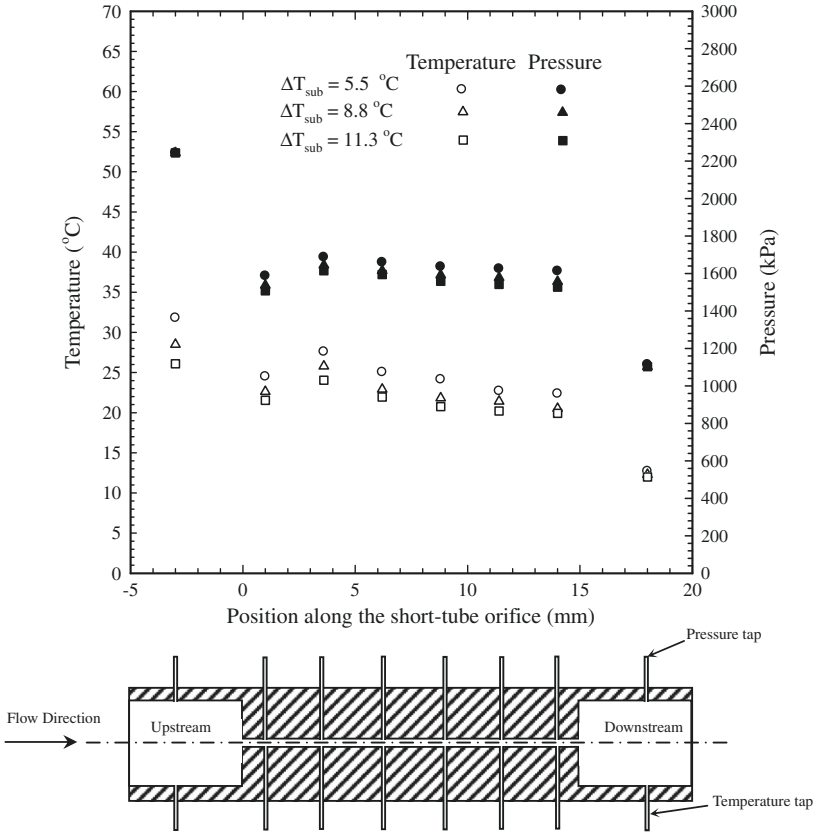

Fig. 6. Effect of degree of subcooling on the pressure and temperature distribution at D = 0.961 mm, L = 15 mm, P_{up} = 2250 kPa and P_{down} = 1100 kPa.

that the increase of the degree of subcooling leads to increases in the density and mass flow rate of refrigerant which result in an increase of pressure loss inside the short-tube orifice.

Considering the pressure and temperature distributions inside the short-tube orifice shown in Fig. 7, it is found that the long length of the short-tube orifice results in increases of recovery pressure and average pressure in the short-tube orifice; however it also leads to a slight decrease of downstream temperature. As mentioned above, it can be noted that the downstream temperature is slightly decreased by increasing the degree of subcooling and the length of the short-tube orifice, but increased by increasing the upstream pressure.

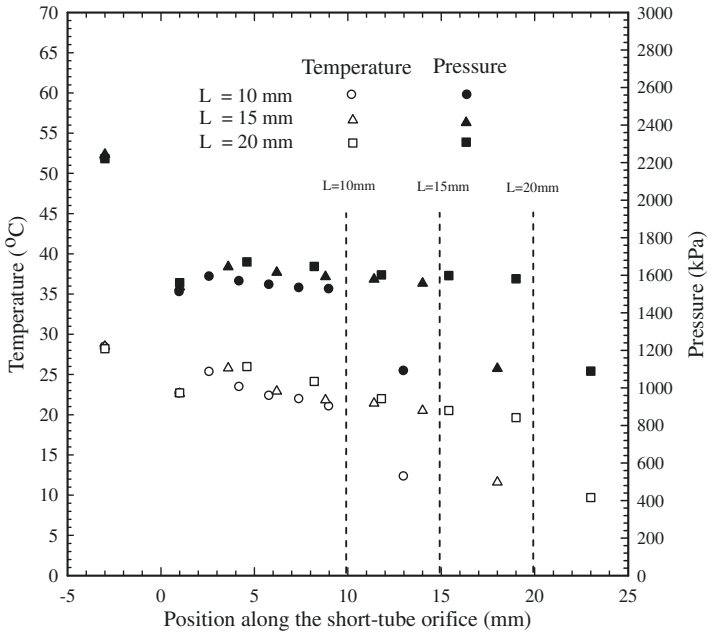

Fig. 7. Effect of short-tube orifice length on the pressure and temperature distribution at D = 0.961 mm, ΔT_{sub} = 7.8–8.5 °C, P_{up} = 2250 kPa and P_{down} = 1100 kPa.

3.2. Metastable flow phenomenon

Metastable flow is the flow phenomenon which occurs during the transition from liquid to vapour state according to a flashing process in the expansion device. In this section, the existence of metastable flow in the short-tube orifice is described.

In order to verify the existence of metastable flow, the relationship between pressure distribution and flow pattern inside the short-tube orifice is presented in Fig. 8. In the photograph of the flow pattern in the figure, the flow of liquid refrigerant is displayed by the bright (white) region, whereas the two-phase refrigerant flow is displayed by the dark (black) region. The increase of darkness level in the dark region represents the high level of quality. As shown in Fig. 8(a), it is found that the conical liquid refrigerant appears in a core of the tube while the other area is covered by the two-phase refrigerant, which consists of tiny bubbles mixed with liquid refrigerant and is similar to a mist. In addition, it is found that the darkness level in the dark region increases along the tube length, especially in the exit plane of the short-tube orifice.

As shown in Fig. 8(b), when the flow of refrigerant passes the entrance region, the measured pressure along the short-tube orifice is lower than the saturation pressure in response to the measured temperature. The result indicates that the refrigerant is in a superheated vapour state after it passes the entrance plane. That is, the subcooled liquid refrigerant ought to be evaporated at 1 mm from the entrance plane. However, after consideration of the flow pattern in Fig. 8(a), it is found that the refrigerant at the core of tube remains in the liquid state. This means that the vaporization of refrig-

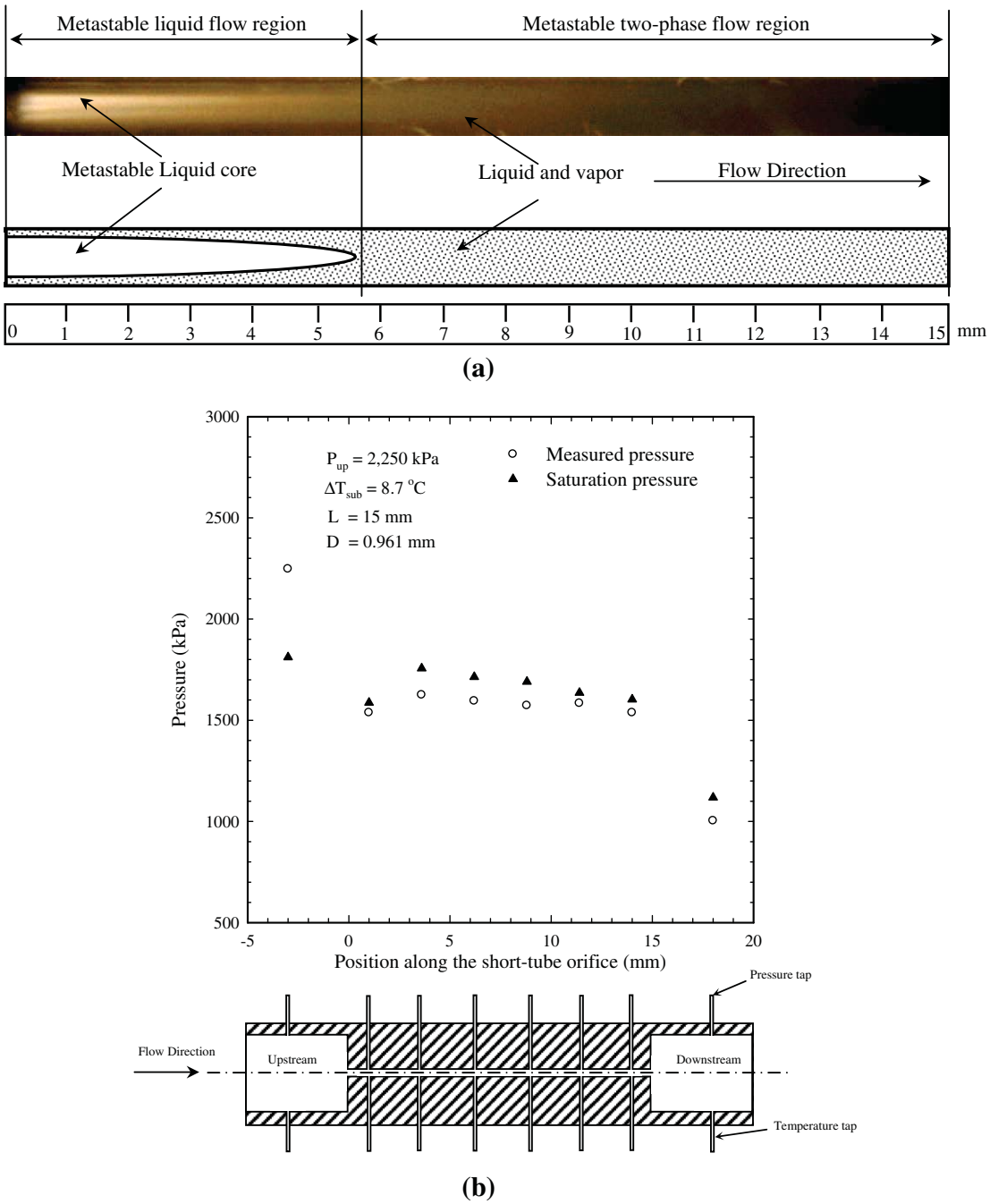

Fig. 8. Flow behaviour of HFC-410A along a short-tube orifice: (a) flow pattern and (b) pressure and temperature distribution.

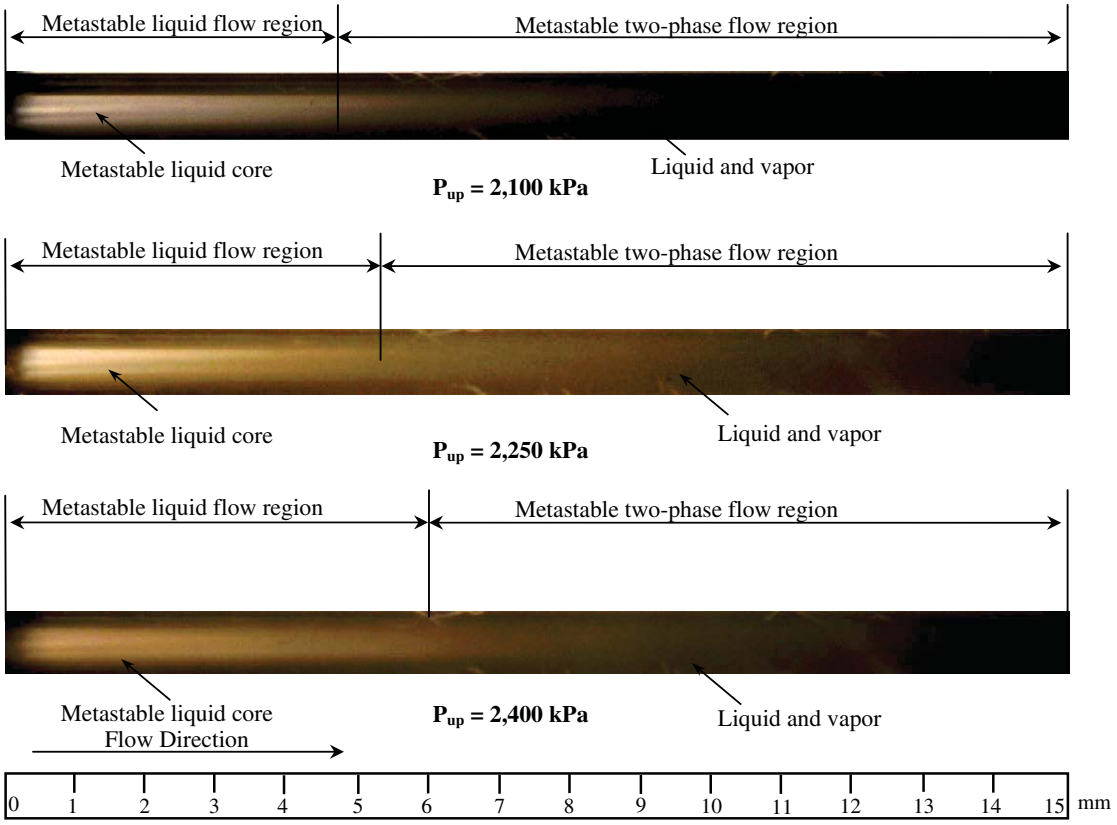

Fig. 9. Effect of upstream pressure on the flow pattern inside a short-tube orifice at $D = 0.961$ mm, $L = 15$ mm, $\Delta T_{sub} = 7.8–8.5$ °C and $P_{down} = 1100$ kPa.

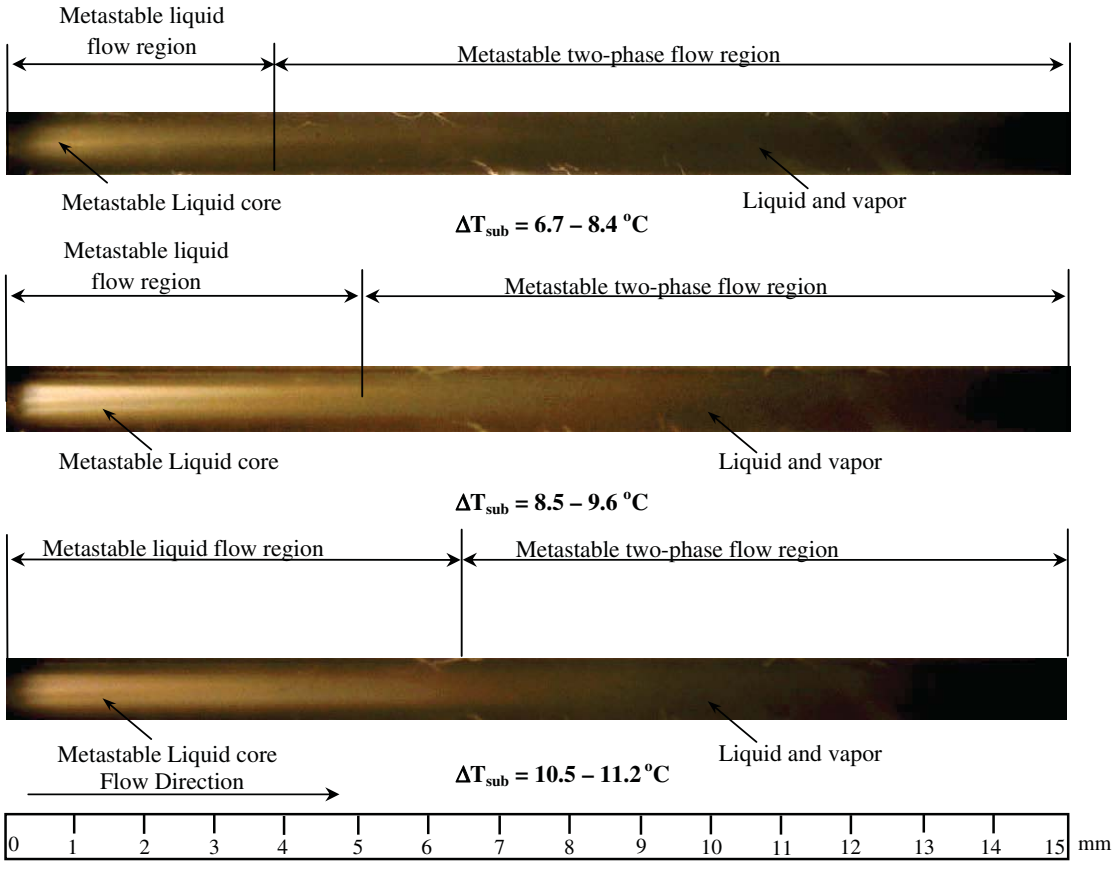

Fig. 10. Effect of degree of subcooling on the flow pattern inside a short-tube orifice at $D = 0.961$ mm, $L = 15$ mm, $P_{up} = 2250$ kPa and $P_{down} = 1100$ kPa.

erant is delayed and the flow of refrigerant inside the short-tube orifice exists under non-equilibrium thermodynamic conditions. Therefore, this flow region is called metastable liquid flow. On the other hand, when the entire flow area of the tube is covered by two-phase liquid–vapour refrigerant, it is called metastable two-phase flow. In order to identify the extent of the metastable liquid flow region, the image was magnified for clearness and the variations in the colour level of liquid refrigerant at the central core of the tube were observed by eye. The end point of metastable liquid flow length is the point where the dark region completely covers the flow area. The average length of metastable liquid flow represented in this paper is obtained from several repetitions.

Figs. 9 and 10 show the flow pattern of refrigerant inside the short-tube orifice which is changed by the upstream pressure and degree of subcooling, respectively. It is discovered that the length of the metastable liquid flow region is extended by increasing the upstream pressure and degree of subcooling. The reason for this is that the difference between upstream pressure and saturation pressure is increased as upstream pressure and degree of subcooling are increased. This means that the inception of flashing is delayed when the upstream pressure and degree of subcooling are increased.

3.3. Mass flow rate

Another purpose of the expansion device is to regulate the mass flow rate of refrigerant flowing from the condenser to the evaporator. In this section, the effects of operating conditions and short-

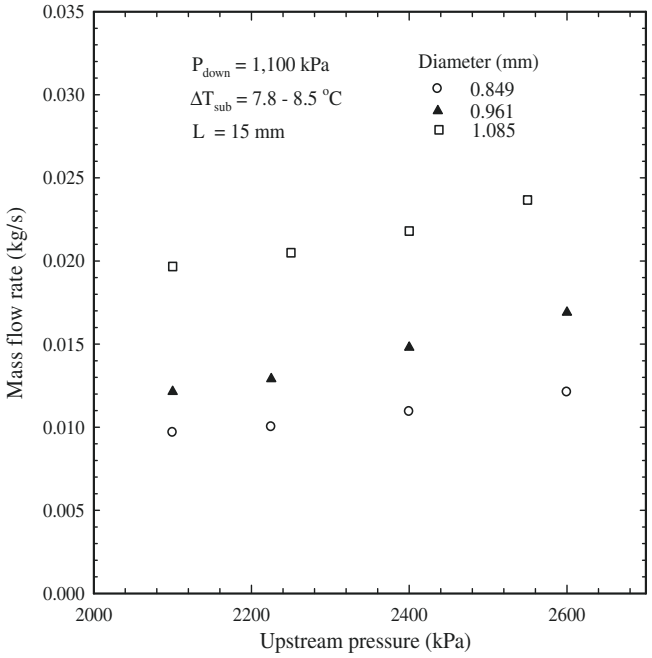

Fig. 11. Effect of upstream pressure on mass flow rate.

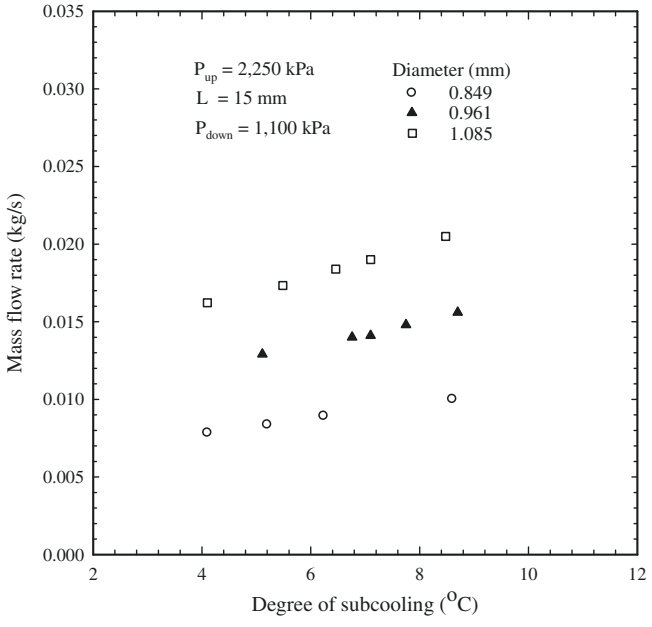

Fig. 12. Effect of degree of subcooling on mass flow rate.

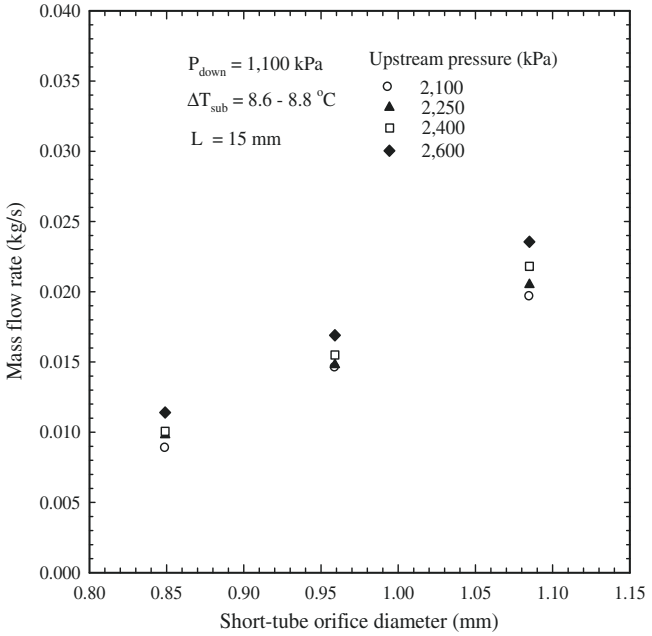

Fig. 13. Effect of short-tube orifice diameter on mass flow rate.

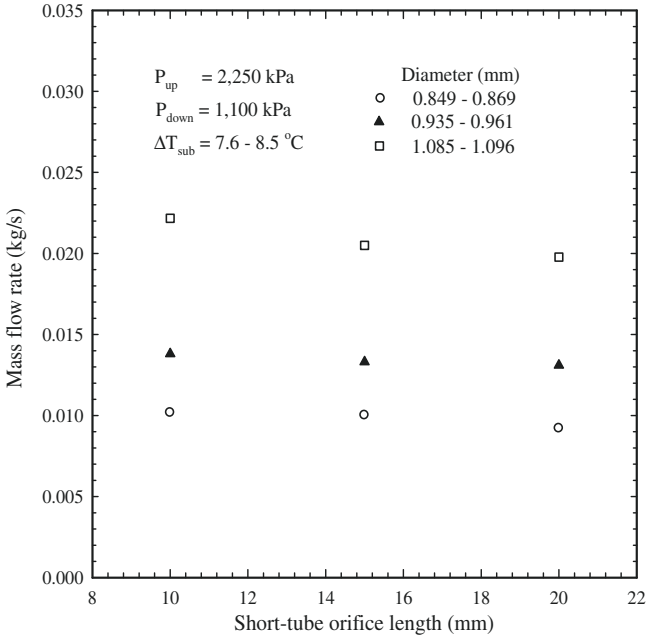

Fig. 14. Effect of short-tube orifice length on mass flow rate.

tube orifice dimensions on the mass flow rate of HFC-410A through short-tube orifices are described.

As shown in Fig. 11, it can be seen that the mass flow rate is increased when the upstream pressure is increased. In addition, it is found that the tendency in the data is dependent on short-tube diameter. That is, the data tendency is lifted when the upstream pressure is increased. The reason for this is that the refrigerant velocity is increased as the upstream pressure is increased, which is responsible for the increase in mass flow rate.

Fig. 12 shows the effect of the degree of subcooling on mass flow rate. The results show that increasing the degree of subcooling produces an increase in mass flow rate. However, it is discovered

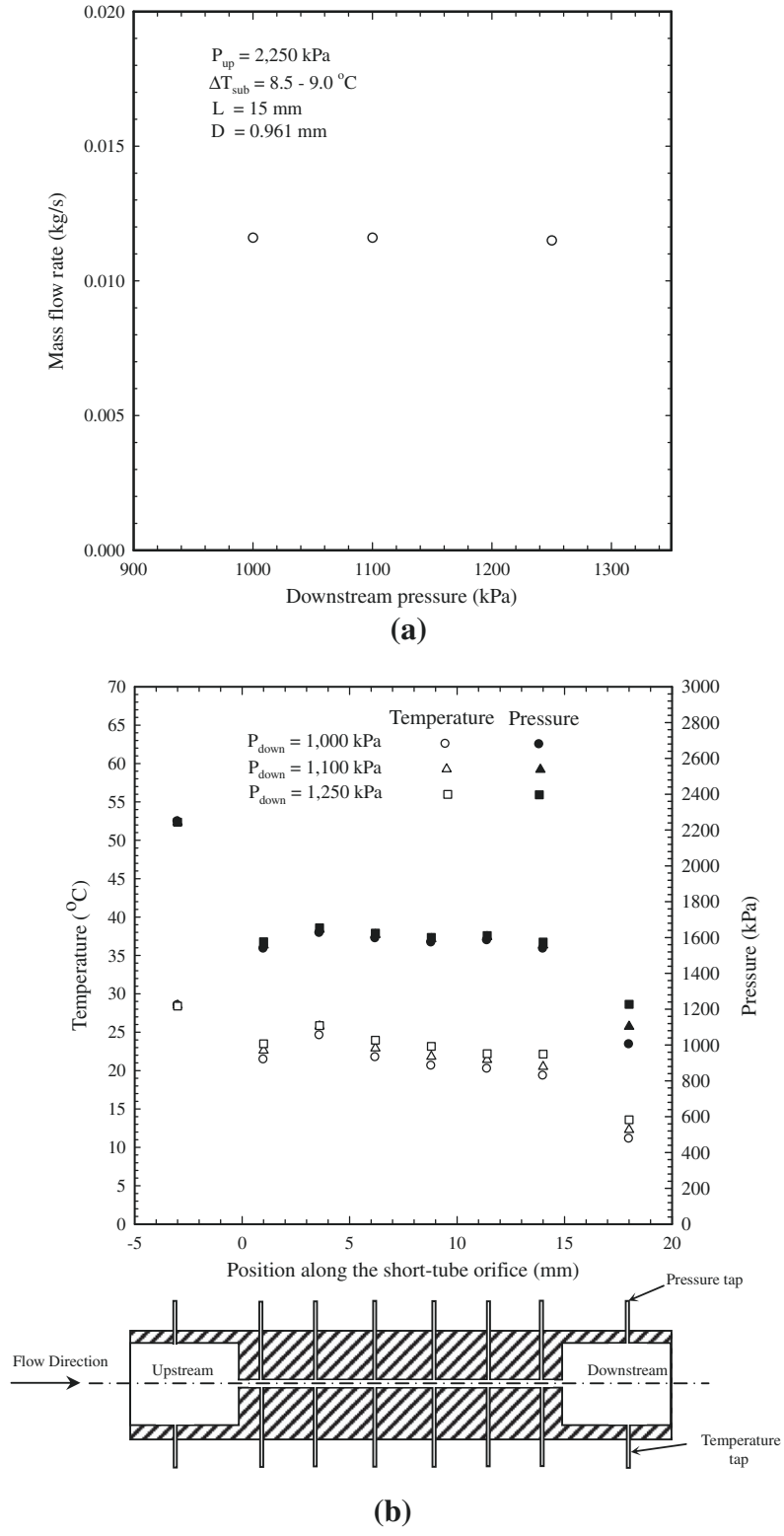

Fig. 15. Effect of downstream pressure on the flow mechanism of HFC-410A inside a short-tube orifice: (a) mass flow rate and (b) pressure and temperature distribution.

that the mass flow rate is related to short-tube diameter. This means that an increase of the short-tube diameter tends to lift the data tendency. This is due to the fact that the refrigerant density is increased as the degree of subcooling is increased. This impact causes the mass flow rate to be increased.

As shown in Fig. 13, the mass flow rate increases greatly as the short-tube orifice diameter is increased. The flow rate is found to change by an average of 173 kg/h/mm. This is because the cross-sectional area is expanded when the short-tube orifice diameter is increased.

The relationship between mass flow rate and short-tube orifice length is shown in Fig. 14. It can be seen that the mass flow rate decreases slightly when the shot-tube length is increased. The average variation of mass flow rate is 0.252 kg/h/mm. This is because the frictional pressure drop is increased when the shot-tube length is increased, which leads to a reduction of the flow rate.

3.4. Choked flow phenomenon

Choked flow is a limiting condition which occurs inside the short-tube orifice when the velocity of refrigerant reaches sonic velocity. Under this condition, the mass flow rate of refrigerant is restricted, although the downstream pressure is decreased. Therefore, this phenomenon is necessary for the flow of HFC-410A inside the short-tube orifice. In this section, the verification of choked flow inside the short-tube orifice is presented.

Considering the effect of downstream pressure on the mass flow rate, pressure distribution, and temperature distribution of HFC-410A in Fig. 15, it can be clearly seen that the mass flow rate and pressure distribution inside the short-tube orifice are nearly constant while the downstream pressure is decreased. Therefore, it can be confirmed that the flow of HFC-410A is choked inside the short-tube orifice. However, it is found that the temperature distribution inside the short-tube orifice is diminished by decreasing the downstream pressure. This flow behaviour is consistent with the results of past researches [4,6]. The results from this study indicate that choked flow appears over the entire range of experimental conditions.

4. Conclusion

This paper presents new experimental data of HFC-410A flow mechanisms, including the pressure distribution, temperature distribution, flow pattern, choked flow phenomenon, metastable flow and mass flow rate inside a short-tube orifice. The influences of upstream pressure, downstream pressure, degree of subcooling, and short-tube orifice length on the flow mechanisms are discussed. The following conclusions can be drawn from this study:

1. The flow pattern with which the liquid refrigerant flows in a conical form at the core of the tube, surrounded by tiny bubbles mixed in the liquid refrigerant, has been discovered inside short-tube orifices.
2. The pressure and temperature of refrigerant decrease rapidly in the entrance and exit regions. However, the pressure and temperature of the refrigerant increase only slightly over a short length and gradually decrease thereafter inside the short-tube orifice.
3. The mass flow rate increases in proportion when the upstream pressure and degree of subcooling are increased, but it is greatly increased by increasing the short-tube diameter.
4. The mass flow rate and pressure distribution inside a short-tube orifice are nearly constant as the downstream pressure is varied. However, the temperature distribution of the refrigerant inside a short-tube orifice is slightly decreased when the downstream pressure is decreased.

Acknowledgements

The authors would like to express their appreciation to the Thailand Research Fund (TRF) and the Office of Higher Education Commission for providing financial support for this study. The authors also wish to thank Mr. Chiatta Supawarasuwat of C-Aircon Tech Company for the valuable donation of the short-tube orifices used in the present study.

References

[1] P.F. Pasqua, Metastable flow of Freon-12, Refrig. Eng. 61 (1953) 1084–1088.
[2] A.A. Aaron, P.A. Domanski, Experimentation analysis and correlation of refrigerant-22 flow through short tube restrictors, ASHRAE Trans. 96 (1990) 29–742.
[3] Y. Kim, Two-phase flow of HFC134a and HCFC22 through short tube orifices, Ph.D. thesis, Texas A&M University, USA, 1993.
[4] K. Nilpueng, S. Wongwises, Experimental investigation of two-phase flow characteristics of HFC-134a through short-tube orifices, Int. J. Refrig. 32 (2009) 854–864.
[5] J.P. Liu, Y.M. Niu, J.P. Chen, Z.J. Chen, X. Feng, Experimental and correlation of R744 two-phase flow through short tubes, Exp. Therm. Fluid Sci. 28 (2004) 565–573.
[6] K. Nilpueng, S. Wongwises, Flow pattern, mass flow rate, pressure distribution, and temperature distribution of two-phase flow of HFC-134a inside short-tube orifices, Int. J. Refrig. 32 (2009) 1864–1875.
[7] V.C. Mei, Short tube refrigerant flow restrictors, ASHRAE Trans. 88 (1982) 157–169.
[8] Y.C. Kim, D.L. O'Neal, Refrigerant flow through flexible short tube orifices, HVAC Res. 8 (2002) 179–190.
[9] G.M. Singh, P.S. Hrnjak, C.W. Bullard, Flow of refrigerant R134a through orifice tubes, Int. J. HVAC Res. 7 (2001) 245–262.
[10] X. Tu, P.S. Hrnjak, C.W. Bullard, Refrigerant 134a liquid flow through micro-scale short tube orifices with/without phase change, Exp. Therm. Fluid Sci. 30 (2006) 253–262.
[11] W.V. Payne, D.L. O'Neal, Mass flow characteristics of R407C through short-tube orifices, ASHRAE Trans. 104 (1998) 197–209.
[12] Y. Kim, V. Payne, J. Choi, P. Domanski, Mass flow of R410A through short tube working near the critical point, Int. J. Refrig. 28 (2005) 547–553.

International Journal of Heat and Mass Transfer 53 (2010) 4023–4038

Contents lists available at ScienceDirect

International Journal of Heat and Mass Transfer

journal homepage: www.elsevier.com/locate/ijhmt

Flow pattern and heat transfer characteristics of R-134a refrigerant during flow boiling in a horizontal circular mini-channel

Sira Saisorn [a,c], Jatuporn Kaew-On [b,c], Somchai Wongwises [c,*]

[a] King Mongkut's Institute of Technology Ladkrabang Chumphon Campus, Chumphon 86160, Thailand
[b] Department of Physics, Faculty of Science, Thaksin University, Phattalung, Thailand
[c] Fluid Mechanics, Thermal Engineering and Multiphase Flow Research Lab. (FUTURE), Department of Mechanical Engineering, King Mongkut's University of Technology Thonburi, Bangmod, Bangkok 10140, Thailand

ARTICLE INFO

Article history:
Received 17 November 2009
Received in revised form 16 April 2010
Accepted 16 April 2010
Available online 9 June 2010

Keywords:
Flow boiling
Mini-channel
Flow pattern
Heat transfer

ABSTRACT

Flow boiling heat transfer of R-134a refrigerant in a circular mini-channel, 600 mm long with a diameter of 1.75 mm, is investigated experimentally in this study. The test section is a stainless steel tube placed horizontally. Flow pattern and heat transfer coefficient data are obtained for a mass flux range of 200–1000 kg/m^2 s, a heat flux range of 1–83 kW/m^2 and saturation pressures of 8, 10, and 13 bar. Five different flow patterns including slug flow, throat-annular flow, churn flow, annular flow and annular-rivulet flow are observed and the heat transfer coefficient data for different flow patterns are presented. The heat transfer coefficient increases with increasing heat flux but is mostly independent of mass flux and vapour quality. In addition, it is indicated from the experiments that the higher the saturation pressure, the lower is the heat transfer coefficient. Comparisons of the present data with the existing correlations are also presented.

1. Introduction

Research on two-phase compact heat exchangers has gained increasing attention over the years because of the advantages of using small channels as summarised in Ribatski et al. [1]. Definitions for various channels have been given by several investigators who proposed channel classifications which are often based on different dimensionless parameters. For instance, arbitrary channel classifications associated with the hydraulic diameter D_h have been proposed. Mehendale et al. [2] employed the hydraulic diameter as an important parameter for defining heat exchangers and Kandlikar [3] proposed criteria for small flow channels used in engineering applications. Most of the criteria based on the hydraulic diameter, however, cannot relate the channel diameter to fluid flow mechanisms. Regarding the experimental data obtained from flow visualisation studies in small channels, Chung and Kawaji [4] found that diameters between 100 and 250 μm seemed to be in the range corresponding to mini-to-micro-scale transitions. Their findings were also confirmed by Saisorn and Wongwises [5]. According to existing criteria which are unclear, further investigation is still required to meet a more general definition dealing with channel classification.

Two-phase flow of refrigerants during flow boiling in ordinarily sized channels has been investigated by various investigators. Greco [6], for instance, conducted experiments to study the major parameters affecting the heat transfer characteristics. The results of more than 2000 data points were obtained based on 250 different operating conditions. The effects of vapour quality, heat flux mass flux, saturation temperature and thermo-physical properties on the heat transfer behavior were analyzed in detail. Compared to the reported two-phase flow and heat transfer characteristics in ordinarily sized channels, which are available in a relatively large number of publications, flow boiling phenomena in mini- and micro-channels tend to show different behaviors due to the effects of the limited and confined space. Also, a scaling analysis of different forces, as discussed in Kandlikar [7], pointed out that surface tension and evaporation momentum forces were significant for two-phase flow phenomena at micro-scale. Although some relevant information is currently available in the literature, a complete understanding has not yet been clarified with regard to the trends and parameters dominating the phase-change heat transfer mechanism in these small-scale channels.

In what follows, recent studies associated with flow boiling heat transfer in small channels are briefly outlined.

Brutin and Tadrist [8] carried out experiments on flow boiling in a rectangular mini-channel with hydraulic diameter of 0.89 mm to investigate the two-phase flow stability. They indicated that a maximum value of the average heat transfer coefficient was obtained under the unsteady state regime. The stability criterion was found to be dependent upon heat flux and mass flow rate.

* Corresponding author. Tel.: +66 2 470 9115; fax: +66 2 470 9111.
E-mail address: somchai.won@kmutt.ac.th (S. Wongwises).

0017-9310/$ - see front matter © 2010 Elsevier Ltd. All rights reserved.
doi:10.1016/j.ijheatmasstransfer.2010.05.022

Nomenclature

B_o	Boiling number, $B_o = q/Gi_{LG}$
C	constant
C_{CO}	convection number, $C_{CO} = (\rho_G/\rho_L)^{0.5}((1-x)/x)^{0.8}$
C_o	confinement number
C_p	specific heat at constant pressure (J/kg K)
D	channel diameter (m)
D_b	capillary length (m)
D_h	hydraulic diameter (m)
F	two-phase convection multiplier
F_{Fl}	fluid-surface parameter
f	fanning friction factor
G	mass flux (kg/m^2 s)
h	heat transfer coefficient (W/m^2 K)
i	specific enthalpy (J/kg)
i_{LG}	latent heat of vapourisation (J/kg)
j	superficial velocity (m/s)
k	thermal conductivity (W/mK)
M	molecular weight (kg/kmol)
MAE	mean absolute error, $\mathrm{MAE} = \frac{1}{N}\sum_1^N \left(\frac{\lvert h_{\mathrm{pre}} - h_{\mathrm{mea}}\rvert}{h_{\mathrm{mea}}} \times 100\right)$
N	number of experimental data
Nu	Nusselt number, $Nu = hD_h/k$
P	pressure (Pa)
P_r	reduced pressure
Pr	Prandtl number, $Pr = \mu C_p/k$
ΔP_{sat}	saturation pressure difference (Pa)
q	heat flux (W/m^2)
Re	Reynolds number, $Re = GD_h/\mu$
S	nucleate boiling suppression factor
T	temperature (°C)
ΔT_{sat}	wall superheat (K)
We	Weber number, $We = G^2 D_{\mathrm{h}}/\rho\sigma$
x	vapour quality

Greek symbols

χ	Lockhart–Martinelli parameter
φ^2	two-phase frictional multiplier
μ	dynamic viscosity (Ns/m^2)
ρ	density (kg/m^3)
σ	surface tension (N/m)

Subscripts

A	annular flow
avg	average
CB	coalescing bubble flow
CBC	convection boiling contribution
G	vapour phase
GO	all-vapour
IB	isolated bubble flow
L	liquid phase
LO	all-liquid
mea	experimental value
NBC	nucleate boiling contribution
pre	predicted value
sat	saturation
wall,in	inner wall

Huo et al. [9] studied experimentally boiling heat transfer of R-134a fluid in small vertical tubes of 2.01 and 4.26 mm in diameter. In the low vapour quality range, the heat transfer coefficient in both tubes increased with increasing heat flux and saturated pressure but was independent of vapour quality. These results were attributed to nucleate boiling being the dominant heat transfer mode. In other ranges of vapour quality, however, the dominant heat transfer mode was not addressed as a result of inconsistency in the experimental data. Under the same controlled conditions, they found that the nucleate boiling heat transfer coefficient was higher for the 2.01 mm tube than for the 4.26 mm tube.

Flow boiling heat transfer characteristics in micro-channels of 540 mm length with 25 circular flow channels of 0.81 mm diameter were investigated by Pettersen [10]. They reported that the increase in heat flux resulted in higher heat transfer coefficient, which could be explained according to the dominant role of nucleate boiling over the low/moderate vapour quality region. Another point observed was that the dry-out temperature became much more significant at higher mass flux and temperature, resulting in a rapidly reduced heat transfer coefficient at high vapour qualities. Besides, pressure drop increased with mass flux and vapour quality but decreased as temperature increased. The comparison of measured data and various correlations was also discussed.

Yun et al. [11] were concerned with flow boiling heat transfer characteristics in rectangular multi-channels with hydraulic diameters ranging from 1.08 to 1.54 mm. Working fluids tested were CO_2 and R-134a. Generally, the average heat transfer coefficient of CO_2 increased around 53% when compared with that of R-134a. The influences of heat flux on the heat transfer coefficient were much more obvious for CO_2 than for R-134a. Dry-out phenomenon was promoted with an increase in mass flux and it was also noted that the effects of mass flux on heat transfer coefficient were less significant than those of heat flux. As expected, heat transfer coefficient increased with a decrease in the hydraulic diameter.

Heat transfer of R-134a refrigerant during flow boiling in horizontal tubes with different diameters including 0.51, 1.12 and 3.1 mm was studied experimentally by Saitoh et al. [12]. Nucleate boiling was reported in the low vapour quality region whereas convective evaporation was dominant in the high vapour quality region. The latter mechanism was found to be less dominant as the tube diameter decreases. The smaller the tube diameter, the higher is the effect of saturation temperature on the heat transfer coefficient. The flow instability was also discussed in this work.

Evaporation heat transfer in horizontal mini-channels was studied experimentally by Lie et al. [13]. A diameter of 0.83 or 2 mm was used for each channel and the working fluids were R-134a and R-407C. The effects of mass flux, vapour quality, saturation temperature and heat flux on the heat transfer coefficient were investigated. Under given experimental conditions, the use of R-407C gave a higher heat transfer coefficient than R-134a.

The experiments with flow boiling of water in a vertical circular tube having a diameter of 1.5 mm were performed by Boye et al. [14]. The wall temperatures of the tube in which the water flows upward were measured using infrared thermography. Nucleate boiling and convective boiling mechanisms were observed in the experiments.

Choi et al. [15] reported the heat transfer characteristics of CO_2 through horizontal mini-channels having diameters of 1.5 and 3 mm. They indicated that nucleate boiling was predominant in the low vapour quality region and a convective boiling heat transfer contribution appeared in moderate and high vapour quality regions. The variation of local heat transfer coefficient with heat flux, mass flux, vapour quality and saturation temperature was discussed. A more active nucleate boiling was addressed when the tube with smaller diameter was used. Flow boiling heat

transfer of different refrigerants was continually carried out by Choi et al. [16]. They indicated that the use of CO_2 caused the heat transfer coefficient to be higher than that of R-134a and R-22.

Shiferaw et al. [17] compared their flow boiling data with existing correlations. The data points were obtained from experiments with R-134a flowing through small tubes having diameters of 4.26 and 2.01 mm. The comparisons revealed that the existing correlations did not predict well their data. Comments and suggestions were provided by the authors for further development of the prediction. Similar experiments were conducted by Shiferaw et al. [18] to compare the results obtained from a 1.1 mm diameter tube with the three-zone flow boiling model developed by Thome et al. [19] and Dupont et al. [20]. Generally, the model predicted well the experimental data, especially at relatively low pressure. Regarding the heat transfer characteristics, an insignificant influence of mass flux and vapour quality was observed while the heat transfer coefficient increased with increasing heat flux and saturation pressure.

Three different refrigerants, R-134a, R-236fa and R-245fa, were tested for flow boiling in a 1.03 mm diameter tube by Ong and Thome [21]. The trends of the data were investigated, showing that the heat transfer coefficient depended on heat flux at low vapour qualities and on mass flux at high vapour qualities. Regarding the refrigerants tested at low vapour qualities, R-134a gave the highest heat transfer coefficient followed by R-236fa and R-245fa, respectively.

From the above review of the literature, relatively little information has been reported on flow boiling in mini-channels under high mass flow conditions ($G > 500$ kg/m^2 s) and the detailed investigations concentrating on the relevance of the two-phase flow structures to the heat transfer characteristics are still lacking. The main objective of the present work is therefore to extend the database to high mass flux conditions corresponding to a value of up to around 1000 kg/m^2 s. In this paper, the typical features of the flow patterns and the relevant heat transfer characteristics are described. The present data will subsequently be compared with prediction methods of different researchers.

2. Experimental apparatus and procedure

The present experimental apparatus, which is modified from that developed by Kaew-On and Wongwises [22] and is shown schematically in Fig. 1, is designed to investigate flow boiling of R-134a in a circular mini-channel placed horizontally. The main components of the system include a test section, refrigerant loop, sub-cooling loop, and a data acquisition system.

For the refrigerant circulating loop, as seen in Fig. 1, liquid refrigerant is pumped by a gear pump which can be regulated by means of an inverter. The refrigerant then passes in series through a filter/dryer, a refrigerant flow meter, pre-heater, sight glass tube, and enters the test section. The inlet quality before entering the test section is controlled by the pre-heater with a DC power supply used to apply heat. Leaving the test section, the refrigerant vapour subsequently condenses in a sub-cooler and then is collected in a receiver; it eventually returns to the refrigerant pump to complete the cycle. Instrumentation is installed at various positions, as shown in Fig. 1, to monitor the state of the refrigerant. All the signals from the thermocouples and differential pressure transducer are recorded by a data logger.

Fig. 2 shows a schematic diagram of the test section, a stainless steel tube which is 600 mm long and 1.75 mm in diameter. The regulated DC power supply generating 80 A at 12 V is used to apply heat to the test section. The voltage and electric current values are measured by a multimeter (Fluke 336 meter) which has an uncertainty of ±2% for voltage and ±1% for current. T-type thermocouples are installed at the inlet and outlet of the test section to measure the system temperature. The 10 thermocouples are installed on the top and bottom sides at equal distances along the tube to measure the wall temperature. All thermocouples on the tube surface are fixed with special glue. The test section is well insulated by using rubber foam with a thermal conductivity of 0.04 W/mK. A variable area type flow meter is specially calibrated in the range 0.02–0.2 LPM for R-134a by the manufacturer. All thermocouples,

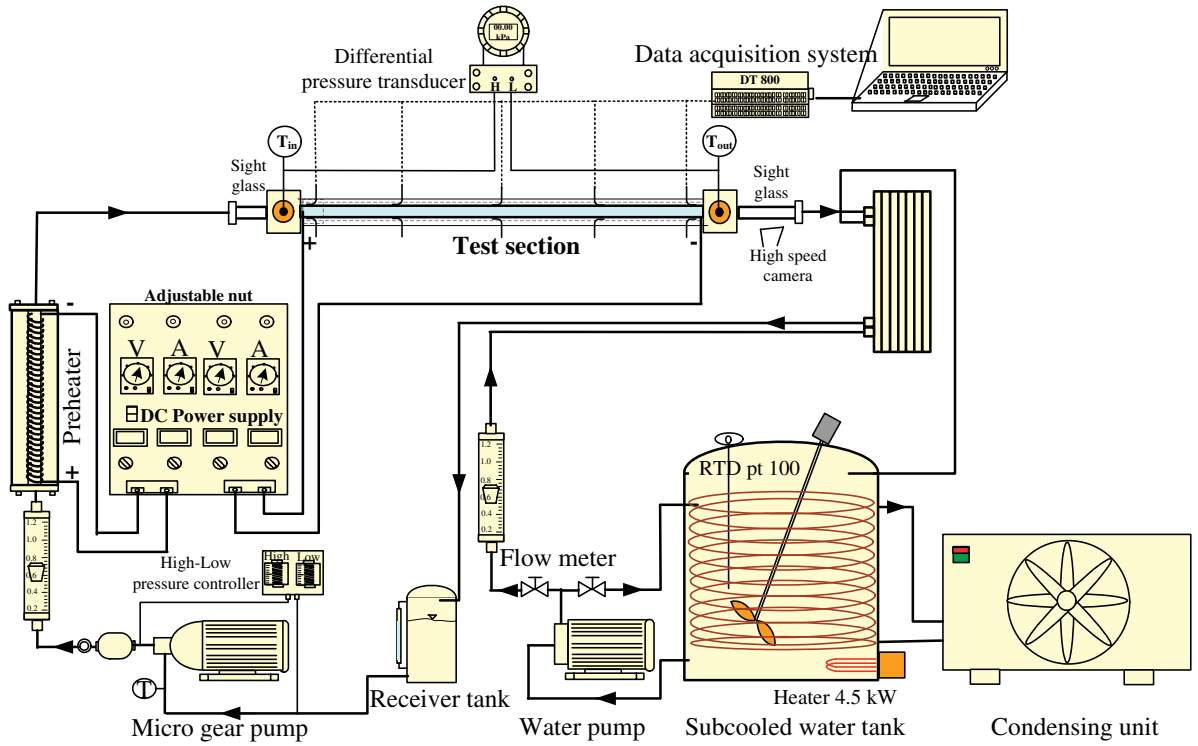

Fig. 1. Schematic diagram of experimental apparatus.

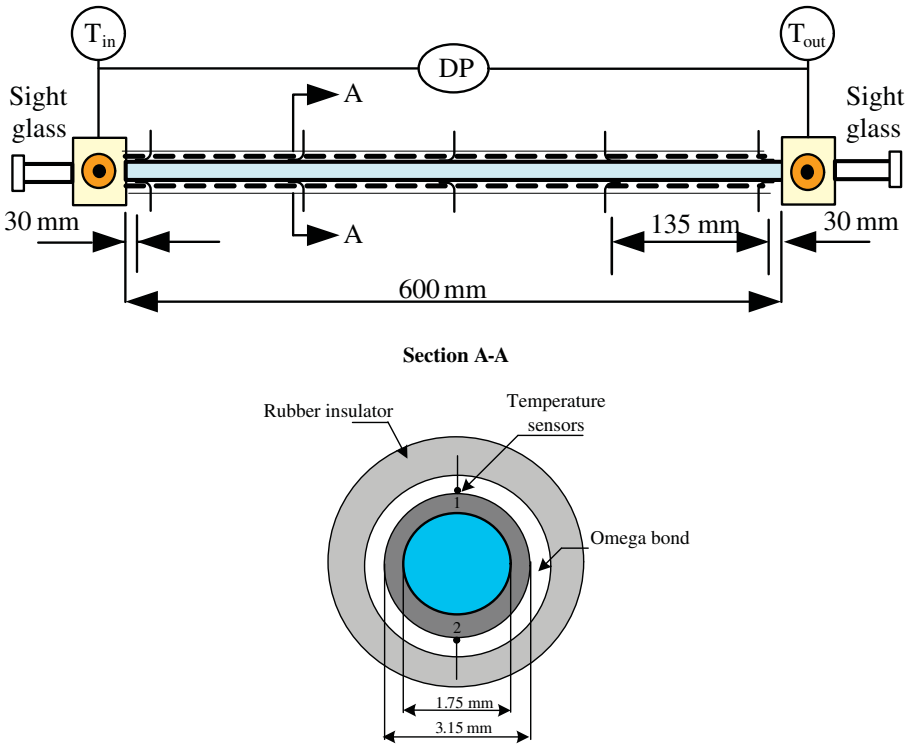

Fig. 2. Schematic diagram of test section.

differential pressure transducer and relevant instruments installed in the experimental apparatus are well calibrated.

A 1.75 mm diameter transparent tube is installed to match up with the test section outlet and to serve as a viewing window for flow visualisation. The detailed formation of each flow pattern is registered by a high quality camera (Fujifilm FinePix S7000) having shutter speeds of 1/15 to 1/10,000 s. The camera together with an adjustable light source consisting of 150 W halogen lamp and dimmer are placed horizontally and normal to the viewing section.

In this work, the experiments are conducted in such a way that the heat applied to the test section is varied by small increments, while the refrigerant flow rate, saturation pressure, and inlet vapour quality in the test section are kept constant at the desired value. The system is allowed to approach a steady state before the flow pattern and relevant data are recorded. During the experiment, the temperature and pressure drop are continuously recorded along the test section by the data logger. The profiles of the temperature help us to know the limit of useful data because a large increase in wall temperature and outlet saturation temperature is observed when dry-out occurs. The range of experimental conditions is presented in Table 1. The uncertainties in the measured quantities and calculated parameters are shown in Table 2.

Table 1
Experimental conditions.

Refrigerant	R-134a
Diameter (mm)	1.75
Length (mm)	600
Mass flux (kg/m^2 s)	200–1000
Heat flux (kW/m^2)	1–83
Saturation pressure (bar)	8–13
Test section material	Stainless steel

Table 2
Uncertainties of measured quantities and calculated parameters.

Parameter	Uncertainty
Temperature	±0.1 (°C)
Mass flow rate of refrigerant	±0.1 **(%)** full scale
Heat transfer rate of test section	±2.25%
Heat transfer rate of pre-heater	±2.25%
Heat transfer coefficient	±8.12%

3. Results and discussion

3.1. Flow pattern

Flow pattern is expected to influence the heat transfer and flow characteristics during the phase-change heat transfer process. A clear understanding of the flow patterns encountered as well as the ability to accurately predict the type of flow are necessary before relevant calculation techniques can be developed. Flow visualisation studies for small channels such as micro- and mini-channels have been carried out by different investigators. A number of the studies concern with flow patterns for gas–liquid flow in small channels and the others concern with those for phase-change process. The flow visualisation for gas–liquid flow in mini- or micro-channel is also considered to be a tool for studying the two-phase flow characteristics because it is not very difficult to control the flow conditions. Gas–liquid flow phenomena are found to be compatible with flow mechanisms based on phase-change process in different aspects. In small channels, for instance, Saisorn and Wongwises [5] indicated that their frictional pressure drop data associated with two-phase gas–liquid flow were fairly predicted by the Muller-Steinhagen and Heck correlation [23] which is working for refrigerants under certain conditions. They also reported the fair agreement between their gas–liquid flow pattern data and the transition lines of Garimella et al. [24] for condensation flow. According to the previous discussion, the present flow

pattern data, which corresponds to flow boiling phenomena, will be subsequently compared with those obtained from gas–liquid flow data to check for the compatibility. The data of Triplett et al. [25] were chosen because of their tube diameter which is comparable to the present one.

In the present study, the boiling flow pattern observations are carried out at system pressures of 8 and 10 bar. The superficial velocities of gas and liquid vary from 0.69 to 16.60 m/s and 0.01 to 0.81 m/s, respectively. By keeping the refrigerant flow rate, saturation pressure and inlet vapour quality constant at a desired value, and increasing the imposed heat flux to the test section by small increments, typical photographs are obtained from the viewing window located downstream of the test section as shown in Fig. 3. The observations show that five different flow patterns are indicated as follows.

Slug flow: elongated bubbles which are larger in length than the channel diameter are developed from small bubbles.

Throat-annular flow: the two consecutive elongated bubbles coalesce into a throat-like gas core.

Churn flow: a disruptive region develops due to the distortion of the elongated bubbles.

Annular flow: liquid film flows on the tube wall and the tube core is occupied by continuous vapour flow.

Annular-rivulet flow: annular flow is observed alternately with flowing of a rivulet-like liquid stream on the tube surface.

It should be noted that peculiar flows such as throat-annular flow and annular-rivulet flow, which have never been observed in ordinarily sized channels, are also reported by Saisorn and Wongwises [26]. However, some discrepancies are normally observed because the present flow patterns are generated by the flow boiling process not by the adiabatic two-phase gas–liquid system used in their experiments.

The usual method in the presentation of flow pattern data is to classify the flow pattern by visual observation and plot the data as a flow pattern map in terms of system parameters. Figs. 4 and 5 illustrate the flow pattern maps which are presented in the superficial velocity of liquid (j_L) versus superficial velocity of vapour (j_G) format. The phase superficial velocities are determined as follows:

$$j_G = \frac{xG}{\rho_G} \tag{1}$$

$$j_L = \frac{(1-x)G}{\rho_L} \tag{2}$$

where x is vapour quality, G is mass flux, ρ_G is vapour density, and ρ_L is liquid density.

The present data are compared with the flow pattern transitions obtained by Triplett et al. [25] for two-phase air–water flow through a 1.45 mm diameter channel. The solid lines along with the flow pattern names indicated on these figures refer to their transition boundaries. In general, the comparisons show inconsistencies between the flow pattern map established from two-phase gas–liquid flow and that from flow boiling. Such inconsistencies were also reported by Martin-Callizo et al. [27] who conducted the visualisation of R-134a during flow boiling in a vertical tube with a diameter of 1.33 mm. Their test section is made from a quartz glass tube coated externally by indium tin oxide (ITO)

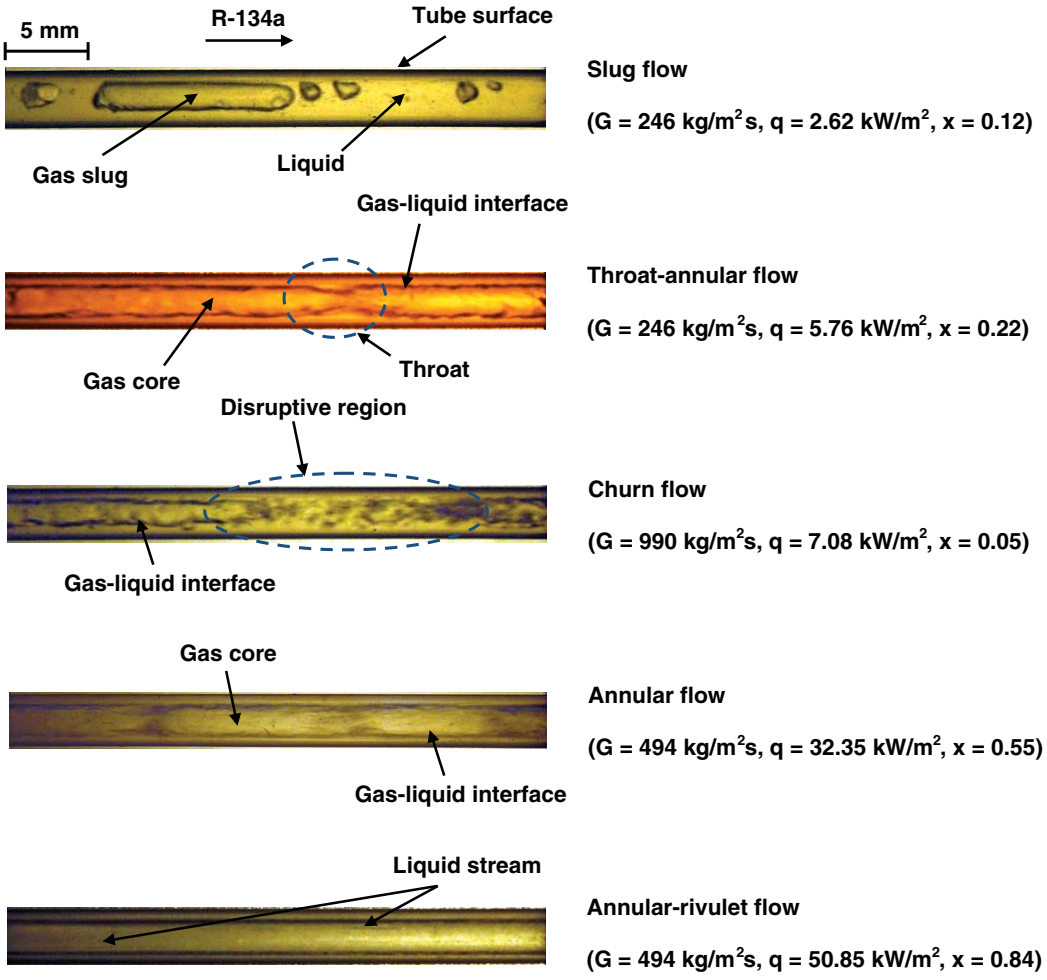

Fig. 3. Flow patterns in flow boiling of R-134a through a 1.75 mm diameter channel under system pressure of 8 bar.

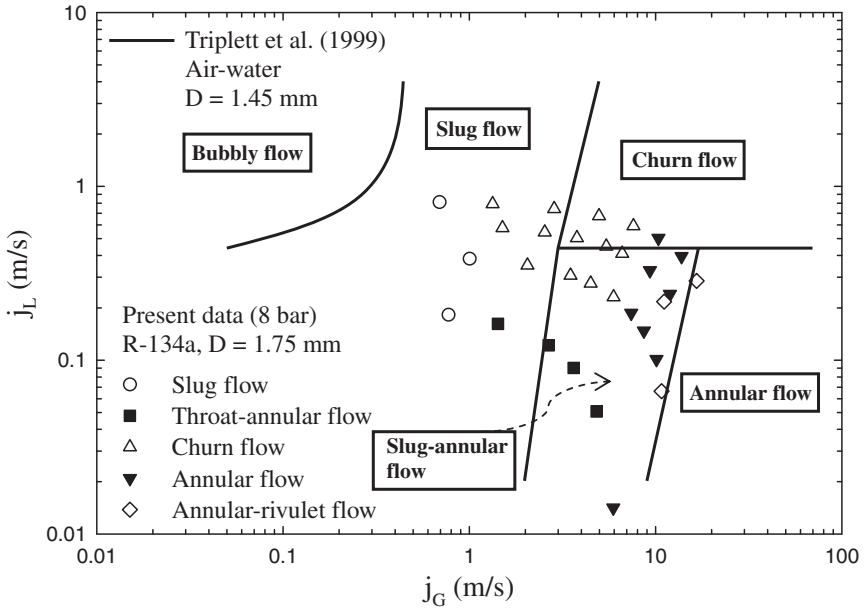

Fig. 4. Comparison of the observed flow patterns at 8 bar with the transition lines by Triplett et al. [25].

which is served as the resistive coating over which a potential difference generated by a DC power supply is applied. Their flow pattern data were also compared with the transition lines of Triplett et al. [25], indicating that the agreement is not satisfactory.

The disagreement can be explained by (i) for gas–liquid flow, the working fluids such as an air–water mixture possess thermophysical properties that are substantially different from the refrigerants used in flow boiling process, (ii) flow patterns generated by an air–water flow system may be possibly based on hydrodynamics of the upstream gas–liquid mixer design, and (iii) the effect of evaporation of the liquid phase taking place in the gas–liquid system could be quite significant in small channels as indicated by Kandlikar [3].

In addition, when the system pressure increases as seen in Fig. 5, a decrease in surface tension results in a degradation of throat-annular flow, especially at high vapour quality.

Recently, a new type of two-phase flow pattern map for flow boiling in micro-channels was developed by Revellin and Thome [28]. The proposed flow regime map comprises different zones according to the bubble coalescence phenomena. The followings are a brief description of each zone located in the flow map.

The isolated bubble (IB) regime corresponds to a relatively high bubble generation rate when compared with the bubble coalescence rate. Either or both of bubbly flow and slug flow are included in this regime. The coalescing bubble (CB) regime is defined when the bubble generation rate is smaller than the bubble coalescence rate.

The isolated bubble (IB) flow to coalescing bubble (CB) flow transition is given by

$$x_{IB/CB} = 0.763\left(\frac{Re_{LO}B_o}{We_{GO}}\right)^{0.41} \tag{3}$$

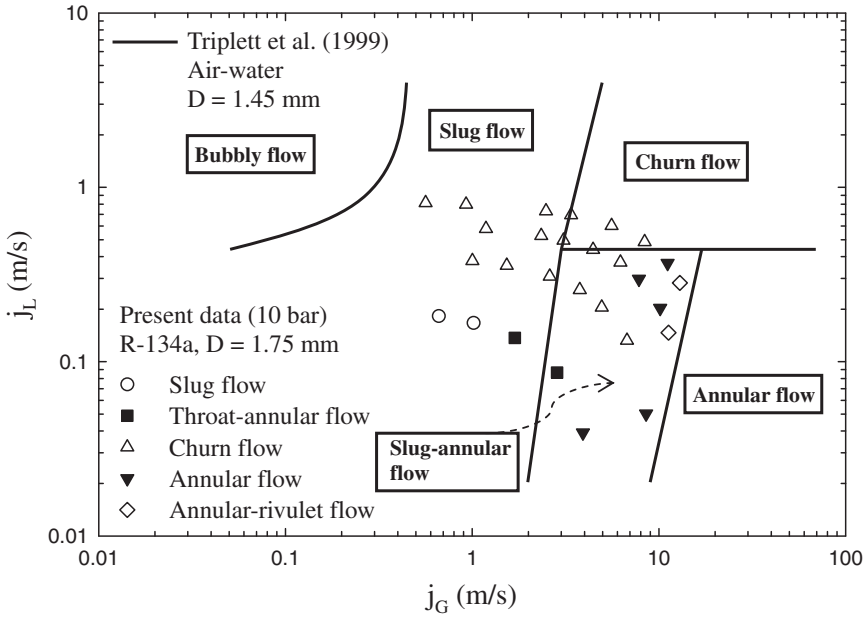

Fig. 5. Comparison of the observed flow patterns at 10 bar with the transition lines by Triplett et al. [25].

where B_o stands for Boiling number, Re_{LO} represents all-liquid Reynolds number and We_{GO} is all-vapour Weber number.

The transition from coalescing bubble flow to annular flow is determined by

$$x_{CB/A} = 0.00014 Re_{LO}^{1.47} We_{LO}^{-1.23} \quad (4)$$

where We_{LO} is all-liquid Weber number.

This correlation takes into account different effects including heat flux, viscosity and surface tension which are represented, respectively, by Boiling number, Reynolds number and Weber number.

The present flow pattern maps in terms of mass flux and vapour quality are presented in Figs. 6 and 7 which are compared with their transition zones. It is found that, in general, the present data correspond well with the transition zones proposed by Revellin and Thome [28]. The regions of churn flow and throat-annular flow obtained from the present study agree fairly well with their coalescing bubble regime whereas our annular flow and annular-rivulet flow are located in their annular region. The present slug flow data are found near the transition zone between their isolated bubble and coalescing bubble regions.

3.2. Flow boiling heat transfer

During two-phase heat transfer experiments, the flow rate, system pressure and inlet vapour quality were set to the desired value and the imposed heat flux was then varied by small increments until dry-out, noticed by a large increase in wall temperature and outlet saturation temperature.

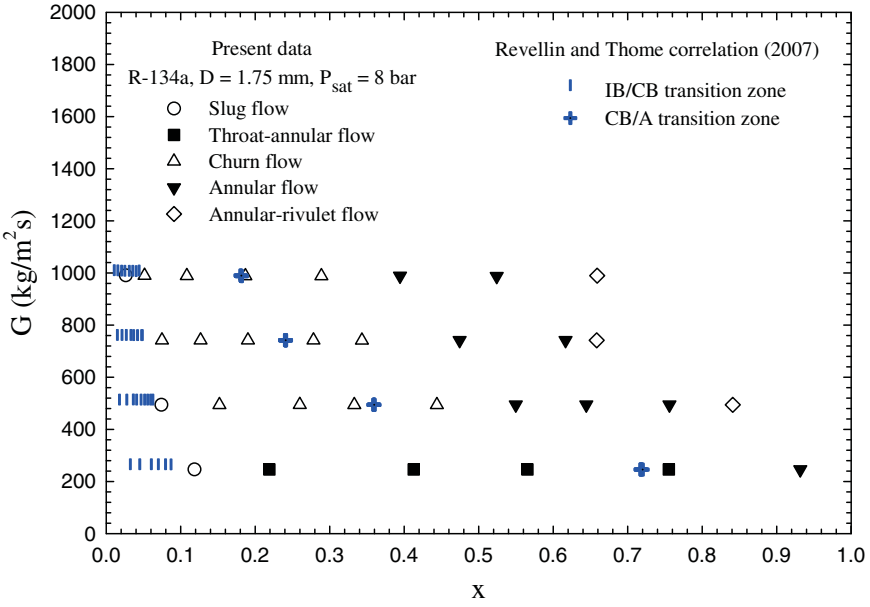

Fig. 6. Comparison of the observed flow patterns at 8 bar with the transition lines by Revellin and Thome correlation [28].

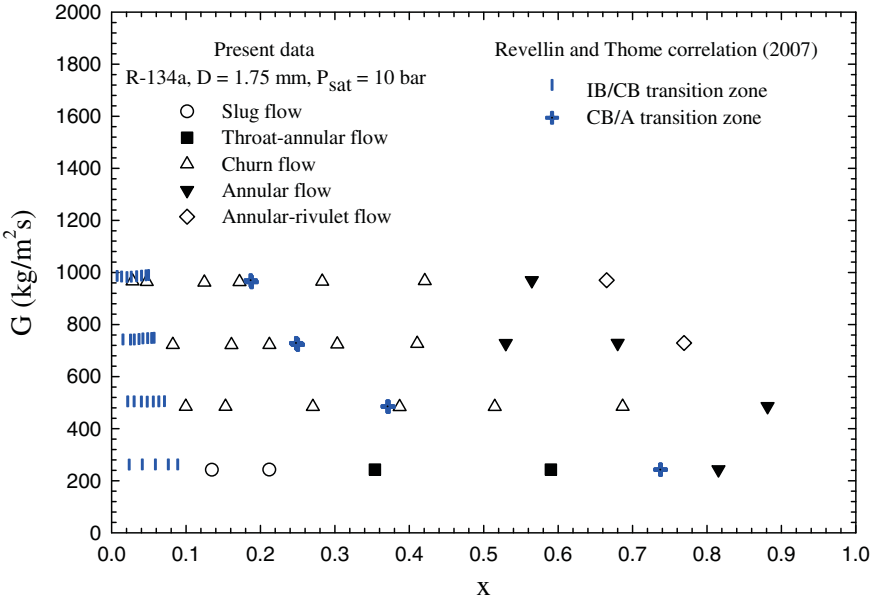

Fig. 7. Comparison of the observed flow patterns at 10 bar with the transition lines by Revellin and Thome correlation [28].

3.2.1. Local heat transfer coefficient

Heat flux, q, transferred to the test section is provided by the regulated DC power supply generating 80 A at 12 V. T-type thermocouples are installed at the inlet and outlet of the test section to measure the refrigerant temperatures. Since, during experiments, the two-phase conditions for flow boiling are provided at the test section inlet by using pre-heater as shown in Fig. 1, the saturation pressures at the test section inlet and outlet are obtained based on the corresponding saturation temperatures. Regarding the assumption of a linear variation of the saturation pressure along the tube, the local saturation temperatures, $T_{sat,loc}$, can subsequently be obtained.

As presented in Fig. 2, the 10 T-type thermocouples are installed on the top and bottom sides at equal distances along the tube to measure the tube surface temperature. For each position where the thermocouple is installed on the tube surface, the inner wall temperature at a given position is determined using the equations for steady-state one-dimensional heat conduction through the tube wall with internal heat generation. At a given distance, hence, the average temperature of the inner wall at the top and bottom sides stands for the local temperature on the inner wall, $T_{wall,in,loc}$. Finally, the local heat transfer coefficient, h_{loc}, for flow boiling of R-134a along the test section is determined using the following equation:

$$h_{loc} = \frac{q}{(T_{wall,in,loc} - T_{sat,loc})} \tag{5}$$

The local vapour quality is determined based on thermodynamic properties, i.e.

$$x = \frac{(i - i_L)}{i_{LG}} \tag{6}$$

where i_L is the specific enthalpy of the saturated liquid, i_{LG} represents the latent heat of vaporisation and the local fluid enthalpy, i is determined from an energy balance.

In the present work, the heat transfer results were taken simultaneously with the flow pattern data. Fig. 8 shows local heat transfer coefficients for different flow patterns. It is found that slug flow appears with the lowest heat transfer coefficient in comparison to the other flow regimes. Although the annular-rivulet flow shows a relatively high heat transfer coefficient, a local dry-out region is observed at high vapour qualities, which is undesirable for a thermal design approach dealing with a cooling system implemented with small channels. Moderate values of heat transfer coefficient are given by throat-annular flow, churn flow and annular flow which might be good choices for the development of these systems. It can be seen from the figure that the flow patterns are expected to influence the flow boiling heat transfer process.

In addition to the flow pattern, the effects of heat flux, mass flux, vapour quality and saturation pressure on the heat transfer characteristics are also addressed as follows.

The dependence of heat transfer coefficients on heat flux is presented in Fig. 9. Regarding the experimental range, the measured results increase with increasing heat flux and are less affected by vapour quality.

In Fig. 10, the heat transfer coefficient is depicted with various values of mass flux. The figure reveals an insignificant effect of mass flux on the measured heat transfer coefficient.

The observed characteristics, presented in Figs. 9 and 10, seem to be the case that nucleate boiling contribution plays an important role on flow boiling heat transfer in mini-channel. Similar observations were also reported by different researchers such as Saitoh et al. [12], Choi et al. [16], Lazarek and Black [29], Wambsganss et al. [30], Bao et al. [31] and Tran et al. [32].

Fig. 11 presents the variation of heat transfer coefficient with vapour quality for saturation pressures of 8, 10 and 13 bar. There is a decrease in heat transfer coefficient with increasing saturation pressure across the experimental range of vapour quality. This may be attributed to the fact that, with an increase in saturation pressure, which corresponds to the smaller latent heat of vaporisation, the lower liquid viscosity can contribute the thinner liquid film on the tube wall to become easily broken and, hence, a decrease in heat transfer coefficient is established. A similar trend regarding the effect of saturation pressure on heat transfer coefficient was also reported by Choi et al. [15] and Kaew-On and Wongwises [22].

3.2.2. Average heat transfer coefficient

The average heat transfer coefficient for the entire 0.6 m long tube is defined as

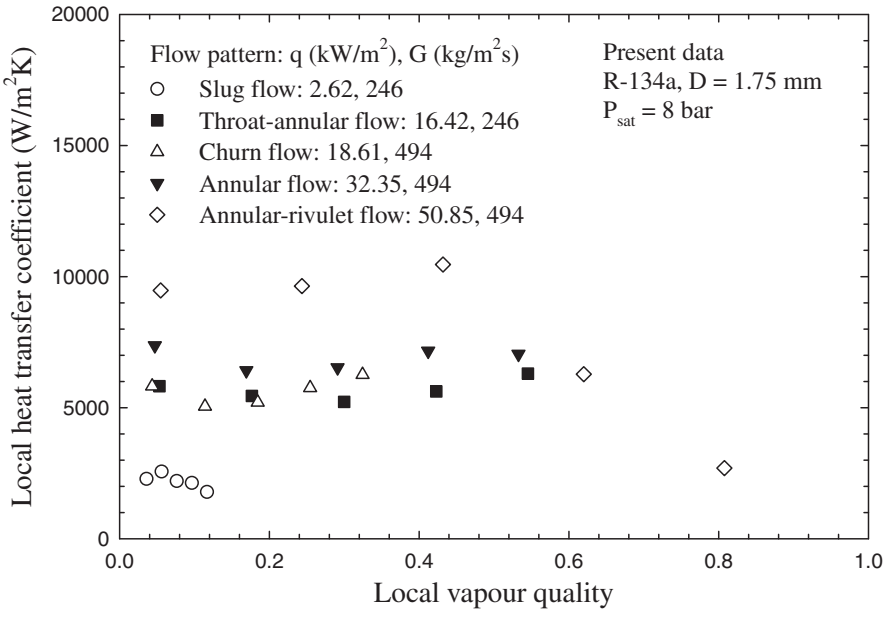

Fig. 8. Local heat transfer coefficient data for various flow patterns.

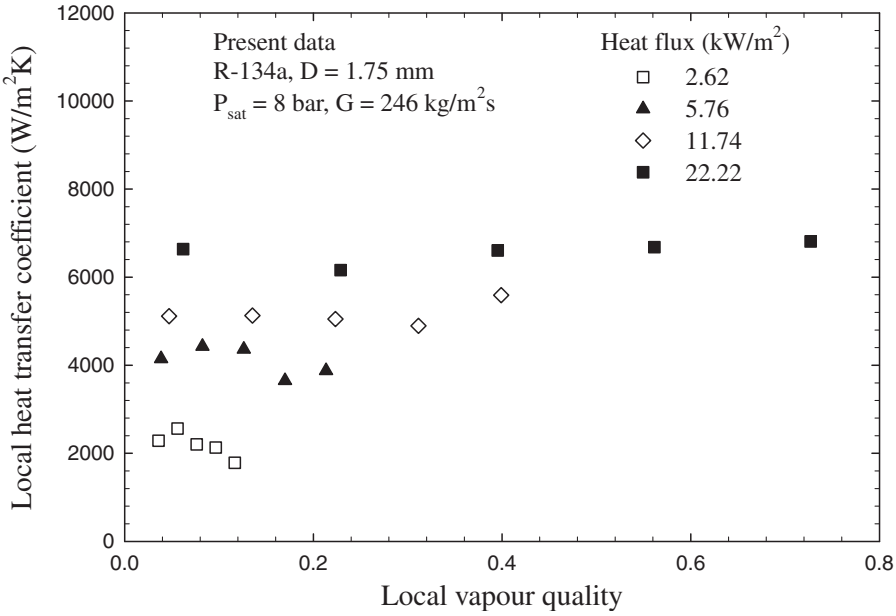

Fig. 9. Local vapour quality versus local heat transfer coefficient for various heat flux values.

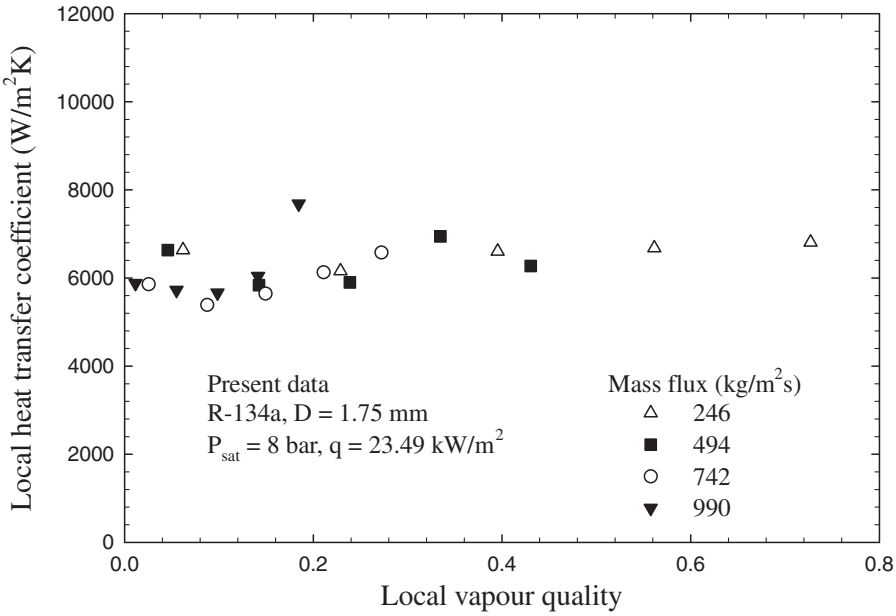

Fig. 10. Local vapour quality versus local heat transfer coefficient for various mass flux values.

$$h_{avg} = \frac{q}{(T_{wall,in,avg} - T_{sat,avg})} \quad (7)$$

There are 10 positions along the tube, at which the inner wall temperatures are determined and thus the average value of the inner wall surface temperature, $T_{wall,in,avg}$, of the test section is obtained using the arithmetic mean of the temperatures along the tube. $T_{sat,avg}$ represents the average temperature of the refrigerant at the test section inlet and outlet.

Fig. 12 presents average heat transfer coefficients plotted as a function of heat flux for different constant values of mass flux. For each mass flux value, the results depend strongly on heat flux. The decreases in heat transfer coefficient which result from the partial dry-out region appearing in the annular-rivulet flow are indicated under mass flux values of 494, 742 and 989 kg/m^2 s.

The interesting point observed from Fig. 12 is that the heat transfer coefficient data are mostly less dependent on mass flux, especially, under heat flux values up to around 40 kW/m^2. This observed behavior reveals that convective contribution does not play dominant role on the heat transfer mechanisms although liquid-turbulent and vapour-turbulent flow are established in the mass flux ranging between 494 and 989 kg/m^2 s (a mass flux value of 246 kg/m^2 s falls in the liquid-laminar and vapour-turbulent region which is a common flow pattern in many applications of mini-channel [33]). To examine such behavior, the confinement number recommended by Kew and Cornwell [34] is used as the transition

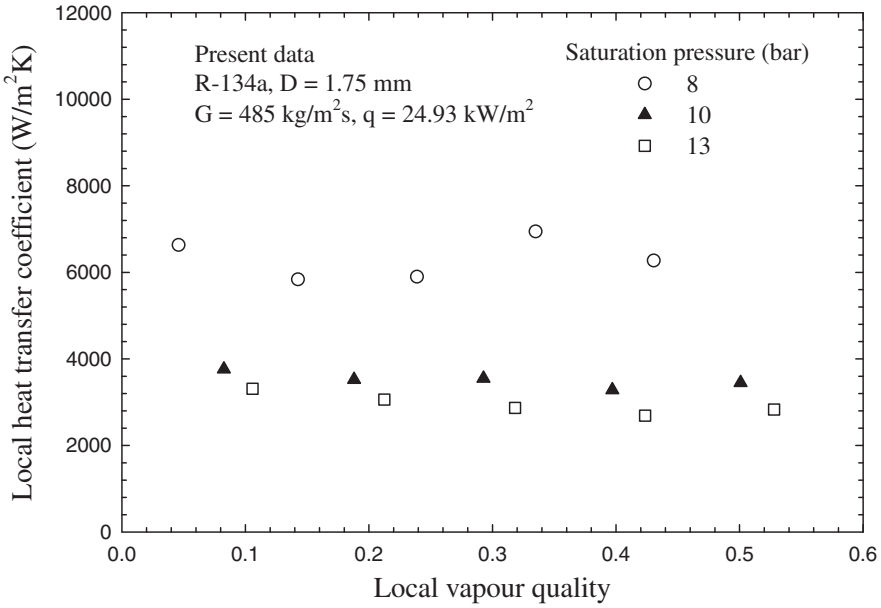

Fig. 11. Local vapour quality versus local heat transfer coefficient for various pressures.

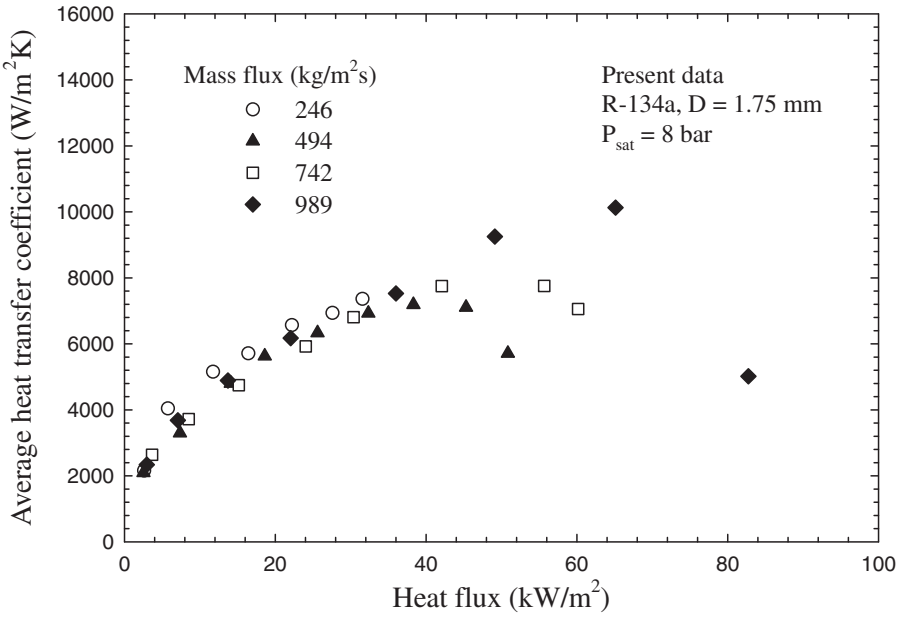

Fig. 12. Heat flux versus average heat transfer coefficient for various mass flux values at P_{sat} = 8 bar.

criterion for checking whether the micro-scale effects are important. The confinement number is defined as

$$C_o = \frac{D_b}{D_h} \tag{8}$$

where D_b is the nominal bubble size or capillary length which is expressed by

$$D_b = \sqrt{\frac{\sigma}{g(\rho_L - \rho_G)}} \tag{9}$$

The confinement number below 0.5 stands for ordinarily sized channel. In the present study, the confinement number for all mass flux values under a saturation pressure of 8 bar is slightly above 0.5, presumably indicating a mini-channel flow.

As heat flux is increased to values larger than 40 kW/m^2, nevertheless, the increase in evaporation momentum force exerted at the evaporating interface tends to enhance convective heat transfer mechanisms, leading to the variation of heat transfer coefficient with mass flux.

For a saturation pressure of 10 bar, the heat flux versus average heat transfer coefficient for various mass flux is illustrated in Fig. 13. The variation of heat transfer coefficient with mass flux is more obvious than that presented in Fig. 12. As expected, the criterion proposed by Kew and Cornwell [34] indicates the macro-scale flow region in which the values of the confinement number are less than 0.5 for all mass flux values.

The results presented in Fig. 14, for heat transfer coefficient plotted against heat flux for different values of saturation pressure show the decrease in heat transfer coefficient with increasing sat-

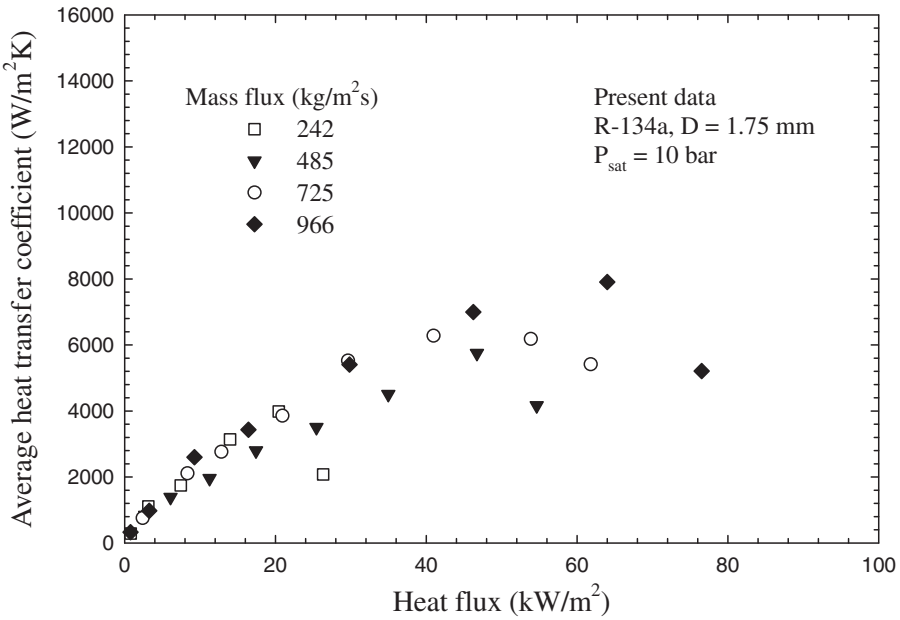

Fig. 13. Heat flux versus average heat transfer coefficient for various mass flux values at P_{sat} = 10 bar.

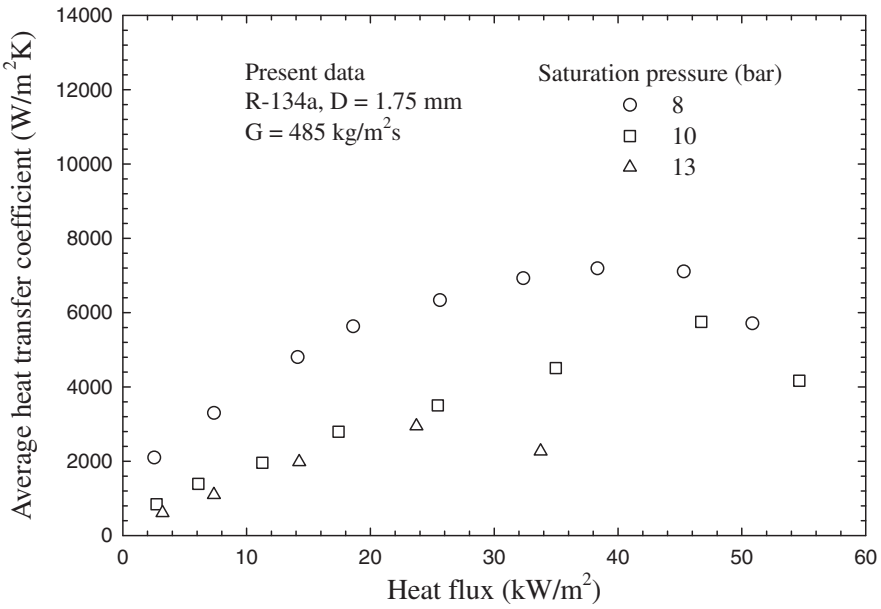

Fig. 14. Heat flux versus average heat transfer coefficient for various pressures.

uration pressure. The results support the trend which is previously discussed as illustrated in Fig. 11. The lower liquid viscosity due to the increment of saturation pressure also leads to the decrease in frictional pressure drop as illustrated in Fig. 15. The frictional pressure drop is determined by subtracting the accelerational pressure drop from the total one which is monitored by the differential pressure transducer.

The average heat transfer coefficient data obtained from the present study are compared with one well-known heat transfer prediction recommended for flow boiling in ordinarily sized channels and with three boiling heat transfer correlations proposed for small flow channels.

One of the widely used correlations for ordinarily sized channels, which is taken as a benchmark in the flow boiling literature, was proposed by Chen [35]. An additive concept for nucleate boiling and forced convective mechanisms was introduced in the correlation which is expressed as

$$h = h_{NBC}S + h_L F \tag{10}$$

where F is a two-phase convection multiplier which is calculated as

$$F = \begin{cases} 1 & \text{for } \frac{1}{\chi} \leqslant 0.1 \\ 2.35\left(\frac{1}{\chi} + 0.213\right)^{0.736} & \text{for } \frac{1}{\chi} > 0.1 \end{cases} \tag{11}$$

χ in Eq. (11) represents the Lockhart–Martinelli parameter determined by:

$$\chi = \left(\frac{1-x}{x}\right)^{0.9}\left(\frac{\rho_G}{\rho_L}\right)^{0.5}\left(\frac{\mu_L}{\mu_G}\right)^{0.1} \tag{12}$$

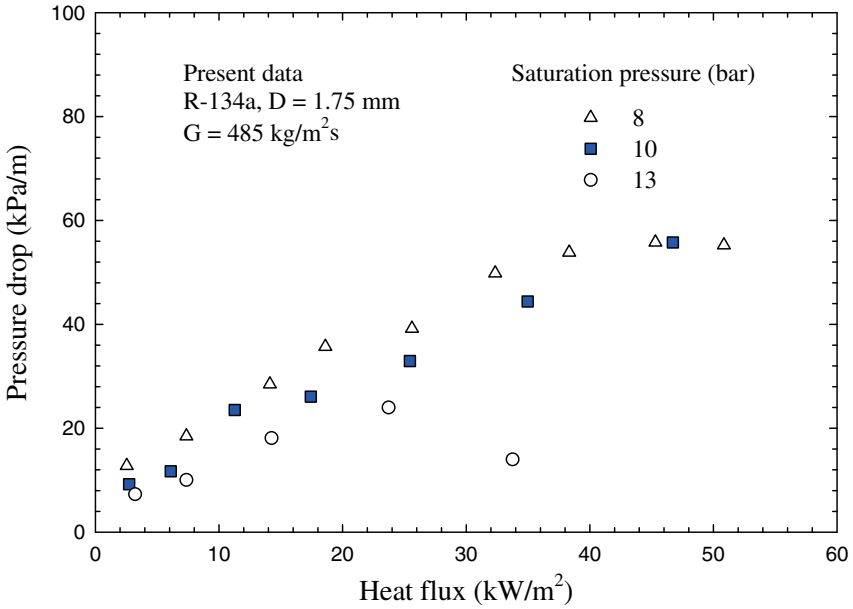

Fig. 15. Heat flux versus frictional pressure drop for various pressures.

The nucleate boiling suppression factor, S, is expressed as

$$S = \frac{1}{1 + 2.53 \times 10^{-6} Re_L^{1.17}} \tag{13}$$

The liquid-phase heat transfer coefficient, h_L, is given by:

$$h_L = 0.023 Re_L^{0.8} \left(\frac{\mu_L C_{pL}}{k_L}\right)^{0.4} \left(\frac{k_L}{D}\right) \tag{14}$$

and nucleate boiling heat transfer coefficient, h_{NBC}, is determined from the following equation:

$$h_{NBC} = 0.00122 \Delta T_{sat}^{0.24} \Delta P_{sat}^{0.75} \left(\frac{k_L^{0.79} C_{pL}^{0.45} \rho_L^{0.49}}{\sigma^{0.5} \mu_L^{0.29} i_{LG}^{0.24} \rho_G^{0.24}}\right) \tag{15}$$

In Eqs. (12)–(15), μ_L is liquid viscosity, μ_G is vapour viscosity, Re_L is liquid Reynolds number, C_{pL} is liquid specific heat capacity, k_L is liquid thermal conductivity, D is channel diameter, σ is surface tension, ΔT_{sat} is wall superheat and ΔP_{sat} stands for the difference between the saturation pressures calculated from wall temperature and fluid temperature.

Later, the Chen correlation [35] was improved by Choi et al. [16] to make it more applicable to small channels. The two-phase convection multiplier, F, which can be related to the two-phase frictional multiplier as indicated in Zhang et al. [36], and the nucleate boiling suppression factor, S, were modified by Choi et al. [16] using a regression method corresponding to their experimental data for mini-channels.

The proposed two-phase convection multiplier and nucleate boiling suppression factor are expressed in Eqs. (16) and (17), respectively:

$$F = 0.042 \phi_L^2 + 0.958 \tag{16}$$

$$S = 469.1689 (\phi_L^2)^{-0.2093} B_o^{0.7402} \tag{17}$$

where ϕ_L^2 represents the two-phase frictional multiplier given by:

$$\phi_L^2 = 1 + \frac{C}{\chi} + \frac{1}{\chi^2} \tag{18}$$

The constant C in this equation is a parameter which indicates the two-phase flow condition. The value of this parameter proposed by Chisholm [37], varying from 5 to 20, depends on the flow condition of the vapour and liquid. $C = 20$ for turbulent liquid and turbulent vapour, $C = 12$ for laminar liquid and turbulent vapour, $C = 10$ for turbulent liquid and laminar vapour, $C = 5$ for laminar liquid and laminar vapour.

Based on the Cooper correlation [38], the nucleate boiling heat transfer coefficient is given by

$$h_{NBC} = 55 P_r^{0.12} (-0.4343 \ln P_r)^{-0.55} M^{-0.5} q^{0.67} \tag{19}$$

where P_r is reduced pressure and M is molecular weight.

Finally, the predicted heat transfer coefficient can be obtained by substituting Eqs. (14), (16), (17), and (19) into (10).

Tran et al. [32] proposed a correlation for flow boiling in circular and rectangular mini-channels. The dominant heat transfer mechanism associated with nucleate boiling was considered to develop a correlation which is written as

$$h = 8.4 \times 10^5 \left(B_o^2 We_{LO}\right)^{0.3} \left(\frac{\rho_L}{\rho_G}\right)^{-0.4} \tag{20}$$

Kandlikar and Balasubramanian [39] modified the correlation proposed by Kandlikar [40] for ordinarily sized channels to extend the prediction to mini- and micro-channels which correspond to the neglected Froude number.

For all-liquid Reynolds numbers higher than 100, their correlation can be expressed as shown below

$$h = \text{larger of} \begin{cases} h_{NBC} \\ h_{CBC} \end{cases} \tag{21}$$

where the heat transfer coefficient based on nucleate boiling contribution, h_{NBC}, and that on forced convective contribution, h_{CBC}, are given by Eqs. (22) and (23), respectively

$$h_{NBC} = 0.6683 C_{CO}^{-0.2} (1-x)^{0.8} h_{LO} + 1058.0 B_o^{0.7} (1-x)^{0.8} F_{FI} h_{LO} \tag{22}$$

$$h_{CBC} = 1.136 C_{CO}^{-0.9} (1-x)^{0.8} h_{LO} + 667.2 B_o^{0.7} (1-x)^{0.8} F_{FI} h_{LO} \tag{23}$$

where C_{CO} represents convection number, F_{FI} stands for a fluid-surface dependent parameter which is equal to 1 for all fluids tested with stainless steel tubes, and h_{LO} for all-liquid flow heat transfer coefficient which is found from Eqs. (24)–(26):

$$h_{LO} = \frac{Re_{LO} Pr_L (f/2)(k_L/D)}{1 + 12.7(Pr_L^{2/3} - 1)(f/2)^{0.5}} \quad \text{for } 10^4 \leqslant Re_{LO} \leqslant 5 \times 10^6 \tag{24}$$

$$h_{LO} = \frac{(Re_{LO} - 1000) Pr_L (f/2)(k_L/D)}{1 + 12.7(Pr_L^{2/3} - 1)(f/2)^{0.5}} \quad \text{for } 3000 \leqslant Re_{LO} \leqslant 10^4 \tag{25}$$

$$h_{LO} = \frac{Nuk_L}{D} \quad \text{for } Re_{LO} \leqslant 1600 \tag{26}$$

Pr_L is the liquid Prandtl number and f appearing in Eqs. (24) and (25) is the friction factor determined by:

$$f = [1.58 \ln(Re_{LO}) - 3.28]^{-2} \tag{27}$$

It is noted that, for laminar flow in a circular channel with constant surface heat flux, the Nusselt number indicated in Eq. (26) is equal to 4.36. In the case of the transition region, the all-liquid flow heat transfer coefficient is established using a linear interpolation between Re_{LO} of 1600 and 3000.

They also proposed a two-phase heat transfer coefficient for very low Reynolds number ($Re_{LO} \leqslant 100$) which is recommended as

$$h = h_{NBC} = 0.6683 C_{CO}^{-0.2} (1-x)^{0.8} h_{LO} + 1058.0 B_o^{0.7} (1-x)^{0.8} F_{FI} h_{LO} \tag{28}$$

where h_{LO} is found from Eq. (26).

Comparisons between the average heat transfer coefficient data and existing correlations are presented in Figs. 16–19 which contain the mean absolute error (MAE) providing the predictive accuracy of the corresponding correlations.

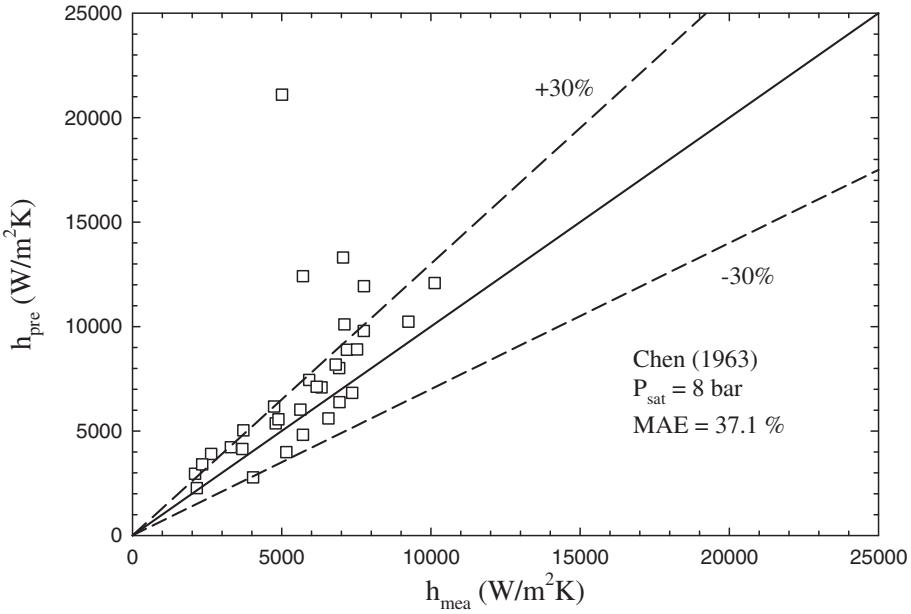

Fig. 16. Comparison between measured and calculated heat transfer coefficient using Chen correlation [35].

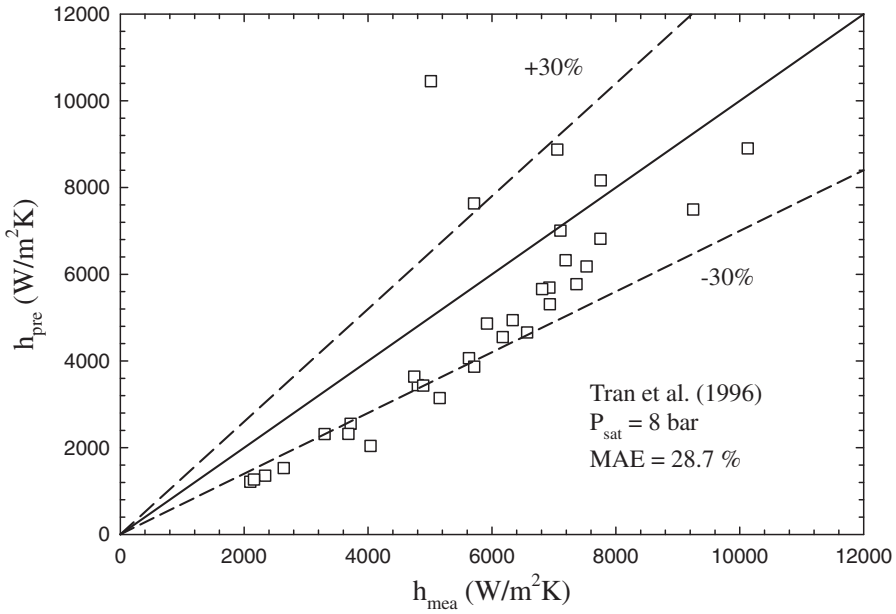

Fig. 17. Comparison between measured and calculated heat transfer coefficient using Tran et al. correlation [32].

The correlations mentioned above were proposed for two-phase heat transfer prediction. The method of Chen [35] were done by assuming that saturated nucleate boiling mechanism and two-phase forced convection mechanism take place to some degree for the entire range of the correlation. The contributions from both mechanisms were also assumed to be additive. Although the method of Chen [35] was developed based on the ordinarily sized channel placed vertically, the applicability of this correlation is examined here. The ordinarily sized channel is often referred to as the channel possessing Bond number (which is in inverse relation to the confinement number) higher than 4.0 for which the effect of the gravitational force is not expected to be small when compared with the surface tension force. In Fig. 16, the correlation proposed by Chen [35] roughly predicts the data. With MAE of 37.1%, the method of Chen [35] captures 68.75% of the data within ±30% error band. The method developed by Tran et al. [32], which is one of the most popular existing correlations, was developed based on flow boiling heat transfer experiments with R-22 in channels having hydraulic diameters of around 2.46 mm, and on the nucleation-dominant mechanism rather than the convection contribution. As presented in Fig. 17, a lower MAE (28.7%) in comparison to that for Chen correlation [35] is due to their method which associates with small channels. However, the Trans et al. correlation [32], which predicts about 65.63% of the data within ±30% error band, deals with the experimental conditions having the Bond number of 9.8 which is nearly three times larger than that for the

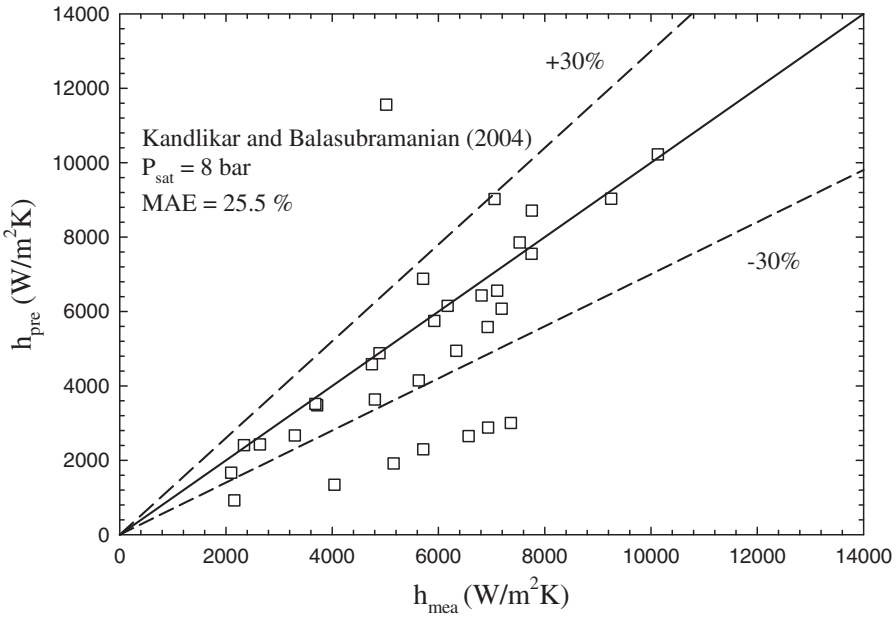

Fig. 18. Comparison between measured and calculated heat transfer coefficient using Kandlikar and Balasubramanian correlation [39].

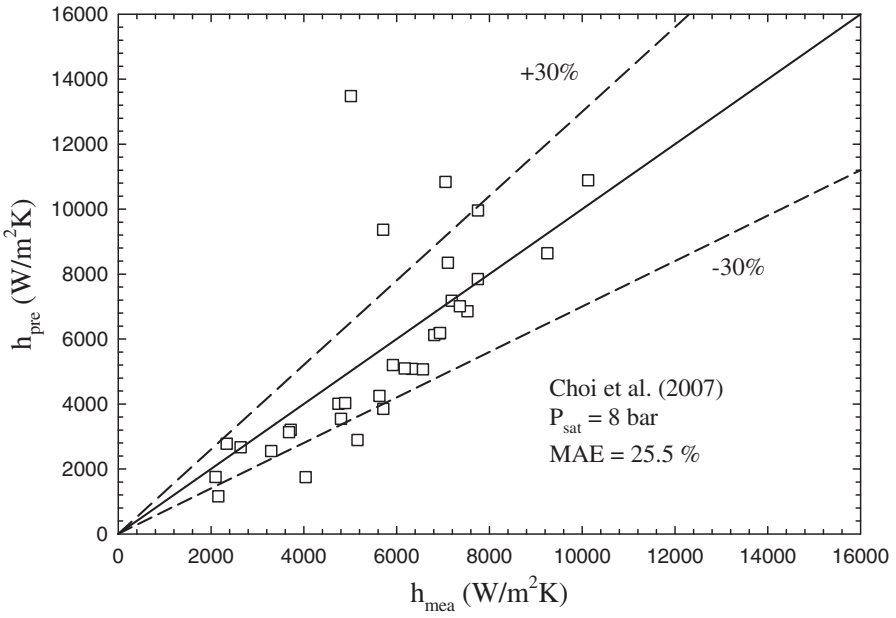

Fig. 19. Comparison between measured and calculated heat transfer coefficient using Choi et al. correlation [16].

Table 3
Mean absolute error (MAE) for different prediction methods.

Prediction method	MAE	
	10 bar	13 bar
Chen [35]	305.5%	670.4%
Tran et al. [32]	71.9%	215.7%
Kandlikar and Balasubramanian [39]	86.5%	154.3%
Choi et al. [15,16]	111.8%	189.7%

present work. The method combining both nucleate boiling and forced convective mechanisms was proposed by Kandlikar and Balasubramanian [39] for predicting heat transfer coefficient in mini- and micro-channels. At a given condition, either heat transfer coefficient based on nucleate boiling contribution or that with respect to forced convective mechanism is representative for the prediction, depending upon which one is larger. With MAE of 25.5%, the correlation developed by Kandlikar and Balasubramanian [39] can predict 75% of the data within ±30% error band as illustrated in Fig. 18. Unlike the method of Kandlikar and Balasubramanian [39], the method for mini-channels proposed by Choi et al. [16] is based on additive concept for nucleate boiling and forced convective contributions under a given condition. In Fig. 19, it seems that the correlation developed by Choi et al. [16] presents the best prediction, with MAE of 25.5% and 78.12% of the predicted data falling within ±30% error band.

The values associated with mean absolute error (MAE) for different prediction methods based on system pressures higher than 8 bar are given in Table 3. As previously discussed, the liquid film under high saturation pressure tends to break up easily, leading to the unstable condition near the tube wall. Such condition, which is not taken into account in these correlations, results in large mean absolute error (MAE) as seen in Table 3.

4. Conclusion

This experimental investigation was conducted to study flow visualisation and heat transfer characteristics of R-134a refrigerant during flow boiling in a stainless steel tube with inner diameter of 1.75 mm and a length of 600 mm. For the flow visualisation study, the flow pattern map is developed from the observed flow patterns, i.e., slug flow, throat-annular flow, churn flow, annular flow and annular-rivulet flow, and is compared with existing transition lines obtained from different working fluids. The heat transfer results for a given flow pattern are presented and the effects of heat flux, mass flux, vapour quality and saturation pressure on the heat transfer coefficient are also discussed in this study. Calculations based on existing heat transfer prediction methods available for ordinarily sized channels and small channels are made to compare the results with the experimental data.

Acknowledgements

The authors would like to express their appreciation to King Mongkut's University of Technology Thonburi, the Thailand Research Fund (TRF) and the Office of Higher Education Commission for providing financial support for this study.

References

[1] G. Ribatski, L. Wojtan, J.R. Thome, An analysis of experimental data and prediction methods for two-phase frictional pressure drop and flow boiling heat transfer in micro-scale channels, Exp. Therm. Fluid Sci. 31 (1) (2006) 1–19.
[2] S.S. Mehendale, A.M. Jacobi, R.K. Ahah, Fluid flow and heat transfer at micro- and meso-scales with application to heat exchanger design, Appl. Mech. Rev. 53 (2000) 175–193.
[3] S.G. Kandlikar, Fundamental issues related to flow boiling in mini-channels and micro-channels, Exp. Therm. Fluid Sci. 26 (7) (2002) 389–407.
[4] P.M.-Y. Chung, M. Kawaji, The effect of channel diameter on adiabatic two-phase flow characteristics in microchannels, Int. J. Multiphase Flow 30 (7–8) (2004) 735–761.
[5] S. Saisorn, S. Wongwises, The effects of channel diameter on flow pattern, void fraction and pressure drop of two-phase air–water flow in circular micro-channels, Exp. Therm. Fluid Sci. 34 (4) (2010) 454–462.
[6] A. Greco, Convective boiling of pure and mixed refrigerants: an experimental study of the major parameters affecting heat transfer, Int. J. Heat Mass Transfer 51 (3–4) (2008) 896–909.
[7] S.G. Kandlikar, Scale effects on flow boiling heat transfer in microchannels: a fundamental perspective, Int. J. Therm. Sci. 49 (7) (2010) 1073–1085.
[8] D. Brutin, L. Tadrist, Pressure drop and heat transfer analysis of flow boiling in a minichannel: influence of the inlet condition on two-phase flow stability, Int. J. Heat Mass Transfer 47 (10–11) (2004) 2365–2377.
[9] X. Huo, L. Chen, Y.S. Tian, T.G. Karayiannis, Flow boiling and flow regimes in small diameter tubes, Appl. Therm. Eng. 24 (8–9) (2004) 1225–1239.
[10] J. Pettersen, Flow vaporization of CO_2 in microchannel tubes, Exp. Therm. Fluid Sci. 28 (2–3) (2004) 111–121.
[11] R. Yun, Y. Kim, M.S. Kim, Convective boiling heat transfer characteristics of CO_2 in microchannels, Int. J. Heat Mass Transfer 48 (2) (2005) 235–242.
[12] S. Saitoh, H. Daiguji, E. Hihara, Effect of tube diameter on boiling heat transfer of R-134a in horizontal small-diameter tubes, Int. J. Heat Mass Transfer 48 (23–24) (2005) 4973–4984.
[13] Y.M. Lie, F.Q. Su, R.L. Lai, T.F. Lin, Experimental study of evaporation heat transfer characteristics of refrigerants R-134a and R-407C, Int. J. Heat Mass Transfer 49 (1–2) (2006) 207–218.
[14] H. Boye, Y. Staate, J. Schmidt, Experimental investigation and modeling of heat transfer during convective boiling in a minichannel, Int. J. Heat Mass Transfer 50 (1–2) (2007) 208–215.
[15] K.I. Choi, A.S. Pamitran, J.T. Oh, Two-phase flow heat transfer of CO_2 vaporization in smooth horizontal minichannels, Int. J. Refrigeration 30 (5) (2007) 767–777.
[16] K.I. Choi, A.S. Pamitran, C.Y. Oh, J.T. Oh, Boiling heat transfer of R-22, R-134a, and CO_2 in horizontal smooth minichannels, Int. J. Refrigeration 30 (8) (2007) 1336–1346.
[17] D. Shiferaw, X. Huo, T.G. Karayiannis, D.B.R. Kenning, Examination of heat transfer correlations and a model for flow boiling of R134a in small diameter tubes, Int. J. Heat Mass Transfer 50 (25–26) (2007) 5177–5193.
[18] D. Shiferaw, T.G. Karayiannis, D.B.R. Kenning, Flow boiling in a 1.1 mm tube with R134a: experimental results and comparison with model, Int. J. Therm. Sci. 48 (2) (2009) 331–341.
[19] J.R. Thome, V. Dupont, A.M. Jacobi, Heat transfer model for evaporation in microchannels. Part I: presentation of the model, Int. J. Heat Mass Transfer 47 (14–16) (2004) 3375–3385.
[20] V. Dupont, J.R. Thome, A.M. Jacobi, Heat transfer model for evaporation in microchannels. Part II: comparison with the database, Int. J. Heat Mass Transfer 47 (14–16) (2004) 3387–3401.
[21] C.L. Ong, J.R. Thome, Flow boiling heat transfer of R134a, R236fa and R245fa in a horizontal 1.030 mm circular channel, Exp. Therm. Fluid Sci. 33 (4) (2009) 651–663.
[22] J. Kaew-On, S. Wongwises, Experimental investigation of evaporation heat transfer coefficient and pressure drop of R-410A in a multiport mini-channel, Int. J. Refrigeration 32 (1) (2009) 124–137.
[23] M. Muller-Steinhagen, K. Heck, A simple friction pressure drop correlation for two-phase flow in pipes, Chem. Eng. Process. 20 (6) (1986) 297–308.
[24] S. Garimella, J.D. Killion, J.W. Coleman, An experimentally validated model for two-phase pressure drop in the intermittent flow regime for circular microchannels, J. Fluid Eng. 124 (1) (2002) 205–214.
[25] K.A. Triplett, S.M. Ghiaasiaan, S.I. Abdel-Khalik, D.L. Sadowski, Gas–liquid two-phase flow in microchannels. Part I: two-phase flow patterns, Int. J. Multiphase Flow 25 (3) (1999) 377–394.
[26] S. Saisorn, S. Wongwises, Flow pattern, void fraction and pressure drop of two-phase air–water flow in a horizontal circular micro-channel, Exp. Therm. Fluid Sci. 32 (3) (2008) 748–760.
[27] C. Martin-Callizo, B. Palm, W. Owhaib, R. Ali, Flow boiling visualization of R-134a in a vertical channel of small diameter, J. Heat Transfer 132 (3) (2010) 1–8.
[28] R. Revellin, J.R. Thome, A new type of diabatic flow pattern map for boiling heat transfer in microchannels, J. Micromech. Microeng. 17 (4) (2007) 788–796.
[29] G.M. Lazarek, S.H. Black, Evaporative heat transfer, pressure drop and critical heat flux in a small diameter vertical tube with R-113, Int. J. Heat Mass Transfer 25 (7) (1982) 945–960.
[30] M.W. Wambsganss, D.M. France, J.A. Jendrzejczyk, T.N. Tran, Boiling heat transfer in a horizontal small-diameter tube, J. Heat Transfer 115 (4) (1993) 963–972.
[31] Z.Y. Bao, D.F. Fletcher, B.S. Haynes, Flow boiling heat transfer of Freon R11 and HCFC123 in narrow passages, Int. J. Heat Mass Transfer 43 (18) (2000) 3347–3358.
[32] T.N. Tran, M.W. Wambsganss, D.M. France, Small circular- and rectangular-channel boiling with two refrigerants, Int. J. Multiphase Flow 22 (3) (1996) 485–498.
[33] W. Li, Z. Wu, A general criterion for evaporative heat transfer in micro/mini-channels, Int. J. Heat Mass Transfer 53 (9–10) (2010) 1967–1976.

[34] P.A. Kew, K. Cornwell, Correlations for the prediction of boiling heat transfer in small-diameter channels, Appl. Therm. Eng. 17 (8–10) (1997) 705–715.
[35] J.C. Chen, A Correlation for Boiling Heat Transfer to Saturated Fluid in Convective Flow, ASME Paper, 63-HT-34, 1963, pp. 1–11.
[36] W. Zhang, T. Hibiki, K. Mishima, Correlation for flow boiling heat transfer in mini-channels, Int. J. Heat Mass Transfer 47 (26) (2004) 5749–5763.
[37] D. Chisholm, A theoretical basis for the Lockhart–Martinelli correlation for two-phase flow, Int. J. Heat Mass Transfer 10 (12) (1967) 1767–1778.
[38] M.G. Cooper, Heat flow rates in saturated nucleate pool boiling – a wide-ranging examination using reduced properties, Adv. Heat Transfer 16 (1984) 157–239.
[39] S.G. Kandlikar, P. Balasubramanian, An extension of the flow boiling correlation to transition, laminar, and deep laminar flows in minichannels and microchannels, Heat Transfer Eng. 25 (3) (2004) 86–93.
[40] S.G. Kandlikar, A general correlation for two-phase flow boiling heat transfer coefficient inside horizontal and vertical tubes, J. Heat Transfer 112 (1) (1990) 219–228.

Applied Thermal Engineering 30 (2010) 1927–1936

Contents lists available at ScienceDirect

Applied Thermal Engineering

journal homepage: www.elsevier.com/locate/apthermeng

Two-phase flow model of refrigerants flowing through helically coiled capillary tubes

Sukkarin Chingulpitak [a,b], Somchai Wongwises [b,*]

[a] The joint Graduate School of Energy and Environment, King Mongkut's University of Technology Thonburi, Bangmod, Bangkok 10140, Thailand
[b] Fluid Mechanics, Thermal Engineering and Multiphase Flow Research Lab. (FUTURE), Department of Mechanical Engineering, King Mongkut's University of Technology Thonburi, Bangmod, Bangkok 10140, Thailand

ARTICLE INFO

Article history:
Received 11 November 2009
Accepted 9 April 2010
Available online 17 June 2010

Keywords:
Capillary tube
Adiabatic
Coiled tube
Friction factor
Homogeneous flow model

ABSTRACT

This paper presents a numerical study of the flow characteristics of refrigerants flowing through adiabatic helically coiled capillary tubes. The theoretical model is based on conservation of mass, energy and momentum of the fluids in the capillary tube. The two-phase flow model developed was based on the homogeneous flow assumption. The viscosity model was also based on recommendations from the literature. The developed model can be considered as an effective tool for designing and optimizing capillary tubes working with newer alternative refrigerants. The model is validated by comparison with the experimental data of Kim et al. (2002) for R-22, R-407C and R-410A, and Zhou and Zhang (2006) for R-22. The results obtained from the present model show reasonable agreement with the experimental data. The proposed model can be used to design helical capillary tubes working with various refrigerants.

1. Introduction

In many small refrigeration systems, a capillary tube is used as the expansion device due to its low cost, low starting torque and low maintenance. Normally, it is used in refrigeration systems with cooling capacities less than 10 kW such as household refrigerators and air conditioners. The nominal size of the capillary tube typically ranges between 0.5 and 2.0 mm in diameter and 2–5 m in length.

Several decades ago, the flow characteristics of various refrigerants flowing through capillary tubes were studied both experimentally and theoretically. The most recent articles describing investigations of capillary tubes are summarized as follows:

Wong and Ooi [1] presented comparisons between the predicted results from homogeneous and separated flow models and experimental results from a number of researchers. The separated flow model which uses Miropolskiy's slip ratio combined with Lin's equation for frictional pressure gradient gave better predictions compared to the homogeneous flow model.

Bansal and Rupasinghe [2] investigated a homogeneous two-phase flow model which is called the "CAPIL model" to study the performance of adiabatic capillary tubes using R-134a as working fluid. The REFPROP program was used to calculate the refrigerant properties.

Sami and Tribes [3] reported a numerical model for predicting capillary tube performance for some azeotropic and zeotropic binary mixtures as well as pure HFC refrigerants.

In 1999, Melo et al. [4] studied experimentally the effect of capillary length, diameter, refrigerant subcooling, condensing pressure and type of refrigerant (CFC-12, HFC-134a and HC-600a) on the mass flow rates through capillary tubes. In addition, they proposed correlations to predict the mass flow rate of various refrigerants. The proposed correlations were found to be in good agreement with those obtained from the measured data and other studies in the open literature.

Wongwises et al. [5] developed a two-phase flow model based on homogeneous flow to study the flow characteristics of many pairs of refrigerants flowing through adiabatic capillary tubes. The Colebrook equation was used to determine the two-phase friction factor. It was found that the traditional refrigerants consistently gave lower pressure drops for both single-phase and two-phase regions which resulted from longer capillary tube lengths.

Wongwises et al. [6] presented a two-phase separated flow model to describe the refrigerant flow characteristics in the capillary tubes of refrigeration systems. The agreement between experimental data and simulation results obtained for flows of R-12, R-22 and R-134a through capillary tubes indicated that the separated flow model with appropriate correlations of the frictional pressure gradient and slip ratio can be used to predict the two-phase flow behaviour of refrigerant flowing through capillary tubes.

* Corresponding author. Tel.: +66 2 470 9115; fax: +66 2 470 9111.
E-mail address: somchai.won@kmutt.ac.th (S. Wongwises).

1359-4311/$ – see front matter © 2010 Elsevier Ltd. All rights reserved.
doi:10.1016/j.applthermaleng.2010.04.026

Nomenclature

A	cross sectional area of capillary tube (m^2)
d_i	capillary tube internal diameter (m)
D_C	coil diameter (m)
De	Dean Number, $De = \mathrm{Re}\sqrt{(d_i/D_C)}$
e/d_i	relative roughness
$\triangle T_{sub}$	degree of subcooling (°C)
f	friction factor
g	gravitational acceleration (m/s^2)
G	mass flow rate per unit area ($kg/s\text{-}m^2$)
h	specific enthalpy (J/kg)
H_{loss}	head loss (m)
He	Helical number, $He = \mathrm{Re}[(d_i/D_C)/\{1+(p/\pi D_C)^2\}]^{1/2}$
k	entrance loss coefficient
L	length (m)
m	mass flow rate (kg/s)
P	pressure (Pa)
Re	Reynolds number
s	specific entropy (J/kg-K)
T	temperature (°C)
V	velocity (m/s)
x	quality

Greek letters

τ_w	shear stress at wall (N/m^2)
v	specific volume (m^3/kg)
μ	dynamic viscosity (kg/m-s)
ρ	density (kg/m^3)

Subscripts

cond, evap	condenser and evaporator, respectively
f, g	liquid phase and gas phase, respectively
h	homogeneous flow
i	capillary inlet condition
sp, tp	single-phase and two-phase, respective

Wongwises and Pirompak [7] studied the flow characteristics of alternative refrigerants in adiabatic capillary tubes by using an adiabatic capillary tube model. Moreover, they also proposed selection charts for selecting the size of capillary tube based on the flow rate and flow condition. In addition to tube size, the charts are very useful for determining the mass flow rate directly.

In 2001, Liang and Wong [8] introduced the homogeneous flow model based on a drift flux model to predict the flow characteristics of R-134a flowing through an adiabatic capillary tube. This model was validated by comparisons between numerical and experimental results by Li et al. [9] and Mikol et al. [10] using R-12 as working fluid.

Jung et al. [11] proposed a model to calculate the size of capillary tubes for various refrigerants of R-22, R-134a, R-407C and R-410A. In their model, the Stocker model was modified and took several factors into account such as area contraction, different equations for viscosity and friction factors, and mixing effects. Numerical results indicated that using the McAdam model for the viscosity equation gave a better calculation than the Dukler model. Finally, semi-empirical correlations for predicting mass flow rate, condensing temperature and subcooling of refrigerant were proposed.

Sinpiboon and Wongwises [12] presented a model to study the flow characteristics in non-adiabatic capillary tubes. In this study, the mathematical model was categorized into three different cases, depending on the position of the heat exchange process. The first case is used when the heat exchange process starts in the single-phase flow region. The second case is determined when the heat exchange process starts at the end of the single-phase flow region. Finally, the last case is considered when the heat exchange process takes place in the two-phase flow region. A set of differential equations were solved by an explicit method in a finite-difference scheme.

Fiorelli et al. [13] performed an experimental study to evaluate the performance of R-22 and its alternatives, such as R-407C and R-410A flowing through adiabatic capillary tubes. The results showed that the performance of capillary tubes for R-410A and R-407C were similar under given conditions. Moreover, they also determined the effect of geometry on the behaviour of capillary tubes. Finally, differences in the flow behaviour of R-410A and R-407C were evaluated.

Bansal and Wang [14] presented a homogeneous and metastable simulation model. The first law of thermodynamics, some fluid mechanics and empirical relations were incorporated into this model. Compared with published experimental data, this model shows good agreement within ±7% for R-22, R-134a and R-600. Moreover, a new numerical analysis for simulating the choked flow of refrigerant under adiabatic conditions was proposed.

Choi et al. [15] presented a generalized mass flow rate correlation based on their experimental data for R-22, R-290 and R-407C. Dimensionless parameters were derived from the Buckingham π theorem by considering the effect of refrigerant properties, capillary tube geometry and inlet conditions.

Similarly, Yang and Wang [16] proposed a generalized mass flow rate correlation based on extensive data for R-12, R-22, R-134a, R-290, R-600a, R-410A, R-407C, and R-404A. The simulation conditions used in their study are as follows: 1) the inner diameter ranges between 0.5 and 2 mm, 2) the tube length ranges between 0.5 and 5 m, 3) the condensing temperature ranges between 20 °C and 60 °C, 4) the subcooling temperature is between 0 °C and 20 °C and 5) Inlet quality varies approximately in the range from 0 to 0.3. Their results showed that the predicted values agree well with the experimental data in the open literature for R-12, R-22, R-134a, R-290, R-407C, R-410A and R-404A refrigerants. Moreover, the model presented gave average and standard deviations of 0.83% and 9.02% compared with the ASHRAE [17] and Choi et al. [15] equations, respectively.

Seixlack and Barbazelli [18] presented a numerical model to predict refrigerant flow along non-adiabatic capillary tubes using a two-fluid model. The flow along the straight and horizontal capillary tube is divided into two regions: single-phase and two-phase flow regions. In comparisons between numerical results and experimental data, the results gave good predictions of the refrigerant mass flow rate. In addition, comparisons with a homogeneous model were also made.

It can be noted that the theoretical and experimental investigations found in the literature and described above have focused on the study of the flow characteristics in horizontal straight capillary tubes; the flow characteristics in coiled capillary tubes has received comparatively little attention in the literature. The most productive studies of coiled capillary tubes have been continuously carried out by the following researchers.

Ali [19] proposed pressure drop correlations which were developed in terms of fluid properties (ρ and μ), flow rate (V) and tube geometry (d_i, D_C, p and L). It should be noted that in most of the

previous works, the relevant correlations were developed in terms of Dean number (*De*), Helical number (*He*), curvature ratio (D_C/d_i), Euler number (*Eu*), Reynolds number, *Re*, and the obtained geometrical group.

Kim et al. [20] presented a mass flow rate correlation based on the Buckingham π theorem for R-22 and its alternatives, R-407C and R-410A. Their results indicated that the mass flow rates of R-407C and R-410A were higher than those of R-22 by about 4.0% and 23%, respectively. In addition, the mass flow rates in straight capillary tubes are quite a lot higher than those in coiled capillary tubes, especially at smaller coil diameters. For instance, mass flow rates through a 40 mm coil diameter are smaller than through straight capillary tubes by approximately 9.0%.

Zhou and Zhang [21,22] studied the performance of coiled adiabatic capillary tubes both theoretically and experimentally. The results were compared with the straight capillary data. The results showed that the refrigerant mass flow rate substantially increases with increasing coil diameter. However, little change was observed for coil diameters larger than 300 mm.

Park et al. [23] studied the flow characteristics of coiled capillary tubes for R-22 and developed a mass flow rate correlation for coiled capillary tubes. Under the same operating conditions, they found that the mass flow rates of coiled capillary tubes decreased by 5–16% more than those of straight capillary tubes. The Buckingham π theorem was used to form a generalized correlation to calculate the refrigerant mass flow rate for both straight and coiled capillary tubes. The effects of inlet condition, refrigerant property, and coiled tube geometry were considered. For both straight and coiled capillary tubes, the results showed that the proposed correlation gave satisfactory agreement with the experimental data for R-22, R-407C and R-410A. The average and standard deviations were around 0.24% and 4.4%, respectively.

García-Valladares [24] presented numerical simulations based on a finite volume formulation for describing the flow characteristics of coiled adiabatic capillary tubes. The numerical model considered various aspects such as geometry, type of fluid (pure substances and mixtures), critical or non-critical flow conditions, metastable region, and transient behaviour.

Although some information is currently available on the flow characteristics of refrigerants in coiled capillary tubes, there still remains room for further research, especially in discussing which friction factor used in the calculation will give reliable predictions of flow characteristics. The purpose of this work is to develop a mathematical model to describe the flow characteristics of a refrigerant flowing through an adiabatic helically coiled capillary tube. A number of relevant friction factors, which have never been seen before, are collected together and used in the mathematical model. The simulation results are verified against the limited data available in the literature.

2. Mathematical modelling

As shown in Fig. 1, the flow of refrigerant through a capillary tube can be divided into two distinct regions; single-phase subcooled liquid and two-phase flow. In the model, the physical method used to describe the flow characteristics is developed from the conservation of mass, energy and momentum. Moreover, the model includes the effects of the condenser and evaporator temperatures, inner diameter, degree of subcooling and mass flow rate of refrigerant.

As shown in Fig. 1, the portion between points 1 and 2 is the capillary tube inlet where there is a pressure drop due to the sudden contraction. Similarly, the portion between points 2 and 3 is the single-phase subcooled liquid region and the portion between points 3 and 4 is the two-phase region where liquid and vapour coexist. The developed model is based on the following assumptions:

- the horizontal helical coiled tube has constant diameter
- the inner diameter and surface roughness of the capillary tube are constant
- adiabatic and homogeneous two-phase flow
- non-metastable liquid region
- one-dimensional steady flow
- thermodynamic equilibrium through the capillary tube

The governing equations used in describing the flow characteristics in the single-phase and two-phase flow regions are presented next.

2.1. Single-phase flow region

The pressure loss due to the sudden contraction at the inlet between points 1 and 2 is determined from:

$$P_1 - P_2 = k\frac{\rho V^2}{2g}, \tag{1}$$

where k is the entrance loss coefficient (for square edge, $k = 0.5$).

The steady flow energy equation between points 2 and 3 can be expressed as.

$$\frac{P_2}{\rho_2 g} + \frac{V_2^2}{2g} + z_2 = \frac{P_3}{\rho_3 g} + \frac{V_3^2}{2g} + z_3 + H_{loss}, \tag{2}$$

The head loss can be determined from:

$$H_{loss} = f_{sp}\frac{L_{sp}}{d_i}\frac{V^2}{2g}. \tag{3}$$

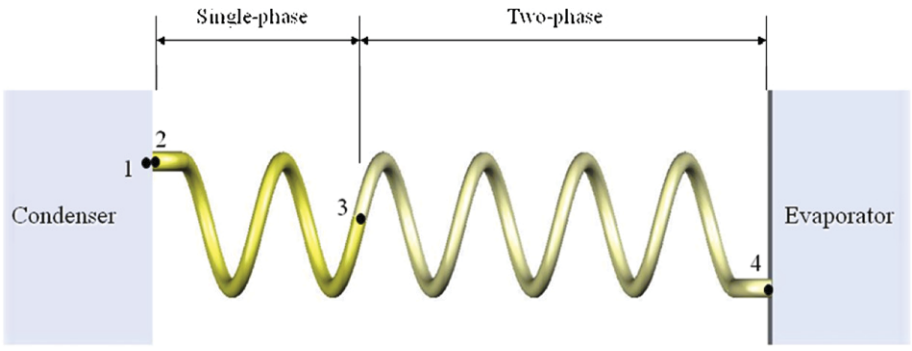

Fig. 1. Schematic diagram of an adiabatic helical capillary tube.

where H_{loss} is the head loss due to friction along the capillary tube and f_{sp} is the single-phase friction factor.

For an incompressible fluid, $\rho_2 \cong \rho_3 = \rho$ the continuity equation is presented in the following equation:

$$m = \rho_2 V_2 A = \rho_3 V_3 A = \rho V A. \tag{4}$$

Re-arranging Eqs. (2)–(4) yields:

$$P_2 = P_3 + \rho g(z_3 - z_2) + \left(\frac{f_{sp}L}{d_i}\right)\left(\frac{\rho V^2}{2}\right), \tag{5}$$

For $z_2 = z_3$ (horizontal tube), substituting Eq. (5) into Eq. (1), gives:

$$L_{sp} = \frac{d_i}{f_{sp}}\left[\frac{2}{\rho V^2}(P_1 - P_3) - (k+1)\right]. \tag{6}$$

The important parameter is the single-phase friction factor (f_{sp}), which can be calculated from twenty six different friction factor models. These equations are expressed as follows (where f_c is the friction factor for a coiled capillary tube and f_s is the friction factor for a straight capillary tube):

1. Dean [25]

$$f_c/f_s = 1.03058\left(De^2/288\right)^2 + 0.01195\left(De^2/288\right)^4, \tag{7}$$

where $De = \mathrm{Re}\sqrt{(d_i/D_C)}$

2. White [26]

$$f_s/f_c = 1 - \left[1 - (11.6/De)^{0.45}\right]^{1/0.45}, \tag{8}$$

3. White [27]

$$f_c = 0.08\mathrm{Re}^{-1/4} + 0.012\sqrt{(d_i/D_C)}, \tag{9}$$

4. Adler [28]

$$f_c/f_s = 0.1064\sqrt{De}, \tag{10}$$

5. Prandtl [29]

$$f_c/f_s = 0.37(0.5De)^{0.36}, \tag{11}$$

6. Hasson [30]

$$f_c/f_s = 0.556 + 0.0969\sqrt{De}, \tag{12}$$

7. Ito [31]

$$f_c/f_s = 21.5De/[1.56 + \log_{10}De]^{5.73}, \tag{13}$$

$$f_c\sqrt{(D_C/d_i)} = 0.0791\left[\mathrm{Re}(d_i/D_C)^2\right]^{-0.2}, \tag{14}$$

$$4f_c\sqrt{(D_C/d_i)} = 0.029 + 0.304 \times \left\{\mathrm{Re}(d_i/D_C)^2\right\}^{-1/4}, \tag{15}$$

8. Kubair and Varrier [32]

$$f_c = 0.7716\exp(3.553d_i/D_C)\mathrm{Re}^{-0.5}, \tag{16}$$

$$f_c = 0.003538\mathrm{Re}^{0.09}\exp(1.887d_i/D_C), \tag{17}$$

9. Barua [33]

$$f_c/f_s = 0.509 + 0.0918\sqrt{De}, \tag{18}$$

10. Mori and Nakayama [34]

$$f_c/f_s = 0.1080\sqrt{De}/\left[1 - 3.253/\sqrt{De}\right], \tag{19}$$

11. Mori and Nakayama [35]

$$f_c\sqrt{(D_C/d_i)} = 0.075\left[\mathrm{Re}(d_i/D_C)^2\right] - 0.2\left\{1 + 0.112 \times \left[\mathrm{Re}(d_i/D_C)^2\right]\right\}^{-0.2}, \tag{20}$$

$$f_c = \frac{0.192(d_i/D_C)^{0.5}}{\left[\mathrm{Re}(d_i/D_C)^{2.5}\right]^{1/6}}\left\{1 + \frac{0.068}{\left[\mathrm{Re}(d_i/D_C)^{2.5}\right]^{1/6}}\right\}, \tag{21}$$

$$f_c = \frac{C_1(d_i/D_C)^{0.5}}{\left[\mathrm{Re}(d_i/D_C)^{2.5}\right]^{1/6}}\left\{1 + \frac{C_2}{\left[\mathrm{Re}(d_i/D_C)^{2.5}\right]^{1/6}}\right\}, \tag{22}$$

$$C_1 = 1.88411177 \times 10^{-1} + 85.2472168(\varepsilon/d_i) - 4.63030629 \times 10^4(\varepsilon/d_i)^2 + 1.31570014 \times 10^7(\varepsilon/d_i)^3,$$

$$C_2 = 6.79778633 \times 10^{-2} + 25.3880380(\varepsilon/d_i) - 1.06133140 \times 10^4(\varepsilon/d_i)^2 + 2.54555343 \times 10^6(\varepsilon/d_i)^3,$$

12. Schmidt [36]

$$f_c/f_s = 1 + 0.14\mathrm{Re}^x, \tag{23}$$

where $x = [1 - 0.0644/(D_C/d_i)^{0.312}]/(D_C/d_i)^{0.97}$,

13. Srinivasan et al. [37]

(a) $$f_c = 5.22\left(\mathrm{Re}\sqrt{(D_C/d_i)}\right)^{-0.6}, \tag{24}$$

(b) $$f_c = 1.8\left(\mathrm{Re}\sqrt{(D_C/d_i)}\right)^{-0.5}, \tag{25}$$

(c) $$f_c = 1.084\left(\mathrm{Re}\sqrt{(D_C/d_i)}\right)^{-0.2}, \tag{26}$$

14. Ito [38]

$$f_c/f_s = 0.1033\sqrt{De}\left[(1 + 1.729/De)^{0.5} - (1.729/De)^{0.5}\right]^{-3}, \tag{27}$$

15. Collins and Dennis [39]

$$f_c/f_s = 0.38 + 0.1028\sqrt{De}, \tag{28}$$

16. Van Dyke [40]

$$f_c/f_s = 0.47136De^{1/4}, \tag{29}$$

17. Mishra and Gupta [41]

$$f_c/f_s = 1 + 0.033[\log_{10}He]^4, \tag{30}$$

$$f_c = 0.0791\mathrm{Re}^{-1/4} + 0.0075\sqrt{(d_i/D_C)}, \tag{31}$$

where $He = \mathrm{Re}[(d_i/D_C)/\{1 + (p/\pi D_C)^2\}]^{1/2}$,

18. Dennis [42]

$$f_c/f_s = 0.388 + 0.1015\sqrt{De}, \tag{32}$$

19. Manlapaz and Churchill [43]

$$f_c/f_s = \left[\left(1 - 0.18/\left\{1 + (35/He)^2\right\}^{0.5}\right)^m + (1 + d_i/\{3D_C\})^2(He/88.33)\right]^{0.5}, \tag{33}$$

where $m = 2$ for $De < 20$, $m = 1$ for $20 < De < 40$, $m = 0$ for $De > 40$,

20. Yanase et al. [44]

$$f_c/f_s = 0.557 + 0.0938\sqrt{De}, \tag{34}$$

21. Giri [45]

$$f_c = 1.1258/\left[\mathrm{Re}^{0.1938}(D_C/d_i)^{0.5391}\right], \tag{35}$$

22. Liu and Masliyah [46]

$$f_c\mathrm{Re} = \left[16 + \left(0.378\mathrm{De}\lambda^{1/4} + 12.1\right)\mathrm{De}^{1/2}\lambda^{1/2}\gamma^2\right] \times \left[1 + \left\{\left(0.0908 + 0.0233\lambda^{1/2}\right)\mathrm{De}^{1/2} - 0.132\lambda^{1/2} + 0.37\lambda - 0.2\right\}/(1 + 49/\mathrm{De})\right], \tag{36}$$

where $\lambda = (D_C/2)/[(D_C/2)^2 + (p/2\pi)^2]$,

$\gamma = \eta/(\lambda De)^{1/2}$,

$\eta = (p/2\pi)/\left[(D_C/2)^2 + (p/2\pi)^2\right]$.

2.2. Two-phase flow region

In this region, the capillary tube is divided into a number of elements as shown in Fig. 2. The following equations are based on control volume considerations in the two-phase region.

The conservation of mass can be calculated using the following equation:

$$m = \frac{AV_i}{v_i} = \frac{AV_{i+1}}{v_{i+1}}. \tag{37}$$

By neglecting the difference in elevation, the conservation of energy for steady-state adiabatic conditions without external work can be expressed as follows:

$$\left(\frac{P_3}{\rho_3 g} + z_3 + \frac{V_3^2}{2g} + u_3\right) = \left(\frac{P_i}{\rho_i g} + z_i + \frac{V_i^2}{2g} + u_i\right). \tag{38}$$

where u is internal energy. Re-arranging Eq. (38) and using the relation $h = Pv + u$,

$$\left(h_3 + gz_3 + \frac{V_3^2}{2}\right) = \left(h_i + gz_i + \frac{V_i^2}{2}\right) = \text{constant},$$

$$h + \frac{V^2}{2} = \text{constant} \tag{39}$$

where h and V are the enthalpy and fluid velocity at any point, respectively.

Due to the fact that the refrigerant flows along the capillary tube, the pressure gradually drops and the liquid flashes into vapour arising purely from the reduced pressure, at any point. Hence,

$$h_i = h_{fi}(1 - x_i) + h_{gi}x_i, \quad v_i = v_{fi}(1 - x_i) + v_{gi}x_i. \tag{40}$$

also, $m = \rho VA = \text{constant}$

$$V = \frac{m}{\rho A} = \frac{G}{\rho} = Gv. \tag{41}$$

The energy balance between point 3 and at any point along the capillary tube in the two-phase flow region can be calculated by substituting Eqs. (40) and (41) into Eq. (39) to give:

$$h_3 + \frac{V_3^2}{2} = h_f + x\left(h_g - h_f\right) + \frac{G^2}{2}\left(v_f(1 - x) + v_g x\right)^2. \tag{42}$$

Expanding the right-hand side of Eq. (42) and rearranging, yields:

$$\left[\left(v_g - v_f\right)^2\frac{G^2}{2}\right]x^2 + \left[G^2 v_f\left(v_g - v_f\right) + \left(h_g - h_f\right)\right]x + \left[\frac{G^2 v_f^2}{2} - h_3 - \frac{V_3^2}{2} + h_f\right] = 0. \tag{43}$$

The quality (x) can be expressed in the form of a quadratic equation as shown in Eq. (44).

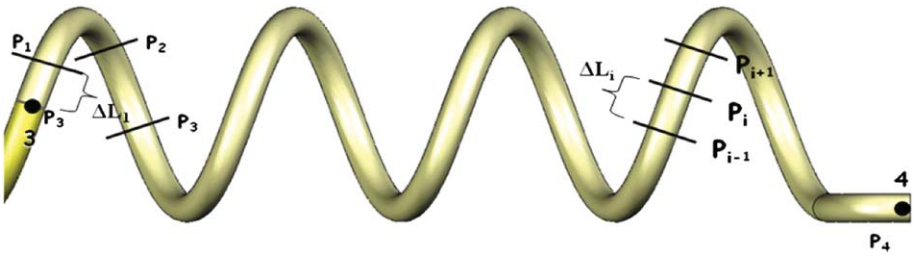

Fig. 2. Schematic diagram of simulation approach for an adiabatic two-phase flow region.

$$x = \frac{-h_{fg} - G^2 v_f v_{fg} + \sqrt{\left(G^2 v_f v_{fg} + h_{fg}\right)^2 - \left(2G^2 v_{fg}^2\right)\left[\frac{G^2 v_f^2}{2} - h_3 - \frac{V_3^2}{2} + h_f\right]}}{G^2 v_{fg}^2}, \quad (44)$$

where $h_{fg} = h_g - h_f$ and $v_{fg} = v_g - v_f$.

Again, the conservation of momentum can be expressed by reconsidering the element of fluid as shown in Fig. 2.

$$\left(P\frac{\pi d_i^2}{4}\right) - (P + dP)\frac{\pi d_i^2}{4} - \tau_w d_i \pi dL = mdV, \quad (45)$$

where τ_w is the wall shear stress which is defined as follows:

$$\tau_w = \frac{f_{tp}\rho V^2}{8}. \quad (46)$$

Substituting Eq. (46) into Eq. (45), we get.

$$-\frac{\pi d_i^2}{4}dP - \frac{f_{tp}}{8}\rho V^2 d_i \pi dL = mdV \quad (47)$$

or:

$$dL = \frac{d_i}{f_{tp}}\left[\frac{2dP}{\rho V^2} + \frac{2mdV}{\rho A V^2}\right]. \quad (48)$$

where f_{tp} is the two-phase friction factor

For constant mass flow rate, $dm = 0$, Eq. (49) is obtained.

$$\frac{-dV}{V} = \frac{d\rho}{\rho}. \quad (49)$$

Substituting Eq. (49) into Eq. (48) gives.

$$dL = \frac{2d_i}{f_{tp}}\left[\frac{-\rho dP}{\rho V^2} + \frac{d\rho}{\rho}\right]. \quad (50)$$

3. Solution method

As shown in Fig. 2, the capillary tube between points 3 and 4 can be divided into numerous sections. Since P_3 is known (saturated liquid), the pressure at any section 'i' can be calculated from the following equation:

$$P_i = P_3 - i\triangle P. \quad (51)$$

With the pressure (P_i) and the quality (x_i) calculated from Eq. (44), the entropy of each section can be calculated from:

$$s_i = s_{if}(1 - x) + s_{ig}x. \quad (52)$$

The Reynolds number in the two-phase region is determined by:

$$\mathrm{Re}_{tp} = \frac{Vd_i}{\mu_{tp} v_{tp}}, \quad (53)$$

where

$$V = Gv_{tp} = G(xv_g) + (1 - x)v_f. \quad (54)$$

The two-phase dynamic viscosity correlation proposed by McAdams [47] is presented as follows:

$$\frac{1}{\mu_{tp}} = \frac{x}{\mu_g} + \frac{1 - x}{\mu_f}. \quad (55)$$

A gradual increase of entropy is obtained along the capillary tube. When the entropy reaches the maximum value, the fluid velocity is equal to the local speed of sound and the flow is choked. As a consequence, the calculation is ended at this point.

The pressure of the element where the entropy has a maximum value $(P_i)_{s\ max}$, is then compared to the evaporator pressure (P_{evap}) given by.

if $P_{i,smax} = P_{evap}$ then $P_4 = P_{evap}$,
if $P_{i,smax} \neq P_{evap}$ then $P_4 = P_{i,smax}$

Thus, from Eq. (50), the two-phase length can be expressed as follows:

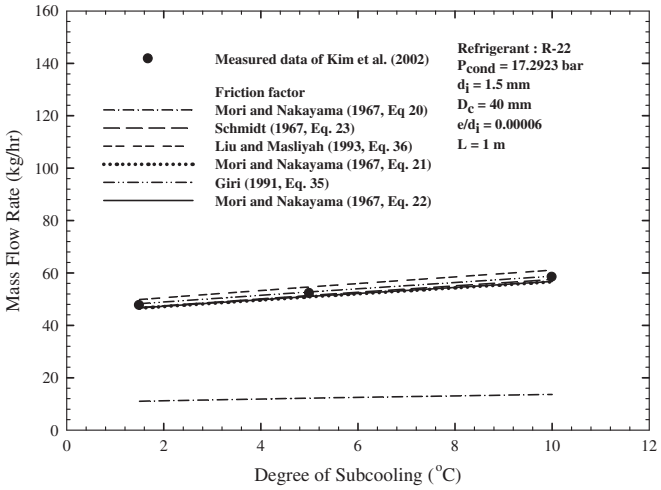

Fig. 3. Comparison of the present numerical results with the measured mass flow rates.

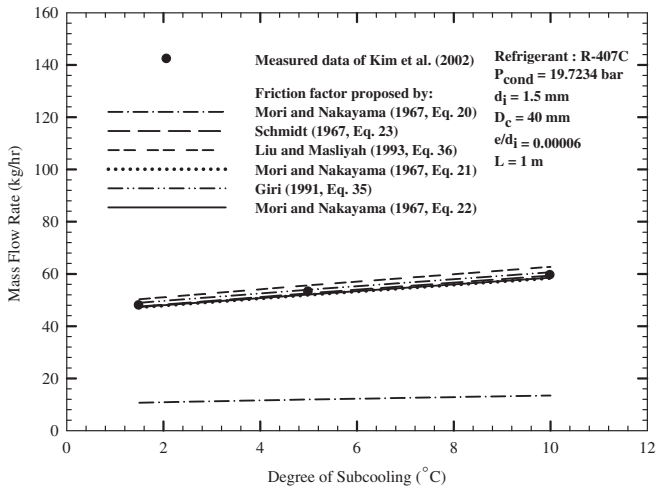

Fig. 4. Comparison of the present numerical results with the measured mass flow rates.

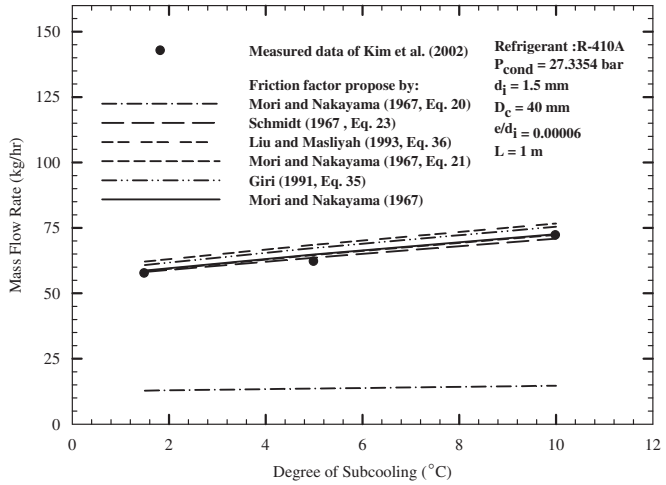

Fig. 5. Comparison of the present numerical results with the measured mass flow rates.

$$L_{tp} = d_i\left[\frac{-2}{G^2}\int_{P_3}^{P_{smax}}\frac{\rho}{f_{tp}}dp + 2\int_{P_3}^{P_{smax}}\frac{d\rho}{\rho f_{tp}}\right], \tag{56}$$

The capillary length of each section is calculated from:

$$\Delta L_i = \frac{2d_i}{f_{tp,i}}\left(\frac{-\rho_i \Delta P}{G^2} + \frac{\Delta \rho}{\rho_i}\right). \tag{57}$$

The total length of the two-phase region is determined from:

$$L_{tp} = \sum_{i=1}^{n} \Delta L_i, \tag{58}$$

Finally, the total length of capillary tube is the sum of the single-phase and two-phase lengths which are defined as follows:

$$L_{total} = L_{sp} + L_{tp}. \tag{59}$$

All refrigerant properties are taken from the REFPROP computer program [48] and are developed in the function of pressure.

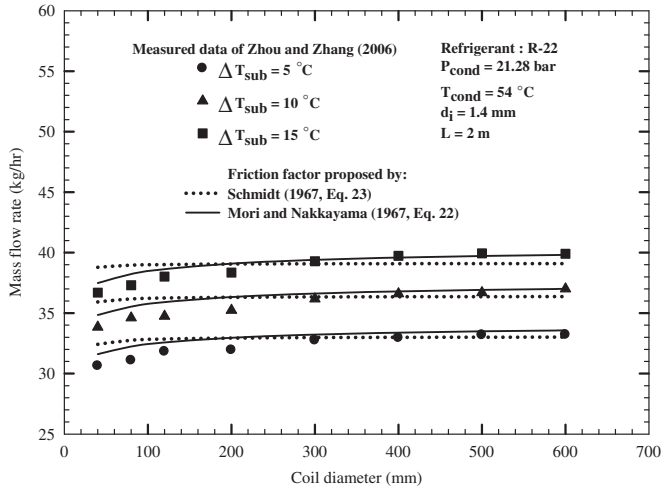

Fig. 6. Comparison of the present numerical results with the measured mass flow rate at different coil diameters and degrees of subcooling.

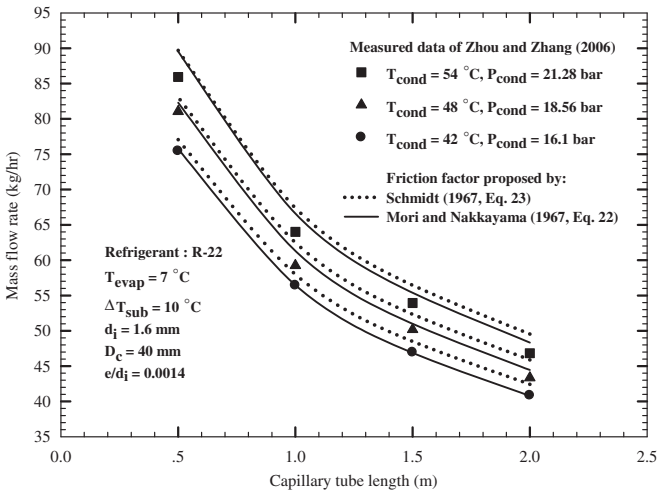

Fig. 7. Comparison of the present numerical results with the measured mass flow rates at different capillary tube lengths and condensing temperatures.

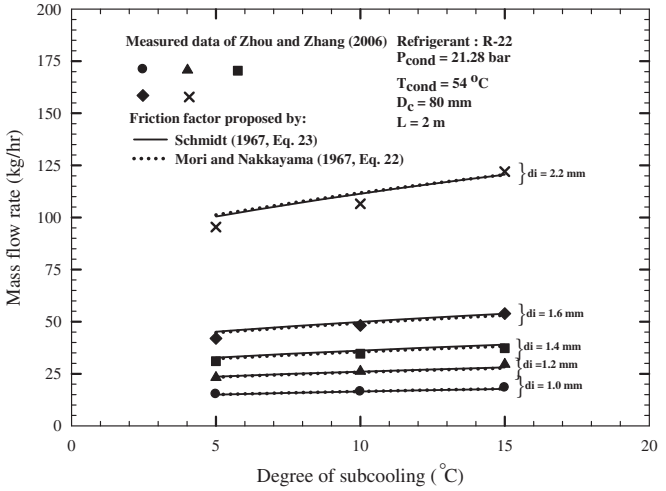

Fig. 8. Comparison of the present numerical results with the measured mass flow rates at different capillary tube diameters and degrees of subcooling.

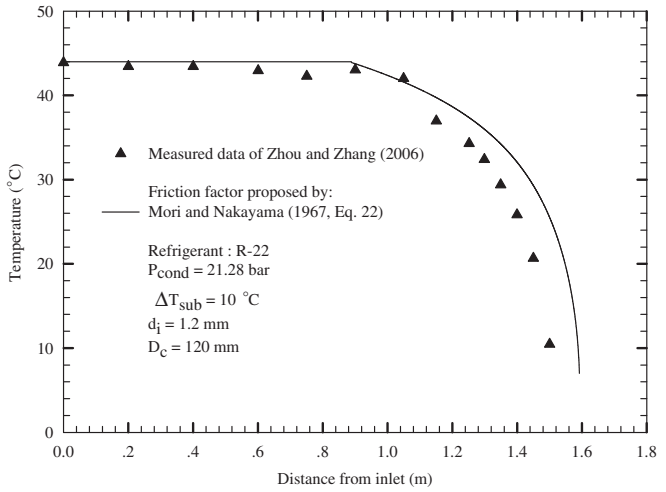

Fig. 9. Comparison of measured temperature distributions with present numerical results.

4. Results and discussion

In order to validate the present model, comparisons are made with the limited available experimental data of Kim et al. [15] for R-22, R-407C and R-410A and of Zhou and Zhang [21] for R-22.

Figs. 3–5 present the mass flow rate variation versus degree of subcooling by comparing the numerical results with the experimental data of Kim et al. [15] for R-22 ($D_c = 200, 120$ and 40 mm). In the present model, friction factors are calculated by the twenty six different models presented in Section 2.1. In this case, the mass flow rate is plotted with the degree of subcooling for fixed total lengths of the helical capillary tube. It is clearly seen that mass flow rate decreases with decreasing subcooling temperature. This is due to the friction loss in the capillary tube increases as the temperature increases which results in the decrease of the refrigerant mass flow rate entering the tube. The model is found to fit the data very well and, in particular, the friction factor models of Mori and Nakayama [35] (Eqs. (20–22)) and Schmidt [36] (Eq. (23)) agree well with the data of Kim et al. [15] for R-22.

Fig. 6 presents comparisons between the present results and the experimental data of Zhou and Zhang [21] for R-22 at different coil diameters and degrees of subcooling. The results show that the calculated mass flow rate of R-22 deviates from the experimental results. Moreover, the results also indicate that the mass flow rate obtained from the present model is fitted very well with the data and in particular, the friction factor of Mori and Nakayama [35] (Eq.

Table 1
Comparison of the present numerical results with the experimental data of Kim et al. [15] for R-22.

Conditions	L (m)	d_i (mm)	ε/d_i	P_{con} (bar)	T_{con} (°C)	ΔT_{sc} (°C)	D_c (mm)	$\dot{m}_{exp}$ (kg/h)
No.1	1.0	1.5	6×10^{-5}	17.2923	45	1.5	200	50.65
No.2						5.0	200	55.04
No.3						10.0	200	61.85
No.4						1.5	120	49.10
No.5						5.0	120	53.68
No.6						10.0	120	60.26
No.7						1.5	40	47.56
No.8						5.0	40	52.20
No.9						10.0	40	58.36

Author	Error (%)									MAE
Conditions	No.1	No.2	No.3	No.4	No.5	No.6	No.7	No.8	No.9	
1. Dean [25] Eq. (7)	−99.10	−99.08	−99.10	−99.25	−99.25	−99.26	−99.53	−99.52	−99.53	99.3
2. White [26] Eq. (8)	−59.55	−59.18	−59.59	−60.40	−60.25	−60.61	−63.16	−63.18	−63.36	61.0
3. White [27] Eq. (9)	50.98	56.32	65.90	53.06	57.17	65.57	50.14	52.65	58.66	56.7
4. Adler [28] Eq. (10)	−60.30	−59.87	−60.23	−61.21	−61.03	−61.35	−64.37	−64.36	−64.52	61.9
5. Prandtl [29] Eq. (11)	−57.16	−56.78	−57.24	−57.58	−57.47	−57.89	−59.93	−59.99	−60.23	58.3
6. Hasson [30] Eq. (12)	−60.17	−59.77	−60.14	−60.95	−60.78	−61.12	−63.90	−63.91	−64.07	61.6
7. Ito [31] Eq. (13)	−61.17	−60.75	−61.09	−62.14	−61.95	−62.25	−65.45	−65.42	−65.55	62.9
8. Ito [31] Eq. (14)	56.94	63.51	77.76	59.51	64.79	77.43	59.45	63.23	73.41	66.2
9. Ito [31] Eq. (15)	56.81	63.33	77.60	59.86	65.21	78.19	59.28	63.07	73.09	66.3
10. Kubair and Varrier [32]										
(a) Eq. (16)	95.51	127.09	209.53	100.81	130.41	213.93	102.84	126.17	205.55	145.8
(b) Eq. (17)	20.87	23.16	24.16	24.29	25.89	26.98	26.36	27.36	28.84	25.3
11. Barua [33] Eq. (18)	−59.18	−58.77	−59.15	−59.98	−59.81	−60.16	−63.01	−63.02	−63.18	60.7
12. Mori and Nakayama [34] Eq. (19)	−61.43	−61.03	−61.39	−62.23	−62.07	−62.39	−65.18	−65.18	−65.33	62.9
13. Mori and Nakayama [35] Eq. (20)	−6.87	−4.76	−5.07	−40.99	−40.19	−40.39	−76.81	−76.64	−76.64	40.9
14. Mori and Nakayama [35] Eq. (21)	−4.33	−3.77	−4.58	−2.46	−2.48	−3.26	−2.10	−2.57	−3.03	**3.2**
15. Mori and Nakayama [35] Eq. (22)	−4.01	−3.43	−4.23	−2.14	−2.14	−2.91	−1.79	−2.25	−2.70	**2.8**
16. Schmidt [36] Eq. (23)	−5.73	−5.38	−6.41	−3.05	−3.17	−4.05	−1.59	−1.55	−1.51	**3.6**
17. Srinivasan et al. [37]										
(a) Eq. (24)	134.41	304.72	466.72	133.83	271.99	421.31	124.37	202.28	325.43	265.0
(b) Eq. (25)	114.62	196.93	304.88	115.14	179.65	281.61	108.26	139.52	228.15	185.4
(c) Eq. (26)	−44.22	−44.13	−45.04	−43.92	−44.16	−45.04	−45.22	−45.69	−46.33	44.86
18. Ito [38] Eq. (27)	−60.84	−60.44	−60.81	−61.64	−61.47	−61.81	−64.61	−64.61	−64.77	62.3
19. Collins and Dennis [39] Eq. (28)	−60.67	−60.12	−60.51	−61.32	−61.18	−61.52	−64.33	−64.34	−64.51	62.1
20. Van Dyke [40] Eq. (29)	−47.40	−47.05	−47.68	−47.29	−47.25	−47.85	−48.89	−49.08	−49.45	48.0
21. Mishra and Gupta [41]										
(a) Eq. (30)	−41.45	−40.86	−41.39	−36.94	−36.68	−37.18	−28.68	−28.66	−28.89	35.6
(b) Eq. (31)	55.04	61.17	73.81	58.05	63.04	74.59	57.46	60.95	70.01	63.8
22. Dennis [42] Eq. (32)	−60.33	−59.94	−60.32	−61.14	−60.99	−61.34	−64.15	−64.17	−64.34	61.9
23. Manlapaz and Churchill [43]										
(a) m=2 Eq. (33)	−39.79	−39.13	−39.63	−34.96	−34.64	−35.11	−26.18	−26.11	−26.29	33.5
(b) m=1 Eq. (33)	−39.98	−39.34	−39.83	−35.21	−34.90	−35.37	−26.59	−26.53	−26.73	33.8
(c) m=0 Eq. (33)	−40.21	−39.58	−40.08	−35.51	−35.21	−35.69	−27.07	−27.03	−27.24	34.2
24. Yanase et al. [44] Eq. (34)	−59.49	−59.11	−59.50	−60.28	−60.13	−60.49	−63.27	−63.29	−63.47	61.0
25. Giri [45] Eq. (35)	31.12	33.71	36.15	23.07	23.99	24.77	1.48	1.03	0.65	19.6
26. Liu and Masliyah [46] Eq. (36)	41.08	44.97	49.93	31.25	32.95	34.88	4.82	4.68	4.61	27.7

$$\text{Error}(\%) = \left(\frac{M_{num} - M_{exp}}{M_{exp}}\right) \times 100$$

$$\text{MAE}(\%) = \frac{1}{N}\sum_{N}\frac{\|M_{num} - M_{exp}\|}{M_{exp}} \times 100$$

(22)) gives the best result which is in agreement with the results of Zhou and Zhang [21] for R-22. Moreover, the friction factor of Mori and Nakayama [35] (Eq. (22)) gives a mean absolute error of 1.58%. In case of a coil diameter less than 300 mm, the experimental data show that the mass flow rate of refrigerant decreases with decreasing coil diameter. Between the coil diameters of 40 and 300 mm, the change in the mass flow rate is about 6–7%.

On the other hand, the mass flow rate of refrigerants is increased by a minuscule amount around 1–2% for a coil diameter ranging between 300 and 600 mm.

Fig. 7 shows a comparison of mass flow rate between the present model and the experimental data of Zhou and Zhang [21] for R-22 flowing through a coiled capillary tube with different capillary tube lengths and condensing temperatures. Similar to the straight tube, the mass flow rate of the coiled capillary decreases rapidly as the tube length increases, but it increases with increasing condensing temperature. The figure also shows that the friction factor of Mori and Nakayama [35] (Eq. (22)) gives reasonable predictions compared with the experimental data.

Similarly, Fig. 8 shows a comparison of mass flow rate between the present model and the experimental data of Zhou and Zhang [21] for R-22 flowing through a coiled capillary tube with different capillary tube diameters and degrees of subcooling. Similarly, the mass flow rate of the coiled capillary tube increases rapidly as the capillary tube diameter increases. Moreover, the results show that the friction factor of Mori and Nakayama [35] (Eq. (22)) gives reasonable predictions compared with experimental data. The results from the present model using the friction factor of Mori and Nakayama [22] are compared with the measured data of Zhou and Zhang [21] as shown in Fig. 8. The results give the mean absolute error of 3%. While comparison between the measured data of Zhou and Zhang [21] and their simulation results give an average deviation of −4.53%. It is clear that the present model shows good prediction than the model of Zhou and Zhang [22].

Fig. 9 shows comparisons between the present model and the experimental data of Zhou and Zhang [21] to validate the temperature distribution along the capillary tube length. In the subcooled liquid region, the temperature remains nearly constant along the tube, while it decreases rapidly after the refrigerant flashes. The deviations between the simulated results with the measured values may be due to the fact that the model was developed based on many assumptions, for example, the metastable liquid region is neglected. This phenomena occurs when the pressure of the liquid approach to the saturation pressure, but the fluid is still in the liquid phase. It can be clearly seen from Fig. 9 that the metastable phenomena may occur. Moreover, the viscosities calculated from various models may cause the error, for example, the McAdam equation which was used to calculate the viscosity of the refrigerant was established under the different conditions compared with the Zhou and Zhang [21] experiment.

Table 1 gives comparisons between the present results and the experimental data of Kim et al. [15] for R-22 ($L = 1.0$ m, $d_i = 1.5$ mm, $\varepsilon/d_i = 6$ and $T_{cond} = 45$ °C) at various coil diameters and degrees of subcooling, using the twenty six friction factor equations. From this table, it is evident that the Mori and Nakayama and Schmidt equations give the smallest error values compared with the other equations.

It is clear that the Mori and Nakayama [35] and Schmidt [36] correlations fit the best to experimental data. This is due to the fact that the correlations were obtained from the measured data at the d_i/D_c ranging between 0.02 and 0.3 which correspond to the experimental conditions performed by Kim et al. [15] and Zhou and Zhang [21]. Other correlations presented in the manuscript were developed based on the curvature ratios which are different from the measured data.

5. Conclusion

In the present study, a model has been developed to determine the refrigerant flow characteristics in adiabatic helical capillary tubes. From the results, it is evident that the most suitable equations for calculating the friction factor are those due to Mori and Nakayama [35] (Eqs. (21,22)) and Schmidt [36] (Eq. (23)). These equations gave a deviation ranging between 1 and 4%. The present model was validated by comparing the results with the experimental data of Kim et al. [15] for R-22, R-407C and R-410A, and the data of Zhou and Zhang [21] for R-22, and was found to give an average discrepancy of around 4%.

Acknowledgement

The authors are indebted to King Mongkut's University of Technology Thonburi (KMUTT), the Thailand Research Fund (TRF) and the Office of the Higher Education Commission for supporting this study.

References

[1] T.N. Wong, K.T. Ooi, Adiabatic capillary tube expansion devices: a comparison of the homogeneous flow and the separated flow models. Applied Thermal Engineering 16 (7) (1996) 625–634.
[2] P.K. Bansal, A.S. Rupasinghe, A homogeneous model for adiabatic capillary tubes. Applied Thermal Engineering 18 (3–4) (1998) 207–219.
[3] S.M. Sami, C. Tribes, Numerical prediction of capillary tube behavior with pure and binary alternative refrigerants. Applied Thermal Engineering 18 (1998) 491–502.
[4] C. Melo, R.T.S. Ferreira, C. Boabaid Neto, J.M. Goncalves, M.M. Mezavi, An experimental analysis of adiabatic capillary tubes. Applied Thermal Engineering 19 (1999) 669–684.
[5] S. Wongwises, T. Songnetichaovalit, N. Lokathada, P. Kritsadathikarn, M. Suchatawat, W. Pirompak, A comparison of the flow characteristics of refrigerants flowing through adiabatic capillary tubes. International Communications in Heat and Mass Transfer 27 (2000) 611–621.
[6] S. Wongwises, P. Chan, N. Luesuwanatat, T. Purattanarak, Two-phase separated flow model of refrigerants flowing through capillary tubes. International Communications in Heat and Mass Transfer 27 (2000) 343–356.
[7] S. Wongwises, W. Pirompak, Flow characteristics of pure refrigerants and refrigerant mixtures in adiabatic capillary tubes. Applied Thermal Engineering 21 (8) (2001) 845–861.
[8] S.M. Liang, T.N. Wong, Numerical modeling of two-phase refrigerant flow through adiabatic capillary tubes. Applied Thermal Engineering 21 (2001) 1035–1048.
[9] R.Y. Li, S. Lin, Z.H. Chen, Numerical modeling of thermodynamic non-equilibrium flow of refrigerant through capillary tubes. ASHRAE Transaction 96 (1990) 542–549.
[10] E.P. Mikol, Adiabatic single and two-phase flow in small bore tubes. ASHRAE Journal 5 (1963) 75–86.
[11] D. Jung, C. Park, B. Park, Capillary tube selection for HCFC22 alternatives. International Journal of Refrigeration 22 (1999) 604–614.
[12] J. Sinpiboon, S. Wongwises, Numerical investigation of refrigerant flow through non-adiabatic capillary tubes. Applied Thermal Engineering 22 (2002) 2015–2032.
[13] F.A.S. Fiorelli, A.A.S. Huerta, O.M. Silvares, Experimental analysis of refrigerant mixtures flow through adiabatic capillary tubes. Experimental Thermal and Fluid Science 26 (2002) 499–512.
[14] P.K. Bansal, G. Wang, Numerical analysis of choked refrigerant flow in adiabatic capillary tubes. Applied Thermal Engineering 24 (2004) 851–863.
[15] J. Choi, Y. Kim, J.T. Chung, An empirical correlation and rating charts for the performance of adiabatic capillary tubes with alternative refrigerants. Applied Thermal Engineering 24 (2004) 29–41.
[16] L. Yang, W. Wang, A generalized correlation for the characteristics of adiabatic capillary tubes. International Journal of Refrigeration 31 (2008) 197–203.
[17] ASHRAE Handbook – Refrigeration. American Society of Heating, Refrigerating and Air-Conditioning Engineer Inc, 2002, (Chapter 45).
[18] A.L. Seixlack, M.R. Barbazelli, Numerical analysis of refrigerant flow along non-adiabatic capillary tubes using a two-fluid model. Applied Thermal Engineering 29 (2009) 523–531.
[19] S. Ali, Pressure drop correlations for flow through regular helical coil tubes. Fluid Dynamics Research 28 (2001) 295–310.
[20] S.G. Kim, S.T. Ro, M.S. Kim, Experimental investigation of the performance of R-22, R-407C and R-410A in several capillary tubes for air-conditioners. International Journal of Refrigeration 25 (2002) 521–531.
[21] G. Zhou, Y. Zhang, Experimental investigation on hysteresis effect of refrigerant flowing through a coiled adiabatic capillary tube. Energy Conversion and Management 47 (2006) 3084–3093.

[22] G. Zhou, Y. Zhang, Numerical and experimental investigations on the performance of coiled adiabatic capillary tubes. Applied Thermal Engineering 26 (2006) 1106–1114.
[23] C. Park, S. Lee, H. Kang, Y. Kim, Experimentation and odelling of refrigerant flow through coiled capillary tubes. International Journal of Refrigeration 30 (2007) 1168–1175.
[24] G. Valladares, Numerical simulation and experimental validation of coiled adiabatic capillary tubes. Applied Thermal Engineering 27 (2007) 1062–1071.
[25] W.R. Dean, The streamline motion of fluid in a curved pipe. Philosophy Magazine 5 (1928) 673–695.
[26] C.M. White, Streamline flow through curved pipe. Proceedings of the Royal Society of London Series A 123 (1929) 645–663.
[27] C.M. White, Fluid Friction and Its Relation to Heat Transfer, vol. 10, Transactions of Institution of Chemical Engineering, London, 1932, pp. 66–86.
[28] M. Adler, Stromung in Gekrummten Rohren. ZAMM-Journal of Applied Mathematics and Mechanics 14 (1934) 257–275.
[29] L. Prandtl, Fuhrer Dmchdie Stromungslehre 1954, , In: Braunsschweigh; English Transl., Essentials of Fluid Dynamics, third ed., vol. 168, Blackie and Son, London, 1949, 159.
[30] D. Hasson, Streamline flow resistance in coils, Research Correspondence 1 S1 (1955).
[31] H. Ito, Friction factors for turbulent flow in curved pipes. ASME Journal of Basic Engineering 81 (1959) 123–134.
[32] V. Kubair, C.B.S. Varrier, Pressure drop for liquid flow in helical coils. Indian Institute of Chemical Engineer Journal, Transactions 14 (1961/1962) 93–97.
[33] S.N. Barua, On secondary flow in stationary curved pipes. The Quarterly Journal of Mechanics and Applied Mathematics 16 (1963) 61–77.
[34] Y. Mori, W. Nakayama, Study on forced convective heat transfer in curve pipes I. International Journal of Heat and Mass Transfer 8 (1965) 67–82.
[35] Y. Mori, W. Nakayama, Study on forced convective heat transfer in curve pipes II. International Journal of Heat and Mass Transfer 10 (1967) 37–59.
[36] E.F. Schmidt, Warmeubergang and Druckverlust in Rohrschlangen. The Chemical Engineering and Technology 13 (1967) 781–789.
[37] P.S. Srinivasan, S.S. Nandapurkar, F.A. Holland, Pressure drop and heat transfer in coils. The Chemical Engineering (London) 218 (1968) 113–119.
[38] H. Ito, Laminar flow in curved pipes. ZAMM Journal of Applied Mathematics and Mechanics 11 (1969) 653–663.
[39] W.M. Collins, S.C.R. Dennis, The steady motion of a viscous fluid in a curved tube. The Quarterly Journal of Mechanics and Applied Mathematics 28 (1975) 133–156.
[40] M. Van Dyke, Extended stokes-series laminar flow through a loosely coiled pipe. Journal of Fluid Mechanics 86 (1978) 129–145.
[41] P. Mishra, S.N. Gupta, Momentum transfer in curved pipes 1. Newtonian fluids; 2. Non-Newtonian fluids. Industrial and Engineering Chemistry Process Design and Development 18 (1979) 130–142.
[42] S.C.R. Dennis, Calculation of the steady flow through a curved tube using a new finite difference method. Journal of Fluid Mechanics 99 (1980) 449–467.
[43] R.L. Manlapaz, S.E.W. Churchill, Fully developed laminar flow in a helically coiled tube of finite pitch. Chemical Engineering Communications 7 (1980) 57–78.
[44] S. Yanase, N. Goto, K. Yamamoto, Dual solutions of the flow through a curved tube. Fluid Dynamics Research 5 (1989) 191–201.
[45] J.N. Gorasia, N. Dubey, K.K. Jain, Computer-aided design of capillaries of different configurations. ASHRAE Transactions(pt 1) (1991) 132–138.
[46] S. Liu, J.M. Masliyah, Axially invariant laminar flow in helical pipes with finite pitch. Journal of Fluid Mechanics 251 (1993) 315–353.
[47] W.H. McAdams, W.K. Wood, R.L. Bryan, Vaporization inside horizontal tubes. II, Benzence-oil mixture. Transaction ASME 64 (1942) 193.
[48] McLinden, M.O., Klein, S.A., Lemmon, E.W., 1998. REFPROP – thermodynamic and transport properties of refrigerants and refrigerant mixtures, NIST Standard Reference Database – version 6.01.

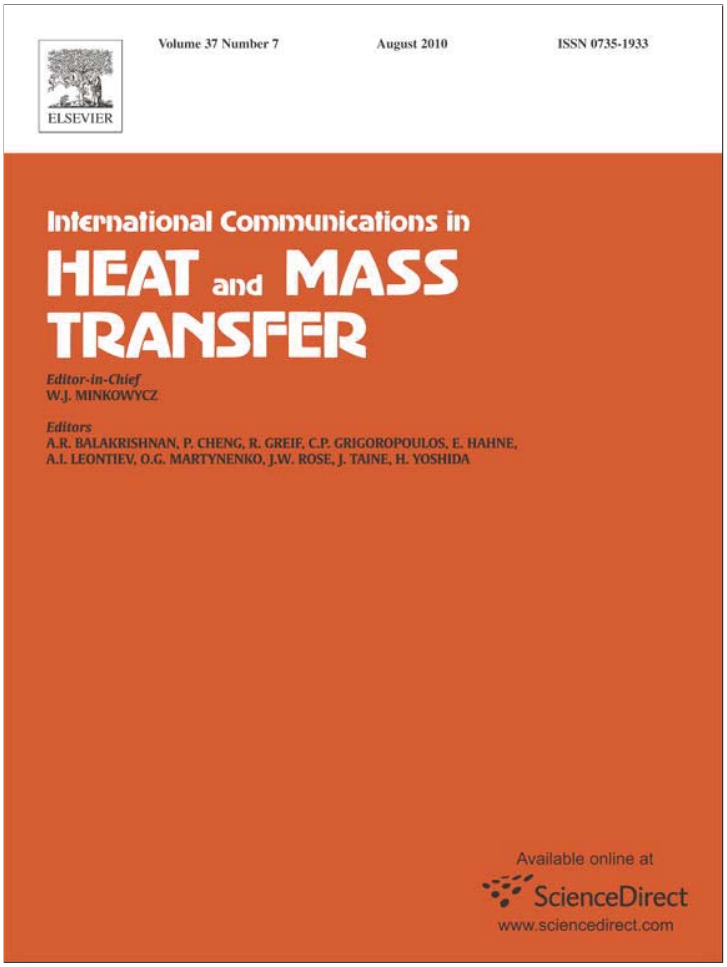

International Communications in Heat and Mass Transfer 37 (2010) 827–834

Contents lists available at ScienceDirect

International Communications in Heat and Mass Transfer

journal homepage: www.elsevier.com/locate/ichmt

Validation of void fraction models and correlations using a flow pattern transition mechanism model in relation to the identification of annular vertical downflow in-tube condensation of R134a ☆

A.S. Dalkilic [a,*], S. Wongwises [b,*]

[a] Heat and Thermodynamics Division, Department of Mechanical Engineering, Yildiz Technical University (YTU), Yildiz, Besiktas, Istanbul, 34349, Turkey
[b] Fluid Mechanics, Thermal Engineering and Multiphase Flow Research Laboratory (FUTURE), Department of Mechanical Engineering, King Mongkut's University of Technology Thonburi (KMUTT), Bangmod, Bangkok 10140, Thailand

ARTICLE INFO

Available online 7 July 2010

Keywords:
Condensation
Flow regime map
Vertical down flow
R134a
Phase change

ABSTRACT

This paper reports the experimental investigation of a model for predicting flow pattern transitions and for the validation of void fraction models and correlations proposed in the authors' previous publications and for the identification of flow regimes in data corresponding to annular flow downward condensation of R134a in a vertical smooth copper tube having an inner diameter of 8.1 mm and a length of 500 mm. R134a and water are used as working fluids on the tube side and annular side, respectively, of a double tube heat exchanger. Condensation experiments are done at mass fluxes of 260 and 515 kg m^{-2} s^{-1} in the high mass flux region of R134a. The condensing temperatures are between 40 and 50 °C; heat fluxes are between 10.16 and 66.61 kW m^{-2}. A mathematical model proposed by Soliman based on the models of Kosky and Lockhart–Martinelli is used to determine the condensation film thickness of R134a. Comparative void fraction values are determined indirectly using the measured data under laminar and turbulent flow conditions together with various void fraction models and correlations reported in the literature. There is good agreement between the void fraction results obtained from the theoretical model and those obtained from the void fraction models of Soliman, Chisholm and Armand, Turner and Wallis, Smith, Spedding and Spence previously proposed in the authors' publications and tested against their experimental database. Various well-known flow regime correlations from the literature are investigated to identify the flow regime occurring in the test tube, the correlations of Taitel and Dukler, Dobson, Akbar et al., Breber et al., Cavallini et al., and Sardesai et al. can provide accurate estimates of the annular flow conditions in spite of their different working conditions.

1. Introduction

Many industrial applications are concerned with heat exchange in two-phase flow occurring in condensers and evaporators. The correct calculation of heat transfer rates and pressure drops are necessary for the accurate design of compact heat exchangers. The pressure drop and heat transfer characteristics are strongly dependent on the two-phase flow patterns, their transitions and void fraction during condensation. Most of the analytical or empirical two-phase heat transfer correlations available in the literature are developed for a certain flow pattern. For this reason, the use of specific heat transfer correlations, developed for a certain flow pattern, under incompatible operating conditions can cause significant errors in magnitude and trend. Finally, flow pattern identification inside a condenser and determination of void fraction are important to investigate heat transfer characteristics under certain flow conditions. Although there are a large number of flow pattern identifications by means of maps or correlations and also void fraction studies of horizontal and upward flow, few researchers have examined them for downward flow using new generation refrigerants in small diameter tubes. The most widely recommended flow pattern maps for vertical tubes are those of Barnea et al. [1], Fair [2], Hewitt and Roberts [3], Chen et al. [4] and Zahao and Bi [5].

The orientation and interaction of the liquid and vapor phases inside the tubes are among the most significant characteristics of two-phase flow. These phenomena are related to flow regime and flow pattern. A specific kind of geometric distribution of the phases is called a flow pattern or flow regime. The interfacial area of the phases is affected by geometry, and thus mass, momentum, and energy exchange between phases have come to play important roles in design. Different flow patterns may occur depending on tube position, tube geometry, flow rates, superficial velocities and physical properties such as density, viscosity, and surface tension of the two phases.

☆ Communicated by W.J. Minkowycz.

* Corresponding authors.
E-mail addresses: dalkilic@yildiz.edu.tr (A.S. Dalkilic), somchai.won@kmutt.ac.th (S. Wongwises).

0735-1933/$ – see front matter © 2010 Published by Elsevier Ltd.
doi:10.1016/j.icheatmasstransfer.2010.02.010

Nomenclature

A	inside surface area, m^{-2}
c_p	specific heat, J kg^{-1} K^{-1}
d	internal tube diameter, m
F_r	Froude rate parameter
G	mass flux, kg m^{-2} s^{-1}
Ga	Galileo number
g	gravitational constant, m s^{-2}
h	heat transfer coefficient, W m^{-2} K^{-1}
i	enthalpy, J kg^{-1}
i_{fg}	latent heat of condensation, J kg^{-1}
K	coefficient in Smith correlation
L	length of test tube, m
m	mass flow rate, kg s^{-1}
r	internal tube radius, m
Re	Reynolds number
S	slip ratio
T	temperature, °C
Q	heat transfer rate, W
u	velocity, m s^{-1}
u^*	frictional velocity, m s^{-1}
x	mean vapor quality
X	Lockhart–Martinelli parameter
We	Weber number
ΔP	pressure drop, Pa
ΔT	vapor side temperature difference, $T_{sat} - T_{wi}$, °C

Greek symbols

σ	surface tension, N m^{-1}
ρ	density, kg m^{-3}
μ	dynamic viscosity, kg m^{-1} s^{-1}
δ	film thickness, m
δ^+	dimensionless form of film thickness
α	void fraction
τ	shear stress, N m^{-2}
ν	kinematics viscosity m^2 s^{-1}
ϕ	two-phase multiplier

Subscripts

cond	condensate
exp	measured
f	frictional
g	gas/vapor
H	homogen
h	hydraulic
i	inlet
l	liquid
o	outlet
ph	preheater
ref	refrigerant
s	superficial for one phase flow alone in the pipe
sat	saturation
so	Soliman
T	total
TS	test section
w	water
wi	inner wall

Generally, flow patterns are observed by visual inspection and include bubble flow, slug flow, churn flow, wispy–annular flow, and annular flow in a vertical configuration, and bubble flow, plug flow, stratified flow, wavy flow, slug flow, and annular flow in a horizontal configuration. However, Hubbard and Dukler [6] classified the flow patterns as separated flow patterns (stratified flow, annular flow), intermittent flow patterns (elongated bubble flow, slug/plug flow, churn/froth flow), and dispersed flow patterns (bubble flow, dispersed bubble flow). The prediction of flow patterns during gas–liquid flow is achieved by one of three approaches: empirical correlations, visual examination, flow regime maps. In this paper, the applicability of some well-known empirical correlations such as Jaster and Kosky [7], Traviss and Rohsenow [8], Taitel and Dukler [9], Dobson [10], Akbar et al. [11], Breber et al. [12], Cavallini et al. [13], Chisholm and Sutherland [14], Soliman [15], Tandon et al. [16], Sardesai et al. [17], and Soliman [18] in Table 1 are investigated to determine the flow pattern during condensation of R134a in the test tube.

Two-phase annular flow occurs widely in film heating and cooling processes, particularly in power generation and especially in nuclear reactors. This flow regime has received the most attention, both analytically and experimentally, because of its practical importance and the relative ease with which analytical treatment may be applied. Annular two-phase flow is characterized by a phase interface separating a thin liquid film from the gas flow in the core region. In addition to this, the condensate distribution inside the tube wall is almost symmetric and there is high velocity vapor flow in the core during annular flow.

Void fraction is an important parameter and is always used to determine the flow pattern transition, heat transfer coefficient and two-phase pressure drop, and is defined as the cross-sectional area occupied by the vapor in relation to the area of the flow channel. Two-phase separated flow is commonly analyzed using the slip flow model. In this model, it is assumed that the separated phases have different uniform velocities. By contrast, the homogeneous model is defined as an ideal case, as it assumes a homogeneous mixture providing uniform velocities for both phases, and for that reason it is the simplest method of determination of the void fraction.

In the technical literature, numerous studies have been carried out on the modeling of the void fraction and can be divided into several groups: general void fraction models and correlations, $K\varepsilon_H$ parameter-based void fraction models and correlations, flow regime-based void fraction models and correlations, Lockhart and Martinelli parameter-based void fraction models and correlations and slip ratio void fraction models and correlations. It should be noted that the most predictive void fraction models and correlations according to the authors' experimental database, revealed in the authors' previous publications, such as Chisholm [19], Turner and Wallis [20], Smith [21], Spedding and Spence [22] in Table 2, are used for comparison in this paper. A brief and comprehensive overview of these works is presented in the authors' previous publications [23–26].

This paper gives a validation of the most agreeable void fraction models and correlations, previously explained in the authors' publications, against the heat transfer database in relation to a flow transition model having a relationship between the film thickness and void fraction models and correlations. The experiments include a wide range of high mass fluxes with different saturation temperatures as they relate to 380 data points of R134a belonging to the condensation heat transfer database of FUTURE Lab in KMUTT. Apart from the authors' previous publications [23–36], few studies exist in the literature on the investigation of heat transfer characteristics in a small diameter vertical tube during co-current down flow condensation, and besides this, there is no study with the experimental parameters of this work and its content in the open literature. In this study, determination of the void fraction is presented by means of the model of Soliman [18] and verified by relating the void fraction models and correlations. In addition to this, flow regime identification is performed using various flow pattern correlations valid for horizontal and vertical tubes to show the independence of the annular flow regime from tube orientation [33,35].

Table 1
Flow pattern correlations.

Number	Flow pattern correlation	Model/correlation
1	Jaster and Kosky [7]	$\tau'>29$ for annular flow regime $\tau' = \frac{\tau_{wall}}{(\rho_l g\delta)}$ Eq. (7) is used for τ_{wall}, Eq. (5) is used for δ
2	Traviss and Rohsenow [8]	Fr>45 for annular/semi-annular flow regime $Fr = \frac{u_l}{\sqrt{g\delta}}$ Eq. (5) is used for δ
3	Taitel and Dukler [9]	F>1.5 for annular flow regime $F = \sqrt{\frac{\rho_g}{(\rho_l-\rho_g)}}\left(\frac{u_{vs}}{\sqrt{gd}}\right)$ $u_{vs} = 14.63\rho_g^{-0.23}u_{ls}^{-0.287}d^{0.414}[\sigma(\rho_l-\rho_g)]^{0.115}$ $u_l = \frac{u_{ls}}{4\left(\bar{\delta}-\bar{\delta}^2\right)}$ $m_{cond} = \rho_l A_l u_l$ $\delta^+ = \frac{\delta}{d}$ Eq. (5) is used for δ
4	Dobson [10]	Fr_{so}>20 for annular flow regime $Fr_{so} = 0.025\mathrm{Re}_l^{1.59}\left(\frac{1+1.09X^{0.039}}{X}\right)1.5\frac{1}{Ga^{0.5}}$ for $Re_l \le 1250$ $Fr_{so} = 1.26Re_l^{1.04}\left(\frac{1+1.09X^{0.039}}{X}\right)1.5\frac{1}{Ga^{0.5}}$ for $Re_l > 1250$ $Ga = g\rho_l(\rho_l-\rho_g)\frac{(\sqrt{\alpha}d)^3}{\mu_l^2}X = \left(\frac{1-x}{x}\right)^{0.9}\left(\frac{\rho_g}{\rho_l}\right)^{0.5}\left(\frac{\mu_l}{\mu_g}\right)^{0.1}$ $\alpha = \left[1+\frac{1-x}{x}\left(\frac{\rho_g}{\rho_l}\right)^{\frac{2}{3}}\right]^{-1}$ $Re_l = \frac{Gd(1-x)}{\mu_l}$
5	Akbar et al. [11]	$\mathrm{We}_{gs} \ge 11.0\mathrm{We}_{ls}^{0.14}$ and $\mathrm{We}_{ls} \le 3.0$ for annular flow regime $We_{ls} = \frac{u_{ls}^2 d_h \rho_l}{\sigma}$ $We_{gs} = \frac{u_{gs}^2 d\rho_g}{\sigma}$ $u_l = \frac{u_{ls}}{4(\delta^+-\delta^{+2})}$ $m_{cond} = \rho_l A_l u_l$ $\delta^+ = \frac{\delta}{d}$ Eq. (5) is used for δ
6	Breber et al. [12]	j_g^*>1.5 and X<1.0 for annular regime $j_g^* = \frac{Gx}{\sqrt{(dg\rho_g(\rho_l-\rho_g)}}$ and $X = \left(\frac{1-x}{x}\right)^{0.9}\left(\frac{\rho_g}{\rho_l}\right)^{0.5}\left(\frac{\mu_l}{\mu_g}\right)^{0.1}$
7	Cavallini et al. [13]	j_g^*>2.5 and X<1.6 for annular regime $j_g^* = \frac{Gx}{\sqrt{(dg\rho_g(\rho_l-\rho_g)}}$ and $X = \left(\frac{1-x}{x}\right)^{0.9}\left(\frac{\rho_g}{\rho_l}\right)^{0.5}\left(\frac{\mu_l}{\mu_g}\right)^{0.1}$
8	Chisholm and Sutherland [14]	$\phi_g^2 F$>1.75 for annular flow regime $\phi_g^2 = 0.7X^2+2X+0.85$ and $X = \left(\frac{1-x}{x}\right)^{0.9}\left(\frac{\rho_g}{\rho_l}\right)^{0.5}\left(\frac{\mu_l}{\mu_g}\right)^{0.1}$ $F = \sqrt{\frac{\rho_g}{\rho_l-\rho_g}}\frac{u_{gs}}{\sqrt{dg}}$ $u_g = \frac{4u_{gs}}{1-4\delta^+ + 4\delta^{+2}}$ $m_g = \rho_g A_g u_g$ $m_g = xm_T$ $x = \frac{x_{TS,i}+x_{TS,o}}{2}$ $\delta^+ = \frac{\delta}{d}$
9	Soliman [15]	We<20 for annular flow regime $We = 2.45Re_g^{0.64}\left(\frac{\mu_g^2}{\rho_g\sigma d}\right)^{0.3}\phi_g^{-0.4}$ for $Re_l \le 1250$ $We = 0.85Re_g^{0.79}\left(\frac{\mu_g^2}{\rho_g\sigma d}\right)^{0.3}\left[\left(\frac{\mu_g^2}{\rho_g\sigma d}\right)^2\left(\frac{\rho_l}{\rho_g}\right)\right]^{0.0884}\left(X/\phi_g^{2.55}\right)^{0.157}$ for $Re_l > 1250X = \left(\frac{1-x}{x}\right)^{0.9}\left(\frac{\rho_g}{\rho_l}\right)^{0.5}\left(\frac{\mu_l}{\mu_g}\right)^{0.1}$ Eqs. (1) and (2) are used for Re_l and Re_g respectively. Eq. (12) is used for ϕ_g
10	Tandon et al. [16]	$1 \le j_g^* \le 6$ and $\frac{1-\alpha}{\alpha} \le 0.5$ for annular/semi-annular regime $j_g^* = \frac{Gx}{\sqrt{(dg\rho_g(\rho_l-\rho_g)}}$ $\alpha = \left\{1+\left(\frac{\rho_g}{\rho_l}\right)K\left(\frac{1}{x}-1\right)+\left(\frac{\rho_g}{\rho_l}\right)(1-K)\left(\frac{1}{x}-1\right)\left[\frac{\left(\frac{\rho_l}{\rho_g}\right)+K\left(\frac{1}{x}-1\right)}{1+K\left(\frac{1}{x}-1\right)}\right]\right\}^{-1}$ $K = 0.4$
11	Sardesai et al. [17]	$\beta \ge 1.75$ for annular flow regime $\beta = (0.7X^2+2X+0.85)F$ $X = \left(\frac{1-x}{x}\right)^{0.9}\left(\frac{\rho_g}{\rho_l}\right)^{0.5}\left(\frac{\mu_l}{\mu_g}\right)^{0.1}$ $F = \sqrt{\frac{\rho_g}{\rho_l-\rho_g}}\frac{j_g}{\sqrt{dg}}$ $j_g = \frac{xG}{\rho_g}$
12	Soliman [18]	Fr>45 for annular/semi-annular flow regime $Fr = \frac{0.25Re_l\left(\frac{u^*}{\delta^+}\right)^{1.5}}{\sqrt{gv_l}}$ $Re_l = \frac{Gd(1-x)}{\mu_l}$ Eq. (6) is used for u^*, Eqs. (3) and (4) are used for δ^+

Table 2
Void fraction models and correlations.

Number	Void fraction model/correlation	Model/correlation
1	Homogeneous model	$\alpha_H = \frac{1}{1+\left(\frac{1-x}{x}\right)\left(\frac{\rho_g}{\rho_l}\right)S} \quad S=1$
2	Soliman [18]	$G(1-x) = 4\rho_l u_l\left(\frac{\delta}{d}\right) \quad \alpha = 1-\frac{4\delta}{d}$
3	Chisholm [19]	$\alpha = \frac{1}{\alpha_H + (1-\alpha_H)^{0.5}}\alpha_H$
4	Turner and Wallis [20]	$\frac{1-\alpha}{\alpha} = A\left(\frac{1-x}{x}\right)^p\left(\frac{\rho_g}{\rho_l}\right)^q\left(\frac{\mu_l}{\mu_g}\right)^r$

Correlation or model	A	p	q	r
Homogeneous	1	1	1	0
Zivi	1	1	0.67	0
Turner–Wallis	1	0.72	0.4	0.08
Lockhart–Martinelli	0.28	0.64	0.36	0.07
Thom	1	1	0.89	0.18
Baroczy	1	0.74	0.65	0.13

5	Smith [21]	$\alpha = \left\{1+\left(\frac{\rho_g}{\rho_l}\right)K\left(\frac{1}{x}-1\right)+\left(\frac{\rho_g}{\rho_l}\right)(1-K)\left(\frac{1}{x}-1\right)\left[\frac{\left(\frac{\rho_l}{\rho_g}\right)+K\left(\frac{1}{x}-1\right)}{1+K\left(\frac{1}{x}-1\right)}\right]\right\}^{-1}$ $K=0.4$
6	Spedding and Spence [22]	$\alpha = \left(1+2.22\left(\frac{1-x}{x}\right)^{0.65}\left(\frac{\rho_g}{\rho_l}\right)^{0.65}\right)^{-1}$

2. Experimental apparatus and method

Due to space limitations, detailed descriptions of the experimental apparatus and test section for studying the condensation of R134a inside a vertical tube can be found in the authors' previous publications.

3. Data reduction

The data reduction of the measured results such as inlet and outlet vapor qualities of the test section, average heat transfer coefficient can be seen from the authors' previous publications in detail.

3.1. Calculation procedure for annular flow model

To confirm the annular flow pattern during condensation of refrigerant in the test section, the experimental results at a mass flux of 260–515 kg m^{-2} s^{-1} and condensing temperature of 40–50 °C are checked with the flow regime maps of Hewitt and Roberts [3], Chen et al. [4], Barnea et al. [38], Baker [39], Thome [40] and Kattan et al. [41], and they are also checked through sight glasses at the inlet and outlet of the test section. Plotting the data points on this flow regime map, it is found to be in very good agreement qualitatively. The data points are located in the region of the annular flow pattern although some flow regime maps are developed for two-phase flow in horizontal tubes. Hence, the discussion section will address only the heat transfer mechanism in this flow pattern.

In the present study, annular flow pattern models and correlations are used to show the similarity of annular flow correlations which are independent of tube orientation (horizontal or vertical). Chen et al. [37] also mentioned this similarity in their article. They developed a general correlation by relating the interfacial shear stress to flow conditions for annular film condensation inside horizontal and vertical tubes using correction factors.

Details of the development of the relationship between film thickness, void fraction and flow parameters on one hand, and flow pattern transition mechanisms on the other, can be seen in Soliman [18], Kosky [42], Lockhart–Martinelli [43] and Azer et al. [44].

Liquid and vapor Reynolds numbers can be determined respectively as follows:

$$Re_l = \frac{Gd(1-x)}{\mu_l} \tag{1}$$

$$Re_g = \frac{Gdx}{\mu_g} \tag{2}$$

Kosky [42] developed a model for the determination of liquid film thickness in co-current flow under simultaneous shear and gravity forces which has also been validated experimentally by Soliman [18]. Calculation of liquid film thickness is defined as follows:

$$\delta^+ = 0.707(Re_l)^{0.5} \quad \text{for} \quad Re_l \le 1250 \tag{3}$$

$$\delta^+ = 0.0504Re_l^{0.875} \quad \text{for} \quad Re_l > 1250 \tag{4}$$

where the dimensionless film thickness value is shown in Eq. (5):

$$\delta^+ = \frac{\delta u^*}{\nu_l} \tag{5}$$

Table 3
Standard deviation and mean error between predicted void fraction values for $T_{sat}=40$ °C and $G=300$–515 kg m^{-2} s^{-1}.

Void fraction models and correlations	$G=300$ kg m^{-2} s^{-1}		$G=515$ kg m^{-2} s^{-1}	
	Mean error (%)	Standard deviation	Mean error (%)	Standard deviation
Soliman [18]	−0.376	0.021	−0.845	0.0137
Chisholm [19]	−4.63	0.022	−4.38	0.013
Turner and Wallis [20]	−5.861	0.035	−4.791	0.02
Smith [21]	−6.384	0.045	−4.564	0.025
Spedding and Spence [22]	−5.123	0.03	−4.397	0.017

and the frictional velocity is determined as:

$$u^* = \sqrt{\frac{\tau_{wall}}{\rho_l}} \tag{6}$$

where the wall shear stress can be calculated as follows:

$$\tau_{wall} = \frac{-d\left(\frac{dp}{dz}\right)_f}{4} \tag{7}$$

Mandhane et al. [45] reported that the determination of the two-phase frictional pressure drop depends strongly on the flow pattern. Lockhart and Martinelli's correlation [43] is recommended for the annular flow regime and shown in Eq. (8):

$$\left(\frac{dp}{dz}\right)_f = \phi_g^2 \left(\frac{dp}{dz}\right)_{gs} \tag{8}$$

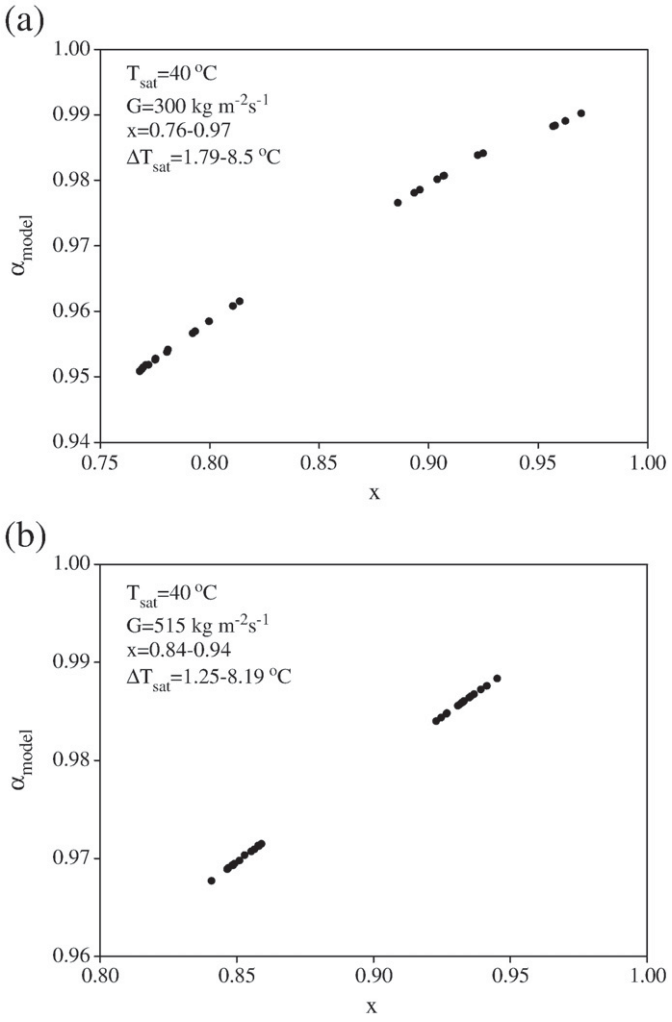

Fig. 1. Void fraction values from model vs. average vapor quality for $G = 300$ kg m^{-2} s^{-1} (a) and 515 kg m^{-2} s^{-1} (b) at the condensing temperature of 40 °C using laminar and turbulent flow data.

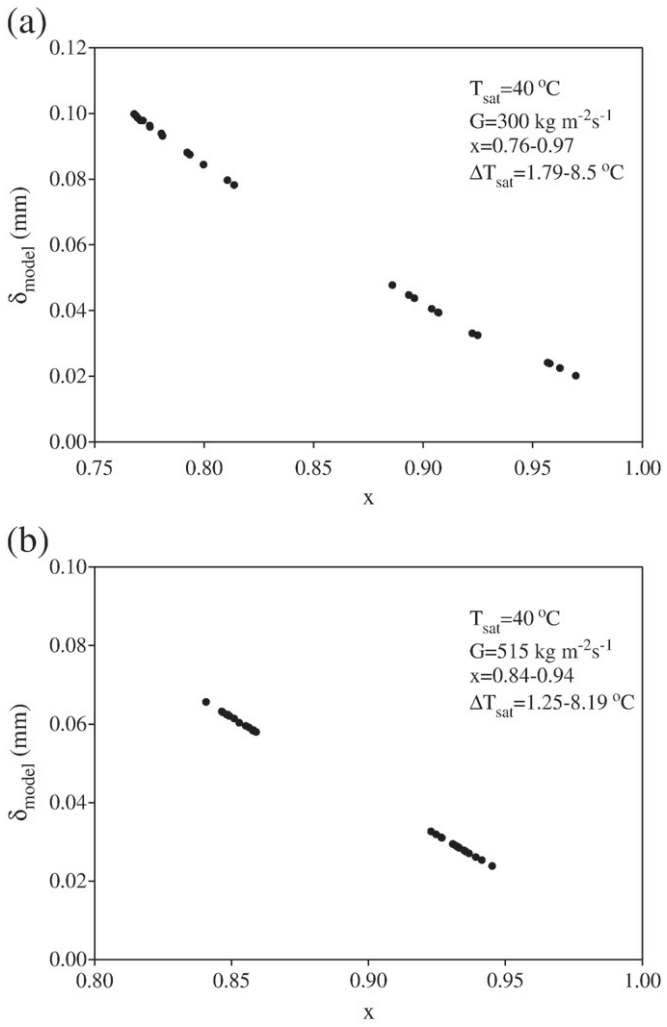

Fig. 2. Film thickness values from model vs. average vapor quality for $G = 300$ kg m^{-2} s^{-1} (a) and 515 kg m^{-2} s^{-1} (b) at the condensing temperature of 40 °C using laminar and turbulent flow data.

where the superficial vapor pressure drop is obtained as follows:

$$\left(\frac{dp}{dz}\right)_{gs} = -\left(\frac{2}{d}\right)\left(\frac{0.045}{Re_g^{0.2}}\right)\left(\frac{G^2x^2}{\rho_g}\right) \tag{9}$$

Substituting Eqs. (7)–(9) into Eq. (6), and simplifying gives:

$$u^* = 0.15\left(\frac{\nu_l}{d}\right)\left(\frac{\phi_g}{X}\right)Re_l^{10.9} \tag{10}$$

where the Lockhart–Martinelli [43] parameter is expressed as follows:

$$X = \left(\frac{1-x}{x}\right)^{0.9}\left(\frac{\rho_g}{\rho_l}\right)^{0.5}\left(\frac{\mu_l}{\mu_g}\right)^{0.1} \tag{11}$$

Soliman [18] used the two-phase multiplier of Azer et al. [44] in his analysis and reported that it was the most consistent one for data of annular flow condensation inside a horizontal tube, it should be noted that Eqs. (6) and (10) give exactly the same results as the two-phase multiplier of Azer et al. [44]. On the other hand, it is found that other two-phase multiplier correlations do not give satisfactory results according to the authors' analysis and the most predictive two-phase

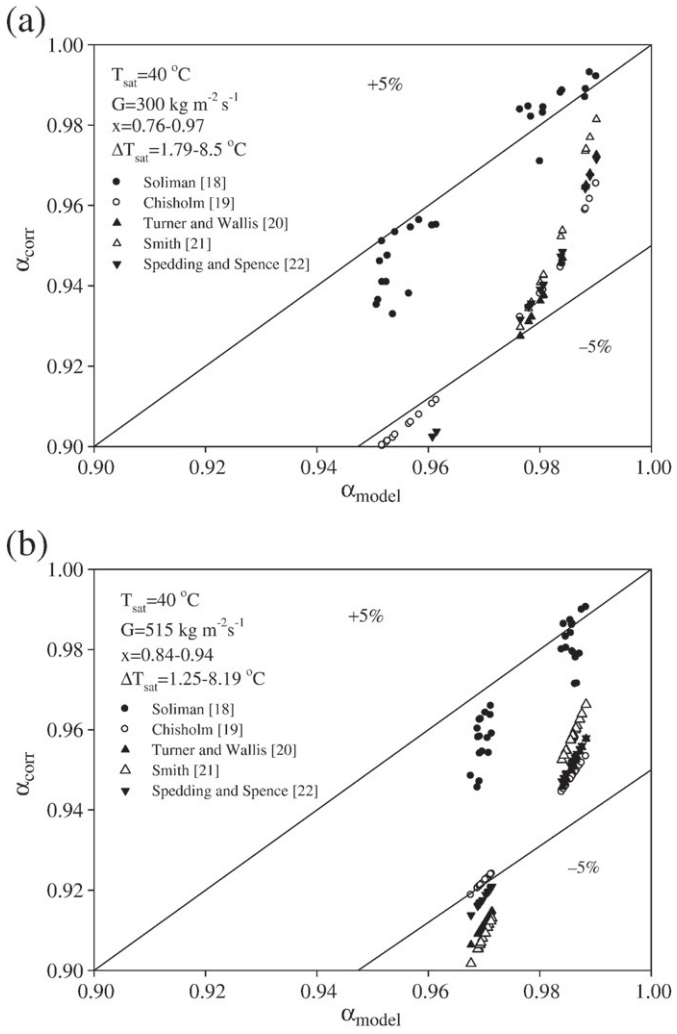

Fig. 3. Comparisons between the model and calculated void fraction values for the mass flux of 300 kg m^{-2} s^{-1} (a) and 515 kg m^{-2} s^{-1} (b) at the condensing temperature of 40 °C using laminar and turbulent flow data.

multiplier for this model by Azer et al. [44] can be seen from Eq. (12) as follows:

$$\phi_g = 1 + 1.09X^{0.039} \tag{12}$$

The void fraction value from the model is estimated using an estimated film thickness value calculated by Eq. (5), assuming $\delta \ll d$ as follows [23–26]:

$$\alpha = \frac{A_g}{A} = \left(1-\frac{\delta}{r}\right)^2 = 1-\frac{4\delta}{d} \tag{13}$$

Moreover mean errors between predicted void fraction values are shown in Table 3 and are calculated as follows:

$$\text{Error} = \left(\frac{\alpha_{corr}-\alpha_{model}}{\alpha_{model}}\right)100 \tag{14}$$

$$\text{Mean Error} = \frac{\sum \text{Error}}{\text{data}} \tag{15}$$

It should also be noted that void fraction values obtained from the model by means of Eq. (13) are assumed as comparative values for the error analysis.

Table 4
Prediction analysis of annular flow pattern for T_{sat} = 40 °C and G = 300–515 kg m^{-2} s^{-1}.

Flow pattern correlation	Predictability of data points	
	G = 300 kg m^{-2} s^{-1}	G = 515 kg m^{-2} s^{-1}
Jaster and Kosky [7]	6/26	32/32
Traviss and Rohsenow [8]	0/26	0/32
Taitel and Dukler [9]	26/26	32/32
Dobson [10]	26/26	32/32
Akbar et al. [11]	26/26	32/32
Breber et al. [12]	26/26	32/32
Cavallini et al. [13]	26/26	32/32
Chisholm and Sutherland [14]	0/26	29/32
Soliman [15]	0/26	0/32
Tandon et al. [16]	26/26	0/32
Sardesai et al. [17]	26/26	0/32
Soliman [18]	12/26	32/32

3.2. Uncertainties

The uncertainties in the Nusselt number and condensation heat transfer coefficient in the test tube varied from ±7.64% to ±10.71%. It should be noted that a similar range of uncertainty with minimum and maximum values exists in the literature. The procedures of Kline and McClintock [46] were used for the calculation of all uncertainties. Various uncertainty values of the study can be seen in the authors' previous works [28,31,33].

4. Results and discussion

In order to investigate the validation of the void fraction models and correlations proposed in the authors' previous publications in the annular flow regime, checked by sight glasses located at the inlet and outlet of the test tube, using a large number of experimental data points for the downward two-phase flow of R134a in a vertical round tube with an inner diameter of 8.1 mm, the present study was performed at the Fluid Mechanics, Thermal Engineering and Multiphase Flow Research Lab. (FUTURE) in KMUTT. Pure HFC-134a was used in the experiments. Discussion of the results will be given in turn as follows:

The present study was performed to study the relationship between void fraction models and the annular flow model of Soliman [18] and to investigate the well-known flow pattern correlations to verify the annular flow conditions of experimental data for downward two-phase flow of R134a in a vertical round tube. The effects of the temperature difference between the saturated temperature of the vapor and the inlet wall temperature of the tube (ΔT_{sat}), mass flux, vapor quality, and condensation temperature on the heat transfer coefficients, pressure drop and void fraction can be seen in the authors' previous studies in detail [23–34]. It should be noted that R134a enters the test section as a pure saturated vapor during laminar flow experiments. Verification of the reliability of the calculated film thickness, void fraction from the model and annular flow pattern identification are checked using different condensing temperatures and mass fluxes.

Figs. 1 and 2 show the relationship between void fraction (Eq. (13)) and film thickness (Eq. (5)) obtained from the model of Soliman [18] and vapor quality in the test tube for mass fluxes of 300 kg m^{-2} s^{-1} (a) and 515 kg m^{-2} s^{-1} (b) and a condensing temperature of 40 °C. Comparison of the void fraction at higher and lower average vapor qualities and smaller liquid film thickness together with higher vapor velocity at the vapor–liquid interface shows an increase in the void fraction when the average quality is higher. In addition to this, the film thickness values increase with decreasing vapor quality. Trend lines of data are in accordance with this basic knowledge of in-tube condensation. It is shown in the authors' previous publications that film thickness decreases with increasing heat transfer coefficient; in other words, film thickness

decreases with decreases in ΔT_{sat} for similar test conditions. The increase in heat flux in relation to ΔT_{sat} increases the condensation rate. In other words, the film thickness on the tube wall increases due to the constant latent heat of condensation for a specific saturation temperature of condensation.

In Fig. 3, comparison of the void fraction values obtained from the model of Soliman [18] with the most predictive void fraction and correlations shown in Table 2 are presented with a 5% deviation line for the minimum mass flux of 300 kg m^{-2} s^{-1} (Fig. 3a) and the maximum mass flux of 515 kg m^{-2} s^{-1} (Fig. 3b) according to the condensation temperature of 40 °C. It is clearly seen from the figures that the void fraction models and correlations of Chisholm [19], Turner and Wallis [20], Smith [21] and Spedding and Chen [22] give the best predictability of experimental data among 35 void fraction models and correlations given in the authors' previous publications [23–26]. In addition to this, the majority of the data calculated by the void fraction models and correlations of them fall within ±5% and are in good agreement with experimental data. Table 3 also shows the accuracy of investigated void fraction models and correlations for the tested experimental conditions.

In Table 1, well-known flow pattern models and correlations valid for horizontal and vertical tube orientations are presented with the plotted experimental data of the current study. Verification by visual control of the flow regime in the test tube is done using these flow pattern models and correlations in the literature. Table 4 shows the comparison of annular flow regime correlations for mass fluxes of 300–515 kg m^{-2} s^{-1} at a condensing temperature of 40 °C. The predictability ratio of Jaster and Kosky [7] for the determination of annular flow regime is 6 out of 26 data points for a mass flux of 300 kg m^{-2} s^{-1}, whereas it is 32 of 32 data points for a mass flux of 515 kg m^{-2} s^{-1}. A heat-momentum transfer analogy (for annular flow) is developed for the two-phase multiplier for shear stress using steam in a 12.5 mm i.d. horizontal tube for mass fluxes between 12.6 and 145 kg m^{-2} s^{-1}. Traviss and Rohsenow's model [8] cannot predict the annular flow regime for the tested experimental conditions. They condensed R12 in an 8 mm i.d. horizontal tube for mass fluxes between 100 and 990 kg m^{-2} s^{-1} at saturation temperatures of 10–40.6 °C. Dispersed, annular, semi-annular and slug flow are observed in their study. The Froude number and von Karman velocity profile are used in their condensation analysis. Taitel and Dukler's [9] model predicts all the tested data successfully for annular flow conditions. They investigated adiabatic flow of air–water in conventional tubes developing a theoretical approach to flow regime mapping using a momentum balance on a stratified flow pattern. Many researchers benefited from their analysis in the literature. Dobson's model [10] is found to be consistent with experimental data for the determination of the annular flow regime. He used R12, R134a, R22, R32/R125 as condensing test fluids in 3.14, 4.6, 7.04 mm i.d. horizontal tubes at mass fluxes between 25 and 800 kg m^{-2} s^{-1} at condensing temperatures of 35–60 °C. His results were in good agreement with the flow regime map of Mandhane et al. [45]. A modified Soliman number and mass flux are used in his analysis. The model of Akbar et al. [11] predicts annular flow experimental data successfully. They divided the entire flow regime map into four regions: the surface tension-dominated region, including bubble, plug, and slug, inertia-dominated zone 1, annular and wavy–annular regimes, inertia-dominated zone 2, and dispersed flow regimes and a transition zone. The model of Breber et al. [12] is good at predicting annular flow experimental data. He performed condensation experiments using R11, R12, R113, steam, n-pentane in several tubes with i.d.'s between 4.8 and 50.8 mm at mass fluxes between 17.6 and 990 kg m^{-2} s^{-1}. They benefited from Taitel and Dukler's flow regime map [9] to develop simple criteria for condensation in horizontal tubes. The analysis of Cavallini et al. [13] is successful at predicting annular flow experimental data. They performed condensation tests using data of R22, R134a, R125, R32, R236ea, R407C, R 410A in an 8 mm i.d. horizontal tube for mass flux between 100 and 750 kg m^{-2} s^{-1} at condensation temperatures of 30–50 °C. Kosky and Staub's model [47] is recommended for annular flow and the model of Breber et al. [12] is considered for the observed flow regimes of annular, stratified, wavy, and slug. Chisholm and Sutherland's model [14] was not successful for the minimum mass flux of R134a, whereas it was successful for the maximum mass flux of R134a. They developed a model using a two-phase multiplier and Froude number for gravity-controlled condensation and annular flow. Soliman's model [15] could not predict annular flow experimental data. Soliman condensed R12, R113 and steam in 4.8–15.9 mm i.d. tubes. He used a Froude number for annular–wavy flow and Weber number for mist–annular flow. Soliman's model [18] also has poor predictability for annular flow experimental data. The model of Tandon et al. [16] was not successful for the maximum mass flux of R134a, whereas it was successful for the minimum mass flux of R134a. They did experiments using several refrigerants such as R12, R113, and R22 in 4.8–15.9 mm i.d. horizontal tubes at pressures between 570 and1960 kPa. They observed annular, semi-annular and wavy flows during their experiments. The model of Sardesai et al. [17] was not successful for the maximum mass flux of R134a, whereas it was successful for the minimum mass flux of R134a. They condensed R113, steam, propane, methanol, n-pentane in a 24.4 mm i.d. horizontal tube. An annular-stratified/wavy transition is investigated in their analysis based on Taitel and Dukler [9].

A large number of graphs could be generated from the output of the calculations; however, due to space limitations, only typical results are shown for limited data. It should also be noted that detailed information on the explanations above and some additional figures with different experimental parameters related to this study can be seen in the authors' previous publications [23–36].

5. Conclusion

Co-current downward condensation heat transfer of R134a was experimentally investigated in an 8.1 mm i.d. vertical smooth tube. Accurate and repeatable heat transfer data during annular flow were obtained. There are few research studies on the parameters and content of such cases in the literature. For this reason, the results of this study are expected to fill a gap. This paper provides a comprehensive review of the published literature on flow regime correlations in relation to a flow transition model connected to film thickness and void fraction models and correlations. Validation of the annular flow model was accomplished by using a large number of data points. The following results were obtained:

1– A study of the theoretical model of the flow regime transition mechanism of Soliman [18], performed for condensation in horizontal tubes, was done using experimental data to determine accurate film thickness and void fraction values under various test conditions. Calculated void fraction and film thickness values from the model are found to be in good agreement in the range of ±5%.
2– The effect of vapor quality on film thickness and void fraction is discussed and investigated in detail. Void fraction values obtained from the theoretical model increase with increasing vapor quality and film thickness values obtained from the theoretical model increase with decreasing vapor quality as expected.
3– In order to verify the results of calculations, the data obtained from void fraction correlations previously proposed in the authors' publications with void fraction values from the mode were compared. The majority of data obtained from the void fraction models and correlations of Chisholm [19], Turner and Wallis [20], Smith [21] and Spedding and Chen [22] are found to be in good agreement with the void fraction values obtained from the model of Soliman [18] within the ±5% error band. These results also validate the accuracy of previously proposed consistent void

fraction correlations with the condensation database of KMUTT by the authors.

4– According to the analysis of flow regime identification in this paper, the flow pattern correlations of Taitel and Dukler [9], Dobson [10], Akbar et al. [11], Breber et al. [12], Cavallini et al. [13] and Sardesai et al. [17] are capable of predicting the annular flow regime conditions, as verified through sight glasses in the experimental apparatus and also checked with various flow regime maps for the high mass region of R134a in a vertical tube.

5– According to the analysis in this paper, it is shown that the annular flow model does not depend on tube orientation provided that an annular flow regime exists along the tube length and is capable of predicting condensation film thickness, void fraction and flow pattern inside the test tube.

Acknowledgements

The authors are indebted to King Mongkut's University of Technology Thonburi (KMUTT), the Thailand Research Fund and the Office of Higher Education Commission for supporting this study. Especially, the first author wishes to thank KMUTT for providing him with a Post-doctoral fellowship.

References

[1] D. Barnea, O. Shoham, Y. Taitel, Flow pattern transition for vertical downward two phase flow, Chemical Engineering Science 37 (1982) 741–744.
[2] J.R. Fair, What you need to know to design thermosyphon reboilers, Petroleum Refiner, 39 no:2, 1960, p. 105.
[3] G.F. Hewitt, D.N. Robertson, Studies of two-phase flow patterns by simultaneous x-ray and flash photography, Rept AERE-M2159, UKAEA, Harwell, 1969.
[4] L. Chen, Y.S. Tian, T.G. Karayiannis, The effect of tube diameter on vertical two-phase flow regimes in small tubes, International Journal of Heat and Mass Transfer 49 (2006) 4220–4230.
[5] T.S. Zhao, Q.C. Bi, Co-current air–water two-phase flow patterns in vertical triangular microchannels, International Journal of Multiphase Flow 27 (2001) 765–782.
[6] M.G. Hubbard, A.E. Dukler, The characterization of flow regimes for horizontal twophase flow, Proc. Heat Transfer and Fluid Mech. Inst., Standford University Press, 1966.
[7] H. Jaster, P.G. Kosky, Condensation heat transfer in a mixed flow regime, International Journal of Heat and Mass Transfer 19 (1976) 95–99.
[8] D.P. Traviss, W.M. Rohsenow, Flow regimes in horizontal two-phase flow with condensation, ASHRAE Transactions 79 (1973) 31–39.
[9] Y. Taitel, A.E. Dukler, A model for predicting flow regime transitions in horizontal and near horizontal gas–liquid flow, AIChE Journal 22 (1976) 47–55.
[10] M.K. Dobson, Heat transfer and flow regimes during condensation in horizontal tubes, PhD Thesis, Mechanical and Industrial Engineering, University of Illinois at Urbana-Champaign, Urbana-Champaign, IL, 1994.
[11] M.K. Akbar, D.A. Plummer, S.M. Ghiaasiaan, On gas–liquid two-phase flow regimes in microchannels, International Journal of Multiphase Flow 29 (2003) 855–865.
[12] G. Breber, J.W. Palen, J. Taborek, Prediction of horizontal tube side condensation of pure components using flow regime criteria, Journal of Heat Transfer Transactions of ASME 102 (1980) 471–476.
[13] A. Cavallini, G. Censi, D. Del Col, L. Doretti, G.A. Longo, L. Rossetto, Experimental investigation on condensation heat transfer and pressure drop of new HFC refrigerants (R134a, R125, R32, R410A, R236ea) in a horizontal smooth tube, International Journal of Refrigeration 24 (2001) 73–87.
[14] D. Chisholm, L.A. Sutherland, Prediction of pressure gradients in pipeline systems during two-phase flow, Proceedings of the Institution of Mechanical Engineering 184 (1969–1970) 24–32.
[15] H.M. Soliman, Mist–annular transition during condensation and its influence on the heat transfer mechanism, International Journal of Multiphase Flow 12 (1986) 277–288.
[16] T.N. Tandon, H.K. Varma, C.P. Gupta, New flow regimes map for condensation inside horizontal tubes, Journal of Heat Transfer 104 (1982) 763–768.
[17] R.G. Sardesai, R.G. Owen, D.J. Pulling, Flow regimes for condensation of a vapour inside a horizontal tube, Chemical Engineering Science 36 (1981) 1173–1180.
[18] H.M. Soliman, On the annular-to-wavy flow pattern transition during condensation inside horizontal tubes, The Canadian Journal of Chemical Engineering 60 (1982) 475–481.
[19] D. Chisholm, Two Phase Flow in Pipelines and Heat Exchangers, George Godwin in association with The Institution of Chemical Engineers, London, 1983.
[20] J.M. Turner, G.B. Wallis, The Separate-Cylinders Model of Two-Phase Flow, Paper No. NYO-3114-6, Thayer's School Eng.,Dartmouth College, Hanover, NH, USA, 1965.
[21] S.L. Smith, Void fractions in two-phase flow: a correlation based upon an equal velocity head model, Proceedings of the Institution of Mechanical Engineers 36 (1969) 647–664.
[22] P.L. Spedding, D.R. Spence, Prediction of holdup in two phase flow, International Journal of Engineering Fluid Mechanics 2 (1989) 109–118.
[23] A.S. Dalkilic, S. Laohalertdecha, S. Wongwises, Effect of void fraction models on the two-phase friction factor of R134a during condensation in vertical downward flow in a smooth tube, International Communications in Heat and Mass Transfer 35 (2008) 921–927.
[24] A.S. Dalkilic, S. Laohalertdecha, S. Wongwises, Effect of void fraction models on the film thickness of R134a during downward condensation in a vertical smooth tube, International Communications in Heat and Mass Transfer 36 (2009) 172–179.
[25] A.S. Dalkilic, S. Laohalertdecha, S. Wongwises, A comparison of the void fraction correlations of R134a during condensation in vertical downward laminar flow in a smooth and micro-fin tube, Proceedings of the 1st International Conference on Micro/Nanoscale Heat Transfer, ASME, 2008, January 06-09, Taiwan.
[26] A.S. Dalkilic, S. Laohalertdecha, S. Wongwises, Two-phase friction factor obtained from various void fraction models of R-134a during condensation in vertical downward flow at high mass flux, Proceedings of the 1st International Conference on Heat Transfer, ASME, 2008, August 10–14, USA.
[27] A.S. Dalkilic, S. Wongwises, Intensive literature review of condensation inside smooth and enhanced tubes, International Heat and Mass Transfer 52 (2009) 3409–3426.
[28] A.S. Dalkilic, S. Yildiz, S. Wongwises, Experimental investigation of convective heat transfer coefficient during downward laminar flow condensation of R134a in a vertical smooth tube, International Journal of Heat and Mass Transfer 52 (2009) 142–150.
[29] A.S. Dalkilic, S. Laohalertdecha, S. Wongwises, Two-phase friction factor in vertical downward flow in high mass flux region of refrigerant HFC-134a during condensation, International Communications in Heat and Mass Transfer 35 (2008) 1147–1152.
[30] A.S. Dalkilic, S. Laohalertdecha, S. Wongwises, Experimental investigation on heat transfer coefficient of R134a during condensation in vertical downward flow at high mass flux in a smooth tube, International Communications in Heat and Mass Transfer 36 (2009) 1036–1043.
[31] A.S. Dalkilic, S. Laohalertdecha, S. Wongwises, Experimental investigation on the condensation heat transfer and pressure drop characteristics of R134a at high mass flux conditions during annular flow regime inside a vertical smooth tube, Summer Heat Transfer Conference, ASME, July 19–23, USA, 2009.
[32] A.S. Dalkilic, O. Agra, Experimental apparatus for the determination of condensation heat transfer coefficient for R134a and R600a flowing inside vertical and horizontal tubes, Summer Heat Transfer Conference, ASME, July 19–23, USA, 2009.
[33] A.S. Dalkilic, S. Laohalertdecha, S. Wongwises, Experimental research on the similarity of annular flow models and correlations for the condensation of R134a at high mass flux inside vertical and horizontal tubes, International Mechanical Engineering Congress and Exposition, ASME, November 13–19, USA, 2009.
[34] A.S. Dalkilic, S. Wongwises, A heat transfer model for co-current downward laminar film condensation of R134a in a vertical micro-fin tube during annular flow regime, Eleventh UK National Heat Transfer Conference, September 6–8, Queen Mary University of London, 2009.
[35] A.S. Dalkilic, O. Agra, I. Teke, S. Wongwises, Comparison of frictional pressure drop models during annular flow condensation of R600a in a horizontal tube at low mass flux and of R134a in a vertical tube at high mass flux, International Journal of Heat and Mass Transfer, http://dx.doi.org/10.1016/j.ijheatmasstransfer.2009.12.051, 2010.
[36] A.S. Dalkilic, S. Wongwises, An investigation of a model of the flow pattern transition mechanism in relation to the identification of annular flow of R134a in a vertical tube using various void fraction models and flow regime maps, Experimental Thermal and Fluid Science, http://dx.doi.org/10.1016/j.expthermflusci.2009.12.011, 2010.
[37] S.L. Chen, F.M. Gerner, C.L. Tien, General film condensation correlations, Experimental Heat Transfer 1 (1987) 93–107.
[38] D. Barnea, O. Shoham, Y. Taitel, Flow pattern transition for vertical downward two phase flow, Chemical Engineering Science 37 (1982) 741–744.
[39] O. Baker, Design of pipe lines for simultaneous flow of oil and gas, Oil and Gas Journal 26 (1954) 185–195.
[40] J.R. Thome, Update on advances in flow pattern based two-phase heat transfer models, International Journal of Heat and Mass Transfer 29 (2005) 341–349.
[41] N. Kattan, J.R. Thome, D. Favrat, Flow boiling in horizontal tubes. Part 1: development of a diabatic two-phase flow pattern map, Journal of Heat Transfer 120 (1998) 140–147.
[42] P.G. Kosky, Thin liquid films under simultaneous shear and gravity forces, International Journal of Heat Mass Transfer 14 (1971) 1220–1224.
[43] R.W. Lockhart, R.C. Martinelli, Proposed correlation of data for isothermal two-phase, two-component flow in pipes, Chemical Engineering Progress 45 (1949) 39–45.
[44] N.Z. Azer, L.V. Abis, H.M. Soliman, Local heat transfer coefficients during annular flow condensation, ASHRAE Transactions 78 (1972) 135–143.
[45] J.M. Mandhane, G.A. Gregory, K. Aziz, Critical evaluation of friction pressure drop prediction methods for gas–liquid flow in horizontal pipes, Journal of Petroleum Technology 29 (1977) 1348–1358.
[46] S.J. Kline, F.A. McClintock, Describing uncertainties in single sample experiments, Mechanical Engineering 75 (1953) 3–8.
[47] P.G. Kosky, F.W. Staub, Local condensing heat transfer coefficients in the annular flow regime, AIChE Journal 17 (1971) 1037–1043.

International Communications in Heat and Mass Transfer 37 (2010) 822–826

Contents lists available at ScienceDirect

International Communications in Heat and Mass Transfer

journal homepage: www.elsevier.com/locate/ichmt

Investigation on the jet liquid impingement heat transfer for the central processing unit of personal computers ☆

Paisarn Naphon [a,*], Somchai Wongwises [b]

[a] Thermo-Fluids and Heat Transfer Enhancement Lab. (TFHT), Department of Mechanical Engineering, Faculty of Engineering, Srinakharinwirot University, 63 Rangsit-Nakhornnayok Rd., Ongkharak, Nakhorn-Nayok, 26120, Thailand

[b] Fluid Mechanics, Thermal Engineering and Multiphase Flow Research Lab. (FUTURE), Department of Mechanical Engineering, King Mongkut's University of Technology Thonburi, 91 Suksawas 48, Bangmod, Bangkok 10140, Thailand

ARTICLE INFO

Available online 10 June 2010

Keywords:
Jet impingement
Mini-rectangular fin heat sink
Central processing unit

ABSTRACT

In this paper, the jet liquid impingement heat transfer characteristics in the mini-rectangular fin heat sink for the central processing unit of a personal computer are experimentally investigated. The experiments are tested with three different channel width heat sinks under real operating conditions: no load and full load conditions. The jet liquid impingement cooling with mini-rectangular fin heat sink system is introduced as the active and passive heat transfer enhancement techniques. Effects of relevant parameters on the central processing unit temperature are considered. It is found that the central processing unit temperatures obtained from the jet liquid impingement cooling system are lower than those from the conventional liquid cooling system; however, the energy consumption also increases. The results of this study are of technological importance for the efficient design of cooling systems of personal computers or electronic devices to enhance cooling performance.

1. Introduction

In order to ensure reliable operation, the personal computer (PC) or electronic devices must be operated in specific temperature ranges. The exceeding maximum allowable temperature is a serious problem for these devices. Therefore, in order to keep the operated temperature constant, the cooling system must dissipate generated heat equal or higher than the generated heat of these devices. There are many techniques to dissipate the generated heat. The development of the miniaturized technology, mini and micro-components has been introduced as one of the techniques. The heat transfer and pressure drop in the mini and micro-channel have been widely studied by researchers. Guglielmini et al. [1] studied the pool boiling heat transfer of the finned copper surfaces immersed in a dielectric fluid. Zhao and Lu [2] analytically and numerically studied the effect of porosity on the thermal performance of the micro channel heat sink. Bhowmil [3] investigated on the convective heat transfer of electronic chips in a vertical rectangular channel. Zhang et al. [4] reported the study of a single-phase heat transfer of micro channel heat sink. Yu [5] studied on the thermal performance of a plate-pin fin heat sink and a plate fin heat sink. Peles et al. [6] investigated on the heat transfer and pressure drop over a bank of micro pin fins. Kosar and Peles [7,8] considered the single-phase and two-phase heat transfer, and pressure drop of R-123 over a bank of the micro pin fins. Yakut et al. [9] considered effects of the heights, widths of the hexagonal fins on thermal resistance and pressure drop characteristics. Mohamed [10] investigated on air-cooling characteristics of an electronic device with various square modules array heat sinks. Didarul [11] investigated on the heat transfer and fluid flow characteristics of finned surfaces. Chein and Chuang [12] studied on the micro channel heat sink performance with and without thermoelectric using nanofluids as coolants. Jeng and Tzeng [13] determined the pressure drop and heat transfer of a square pin-fin array. Lie et al. [14] investigated the flow boiling heat transfer of FC-72 on a heated micro-pin-finned silicon chip. Naphon et al. [15,16] numerically and experimentally studied on the heat transfer and flow characteristics in the mini-fin heat sink for CPU with and without thermoelectric. There is reasonable agreement from the comparison between the measured data and the predicted results.

The numerous papers presented the jet impingement heat transfer enhancement. Kobus and Oshio [17] studied on the thermal performance of a pin-fin heat sink with various geometrical. Li et al. [18] determined the thermal performance of heat sinks with confined impingement cooling. The effects of the impinging Reynolds number, the width and the height of the fins, the distance between the nozzle and the tip of the fins on the thermal resistance were investigated. Geedipalli et al. [19] simulated the combination heating of food using microwave and jet impingement by coupling Maxwell's equations. Sung and Mudawar [20,21] studied on the jet impingement single-phase and two-phase heat transfer characteristics. Reasonable

☆ Communicated by W.J. Minkowycz.

* Corresponding author.
E-mail address: paisarnn@swu.ac.th (P. Naphon).

0735-1933/$ – see front matter © 2010 Elsevier Ltd. All rights reserved.
doi:10.1016/j.icheatmasstransfer.2010.05.004

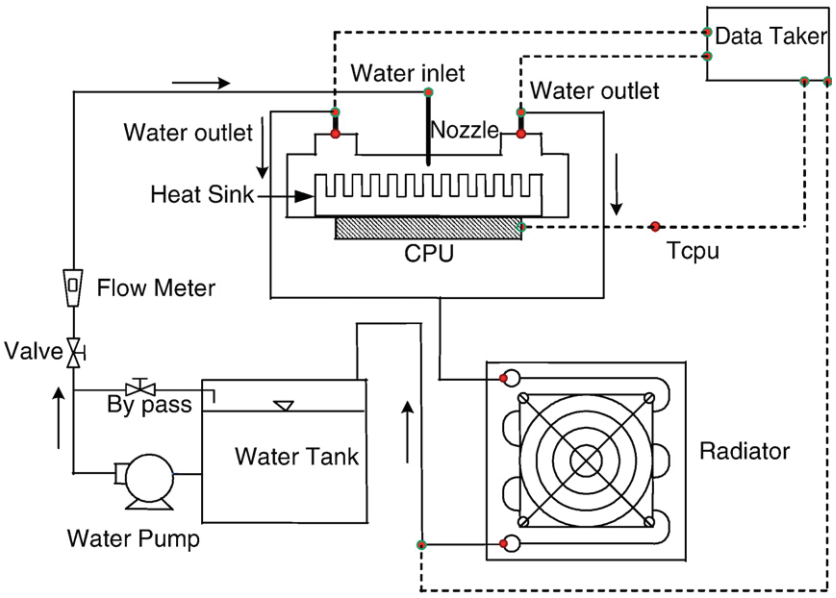

Fig. 1. Schematic diagram of experimental apparatus.

agreement was obtained between the predicted results and the measured data. Koseoglu and Baskaya [22] applied Laser Doppler Anemometry to observe the jet flow field and turbulence on heat transfer characteristics. Katti and Prabhu [23] carried out to study the jet heat transfer enhancement from a flat surface. Kanna and Das [24] simulated the heat transfer from the flat plate by a two-dimensional laminar incompressible offset jet. Goodro et al. [25] considered effects of the hole spacing on the spatially-resolved jet array impingement heat transfer. Cirillo and Isopi [26] experimentally and numerically studied air jet heat transfer characteristics on a flat plate. Effects of jet diameter, air velocity, jet-to-jet spacing, jet-to-plate distance and nozzle height were considered. Jeng et al. [27] experimentally investigated on the jet air flow and heat transfer behaviors of a rotating heat sink. Wong and Saeid [28,29] applied the Brinkman-extended Darcy model to simulate the mixed convection on jet impingement cooling in a horizontal porous layer. Hewakandamby [30] numerically studied on the enhanced heat transfer of oscillatory impinging jets. Nguyen et al. [31] performed to study the enhanced heat transfer of nanofluid in a confined and submerged impinging jet on a flat, horizontal and circular heated surface. Koseoglu and Baskaya [32] experimentally and numerically investigated on the impinging jet heat transfer. Chang et al. [33] studied the jet-array impingement heat transfer in a concentric annular channel with rotating inner cylinder. Sharif and Banerjee [34] applied the k–ε turbulence model to analyze the heat transfer of the confined slot-jet impingement on a moving plate. Whelan and Robinson [35] used the jet liquid impingement for cooling the electronic devices.

As mentioned above, the numerous papers presented the study on heat transfer and pressure drop in the mini-and micro-channel or jet impingement heat transfer on the flat plate. Almost all the works reported on the study of jet air impingement heat transfer. However, heat transfer capability is limited by the working fluid transport properties. At present there is limited data available for jet liquid impingement heat transfer especially for the central processing unit (CPU) of personal computers (PC). Furthermore, the paper focuses on the experimental study on the jet liquid impingement heat transfer characteristics of the mini-rectangular fin heat sink of a CPU based on the real operating conditions of a PC. Effects of channel width, nozzle diameter, and coolant flow rate on the CPU temperature are considered. The results obtained from the jet liquid impingement cooling system are compared with those from the conventional liquid cooling system.

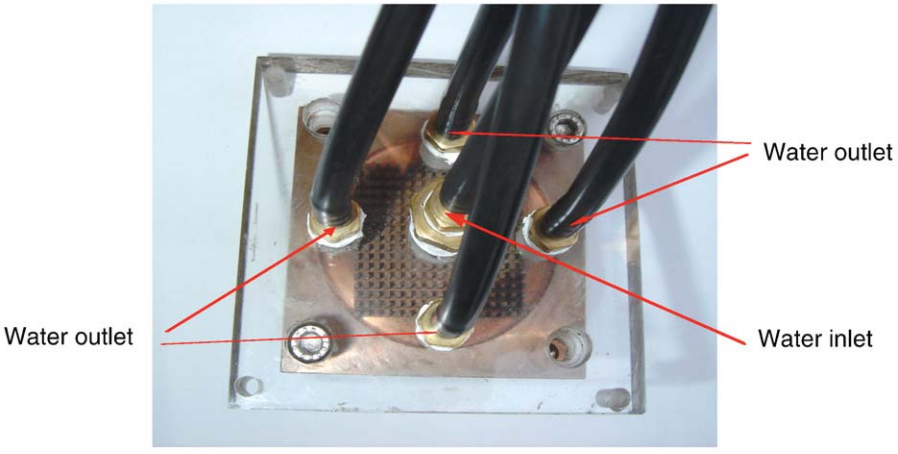

Fig. 2. Photograph of the mini-rectangular fin heat sink unit for cooling the CPU of the PC.

Table 1
Accuracy and uncertainty of measurements.

Instruments	Accuracy	Uncertainty
Voltage supplied by power source (volt)	0.2%	±0.5
Current supplied by power source (ampere)	0.2%	±0.5
Water flow meter	0.2%	±0.5
Thermocouple type T, data logger, (°C)	0.1%	±0.1

2. Experimental apparatus and method

A schematic diagram of the experimental apparatus is shown in Fig. 1. The test loop consists of a set of PC, cooling de-ionized water loop and data acquisition system. The close-loop of de-ionized water consists of a 10^{-3} m^3 storage tank, water pump, flow meter, and radiator. The de-ionized water in the radiator is chilled by the atmospheric air. After the temperatures of the water are cooled to achieve the desired level, the cooling water is pumped out of the storage tank, passed through a flow meter and the CPU, and returned to the storage tank. Three nozzles with diameters of 1.00, 1.40, and 1.80 mm are tested. The flow rates of the cooling water are controlled by adjusting the valve and measured by the flow meter with an accuracy of ±0.2% of full scale. The test sections are fabricated from the blocks of copper by a wire electrical discharge machine (WEDM) with channel widths of 0.50, 1.00, and 1.25 mm. The inlet and outlet plenums are shown in Fig. 2. In Fig.1, the type T copper-constantan thermocouples with an accuracy of 0.1% of full scale are employed to measure the temperatures at various positions. The CPU temperatures are measured by two type-T copper-constantan thermocouples. All thermocouples are pre-calibrated with a dry box temperature calibrator.

The de-ionized water was pumped into the mini-rectangular fin heat sink which was installed on the CPU of the PC in the normal direction. The inlet temperature of coolant water before entering the cooling section was kept nearly constant at 28–30 °C. Experiments were conducted with various cooling water flow rates, channel width of heat sink, and operating condition of PC. The supplied load into the CPU was adjusted to achieve the desired level by setting the operating conditions of the PC. The operating conditions of the computer can be controlled by setting the software of computer system. The energy consumption of the PC was measured by the watt–hour meter. The temperatures at each position and energy consumption were recorded in the period time of 200 min. Data collection was carried out using a data acquisition system (DataTaker). The uncertainty and accuracy of the measurement are given in Table 1.

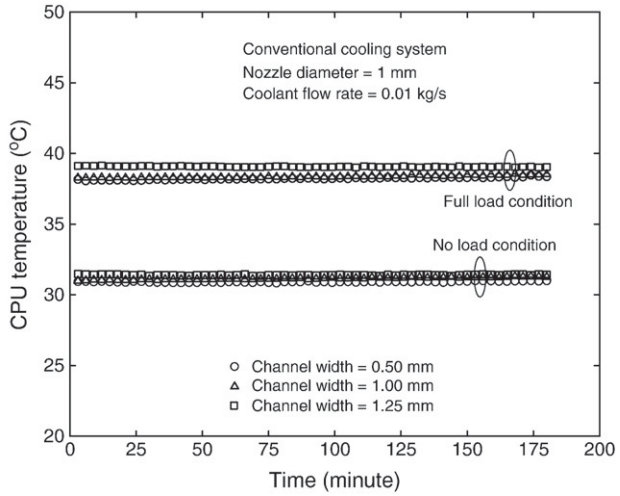

Fig. 3. Effects of channel width of heat sink on CPU temperature of the conventional cooling system for no load and full load conditions.

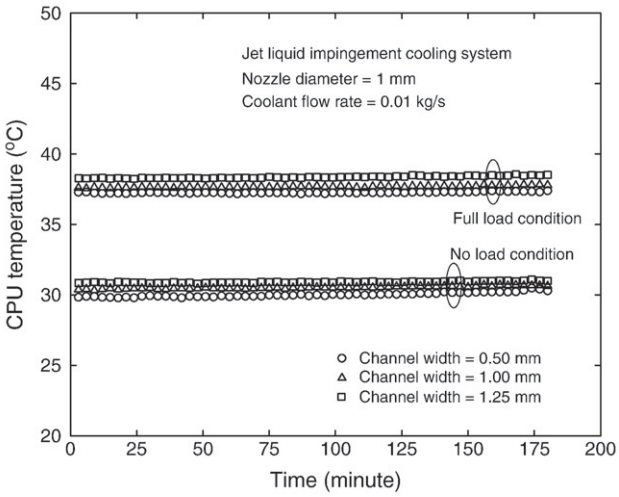

Fig. 4. Effects of channel width of heat sink on CPU temperature of the jet liquid impingement cooling system for no load and full load conditions.

3. Results and discussion

The supplied load into the CPU was adjusted by setting the operating condition of the PC: full load and no load conditions. The relevant parameters are measured in the period time of 200 min. In general, based on the real operating conditions of a PC, it is difficult to know the generated heat of the CPU. In the present experiment, average CPU temperature is measured with type-T copper-constantan thermocouples in the period time of 200 min. Figs. 3–4 show the effect of the channel width of the heat sink on the CPU temperatures for the conventional liquid cooling system and for the jet liquid impingement cooling system, respectively. Due to higher surface area, the heat transfer rate from the CPU to the heat sink increases. Therefore, the CPU temperatures obtained from the heat sink with the channel width of 0.5 mm are lower than those from the higher ones. As expected, the CPU temperatures from the full load condition are higher than those from the no load condition for the whole range of the period time. At the same condition, the CPU temperatures obtained from the jet liquid impingement cooling system are lower than those from the conventional liquid cooling system. From Fig. 2, it can be seen that fluid flows in and flows out the heat sink in the normal direction. At the inlet plenum, it looks like a jet impinging on the bottom of the

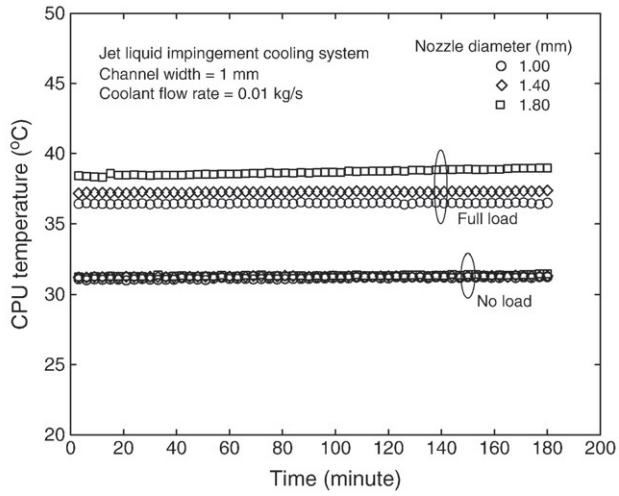

Fig. 5. Effects of nozzle diameter on the CPU temperature for no load and full load conditions.

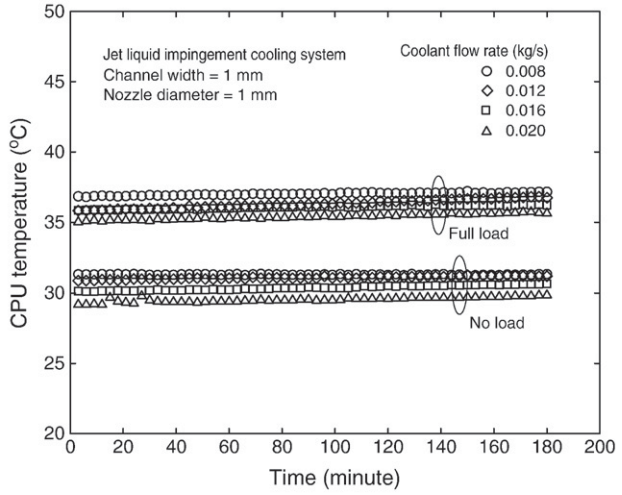

Fig. 6. Effects of coolant flow rate on the CPU temperature for no load and full load conditions.

heat sink. The recirculation zones appear in the inlet and outlet plenums.

In addition, a larger velocity in the heat sink results in higher heat transfer coefficient. Therefore, the jet liquid impingement cooling system gives CPU temperatures lower than the conventional liquid cooling system. Fig. 5 shows the variation of the CPU temperature from the jet liquid impingement cooling system for different nozzle diameters. Due to higher velocity, the heat transfer rate increases with decreasing nozzle diameter. Therefore, the lower nozzle diameter gives CPU temperatures lower than the higher ones. Effects of coolant flow rate on the CPU temperatures for different load conditions are shown in Fig. 6. For the four different coolant flow rates, a larger CPU temperature drop is found for a larger coolant flow rate. The reason for this is because a larger coolant flow rate results in lower capacity resistance and consequently lower heat sink thermal resistance ($R = \Delta T/Q$) as shown in Fig. 7.

The CPU temperature and the energy consumption obtained from the jet liquid impingement cooling system are compared with those from the conventional liquid cooling system. As seen in Table 2, the plus symbol represented the higher values while the minus symbol represented the lower values as compared with those from the

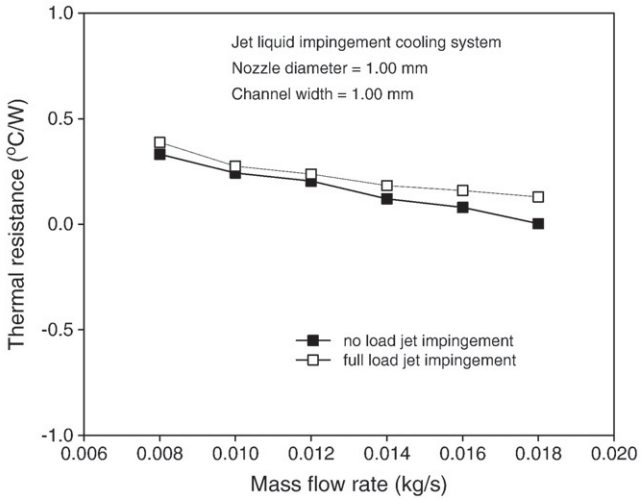

Fig. 7. Variation of thermal resistance with coolant mass flow rate.

Table 2
Comparison of the energy consumption between jet liquid impingement cooling system with conventional liquid cooling system.

Cooling techniques	CPU temperature		Energy consumption	
	No load	Full load	No load	Full load
Jet liquid impingement heat transfer system with the channel width of 0.5 mm	−2.90%	−2.36%	+9.30%	+16.67%
Jet liquid impingement heat transfer system with the channel width of 1.00 mm	−2.04%	−2.26%	+9.30%	+16.67%
Jet liquid impingement heat transfer system with the channel width of 1.25 mm	−1.57%	−3.59%	+9.30%	+16.67%

conventional liquid cooling system. It can be seen that the CPU temperatures obtained from the jet liquid impingement cooling system are lower than those from the conventional liquid system and with the same explanation as mentioned above. However, the energy consumption also increases.

4. Conclusions

Due to high levels of heat generation, space limitation for the set up of the cooling system, and air cooling limitation, the jet liquid impingement cooling in the mini-rectangular fin channel heat sink for CPUs of PCs has been investigated. The jet liquid impingement cooling with mini-rectangular fin heat sink system is introduced as the couple active and passive heat transfer enhancement techniques. The effect of channel width of heat sink, coolant flow rate and operating condition of the PC on the CPU temperature are considered. It is found that the CPU temperatures obtained from the jet liquid impingement cooling system are lower than those from the conventional liquid system. However, this technique requires higher energy consumption. The results of this study are expected to lead to guidelines that will allow the design of a cooling system with improved thermal cooling performance for ensuring that these devices are in the specific temperature ranges.

Acknowledgements

The authors would like to express their appreciation to the Thailand Research Fund (TRF) and Srinakharinwirot University (SWU) for providing financial support for this study.

References

[1] G. Guglielmini, M. Misale, C. Schenone, Boiling of saturated FC-72 on square pin fin arrays, International Journal of Thermal Sciences 41 (2002) 599–608.
[2] C.Y. Zhao, T.J. Lu, Analysis of microchannel heat sink for electronics cooling, International Journal of Heat and Mass Transfer 45 (2002) 4857–4869.
[3] H. Bhowmil, Convection heat transfer from discrete heat sourced in a liquid cooled rectangular channel, Applied Thermal Engineering 25 (2005) 2532–2542.
[4] H.Y. Zhang, D. Pingala, T.N. Wong, K.C. Toh, Y.K. Joshi, Single-phase liquid cooled micro channel heat sink for electronic packages, Applied Thermal Engineering 25 (2005) 1472–1487.
[5] X. Yu, Development of a plate-pin fin heat sink and its performance comparisons with a plate fin heat sink, Applied Thermal Engineering 25 (2005) 173–182.
[6] Y. Peles, A. Kosor, C. Mishra, C.J. Kuo, B. Schneider, Forced convective heat transfer across a pin fin micro heat sink, International Journal of Heat and Mass Transfer 48 (2005) 3615–3627.
[7] A. Kosar, Y. Peles, Convective flow of refrigerant (R123) across a bank of micro pin fins, International Journal of Heat and Mass Transfer 49 (2006) 3142–3155.
[8] A. Kosar, Y. Peles, Boiling heat transfer in a hydrofoil-based micro pin fin heat sink, International Journal of Heat and Mass Transfer 50 (2007) 1018–1034.
[9] K. Yukut, Experimental investigation of thermal resistance of a heat sink with hexagonal fins, Applied Thermal Engineering 26 (2006) 2262–2271.
[10] M.M. Mohamed, Air cooling characteristics of a uniform square modules array for electronic device heat sink, Applied Thermal Engineering 26 (2006) 486–493.

[11] I.M. Didarul, Study on heat transfer and fluid flow characteristics with short rectangular plate fin of different pattern, Experimental Thermal and Fluid Science 31 (2007) 367–379.
[12] R. Chein, J. Chuang, Experimental microchannel heat sink performance studies using nanofluids, International Journal of Thermal Sciences 46 (2007) 57–66.
[13] T.M. Jeng, S.C. Tzeng, Pressure drop and heat transfer of square pin-fin arrays in in-line and staggered arrangements, International Journal of Heat and Mass Transfer 50 (2007) 2364–2375.
[14] Y.M. Lie, Saturated flow boiling heat transfer and associated bubble characteristics of FC-72 on a heated micro-pin-fined silicon chip, International Journal of Heat and Mass Transfer 50 (2007) 3862–3876.
[15] P. Naphon, S. Wiriyasart, Liquid cooling in the mini-rectangular fin heat sink with and without thermoelectric for CPU, International Communications in Heat and Mass Transfer 36 (2009) 166–171.
[16] P. Naphon, S. Klangchart, S. Wongwises, Numerical investigation on the heat transfer and flow in the mini-fin heat sink for CPU, International Communications in Heat and Mass Transfer 36 (2009) 834–840.
[17] C.J. Kobus, T. Oshio, Development of a theoretical model for predicting the thermal performance characteristics of a vertical pin-fin array heat sink under combined forced and natural convection with impinging flow, International Journal of Heat and Mass Transfer 48 (2005) 1053–1063.
[18] H.Y. Li, S.M. Chao, G.L. Tsai, Thermal performance measurement of Heat sinks with confined impinging jet by infrared thermography, International Journal of Heat and Mass Transfer 48 (2005) 5386–5394.
[19] S. Geedipalli, A.K. Datta, V. Rakesh, Heat transfer in a combination microwave–jet impingement oven, Food and Bioproducts Processing 86 (2008) 53–63.
[20] M.K. Sung, I. Mudawar, Single-phase and two-phase heat transfer characteristics of low temperature hybrid micro-channel/micro-jet impingement cooling module, International Journal of Heat and Mass Transfer 51 (2008) 3882–3895.
[21] M.K. Sung, I. Mudawar, Single-phase hybrid micro-channel/micro-jet impingement cooling, International Journal of Heat and Mass Transfer 51 (2008) 4342–4352.
[22] M.F. Koseoglu, S. Baskaya, The effect of flow field and turbulence on heat transfer characteristics of confined circular and elliptic impinging jets, International Journal of Thermal Sciences 47 (2008) 1332–1346.
[23] V. Katti, S.V. Prabhu, Heat transfer enhancement on a flat surface with axisymmetric detached ribs by normal impingement of circular air jet, International Journal of Heat and Fluid Flow 29 (2008) 1279–1294.
[24] P.R. Kanna, M.K. Das, Heat transfer study of two-dimensional laminar incompressible offset jet flows, International Journal of Thermal Sciences 47 (2008) 1620–1629.
[25] M. Goodro, J. Park, P. Ligrani, M. Fox, H.K. Moon, Effects of hole spacing on spatially-resolved jet array impingement heat transfer, International Journal of Heat and Mass Transfer 51 (2008) 6243–6253.
[26] F. Cirillo, G.M. Isopi, Glass tempering heat transfer coefficient evaluation and air jets parameter optimization, Applied Thermal Engineering 29 (2009) 1173–1179.
[27] T.M. Jeng, S.C. Tzeng, H.R. Liao, Flow visualizations and heat transfer measurements for a rotating pin-fin heat sink with a circular impinging jet, International Journal of Heat and Mass Transfer 52 (2009) 2119–2131.
[28] K.C. Wong, N.H. Saeid, Numerical study of mixed convection on jet impingement cooling in a horizontal porous layer-using Brinkman-extended Darcy model, International Journal of Thermal Sciences 48 (2009) 96–104.
[29] K.C. Wong, N.H. Saeid, Numerical study of non-Darcian effects on jet impingement cooling in a horizontal porous layer in the mixed convection regime, International Communications in Heat and Mass Transfer 36 (2009) 45–50.
[30] B.N. Hewakandamby, A numerical study of heat transfer performance of oscillatory impinging jets, International Journal of Heat and Mass Transfer 52 (2009) 396–406.
[31] C.T. Nguyen, N. Galanis, G. Polidori, S. Fohanno, C.V. Popa, A.L. Bechec, An experimental study of a confined and submerged impinging jet heat transfer using Al2O3-water nanofluids, International Journal of Thermal Sciences 48 (2009) 401–411.
[32] M.F. Koseoglu, S. Baskaya, Experimental and numerical investigation of natural convection effects on confined impinging jet heat transfer, International Journal of Heat and Mass Transfer 52 (2009) 1326–1336.
[33] S.W. Chang, T.L. Yang, D.W. Shih, Jet-array impingement heat transfer in a concentric annular channel with rotating inner cylinder, International Journal of Heat and Mass Transfer 52 (2009) 1254–1267.
[34] M.A.R. Sharif, A. Banerjee, Numerical analysis of heat transfer due to confined slot-jet impingement on a moving plate, Applied Thermal Engineering 29 (2009) 532–540.
[35] B.P. Whelan, A.J. Robinson, Nozzle geometry effects in liquid jet array impingement, Applied Thermal Engineering 29 (2009) 2211–2221.

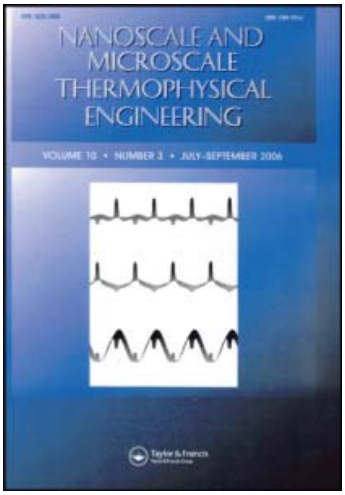

Nanoscale and Microscale Thermophysical Engineering
Publication details, including instructions for authors and subscription information:
http://www.informaworld.com/smpp/title~content=t713774103

Measurement of Thermo Physical Properties of Metallic Nanofluids for High Temperature Applications

Lazarus Godson[a]; D. Mohan Lal[a]; Somchai Wongwises[b]
[a] R&AC Division, Department of Mechanical Engineering, College of Engineering, Guindy, Anna University, Chennai, India [b] Fluid Mechanics, Thermal Engineering and Multiphase Flow Research Lab (FUTURE), Department of Mechanical Engineering, King Mongkut's University of Technology Thonburi, Bangmod, Bangkok, Thailand

Online publication date: 25 August 2010

To cite this Article Godson, Lazarus , Lal, D. Mohan and Wongwises, Somchai(2010) 'Measurement of Thermo Physical Properties of Metallic Nanofluids for High Temperature Applications', Nanoscale and Microscale Thermophysical Engineering, 14: 3, 152 — 173
To link to this Article: DOI: 10.1080/15567265.2010.500319
URL: http://dx.doi.org/10.1080/15567265.2010.500319

Nanoscale and Microscale Thermophysical Engineering, 14: 152–173, 2010

ISSN: 1556-7265 print / 1556-7273 online
DOI: 10.1080/15567265.2010.500319

Taylor & Francis
Taylor & Francis Group

MEASUREMENT OF THERMO PHYSICAL PROPERTIES OF METALLIC NANOFLUIDS FOR HIGH TEMPERATURE APPLICATIONS

Lazarus Godson[1], D. Mohan Lal[1], and Somchai Wongwises[2]
[1]*R&AC Division, Department of Mechanical Engineering, College of Engineering, Guindy, Anna University, Chennai, India*
[2]*Fluid Mechanics, Thermal Engineering and Multiphase Flow Research Lab (FUTURE), Department of Mechanical Engineering, King Mongkut's University of Technology Thonburi, Bangmod, Bangkok, Thailand*

This article presents the measurement of thermal conductivity and viscosity of nanofluids experimentally. Silver nanoparticles dispersed in water with volume concentrations of 0.3, 0.4, 0.6, 0.8, 0.9, and 1.2 vol% are used in the present study. A transient hot-wire apparatus is used for measuring the thermal conductivity of nanofluids and a Cannon-Fenske viscometer is used to measure the kinematic viscosity of nanofluids. The data are collected for temperatures ranging from 50 to 90°C. The results have shown an increase in the measured thermal conductivity and viscosity of nanofluids as the particle concentrations increase, and the values are higher than the values of the base liquids. The minimum enhancement of 27% for 0.3 vol% and a maximum enhancement of 115% for 1.2 vol% are observed at an average temperature of 70°C when compared with pure water for the same temperature. Further, the thermal conductivity of nanofluids increases with the increase in nanofluid temperatures and, conversely, the viscosity of nanofluids decreases with the increase in temperature of nanofluids. An experimental correlation is developed based on the experimental data for thermal conductivity and viscosity that relates the particle volume concentration and nanofluid temperature.

KEY WORDS: thermal conductivity, viscosity, silver, nanofluid, temperature, nanoparticle enhancement

INTRODUCTION

Conventional heat transfer fluids such as water, mineral oil, and ethylene glycol play a vital role in many industrial applications, including power generation, chemical processes, heating or cooling processes, and microelectronic devices. The operational speed of these devices depends on the cooling rate. Low heat transfer performance of these conventional fluids affects the enhancement of performance and in turn the compactness of heat exchangers. Therefore, further enhancement in heat transfer is always in demand. Energy-efficient fluids with greater potential to improve flow and

Manuscript received 2 July 2009.
The third author would like to thank the Thailand Research Fund and the Office of Higher Education Commission for their support.
Address correspondence to Lazarus Godson, R&AC Division, Department of Mechanical Engineering, College of Engineering, Anna University, Chennai, Tamil Nadu, 600 025, India. E-mail: godasir@yahoo.co.in

NOMENCLATURE

A	surface area, m^2
g	acceleration of gravity, m s^{-2}
h	free surface elevation difference, m
k	thermal conductivity, W/mK
l	length of the capillary section, m
n	empirical shape factor
q	heat flux, W/m
r	radial distance, m
T	final temperature, °C
T_0	initial temperature, °C
t	time, s

Greek Symbols

γ	particle size, nm
μ	dynamic viscosity, mPa.s
ν	kinematic viscosity, m^2/s
ρ	density, kg/m^3
φ	volume fraction

Subscripts

nf	nanofluid
p	particle
w	water

thermal characteristics are the option to enhance heat transfer rate. In the development of any energy-efficient heat transfer fluids for enhanced heat transfer performance, in practical applications, a detailed study on the thermophysical properties such as thermal conductivity and viscosity is necessary. Improving the thermophysical properties is the key idea to improve the heat transfer characteristics of the conventional fluids.

The use of nanosize solid particles as an additive suspended in the base fluid (nanofluids) is a technique for the heat transfer enhancement [1]. Besides the enhancement it is found that the nanofluids eliminate most of the problems arising with microsize slurries, like sedimentation, clogging of small channels, erosion, excessive pressure drop, etc. Thus, nanofluids have greater potential for heat transfer enhancement and are highly suited to application in practical heat transfer processes. Nanofluid thermophysical properties such as thermal conductivity and dynamic viscosity are of significant importance in every heat transfer application involving a fluid system. The heat transfer resistance of a flowing fluid is often represented by a Nusselt number, which takes into account the fluid thermal conductivity sometimes directly and usually indirectly as well through the Prandtl number. Thus, the first assessment of the heat transfer potential of a nanofluid is to consider its thermal conductivity.

The thermal conductivity of nanofluids is more temperature sensitive than that of the base fluid. Consequently, the thermal conductivity enhancement of nanofluids is temperature sensitive. Recently, many researchers have investigated the enhancement of thermal conductivity and observed that the thermal conductivity of the suspension of nanoparticles has increased more than 20% even with the low nanoparticle concentrations [2, 3]. Maxwell's theoretical model showed that the effective thermal conductivity of suspensions containing spherical particles increases with particle volume concentration [4]. Hamilton and Crosser's and the modified Maxwell model showed the effect of particle shape and particle volume concentration on thermal conductivity of fluid containing solid particles [5]. Recent research has focused on both the effect of particle size on the heat transport mechanism and the effect of a solid–-liquid interface and temperature effect on thermal conductivity enhancement. Lee et al. [6] investigated the effective thermal conductivity and viscosities of Al_2O_3 nanoparticles with volume fraction of 0.01–0.3 vol% dispersed in water. The transient hot-wire technique was used to measure the thermal conductivity and an oscillation viscometer was used to measure the viscosity of nanofluids. All data were collected for temperatures ranging between 20 and 40°C. The results showed that the thermal

conductivity of nanofluids increases nearly linearly with the particle volume fraction. The viscosity of nanofluids significantly decreases with increasing temperature. Moreover, the authors found that the measured viscosities of nanofluids exhibited a nonlinear relation with the particle concentration and increase with increase in particle concentrations. Das et al. [7] investigated the thermal conductivity of Al_2O_3 and CuO nanoparticles suspended in water as a function of temperature. The temperature oscillation technique was used for measuring the thermal conductivity of nanofluids at different temperatures ranging from 21 to 51°C. The results showed that the thermal conductivity increased with increase in nanofluid temperature as well as particle concentrations. Thus, fluids containing suspended metal particles are found to manifest enhanced thermal conductivities compared to pure fluids [8]. Masuda et al. [9] dispersed oxide nanoparticles (γ-Al_2O_3 and TiO_2 with $\varphi = 4.3\%$) in liquid and showed the increase in the thermal conductivity to be 32 and 11%, respectively. Grimm [10] dispersed aluminum particles ($\gamma = 80$ nm to 1 μm) in a fluid and claimed a 100% increase in the thermal conductivity of the fluid for $\varphi = 0.5$–10 vol%.

Choi and Eastman [11] measured the thermal conductivity of multiwalled carbon nanotubes (MWCNTs) of diameter 25 nm and length 50 μm. The thermal conductivity was measured by a transient hot-wire method for 1 vol% nanotube loading. The results showed 159% enhancement in the thermal conductivity with 1 vol% fraction of MWCNT. The important feature of this enhancement was the increasing slope of the enhancement curve. Eastman et al. [3] showed that Cu-ethylene glycol (nanoparticles coated with thioglycolic acid) with $\varphi = 0.3\%$ gave a 40% increase in thermal conductivity. Recently, an investigation on thermal conductivity of magnetic nanoparticles (Fe_3O_4 coated with oleic acid) suspended in the base fluid (hexadecane) was conducted at the Indira Gandhi Centre for Atomic Research (IGCAR). The results showed 300% enhancement in the thermal conductivity of nanofluids containing magnetic nanoparticles [12]. Further, it was proved that the thermal properties are tunable for magnetically polarizable nanofluids that consist of a colloidal suspension of magnetite nanoparticles. These enhancements depend on factors such as particle shape, particle size, and volume fraction of particles and temperature and thermal properties of solid and liquid materials.

Viscosity is an important parameter for fluid flow. Determining the viscosity of the nanofluid is essential in establishing adequate pumping power as well as the convective heat transfer coefficient, because the Prandtl and Reynolds numbers (functions of viscosity) will be influenced by these. Until now, only a few studies have addressed the viscous properties of nanoparticle suspensions at different temperatures. Masuda et al. [9] were the first who measured viscosity of water-based nanofluids for temperatures varying from the ambient to 60°C, which was then followed by Pak and Cho [13], who presented some additional data for Al_2O_3–water nanofluid. Wang et al. [14] measured the viscosity using three different dispersion techniques for Al_2O_3–water and Al_2O_3–ethylene glycol mixtures at ambient temperature. Putra et al. [15] have provided some limited data showing the temperature effect on Al_2O_3–water nanofluid viscosity. Recently, Maré et al. [16] have obtained some new temperature-dependent viscosity data for Al_2O_3–water with relatively high particle concentrations. Lu and Fan [17], Kwak and Kim [18], Nguyen et al. [19], Namburu et al. [20], and Avsec and Oblak [21] have studied the viscosity of nanofluids with various metallic and oxide nanoparticles and found that the viscosity of nanofluids increases with particle loading and decreases with increase in temperature. Lee et al. [6] measured viscosity of

Al_2O_3–water nanofluids with low volume concentrations ranging from 0.01 to 0.3%. Results showed that the viscosity decreased with increasing temperature. Furthermore, the measured viscosities of the Al_2O_3–water nanofluids showed a nonlinear relation even in the low volume concentration, whereas the Einstein viscosity model clearly predicts a linear relation. Murshed et al. [22] measured the viscosity of nanofluids and found that the viscosity increased with the volumetric loading of nanoparticles. The results were compared with different models and experimental data. The results showed a substantial increase in the viscosity. Such enhancement of viscosity may diminish the potential benefits of nanofluids. Most recently, Duangthongsuk and Wongwises [23] experimentally investigated the thermal conductivity and dynamic viscosity of TiO_2 nanoparticles dispersed in water with volume concentration of 0.2–2 vol% for temperatures ranging from 15 to 35°C. Detailed information regarding measurement techniques of thermal conductivity, viscosity, and particle size are shown in Duangthongsuk and Wongwises [23], which belong to one of coauthors. The results showed that the measured viscosity and thermal conductivity of nanofluids increased as the particle concentrations increased and are higher than the values of the base liquids. Finally, new thermophysical correlations are proposed for predicting the thermal conductivity and viscosity of nanofluids [23].

Based on the above, it is clearly seen that the nanofluids show higher thermal conductivity and viscosity than the base fluids. However, the inconsistency has been the subject of many published literature works with respect to the thermal conductivity and viscosity of nanofluids. For example, some researchers have suggested that the existing theoretical models can be used to predict the thermal conductivity and viscosity of nanofluids, whereas many other researchers have indicated that these models fail to predict the thermophysical properties of nanofluids. Likewise, the enhancements of the thermophysical properties of nanofluids have been explained by a number of mechanisms and models but no agreement has been reached between the experimental and theoretical results. Also, the thermophysical properties of nanofluids depend on various factors such as particle size, particle shape, metallic or nonmetallic (oxide) material, pH value, etc. For example, nanoparticles with a cylindrical shape have higher thermal conductivity enhancement than spherical-shaped nanoparticles. Nanofluids with smaller nanoparticle size exhibit greater thermal conductivity [24]. Nanofluids with metallic nanoparticles give higher thermal conductivity than nanofluids with nonmetallic nanoparticles [22]. The lower pH value gives higher heat transport than the higher pH value [25]. Furthermore, the thermophysical properties of nanofluids are strongly dependent on temperature. Only a few articles [6, 7, 22, 26] have reported the effect of temperature on the thermal conductivity and viscosity of nanofluids and more experimental investigations are needed to address the effect of the temperature and particle volume concentrations on the thermophysical properties of nanofluids. Therefore, in the present work, the temperature-dependent properties such as the thermal conductivity and viscosity of silver nanoparticles suspended in water are measured. The experiments were carried out over temperatures ranging from 50 to 90°C with 0.3, 0.4, 0.6, 0.8, 0.9, and 1.2% volume concentrations. The thermal conductivity was measured by the transient hot-wire method and the viscosity was measured with a Cannon-Fenske viscometer (Shambhavi Impex, Mumbai, India). Further, the measured data of the thermal conductivity and viscosity of nanofluids are used for comparison with the predicted values of the existing classical models. Finally, new correlations for predicting the thermal conductivity and viscosity of silver–water nanofluids are proposed.

PREPARATION AND CHARACTERIZATION OF SILVER–WATER NANOFLUID

Some important conditions in the preparation of nanofluid are stable suspension ability to withstand any chemical change and low agglomeration of particles. Common methods used for the preparation of nanofluids are (1) addition of acid or base to change the pH value of the suspension; (2) addition of surfactants to disperse particles into fluid; and (3) the use of ultrasonic vibration. Addition of some other materials (surfactants) may have negative effects because of the structural change of solid–liquid interface. Therefore, the ultrasonic vibration method is used for the preparation of nanofluids and also to prevent the structural change of nanofluids in this experiment. The ultrasonic vibration is carried out for 5 h using an ultrasonic processor (Roop-Telsonic TEC-40 model [Roop Telsonic Ultrasonix Limited, USA]; power density 750 W, frequency 20 kHz). The silver nanoparticles were directly purchased from Sigma Aldrich, Bangalore, India (product number 576832, xilver nanopowder, $<$100 nm, 99.5% metals). The silver nanoparticles were mixed directly with deionized water under ultrasonic vibration without any additive or stabilizer. The nanofluid was not transparent and it was black in color. The long-term stability of nanoparticles in suspension is not important to measure the thermal conductivity of nanofluid by the transient hot-wire method because the thermal conductivity measurement is carried out within 10 s. Moreover, the nanofluid used in this experiment was not settled for one day. To validate this, a stability test was conducted by taking a small sample of nanofluid with the maximum concentration of 1.2% volume fraction and physically observing to see whether any settling occurred. Photos were taken 1 h after preparing the sample and after 24 h as shown in Figure 1. From the figure it is clearly seen that settling did not occur in 24 h. Hence, the nanofluid is assumed as a stable fluid in the experiment. The pH value of the nanofluid is also measured by using a pH meter (ELICO, LI120, Elico Limited, Hyderabad, India), which is capable of measuring pH values ranging from 2 to 14. The glass electrode that is connected to the pH meter is inserted into the liquid and the measured value is displayed in the indicator of the pH meter. The desired volume concentrations used in this study are 0.3, 0.4, 0.6, 0.8, 0.9,

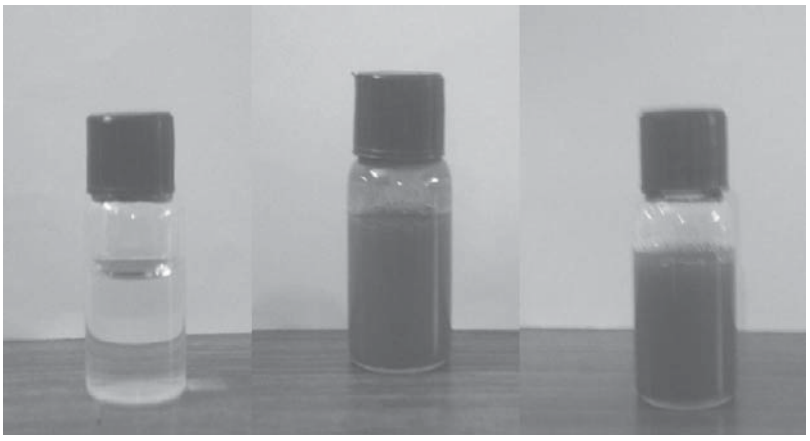

Figure 1 Stability test of silver–water nanofluids.

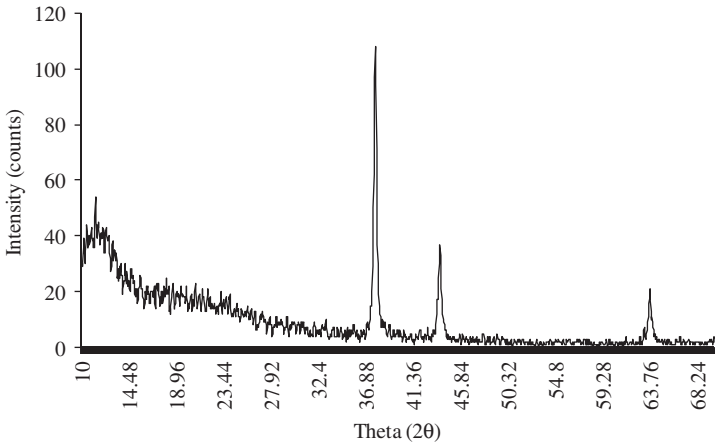

Figure 2 XRD patterns of silver nanoparticles.

and 1.2 vol% with pH values of 7.4, 7.3, 7.1, 6.9, 6.8, and 6.7, respectively. From the pH values, it can be seen that the solution chemistry of nanofluids is nearly neutral in nature. Powder X-ray diffraction (PXRD) as shown in Figure 2 is used in the present study for characterizing silver nanoparticles. As the name suggests, the sample is in powder form, consisting of fine grains in the form of single crystallites. The term *powder* really means that the crystalline domains are randomly oriented in the sample. In Figure 2, The XRD plot is between the intensity (counts) and 2θ, in degrees. The wavelength is 1.54 nm and the shape factor is 0.9. When a two-dimensional (2D) diffraction pattern is recorded, it shows concentric rings of scattering peaks corresponding to the various *d*-spacings in the crystalline lattice. The positions and the intensities of the peaks are used for identifying the underlying structure (or phase) of a solid material. From the Scherrer equation the average size of calculated silver nanoparticles was 63 nm, which is consistent with the identified value from the manufacturer.

THERMAL CONDUCTIVITY MEASUREMENT

Description of the Transient Hot-Wire Method/Apparatus

A transient hot-wire method is the most appropriate and widely used method to determine the thermal conductivity of liquids. This method eliminates the effects of natural convection, whose unwanted presence creates problems for measurements made with a steady-state apparatus. A constant current is supplied to the wire (platinum) to generate the essential temperature rise. The wire serves as both the heat source and the temperature sensor. The wire is surrounded by a liquid, whose thermal conductivity is to be measured. The heat dissipated in the wire increases the temperature of the wire and that of the liquid. The rise in temperature of the wire depends on the thermal conductivity of the liquid in which the wire is immersed.

Normally a platinum wire is chosen because of its capable resistance–temperature relationship over a wide temperature range. The resistance–temperature coefficient of platinum wire is 0.0039092°C. A 75-μm diameter is used in the present study.

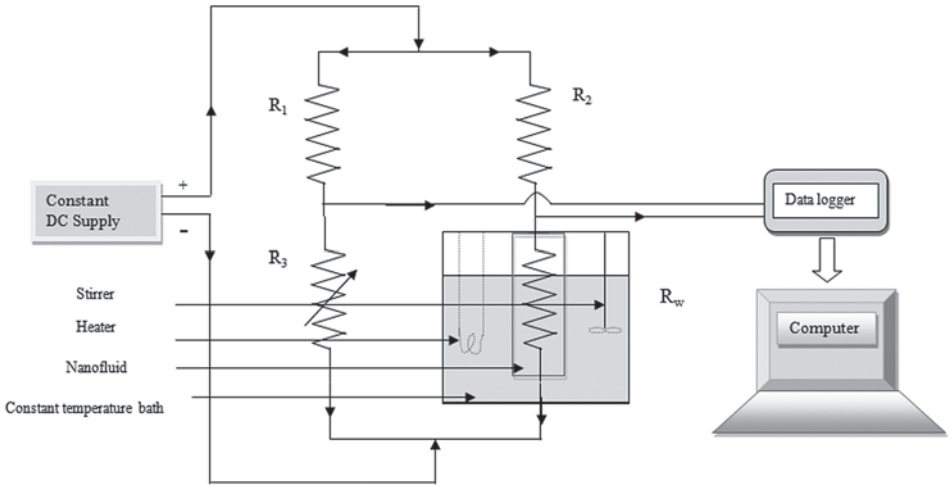

Figure 3 Transient hot-wire setup for measuring the thermal conductivity of nanofluids.

Because the nanofluids are electrically conductive, Teflon spray is used for easy and convenient coating of the platinum wire to act as an electric insulation. The Teflon-coated platinum wire was directly purchased and the 7.5-μm Teflon coating was given as per the specification from the manufacturer. A schematic diagram of the transient hot-wire apparatus is shown in Figure 3. The main experimental cell is actually a part of the Wheatstone bridge circuit because the wire (hot-wire) is used as one arm of the bridge circuit. In the bridge R_1 and R_2 are the fixed resistors having 1,000Ω and 16Ω resistance; R_3 is the variable resistor with maximum of 1,000Ω resistance connected to the Wheatstone bridge circuit; and R_w is the resistance of the wire that is to be measured. A 100-mL glass tube having a cylinder cavity of 2.9 cm in diameter and 23 cm length is used as the nanofluid container, which is filled with fluid whose thermal conductivity is to be measured. The Pplatinum wire is placed at the center of the nanofluid container and is placed inside the constant-temperature bath. The size of the bath is 17.5 cm diameter and 24.5 cm length. The constant-temperature bath consists of a heater, a stirrer, and temperature sensors to ensure that a constant temperature is maintained in the bath. Water is used as the heating fluid in the bath. The constant-temperature bath is also thermally insulated.

Principle of Transient Hot-Wire Method

Because the experiment lasts for just 5 s, the total quantity of heat going to the liquid per second is very small. Hence, the diameter of the container is sufficient to assume the liquid to be a thermally semi-infinite medium. An infinitely long and thin wire is used as a line source for dissipating heat into a semi-infinite medium, with constant heat generation. The working equation is based on a specific solution of Fourier's law [27].

Following is the general Fourier's equation for one-dimensional radial heat conduction:

$$\frac{1}{\alpha_f}\frac{\partial \Delta T}{\partial t} = \frac{1}{r}\frac{\partial}{\partial r}\left(r\frac{\partial \Delta T}{\partial r}\right) \tag{1}$$

with boundary conditions

$$\lim_{r\to 0}\left\{r\left(\frac{\partial T}{\partial r}\right)\right\} = -\frac{q}{2\pi k_f} \tag{2}$$

where $t = 0$ and $r = 0$.

$$\lim_{r\to\infty}\{\Delta T(r,t)\} = 0 \tag{3}$$

where $t \geq 0$ and $r = \infty$ and $\Delta T = T - T_0$.

If temperatures of the heat source at time t_1 and t_2 are T_1 and T_2, respectively, then the thermal conductivity of liquid may be given as

$$k = \frac{q}{4\pi(T_2 - T_1)}\ln\frac{t_2}{t_1} \tag{4}$$

Experimental Procedure

Initially, the experiment was conducted and the readings were recorded up to 10 s and the actual calculation was carried out for less than 5 s after reaching the required temperature in the bath in order to avoid natural convection of the wire and fluid. Measurements were taken at different temperatures ranging from 50 to 90°C. It took nearly 15 to 20 min to reach each temperature range chosen for the study. The nanofluid was heated to the desired temperature after sonication. After taking the reading for each concentration, the nanofluid was taken out and sonicated well before conducting the experiment for the next concentration. During the experimentation, we did not find any agglomeration for the nanofluid tested. However, some particles stuck to the glass tube.

Once the required temperature was reached in the constant-temperature bath, the power supply was switched ON. The Wheatstone bridge circuit was balanced (i.e., until the galvanometer showed zero deflection) by adjusting the variable resistor R_3. Then the DC supply was given to the bridge, which caused a change of voltage in the bridge through the platinum wire. As the current flowed through the circuit the resistance of the wire increased, which in turn produced an emf between the arms, thus causing an unbalanced condition in the circuit. This change in voltage over time was recorded by the data logger (Agilent Technologies Ltd.) at the sampling rate of 10 readings per second. The change in resistance of the wire was calculated from the Ohm's law using the measured voltage change over time. From the temperature–resistance relation of the platinum wire the temperature variation of the wire was calculated. The calculated temperature variation vs. natural logarithm of time was plotted and a sample plot

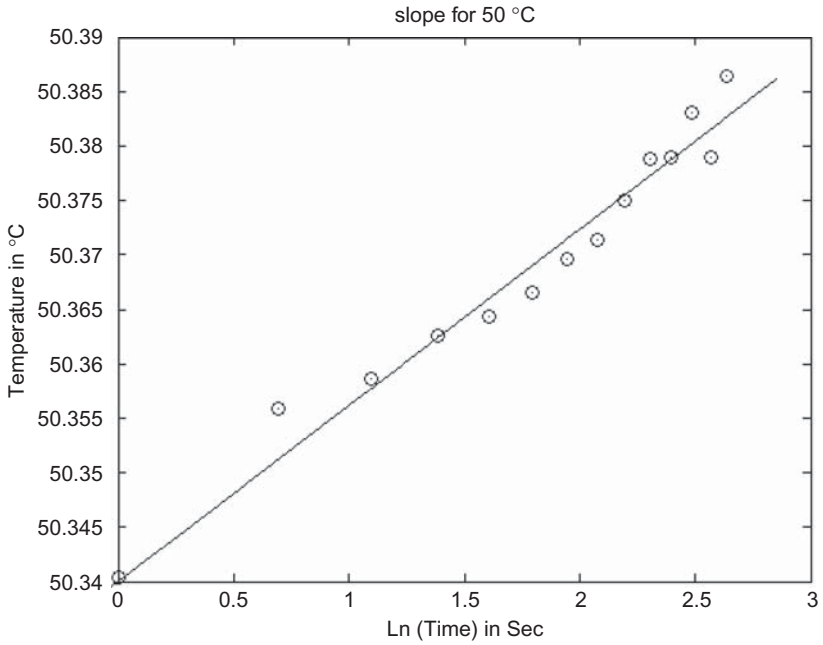

Figure 4 Plot of the temperature variation vs. natural logarithm of time.

of the same is shown in Figure 4. The thermal conductivity was then calculated from the slope of the linear fitted curve and the other known parameters. For every concentration of the nanofluid measurement the glass tube for measuring the thermal conductivity was cleaned and kept for some time to be dried. Then the measurements awere taken for different concentrations. The above procedure was repeated for different temperatures and different volume concentrations of silver water nanofluid.

Uncertainty Analysis

Various measured entities with their average values and uncertainties are as given below, including resistances:

$$\sigma_{\Delta R_W} = \pm\sqrt{\left(\frac{\partial \Delta R_W}{\partial V}\sigma_V\right)^2 + \left(\frac{\partial \Delta R_W}{\partial R_3}\sigma_{R_3}\right)^2 + \left(\frac{\partial \Delta R_W}{\partial R_W}\sigma_{Rw}\right)^2 + \left(\frac{\partial \Delta R_W}{\partial \Delta V}\sigma_{\Delta V}\right)^2} \quad (5)$$

$$\sigma_{\Delta R_W} = \pm 5.0227 \times 10 \times \mathrm{e}^{-4}\ \Omega$$

For example, the thermal conductivity of water at 70°C is calculated as $k = 0.6616$ W/mK, which is the average value from 50 to 90°C. The uncertainty in this value is calculated as

$$\sigma_k = \pm\sqrt{\left(\frac{\partial k}{\partial q}\sigma_q\right)^2 + \left(\frac{\partial k}{\partial slope}\sigma_{slope}\right)^2} = \pm 0.01013\,\mathrm{W/mK}. \tag{6}$$

$$\mathrm{k} = 0.6616 \pm 0.01013\ \mathrm{W/mK}$$

Thus, the uncertainty in the value of thermal conductivity of liquid measured by this equipment is less than 1.6% of its mean value. Then, the measured thermal conductivity of nanofluids is used for comparison with those obtained from the existing correlations, which are defined as follows.

Hamilton and Crosser [5] proposed a model for calculating the thermal conductivity of nanofluids for spherical and nonspherical (cylindrical) particles where $n = 3$ for spheres, $n = 6$ for cylinders, which is expressed in the following form:

$$\frac{k_{nf}}{k_w} = \frac{k_p + (n-1)k_w - (n-1)\varphi(k_w - k_p)}{k_p + (n-1)k_w + \varphi(k_w - k_p)} \tag{7}$$

Timofeeva et al. [28] suggested the effective medium theory to calculate thermal conductivity of nanofluids, which is expressed as follows:

$$k_{nf} = (1 + 3\varphi)k_w \tag{8}$$

Wasp [29] proposed a model for calculating the thermal conductivity of nanofluids, which is expressed as follows:

$$\frac{k_{nf}}{k_w} = \frac{k_p + 2k_w - 2\varphi(k_w - k_p)}{k_p + 2k_w + \varphi(k_w - k_p)} \tag{9}$$

VISCOSITY MEASUREMENT

Principle of Cannon-Fenske Viscometer

Various methods can be used for the experimental determination of viscosity. Concentric cylinders or cone and plate methods are very similar to the parallel plate visualization for measuring the shear viscosity.

The capillary viscometer follows Oswald flow where the kinematic viscosity is given by the formula

$$\nu = \frac{4\pi r^4 gh/8l}{dv/dt} \tag{10}$$

Each glass viscometer size has a coefficient of calibration. The coefficient is multiplied by the time taken for the fluid sample to pass between the different marks on the viscometer. This value determines the kinematic viscosity, which can be converted into the dynamic viscosity by multiplying the density of the fluid. An